MICROBIAL BIOENERGETICS

EDITED BY: Davide Zannoni, Fevzi Daldal, Wolfgang Nitschke and Catarina M. Paquete

PUBLISHED IN: Frontiers in Microbiology

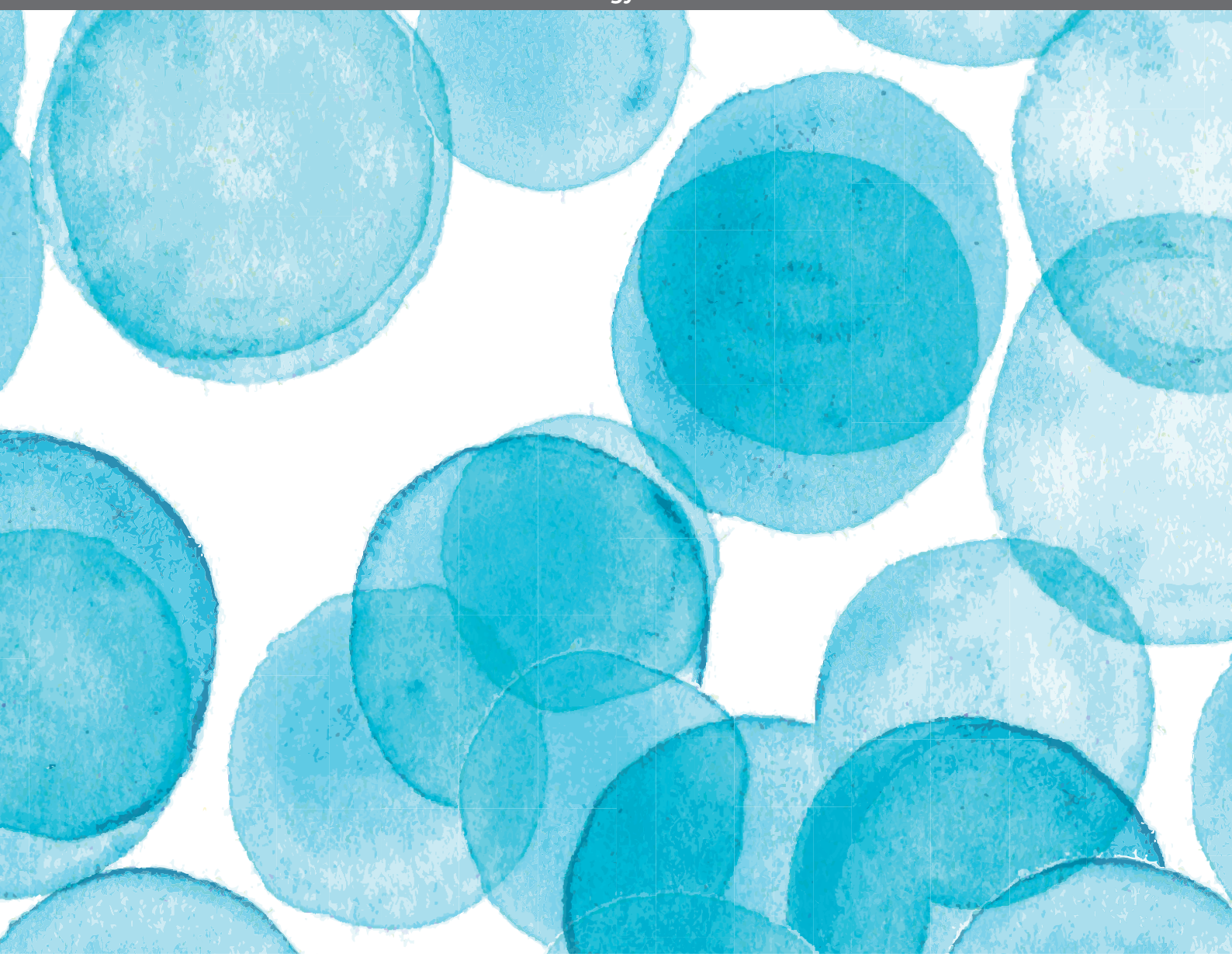

frontiers Research Topics

ISSN 1664-8714
ISBN 978-2-88974-042-0
DOI 10.3389/978-2-88974-042-0

About Frontiers

Frontiers is more than just an open-access publisher of scholarly articles: it is a pioneering approach to the world of academia, radically improving the way scholarly research is managed. The grand vision of Frontiers is a world where all people have an equal opportunity to seek, share and generate knowledge. Frontiers provides immediate and permanent online open access to all its publications, but this alone is not enough to realize our grand goals.

Frontiers Journal Series

The Frontiers Journal Series is a multi-tier and interdisciplinary set of open-access, online journals, promising a paradigm shift from the current review, selection and dissemination processes in academic publishing. All Frontiers journals are driven by researchers for researchers; therefore, they constitute a service to the scholarly community. At the same time, the Frontiers Journal Series operates on a revolutionary invention, the tiered publishing system, initially addressing specific communities of scholars, and gradually climbing up to broader public understanding, thus serving the interests of the lay society, too.

Dedication to Quality

Each Frontiers article is a landmark of the highest quality, thanks to genuinely collaborative interactions between authors and review editors, who include some of the world's best academicians. Research must be certified by peers before entering a stream of knowledge that may eventually reach the public - and shape society; therefore, Frontiers only applies the most rigorous and unbiased reviews.
Frontiers revolutionizes research publishing by freely delivering the most outstanding research, evaluated with no bias from both the academic and social point of view. By applying the most advanced information technologies, Frontiers is catapulting scholarly publishing into a new generation.

What are Frontiers Research Topics?

Frontiers Research Topics are very popular trademarks of the Frontiers Journals Series: they are collections of at least ten articles, all centered on a particular subject. With their unique mix of varied contributions from Original Research to Review Articles, Frontiers Research Topics unify the most influential researchers, the latest key findings and historical advances in a hot research area! Find out more on how to host your own Frontiers Research Topic or contribute to one as an author by contacting the Frontiers Editorial Office: frontiersin.org/about/contact

MICROBIAL BIOENERGETICS

Topic Editors:
Davide Zannoni, University of Bologna, Italy
Fevzi Daldal, University of Pennsylvania, United States
Wolfgang Nitschke, Centre National de la Recherche Scientifique (CNRS), France
Catarina M. Paquete, Universidade Nova de Lisboa, Portugal

Citation: Zannoni, D., Daldal, F., Nitschke, W., Paquete, C. M., eds. (2022). Microbial Bioenergetics. Lausanne: Frontiers Media SA. doi: 10.3389/978-2-88974-042-0

Table of Contents

frontiers in Microbiology

EDITORIAL
published: 22 November 2021
doi: 10.3389/fmicb.2021.793917

Editorial: Microbial Bioenergetics

Catarina M. Paquete[1]*, *Wolfgang Nitschke*[2], *Fevzi Daldal*[3] and *Davide Zannoni*[4]

[1] Instituto de Tecnologia Química e Biológica António Xavier, Universidade Nova de Lisboa, Oeiras, Portugal, [2] Aix Marseille Université, CNRS, BIP (UMR 7281), Marseille, France, [3] Department of Biology, University of Pennsylvania, Philadelphia, PA, United States, [4] Department of Pharmacy and Biotechnology, University of Bologna, Bologna, Italy

Keywords: bioenergetics, respiration, electron transfer, energy transduction systems, microorganism

Editorial on the Research Topic

Microbial Bioenergetics

In nature, microorganisms use different processes to harness energy from a variety of metabolic pathways, converting, or storing it into chemical or electrochemical forms. Some organisms are capable of acquiring energy from light through photosynthesis, whereas others break down the chemical bonds of organic compounds to release energy. The variety of environments in which microorganisms can thrive is enormous, ranging from extreme pH and ionic strengths, pressure, and temperature to conditions where oxygen is scarce or even absent. *Microbial bioenergetics* aims to understand how microorganisms efficiently coordinate their energy needs with their different cellular physiologies, including respiration, metabolism, storage, and other biological processes. The scope of this special issue on this Research Topic is to focus on recent advances of structural, functional, and molecular biological natures of energy transduction systems in microbes. It consists of 13 articles by several groups actively engaged on these topics, with 10 of them describing original research while the remaining are reviews and method description.

The review by Buckel covers energy conservation during fermentation in anaerobic bacteria focusing on electrochemical ion gradients for ATP synthesis. These processes can be catalyzed by ubiquitous H^+-or Na^+-dependent ATP-synthases, documenting that anaerobes can be more efficient than aerobes. In particular, comprehensive descriptions of the biotin-containing decarboxylases and NAD:ferredoxin oxidoreductases are provided in this review, and the mechanisms of the recently discovered electron bifurcation are examined in detail.

Respiration being a major process shaping the biology of many environments, Esposti et al. focuses on heme A containing cytochrome oxidases (COX), with the aim of elucidating the evolutionary origin of COX in bacteria. Toward this, the authors used extensive sequence and phylogenetic analyses to show that the ancestors of extant iron-oxidizers were the first species to evolve a COX, suggesting that the earliest geochemical evidence for bacterial respiration seems to originate from acidophilic iron-oxidizing prokaryotes.

Several organisms, including bacteria, archaea, and fungi perform efficient extracellular electron transfer processes. In their research article, Tanaka et al. described these processes for the photosynthetic cyanobacterium *Synechocystis* sp. PCC 6803. The authors investigate the capabilities of this species in reducing iron hydroxides and generating (photo)electricity under a variety of physiological conditions. Their study reveals that photosynthetic microorganisms can perform, in glucose-enriched environments, ferrihydrite reduction by extracellular electron transfer processes. Bertling et al. studied the aerobic respiration carried out by the facultative anaerobe *Shewanella oneidensis* MR-1, showing that in this species the aa_3-type cytochrome *c* oxidase, which is the primary oxygen reductase in aerobiosis in many bacteria, does not appear to contribute to aerobic growth in *Shewanella*. Instead, this activity and its contribution to aerobic growth is dependent on the energy and carbon source that the bacterium uses. In addition, the authors also examine the role of cAMP-receptor protein CRP and phosphodiesterase CpdA in regulating respiration

OPEN ACCESS

Edited by:
Nicole Buan,
University of Nebraska-Lincoln,
United States

Reviewed by:
Ricardo Jasso-Chávez,
Instituto Nacional de Cardiologia Ignacio Chavez, Mexico
Oscar Juarez,
Illinois Institute of Technology,
United States

***Correspondence:**
Catarina M. Paquete
cpaquete@itqb.unl.pt

Specialty section:
This article was submitted to Microbial Physiology and Metabolism, a section of the journal Frontiers in Microbiology

Received: *12 October 2021*
Accepted: *22 October 2021*
Published: *22 November 2021*

Citation:
Paquete CM, Nitschke W, Daldal F and Zannoni D (2021) Editorial: Microbial Bioenergetics. Front. Microbiol. 12:793917. doi: 10.3389/fmicb.2021.793917

in *Shewanella*, demonstrating that CRP proteins are important for aerobic respiration. In respect to extracellular electron transfer, it is known that *Shewanella* transfers electrons outside of the cell using the outer membrane-associated MTR complex, composed of the decaheme cytochromes MtrA and MtrC together with the 26-strand beta-barrel protein MtrB. Earlier studies have shown that *in vitro* mixing of purified MtrAB with soluble MtrC results in spontaneous formation of a stable high-affinity complex. In their research article Piper et al. now demonstrate that the complex thus formed has a similar structure and rate of electron transfer as compared with the MTR complex directly purified from *S. oneidensis* MR-1.

Leptospirillum spp. are Gram-negative, obligately acidophilic chemoautotrophic prokaryotes that can respire aerobically using reduced soluble iron or ferrous iron-containing sulfide minerals. Blake et al. explore in details the respiratory chain components of these organisms, identifying the periplasmic cytochrome 579 as a possible candidate involved in this process. Their research article describes selected structural and functional properties of cytochrome 579 after its purification to electrophoretic homogeneity from cell-free extracts. The results obtained support the hypothesis that cytochrome 579 is a periplasmic electron conductor from the outer membrane associated initial iron oxidation to a terminal reductase in the plasma membrane of *Leptospirillum*.

Copper (Cu) is a micronutrient that is an essential cofactor in numerous redox enzymes in all domains of life, but it can also be deleterious to cells in excess. Thus, cells have developed sophisticated Cu homeostasis processes to efficiently provide Cu to cuproproteins while controlling its toxicity. The work of Öztürk et al. investigates the maturation of an extracytoplasmic multicopper oxidase CutO from the Gram-negative facultative phototroph *Rhodobacter capsulatus*, involved in periplasmic Cu detoxification. The laccase-like multicopper oxidases are unique because Cu is both a substrate and a cofactor for these enzymes, yet how they acquire Cu essential for their activities remain unknown. In this research article, the authors investigated the cellular source of Cu for CutO assembly and found that it is partly provided by Cu detoxification pathway centered around the Cu-transporting P_{1B}-type ATPase, CopA1. Moreover, they showed that a small protein CutF, clustered with *cutO* structural gene on some bacterial genomes, is required for maturation of CutO activity. Bacterial species often contain multiple P_{1B}P1-type ATPases, with CopA1-type dedicated to cytoplasmic detoxification and CopA2-type providing Cu to some cuproenzymes. The heme-copper oxidases of aa_3- or cbb_3-types are proton-translocating respiratory cytochrome oxidases that contain a binuclear heme-copper site where oxygen reduction occurs. In a related work, Andrei et al. investigated the $CopA_2$-type P_{1B}-type ATPases, and showed that, as predicted, they provide Cu for maturation of the cbb_3-type cytochrome oxidases. By reconstituting the purified membrane-integral $CopA_2$-type ATPase CcoI from *R. capsulatus* into liposomes and monitoring Cu transport by solid-supported membrane electrophysiology, the authors demonstrate that CcoI provides the link between the cytosolic Cu and the periplasmic Cu chaperones networks during the maturation of cbb_3-type cytochrome oxidase. Remarkably, the pathogenic bacterium *Campylobacter jejuni* is among the few bacterial species that contain only a cbb_3-type cytochrome oxidase. Garg et al. identified the genes involved in the assembly, and activity, of this type cytochrome oxidase, and used mutagenesis to confirm their involvements in these processes. Most, not all, of these genes are highly homologous to their counterparts in other species, linking copper homeostasis, and cytochrome oxidase maturation in this pathogen.

Respiratory processes also play important roles in mycobacterial growth and survival as well as their response and adaptation to different environmental niche and stress, often leading to selection of "persisters" cell population in infected patients. Patil and Jain investigated in detail the mechanisms involved in transitioning to an energy-compromised state in this species upon deletion of the *atp*D gene, revealing that a tight relationship between energy metabolism, redox homeostasis, and lipid biosynthesis exist during ATP-depleted states of mycobacterial cells. This information may be crucial to identify and develop novel therapeutic drug targets to counter mycobacterial infections.

The review article by Gorka et al. surveys the structures and functions of primary electron donors in Type I- and Type II-photosynthetic reaction centers using the vast body of spectroscopic research that has been performed to date. In this review, density functional theory calculations on each oxidized primary donor are used to analyse the electronic properties of the involved electron donors, and the properties thus defined are used to compare and contrast the hetero- and homodimeric photosynthetic reaction centers.

In order to investigate the role of microbial rhodopsin in the heterotrophic growth via phototrophy by *Actinobacteria*, Chuon et al. isolated and characterized the actinorhodopsin ActR-13023 from *Candidatus Aquiluna* sp. IMCC13023. Their research article demonstrated that purified ActR-13023 could be reconstituted with actinobacterial carotenoids for additional light-harvesting, confirming the functional role of this gene and its product, ActR. The role of ActR for solar energy capture by microbial communities is also highlighted in this study. Lastly, Cypionka and Reese contribute a methods article, which describes a freeware app, proton.exe that can be used to assess metabolic activities associated with proton uptake/release processes based on Michaelis-Menten kinetics or first order kinetics. *Proton.exe* models ATP gain and proton-motive force changes in cells, allowing researchers to study proton-related metabolism in mitochondria, phototrophic bacteria, and chloroplasts. The authors used *Desulfovibrio desulfuricans* CNS to validate their model for different biological processes: sulfate uptake by proton-sulfate symport, scalar alkalinization by sulfate reduction to sulfide, nitrate, and nitrite reduction to ammonia as well as electron transport-coupled proton translocation.

Overall, this special issue greatly contributes to the current knowledge of various *microbial bioenergetics* subfields and provides the readers with a wealth of mostly current information to extend their understanding and

appreciation of these vibrant and ever developing areas of the microbial world.

AUTHOR CONTRIBUTIONS

CP wrote the first draft of the manuscript. CP, WN, FD, and DZ contributed to the final version of the manuscript. All authors contributed to the article and approved the submitted version.

Conflict of Interest: The authors declare that the research was conducted in the absence of any commercial or financial relationships that could be construed as a potential conflict of interest.

Publisher's Note: All claims expressed in this article are solely those of the authors and do not necessarily represent those of their affiliated organizations, or those of the publisher, the editors and the reviewers. Any product that may be evaluated in this article, or claim that may be made by its manufacturer, is not guaranteed or endorsed by the publisher.

frontiers in Microbiology

ORIGINAL RESEARCH
published: 08 March 2021
doi: 10.3389/fmicb.2021.650832

Ferrihydrite Reduction by Photosynthetic *Synechocystis* sp. PCC 6803 and Its Correlation With Electricity Generation

*Kenya Tanaka[1], Ginga Shimakawa[2], Shoko Kusama[2], Takashi Harada[2], Souichiro Kato[2,3] and Shuji Nakanishi[1,2]**

[1] Graduate School of Engineering Science, Osaka University, Toyonaka, Japan, [2] Research Center for Solar Energy Chemistry, Osaka University, Toyonaka, Japan, [3] Bioproduction Research Institute, National Institute of Advanced Industrial Science and Technology, Sapporo, Japan

Microbial extracellular electron transfer (EET) to solid-state electron acceptors such as anodes and metal oxides, which was originally identified in dissimilatory metal-reducing bacteria, is a key process in microbial electricity generation and the biogeochemical cycling of metals. Although it is now known that photosynthetic microorganisms can also generate (photo)currents via EET, which has attracted much interest in the field of biophotovoltaics, little is known about the reduction of metal (hydr)oxides via photosynthetic microbial EET. The present work quantitatively assessed the reduction of ferrihydrite in conjunction with the EET of the photosynthetic microbe *Synechocystis* sp. PCC 6803. Microbial reduction of ferrihydrite was found to be initiated in response to light but proceeded at higher rates when exogenous glucose was added, even under dark conditions. These results indicate that current generation from *Synechocystis* cells does not always need light irradiation. The qualitative trends exhibited by the ferrihydrite reduction rates under various conditions showed significant correlation with those of the microbial currents. Notably, the maximum concentration of Fe(II) generated by the cyanobacterial cells under dark conditions in the presence of glucose was comparable to the levels observed in the photic layers of Fe-rich microbial mats.

Keywords: cyanobacteria, iron redox cycle, biophotovoltaics, extracellular electron transfer, *Synechocystis*

OPEN ACCESS

Edited by:
Davide Zannoni, University of Bologna, Italy

Reviewed by:
Paolo Bombelli, University of Cambridge, United Kingdom
Yang-Chun Yong, Jiangsu University, China

***Correspondence:**
Shuji Nakanishi
nakanishi@chem.es.osaka-u.ac.jp

Specialty section:
This article was submitted to Microbial Physiology and Metabolism, a section of the journal Frontiers in Microbiology

Received: *08 January 2021*
Accepted: *16 February 2021*
Published: *08 March 2021*

Citation:
Tanaka K, Shimakawa G, Kusama S, Harada T, Kato S and Nakanishi S (2021) Ferrihydrite Reduction by Photosynthetic Synechocystis sp. PCC 6803 and Its Correlation With Electricity Generation. Front. Microbiol. 12:650832. doi: 10.3389/fmicb.2021.650832

INTRODUCTION

Photosynthetic microorganisms are able to transport intracellular electrons to an anode and this process, known as extracellular electron transfer (EET), has received attention within the field of biophotovoltaics (BPVs), as summarized in recent reviews (Rosenbaum et al., 2010; McCormick et al., 2015; Tschörtner et al., 2019). In a typical BPV system, oxygenic photosynthetic microorganisms such as cyanobacteria and green algae serve both as light absorbers and living anodes/catalysts for water oxidation. Previous researches have suggested that electrons are transferred from NADPH and/or electron transfer chain via some electron mediators, and/or Type IV pili (Lamb et al., 2014; Saper et al., 2018; Zhang et al., 2018). In cyanobacteria, due

to the lack of organelles, both respiration and photosynthesis proceed in one cell, and they depend mutually in the cytosolic metabolism and in the electron transfer chain in the thylakoid membrane (**Figure 1**). Photosynthetic and respiratory electron transfer chains share the interchain components plastoquinone, the cytochrome b_6/f complex, plastocyanin, and cytochrome *c* (Binder, 1982; Peschek et al., 2004). Therefore, not only photosynthetic reactions but respiratory reactions can affect EET flux. The electrons injected into the anode via EET are transferred to the cathode where oxygen reduction occurs, generating electricity. Thus, light to electrical energy conversion in BPVs is achieved on the basis of the functions of living photosynthetic microorganisms.

Microbial EET was originally identified and has been extensively studied in dissimilatory metal-reducing bacteria (DMRB) such as *Shewanella* spp. and *Geobacter* spp. (Lovley et al., 2004; Weber et al., 2006; Kato, 2015; Shi et al., 2016). DMRB are capable of utilizing solid-state Fe(III) (hydr)oxides as respiratory electron acceptors via EET in anaerobic environments, and redox-active proteins expressed in the outer membranes of these microbes are known to play an essential role in this process (Kato, 2015; Shi et al., 2016). Since Fe(II) ions are released to the environment as a consequence of EET to Fe(III) (hydr)oxides, EET from DMRB can have a significant impact on the Fe cycle in natural ecosystems (Lovley et al., 2004; Weber et al., 2006; Melton et al., 2014). In general, the capacity of DRMB to reduce metal oxides is closely correlated with the ability of the microbes to generate electricity (Bond and Lovley, 2003; Bretschger et al., 2007; Liu et al., 2010). Specifically, microorganisms that can reduce Fe(III) (hydr)oxides at a higher rate exhibit superior electricity generation characteristics, and *vice versa*. However, it is uncertain whether or not the (photo)electricity generation ability of photosynthetic microorganisms correlates with the capacity of such organisms to reduce Fe(III) (hydr)oxides. This is because the oxygen evolved as a consequence of photosynthetic activity rapidly oxidizes Fe(II) at pH values close to neutral, forming Fe(III) (hydr)oxides. Furthermore, none of the genes associated with EET in DMRB have been confirmed to appear in cyanobacteria (Kranzler et al., 2014).

The cyanobacterium *Synechocystis* sp. PCC 6803 (S6803) is an ideal model species for studying the correlation between the generation of (photo)electricity and the reduction of Fe(III) (hydr)oxides. S6803 is known to take up iron via the reduction of trace amounts of dissolved Fe(III) species using alternate respiratory terminal oxidase (ARTO) (Kranzler et al., 2011, 2014; **Figure 1**), and can grow using insoluble iron oxides as its sole iron source (Lamb et al., 2014). Furthermore, S6803 has been found to express electrically-conductive nanowires that are associated with the appearance of EET in DMRB (Gorby et al., 2006). Even so, there have been no attempts to quantitatively assess the ability of S6803 to reduce Fe(III) (hydr)oxides or to examine the correlation of such reduction with (photo)electricity generation. Therefore, the present work investigated the appearance of these phenomena in this microbe under a variety of conditions, such as by varying the light intensity and concentrations of oxygen and exogenous glucose. The aim of this study was to clarify the correlation between these two EET-related capabilities.

MATERIALS AND METHODS

Bacterial Strains and Cell Culture Conditions

This work employed a glucose-tolerant, wild strain of S6803 (Williams, 1988; Shimakawa et al., 2014) that was grown and stored on solid BG-11 media plates (1.5% Bacto agar). Preculturing was performed by inoculating 30 mL portions of the liquid BG-11 medium in 100 mL flasks with cells from the agar plates. These flasks were then heated at 30°C with air bubbling under white light at an intensity of 20 μmol $m^{-2}s^{-1}$ to promote microbe growth. The main culture was obtained by inoculation of a 30 mL quantity of the BG11 medium to give an optical density of 0.02 at 730 nm (OD_{730}), applying the same conditions as employed to produce the preculture.

Electrochemical Analysis and Chlorophyll Fluorescence Measurements

The electrochemical measurements were carried out at 30°C in a single-chamber electrochemical cell with an indium-tin oxide (ITO) working electrode (3 cm^2), an Ag/AgCl (saturated KCl) reference electrode and a platinum counter wire (**Supplementary Figure 1**). In preparation, S6803 cells were collected from the main culture with OD_{730} of 2–4 by centrifugation, washed twice with a 20 mM TES buffer (pH 7.5) and suspended in the same buffer. Following this, a 3.7 mL quantity of the TES buffer was added to the electrochemical cell, followed by the introduction of the cell suspension to the bottom of the cell to give an OD_{730} of 10. Situating the cells on the bottom working electrode was expected to increase the current obtained from this system. The generation of an anodic current was monitored using a potentiostat (HA-1510, Hokuto Denko, Tokyo, Japan) with the working electrode potential set at + 0.25 V relative to the reference electrode.

The chlorophyll fluorescence was assessed simultaneously using "e-PAM" set-up described previously (Beauzamy et al., 2020). Briefly, the signal collection fiber of dual PAM/Fiber fluorometer (Heintz Walz, Effeltrich, Germany) was positioned on the bottom ITO working electrode of the electrochemical cell (**Supplementary Figure 1**). Photosynthetic electron transport was driven by actinic light (635 nm), and the fluorescence signal (F) was originated from pulse-modulated measuring light (620 nm). For assessment of the fluorescence yield for cells adapted in dark conditions, the effective intensity of measuring light is set at very low level (Schreiber, 2004). The maximum fluorescence level obtained with fully reduced Q_A (Fm'), the primary quinone acceptor of photosystem (PS) II, was determined by applying 300 ms pulses of saturation light (7,000 μmol m^{-2} s^{-1}). The effective quantum yield of the PSII [Y(II)] was calculated as (Fm'-F)/Fm' (Baker, 2008).

Fe(III) Reduction Assay

In preparation for these experiments, S6803 cells were collected by centrifugation, washed twice with Fe-free BG11 and suspended in the same medium such that the optical density at 730 nm was 5. Ferrihydrite was prepared following a process described in a previous publication (Lovley and Phillips, 1986)

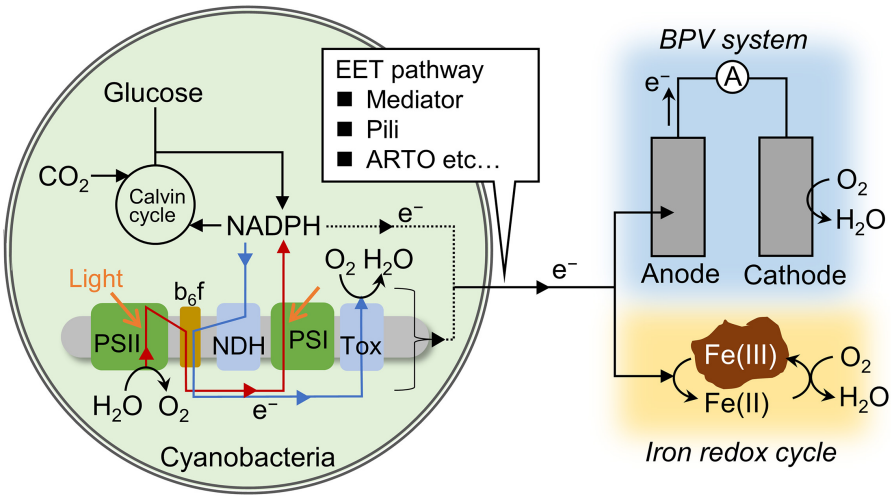

FIGURE 1 | Schematic of the electron flux pathways related to anodic current generation and iron reduction. Red and blue arrows indicate photosynthetic and respiratory electron transfer chain. In photosynthetic electron transfer chain, electrons are transported from photosystem (PS) II to I *via* the interchain components, including plastoquinone, the cytochrome b_6/f complex, and plastocyanin (or cytochrome *c*). In respiratory electron transfer chain, electrons are transported from NAD(P)H dehydrogenase (NDH) or succinate dehydrogenase to terminal oxidases (Tox) *via* the interchain components. Redox mediators, Type IV pili, and alternate respiratory terminal oxidase (ARTO) are suggested to function at the step of extracellular electron transfer (EET).

and added to the cell suspension to give a final concentration of 15 mM Fe, after which a portion of a sterilized stock solution of glucose was added. The cell suspension was subsequently incubated in darkness at 30°C under a N_2 atmosphere with shaking, following which the concentration of Fe(II) was determined by the ferrozine method, as described previously (Lovley and Phillips, 1987). Briefly, the harvested cell suspension was mixed with an HCl solution to give a final concentration of 0.5 M. After incubation for 15 min, the suspension was centrifuged. A 10 μL aliquot of the resulting supernatant was added to 190 μL of a 50 mM HEPES buffer (pH 7.0) containing 2 mM ferrozine. The absorption of this solution at 562 nm was measured and the Fe(II) concentration was calculated according to a standard calibration curve prepared using known concentrations of $FeSO_4$ in solution.

RESULTS

We initially measured the anodic current to ascertain the conditions under which the S6803 exhibited the capacity to reduce Fe(III) (hydr)oxides (**Figure 1**). The anodic current was found to slightly increase in response to light exposure under aerobic conditions, in agreement with previous reports (**Figure 2A**, inset) (McCormick et al., 2011; Cereda et al., 2014; Sekar et al., 2016; Wei et al., 2016; Saper et al., 2018; Zhang et al., 2018). When irradiation was ceased, the current sharply decreased. The current was also observed to gradually increase following the addition of glucose, while the current produced by the control sample without glucose was stable (**Figure 2A**). The anodic current was not observed in the presence of cells or in the presence of dead cells even when the glucose was added into the system (**Supplementary Figure 2**). These results clearly show that S6803 can generate EET current through dissimilation of glucose in darkness. Since the respiratory electron chain share some components with photosynthetic electron chain in S6803 cells (Lea-Smith et al., 2016; **Figure 1**), the effect of glucose addition can be assessed by simultaneously monitoring the chlorophyll fluorescence signal. In the absence of exogenous glucose, the chlorophyll fluorescence output decreased monotonically when the light was off while, in the presence of glucose, the fluorescence initially decreased and then increased after irradiation was ceased (**Figures 2B,C**, black lines). In addition, although the Y(II) in darkness was almost constant over time without glucose, this value decreased in the presence of glucose (**Figures 2B,C**, blue lines). The data acquired under the dark conditions indicate that exogenous glucose was metabolized in the S6803 cells, and that the respiratory electron transfer chain became reductive.

Based on the above results, it was expected that the cyanobacterial reduction of Fe(III) (hydr)oxides would occur to the greatest extent under dark conditions in the presence of glucose. Therefore, we subsequently attempted to quantitatively investigate the effect of glucose on ferrihydrite reduction in the absence of light. **Figure 3** plots Fe(II) concentrations over time (as determined by the ferrozine assay) in cell suspensions containing ferrihydrite. Increases in the Fe(II) concentration are evident in those samples incubated under both aerobic and anaerobic conditions (**Figure 3A**). Notably, ferrihydrite reduction was also observed in a batch of fresh BG-11 medium containing ferrihydrite and glucose but not S6803 cells (**Supplementary Figure 3**). In addition, when a cell suspension incubated with glucose but without ferrihydrite was mixed with ferrihydrite just prior to the ferrozine assay, the reduction of ferrihydrite did not occur (**Supplementary Figure 4**). This result demonstrates that the Fe(II) increase in **Figure 3A** did not result from ferrihydrite

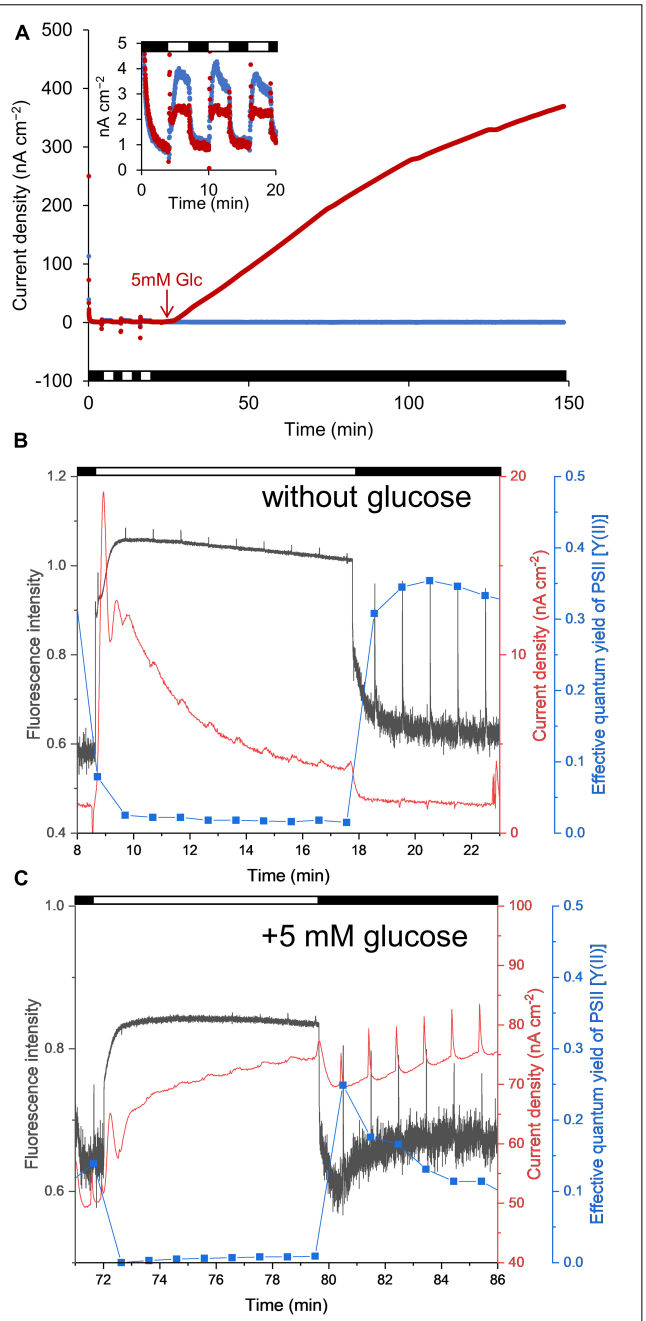

FIGURE 2 | (A) Time courses of anodic current generation from S6803 cells at + 0.25 V vs. Ag/AgCl. Red and blue lines indicate the current with and without 5 mM glucose, respectively, added at the point indicated by the red arrow. The inset shows an enlarged view of the data up to 20 min. **(B,C)** Chlorophyll fluorescence (black lines), current (red lines) and effective quantum yield of the PSII complex [Y(II)] (blue lines) as functions of time with and without glucose. The spikes observed at every 1 min resulted from saturation pulses. The horizontal white and black bars in each graph indicate light [**(A)** 200 μmol m^{-2} s^{-1} **(B,C)** 260 μmol m^{-2} s^{-1}] and dark conditions.

reduction by intracellular reducing equivalents. Thus, the above data indicate that S6803 was able to reduce extracellular solid-state ferrihydrite in the presence of glucose.

The effect of the glucose concentration on the ability of the S6803 to reduce ferrihydrite under dark conditions was subsequently examined. Because the end amount of reduced ferrihydrite in samples incubated under aerobic conditions was lower than that under anaerobic conditions (**Figure 3A**), the effect of glucose was examined under anaerobic conditions. Trials were performed by adding 15 mM ferrihydrite, S6803 cells and glucose to BG-11 medium followed by incubation under anaerobic conditions, and higher glucose concentrations were found to promote ferrihydrite reduction (**Figure 3B**). The chlorophyll concentration during incubation remained relatively constant, and so it is probable that the S6803 cells maintained their cellular components during these experiments even under continuous anaerobic, dark conditions (**Supplementary Figure 5**). These results establish that the cyanobacterial ferrihydrite reduction process was affected by the exogenous glucose concentration. In the case that a suspension of cells containing 5 mM glucose was exposed to light, ferrihydrite reduction under aerobic conditions was found to be slower than that under anaerobic dark conditions, although the rate of the reductive generation of Fe(II) was greater than that observed in a control experiment without cells (**Supplementary Figure 3**). These results suggest that cyanobacteria can reduce insoluble Fe(III) (hydr)oxides even in aerobic environments.

Based on the above results, the growth of S6803 cells was measured in the presence of both ferrihydrite and glucose under anaerobic conditions. Cells were grown under light irradiation at an intensity of 100 μmol m^{-2} s^{-1} while oxygen was continuously removed by nitrogen bubbling. During these trials, ferrihydrite was added to the BG11 medium as the sole iron source. Cells in cultures without ferrihydrite did not grow, as expected (**Figure 4A**, gray line) while, in contrast, cells in cultures with ferrihydrite grew well under anaerobic conditions (**Figure 4A**, red and blue dotted lines). In agreement with a previous report that S6803 can grow using insoluble iron oxides as the sole iron source (Lamb et al., 2014), S6803 was found to be capable of utilizing ferrihydrite as its iron source even under anaerobic conditions. Although the growth rate was unaffected by the addition of 5 mM glucose, the amount of Fe(II) slightly increased in the early stage of culturing in the presence of glucose (**Figure 4A**, red solid line). After the light intensity was decreased to 5 μmol m^{-2}s^{-1} to mimic dim light conditions in a typical internal microbial ecosystem (Fourçans et al., 2004; Ciani et al., 2005; Ohkubo and Miyashita, 2017), the chlorophyll concentration remained almost constant both with and without glucose (**Figure 4B**, red and blue dotted lines). Following this transition to dim light conditions, the glucose concentration was increased to 10 mM, causing a rapid increase in the amount of Fe(II) (**Figure 4B**, red broken and solid lines). The above results suggest that ferrihydrite reduction sufficient for iron acquisition and cell growth (Kranzler et al., 2011, 2014; Lamb et al., 2014) is possible without exogenous glucose, although glucose can promote ferrihydrite reduction to generate an excess of Fe(II) for S6803 growth. In fact, the ferrihydrite reduction rates obtained with 3–15 mM glucose were about 100 times larger than the value reported for dissolved Fe(III) species without glucose (Kranzler et al., 2014; **Supplementary Figure 6**).

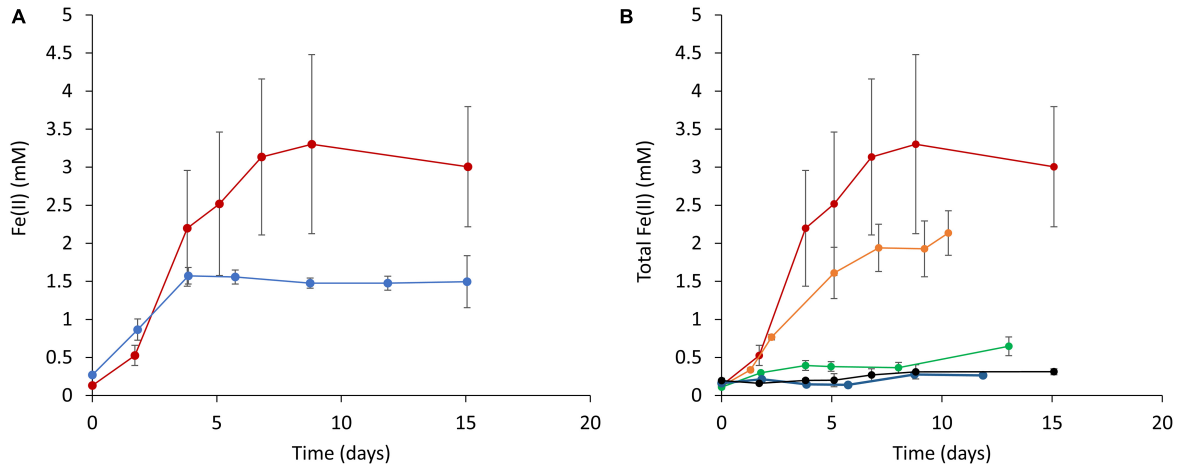

FIGURE 3 | Time courses of ferrihydrite reduction determined using a ferrozine assay. **(A)** A comparison of ferrihydrite reduction under anaerobic (red line) and aerobic (blue line) conditions. **(B)** The effect of glucose concentration on ferrihydrite reduction by S6803 cells. Red, orange, green, blue, and black lines indicate initial glucose concentrations of 15, 5, 3, 1, and 0 mM, respectively. Red lines in **(A,B)** are identical data. Values are means ± one standard deviation (error bars) of three replicate trials.

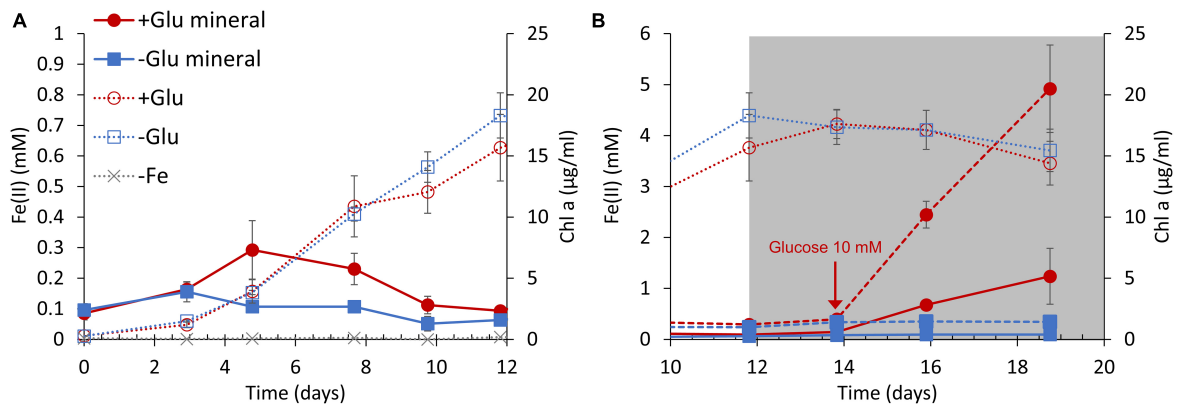

FIGURE 4 | S6803 and Fe(II) concentrations over time under anaerobic conditions with ferrihydrite as the sole iron source. The S6803 cells were inoculated to give an optical density at 730 nm of 0.1 and grown with N_2 bubbling. **(A)** The rapid growth phase under 100 μmol m^{-2} s^{-1} light irradiation. **(B)** The stationary phase under dim light irradiation (gray background). The red and blue lines indicate data obtained with and without glucose, respectively. The solid and broken lines indicate the Fe(II) concentrations in cell suspension and solid iron samples (see also **Supplementary Figure 8**), respectively. The dotted lines indicate chlorophyll concentration and the gray dotted lines indicate chlorophyll concentration in cultures without ferrihydrite. Values are means ± one standard deviation (error bars) of three replicate trials.

DISCUSSION

In contrast to the light-dependent current increases reported elsewhere, the current in the present work was found to increase under dark conditions upon the addition of glucose. This result clearly shows that the EET current in S6803 can be also generated through dissimilation of glucose. Details of mutual relationship between the light-dependent and glucose-dependent EET pathways remains unknown. However, given that the photosynthetic and respiratory electron transport share some components in S6803 (Lea-Smith et al., 2016), it is reasonable to consider that the light-dependent and glucose-dependent EET pathways are also mutually correlated each other, as schematically shown in **Figure 1**. In fact, it was reported that respiratory systems and NADPH are known to participate in the electron pathways of photocurrent generation (Bombelli et al., 2011; Bradley et al., 2013; Saper et al., 2018). The molecular mechanisms that occur in conjunction with EET to Fe(III) (hydr)oxides in DMRB have been well investigated, and it is now known that outer membrane cytochromes play an essential role (Weber et al., 2006; Kato, 2015; Shi et al., 2016). However, these redox-active proteins have not yet been identified in S6803. It has been suggested that ARTO and/or Type IV pili are involved in the iron uptake process in S6803 (Kranzler et al., 2014; Lamb et al., 2014), and such factors may also contribute to ferrihydrite reduction and electricity generation by this microbe (**Figure 1**) [of note, a recent paper reported that pili has little impact on the photo-current generation capability (Thirumurthy et al., 2020)].

Another possibility is that a diffusive electron mediator excreted from the cells was responsible for ferrihydrite reduction. In fact, some redox peaks were observed in cyclic voltammograms obtained from these cells (**Supplementary Figure 7**). These peaks are consistent with previous reports and are attributed to small redox-active metabolites related to EET capability (Saper et al., 2018; Zhang et al., 2018).

It is also helpful to examine the possible effects of cyanobacterial ferrihydrite reduction on microbial ecosystems. Since cyanobacterial habitats become aerobic as a result of oxygenic photosynthesis, cyanobacteria have been regarded as oxidizers of Fe(II) in natural environments. However, the present study demonstrates that cyanobacteria can also act as reducers of Fe(III). In fact, Fe(II) has been detected in aerobic regions within sediment, microbial mats and seawater where cyanobacteria are also found (O'Sullivan et al., 1991; Wieland et al., 2005; Rentz et al., 2007). Although a certain amount of Fe(II) can be generated abiotically by photo-generated superoxides or photo-reaction with Fe(III)-binding ligands (Voelker and Sedlak, 1995; Barbeau, 2006), the present work suggests that Fe(II) can also be produced by EET associated with photosynthetic microorganisms in environments where glucose is present. Microbial mats are one such ecosystem, and *Synechocystis* species are often found in microbial mats (Fourçans et al., 2004; Singh et al., 2011) where they produce a polysaccharide as an extracellular polymeric substance (EPS) (Flemming and Wingender, 2010; Stuart et al., 2016). It has been estimated that the concentration of carbohydrates in this EPS is 45 mg/g on a wet basis, and that glucose residues account for almost all the carbohydrate (Stuart et al., 2016). This amount therefore corresponds to approximately 250 mM glucose. The present study revealed that ferrihydrite reduction occurred in the presence of glucose at a concentration of only 3–15 mM (**Figure 3**). Together, these data suggest that cyanobacterial Fe(III) reduction could be promoted by exogenous glucose even in natural microbial mats.

It is also of interest to compare the Fe(II) concentration range observed in our laboratory experiments with those found in natural environments. In iron-rich microbial mats containing cyanobacteria, Fe(II) has been found at concentrations from 1 to 10 mM even in the aerobic top 2.0 mm of the mats (Wieland et al., 2005). In our experiments, the maximum concentration of Fe(II) generated by the S6803 cells in the absence of light was comparable to the level in the aerobic layers of such iron-rich microbial mats (**Figure 3B**). Thus, the cyanobacterial reduction of insoluble Fe(III) may help maintain the concentration of Fe(II) in the photic layers of microbial mats (**Supplementary Figure 8**).

Although soluble Fe(II) is typically almost completely oxidized by abiotic reactions with oxygen under aerobic conditions, the Fe(II) concentration was increased and then maintained by S6803 cells even under aerobic dark conditions (**Figure 3A**). There are two possible explanations for this result. Firstly, the ferrihydrite reduction rate may have been faster than the abiotic Fe(II) oxidation rate and, secondly, the Fe(II) that was generated could have been poorly reactive with oxygen. The oxidation rate of dissolved Fe(II) at a concentration of 1 mM in a pH 7 solution under ambient air is estimated to be 9.6 mM h^{-1} (Rentz et al., 2007), which is much faster than the rate of reduction by the S6803 cells, indicating that the first possibility can be excluded. Although we tried to confirm the presence of Fe(II) in solid phase by X-ray diffraction (XRD) and transmission electron microscope (TEM), characteristic signal for crystallization of Fe(II) could not observed due to small particle size (<5 nm) (**Supplementary Figure 9**). However, an increase in Fe(II) in the solid fraction was observed during the ferrihydrite reduction experiments (**Supplementary Figure 10**). Thus, it is likely that Fe(II) was protected from oxygen in the solid phase and thus stabilized.

In summary, the present work demonstrated that S6803 can reduce ferrihydrite via EET. Both the reduction rate of ferrihydrite and the microbial current were higher under dark conditions in the presence of glucose than under light conditions. Thus, the accumulation of organic substances in local environments surrounding photosynthetic microbes could be important in terms of the enhanced reduction of iron (hydr)oxides and the generation of microbial electricity. We anticipate that further studies along these lines will provide a deeper understanding of the biogeochemical cycling of iron in nature and will also assist in the development of biophotovoltaics.

DATA AVAILABILITY STATEMENT

The original contributions presented in the study are included in the article/**Supplementary Material**, further inquiries can be directed to the corresponding author/s.

AUTHOR CONTRIBUTIONS

KT, GS, and SN designed the research. KT, GS, and TH performed the research. KT, GS, TH, ShK, SoK and SN analyzed the data. KT, GS and SN wrote the manuscript. All authors contributed to the article and approved the submitted version.

FUNDING

This work was partially supported by the Advanced Low Carbon Technology Research and Development Program (JPMJAL1402) of the Japan Science and Technology Agency (JST), and JSPS KAKENHI grant numbers 18J20176 and 20J00105.

ACKNOWLEDGMENTS

TEM measurement was carried out by using a facility in the Research Center for Ultra-High Voltage Electron Microscopy, Osaka University and TEM observation was supported by Dr. Takao Sakata.

SUPPLEMENTARY MATERIAL

The Supplementary Material for this article can be found online at: https://www.frontiersin.org/articles/10.3389/fmicb.2021.650832/full#supplementary-material

REFERENCES

Baker, N. R. (2008). Chlorophyll fluorescence: a probe of photosynthesis in vivo. *Annu. Rev. Plant Biol.* 59, 89–113. doi: 10.1146/annurev.arplant.59.032607.092759

Barbeau, K. (2006). Photochemistry of organic iron(III) complexing ligands in oceanic systems. *Photochem. Photobiol.* 82, 1505–1516. doi: 10.1562/2006-06-16-IR-935

Beauzamy, L., Delacotte, J., Bailleul, B., Tanaka, K., Nakanishi, S., Wollman, F. A., et al. (2020). Mediator-microorganism interaction in microbial solar cell: a Fluo-electrochemical insight. *Anal. Chem.* 92, 7532–7539. doi: 10.1021/acs.analchem.9b05808

Binder, A. (1982). Respiration and photosynthesis in energy-transducing membranes of cyanobacteria. *J. Bioenerg. Biomembr.* 14, 271–286. doi: 10.1007/BF00743057

Bombelli, P., Bradley, R. W., Scott, A. M., Philips, A. J., McCormick, A. J., Cruz, S. M., et al. (2011). Quantitative analysis of the factors limiting solar power transduction by *Synechocystis* sp. PCC 6803 in biological photovoltaic devices. *Energy Environ. Sci.* 4, 4690–4698. doi: 10.1039/c1ee02531g

Bond, D. R., and Lovley, D. R. (2003). Electricity production by *Geobacter sulfurreducens* attached to electrodes. *Appl. Environ. Microbiol.* 69, 1548–1555. doi: 10.1128/aem.69.3.1548-1555.2003

Bradley, R. W., Bombelli, P., Lea-Smith, D. J., and Howe, C. J. (2013). Terminal oxidase mutants of the cyanobacterium *Synechocystis* sp. PCC 6803 show increased electrogenic activity in biological photo-voltaic systems. *Phys. Chem. Chem. Phys.* 15, 13611–13618. doi: 10.1039/c3cp52438h

Bretschger, O., Obraztsova, A., Sturm, C. A., Chang, I. S., Gorby, Y. A., Reed, S. B., et al. (2007). Current production and metal oxide reduction by *Shewanella oneidensis* MR-1 wild type and mutants. *Appl. Environ. Microbiol.* 73, 7003–7012. doi: 10.1128/AEM.01087-07

Cereda, A., Hitchcock, A., Symes, M. D., Cronin, L., Bibby, T. S., and Jones, A. K. (2014). A bioelectrochemical approach to characterize extracellular electron transfer by *Synechocystis* sp. PCC6803. *PLoS One* 9:e91484. doi: 10.1371/journal.pone.0091484

Ciani, A., Goss, K. U., and Schwarzenbach, R. P. (2005). Light penetration in soil and particulate minerals. *Eur. J. Soil Sci.* 56, 561–574. doi: 10.1111/j.1365-2389.2005.00688.x

Flemming, H. C., and Wingender, J. (2010). The biofilm matrix. *Nat. Rev. Microbiol.* 8, 623–633. doi: 10.1038/nrmicro2415

Fourçans, A., De Oteyza, T. G., Wieland, A., Solé, A., Diestra, E., Van Bleijswijk, J., et al. (2004).). Characterization of functional bacterial groups in a hypersaline microbial mat community (Salins-de-Giraud, Camargue, France). *FEMS Microbiol. Ecol.* 51, 55–70. doi: 10.1016/j.femsec.2004.07.012

Gorby, Y. A., Yanina, S., McLean, J. S., Rosso, K. M., Moyles, D., Dohnalkova, A., et al. (2006). Electrically conductive bacterial nanowires produced by *Shewanella oneidensis* strain MR-1 and other microorganisms. *Proc. Natl. Acad. Sci. U.S.A.* 103, 11358–11363. doi: 10.1073/pnas.0903426106

Kato, S. (2015). Biotechnological aspects of microbial extracellular electron transfer. *Microbes Environ.* 30, 133–139. doi: 10.1264/jsme2.ME15028

Kranzler, C., Lis, H., Finkel, O. M., Schmetterer, G., Shaked, Y., and Keren, N., (2014). Coordinated transporter activity shapes high-affinity iron acquisition in cyanobacteria. *ISME J.* 8, 409–417. doi: 10.1038/ismej.2013.161

Kranzler, C., Lis, H., Shaked, Y., and Keren, N. (2011). The role of reduction in iron uptake processes in a unicellular, planktonic cyanobacterium. *Environ. Microbiol.* 13, 2990–2999. doi: 10.1111/j.1462-2920.2011.02572.x

Lamb, J. J., Hill, R. E., Eaton-Rye, J. J., and Hohmann-Marriott, M. F. (2014). Functional role of PilA in iron acquisition in the cyanobacterium *Synechocystis* sp. PCC 6803. *PLoS One* 9:e105761. doi: 10.1371/journal.pone.0105761

Lea-Smith, D. J., Bombelli, P., Vasudevan, R., and Howe, C. J. (2016). Photosynthetic, respiratory and extracellular electron transport pathways in cyanobacteria. *Biochim Biophys Acta.* 1857, 247–255. doi: 10.1016/j.bbabio.2015.10.007

Liu, H., Matsuda, S., Kato, S., Hashimoto, K., and Nakanishi, S. (2010). Redox-responsive switching in bacterial respiratory pathways involving extracellular electron transfer. *ChemSusChem*. 3, 1253–1256. doi: 10.1002/cssc.201000213

Lovley, D. R., Holmes, D. E., and Nevin, K. P. (2004). Dissimilatory Fe(III) and Mn(IV) reduction. *Adv. Microb. Physiol.* 49, 219–286. doi: 10.1016/S0065-2911(04)49005-5

Lovley, D. R., and Phillips, E. J. (1986). Organic matter mineralization with reduction of ferric iron in anaerobic sediments. *Appl. Environ. Microbiol.* 51, 683–689. doi: 10.1128/AEM.51.4.683-689.1986

Lovley, D. R., and Phillips, E. J. (1987). Rapid assay for microbially reducible ferric iron in aquatic sediments. *Appl. Environ. Microbiol.* 53, 1536–1540. doi: 10.1128/AEM.53.7.1536-1540.1987

McCormick, A. J., Bombelli, P., Bradley, R. W., Thorne, R., Wenzel, T., and Howe, C. J. (2015). Biophotovoltaics: oxygenic photosynthetic organisms in the world of bioelectrochemical systems. *Energy Environ. Sci.* 8, 1092–1109. doi: 10.1039/c4ee03875d

McCormick, A. J., Bombelli, P., Scott, A. M., Philips, A. J., Smith, A. G., Fisher, A. C., et al. (2011). Photosynthetic biofilms in pure culture harness solar energy in a mediatorless bio-photovoltaic cell (BPV) system. *Energy Environ. Sci.* 4, 4699–4709. doi: 10.1039/c1ee01965a

Melton, E. D., Swanner, E. D., Behrens, S., Schmidt, C., and Kappler, A. (2014). The interplay of microbially mediated and abiotic reactions in the biogeochemical Fe cycle. *Nat. Rev. Microbiol.* 12, 797–808. doi: 10.1038/nrmicro3347

Ohkubo, S., and Miyashita, H. (2017). A niche for cyanobacteria producing chlorophyll f within a microbial mat. *ISME J.* 11, 2368–2378. doi: 10.1038/ismej.2017.98

O'Sullivan, D. W., Hanson, A. K., Miller, W. L., and Kester, D. R. (1991). Measurement of Fe(II) in surface water of the equatorial Pacific. *Limnol. Oceanogr.* 36, 1727–1741. doi: 10.4319/lo.1991.36.8.1727

Peschek, G. A., Obinger, C., and Paumann, M. (2004). The respiratory chain of blue-green algae (cyanobacteria). *Physiol. Plant.* 120, 358–369. doi: 10.1111/j.1399-3054.2004.00274.x

Rentz, J. A., Kraiya, C., Luther, G. W. III, and Emerson, D. (2007). Control of ferrous iron oxidation within circumneutral microbial iron mats by cellular activity and autocatalysis. *Environ. Sci. Technol.* 41, 6084–6089. doi: 10.1021/es062203e

Rosenbaum, M., He, Z., and Angenent, L. T. (2010). Light energy to bioelectricity: photosynthetic microbial fuel cells. *Curr. Opin. Biotechnol.* 21, 259–264. doi: 10.1016/j.copbio.2010.03.010

Saper, G., Kallmann, D., Conzuelo, F., Zhao, F., Tóth, T. N., Liveanu, V., et al. (2018). Live cyanobacteria produce photocurrent and hydrogen using both the respiratory and photosynthetic systems. *Nat. Commun.* 9:2168. doi: 10.1038/s41467-018-04613-x

Schreiber, U. (2004). "Pulse-Amplitude-Modulation (PAM) fluorometry and saturation pulse method: an overview," in *Chlorophyll a Fluorescence. Advances in Photosynthesis and Respiration*, eds G. C. Papageorgiou and Govindjee (Dordrecht: Springer), 279–319.

Sekar, N., Jain, R., Yan, Y., and Ramasamy, R. P. (2016). Enhanced photobioelectrochemical energy conversion by genetically engineered cyanobacteria. *Biotechnol. Bioeng.* 113, 675–679. doi: 10.1002/bit.25829

Shi, L., Dong, H., Reguera, G., Beyenal, H., Lu, A., Liu, J., et al. (2016). Extracellular electron transfer mechanisms between microorganisms and minerals. *Nat. Rev. Microbiol.* 14, 651–662. doi: 10.1038/nrmicro.2016.93

Shimakawa, G., Hasunuma, T., Kondo, A., Matsuda, M., Makino, A., and Miyake, C. (2014). Respiration accumulates Calvin cycle intermediates for the rapid start of photosynthesis in *Synechocystis* sp. PCC 6803. *Biosci. Biotechnol. Biochem.* 78, 1997–2007. doi: 10.1080/09168451.2014.943648

Singh, D. P., Khattar, J. I. S., Nadda, J., Singh, Y., Garg, A., Kaur, N., et al. (2011). Chlorpyrifos degradation by the cyanobacterium *Synechocystis* sp. strain PUPCCC 64. *Environ. Sci. Pollut. Res. Int.* 18, 1351–1359. doi: 10.1007/s11356-011-0472-x

Stuart, R. K., Mayali, X., Lee, J. Z., Craig Everroad, R., Hwang, M., Bebout, B. M., et al. (2016). Cyanobacterial reuse of extracellular organic carbon in microbial mats. *ISME J.* 10, 1240–1251. doi: 10.1038/ismej.2015.180

Thirumurthy, M. A., Hitchcock, A., Cereda, A., Liu, J., Chavez, M. S., Doss, B. L., et al. (2020). Type IV pili-independent photocurrent production by the cyanobacterium *Synechocystis* sp. PCC 6803. *Front. Microbiol.* 11:1344. doi: 10.3389/fmicb.2020.01344

Tschörtner, J., Lai, B., and Krömer, J. O. (2019). Biophotovoltaics: green power generation from sunlight and water. *Front. Microbiol.* 10:866. doi: 10.3389/fmicb.2019.00866

Voelker, B. M., and Sedlak, D. L. (1995). Iron reduction by photoproduced superoxide in seawater. *Mar. Chem.* 50, 93–102. doi: 10.1016/0304-4203(95)00029-Q

Weber, K. A., Achenbach, L. A., and Coates, J. D. (2006). Microorganisms pumping iron: anaerobic microbial iron oxidation and reduction. *Nat. Rev. Microbiol.* 4, 752–764. doi: 10.1038/nrmicro1490

Wei, X., Lee, H., and Choi, S. (2016). Biopower generation in a microfluidic bio-solar panel. *Sens. Actuators B Chem.* 228, 151–155. doi: 10.1016/j.snb.2015.12.103

Wieland, A., Zopfi, J., Benthien, M., and Kühl, M. (2005). Biogeochemistry of an iron-rich hypersaline microbial mat (Camargue, France). *Microb. Ecol.* 49, 34–49. doi: 10.1007/s00248-003-2033-4

Williams, J. G. K. (1988). Construction of specific mutations in photosystem II photosynthetic reaction center by genetic engineering methods in *Synechocystis* 6803. *Methods Enzymol.* 167, 766–778. doi: 10.1016/0076-6879(88)67088-1

Zhang, J. Z., Bombelli, P., Sokol, K. P., Fantuzzi, A., Rutherford, A. W., Howe, C. J., et al. (2018). Photoelectrochemistry of photosystem II in vitro vs in vivo. *J. Am. Chem. Soc.* 140, 6–9. doi: 10.1021/jacs.7b08563

Conflict of Interest: The authors declare that the research was conducted in the absence of any commercial or financial relationships that could be construed as a potential conflict of interest.

frontiers in Microbiology

ORIGINAL RESEARCH
published: 28 April 2021
doi: 10.3389/fmicb.2021.652328

Assembly of Natively Synthesized Dual Chromophores Into Functional Actinorhodopsin

*Kimleng Chuon[1], So Young Kim[2], Seanghun Meas[1], Jin-gon Shim[1], Shin-Gyu Cho[1], Kun-Wook Kang[1], Ji-Hyun Kim[1], Hyun-Suk Cho[1] and Kwang-Hwan Jung[1]**

[1]Department of Life Science and Institute of Biological Interfaces, Sogang University, Seoul, South Korea, [2]Research Institute of Basic Sciences, Seoul National University, Seoul, South Korea

Microbial rhodopsin is a simple solar energy-capturing molecule compared to the complex photosynthesis apparatus. Light-driven proton pumping across the cell membrane is a crucial mechanism underlying microbial energy production. *Actinobacteria* is one of the highly abundant bacterial phyla in freshwater habitats, and members of this lineage are considered to boost heterotrophic growth *via* phototrophy, as indicated by the presence of actino-opsin (ActR) genes in their genome. However, it is difficult to validate their function under laboratory settings because *Actinobacteria* are not consistently cultivable. Based on the published genome sequence of *Candidatus aquiluna* sp. strain IMCC13023, actinorhodopsin from the strain (ActR-13023) was isolated and characterized in this study. Notably, ActR-13023 assembled with natively synthesized carotenoid/retinal (used as a dual chromophore) and functioned as a light-driven outward proton pump. The ActR-13023 gene and putative genes involved in the chromophore (retinal/carotenoid) biosynthetic pathway were detected in the genome, indicating the functional expression ActR-13023 under natural conditions for the utilization of solar energy for proton translocation. Heterologous expressed ActR-13023 exhibited maximum absorption at 565 nm with practical proton pumping ability. Purified ActR-13023 could be reconstituted with actinobacterial carotenoids for additional light-harvesting. The existence of actinorhodopsin and its chromophore synthesis machinery in *Actinobacteria* indicates the inherent photo-energy conversion function of this microorganism. The assembly of ActR-13023 to its synthesized chromophores validated the microbial community's importance in the energy cycle.

Keywords: actinobacteria, microbial rhodopsin, light-driven proton pumps, retinal, carotenoid, dual chromophore actinorhodopsin

OPEN ACCESS

Edited by:
Davide Zannoni, University of Bologna, Italy

Reviewed by:
Willem J. De Grip, Leiden University, Netherlands
Katrina T. Forest, University of Wisconsin-Madison, United States

***Correspondence:**
Kwang-Hwan Jung
kjung@sogang.ac.kr

Specialty section:
This article was submitted to Microbial Physiology and Metabolism, a section of the journal Frontiers in Microbiology

Received: *12 January 2021*
Accepted: *06 April 2021*
Published: *28 April 2021*

Citation:
Chuon K, Kim SY, Meas S, Shim J-g, Cho S-G, Kang K-W, Kim J-H, Cho H-S and Jung K-H (2021) Assembly of Natively Synthesized Dual Chromophores Into Functional Actinorhodopsin. Front. Microbiol. 12:652328. doi: 10.3389/fmicb.2021.652328

INTRODUCTION

Actinobacteria are found in various terrestrial and aquatic environments. They are the most morphologically diverse prokaryotes (Servin et al., 2008). The unique genes and novel metabolic pathways present in the organism are beneficial for natural adaptation. Also, marine *Actinobacteria* are distributed in various marine habitats, such as marine sediments (Claverías et al., 2015),

seawater (Subramani and Aalbersberg, 2013), freshwater ecosystems (Allgaier and Grossart, 2006), and melting sea ice (Fernández-Gómez et al., 2019). The *Actinobacteria* clade (OM1 clade; Rappé et al., 1998), constituted by members of the class Actinobacteria, had been recognized as a contributor to marine microbial communities in culture-independent studies, which involved 16S rRNA gene pyrosequencing, metagenome sequencing, and metaproteomic experiments (Jensen and Lauro, 2008). The *Actinobacteria* strain IMCC13023 was isolated from a surface seawater sample collected from Kongsfjorden (Svalvard, Norway) during the glacier-melting season using high-throughput extinction-to-dilution culturing. The strain was classified under the current name *Candidatus Aquiluna* sp. IMCC13023, candidatus name (Cho and Giovannoni, 2004; Kang et al., 2012). A protein-centric comparative metaproteomic approach adopted on an oceanic scale, targeting membrane proteins, suggested the involvement of the bacteria in nutrient transport and energy transduction, which altered our understanding of the bacterial community structure, nutrient utilization, and energy transduction, as well as viral and archaeal activities (Morris et al., 2010).

Light is a source of energy and an environmental cue that available in excess in most surface environments. In prokaryotic systems, it has been utilized by photoautotrophs and photoheterotrophs. However, the conversion of light to cellular energy has been characterized in only a few species. Freshwater actinobacteria are ubiquitous in light-illuminated aquatic environments and grow more rapidly in the absence of functional photosystems, likely because sugar transport is upregulated in light (Maresca et al., 2019). In a previous report, the actinobacterium *Rhodoluna planktonica* was shown to encode one actinorhodopsin (RpActR), and the functional expression of RpActR was demonstrated in native cells. Illumination induced the acidification of actinobacteria cell culture and elevated the cellular ATP content, indicating ActR-based phototrophy in native actinobacteria (Nakamura et al., 2016). Rhodopsins found in Archaea, Bacteria, and Eukaryotes, which contained opsin and a covalently bound retinal as a chromophore to absorb photons for energy conversion or the initiation of intra or intercellular signaling (Spudich et al., 2000). Microbial communities utilized the microbial rhodopsin or typed I rhodopsin with all-trans-retinal for various purposes. At the same time, animals solely used a different rhodopsin family with 11-cis retinal for visual and nonvisual phototransduction, classified as type II rhodopsin (Palczewski, 2006; Shichida and Matsuyama, 2009). Rhodopsins had been divided for microbial and animal rhodopsin, also known as type-I and type-II rhodopsin, respectively (Ernst et al., 2014). The gene for actinorhodopsin, a type I rhodopsin-family protein previously detected in actinobacteria isolates, was also found in the strain IMCC13023 (Sharma et al., 2008, 2009). Here, we demonstrated that ActR-13023 exhibited phototrophy in native actinobacterium, which confirmed the functional expression of the ActR-13023 gene, and light illumination induced the acidification of the actinobacterial cell culture. ActR-13023 expressed heterologously in *Escherichia coli* facilitated accurate characterization, and the findings suggested the assembly of this actinorhodopsin with retinal/carotenoid as a light-harvesting protein.

MATERIALS AND METHODS

Molecular Cloning

Candidatus Aquiluna sp. IMCC13023 cells were generously provided by Jang-Cheon Cho from the Department of Biology, Inha University, Korea. PCR primers with restriction enzyme sites and his-tag sequences were used for colony PCR. The expression vector pKA001 (Pushkarev et al., 2018) under the IPTG inducible promoter was used to express the ActR-13023 gene. pACK-*blh* was used to express the β-carotene dioxygenase gene, and pACK-ctrw7120 was used to expressing the β-carotene ketolase genes from *Nostoc* sp. PCC7120 (for canthaxanthin production; Jang et al., 2011; Yang and Guo, 2014; Gao et al., 2020). The expression vector for carotenoid was successfully constructed with an addition of a multiple cloning site under an inducible promoter into an original pAC-BETA plasmid (Addgene, United States). The detailed information of primers sequences and a global map of the expression vectors with restriction enzyme sites were documented in supplementary data (**Supplementary Figure S1**).

Protein Expression and Purification

Escherichia coli strain UT5600 was used for the expression system. The cloned plasmid, containing the recombinant ActR-13023 sequence, was transformed into *E. coli*. To express these proteins, the transformed *E. coli* cells were cultured in LB media until OD_{600nm} = 0.4. Then, protein expression was achieved by inducing 1 mM of IPTG (Applichem, United States) and 5 μM all-*trans*-retinal (Sigma, United States), and culture for 5 h at 37°C with shaking at 240 rpm. The cells were collected and sonicated (Branson Sonifier 250, United States), and the membrane fraction was collected by ultracentrifugation for 1 h at 35,000 × *g*. The membrane fraction was mixed with 2% n-dodecyl-*β*-D-maltopyranoside (DDM) in the same volume to obtain a final solution of 1% DDM (Anatrace, United States), and the sample was continuously inverted in a chamber at 4°C for 4 h. After detergent solubilization, the sample was centrifuged at 20,000 × *g* for 15 min at 4°C to separate solubilized protein from the cell membrane. Then, the supernatant was collected and treated with 1 ml volume of Ni^{+2}-NTA resin (Qiagen, Korea). Immobilized metal affinity chromatography (IMAC) for the His-tag fusion protein technique was applied to extract the pure target protein. The protein bound to the Ni^{+2}-NTA resin was loaded to the affinity column, and the sample was washed with 25 mM imidazole (Sigma) in 0.02% DDM twice to remove non-specific binding random histidine. Finally, the target protein was eluted with 250 mM imidazole in 0.02% DDM, and the sample was filtered by Amicon centrifugal filter (Merckmilliphore, Germany). The eluted protein was washed and concentrated through Amicon centrifugal filter with a 10 kDa molecular weight cutoff membrane. The sample

was washed using 5 ml of 0.02% DDM buffer to push through, and concentrated sample to 0.3~0.5 ml and then resuspended with another 5 ml of the same buffer to continuously repeat the process three times. Purified rhodopsin showed purple color in the 0.02% DDM solution, and the SDS-PAGE of the purified sample was assessed to confirm the protein's molecular mass and purity. Purified rhodopsin was kept in 0.02% DDM at 4°C.

Absorption Spectroscopy and pKa Measurements

UV/VIS spectrophotometer (Shimadzu, UV-2550) was used to measure the absorbance spectra of purified ActR-13023 in DDM solution. To measure the entire spectrum, 0.02% DDM solution was used for baseline, and the sample was measured every 0.5 nm wavelength from 350 to 750 nm. The absorption spectra of wild-type and mutants in DDM were recorded in various pH conditions. Samples were divided into two sets, and one set started with pH 7.0 down to pH 4.0 with a 0.5 pH change that was adjusted by adding a tiny amount of HCL. The other set with the same condition started from pH 7.0 up to pH 10.0 with a 0.5 pH change adjusted by adding a tiny NaOH amount. Together, we collected the spectroscopic titration data of ActR-13023 wild-type and mutants dependent on pH changes. The maximum absorption of microbial rhodopsin is shifted upon protonated and deprotonated states of the Schiff base (SB) counter-ion as previously described (Spassov et al., 2001). The data were fitted with a function containing pKa component as the following equation $y = A/\left(1+10^{pH-pKa}\right)$ where A is maximum absorbance changes in Origin Pro 7.0.

Hydroxylamine reactions were carried out at pH 7.0 in a mixture of 10 mM Tris-HCL (using a small amount of HLC to adjust Tris containing pH to 7.0), 0.1% DDM, 150 mM NaCl, and 0.2 M hydroxylamine. The sample was stirred continuously along with white light irradiation at an intensity of 100 W/m^2 using a short wavelength cutoff filter (>440 nm, Sigma Koki SCF-50S-44Y, Japan) for 30 min. After the reaction, the cell sample was collected by centrifuge at 4,000 rpm at 4°C for 15 min, following cell wash with 15% ethanol one time then collected in the same condition.

Proton Pumping Measurements

Proton pumping experiments were performed using whole-cell and spheroplast vesicles, as previously described (Zhu et al., 2013; Maresca et al., 2016). The spheroplast vesicles were isolated by centrifugation at 30,000 × g for 1 h at 4°C (Beckman XL-90 ultracentrifuge) and washed by 3 ml of 10 mM NaCl, 10 mM $MgSO_4.7H_2O$, and 100 μM $CaCl_2$ (Wang et al., 2003). About 30 μl of carotenoid in ethanol with maximum absorbance density at 3 units (OD = 3) was added to 3 ml of ActR-13023-expressing spheroplasts by vigorously stirring in 50 mM $MgSO_4$ and 50 mM Na-EDTA for an additional 30 min, followed by further incubation for 16 h at 4°C, washing twice with sonication buffer (50 mM Tris, 150 mM NaCl, pH 7), and resuspension in an unbuffered solution (10 mM NaCl, 10 mM $MgSO_4.7H_2O$, and 100 μM $CaCl_2$). The samples were maintained in an unbuffered solution, and the pH of the solution was recorded. The sample solution was illuminated at an intensity of 100 W/m^2 using a short wavelength cutoff filter (>440 nm, Sigma Koki SCF-50S-44Y, Japan) in combination with a focusing convex lens and heat protecting ($CuSO_4$) filter, and the pH values were monitored using a Horiba pH meter F-51. The sample was stored in the dark for 5 min, and the pH values were measured in the initial dark state followed by illumination for 3 min and 3 min of darkness after illumination, and 10 μM of carbonyl cyanide m-chlorophenyl hydrazine (CCCP) was used in CCCP treated experiments. Proton change was converted by $10^{-\Delta pH}$ and then multiply with 10^{pH} (initial pH), and the average data were calculated and fitted using Origin Pro 7.0.

Light-Induced Differential Spectroscopy and Photocycle Measurements

The purified ActR-13023 wild-type and mutants were stored in 0.02% DDM, and then had been measured by the time-based kinetic function of Scinco spectrophotometer (Scinco, Korea) upon light illumination. The samples had been prepared in 1 ml volume cuvette at 0.5 OD and kept in the dark conditions for 10 min at 4°C. The dark-adapted samples were used for baseline spectrum; then, the samples were illuminated with white light at an intensity of 100 W/m^2 guided by an optical tube for 1 min. The light-induced absorption differences were measured every 700 msec for 60 times, and the signals were averaged as one data. Three experiments were repeated and fitted the overall differential spectra in Origin Pro 7.0.

Sample preparation and experimental set-up for photocycle had been performed by flash-induced transient absorption changes using RSM 1000 spectrophotometer (Olis, United States). ActR-13023 expressed cells were sonicated (Branson Sonifier 250, United States) three times at 45% amplitude for 2:30 min in 30-s intervals. The sample was centrifuged to check for cell lysis at 4,000 rpm at °C for 15 min, and the supernatant was collected. The pellet containing the unbroken cell was discarded. The broken membrane fragments were then collected with ultracentrifuge at 20,000 rpm at 4°C for 1 h. Flash-photolysis experiments were performed on the membrane fragments encased within polyacrylamide gel. Membrane fragments were resuspended in 0.4 ml of pH 8.0 (50 mM Tris and 150 mM NaCl), and then added 0.3 ml of 33% acrylamide and 1% bis-acrylamide solution (Dynebio, Korea), 2.4 μl of 10% ammonium persulfate (AP), and 3 μl of TEMED (N, N, N′, N′ tetramethylethylenediamine), which was used to study photocycle of microbial rhodopsin to the closest native form in *E. coli* membrane previously (Miranda et al., 2009). The samples were placed in plastic cases that mimic the cuvette shape and size. After solidification, the gel was removed and washed with deionized water (DIW) for 4 h at 23°C and store at 4°C for the next experiment. The samples were soaked in pH 7–8 buffer solution (50 mM Tris and 150 mM NaCl), pH adjustment using HCL solution. The experiment was conducted by a custom-built single-wavelength spectrometer described before (Waschuk et al., 2005). In short,

the photocycle experiment started with 6 ns pulses of an Nd-YAG pulse laser (Continuum, Mini-light II, 532 nm, 6 ns, 25 mJ), and optical filters were applied for selected wavelengths. At least 30 signals were averaged for each data points before the fitting process.

Carotenoid Interaction Measurement

Salinibacter ruber was used to isolate salinixanthin, and the cells were grown at 37°C in a shaking incubator (180 rpm) in 200 ml Erlenmeyer flasks containing 50 ml medium of the following composition NaCl, 195; $MgSO_4.7H_2O$,25; $MgCl_26H_2O$,16.3; $CaCl_22H_2O$,1.25; KCl,5.0; $NaHCO_3$,0.25; NaBr,0.625; yeast extract, 1.0 (all concentrations in g/L), and adjusted to pH 7.0 by HCL. Jang-Cheon Cho generously provided the actinobacteria strain IMCC13023, Inha University, Korea. The samples were collected and washed with DIW (10 ml). The cells were then sonicated (Branson Sonifier 250, United States) in DIW, and the cell lysis then mixes with methanol/acetone (3:7). The samples were centrifuged at 35,000 rpm, and the supernatant was taken to dryness. Then was dissolved in methanol and spotted on a silica gel 60 TLC plate (Sigma). The plate was developed by immersion in the corresponding solvents [100:1 ethyl acetate:ethanol and hexane (5:1 v/v)]. The carotenoid target samples were isolated from the plate and dissolved in petroleum ether, applied to the Symmetry C18 column (3.9 mm × 150 mm; Agilent, United States), and eluted with a mixture of acetonitrile and dichloromethane (31, v/v) at a flow rate of 1 ml/min. The product was confirmed based on high-resolution mass spectra data obtained from the Organic Chemistry Research Center, Sogang University, Orbitrap Mass Spectrometer, LTQ Orbitrap XL, Thermo Fisher Scientific, Korea.

The 3D structure prediction of ActR-13023 was modeled by automated protein structure homology SWISS-MODEL (PDB: 3ddl as a template), and an optimized PDB file was obtained for molecular docking prediction. Protein PDB file and carotenoid (canthaxanthin, PubChem ID: 5281227) were uploaded to an integrated docking server[1] using the PM6 method by Mozyme function of MOPAC2009 as described by Bikadi and Hazai (2009). After each docking calculation, the RMSD between the lowest energy docked ligand, and the complex crystal structure was evaluated. Docking calculations were carried out using DockingServer. The MMFF94 force field (Kaminski and Jorgensen, 1996) was used for energy minimization of ligand molecule (***canthaxanthin***) using DockingServer. Gasteiger partial charges were added to the ligand atoms. Non-polar hydrogen atoms were merged, and rotatable bonds were defined. Docking calculations were carried out on the ***ActR-13023-optimized*** protein model. Essential hydrogen atoms, Kollman united atom type charges, and solvation parameters were added with AutoDock tools' aid (Morris et al., 2009). Affinity (grid) maps of 20 × 20 × 20 Å grid points and 0.375 Å spacing were generated using the Autogrid program (Morris et al., 1998). AutoDock parameter set- and distance-dependent dielectric functions were used to calculate the van der Waals and the electrostatic terms, respectively. Docking simulations were performed using the Lamarckian genetic algorithm (LGA) and the Solis and Wets local search method (Solis and Wets, 1981). The initial position, orientation, and torsions of the ligand molecules were set randomly. Each docking experiment was derived from two different runs set to terminate after a maximum of 250,000 energy evaluations. The population size was set to 150. A translational step of 0.2 Å and quaternion and torsion steps of 5 was applied during the search.

[1]www.dockingserver.com

RESULTS

Features of ActR-13023 vs. Other Microbial Rhodopsins

Rhodopsin is a retinal-binding protein ubiquitous in unicellular microorganisms (Heberle et al., 2014). ActR-13023 from strain IMCC13023 contained all critical residues for function and secondary chromophore assembly. The newly discovered microbial rhodopsin's photochemical and physiological characterization was essential to determine the protein's potential as an important molecule in the microbial community. Proton pumps are associated with the most significant functional class of microbial rhodopsins and are widely distributed among microorganisms inhabiting a broad range of environments (Nakamura et al., 2016). The amino acid sequence comparison of ActR-13023 to bacteriorhodopsin (BR; Khorana et al., 1979), green-light absorption proteorhodopsin (PR; Bamann et al., 2014), xanthorhodopsin (XR; Luecke et al., 2008), and actinorhodopsin (ActR; Dwulit-Smith et al., 2018) revealed the DTE motif that associated to the proton-pumping process. ActR-13023 is a typical seven α-helical membrane protein with a chromophore, all-*trans*-retinal, covalently bound to lysine K224 (K216 in BR). The essential residues for proton transfer, aspartic acid D85 (D85 in BR; primary proton acceptor), and glutamic acid E96 (D96 in BR), were also conserved. **Figure 1A** showed the alignment of ActR-13023 to other microbial rhodopsin, including BR; however, the whole sequence of BR was used for the sequence alignment that why the position of D85 and D96 were not matched. Since the original position is different from the commonly used position reported by the crystal structure of BR using truncated form protein [complete sequence bacteriorhodopsin; Pinhassi et al., 2016; accession: WP_010903069]. The protein sequence alignment of ActR-13023 to BR, PR, and XR from *S. ruber* (PDB: 3ddl) that was reported for carotenoid interaction (Luecke et al., 2008), and other actinorhodopsins (Dwulit-Smith et al., 2018) showed that ActR-13023 shared 11 out of 18 residues that were reported for carotenoid interaction in XR. ActR-13023 had more conserved residues to XR than PR and BR, and the phylogenetic tree suggested a smaller distance to XR than the other microbial rhodopsin. A Pro residue in the middle of helix D is known to differentiate ActR from XR (Dwulit-Smith et al., 2018; **Figure 1A**). Structural alignment of modeling ActR-13023 to XR (PDB: 3ddl) helped to visualize the protein

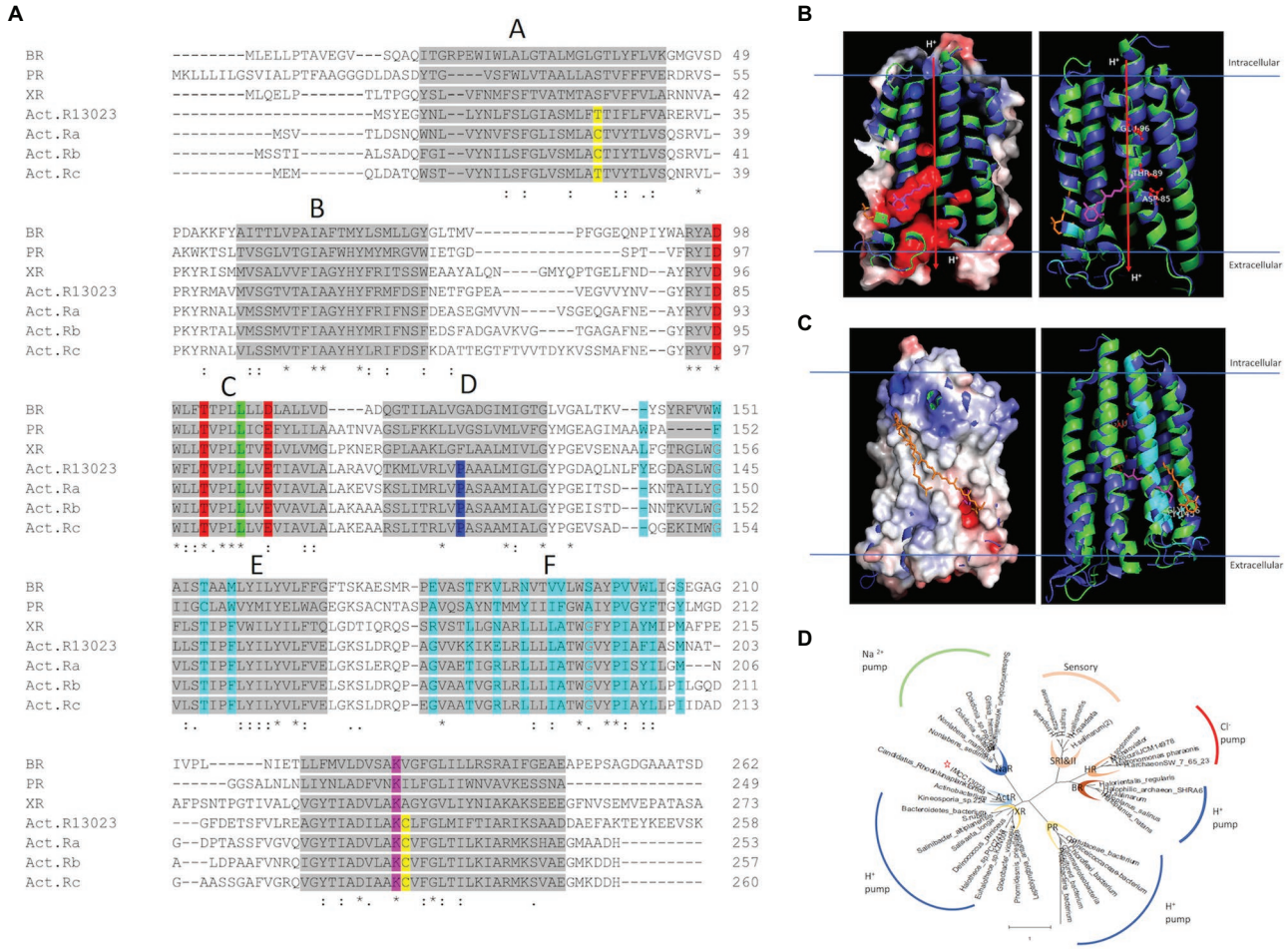

FIGURE 1 | Features of ActR-13023 vs. other microbial rhodopsins. **(A)** Multiple sequence alignment of ActR-13023 with bacteriorhodopsin (BR), proteorhodopsin (PR), xanthorhodopsin (XR), and actinorhodopsin from acI actinobacteria clades A, B, and C (ActR a–c). Gray highlights and the alphabet represent the helical segment. Cys/Thr on helix A and G (disulfide bond in ActR) is marked in yellow, DTE motifs in red, color tuning residue in green, phylogenetically differentiated ActR XR, Pro in blue, carotenoid interaction residues in cyan, and retinal-bound Lys in pink. **(B)** Functional visualization of ActR-13023 compared to light-driven outward proton pump. **(C)** Carotenoid interaction potential of ActR-13023. **(D)** Phylogenetic tree of ActR-13023 vs. other microbial rhodopsins (the tree was generated using MEGA X 10.1).

similarity, where electrostatic map revealed the negatively charged regions represented the DTE motifs of ActR-13023; each residue was marked in red and labeled (**Figures 1A,B**). The surface view of ActR-13023 with the carotenoid antenna-salinixanthin of XR revealed an interaction pattern, where Gly replaced a bulky residue (such as Trp in case of BR) introduced specifically in an interactive pocket for carotenoid to protein and retinal. Gly145 of ActR-13023 aligned perfectly with G156 of XR and created space for docking the keto-ring of SAL into the protein (**Figure 1C**). Phylogenetic analysis suggested that ActR-13023 shared a close evolutionary relationship with XR, which functions as proton-pumping rhodopsin (**Figure 1D**).

Functional Expression of ActR-13023

Based on primary and 3D structural modeling, ActR-13023 was predicted to be a light-driven proton pump functioning as a single molecule and assembling with retinal and carotenoids. The function of this protein was studied in native cells. The UV-visible spectrum of native cells showed maximum absorption (λmax) in the blue-green region; λmax was observed at 512 nm and the formation of a blue shoulder peak at 482 nm, a green shoulder peak at 550 nm (**Figure 2**). To confirm the expression of ActR-13023 in strain IMCC13023, the chromophores were removed from the native membrane using hydroxylamine and reconstituted with all-*trans*-retinal. As anticipated, the absorbance at 566 nm (green region) with a minor shoulder absorption peak formed at 526 nm (blue region) increased upon incubation with all-*trans*-retinal. Chromophore reconstitution confirmed the natural expression of ActR-13023 in native cells. Opsin-bound retinal usually produces a single peak, yet multiple absorbance readings were observed here. After 1 h of reconstitution, the absorbance at 566 nm was increased, then after 2 days of reconstitution, the height of the shoulder peak

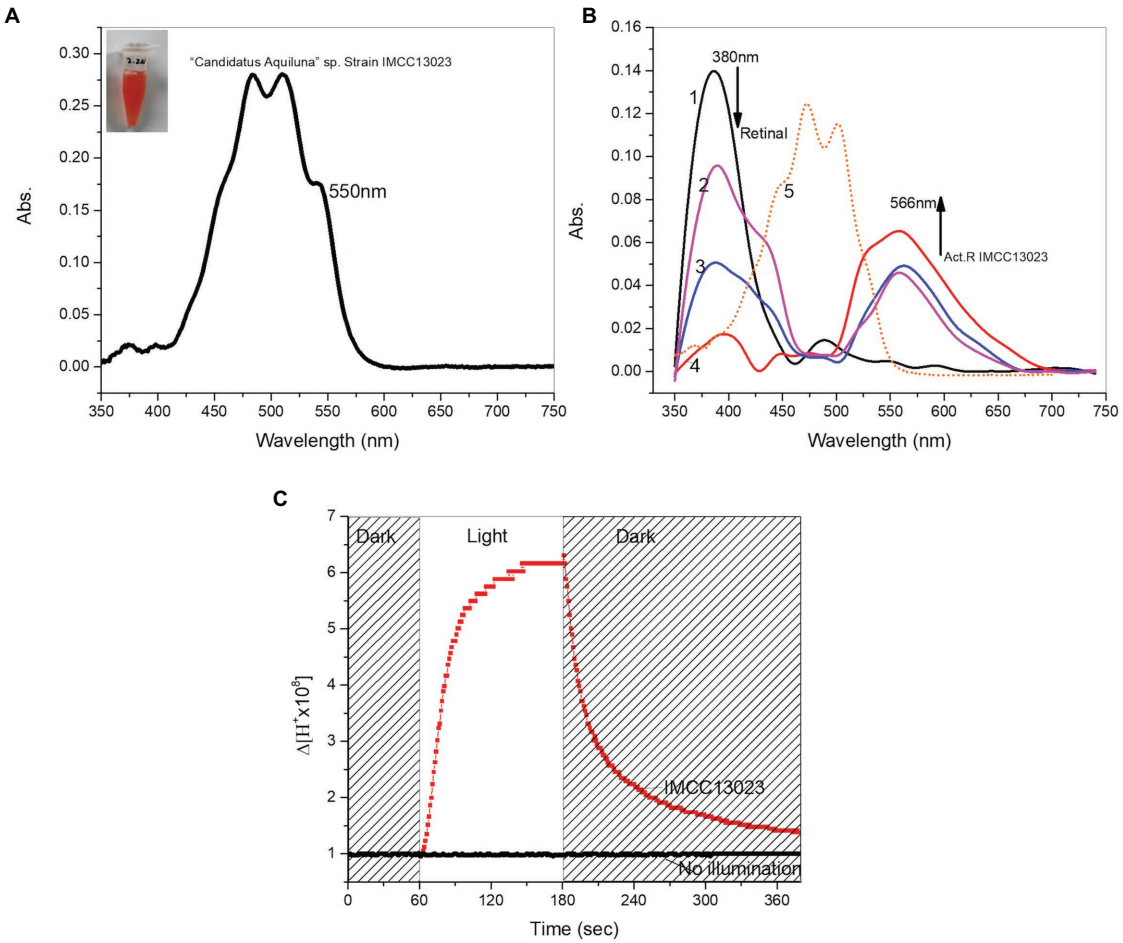

FIGURE 2 | Characterization of ActR-13023 in *Candidatus aquiluna*. **(A)** *C. aquiluna* whole-cell spectrum (black) and expected ActR-13023 peak in the native cell (red). **(B)** Chromophore removal from *C. aquiluna* membrane and reconstitution with all-*trans*-retinal (1) membrane fraction with chromophore removed, (2) 1 h, (3) 24 h, and (4) 48 h after reconstitution, (5) carotenoid isolated from *C. aquiluna*. **(C)** Measurement of proton pumping potential of *C. aquiluna*.

in the blue region was also increased, suggesting the interaction of carotenoid. As shown in **Figure 2B**, the membrane of native cells showed minor absorption peaks in the blue region, suggesting that the endogenously synthesized carotenoid was retained in the membrane after retinal removal (**Figure 2B** graph 1). After 1 h of reconstitution (graph 2), a sharp peak was formed at 566 nm, and after 24 and 48 h (graphs 3 and 4, respectively), the absorbances in the blue region were increased. The carotenoid isolated from the native membrane formed peaks at 472 and 501 nm (**Figure 2** graph 5). In this study, the molecule was named "actinobacterial carotenoid" (**Figure 2B**). The natural expression of ActR-13023 revealed the importance of this protein since the corresponding gene was encoded in the genome even this strain genome is considerably compact (the summed length of the contigs is 1,359,862 bp, the smallest genome size ever reported for free-living actinobacteria, as of April 2012; Kang et al., 2012). The native cells were suspended in unbuffered solution (10 mM NaCl, 10 mM $MgSO_4$, and 10 μM $CaCl_2$), and light illumination to the sample induced acidification suggesting a light-driven outward proton-pumping activity (**Figure 2C**). Collectively, the findings indicated that ActR-13023 inherently functions as an outward proton pump for phototrophy.

Heterologous Expression and Biochemical Characterization of ActR-13023

The opsin apoprotein cannot absorb light independently in the absence of a chromophore. Therefore, we hypothesized that the strain IMCC13023 could naturally synthesize retinal as a chromophore for apo-actinorhodopsin (holo-ActR). The *Actinobacteria* genome harbors a bacterio-opsin related protein homolog (*blh*) gene that encodes a β-carotene 15,15′ dioxygenase along with carotenoid synthesis genes and the *actR* gene. Transcription analysis of acI actinobacteria (acI lineage of the phylum Actinobacteria, the most abundant bacterial group in most freshwater lakes; Kang et al., 2017) revealed that all retinal and carotenoid operon genes were transcribed and *actR* was among the most highly transcribed acI genes (Dwulit-Smith et al., 2018). Genome comparison of *Candidatus Aquiluna* sp. IMCC13023 to other acI actinobacteria facilitated identifying

the chromophore's synthesis pathway and retinal-producing β-carotene dioxygenase (accession no. WP_007542589.1), suggesting the presence of the natively synthesized dual chromophores retinal/carotenoid (**Supplementary Figures S1A**, **S2**). Heterologously expressed ActR-13023 in *E. coli* cultured in the presence of an exogenously supplemented or endogenously synthesized retinal showed the identical optical spectra with λmax at 565 nm pH = 7.0 when the protein was solubilized in detergent solution (**Figure 3A**). The *blh* gene from strain IMCC13023 was cloned in a pACK-*blh* plasmid together with other genes encoding proteins participating in the β-carotene-producing pathway. The expression of pAC-BETA (Cunningham et al., 1996) produced β-carotene with maximum absorption at 449 nm (orange). The pigment was treated with β-carotene 15,15′ dioxygenase, which led to the conversion of β-carotene to retinol (red) with λmax at 328 nm; the absorbance of reference retinol was measured for comparison (green; **Figure 3B**). The co-expression of *actR* and *blh* genes

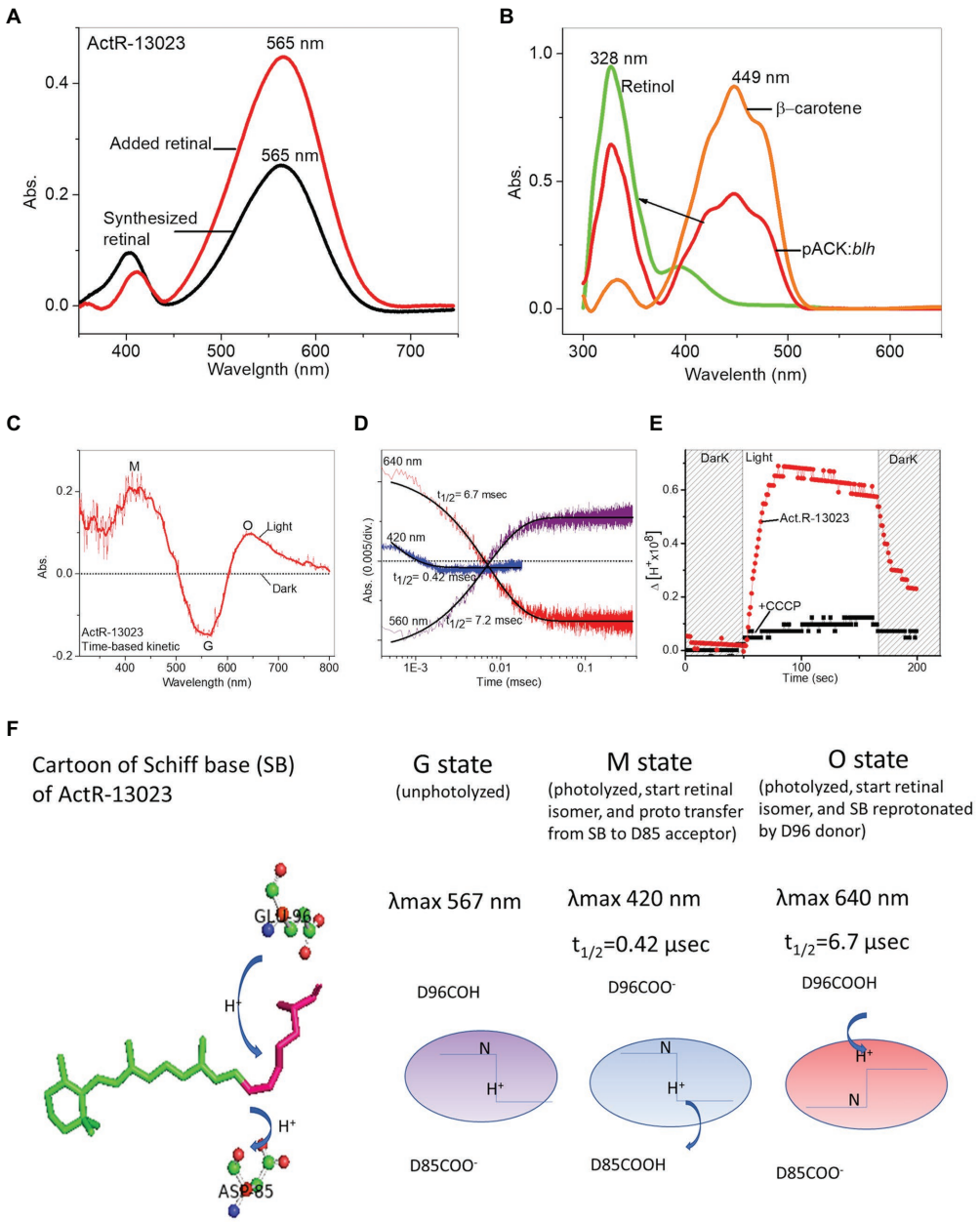

FIGURE 3 | Characterization of heterologously expressed ActR-13023. **(A)** Expression with additional all-*trans*-retinal (red) and bio-synthesized retinal (black). **(B)** Retinol conversion from β-carotene using the enzyme encoded by the *C. aquiluna blh* gene. **(C)** A light-induced differential spectrum of purified ActR-13023. **(D)** Flash-induced transient absorbance changes during the photocycle. **(E)** Proton pumping activity of heterologously expressed ActR-13023. **(F)** Illustration of naturally functional ActR-13023 as a light-driven outward proton pump.

generated functional actinorhodopsin, and light-induced differential spectra of ActR-13023 revealed the light-dependent molecular photochemical changes. Upon light absorption, ActR-13023 entered a photocycle with the formation of several distinct photo intermediates (typical intermediates are M and O) initiated by the isomerization of all-*trans*-retinal to 13-*cis*-retinal. This cycle has been associated with the proton pumping mechanism (Lanyi, 1993). The ActR-13023 light-induced differential spectra showed a clear accumulation of O intermediate with absorption at 645 nm, along with depletion of the ground-state absorption at 560 nm and increase in the M intermediate components with absorption at 420 nm (**Figure 3C**). Photocycle measurement revealed the rapid formation of kinetic intermediates [M intermediate ($t_{1/2} \approx 0.42$ ms), O intermediate ($t_{1/2} \approx 6.7$ ms), and return to ground state ($t_{1/2} \approx 7.2$ ms)], which is indicative of the highly efficient proton-pumping activity (**Figure 3D**). ActR-13023-expressed *E. coli* cell showed acidification upon light illumination followed by a dark-light cycle, and the proton pumping activity was abolished upon treatment with carbonyl cyanide m-chlorophenyl hydrazine (Sapra et al., 2003; **Figure 3E**). Therefore, based on the changes in the differential spectrum and acidification of both native cell and ActR-13023 containing *E. coli*, we concluded that ActR-13023 is a natural light-driven outward proton pump functioning with natively synthesized retinal (**Figure 3F**).

The high-resolution crystal structure of bacteriorhodopsin revealed the hydrogen bond network's characteristics and the critical mechanism underlying proton pumping associated with the retinal SB, a proton acceptor (D85), and a proton donor (D96). A mutation in ActR-13023 at the proton acceptor and donor positions inhibited the light-driven proton-pumping activity and significantly altered the protein kinetics. D85N mutant led to the loss of protonation ability from SB. The first essential process for proton transfer from SB to D85 led to the M intermediate. In the case of the D85N mutant, no proton acceptor can be protonated by SB, so no M intermediate was detected in the light-induced spectra. Proton uptake from the proton donor D96 occurred during the transition from the M to O intermediate. When wild-type ActR-13023 was used, the O intermediate absorbed light at 640 nm. However, this absorbance was not observed for the E96Q mutant. Functional mutation studies on ActR-13023 revealed a typical primary proton donor and proton acceptor in the pumping mechanism. The mutants expressed no acidification due to the absence of proton translocation across the membrane, which indicated the central roles of these residues in the hydrogen network and the pumping mechanism. The maximum absorption of ActR-13023 depends on the environmental pH, and pKa of the primary proton acceptor can be calculated in pH titration experiments. The pH-dependent shifting of ActR-13023 absorbance allowed us to calculate the pKa of SB counter-ion residues (D85). ActR-13023 showed maximum absorption at 570 nm at pH 4.0 and 550 nm at pH 10.0. The pKa $\approx$ 7.81 of SB counter-ion D85 as primary proton acceptor was shown in **Figure 4E**. In contrast, the pKa of the D85N mutant could not be calculated (notably, the small maximum shifted were observed due to the absence of protonatable acceptor residue), and the pKa for the E96Q mutant was 7.67 (**Figure 4**).

ActR-13023 Is a Dual Chromophore Rhodopsin

The proton pumping activity of heterologously expressed ActR-13023 is comparable to that of other proton-pumping rhodopsins. Proteorhodopsin (PR) was expressed, and the protein expression level and proton pumping of the two rhodopsins were shown in **Supplementary Figure S5**. Interestingly, the native cells exhibited more buffer acidification in similar light sources and optical cell density at 600 nm. The orange color of the native cell and carotenoid-related genes in the genome suggested carotenoids' expression in this strain. Like, XR from *S. ruber* that assembles with salinixanthin as a secondary light-harvesting antenna, ActR-13023 was expected for the possibility of carotenoids binding, which may functionally maximize its potential. A carotenoid molecule isolated from the strain showed a molecular weight of 591.4946 mz, and the absorption peaks were formed at 472 and 501 nm in the UV-visible spectrum (**Figure 2B**, graph 5). Thermodynamic insights from isothermal titration calorimetry experiments indicated a significant interaction between ActR-13023 and the carotenoid. The isolated carotenoid was titrated against ActR-13023 (as a ligand and receptor), and the essential enthalpy changes were measured after every injection. The titration profile could be best fitted using a nonlinear least-squares approach to the "one set of sites" binding model, which yielded the association constant (K_a), the stoichiometry of binding (n), thermodynamic parameters, enthalpy of binding (ΔH), and entropy of binding (ΔS) values. Measurements at 30°C yielded the following values for K_a, n, ΔH, and ΔS: 2.72 ($\pm$0.8) $\times$ 10^4 M^{-1}, 0.751 ($\pm$0.03), -6.72×10^4 ($\pm$0.83) cal.mol^{-1}, and -201 cal.mol^{-1}.deg.$^{-1}$, respectively, and the calculated changes in Gibb's free energy (ΔG) was -6.26 kcal/mol^{-1} (**Figure 5A**). After the isothermal titration calorimetry experiment, the samples were speculated by UV-VIS spectrometer, and the absorption spectrum showed carotenoid binding characteristic where maximum absorption was observed at 512 nm accompany the shoulder shape (**Figure 5B**). These results indicated that purified ActR-13023 could be reconstituted with isolated carotenoids. We tried to express ActR-13023 by exogenously added the carotenoid. However, after purification, no binding complex could be isolated. This indicated that the carotenoid barely penetrated the cellular membrane, so the carotenoid was added during spheroplast preparation (see Materials and Methods section) to maximize the possibility of penetration, and samples were incubated overnight for the reaction. The absorption spectra of spheroplast showed optical shifts owing to carotenoid engagement. The ActR-13023 spheroplast showed maximum absorption at 557 nm, which shifted to 516 nm upon carotenoid binding. The addition of carotenoids gave no significant enhancement to total pH change in buffer acidification but notably improved the initial pumping rate of ActR-13023 (**Figure 5C**). In contrast, when salinixanthin was added to the samples, we did not see the enhancement,

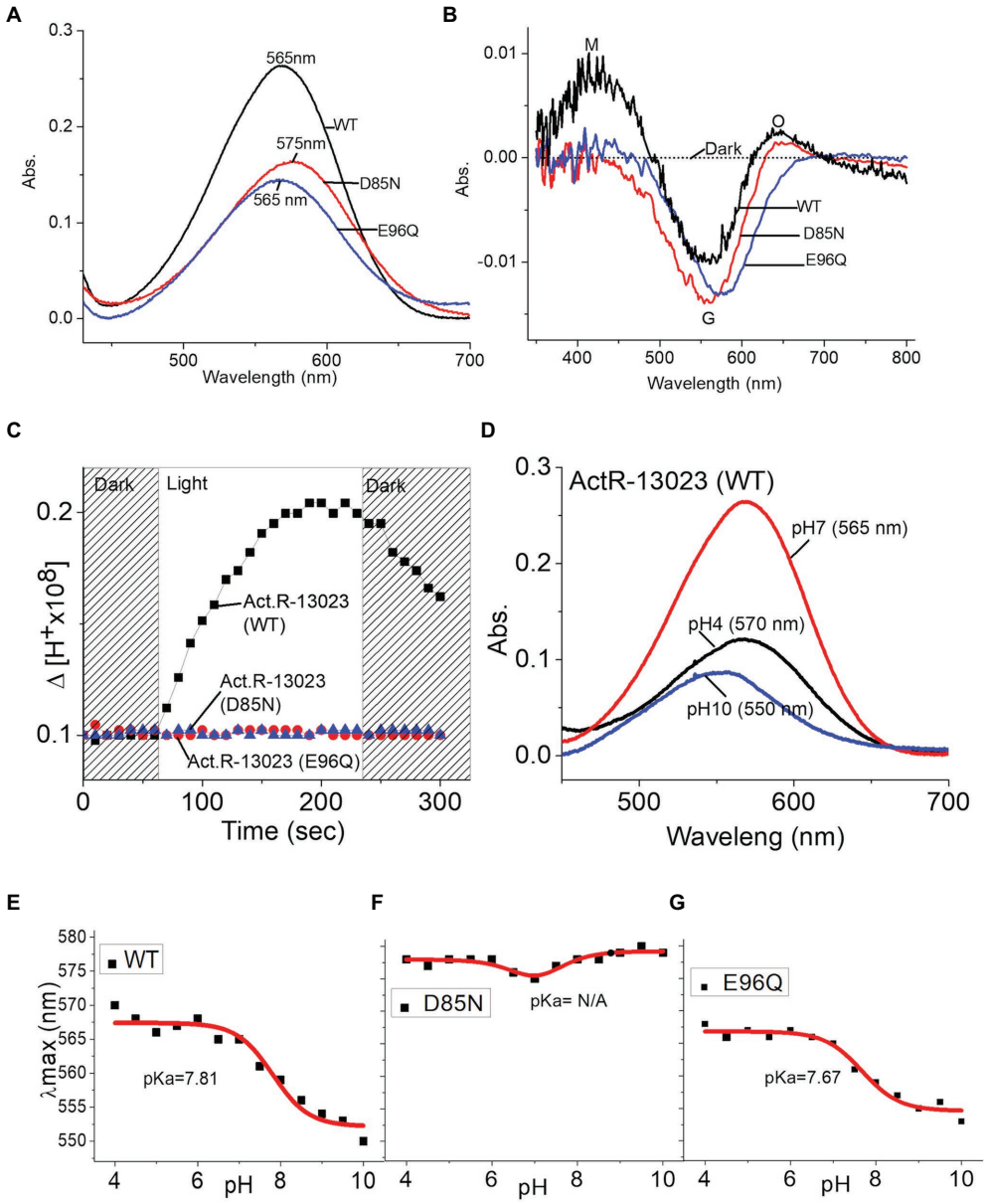

FIGURE 4 | Mutation studies of ActR-13023, wild-type ActR-13023, D85N, and E96Q mutants. **(A)** UV-visible spectra. **(B)** Light-induced differential spectra. **(C)** Proton pumping activities. pH titration and pKa calculation: **(D)** ActR-13023 spectra at pH 4, 7, and 10, **(E)** pKa value of ActR-13023, **(F)** pKa value of the D85N mutant, and **(G)** pKa value of the E96Q mutant.

but a lower proton pumping rate was observed (**Supplementary Figure S5**). This gave an interesting question about carotenoid interaction with rhodopsin and its impacts on protein function. However, further study is required to answer this phenomenon.

DISCUSSION

The high abundance of actinobacteria in aquatic habitats, seawater, sea ice, and freshwater has led to establishing a cellular adaptation model for energy scavenging fitness. The actinorhodopsin-encoding gene has been detected in the compact genome of *Candidatus Aquiluna* sp. IMCC13023, along with the retinal and carotenoid biosynthesis genes. Our results validated the importance of ActR in actinobacteria for solar energy capture and indicated its utility under nutrient stress. The biosynthetic pathways of retinal and its carotenoid precursors have been reported based on findings from the assessment of single-cell genome and metagenome sequences of freshwater-isolated actinobacteria categorized in the acI lineage clades A and B (Dwulit-Smith et al., 2018). Unlike other bacteria that

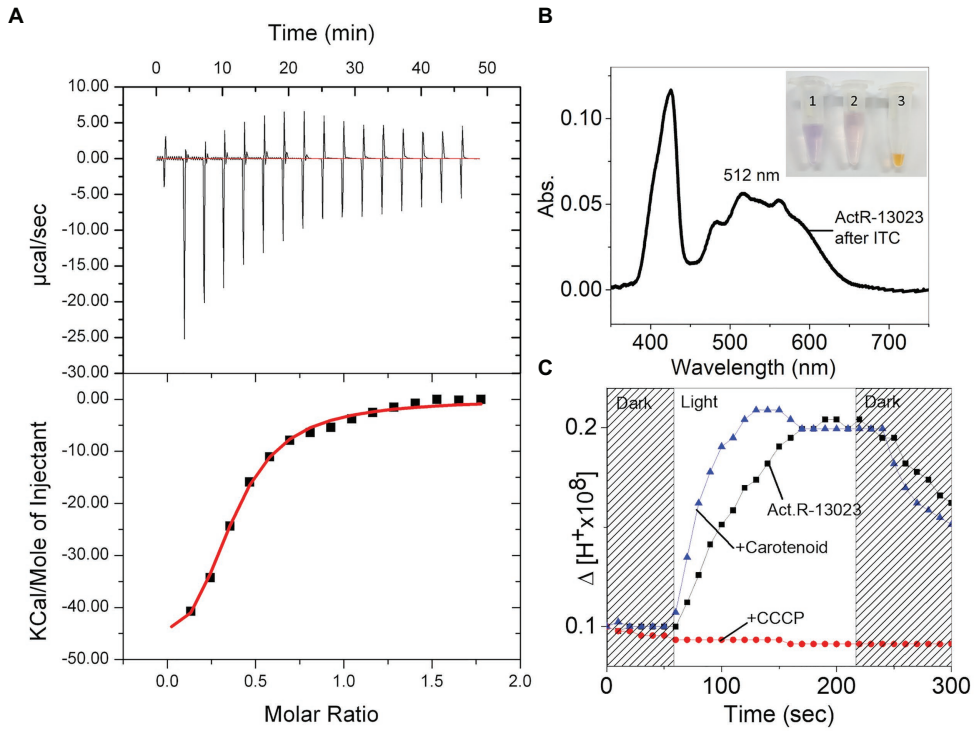

FIGURE 5 | Interaction between ActR-13023 and actinobacterial carotenoid. **(A)** Isothermal titration calorimetry (ITC) of ActR-13023 and the carotenoid. **(B)** UV-Vis spectrum of ActR-13023 after ITC experiment; the samples were shown in e-tube (1) purifiedActR-13023, (2) ActR-13023 after ITC experiment with carotenoid, and (3) the carotenoid as the ligand. **(C)** Comparison of proton pumping in the presence, absence of the carotenoid, and ActR-13023 treated with carbonyl cyanide m-chlorophenyl hydrazine (+CCCP).

encode opsins but may acquire retinal exogenously, actinorhodopsins had their chromophore synthesis machinery.

Interestingly, ActR-13023 is natively expressed with retinal and interacts with natively synthesized carotenoids as secondary chromophores. Seven genes in the actinobacteria genome are considered to encode proteins associated with retinal synthesis. Other genes that encode proteins for the synthesis of complex carotenoids, such as the β-carotene ketolase gene, have also been detected (Klassen, 2010). Consequently, ActR-13023 might be bound to retinal and complex carotenoids. The 4 keto-ring of complex carotenoids salinixanthin, canthaxanthin, and echinenone have been reported to be critical components for rhodopsin binding (Balashov et al., 2010). However, the co-expression of ActR-13023 and canthaxanthin in *E. coli* did not lead to the production of a binding complex (data not shown). We also stimulated ActR-13023 with canthaxanthin for evaluating its binding properties. Molecular docking studies suggested that the docking surface was in a position like that in XR; binding with salinixanthin was promoted; however, the binding constant could not be estimated (**Supplementary Figure S1C**). The carotenoid's molecular weight isolated from the strain showed 591.4946 in molecular mass, which was greater than those of lycopene (536.8) and canthaxanthin (564.8), suggesting a distinct structure of this carotenoid. AcI actinobacterial gene transcription has been challenging to study. While the isolation of several carotenoid-related genes from the strain had been attempted, but the carotenoid had been unsuccessful. Light-driven outward proton pumping by native cell was significantly stronger than that in ActR-13023-overexpressed *E. coli*, which suggested the carotenoid's critical role for light-driven proton pumping by ActR-13023. Molecular docking results suggested the interaction of canthaxanthin containing helices E, F, and G. However, the titration of canthaxanthin with purified ActR-13023 and co-expression did not show the binding property. This suggested that despite a similar binding pocket on helices E and F, microbial rhodopsin might exhibit selectivity toward secondary chromophores. The carotenoid from the strain may contain a unique structure compatible with ActR-13023. It will be interesting to elucidate the mechanism of dual chromophores (retinal/carotenoid) in actinorhodopsin. Our results showed that the actinobacterial carotenoid barely penetrated the cell membrane; therefore, the secondary antenna might be synthesized within the cell, or a specific carotenoid uptake mechanism may be acquired to obtain it *via* exogenous sources. Notably, ActR-13023 followed a rapid photocycle with the return to the ground state with a half-time of 7.2 msec. It exhibited proton pumping activity comparable to that of other well-known proton pumps such as proteorhodopsin. The potential of actinorhodopsin with dual chromophores in the aquatic environment on the earth's surface may play a critical role in solar energy capture. Effective solar bio-energy conversion may

serve as a helpful strategy against climate change issues, besides having other applications, and the role of ActR for solar energy capture in microbial communities could be the contribution to the ecosystem.

DATA AVAILABILITY STATEMENT

The original contributions presented in the study are included in the article/**Supplementary Material**, further inquiries can be directed to the corresponding author.

AUTHOR CONTRIBUTIONS

KC and K-HJ developed the concept and supervised the experiments. SK provided support in the cloning and plasmid preparation experiments. J-gS, S-GC, K-WK, J-HK, SM, and H-SC provided support in the protein expression and purification experiments. All authors contributed to the article and approved the submitted version.

FUNDING

The Basic Science Research Program supported this work through the National Research Foundation of Korea (NRF), funded by the Ministry of Education (2018R1A6A1A03024940, 2019R1F1A1061031, and NRF-2020R1A2C2008197).

ACKNOWLEDGMENTS

We thank Jang-Cheon Cho, Dept. Biology, Inha University, Korea for providing *Candidatus aquiluna* sp. strain IMCC13023. We would also like to thank Editage (www.editage.com) for English language editing.

SUPPLEMENTARY MATERIAL

The Supplementary Material for this article can be found online at: https://www.frontiersin.org/articles/10.3389/fmicb.2021.652328/full#supplementary-material

REFERENCES

Allgaier, M., and Grossart, H.-P. (2006). Diversity and seasonal dynamics of *Actinobacteria* populations in four lakes in northeastern Germany. *Appl. Environ. Microbiol.* 72, 3489–3497. doi: 10.1128/AEM.72.5.3489-3497.2006

Balashov, S. P., Imasheva, E. S., Choi, A. R., Jung, K.-H., Liaaen-Jensen, S., and Lanyi, J. K. (2010). Reconstitution of *gloeobacter* rhodopsin with echinenone: role of the 4-keto group. *Biochemistry* 49, 9792–9799. doi: 10.1021/bi1014166

Bamann, C., Bamberg, E., Wachtveitl, J., and Glaubitz, C. (2014). Proteorhodopsin. *Biochim. Biophys. Acta* 1837, 614–625. doi: 10.1016/j.bbabio.2013.09.010

Bikadi, Z., and Hazai, E. (2009). Application of the PM6 semi-empirical method to modeling proteins enhances docking accuracy of AutoDock. *J. Cheminform.* 1:15. doi: 10.1186/1758-2946-1-15

Cho, J.-C., and Giovannoni, S. J. (2004). Cultivation and growth characteristics of a diverse group of oligotrophic marine gammaproteobacteria. *Appl. Environ. Microbiol.* 70, 432–440. doi: 10.1128/aem.70.1.432-440.2004

Claverías, F. P., Undabarrena, A., González, M., Seeger, M., and Cámara, B. (2015). Culturable diversity and antimicrobial activity of *Actinobacteria* from marine sediments in Valparaíso bay, Chile. *Front. Microbiol.* 6:737. doi: 10.3389/fmicb.2015.00737

Cunningham, F. X., Pogson, B., Sun, Z., McDonald, K. A., DellaPenna, D., and Gantt, E. (1996). Functional analysis of the beta and epsilon lycopene cyclase enzymes of *Arabidopsis* reveals a mechanism for control of cyclic carotenoid formation. *Plant Cell* 8, 1613–1626.

Dwulit-Smith, J. R., Hamilton, J. J., Stevenson, D. M., He, S., Oyserman, B. O., Moya-Flores, F., et al. (2018). acI *Actinobacteria* assemble a functional actinorhodopsin with natively synthesized retinal. *Appl. Environ. Microbiol.* 84, e01678–e01618. doi: 10.1128/AEM.01678-18

Ernst, O. P., Lodowski, D. T., Elstner, M., Hegemann, P., Brown, L. S., and Kandori, H. (2014). Microbial and animal rhodopsins: structures, functions, and molecular mechanisms. *Chem. Rev.* 114, 126–163. doi: 10.1021/cr4003769

Fernández-Gómez, B., Díez, B., Polz, M. F., Arroyo, J. I., Alfaro, F. D., Marchandon, G., et al. (2019). Bacterial community structure in a sympagic habitat expanding with global warming: brackish ice brine at 85–90 °N. *ISME J.* 13, 316–333. doi: 10.1038/s41396-018-0268-9

Gao, X., Xu, H., Zhu, Z., She, Y., and Ye, S. (2020). Improved production of echinenone and canthaxanthin in transgenic *Nostoc sp*. PCC 7120 overexpressing a heterologous *crtO* gene from *Nostoc flagelliforme*. *Microbiol. Res.* 236:126455. doi: 10.1016/j.micres.2020.126455

Heberle, J., Deupi, X., and Schertler, G. (2014). Retinal proteins - you can teach an old dog new tricks. *Biochim. Biophys. Acta* 1837, 531–532. doi: 10.1016/j.bbabio.2014.02.019

Jang, H.-J., Yoon, S.-H., Ryu, H.-K., Kim, J.-H., Wang, C.-L., Kim, J.-Y., et al. (2011). Retinoid production using metabolically engineered *Escherichia coli* with a two-phase culture system. *Microb. Cell Factories* 10:59. doi: 10.1186/1475-2859-10-59

Jensen, P. R., and Lauro, F. M. (2008). An assessment of actinobacterial diversity in the marine environment. *Antonie Van Leeuwenhoek* 94, 51–62. doi: 10.1007/s10482-008-9239-x

Kaminski, G., and Jorgensen, W. L. (1996). Performance of the AMBER94, MMFF94, and OPLS-AA force fields for modeling organic liquids. *J. Phys. Chem.* 100, 18010–18013.

Kang, I., Kim, S., Islam M, R., and Cho, J.-C. (2017). The first complete genome sequences of the acI lineage, the most abundant freshwater *Actinobacteria*, obtained by whole-genome-amplification of dilution-to-extinction cultures. *Sci. Rep.* 7:42252. doi: 10.1038/srep42252

Kang, I., Lee, K., Yang, S.-J., Choi, A., Kang, D., Lee, Y. K., et al. (2012). Genome sequence of "*Candidatus Aquiluna*" sp. strain IMCC13023, a marine member of the *Actinobacteria* isolated from an arctic fjord. *J. Bacteriol.* 194, 3550–3551. doi: 10.1128/JB.00586-12

Khorana, H. G., Gerber, G. E., Herlihy, W. C., Gray, C. P., Anderegg, R. J., Nihei, K., et al. (1979). Amino acid sequence of bacteriorhodopsin. *Proc. Natl. Acad. Sci. U. S. A.* 76, 5046–5050. doi: 10.1073/pnas.76.10.5046

Klassen, J. L. (2010). Phylogenetic and evolutionary patterns in microbial carotenoid biosynthesis are revealed by comparative genomics. *PLoS One* 5:e11257. doi: 10.1371/journal.pone.0011257

Lanyi, J. K. (1993). Pathways of proton transfer in the light-driven pump bacteriorhodopsin. *Experientia* 49, 514–517. doi: 10.1007/BF01955153

Luecke, H., Schobert, B., Stagno, J., Imasheva, E. S., Wang, J. M., Balashov, S. P., et al. (2008). Crystallographic structure of xanthorhodopsin, the light-driven proton pump with a dual chromophore. *PNAS* 105, 16561–16565. doi: 10.1073/pnas.0807162105

Maresca, J. A., Keffer, J. L., Hempel, P. P., Polson, S. W., Shevchenko, O., Bhavsar, J., et al. (2019). Light modulates the physiology of nonphototrophic *Actinobacteria*. *J. Bacteriol.* 201, e00740–e00718. doi: 10.1128/JB.00740-18

Maresca, J. A., Keffer, J. L., and Miller, K. J. (2016). Biochemical analysis of microbial rhodopsins. *Curr. Protoc. Microbiol.* 41, 1F.4.1–1F.4.18. doi: 10.1002/cpmc.5

Miranda, M. R. M., Choi, A. R., Shi, L., Bezerra, A. G., Jung, K.-H., and Brown, L. S. (2009). The Photocycle and proton translocation pathway in

a cyanobacterial ion-pumping rhodopsin. *Biophys. J.* 96, 1471–1481. doi: 10.1016/j.bpj.2008.11.026

Morris, G. M., Goodsell, D. S., Halliday, R. S., Huey, R., Hart, W. E., Belew, R. K., et al. (1998). Automated docking using a Lamarckian genetic algorithm and an empirical binding free energy function. *J. Comput. Chem.* 19, 1639–1662. doi: 10.1002/(SICI)1096-987X(19981115)19:14<1639::AID-JCC10>3.0.CO;2-B

Morris, G. M., Huey, R., Lindstrom, W., Sanner, M. F., Belew, R. K., Goodsell, D. S., et al. (2009). AutoDock4 and AutoDockTools4: automated docking with selective receptor flexibility. *J. Comput. Chem.* 30, 2785–2791. doi: 10.1002/jcc.21256

Morris, R. M., Nunn, B. L., Frazar, C., Goodlett, D. R., Ting, Y. S., and Rocap, G. (2010). Comparative metaproteomics reveals ocean-scale shifts in microbial nutrient utilization and energy transduction. *ISME J.* 4, 673–685. doi: 10.1038/ismej.2010.4

Nakamura, S., Kikukawa, T., Tamogami, J., Kamiya, M., Aizawa, T., Hahn, M. W., et al. (2016). Photochemical characterization of actinorhodopsin and its functional existence in the natural host. *Biochim. Biophys. Acta* 1857, 1900–1908. doi: 10.1016/j.bbabio.2016.09.006

Palczewski, K. (2006). G protein–coupled receptor rhodopsin. *Annu. Rev. Biochem.* 75, 743–767. doi: 10.1146/annurev.biochem.75.103004.142743

Pinhassi, J., DeLong, E. F., Béjà, O., González, J. M., and Pedrós-Alió, C. (2016). Marine bacterial and archaeal ion-pumping rhodopsins: genetic diversity, physiology, and ecology. *Microbiol. Mol. Biol. Rev.* 80, 929–954. doi: 10.1128/MMBR.00003-16

Pushkarev, A., Hevroni, G., Roitman, S., Shim, J., Choi, A., Jung, K.-H., et al. (2018). The use of a chimeric rhodopsin vector for the detection of new proteorhodopsins based on color. *Front. Microbiol.* 9:439. doi: 10.3389/fmicb.2018.00439

Rappé, M. S., Suzuki, M. T., Vergin, K. L., and Giovannoni, S. J. (1998). Phylogenetic diversity of Ultraplankton plastid small-subunit rRNA genes recovered in environmental nucleic acid samples from the Pacific and Atlantic coasts of the United States. *Appl. Environ. Microbiol.* 64, 294–303. doi: 10.1128/AEM.64.1.294-303.1998

Sapra, R., Bagramyan, K., and Adams, M. W. W. (2003). A simple energy-conserving system: proton reduction coupled to proton translocation. *PNAS* 100, 7545–7550. doi: 10.1073/pnas.1331436100

Servin, J. A., Herbold, C. W., Skophammer, R. G., and Lake, J. A. (2008). Evidence excluding the root of the tree of life from the *Actinobacteria*. *Mol. Biol. Evol.* 25, 1–4. doi: 10.1093/molbev/msm249

Sharma, A. K., Sommerfeld, K., Bullerjahn, G. S., Matteson, A. R., Wilhelm, S. W., Jezbera, J., et al. (2009). Actinorhodopsin genes discovered in diverse freshwater habitats and among cultivated freshwater *Actinobacteria*. *ISME J.* 3, 726–737. doi: 10.1038/ismej.2009.13

Sharma, A. K., Zhaxybayeva, O., Papke, R. T., and Doolittle, W. F. (2008). Actinorhodopsins: proteorhodopsin-like gene sequences found predominantly in non-marine environments. *Environ. Microbiol.* 10, 1039–1056. doi: 10.1111/j.1462-2920.2007.01525.x

Shichida, Y., and Matsuyama, T. (2009). Evolution of opsins and phototransduction. *Philos. Trans. R. Soc. Lond. Ser. B Biol. Sci.* 364, 2881–2895. doi: 10.1098/rstb.2009.0051

Solis, F. J., and Wets, R. J.-B. (1981). Minimization by random search techniques. *Math. Oper. Res.* 6, 19–30. doi: 10.1287/moor.6.1.19

Spassov, V. Z., Luecke, H., Gerwert, K., and Bashford, D. (2001). pKa calculation suggests storage of an excess proton in a hydrogen-bonded water network in bacteriorhodopsin. *J. Mol. Biol.* 312, 203–219. doi: 10.1006/jmbi.2001.4902

Spudich, J. L., Yang, C. S., Jung, K. H., and Spudich, E. N. (2000). Retinylidene proteins: structures and functions from archaea to humans. *Annu. Rev. Cell Dev. Biol.* 16, 365–392. doi: 10.1146/annurev.cellbio.16.1.365

Subramani, R., and Aalbersberg, W. (2013). Culturable rare Actinomycetes: diversity, isolation, and marine natural product discovery. *Appl. Microbiol. Biotechnol.* 97, 9291–9321. doi: 10.1007/s00253-013-5229-7

Wang, W.-W., Sineshchekov, O. A., Spudich, E. N., and Spudich, J. L. (2003). Spectroscopic and photochemical characterization of a deep ocean proteorhodopsin. *J. Biol. Chem.* 278, 33985–33991. doi: 10.1074/jbc.M305716200

Waschuk, S. A., Bezerra, A. G., Shi, L., and Brown, L. S. (2005). Leptosphaeria rhodopsin: Bacteriorhodopsin-like proton pump from a eukaryote. *Proc. Natl. Acad. Sci.* 102, 6879–6883. doi: 10.1073/pnas.0409659102

Yang, J., and Guo, L. (2014). Biosynthesis of β-carotene in engineered *E. coli* using the MEP and MVA pathways. *Microb. Cell Factories* 13:160. doi: 10.1186/s12934-014-0160-x

Zhu, W., Lan, Y., Lou, X., Han, N., Ran, T., Xu, L., et al. (2013). Isolation of proteorhodopsin-bearing bacterium JL-3 from fresh water and characterization of the proteorhodopsin. *FEMS Microbiol. Lett.* 344, 10–17. doi: 10.1111/1574-6968.12144

Conflict of Interest: The authors declare that the research was conducted in the absence of any commercial or financial relationships that could be construed as a potential conflict of interest.

frontiers in Microbiology

METHODS
published: 29 April 2021
doi: 10.3389/fmicb.2021.654065

Recording and Simulating Proton-Related Metabolism in Bacterial Cell Suspensions

Heribert Cypionka and Jan-Ole Reese*

Institute for Chemistry and Biology of the Marine Environment, Carl-von-Ossietzky University of Oldenburg, Oldenburg, Germany

Proton release and uptake induced by metabolic activities were measured in non-buffered cell suspensions by means of a pH electrode. Recorded data were used for simulating substrate turnover rates by means of a new freeware app (*proton.exe*). The program applies Michaelis-Menten or first-order kinetics to the metabolic processes and allows for parametrization of simultaneously ongoing processes. The simulation includes changes of the transmembrane ΔpH, membrane potential and ATP gains, and demonstrates the principles of chemiosmotic energy conservation. In our experiments, the versatile sulfate-reducing bacterium *Desulfovibrio desulfuricans* CSN (DSM 9104) was used as model organism. We analysed sulfate uptake by proton-sulfate symport, scalar alkalinization by sulfate reduction to sulfide, as well as nitrate and nitrite reduction to ammonia, and electron transport-coupled proton translocation. Two types of experiments were performed: In oxidant pulse experiments, cells were kept under H_2, and micromolar amounts of sulfate, nitrate or nitrite were added. For reductant pulse experiments, small amounts of H_2-saturated KCl were added to cells incubated under N_2 with an excess of one of the above-mentioned electron acceptors. To study electron-transport driven proton translocation, the membrane potential was neutralized by addition of KSCN (100 mM). H^+/e^- ratios of electron-transport driven proton translocation were calculated by simulation with *proton.exe*. This method gave lower but more realistic values than logarithmic extrapolation. We could verify the kinetic simulation parameters found with *proton.exe* using series of increasing additions of the reactants. Our approach allows for studying a broad variety of proton-related metabolic activities at micromolar concentrations and time scales of seconds to minutes.

Keywords: vectorial proton translocation, dissimilatory sulfate reduction, dissimilatory nitrate reduction to ammonia, ATP synthase activity, Desulfovibrio desulfuricans, Michaelis-Menten kinetics, proton-sulfate symport

OPEN ACCESS

Edited by:
Catarina M. Paquete, Institute of Chemical and Biological Technology, New University of Lisbon, Portugal

Reviewed by:
Kai Waldemar Finster, Aarhus University, Denmark
Bradley Gary Lusk, Science the Earth Mesa, United States

****Correspondence:***
Heribert Cypionka
heribert.cypionka@uni-oldenburg.de

Specialty section:
This article was submitted to Microbial Physiology and Metabolism, a section of the journal Frontiers in Microbiology

Received: *15 January 2021*
Accepted: *29 March 2021*
Published: *29 April 2021*

Citation:
Cypionka H and Reese J-O (2021) Recording and Simulating Proton-Related Metabolism in Bacterial Cell Suspensions. Front. Microbiol. 12:654065. doi: 10.3389/fmicb.2021.654065

INTRODUCTION

All living cells, mitochondria, chloroplasts or bacteria cause various types of pH changes. First, production or consumption of acidic or basic metabolites results in permanent pH effects. As such reactions change the amount of protons in the system they are named scalar. By far more common are vectorial processes which translocate protons or metabolites across a membrane without changing their overall amount. The resulting pH effects are transient and compensated

by counteracting cyclic transport processes. Some vectorial processes – named electroneutral – are not going along with a net charge transfer (e.g., transport of an anion A^- in symport with a single proton H^+). By contrast, electrogenic transport (e.g., symport of 2 H^+ per anion A^-) affects the electrical potential across the membrane. The most important electrogenic vectorial processes are proton translocation during respiration and photosynthesis, which build up the proton-motive force (pmf, composed of the trans-membrane proton gradient, and membrane potential). The pmf is then used to drive ATP conservation by the membrane-bound ATP synthase (or simply ATPase), which is also an electrogenic proton transport system. As the ATPase takes up 3–4 H^+ per ATP (Cross and Müller, 2004; Steigmüller et al., 2008; Petersen et al., 2012), which before have been pumped out driven by respiratory or photosynthetic electron transport, proton translocation across a membrane is the most common process in living cells. For example, a bacterium respiring a single molecule of glucose with oxygen gains about 30 ATP (Rich, 2003). This involves vectorial translocation of up to 120 protons by the respiratory chain, which will be taken up again by the ATPase. Thus, up to 240 protons per glucose are translocated across the membrane.

Scalar consumption or production of protons can easily by recorded by means of a pH electrode. Vectorial proton transport, however, often remains invisible as the cyclic compensation processes are rather fast. Particularly, electrogenic protons are drawn back immediately by the membrane potential. Therefore one has to neutralize the membrane potential for measurements of electrogenic proton translocation. For this purpose, potassium thiocyanate (KSCN) can be used (Mitchell and Moyle, 1967, 1968). The chaotropic SCN^- ion is known to be membrane permeant, thus compensating electrogenic processes and slowing down vectorial proton backflow.

In our study we analysed H_2 oxidation by the versatile sulfate reducer *Desulfovibrio desulfuricans*, that is able to utilize nitrate, nitrite, or sulfate as electron acceptor (Steenkamp and Peck, 1981; Seitz and Cypionka, 1986; Dilling and Cypionka, 1990). Both sulfate and nitrate reduction cause scalar alkalinization of the outer bulk medium. While nitrate reduction presumably proceeds in the periplasm (Marietou, 2016), sulfate reduction is known to proceed intracellularly. We have to consider several proton-related transport processes and scalar pH changes (**Figure 1**).

Desulfovibrio species possess periplasmic hydrogenases which allow for generating proton-motive force by a special mechanism named vectorial electron transport (**Figure 1F**, Badziong and Thauer, 1980; Marietou et al., 2005; Duarte et al., 2018). The 2 H^+ produced by H_2 oxidation remain in the periplasm and in equilibrium with the bulk medium until they are taken up via the ATPase (**Figure 1D**). The electrons derived from H_2

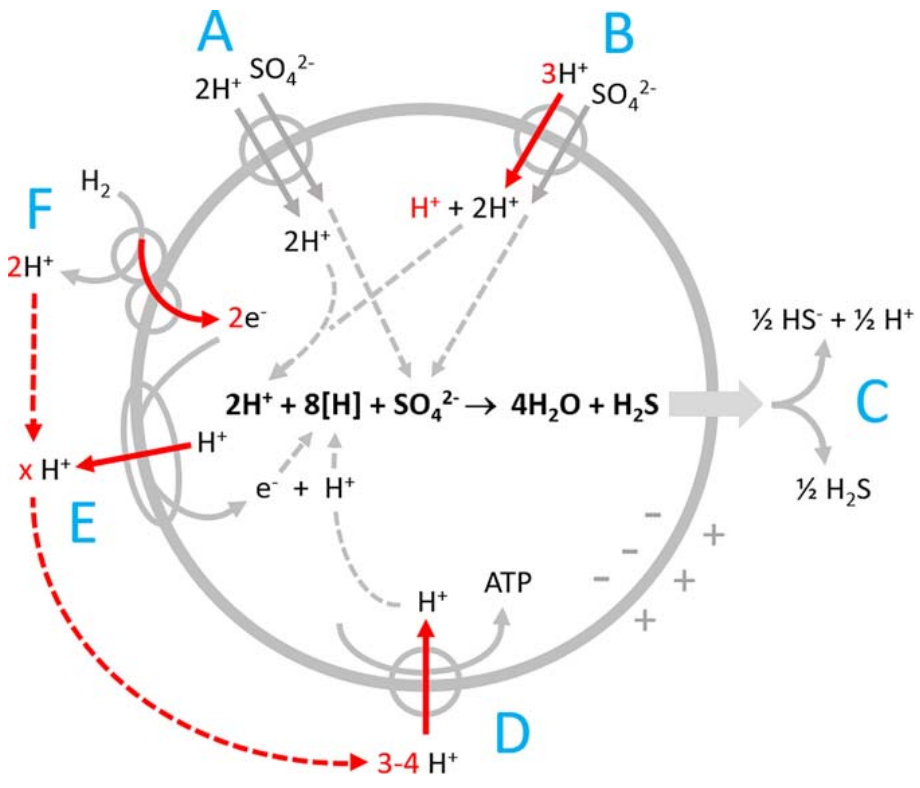

FIGURE 1 | Proton-related processes in *Desulfovibrio* during sulfate reduction with hydrogen. **(A)** Electroneutral proton-sulfate symport; **(B)** electrogenic proton-sulfate symport; **(C)** release of H_2S by diffusion and partial dissociation to $H^+ + HS^-$; **(D)** ATP synthase; **(E)** proton-translocating electron transport chain; and **(F)** periplasmic hydrogenase coupled to cytochrome c that channels electrons into the cell by vectorial electron transport. Red arrows point to electrogenic vectorial processes.

are channeled electrogenically into the cell via cytochrome c. The eight reducing equivalents ($H^+ + e^-$ or [H]) consumed during sulfate reduction are thus entering the cell via electrogenic processes (**Figure 1**). Additionally, sulfate reducers have proton-translocating electron transport chains (**Figure 1E**) allowing for translocation of more than 1 H^+/e^- (the maximum gain possible with vectorial electron transport).

The cells take up sulfate in symport with protons (Cypionka, 1987, 1989, 1994; Marietou et al., 2018). During growth with excess sulfate, the symport is electroneutral (**Figure 1A**), while sulfate limitation induces electrogenic symport, which is faster and allows for 1000-fold intracellular sulfate accumulation (Cypionka, 1995, **Figure 1B**). Sulfate reduction forms cytoplasmic HS^- and H_2S. Unlike HS^-, H_2S is an uncharged small molecule, and membrane permeant. It leaves the cell by diffusion (**Figure 1C**) and thereby exports two bound protons, just the amount taken up during electroneutral symport with sulfate. Sulfate reduction will therefore not affect the intracellular proton balance and pH. Outside, H_2S dissociates partially to 0.5 HS^- + 0.5 H^+ causing a slight acidification. The scalar alkalinization of the bulk medium of 1.5 H^+ per reduced sulfate is thus brought about by loss of 2 H^+ during the initial proton-sulfate symport and a compensation of 0.5 H^+ when the released H_2S partially dissociates in the bulk medium.

Sulfate transport and scalar alkalinization by sulfide production run simultaneously with the different electrogenic processes described in **Figures 1D–F**. To visualize and separately assess the electrogenic processes, we performed experiments with a neutralized membrane potential, and we added pulses of either electron acceptor or donor to non-buffered cell suspensions.

In order to simulate the simultaneously ongoing processes, we developed a freeware app (*proton.exe*) describing the metabolic activities by Michaelis-Menten kinetics or – for the ATPase rate – first order kinetics. With its help one can model the ATP gain and changes of the proton-motive force as well. The simulation is applicable to physiological studies with all bacteria that perform proton-related metabolism, could also be used with mitochondria, phototrophic bacteria or chloroplasts, and demonstrates chemiosmotic energy conservation in general.

MATERIALS AND METHODS

Organism and Cultivation

Experiments were carried out with *Desulfovibrio desulfuricans* strain CSN (DSM 9104), grown in a pH-controlled chemostat as described by Cypionka (1986), but without sulfide recording. The reservoir medium was the freshwater mineral medium described by Cypionka and Pfennig (1986), containing lactate (30 mM) and either sulfate or nitrate as an electron acceptor in limiting concentrations (10 mM). The culture was gassed with N_2. CO_2 was additionally supplied by the pH regulator set to maintain a pH of 7.0.

Preparation of Cell Suspensions

The chemostat outflow was collected on ice under N_2 atmosphere. Cells were harvested by centrifugation (9.950×*g*, 20 min, 4°C, Beckman JA-10), washed once and resuspended in N_2-saturated 150 mM KCl as described by Kirchhoff et al., 2018.

Set-Up for Physiological Experiments

Washed cells were diluted with KCl (150 mM) to obtain an OD_{436} (Biochrom Libra S12 UV/Vis Spectrophotometer) between 5 and 40 and a final volume of 2 ml. Experiments were carried out at 30°C in a reaction chamber equipped with a pH electrode (Inlab Micro, Mettler Toledo) and magnetic stirring. Anoxic conditions were obtained by sealing the chamber with a rubber stopper and flushing it with either H_2 or N_2 by fine cannulas for 10 min. After the suspension was filled into the chamber, it was bubbled with the respective gas and cells were allowed to equilibrate for 30 min. After this pre-incubation, only the headspace was flushed with gas. Proton translocation was measured using the method described in former studies (Cypionka et al., 1984; Fitz and Cypionka, 1989; Kirchhoff et al., 2018). The membrane potential of the cells was neutralized by addition of 100 mM KSCN. As described above, the membrane-permeable SCN^- anions are known to distribute over both sides of the membrane and compensates any electrogenic solute transport by migrating across the membrane. Two types of experiments were performed: In oxidant pulse experiments, cells were incubated under H_2 to provide an excess of the electron donor. Then micromolar pulses of various electron acceptors (Na_2SO_4, $NaNO_3$, and $NaNO_2$) were added from 1 mM N_2-flushed stock solutions. For reductant pulse experiments, the cell suspensions were preincubated with either Na_2SO_4 or $NaNO_3$ (10 mM) under N_2. Subsequently, H_2-saturated KCl (150 mM, assumed to contain 680 μM H_2 at 25°C, Crozier and Yamamoto, 1974) was used to add reductant pulses.

N_2-flushed 1 mM HCl and KOH (in 150 mM KCl) were added to calibrate the pH measurement and to titrate the suspension back to a neutral pH. pH changes were recorded by an AD converter (ADC-16, Pico Technology).

Short Description of *proton.exe*

pH recordings were simulated by means of *proton.exe.* This freeware app (Cypionka, 2021, see **Supplementary Material** for download and tutorial videos) allows for modeling of metabolic processes coupled to chemiosmotic energy conservation in bacterial cells, and generates simulated pH curves resulting from metabolic processes. A freeware app (Glass2k.exe) was used to get semi-transparent windows allowing for overlays of measured and simulated pH curves. For fitting the results with real pH data, one enters technical calibration parameters of the assay like buffering capacity, sensitivity, and response time of the pH electrode. Some biological parameters describe the cell suspension, e.g., cell number and size, membrane potential, number of protons translocated per electron by the electron transport system, as well as the numbers of protons taken up per ATP, and the ATPase rate. If some of these data are not known one can start with arbitrary numbers and learn how those change the simulated pH curves. *proton.exe* can be used without real data. Furthermore, it calculates ATP gains and changes of the proton-motive force. The metabolic reactions are started by (virtual or real) additions of micromolar pulses of electron donors or acceptors.

Uptake and metabolic rates (v) are assumed to depend on the substrate concentration [S] and calculated once per second assuming Michaelis-Menten kinetics according to:

$$V = (V_{max} \cdot [S]) / (K_M + [S])$$

with an estimated maximum rate V_{max}, and Michaelis constant K_M.

For proton uptake rates by the membrane ATPase first-order kinetics is assumed, i.e., the dependence on the proton gradient across the membrane (ΔpH, difference to the start value ΔpH_0, which is assumed to be in equilibrium):

$$H^+\text{uptake} = A \cdot (\Delta pH - \Delta pH_0)$$

with A as the ATPase H^+ uptake rate per sec.

The simulation not only generates virtual pH curves, but also calculates the corresponding concentration changes of reactants and products as well as the ATP gain. The components of the proton-motive force, i.e., ΔpH and membrane potential are calculated as well. The calculated membrane potential, however, is not used as driving parameter for the simulation as the membrane potential in our proton-translocation experiments was neutralized by KSCN. *proton.exe* shows the concentration changes over time graphically and saves the parameters used together with the simulation results in the csv format that can be read by any text editor or spreadsheet program.

Assessment of the Simulation Quality

All experiments were repeated at least four times. Standard deviations between measured and simulated data were determined with Excel by pairwise comparison. The simulations reached similarities to the original data curves of 86–97% (**Supplementary Table 1**), with the deviations mainly arising from scattering of the original data. Lower similarities were obtained for calibration pulses, which can be explained by temporary local concentration peaks, generated when HCl pulses were added close to the pH electrode sensor tip.

To check the relevance of the simulation parameters, we did series of experiments changing only the amounts of added oxidant or reductant. By this approach, the concentrations of the metabolites were changed and gave corresponding reaction kinetics. Simulation was performed the same way with all parameters but the added amounts kept constant. As both Michaelis-Menten and first order kinetics describe concentration-dependent reaction rates the accuracy of our simulations proved that we were applying realistic values.

RESULTS

Scalar pH Changes Caused by Sulfate and Nitrate Reduction

Figure 2 (data from Krekeler and Cypionka, 1995) shows a cell suspension of *Desulfovibrio desulfuricans* reducing additions of sulfate and nitrate with H_2 as electron donor. Nitrate was reduced more rapidly than sulfate. The reactions consume 1.5 H^+ per sulfate and 2 H^+ per nitrate according to the Eqs 1, 2:

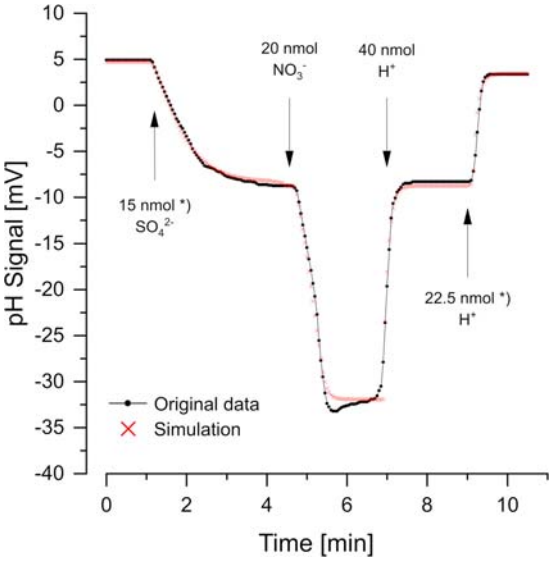

FIGURE 2 | Scalar pH changes correlated with sulfate and nitrate reduction by *Desulfovibrio desulfuricans* CSN. A cell suspension with OD_{436} = 1 was incubated at 30°C in H_2-saturated 150 mM KCl, before small pulses of 1 mM Na_2SO_4, $NaNO_3$, or HCl (in 150 mM N_2-flushed KCl) were added. The red dots show the simulation obtained with *proton.exe* (parameters see **Supplementary Material**, standard deviations see **Supplementary Table 1**). *Data from Krekeler and Cypionka, 1995. Note that a satisfying simulation was obtained only if additions of 15 nmol sulfate and 22.5 nmol H^+ (second calibration pulse) were assumed, while the original publication says 20 nmol sulfate and 30 nmol H^+. Even without simulation by *proton exe*, it is obvious that the second H^+ pulse gave a far smaller response than the 30/40 of the first one of 40 nmol H^+. Further sulfate and H^+ additions in the original experiment (Krekeler and Cypionka, 1995) confirmed the scalar consumption of 1.5 H^+ per reduced sulfate.

$$4\,H_2 + SO_4^{2-} + 1.5\,H^+ \rightarrow 0.5\,HS^- + 0.5\,H_2S + 4\,H_2O \quad (1)$$

$$4\,H_2 + NO_3^- + 2\,H^+ \rightarrow 3\,H_2O + NH_4^+ \quad (2)$$

To obtain the correct scalar pH effects, the equations are written for pH = 7 and regard the pK values of H_2S/HS^- (7.0) and NH_4^+/NH_3 (9.3). Proton quantification was done by adding calibration pulses of a few nanomoles H^+ (as 1 mM HCl in 150 mM N_2-saturated KCl), which also helped to keep the pH of the non-buffered suspension constant. Although not essential for the simple curves in **Figure 2**, we used *proton.exe* to model the reaction kinetics. The scalar pH effects of sulfate and nitrate reduction were compensated by H^+ additions according to the Eqs 1, 2 (see **Supplementary Material** for simulation data files and tutorial #3). However, the simulation led to the discovery of an error in the originally published figure. Both, sulfate reduction and the second H^+ calibration pulse could only be simulated correctly if 25% smaller additions than originally published were assumed (see legend of **Figure 2**). When we had published this

experiment (Krekeler and Cypionka, 1995) the discrepancy had been overlooked.

Transient Vectorial pH Changes Related to Proton-Sulfate Symport

The pH curves during sulfate reduction did not always look like the one in **Figure 2**. Depending on the physiological state of the cells, a rapid and transient initial alkalinization occurred (**Figure 3**). Sulfate limitation is known to induce high-affinity sulfate uptake systems which accumulate sulfate in symport with protons (Cypionka, 1987, 1989, 1994). Furthermore, starved cells often do not reduce added sulfate immediately, probably because they have a low internal level of ATP, which is required for sulfate activation. The initial disappearance of two protons can be explained by rapid sulfate uptake via symport with protons. Intracellular sulfate reduction started with a delay and then caused a slight acidification, when H_2S was diffusing through the membrane and outside partially dissociated to 0.5 HS^- + 0.5 H^+ (**Figure 1C**). The high-accumulating sulfate transport is electrogenic and probably takes up 3 H^+ per sulfate (Cypionka, 1989, 1994). The electrogenic third proton, however, will be invisible as long as the cells have their normal membrane potential that will rapidly compensate electrogenic proton transitions (see section "Discussion" and tutorial videos).

Kinetics of sulfate uptake and subsequent reduction could be modeled by *proton.exe*. An accurate simulation (**Figure 3**, see **Supplementary Material** for the parameters used) was only obtained if it was assumed that sulfate reduction started after completion of sulfate uptake. Sulfate uptake not coupled to immediate reduction has been reported already by Cypionka (1987; 1989; 1994). The delayed sulfide production was verified by means of a sulfide electrode, when this experiment was published first (Cypionka, 1995). The corresponding bulk sulfate and sulfide concentrations were calculated by *proton.exe* as well (**Figure 3**).

Vectorial Proton Translocation Driven by Electron Transport

In order to study electron-transport driven vectorial proton translocation, the membrane potential of the cells was neutralized by preincubation with KSCN, which did not change the overall reaction rates and final scalar pH changes. However, additional peaks indicating electron-transport driven proton translocation became visible (**Figure 4**). As expected, these peaks were transient as the protons simultaneously flow back via the membrane ATPase. The full amount of translocated protons is therefore not detectable by a pH electrode.

Proton uptake by the membrane ATPase is assumed to follow first order kinetics (Mitchell and Moyle, 1967, 1968), i.e., it should be proportional to the proton gradient across the membrane. Normally, one calculates the number of translocated protons by exponential extrapolation from the final phase, when there is no more electron transport but still ATPase activity going on. For our experiments, we used *proton.exe* to simulate these processes applying K_M and V_{max} values to transport and metabolic processes. Simulation gave smaller H^+/e^- values than extrapolation, which, however, are more realistic (see section "Discussion").

Vectorial Proton Translocation in Oxidant Pulse Experiments

Two types of experiments were performed to study electron transport-driven proton translocation with sulfate and nitrate. In oxidant pulse experiments washed cells were incubated with KSCN under H_2, and micromolar pulses of sulfate, nitrate or nitrite were added.

Cells grown with nitrate as electron acceptor performed rapid proton translocation with both nitrate and nitrite (**Figure 4**). The pH curves for nitrate and nitrite reduction looked almost identical which indicated that nitrate reduction to nitrite

$$H_2 + NO_3^- \rightarrow H_2O + NO_2^- \quad (3)$$

is not coupled to proton translocation as already reported by Steenkamp and Peck (1981). Small sulfate pulses added to nitrate-grown cells were not reduced and did not result in proton translocation with nitrate-grown cells (**Figure 4**). The scalar proton consumption during nitrite reduction followed Eq. 4:

$$3\,H_2 + NO_2^- + 2\,H^+ \rightarrow 2\,H_2O + NH_4^+ \quad (4)$$

Simulation of the experiment with *proton.exe* was done based on the model in **Figure 1**, assuming periplasmic nitrate- and nitrite reduction (Marietou et al., 2005). We obtained a simulated vectorial proton translocation of 12.2 H^+ per nitrate or nitrite, while the extrapolation method gave a value of 14.4 H^+. The H^+/H_2 ratio was lower with nitrate (3 H^+/H_2) than with nitrite (4 H^+/H_2) as the nitrate reductase consumes H_2 without coupling to proton translocation.

Reductant Pulse Experiments With H_2

For reductant pulse experiments, the cells were incubated under N_2 with KSCN and with excess sulfate or nitrate. Small pulses of H_2 (added as H_2-saturated KCl) caused vectorial proton translocation. However, the reactions were slower than in oxidant pulse experiment and, depending on the added amount of H_2, steady-state phase of proton translocation and uptake developed (**Figure 5**). There was no pH effect that could be attributed to sulfate uptake, which obviously had been accumulated sufficiently. Furthermore, there was no scalar alkalinization as described by the Eqs 1, 2, 4. By contrast, with both sulfate and nitrate as electron acceptor, a slight acidification was observed as already reported by Fitz and Cypionka (1989). The pH curves could be simulated by *proton.exe*. Experiments with three different H_2 additions confirmed the simulation quality, when the only simulation parameter changed was the amount of electron donor added (**Figure 4**).

For experiments with steady-state phases, electron-transport-driven proton translocation cannot be calculated by the logarithmic extrapolation method (see section "Discussion"). With *proton.exe*, however, we could simulate the experiments applying the same proton translocation of 1 H^+/e^- (or 2 H^+/H_2) for both sulfate and nitrate as electron acceptor.

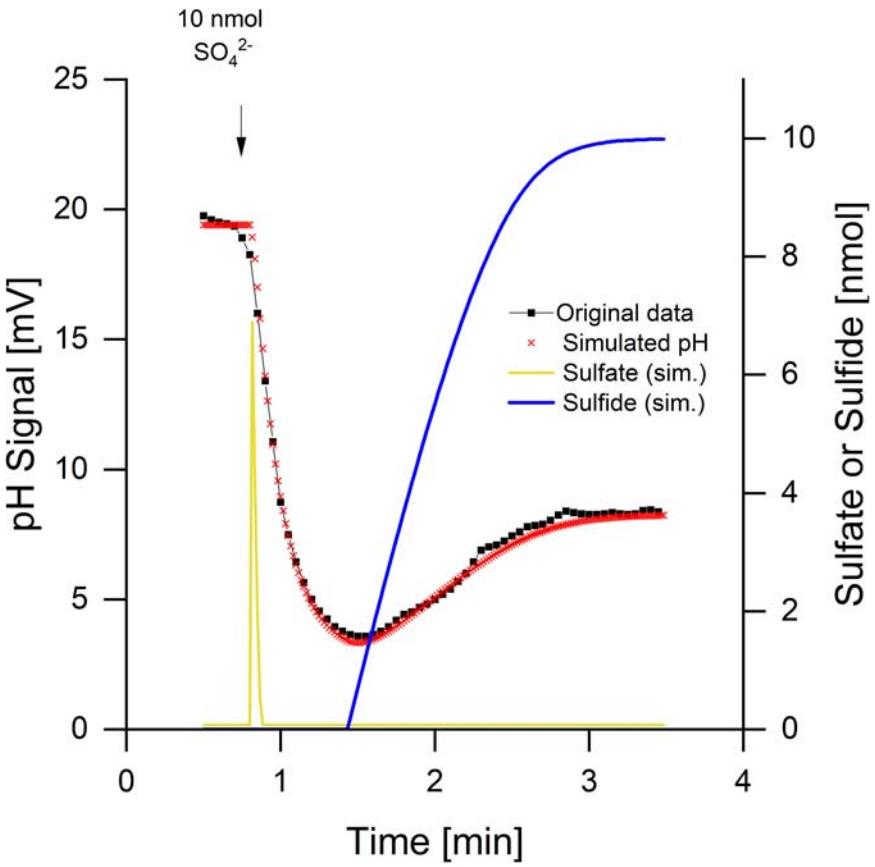

FIGURE 3 | Sulfate reduction by *Desulfovibrio desulfuricans* CSN grown under sulfate limitation. Conditions as described in **Figure 1**, data from Cypionka (1995). Additionally to the pH curve, sulfate uptake and sulfide release were simulated by means of *proton.exe* (parameters see **Supplementary Material**, standard deviations see **Supplementary Table 1**). The simulation includes initial proton-sulfate symport followed by sulfate reduction and release of H_2S part of which dissociating to $H^+ + HS^-$.

This result is in accordance with the assumption that H_2 is oxidized by a periplasmic hydrogenase which channels two electrons per H_2 into the cytoplasm via cytochrome c (Marietou et al., 2005), while the two protons resulting from H_2 oxidation remain extracellular (**Figure 1F**). This so-called vectorial electron transport (Badziong and Thauer, 1980; Duarte et al., 2018) generates a proton-motive force without requiring proton pumps.

DISCUSSION

pH Recording and Simulation as a Powerful Tool

Acid-base titration is a well-known quantitative method, and pH electrodes are rather sensitive tools. For example, changing the pH by one unit from 7 to 8 (i.e., 10^{-7}–10^{-8} mol H^+/l) in a non-buffered assay, corresponds to a H^+ concentration decrease by 90 nM (giving a signal response of −59 mV). The high sensitivity allows for physiological experiments at substrate limitation and natural concentration levels. We demonstrated how to measure the reduction of sulfate and nitrate (**Figure 2**) and nitrate and nitrite (**Figure 4**) in the same assay within a few minutes. As many metabolic reactions cause scalar H^+ consumption or release, there are many more physiological activities that can be recorded by our approach.

Simulation of the pH curves as done in our study is not required if only scalar pH effects are visible. However, as shown in **Figure 2** the simulation lead to the detection and correction of a discrepancy in published data. Although there are several parameters adjustable in *proton.exe*, the calibration pulses and variations of the additions restrict the simulations and lead to reproducible results.

Vectorial Proton Translocation: Extrapolation Versus Simulation

Knowing the number of protons translocated per electron during electron-transport (H^+/e^- ratio) is of fundamental importance for chemiosmotic considerations. It is impossible to measure all translocated protons upon addition of a small electron acceptor pulse because the backflow via the membrane ATPase starts immediately while there are still protons being pumped out. Therefore, the classical way to calculate the

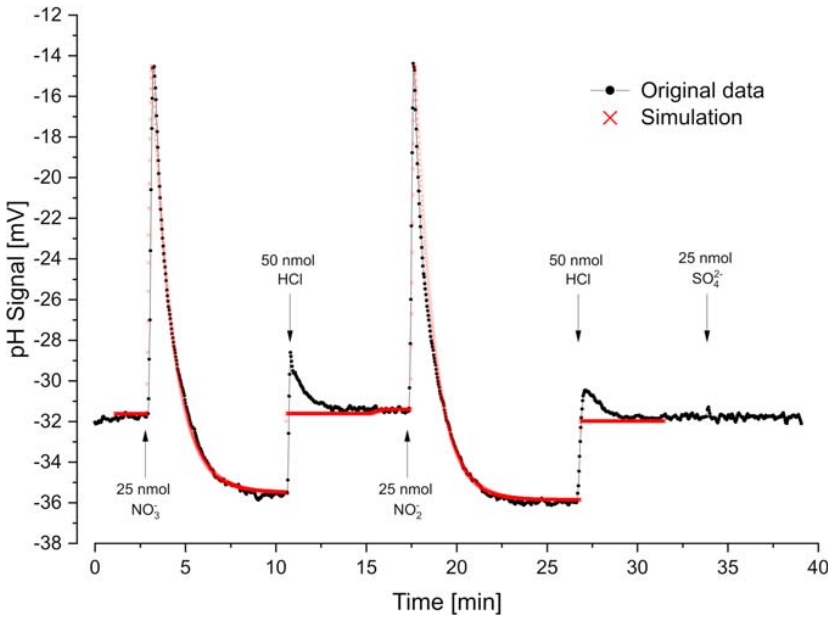

FIGURE 4 | Oxidant pulse experiment. Proton translocation coupled to nitrate- and nitrite reduction. Nitrate-grown cells were incubated under H_2 in the presence of KSCN (100 mM). Sulfate was not metabolized under these conditions. pH curves and proton translocation were simulated by means of *proton.exe* (parameters see **Supplementary Material**, standard deviations see **Supplementary Table 1**). The H^+/e^- ratio was additionally calculated by logarithmic extrapolation back to the time of electron acceptor addition (see **Supplementary Figure 1**).

H^+/e^- ratio is based on a later phase of the pH curve, when there is no more electron transport going on. The backflow rate is assumed to follow first-order kinetics and to depend on the deviation from the initial transmembrane proton gradient, only. To calculate the number of translocated protons, a semi-logarithmic plot of the pH curve is made, the linear part of which is extrapolated to the time of electron acceptor addition.

Simulation by *proton.exe* also applies first order kinetics for proton backflow, but instead of a simple extrapolation to the time of acceptor addition it describes the different processes (uptake, reduction, and oxidation) by means of K_M and V_{max} values. This normally gives lower H^+/e^+ ratios, which, however, are more realistic. It appears obvious that the proton pumps cannot work at maximum rate at time zero, when the preceding steps (transport, sulfate activation etc.) are limiting factors. Furthermore, the simulation can easily mirror scalar pH effects that go on concomitantly.

Steady-State Phases Are Typical for Reductant Pulse Experiments

Although in reductant pulse experiments the same metabolites are offered as in oxidant pulse assays, the physiological state of the cells is quite different. Here we have excess electron acceptors, and a more positive redox potential due to N_2 instead of H_2 saturation of the cell suspensions. During the pre-incubation phase the cells will run into depletion of internal electron donors and form oxidized cytoplasmic metabolites, which were reduced instead of sulfate or nitrate when H_2 became available. This explains why in reductant pulse experiments we did not find the scalar pH effects predicted by the Eqs 1–4.

We observed electron-transport driven proton translocation with different kinetics under these conditions. The rates were lower and there were steady-state phases of equal proton export- and backflow rates, particularly after increasing H_2 additions. Extrapolation of the final phase of proton backflow to calculate the H^+/e^- ratio is not adequate under these conditions and will give too high values. Simulation of the involved processes, however, is an appropriate approach for the assessment of experiments with steady-state phases.

Using *proton.exe* to Understand Chemiosmotic Processes

By means of *proton.exe* not only pH changes and bulk metabolite concentrations are calculated. The simulation also indicates the amounts of conserved ATP with adjustable H^+/ATP ratios as well as changes of the proton-motive force and its components. Trying out simulations with varied parameters (see **Supplementary Material** for the simulation parameters) shows which parameters are limiting the overall reaction rates and provide a deeper understanding of chemiosmotic principles.

Although there are several variables used in *proton.exe,* the search for the best simulation parameters will lead to similar results, particularly with respect to the limiting factors. We could verify the quality of our simulations by doing experiments with

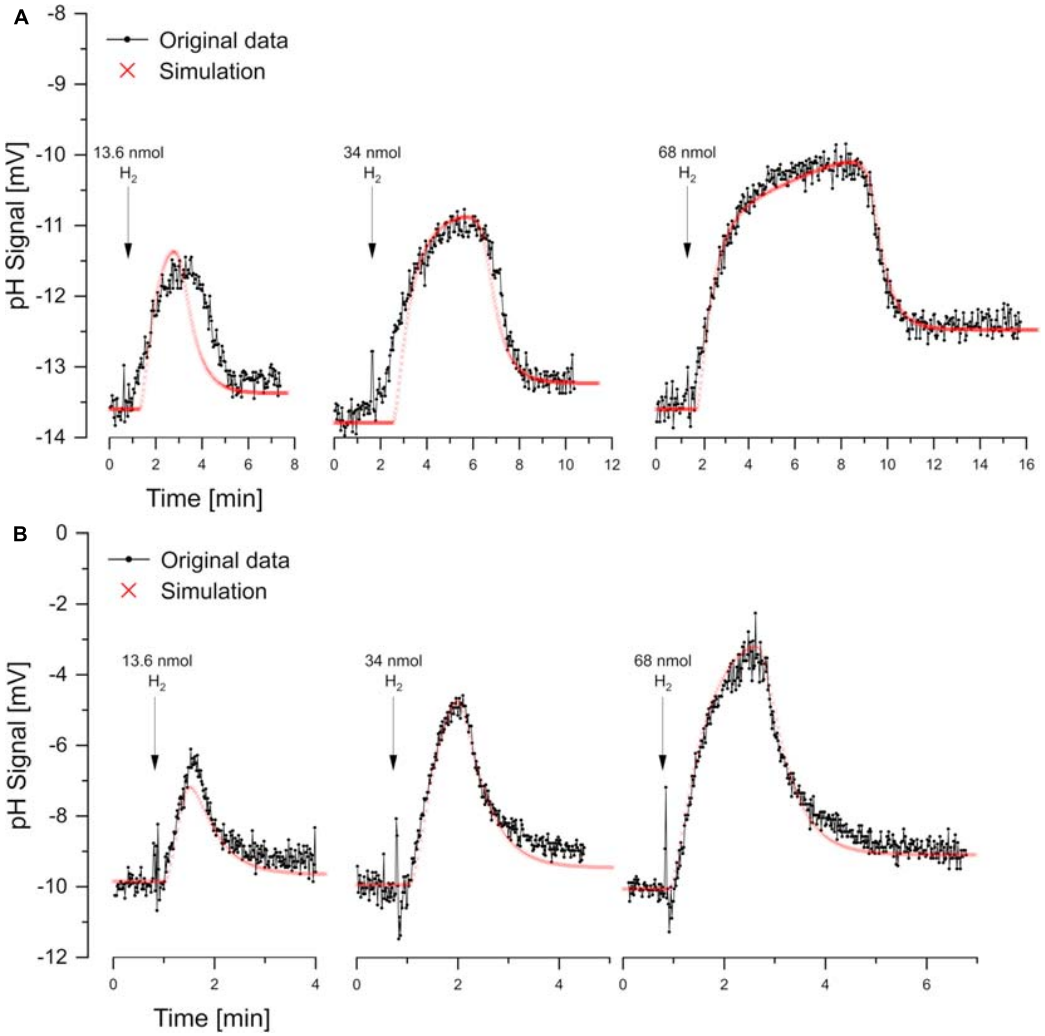

FIGURE 5 | Reductant pulse experiments. Proton translocation induced by H_2 pulses to cell suspensions incubated in N_2-saturated KCl with KSCN (100 mM) and **(A)** sulfate-grown cells with 10 mM Na_2SO_4 or **(B)** nitrate-grown cells with 10 mM $NaNO_3$. Three different H_2 concentrations were added for each electron acceptor. Correspondingly the simulations by *proton.exe* differ only by the amounts of electron donor added (parameters see **Supplementary Material**, standard deviations see **Supplementary Table 1**).

sequentially increasing pulses, thereby challenging the applied kinetic parameters. Variation of non-limiting factors hardly changes the simulation outcome, e.g., if for an oxidant pulse experiment the excess electron donor concentration is varied by a factor of 10 or even 100. Simulation thus unravels the relevant factors (The following examples are explained in the tutorial videos on www.microbial-world.com/proton.htm).

Example: ATPase Rate

It is impossible to simulate the pH curves of oxidant pulse experiments (in the absence of KSCN) if one assumes that there is electron-transport driven proton translocation and an ATPase rate below 0.5 s^{-1} (meaning that half of the translocated protons are flowing back within a second). Otherwise simulated curves will start to look like those obtained with KSCN. However, if one plots the membrane potential as well, it turns out that the ATPase rates must be much closer to 1.0. Even with a value of 0.95 s^{-1}, the simulated membrane potential transiently increases to values beyond −600 mV (e.g., simulation of sulfate reduction in **Figure 1**). The latter value is very unrealistic and would make the membrane leaky as shown by Kirchhoff and Cypionka (2017). With an ATPase rate of 0.99 s^{-1} the membrane potential still changes transiently by −80 mV. In experiments with KSCN, that neutralizes the membrane potential, the ATPase rates in our simulations decreased drastically to values below 0.1 s^{-1}, showing that the membrane potential, and not ΔpH is the major player in chemiosmotic energy conservation.

Example: Cytoplasmic Buffering Capacity

Another simulation result shows the strong buffering capacity of the cytoplasm. Based on unpublished experiments, we assumed

in our simulations a buffering capacity of the cytoplasm (1 mV/mM H^+ added) ten times lower than that reported for bacilli and *Escherichia* coli by Krulwich et al. (1985). However, even if with that assumption and with an ATPase rate of 0.95 s^{-1} (giving the strong response of the membrane potential described above) the cytoplasmic pH changes transiently by only 0.02 units (≅1 mV). This is quite astonishing as a bacterial cell with an cytoplasmic pH of 7.7 harbors only about 5 free H^+ (to calculate this consider that pH 8 means 10^{-8} mol H^+ per liter and that the cytoplasmic volume is below 10^{-15} liter, so there will be 10^{-23} mol or 6 free H^+ in a large bacterium). However, amino acids and nucleic acids effectively buffer the cytoplasm, whereas the membrane potential – although generated by >30,000 charges per cell – is much more sensitive to electrogenic processes.

Example: Electroneutral or Electrogenic Proton-Sulfate Symport

The last example shows why electrogenic proton symport (for example with sulfate) remains invisible to the pH electrode. At non-limiting concentration, sulfate uptake is electroneutral with 2 H^+ per SO_4^{2-} (Cypionka, 1995), and disappearance of two protons per sulfate can be measured with the pH electrode. During growth under sulfate limitation *D. desulfuricans* is known to induce an electrogenic proton-sulfate symport mechanism with 3 H^+ per SO_4^{2-} (Cypionka, 1989, 1994). However, simulation of the two different situations (electroneutrally with 2 H^+ per electron acceptor, or electrogenically with 3 H^+, with the third H^+ lowering the membrane potential by +1 charge) do not show any differences in the pH curves. This can be explained by the extremely fast backflow via the ATPase rate as described above. The only visible change in the simulation is a reduced ATP gain after electrogenic uptake, as one proton less contributes to ATP conservation.

CONCLUSION

Recording and simulating proton-related processes is a powerful approach to assess chemiosmotic energy metabolism at micromolar concentrations and time scales of seconds to minutes. The simulation app *proton.exe* is unique in relating pH curves (1) to biochemical reactions consuming or producing protons, (2) to proton-anion symport, and (3) to electron-transport-driven vectorial proton translocation. The simulation describes the kinetics of the reactions (K_M and V_{max}) and displays possible ATP gains and changes of the transmembrane pH gradient and electrical membrane potential. In our study we demonstrated its use with a sulfate-reducing bacterium as model organism. However, comparable simulations are applicable to all bacteria or mitochondria and easily adaptable to light-driven proton translocation by photosynthetic bacteria or chloroplasts.

DATA AVAILABILITY STATEMENT

The raw data supporting the conclusion of this article will be made available by the authors, without undue reservation.

AUTHOR CONTRIBUTIONS

J-OR performed the experimental work, did the simulations, and wrote a draft version of the manuscript. HC designed the study, wrote the software, and wrote the final version of the manuscript. Both authors contributed to the article and approved the submitted version.

FUNDING

This study was funded and supported by the Institute for Chemistry and Biology of the Marine Environment, University of Oldenburg, Germany.

ACKNOWLEDGMENTS

We thank Frank Meyerjürgens for support with the chemostat set-up, and Karlheinz Altendorf, Josef Gödde, Christian Kirchhoff, and Sina Schorn for helpful comments on the manuscript, and Cora Kohlmeier for valuable statistical advice.

SUPPLEMENTARY MATERIAL

The Supplementary Material for this article can be found online at: https://www.frontiersin.org/articles/10.3389/fmicb.2021.654065/full#supplementary-material

REFERENCES

Badziong, W., and Thauer, R. K. (1980) Vectorial electron transport in *Desulfovibrio vulgaris* (Marburg) growing on hydrogen plus sulfate as sole energy source. *Arch. Microbiol.* 125, 167–174. doi: 10.1007/BF00403215

Cross, R. L., and Müller, V. (2004). The evolution of A-, F-, and V-type ATP synthases and ATPases:reversals in function and changes in the H+/ATP coupling ratio. *FEBS Lett.* 576, 1–4. doi: 10.1016/j.febslet.2004.08.065

Crozier, T. E., and Yamamoto, S. (1974). Solubility of hydrogen in water, sea water, and sodium chloridesolutions. *J. Chem. Eng. Data* 19, 242–244. doi: 10.1021/je60062a007

Cypionka, H. (1986). Sulfide-controlled continuous culture of sulfate-reducing bacteria. *J. Microbiol. Meth.* 5, 1–9. doi: 10.1016/0167-7012(86)90018-7

Cypionka, H. (1987). Uptake of sulfate, sulfite and thiosulfate by proton-anion symport in *Desulfovibrio desulfuricans*. *Arch. Microbiol.* 148, 144–149. doi: 10.1007/bf00425363

Cypionka, H. (1989). Characterization of sulfate transport in *Desulfovibrio desulfuricans*. *Arch. Microbiol.* 152, 237–243. doi: 10.1007/bf00409657

Cypionka, H. (1994). Sulfate transport. *Meth. Enzymol.* 243, 3–14. doi: 10.1016/0076-6879(94)43003-9

Cypionka, H. (1995). "Solute transport and cell energetics," in *Sulfate-reducing bacteria, Biotechnology Handbooks*, ed. L. L. Barton (New York, NY: Plenum Press), 151–184. doi: 10.1007/978-1-4899-1582-5_6

Cypionka, H. (2021). *proton.exe*. Freeware, version 2021-03-03. Available online at www.microbial-world.com/proton.htm

Cypionka, H., and Pfennig, N. (1986). Growth yields of *Desulfotomaculum orientis* with hydrogen in chemostat culture. *Arch. Microbiol.* 143, 396–399. doi: 10.1007/bf00412808

Cypionka, H., van Verseveld, H. W., and Stouthamer, A. H. (1984). Proton translocation coupled to carbon monoxide-insensitive and -sensitive electron transport in *Pseudomonas* carboxydovorans. *FEMS Microbiol. Lett.* 27, 189–193.

Dilling, W., and Cypionka, H. (1990). Aerobic respiration in sulfate-reducing bacteria. *FEMS Microbiol. Lett.* 71, 123–128. doi: 10.1016/0378-1097(90)90043-p

Duarte, A. G., Catarino, T., White, G. F., et al. (2018). An electrogenic redox loop in sulfate reduction reveals a likely widespread mechanism of energy conservation. *Nat. Commun.* 9, 5448. doi: 10.1038/s41467-018-07839-x

Fitz, R. M., and Cypionka, H. (1989). A study on electron transport-driven proton translocation in *Desulfovibrio desulfuricans*. *Arch. Microbiol.* 152, 369–376. doi: 10.1007/bf00425175

Kirchhoff, C., and Cypionka, H. (2017). Propidium ion enters viable cells with high membrane potential during live-dead staining. *J. Microbiol. Meth.* 142, 79–82. doi: 10.1016/j.mimet.2017.09.011

Kirchhoff, C., Ebert, M., Jahn, D., and Cypionka, H. (2018). Chemiosmotic energy conservation in *Dinoroseobacter shibae*: proton translocation driven by aerobic respiration, denitrification, and photosynthetic light reaction. *Front. Microbiol.* 9, 903.

Krekeler, D., and Cypionka, H. (1995). The preferred electron acceptor of *Desulfovibrio desulfuricans* CSN. *FEMS Microbiol. Ecol.* 17, 271–277. doi: 10.1111/j.1574-6941.1995.tb00151.x

Krulwich, T. A., Agus, R., Schneier, M., and Guffanti, A. A. (1985). Buffering capacity of bacilli that grow at different pH ranges. *J. Bacteriol.* 162, 768–772. doi: 10.1128/jb.162.2.768-772.1985

Marietou, A. (2016). Nitrate reduction in sulfate-reducing bacteria. *FEMS Microbiol. Lett.* 363:fnw155. doi: 10.1093/femsle/fnw155

Marietou, A., Richardson, D., Cole, J., and Mohan, S. (2005). Nitrate reduction by *Desulfovibrio desulfuricans*: a periplasmic nitrate reductase system that lacks NapB, but includes a unique tetraheme c-type cytochrome. NapM. *FEMS Microbiol. Lett.* 248, 217–225. doi: 10.1016/j.femsle.2005.05.042

Marietou, A., Røy, H., Jørgensen, B. B., and Kjeldsen, K. U. (2018). Sulfate transporters in dissimilatory sulfate reducing microorganisms: A comparative genomics analysis. *Front Microbiol* 9:309. doi: 10.3389/fmicb.2018.00309

Mitchell, P., and Moyle, J. (1967). Respiration-driven proton translocation in rat liver mitochondria. *Biochem. J.* 105, 1147–1162. doi: 10.1042/bj1051147

Mitchell, P., and Moyle, J. (1968). Proton translocation coupled to ATP hydrolysis in rat liver mitochondria. *Eur. J. Biochem.* 4, 530–539. doi: 10.1111/j.1432-1033.1968.tb00245.x

Petersen, J., Förster, K., Turina, P., and Gräber, P. (2012). Comparison of the H^+/ATP ratios of the H^+-ATP synthases from yeast and from chloroplast. *Proc. Nat. Acad. Scienc.* 109, 11150–11155. doi: 10.1073/pnas.1202799109

Rich, P. R. (2003). The molecular machinery of Keilin's respiratory chain. Biochem. *Soc. Trans.* 31:1095-1105.

Seitz, H. J., and Cypionka, H. (1986). Chemolithotrophic growth of *Desulfovibrio desulfuricans* with hydrogen coupled to ammonification of nitrate or nitrite. *Arch. Microbiol.* 146, 63–67. doi: 10.1007/bf00690160

Steenkamp, D. J., and Peck, H. D. (1981). Proton translocation associated with nitrite respiration in *Desulfovibrio desulfuricans*. *J. Biol. Chem.* 256, 5450–5458. doi: 10.1016/s0021-9258(19)69222-7

Steigmüller, S., Turina, P., and Gräber, P. (2008). The thermodynamic H^+/ATP ratios of the H^+-ATP synthases from chloroplasts and *Escherichia coli*. *Proc. Nat. Acad. Scienc.* 105, 3745–3750. doi: 10.1073/pnas.0708356105

Conflict of Interest: The authors declare that the research was conducted in the absence of any commercial or financial relationships that could be construed as a potential conflict of interest.

frontiers in Microbiology

ORIGINAL RESEARCH
published: 03 May 2021
doi: 10.3389/fmicb.2021.673066

Homogeneous Cytochrome 579 Is an Octamer That Reacts Too Slowly With Soluble Iron to Be the Initial Iron Oxidase in the Respiratory Chain of *Leptospirillum ferriphilum*

Robert C. Blake II[1], John E. Shively[2], Russell Timkovich[3] and Richard Allen White III[4,5,6]*

[1]Division of Basic Pharmaceutical Sciences, Xavier University of Louisiana, New Orleans, LA, United States, [2]Division of Immunology, Beckman Research Institute of the City of Hope, Duarte, CA, United States, [3]Department of Chemistry, University of Alabama, Tuscaloosa, AL, United States, [4]Department of Bioinformatics and Genomics, University of North Carolina, Charlotte, NC, United States, [5]Department of Bioinformatics and Genomics, University of North Carolina, Kannapolis, NC, United States, [6]Australian Centre for Astrobiology, University of New South Wales, Sydney, NSW, Australia

OPEN ACCESS

Edited by:
Davide Zannoni, University of Bologna, Italy

Reviewed by:
Marcus Joseph Edwards, University of Essex, United Kingdom
Takeshi Uchida, Hokkaido University, Japan
Linda Celeste Montemiglio, National Research Council (CNR), Italy

***Correspondence:**
Robert C. Blake II
rblake@xula.edu

Specialty section:
This article was submitted to Microbial Physiology and Metabolism, a section of the journal Frontiers in Microbiology

Received: *26 February 2021*
Accepted: *13 April 2021*
Published: *03 May 2021*

Citation:
Blake RC II, Shively JE, Timkovich R and White RA III (2021) Homogeneous Cytochrome 579 Is an Octamer That Reacts Too Slowly With Soluble Iron to Be the Initial Iron Oxidase in the Respiratory Chain of Leptospirillum ferriphilum. Front. Microbiol. 12:673066. doi: 10.3389/fmicb.2021.673066

The exact role that cytochrome 579 plays in the aerobic iron respiratory chain of *Leptospirillum ferriphilum* is unclear. This paper presents genomic, structural, and kinetic data on the cytochrome 579 purified from cell-free extracts of *L. ferriphilum* cultured on soluble iron. Electrospray mass spectrometry of electrophoretically homogeneous cytochrome 579 yielded two principal peaks at 16,015 and 16,141 Daltons. N-terminal amino acid sequencing of the purified protein yielded data that were used to determine the following: there are seven homologs of cytochrome 579; each homolog possesses the CXXCH heme-binding motif found in *c*-type cytochromes; each of the seven sequenced strains of *L. ferriphilum* expresses only two of the seven homologs of the cytochrome; and each homolog contains an N-terminal signal peptide that directs the mature protein to an extra-cytoplasmic location. Static light scattering and macroion mobility measurements on native cytochrome 579 yielded masses of 125 and 135 kDaltons, respectively. The reduced alkaline pyridine hemochromogen spectrum of the purified cytochrome had an *alpha* absorbance maximum at 567 nm, a property not exhibited by any known heme group. The iron-dependent reduction and oxidation of the octameric cytochrome exhibited positively cooperative kinetic behavior with apparent Hill coefficients of 5.0 and 3.7, respectively, when the purified protein was mixed with mM concentrations of soluble iron. Consequently, the extrapolated rates of reduction at sub-mM iron concentrations were far too slow for cytochrome 579 to be the initial iron oxidase in the aerobic respiratory chain of *L. ferriphilum*. Rather, these observations support the hypothesis that the acid-stable cytochrome 579 is a periplasmic conduit of electrons from initial iron oxidation in the outer membrane of this Gram-negative bacterium to a terminal oxidase in the plasma membrane.

Keywords: *Leptospirillum*, cytochrome 579, electron transport, aerobic respiration, cooperative kinetics

INTRODUCTION

Leptospirillum ferrooxidans (Markosyan, 1972; Hippe, 2000), *Leptospirillum ferriphilum* (Coram and Rawlings, 2002), and *Leptospirillum ferrodiazotrophum* (Tyson et al., 2005) are species of mesophilic, vibrioid, or spiral-shaped Gram-negative prokaryotes that can be acquired as pure cultures from national/commercial culture collections. Other potential species in that genus, *Leptospirillum rubarum* (Goltsman et al., 2009), *Leptospirillum thermoferrooxidans* (Golovacheva et al., 1992; Hippe, 2000), and a group designated as "*Leptospirillum* group IV UBA BS" (Goltsman et al., 2013), have been reported, but none of these strains is generally available at the present time. All of these organisms are obligately acidophilic chemoautotrophs that are only known to respire aerobically on reduced soluble iron or ferrous iron-containing sulfide minerals to obtain biochemical energy, making them among the most metabolically restricted organisms known. Despite these restrictions, these microorganisms are widely distributed in both pristine and industrial bioleaching environments, where they are frequently thought to be the critical biological catalysts in the metal sulfide biooxidation process (Sand et al., 1992; Rawlings et al., 1999; Rawlings and Johnson, 2007; Garcia-Moyano et al., 2008).

The identities and cellular locations of the respiratory chain components that are responsible for iron oxidation in the *Leptospirilli* are poorly understood. Prior reductionist studies reported that cell-free extracts derived from iron-grown *L. ferrooxidans* (Hart et al., 1991), *L. ferriphilum* (Ram et al., 2005), or a microbial biofilm community with a low diversity of microbes that was dominated by *Leptospirillum* group II bacteria (Singer et al., 2008) all contained readily discernible quantities of an acid-stable, acid-soluble cytochrome with an unusual absorbance maximum at 579 nm in the reduced state. Although the likely location of this acid-compatible cytochrome 579 was in the acidic periplasm, incomplete reduction of the protein was noted using 30 mM Fe(II) at pH 2.0. Another novel cytochrome with a unique reduced absorbance maximum at 572 nm was purified from the same biofilm communities (Jeans et al., 2008). Cytochrome 572, which was reported to be localized in the outer membrane, was readily and completely reduced by soluble Fe(II) at low pH. These observations led to the working hypothesis that cytochrome 572 was the initial iron oxidase in the outer membrane, while cytochrome 579 served to shuttle electrons from the outer membrane across the periplasm to a terminal oxidase in the plasma membrane. However, the same group also noted that the reactivity of cytochrome 579 was very dependent on the developmental stage of the biofilm (Singer et al., 2010). Thus, cytochrome 579 isolated from early-stage biofilms was much more reactive with Fe(II) at low pH than was cytochrome 579 isolated from late-stage biofilms, an observation that was consistent with the hypothesis that cytochrome 579 might function as an alternative iron oxidase in early developmental-stage biofilms.

This paper describes selected structural and functional properties of cytochrome 579 that was purified to electrophoretic homogeneity from cell-free extracts of the type strain of *L. ferriphilum*. Although this cytochrome possessed the signature absorbance maximum at 579 nm in the reduced state, it nonetheless differed in a number of ways from the purified cytochromes 579 introduced above. First, the reduced alkaline pyridine hemochromogen spectrum of this protein was different from that of the cytochrome 579 purified from the biofilm community (Singer et al., 2008). Second, this cytochrome appeared to function as an octamer in its native state, while the purified cytochromes 579 from both *L. ferrooxidans* (Hart et al., 1991) and the microbial biofilm (Singer et al., 2008) appeared to be monomeric in their native states. Last, but not least, the observed pseudo-first order rate constants for the iron-dependent reduction and oxidation of the purified cytochrome exhibited extraordinary positive cooperativity, a property not reported for the other cytochromes 579. Thus, while the rates of reduction of this cytochrome were sufficiently rapid *in vitro* to be physiologically significant at the high ferrous concentrations achieved in the laboratory, the corresponding rates of reduction were far too slow to be significant at the concentrations of soluble iron likely to be encountered by *L. ferriphilum* in its natural habitat.

MATERIALS AND METHODS

Cell Culture and Quantification of Bacteria

Leptospirillum ferriphilum DSMZ 14647 was cultured autotrophically on soluble ferrous ions at 35°C in the medium described elsewhere (Tuovinen and Kelly, 1973) adjusted to pH 1.5 and amended with 44 g/L of $FeSO_4 \bullet 7H_2O$. Larger quantities of bacteria for protein purification purposes were cultured in an apparatus that permitted the *in situ* electrochemical reduction of the product ferric ions to achieve enhanced yields of the bacteria (Blake et al., 1994). Cells were cultured on a continuous basis in a 45-liter vessel under an applied current of 30 A with a voltage that varied from 4 to 7 V. When suspensions of cells were removed for further experimental purposes, an equal volume of fresh medium was added back to the culture vessel. Cells thus obtained were harvested by centrifugation, washed three times with 0.02 M H_2SO_4, pH 1.5, and resuspended in sufficient 0.02 M H_2SO_4 to achieve a stock suspension of 1.5×10^{10} cells per ml. Each stock suspension was stored at 4°C for up to 2 weeks while structural or spectroscopic experiments were conducted on aliquots of the cells.

Bacterial growth was monitored by quantifying bacterial carbon with a Dohrmann DC-190 high temperature carbon analyzer (Rosemount Analytical, Inc., Santa Clara, CA, United States). The premise was that any carbon detected in solutions of inorganic media at pH 1.5 must be proportional to the biomass accumulated by the obligate autotrophs that

Abbreviations: SDS-PAGE, Sodium dodecyl sulfate polyacrylamide gel electrophoresis; NCBI, National Center for Biotechnology Information; DSMZ, Deutsche Sammlung von Mikrooranismen und Zellkultuen GmbH; BLAST, Basic Local Alignment Search Tool; BLASTp, BLAST search of protein databases using a protein query; tBLASTn, BLAST search of nucleotide databases using a protein query translated into its corresponding nucleic acid sequence.

thrived on that media. Bacterial, or cell-associated, carbon was taken as the difference between the total organic carbon in the cell suspension minus that remaining after the sample had been filtered through a 0.2 μm pore-size filter.

Absolute numbers of *L. ferriphilum* cells were determined by electrical impedance measurements on a Multisizer 4 particle counter (Beckman Coulter, Inc., Brea, CA, United States) fitted with a 30-μm aperture. The instrument was programmed to siphon 50 μl of sample that contained Isoton II as the electrolyte. The current applied across the aperture was 600 μA. Voltage pulses attendant with impedance changes as particles passed through the aperture were monitored with an instrument gain of 4.

Purification of Red Cytochrome

The purification of cytochrome 579 from cell-free extracts of *L. ferriphilum* cultured on soluble iron was conducted as described elsewhere (Ram et al., 2005). Briefly, cells were resuspended in 0.01 N sulfuric acid (4 ml/g wet cell paste) and subsequently disrupted by sonic oscillation for 1 min/g wet cell paste at a power output of 125 watts. Care was taken to maintain the temperature of the solution below 7°C. Centrifugation of the sonicate at 10,000 × *g* for 10 min yielded a red pellet and a cloudy red supernatant. The pellet was resuspended in 0.01 N sulfuric acid (1.5 ml/g original wet cell paste) and centrifuged as described above; the two supernatants were then combined.

The combined supernatants were then subjected to ammonium sulfate precipitation. The bulk of the red cytochrome precipitated between 45 and 95% saturated ammonium sulfate. A red pellet was obtained by centrifugation of the 95%-saturated solution for 20 min at 20,000 × *g*. The pellet was dissolved in and dialyzed against 0.01 N sodium acetate buffer, pH 5.5. The preparation of red cytochrome was then applied to a column of carboxymethylcellulose equilibrated and developed with the same acetate buffer. All of the colored cytochrome eluted from the column in the void volume. A curious feature of this purification procedure was that the cytochrome that eluted in the void volume of the carboxymethylcellulose column was always observed to be in the yellow-green reduced state, regardless of the oxidation state of the protein when it was applied to the column. The source and identity of the reducing equivalents were not determined. The reduced protein thus obtained was converted back to the red oxidized state after mixing with a few grains of ferric sulfate. The red cytochrome at this point exhibited a single band when analyzed by standard SDS-PAGE. SDS-PAGE under reducing conditions was routinely performed on a Pharmacia Phast™ system using PhastGel gradient 10–15 polyacrylamide gels and PhastGel SDS buffer strips; proteins within the gels were visualized using a standard Coomassie Blue stain. Proteins in solution were quantified using the copper-bicinchoninic acid assay (Smith et al., 1985). The purified red protein was concentrated to approximately 10 mg protein/ml by ultrafiltration through an Amicon Centriprep-30 membrane concentrator and stored at 4°C in 0.001 N sulfuric acid. The red cytochrome remained fully redox-active for at least 6 months under these storage conditions.

Protein Subunit Structural Characterization

Amino terminal microsequencing of the purified red cytochrome was accomplished as described previously (Ronk et al., 1991). BLASTp and tBLASTn sequence similarity searches using default parameters were conducted on non-redundant protein sequences and RefSeq Genome databases, respectively, maintained for those purposes by the NCBI (Claverie and Notredame, 2007). *Leptospirillum ferriphilum* strains and their corresponding RefSeq assembly accession numbers were as follows: DSMZ 14647, GCF_000755505.1; ML-04, GCF_000299235.1; YSK, GCF_000695975.1; Sp-Cl, GCF_001280545.1; DX, GCF_002002505.1; ZJ, GCF_002002665.1; pb_238, GCF_900198525.1; and CF-1, GCF_001186405.1.

The subunit molecular weight of the purified protein was obtained by liquid chromatography coupled with electrospray mass spectrometry. The protein sample (1.0 μl, 14 pmoles) was injected onto a capillary reversed phase HPLC column (25 mm ID, Vydac C18) developed at 2 μl/min with a linear gradient from 22% A (0.1% trifluoroacetic acid) to 82% B (trifluoroacetic acid/water/acetonitrile, 0.1/9.9/90, v/v/v) over 30 min. The absorbance at 200 nm was monitored on an ATI/Kastos UV detector. The sample was mixed with 2-methoxyethanol (2 μl/min) for introduction into the electrospray on a Finnigan TSQ700 triple quadrupole mass spectrometer.

Native Protein Structural Characterization

The apparent molecular mass of the native cytochrome in solution was measured by two means. The first means involved Rayleigh light scattering analyses on a Dawn DSP laser photometer equipped with multiple detectors (Wyatt Technology Corp., Santa Barbara, CA, United States). The instrument was run in the batch mode with 10 ml of cytochrome sample per measurement. The protein concentrations in these static light scattering measurements ranged from 1.15 to 5.77 μg or purified protein per milliliter.

The second means involved macroion mobility measurements of the purified protein using a model 3980C macroIMS macroion mobility spectrometer from TSI, Inc. (Shoreview, MN, United States). The instrument consisted of a model 3480 electrospray aerosol generator, a model 3080C electrostatic classifier, and a model 3776 macroion/nanoparticle detector. Samples of 320 ng protein/ml were prepared by diluting the 10 mg protein/ml stock solution into 20 mM ammonium acetate. Any nonvolatile salts that were present in the stock protein preparations were sufficiently diluted in the resulting dilute samples such that any spurious nonprotein peaks that were observed at low molecular masses did not interfere with the interpretation of the protein spectra. Control analyses using purified protein that had been extensively dialyzed against 20 mM ammonium acetate demonstrated that neither the apparent mass nor the shape of the resulting protein peak in the macroIMS spectrum were changed by the desalting procedure. The ammonium acetate was prepared fresh weekly and passed through a 0.2 μm filter to remove any traces of particulate matter.

Spectral and Kinetic Characterization of Purified Cytochrome 579

Absorbance spectra were obtained on a Cary 14 dual-beam spectrophotometer as described earlier (Blake and Shute, 1987). The alkaline pyridine hemochromogen spectra of cytochrome 579 were obtained as described elsewhere (Bartsch, 1971).

Kinetic measurements were performed on an RSM-1000™ stopped flow spectrophotometer equipped with a rapid-scan module that permitted the collection and analysis of absorbance data as a function of both time and wavelength (Blake and Shute, 1987). The samples of cytochrome 579 and ferrous or ferric ions were prepared in identical solutions of sulfuric acid, pH 1.5, and added to separate syringes of the stopped flow spectrophotometer. The temperature of the driving syringes was maintained at 35 ± 1°C by circulating water; room-temperature solutions were allowed to equilibrate for 15 min in the driving syringes. Reactions were initiated by rapidly mixing 0.14 ml of the solution from each driving syringe. An operational bandwidth of 1.0 nm provided acceptable signal to noise characteristics between 350 and 700 nm.

Global fits of absorbance changes as a function of both time and wavelength over the 230-nm range of 370–600 nm were accomplished by the singular value decomposition method (DeSa and Matheson, 2004) using analysis software provided by On Line Instrument Systems, Inc., Bogart, GA, United States. The output of applying the singular value decomposition method to each three-dimensional data set of absorbance as a function of time and wavelength generated three products as follows: (i) a matrix of spectral eigenvectors that represented the changes in absorbance for the principal absorbing species; (ii) a matrix of kinetic eigenvectors that represented the mechanism that accounted for the time dependencies of the principal absorbance changes; and (iii) a diagonal matrix of eigenvalues that minimized the differences between the calculated and the observed data.

Phylogenetic Analysis

The alignment of different amino acid sequences was conducted using the MAFFT multiple sequence alignment software (v7.271) with option local pair and maximum iterations of 1,000 (Katoh and Standley, 2013). Maximum likelihood phylogenetic trees were constructed using the IQ-TREE stochastic algorithm (1.6.2; Nguyen et al., 2014). Model selection was conducted with the ModelFinder selection method (Kalyaanamoorthy et al., 2017) with a total of 1,000 boot-strap replicates using UFBoot2 (Hoang et al., 2017) and visualized with SeaView4 (Gouy et al., 2009). *Candidatus Manganitrophus noduliformans* (WP_168058047.1) was used as an outgroup for cytochrome 579.

RESULTS

Cell Culture by Electrochemical Reduction

A principal practical barrier to fundamental or applied research on *L. ferriphilum* is simply achieving sufficient cell mass for meaningful studies. Efforts to harvest bacteria cultured on insoluble substrates such as pyrite are hampered by the inability to readily separate the cell mass from the particulate inorganic materials, either insoluble substrates that remain or insoluble products such as jarosite. Efforts to cultivate the same bacteria on soluble ferrous ions at acidic pH are hampered by the discouragingly poor cell yield achieved by typical batch culture. A typical culture of *L. ferriphilum* yields roughly 10–20 mg wet cell paste per liter of acid ferrous sulfate medium. Greatly enhanced yields of *L. ferriphilum* cultured autotrophically on soluble ferrous ions were achieved for these studies by the *in situ* electrochemical reduction of soluble ferric ions using an apparatus described previously (Blake et al., 1994).

Figure 1 shows the accumulation of bacterial carbon as a function of time in electrolyzed ferrous sulfate media inoculated with *L. ferriphilum*. Electrolytic reduction was initiated when the batch culture had achieved stationary phase (the 0,0 intercept in **Figure 1**). By reducing the product ferric ions back to the ferrous state at the cathode, the bacteria in the catholyte experienced an endless supply of the growth substrate and continued to prosper until some other factor in the growth medium became limiting. A notable feature of electrolytic growth was the apparent linear, not exponential, dependence of bacterial growth with time. Such linear rates suggest that bacterial growth was limited by some factor that was introduced in a linear fashion. Because the electrical current necessary to maintain a steady state level of iron reduction increased significantly as the cell numbers increased over the time course of each culture, the most likely growth-limiting candidate was either oxygen or carbon dioxide. In any event, every 100 ppm of bacterial carbon was observed to correspond to approximately 1.3 g wet cell paste/liter medium. Thus, 45 L of electrolyzed medium yielded nearly 60 g of the iron-grown *L. ferriphilum* approximately every 2 weeks.

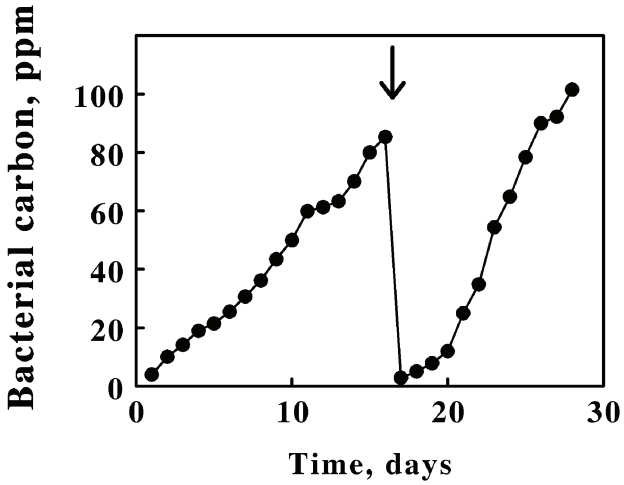

FIGURE 1 | Enhanced yields of *Leptospirillum ferriphilum* achieved by *in situ* electrochemical reduction of soluble iron in the growth medium. Zero time was taken as the start of electrochemical reduction after the culture had already achieved stationary phase on soluble iron in the absence of reduction. The position of the *bold arrow* corresponds to the replacement of 95% of the cell suspension with fresh growth medium.

Structural Properties of the Cytochrome 579 Polypeptide

SDS-PAGE conducted under reducing conditions revealed that the purified protein was comprised of a single polypeptide with an apparent molecular mass of around 16,000 Daltons. **Figure 2A** shows SDS-PAGE analyses conducted on five different concentrations of the purified red cytochrome. The purified protein appeared to be a single, albeit somewhat diffuse, band at all concentrations, with no visible evidence of contaminating proteins as revealed by staining with Coomassie Blue.

Initial evidence for structural heterogeneity in the purified cytochrome 579 came from liquid chromatography coupled with electrospray mass spectrometry. **Figure 2B** shows the positive-ion electrospray mass spectrum of cytochrome 579. The main figure shows the deconvoluted spectrum for the neutral cytochrome(s) obtained using operating and analysis software provided with the mass spectrometer. The principal mass peaks observed at 16,015 and 16,140 Daltons may represent two distinct but nearly identical proteins. Alternatively, the small mass difference could derive from missing amino- or carboxyl-terminal amino acids due to proteolysis activity during preparation or from post-translational modifications of part of the sample.

The uppermost line of text in **Figure 3A** shows the N-terminal amino acid sequence of purified cytochrome 579 as obtained by automated Edman degradation performed on a gas-phase microsequencer. The amino acid chromatograms produced at each cycle of the automated degradation reactions were all consistent with the hypothesis that cytochrome 579 was comprised of a single type of polypeptide chain. That is, each individual chromatogram exhibited one major peak corresponding to the derivatized amino acid released from the polypeptide during that cycle. However, microsequencing analyses performed on internal peptides derived from enzymatic or chemical cleavage of cytochrome 579 also yielded sporadic instances where individual amino acid chromatograms were observed with two major peaks of approximately equal intensity (primary data not shown). These 2-peak chromatograms were frequently interspersed among more routine 1-peak chromatograms generated from the same HPLC-purified peptide(s). One hypothesis that is consistent with these observations was that the purified cytochrome 579 was comprised of two or more different polypeptide chains that were highly homologous, but not quite identical. This apparent heterogeneity in the primary structure of purified cytochrome 579 made the determination of the primary structure by traditional amino terminal microsequencing activities highly unlikely.

The N-terminal sequence of 49 amino acids was used as the query sequence in BLASTp searches of the *L. ferriphilum* species (taxid 178,606) contained in the NCBI non-redundant protein database (**Figure 3A**). These protein-protein searches yielded the sequences of seven different proteins that exhibited a high degree of homology to the query sequence. These seven amino acid sequences are aligned in their entirety in **Supplementary Figure S1**. Each of the seven proteins contained an N-terminal segment of 19–23 amino acids that was tentatively identified as a signal peptide (Ivankov et al., 2013) that targeted the mature protein to the periplasm of this Gram-negative eubacterium. The corresponding N-terminal sequences that remained after the removal of the respective signal peptides are those represented by the seven remaining N-terminal sequences shown in **Figure 3A**. The homology among these amino acid sequence segments is evident. One other noteworthy feature of these sequence comparisons is that every mature protein in **Figure 3A** possesses the CXXCH heme-binding motif (between amino acids 45 and 49) that is the only generally recognized signature sequence that is common to all *c*-type cytochromes.

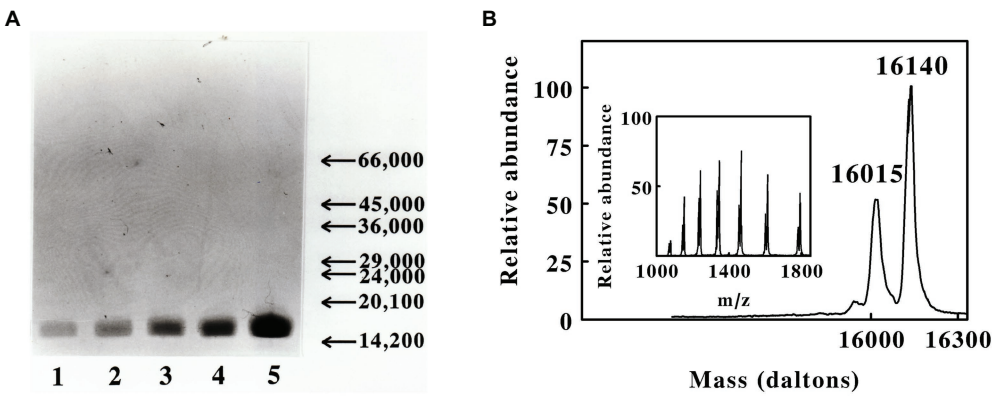

FIGURE 2 | Masses of the polypeptides present in the preparation of cytochrome 579 purified from cell-free extracts of *L. ferriphilum*. **(A)** Sodium dodecyl sulfate-polyacrylamide gel electrophoresis of the purified cytochrome under denaturing and reducing conditions. Protein bands were visualized by staining with Coomassie Blue. *Lanes 1* through *5* represent 0.85, 1.7, 3.3, 7.5, and 15 μg of purified protein, respectively. The *arrows* and *numbers* on the ordinate represent the migration positions and masses, respectively, of stained bands associated with protein molecular mass standards (primary data not shown). The mass standards from high to low were bovine serum albumin, ovalbumin, yeast alcohol dehydrogenase, carbonic anhydrase, bovine chymotrypsin, soybean trypsin inhibitor, and bovine α-lacalbumin. **(B)** Deconvoluted positive-ion electrospray mass spectrum of purified cytochrome 579, showing the masses of the neutral polypeptides. *Inset*, primary data of the electrospray mass spectrum of the purified protein, showing the ions formed by multiple attachment of protons to the molecules.

A

Source of Information	Amino acid sequence (5 10 15 20 25 30 35 40 45 50)
Protein sequencing[&]	AQLDILKPRVPADQLAAAKAMKPPFPVTAAVIAKGKQVFNGA_T_YT_H
WP_101049443.1[‡]	AELDILKPRVPADQLAAAKAMKPPFPVTADMIAKGKEVFNGAGTCYTCH
WP_014961934.1[‡]	AELDILKPRVPADQLAAAKAMKPPFPVTADMIAKGKEVFNGAGTCYTCH
WP_036080593.1[‡]	AELDILKPRVPADQLAAAKAMKPPFPVTADMIAKGKEVFNGAGTCYTCH
AEQ75424.1[‡]	AELDILKPRVPADQTAAAKAMKPPFPVNAATIAKGKEVFNGAGTCYTCH
WP_014961757.1[‡]	AELDILKPRVPADQTAAAKAMKPPFPVTAAVIAKGKEVFNGAGTCYTCH
WP_053765285.1[‡]	AELDILKPRVPADQTAAAKAMKPPFPVTAAVIAKGKEVFNGAGTCYTCH
WP_023524856.1[‡]	AELDILKPRVPADQTAAAKAMKPPFPVTAAVIAKGKEVFNGAGTCYTCH

[&]N-terminal amino acid sequence of purified cytochrome 579

[‡]Accession number that represents a particular NCBI reference sequence

B

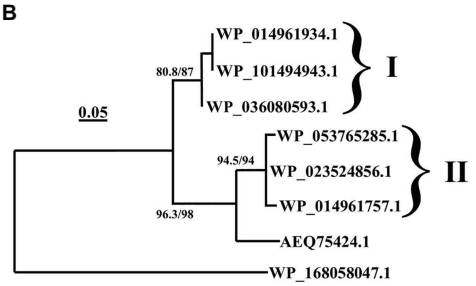

C

Protein Accession Number	14647[‡]/ pb_238[‡]	ML-04	YSK	DX	ZJ	Sp-Cl	CF-1
	L. ferriphilum strain designation						
WP_101494943.1				BOX24_ RS11125			
WP_014961934.1		LFML04_ RS10880	Y981_ RS10405		BOX30_ RS02815	AOA54_ RS09235	ABH19_ RS12215
WP_036080593.1	LPTCAG_ RS02375/ LFTS_ RS06225						
WP_014961757.1	LPTCAG_ RS05430/ LFTS_ RS05275	LFML04_ RS10030					
WP_053765285.1						AOA54_ RS010055	
WP_023524856.1			Y981_ RS09420	BOX24_ RS03035	BOX30_ RS08595		ABH19_ RS11060

[‡]These are the same strains sequenced by two different laboratories.

FIGURE 3 | Sequence comparisons of cytochromes 579 that could be expressed in different strains of *L. ferriphilum*. **(A)** Alignment of amino acid sequences obtained from either the N-terminal amino acid sequencing of cytochrome 579 purified from the type strain of *L. ferriphilum* or from tBLASTn searches of the genomes of purified strains of *L. ferriphilum* that are contained in the NCBI database. The amino acids within each shaded rectangle are those that differ from the corresponding amino acids determined in the protein sequencing data presented herein. Beyond amino acid number 40, the individual amino acid peaks in each round of the sequencing became sufficiently small and irregular so as to prevent a confident identification of the amino acid released during each round of degradation. **(B)** A rooted phylogenetic tree based on seven cytochrome 579 amino acid sequences taken from the proteins represented by the accession numbers shown in **(A)**. The outlying sequence (lowermost item shown in the figure) represents a monoheme *c*-type cytochrome of similar length present in the genomic sequence of *Candidatus Manganitrophus noduliformans*. The tree was inferred using the maximum likelihood method with 1,000 replicates. The *brackets and Roman numerals* identify the two groups of cytochromes 579 that possess different N-terminal signal peptide sequences. **(C)** Identities and genetic loci of the two proteins in each strain of *L. ferriphilum* that bear a high level of sequence homology with the cytochrome 579 purified from the type strain of *L. ferriphilum*. The genetic loci within each rectangle were obtained from the tBLASTn searches conducted on each strain.

Figure 3B shows a rooted phylogenetic tree based on eight complete protein sequences, seven homologs of cytochrome 579 and an outgroup protein comprised of a *c*-type cytochrome present in the genome of *Candidatus Manganitrophus noduliformans*. Six of the seven sequences fell into one of the two groups associated within the two *brackets* or clades in **Figure 3B** that were arbitrarily designated with the Roman numerals *I* and *II*. The three proteins within *clade I* share the same signal peptide sequence, which is different from the signal peptide sequence shared by the three proteins within *clade II*. The protein represented by the accession number AEQ75424.1 has the same signal peptide sequence as those proteins within *clade II*. However, the rest of its primary structure is sufficiently different so as to not warrant its inclusion within either of the two clades. It should be noted that the sequence for this latter protein was derived from a community-wide sequencing project, not from a purified strain of *L. ferriphilum*.

The results of BLASTp searches do not permit one to identify which homologous protein(s) may actually be expressed by individual strains of the same species. Rather, the BLASTp algorithm searches the relevant database for all proteins of all assemblies of the single species, in this case *L. ferriphilum*. It seemed unlikely that every individual strain of *L. ferriphilum* contains the genetic material to express all seven of the highly homologous forms of cytochrome 579 that are present in the species. To determine which cytochromes 579 could be expressed in individual strains of *L. ferriphilum*, translating tBLASTn searches were conducted on the nucleotide assemblies of the seven strains of *L. ferriphilum* that are currently available (Mi et al., 2011; Cardenas et al., 2014; Jiang et al., 2015; Ferrer et al., 2016; Issotta et al., 2016; Zhang et al., 2017; Christel et al., 2018). These searches were limited to those nucleotide assemblies derived from the genomic sequencing of pure strains; no relevant metagenomic sequence data were considered.

The data in **Figure 3C** show the results of conducting tBLASTn searches on each of the seven strains of *L. ferriphilum* that are available in the NCBI database using six of the seven proteins in **Figures 3A**,**B** as the queries. Each strain of *L. ferriphilum* contains the genetic material to express two, and only two, of the seven homologs of cytochrome 579. The corresponding genetic locus for each homolog in each strain is identified in the figure. Further, one of the two genes in each strain codes for a protein contained within one clade in **Figure 3B**, while the other of the two genes codes for a protein contained within the other clade in **Figure 3B**. That is, each strain possesses the genetic codes to express one protein from the contents of each of the two clades in **Figure 3B**. Genomic sequences for the homolog represented by the accession number AEQ75424.1 were not identified in any of these seven strains using the tBLASTn searches.

Structural Properties of the Native Cytochrome 579

The apparent molecular mass of native cytochrome 579 in 0.01 N sulfuric acid was determined by Rayleigh light scattering analysis (Wyatt, 1993). **Figure 4A** shows a Debye plot obtained

with five concentrations of cytochrome 579. Extrapolation of the data to zero angle and zero concentration yielded a weight average molecular mass for the native protein of approximately 125,000 Daltons, a value close to that anticipated for an oligomer composed of eight subunits of approximately 16 kDa each. The oligomeric nature of the native protein was also evident from its chromatographic behavior on gel filtration media. **Supplementary Figure S2** shows the behavior of native cytochrome 579 when the purified protein was subjected to column chromatography on Sephadex G-75. Sephadex G-75 has an effective fractionation range for globular proteins between 3,000 and 80,000 Da. The native cytochrome 579 eluted from the Sephadex G-75 column in the void volume, thus indicating that the molecular mass of the native protein was, at the very least, in excess of 80,000 Da.

Extrapolation of the data in **Figure 4A** to zero angle yielded a value for the second virial coefficient (Wyatt, 1993) of cytochrome 579 of 2.3×10^{-4} mole ml/g^2, indicating that the cytochrome and the solvent interacted in a positive manner, an observation consistent with the observed acid solubility and stability of the protein. Extrapolation of the data to zero concentration yielded a curve that was approximately linear near the ordinate intercept. A value of 10.5 nm was calculated from the linear portion of the curve for the root mean square radius of native cytochrome 579. The root mean square radius (also known as the radius of gyration) is the value of the average distance between each of the light-scattering centers (the individual atoms) in the macromolecule and its center of mass as it exists in the acidic aqueous solvent.

The apparent molecular mass of native cytochrome 579 was also determined by macroion mobility spectrometry (macroIMS). MacroIMS is an electrospray ionization technique whereby macromolecules with masses that can exceed 1 million Daltons are dispersed from dilute solution into droplets of 100–200 nl in volume (van Duijn et al., 2005; Carazzone et al., 2008). Desolvation of these droplets generates highly charged particles that then pass through a neutralizing/charge reduction chamber (Scalf et al., 1999) where they are converted into neutral and singly charged nanoparticles. The resulting reduced-charge particles are then separated in the gas phase according to their electrophoretic mobility and quantified with a condensation particle counter. When the macromolecules are prepared in a buffer amenable to electrospray, even noncovalent polypeptide complexes that are captured within the nl droplet can be transferred intact to the gas phase (van den Heuvel and Heck, 2004).

The macroIMS spectrum obtained with purified cytochrome 579 is shown in **Figure 4B**. A single peak was observed with an apparent molecular mass of 135,000 Daltons. The low protein concentration in the analyte solution, 320 ng/ml, was consistent with the expectation that each 100–200 nl droplet was in the "one analyte per one droplet" operating regime. The 5–6% uncertainty in the absolute accuracy of macromolecular masses as determined by macroIMS measurements (Bacher et al., 2001) meant that these mass results were consistent with those obtained by Rayleigh light scattering analyses.

Spectral Properties of the Purified Cytochrome 579

The absorbance properties of the purified cytochrome are illustrated by the spectra in the visible region shown in **Figure 5A**. The native oxidized cytochrome exhibited a broad absorbance peak at 426 nm. Electrochemical reduction of the cytochrome by soluble Fe(II) produced new absorbance peaks at 441, 540, and 579 nm. These spectral properties are essentially the same as those reported for the prominent cytochromes in cell-free extracts of *L. ferrooxidans* (Hart et al., 1991) and microbial biofilms collected from an acid mine drainage system at the Richmond Mine (Ram et al., 2005; Singer et al., 2008). The *inset* in **Figure 5A** is a difference spectrum of the absolute spectrum of the Fe(II)-reduced cytochrome minus that of the

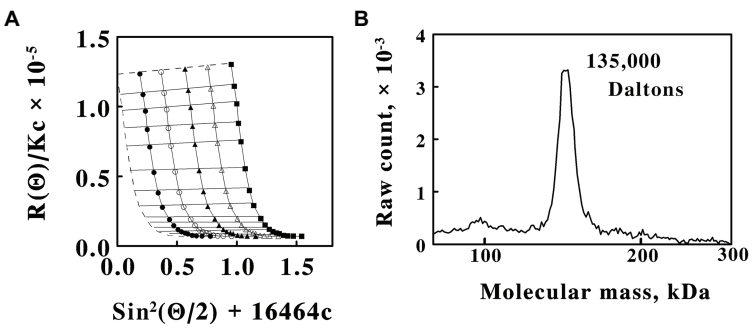

FIGURE 4 | Size analyses of the native cytochrome 579 purified from cell-free extracts of *L. ferriphilum*. **(A)** A Debye plot constructed from static light scattering measurements at different angles and concentrations of purified protein n 0.01 N sulfuric acid. Protein concentrations in μg/ml: 1.15, *closed circles*; 2.31, *open circles*; 3.46, *closed triangles*; 4.62, *open triangles*; and 5.77, *closed squares*. *R*(Ø) is the excess Rayleigh ratio, Ø is the angle between the incident and the scattered light, *K* is an instrument constant that is determined independently, *c* is the concentration of cytochrome 579, and 16,464 is an arbitrary constant that permitted an appropriate spread of the data for plotting and visualizing the results. Each datum represents the mean of at least eight determinations. The concentration variations and the angular data were fit with first and second order polynomials, respectively. The *dashed lines* represent extrapolation to zero angle (*horizontal line*) and zero concentration (*vertical curve*), respectively. **(B)** Macroion mobility spectrum of purified cytochrome 579 conducted at 320 ng/ml. The spectrum consisted of the accumulated counts of 10 repeat scans of 300 s each.

oxidized cytochrome. While the peak at 442 nm in the difference spectrum is reminiscent of that of an *a*-type cytochrome, the peak at 579 nm is considerably blue-shifted from that anticipated for a typical *a*-type cytochrome (Smith, 1978). The visible spectrum of the reduced protein did not change when the protein was exposed to saturating concentrations of carbon monoxide, consistent with an overall pattern of hexa-coordinate, low spin ferric, and ferrous hemes.

The alkaline pyridine hemochromes of cytochrome 579 are shown in **Figure 5B**. The initial spectrum of the ferric protein in alkaline pyridine showed a broad, relatively weak Soret band at 430 nm and a broad visible band at 600 nm (data not shown). This spectrum gradually changed with a half-time of around 6 min to another, more stable, form (*dashed curve*) with a sharp Soret at 418 nm and a weak visible band at 545 nm. The ferrous spectrum (*solid curve*) showed typical absorbance band shapes for a low spin α,β-band ferrous heme, except that the α-band was at the unexpected wavelength of 567 nm. The same ferrous alkaline pyridine hemochromogen spectrum was obtained regardless of whether dithionite was added before, during, or after the slow spontaneous transformation evident in the oxidized alkaline pyridine spectra.

Formation of the reduced pyridine hemochrome spectrum represents a powerful technique used to eliminate those differences in the native absorbance spectra of different heme groups due to the surrounding protein (Bartsch, 1971; Berry and Trumpower, 1987). The unusual α-band at 567 nm in the pyridine hemochrome of cytochrome 579 was significantly higher than those of heme *b* or *c* (557 and 550 nm, respectively; Berry and Trumpower, 1987) or isobacteriochlorin hemes such as siroheme (557 nm; Murphy and Siegel, 1973), yet significantly lower than those in hemes *a* (587 nm) or the *d*-type hemes (618 nm; Berry and Trumpower, 1987; Palmer and Reedijk, 1992). The prosthetic group(s) of cytochrome 579 could not be extracted from the protein by a variety of organic extraction protocols or by thioether bond cleavage reagents typically used to liberate heme *c*, when applied either with or without prior protein denaturation and digestion with proteases. Simultaneous reduction with mercaptoethanol and alkylation in the presence of 4.0 M 4-vinylpyridine (Ozols, 1990) successfully liberated all chromophores from the apoprotein, indicating that the heme may be covalently conjugated to the apoprotein by a novel sulfhydryl bond. Unfortunately, what appeared to be subsequent polymerization of the liberated hemes produced a series of heterogeneous but closely related fractions from which a single purified component has not yet been achieved or characterized. It was evident, however, that cytochrome 579 represents a heme (or hemes) of novel structure that is unique to respiratory iron oxidation in *L. ferriphilum*.

Electron Transfer Reactions Between Cytochrome 579 and Soluble Iron

The oligomeric nature of the native protein was also evident from kinetic studies on the oxidation and reduction reactions of the purified cytochrome with soluble iron. Purified cytochrome 579 was redox-active with ferric and ferrous sulfate at pH 1.5. **Supplementary Figure S3A** shows a series of kinetic scans that were acquired when the purified cytochrome 579 was rapidly mixed with 30 mM Fe(II) in a stopped flow spectrophotometer equipped with a rapid scan module. The Soret peak of the cytochrome shifted from 426 nm in the oxidized state to 441 nm in the Fe(II)-reduced state. Concomitantly, an alpha absorbance band appeared with a maximum at 579 nm. The entire set of kinetic data in **Supplementary Figure S2A** was described by a single exponential function of time (t):

$$\text{absorbance} = \mathrm{B} + (\mathrm{A} - \mathrm{B})\,\mathrm{e}^{-\mathrm{kt}}$$

where *A* and *B* represent the absolute spectrum of the oxidized and reduced cytochrome, respectively, and *k* is the pseudo-first order rate constant for the absorbance change at all wavelengths within the rapid scan. The value of *k* that provided the best fit of the above equation to the kinetic data in **Supplementary Figure S3A** was 2.8 ± 0.2 s^{-1}. **Supplementary Figure S3B** shows a single kinetic trace extracted from a three-dimensional plot such as that shown in

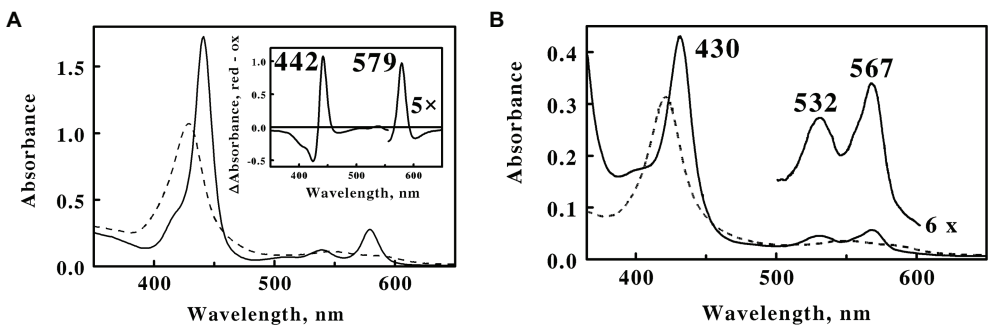

FIGURE 5 | Visible absorbance spectra of cytochrome 579 purified from cell-free extracts of *L. ferriphilum*. **(A)** Spectra of oxidized (*dashed line*) and reduced (*solid line*) cytochrome 579 at 160 μg/ml. Both spectra were determined in 0.01 N sulfuric acid at 25°C. The absorbance spectrum of the reduced cytochrome was determined 10 min after mixing the sample of oxidized cytochrome with an excess of ferrous sulfate. *Inset*, a difference spectrum representing the absolute spectrum of the Fe(II)-reduced cytochrome minus that of the oxidized cytochrome. **(B)** Alkaline pyridine hemochromogen spectra of cytochrome 579 at 45 μg/ml. Spectra: final spectrum of the ferric heme, *dashed curve*; and spectrum of the ferrous heme, *solid curve*.

Supplementary Figure S3A, except that the concentration of soluble ferrous iron in S3B was 60 mM. Like the entire data set at all wavelengths, the increase in absorbance at 579 nm that was concomitant with the reduction of the cytochrome 579 fit a single exponential function of time with a pseudo-first order rate constant to 84 ± 5 s^{-1}.

The dependence of the observed pseudo-first order rate constant for the Fe(II)-dependent reduction of cytochrome 579 on the concentration of Fe(II) is shown in **Figure 6A**. The concentration of ferrous ions had a profound influence on the value of the rate constant. A mere 12-fold increase in the concentration of the reducing agent (5–60 mM) increased the value of the apparent rate constant over 22,000-fold from 3.7×10^{-4} to 84 s^{-1}. The *inset* in **Figure 6A** shows a linear plot of the logarithm of the pseudo-first order rate constant as a function of the logarithm of the soluble ferrous iron concentration. The slope of this log-log plot, 5.0, is effectively the Hill coefficient for the reduction reaction and represents the power to which the concentration of ferrous ion must be raised in order to create a linear correlation among the kinetic data.

Similar results were obtained when analogous kinetic experiments were conducted on the Fe(III)-dependent oxidation of the reduced cytochrome. The dependence of the observed pseudo-first order rate constant for the Fe(III)-dependent oxidation of reduced cytochrome 579 on the concentration of Fe(III) is shown in **Figure 6B**. The concentration of ferric ions also had a strong influence on the value of the rate constant for oxidation of the reduced cytochrome. The same 12-fold increase in the concentration of the oxidizing agent increased the value of the apparent rate constant 13,000-fold from 3.8×10^{-3} to 51 s^{-1}. The *inset* in **Figure 6B** shows a linear plot of the logarithm of the pseudo-first order rate constant as a function of the logarithm of the soluble ferric iron concentration. The slope of this log-log plot, 3.7, is the Hill coefficient for the oxidation reaction and represents the power to which the concentration of ferric ion must be raised in order to create a linear correlation among the oxidation kinetic data.

Figure 6C shows the dependence of the logarithm of the ratio of kinetic rate constants for electron transfer on the logarithm of the concentration of soluble iron. The ratio of the iron-dependent reduction and oxidation rate constants for cytochrome 579 taken from **Figures 6A**,**B**, respectively, comprises the equilibrium constant for the following reaction:

$$\mathrm{Cyt579(III) + Fe(II) \leftrightarrow Cyt579(II) + Fe(III)}$$

The rate and equilibrium constants for this electron transfer reaction are related as follows:

$$\left(\mathrm{RT}/\mathrm{nF}\right)\log\left(\mathrm{k_{red}}/\mathrm{k_{ox}}\right) = \Delta\mathrm{E^0}_{\mathrm{Cyt579}} - \Delta\mathrm{E^0}_{\mathrm{Fe}}$$

where k_{red} and k_{ox} represent the pseudo-first order rate constants for the iron-dependent reduction and oxidation, respectively, of cytochrome 579, ΔE^0_{Cyt579} and ΔE^0_{Fe} represent the standard reduction potentials for cytochrome 579 and soluble iron, respectively, R is the gas constant, T is the temperature, F is Faraday's constant, and n is the number of electrons transferred

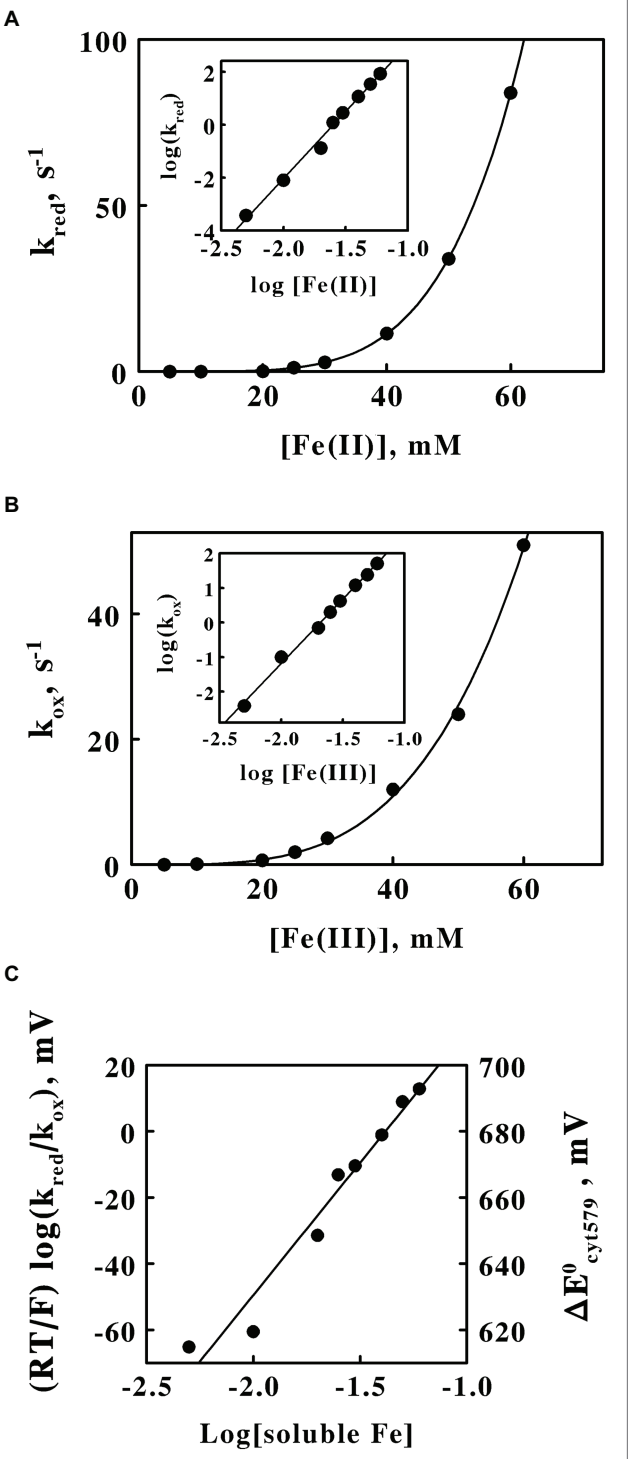

FIGURE 6 | Reactivity of cytochrome 579 with soluble iron at pH 1.5. Absorbance changes were monitored in a stopped flow spectrophotometer when the purified cytochrome was rapidly mixed with a molar excess of soluble iron. **(A)** Dependence of the pseudo-first order rate constant for the reduction of oxidized cytochrome 579 on the concentration of ferrous ions. Final concentrations after mixing: cytochrome 579, 8.6 μM; and sulfuric acid, 0.02 M. The *curve* drawn through the data points was proportional to the concentration of ferrous ions raised to the power of 5.0. *Inset*, the dependence of the logarithm *(Continued)*

FIGURE 6 | of the pseudo-first order rate constant on the logarithm of the molar concentration of ferrous ions. **(B)** Dependence of the pseudo-first order rate constant for the oxidation of reduced cytochrome 579 on the concentration of ferric ions. Final concentrations after mixing: cytochrome 579, 8.2 μM; and sulfuric acid, 0.02 M. The *curve* drawn through the data points was proportional to the concentration of ferric ions raised to the power of 3.7. *Inset*, the dependence of the logarithm of the pseudo-first order rate constant on the logarithm of the molar concentration of ferric ions. **(C)** Dependence of the logarithm of the ratio of the pseudo-first order rate constants for the reduction and oxidation of the cytochrome on the logarithm of the concentration of soluble iron. The reduction potentials for the purified cytochrome on the right ordinate were obtained using a standard reduction potential for the ferric/ferrous couple of 680 mV in 0.02 M sulfuric acid at pH 1.5.

in the reaction, in this case, one. If the data in **Figures 6A**,**B** were simply linear second-order plots, then the resulting logarithm of the ratio of rate constants would be single value that one could use to calculate a single value of ΔE^0_{Cyt579} from the calculated value of ΔE^0_{Fe} = 680 mV in 0.02 M sulfuric acid, pH 1.5 (Blake and Shute, 1987; Blake et al., 1991). However, the striking nonlinearity of the kinetic data in **Figures 6A**,**B** creates the relationship shown in **Figure 6C**, where the logarithm of the ratio of kinetic rate constants is itself a linear function of the logarithm of the concentration of soluble iron. This relationship implies that the standard reduction potential of cytochrome 579 is itself a function of iron concentration, which can only happen if soluble iron binds to the octameric cytochrome and thereby influences its electron transfer reactivity and redox potential. At an iron concentration of approximately 40 mM, where k_{red}/k_{ox} = 1.0, the reduction potential of cytochrome 579 is equal to that of the soluble iron in sulfuric acid, or 680 mV. At iron concentrations higher than 40 mM, the cytochrome 579 has a higher reduction potential than 680 mV and becomes more oxidizing, while at iron concentrations lower than 40 mM, the cytochrome 579 has a lower reduction potential than 680 mV and becomes less oxidizing. These conclusions are summarized by the corresponding calculated changes in the reduction potentials shown on the *right* ordinate in **Figure 6C**.

DISCUSSION

The first notable feature of these results is the unusual absorbance properties of the purified cytochrome. The absorbance maximum at 579 nm in the reduced state is too long for the heme to be a classic *b*- or *c*-type heme protein but too short to be an *a*- or *d*-type heme protein (Palmer and Reedijk, 1992). This observation is particularly interesting because all seven of the homologous cytochromes 579 identified above contain the CXXCH amino acid sequence that is generally acknowledged to represent a signature sequence for heme binding in *c*-type heme proteins. While it is evident from **Figure 3A** that the heme binding motif was only partially sequenced in the purified protein, the amino acids that surrounded the two difficult-to-measure cysteine residues in the motif were nonetheless identical to those in the other cytochrome 579 homologs. Additional evidence that the heme group associated with cytochrome 579 has a unique structure comes from the unexpected absorbance properties of the heme's reduced alkaline pyridine hemochromogen spectrum. When heme proteins are exposed to strong base in the presence of high concentrations of a nitrogenous iron ligand like pyridine, the heme is released from the denatured protein and pyridines become the heme's 5th and 6th axial ligands. The absorbance properties of such hemes are entirely dependent on the structures of the hemes themselves and are no longer influenced by their former native environoments in their respective intact heme proteins (Bartsch, 1971; Berry and Trumpower, 1987). The reduced alkaline pyridine hemochromogen absorbance peaks obtained herein at 567 nm in the absolute spectrum and 568–569 nm in the reduced minus oxidized difference spectrum (data not shown) are well-above those of *b*- and *c*-type hemes (557 and 550 nm, respectively) and well-below that of *a*-type hemes (587 nm; Berry and Trumpower, 1987; Palmer and Reedijk, 1992). The reduced alkaline pyridine hemochromogen spectrum of the cytochrome 579 purified from the community biofilm was reported at 587 nm (Singer et al., 2008), which matches that of an *a*-type heme (Berry and Trumpower, 1987), but does not match that of 567–568 nm reported herein. Of course, the heterogeneous community biofilm could have well-contained relatively higher levels of *a*-type heme proteins.

A cytochrome with a reduced absorbance peak at 572 nm was produced when a recombinant cytochrome *c* from *Thermus thermophilus* was expressed in *Escherichia coli* and heated to 70°C at neutral pH (Fee et al., 2004). Evidence was presented that one of the two vinyl groups in the heme was oxidized to a formyl group. The standard reduction potential of this recombinant cytochrome 572 was 340 mV, approximately 120 mV more positive than that of the recombinant cytochrome *c* with two intact vinyl groups. The reduced alkaline pyridine hemochromogen spectrum of this recombinant, heated cytochrome 572 had an absorbance maximum at 581 nm. However, the peak absorbance of the reduced alkaline pyridine hemochromogen of the native cytochrome 572 purified from the microbial community biofilm was given as 568 nm (Singer et al., 2008), which actually matches that reported herein for cytochrome 579 purified from the type strain of *L. ferriphilum*. It is evident that more experiments are required to clear up these discrepancies. In the meantime, it has become evident that cytochrome 579 represents the product of a novel heme that may potentially interact with the CXXCH sequence motif in a novel manner depending on the nature of any structural modifications in the heme group which have yet to be fully established.

The second notable feature of these results is the realization that the genetic sequences of each of the seven strains of *L. ferriphilum* that are available at the present time only contain the capacity to express two homologs or isozymes per strain of all the seven possible cytochromes 579. Further, each of the two homologs present in each strain is expressed in conjunction with a different signal peptide. The influence, if any, of these two different signal peptides on the eventual extracytoplasmic localization of the respective cytochromes 579 is unknown. There are literally hundreds of different signal peptides tentatively identified in prokaryotes. For example,

careful proteogenomic studies confirmed 156 out of the 337 signal peptides predicted by version 4.0 of SignalP in the complete genome of *E. coli* strain K-12 (Ivankov et al., 2013). Far fewer, if any, putative signal peptides have been confirmed by actual experimentation in lesser-studied organisms like *L. ferriphilum*. Is one homolog of cytochrome 579 destined for the periplasm, while the other homolog is destined for the outer membrane? We simply do not know. What we do hypothesize is that both homologs were co-purified from acidic cell-free extracts of the type strain cultured herein on soluble ferrous ions. This hypothesis is based on the following two observations: (i) the deconvoluted positive-ion electrospray mass spectrum of the purified protein shown in **Figure 2B** provided evidence of two polypeptides that differed by only 125 Da; and (ii) the protein bands in **Figure 2A** that represented the purified cytochrome 579 at different concentrations were sufficiently diffuse so as to suggest the presence of two polypeptides with molecular masses that were not separable by this technique (16,015 vs. 16,140 Da). Because all of the homologs featured in **Supplementary Figure S1** are highly similar with only minor, generally conservative, amino acid differences, it is perhaps not surprising that the kinetic studies conducted herein and elsewhere (Blake and White, 2020) exhibited no evidence of heterogeneity in the purified cytochrome's functional behavior. Whether the purified cytochrome studied herein is a mixture of two homologs, or a mixture of one homolog with varying degrees of post-translational modification, or some combination of both, the fact remains that the purified cytochrome behaves as would a single homogeneous protein.

The sequence of the first 49 amino acids that was obtained using the purified cytochrome 579 was not identical to those of the proteins with accession numbers WP_036080593.1 and WP_014961757.1, the two homologs of cytochrome 579 expected to be expressed by the type strain (**Figure 3C**). Likewise, the molecular masses of the two protein subunits presented in **Figure 2B** did not exactly match those expected from the two homologs in the type strain minus the masses of their respective signal peptides and the associated heme groups. However, it should be noted that others have reported posttranslational modifications and sequence variations of cytochromes 579 present in *Leptospirillum*-dominated biofilms in different stages of development (Singer et al., 2010). One can also note that the type strain of *L. ferriphilum* was received in this laboratory from the DSMZ over 20 years ago as an active culture, and that the culture has been maintained by continually passaging the active planktonic culture the entire time. Consequently, it is entirely possible that slight genetic drift has occurred in the cytochromes 579 during that period compared with the cytochromes 579 present in "identical" strains that have been similarly maintained for long periods of time in other laboratories.

The third notable feature of these results is the observation, by two entirely different analytical methods, that the native cytochrome 579 appeared to be an octameric protein over nearly a 20-fold range in protein concentrations. At the lower end of this range, 320 ng/ml or 20 nM in subunits, macroion mobility spectrometry could easily detect sub-nanomolar concentrations of individual subunits or oligomeric proteins of less than eight subunits. This laboratory previously quantified monoclonal antibodies whose antigen binding sites were occupied with 0, 1, or 2 protein antigens when the total antibody concentration was 5 nM, or 10 nM in binding sites (Blake and Blake, 2012). There were no hints of lower-weight protein intermediates in the spectrum shown in **Figure 4B**. At the higher end of this range, 5.77 μg/ml or 360 nM in subunits, static light scattering measurements could easily detect polymerization of the cytochrome 579 to aggregates greater than eight subunits. If further aggregation had occurred, the weight-average molecular mass on the ordinate intercept would simply have been higher than that shown in **Figure 4A**. The reasons why the other purified cytochromes 579 do not appear to be oligomeric (Hart et al., 1991; Singer et al., 2008) are not known.

What are the advantages, if any, if cytochromes 579 form octamers in the acidic periplasm of *L. ferriphilum*? There is no evidence that bulk ferrous ions enter the neutrophilic cytoplasm when *L. ferriphilum* or related species respire aerobically on their limited range of inorganic electron donors. Thus, whether the electron donor is soluble iron or an insoluble iron-containing sulfide mineral, respiratory electrons must be conducted from the periphery of the Gram-negative organism across the periplasm to a terminal oxidase embedded in the plasma membrane. An impressive volume of work has been reported on prokaryotes that conduct dissimilatory reduction of extracellular soluble and insoluble iron oxides under anaerobic or microaerophilic conditions (Lovley et al., 2004; Weber et al., 2006; Paquete and Louro, 2010, 2014). A comprehensive *in silico* survey of 594 complete prokaryotic genomes identified 1,659 multiheme *c*-type cytochromes in 258 of the organisms (Sharma et al., 2010). A clear subset of these 258 organisms had the capacity to express many different multi-heme *c*-type cytochromes into their periplasm and/or their outer membranes, ostensibly to facilitate the required dissimilatory electron transfer reactions to extracellular soluble and insoluble acceptors. Although *L. ferriphilum* has not been shown to conduct dissimilatory electron transfer to extracellular acceptors (Weber et al., 2006), its aerobic energy metabolism is totally dependent on electron flow in the opposite direction from extracellular electron donors to the cytoplasmic membrane. Whether an organism expresses one large multiheme protein with 6–10 hemes or eight smaller monoheme proteins that form a stable octamer would seem to make little difference in the final product. We hypothesize that this eight-heme octamer functions to facilitate electron flow across the periplasm of *L. ferriphilum* during aerobic respiration on extracellular reduced iron.

The oligomeric nature of the native cytochrome 579 was also evident from the fourth notable feature of these results, the extraordinary dependencies of the rate constants for the iron-dependent reduction and oxidation of the cytochrome on the concentrations of soluble iron. The strong kinetic synergy in the reduction and oxidation of the oligomeric protein suggested that there is facile communication among the redox states of the eight heme groups, just as is hypothesized for the individual hemes in the decaheme cytochromes *c* in

Shewanella (Paquete and Louro, 2010, 2014). Although the rates of the reduction of the purified cytochrome at Fe(II) concentrations in excess of 30 mM were clearly sufficiently rapid to be of physiological significance, the corresponding rates of reduction at sub-mM concentrations of Fe(II), conditions that are more likely to be of physiological significance to the intact organism, were far too slow to account for the overall rate of oxygen consumption by these organisms. Others have noted that the iron-dependent reduction of cytochrome 579 is faster and more complete in proteins extracted from early-stage biofilms as opposed to proteins taken from more mature biofilms (Singer et al., 2008). It has even been proposed that the slightly different cytochrome 579 that is expressed in early-stage biofilms could serve as an alternative initial oxidant of soluble iron, along with the cytochrome 572 in the outer membrane (Singer et al., 2010). Do planktonic *L. ferriphilum* behave more like organisms in early-stage biofilms than do those in later stages of biofilm development?

Of course, conditions experienced by the cytochrome 579 in the crowded, gel-like environment of the periplasm may not have been duplicated by the *in vitro* kinetic experiments conducted on purified proteins in dilute solutions. Rather, the functional properties of an intact electron transport chain that consists of the sequential transfer of electrons from iron to cytochrome 572 to cytochrome 579 to a terminal oxidase in the plasma membrane are inferred from observations on isolated biomolecules in dilute solutions. This laboratory has utilized an integrating cavity absorption meter to monitor absorbance changes in intact microorganisms as they respire aerobically on reduced iron (Blake and Griff, 2012; Li et al., 2015; Blake et al., 2016; Blake and White, 2020). Kinetic studies conducted on intact *L. ferrooxidans* (Blake and Griff, 2012) and intact *L. ferriphilum* (Blake and White, 2020) were both consistent with the hypothesis that reduced cytochrome 579 was an obligatory intermediate in the aerobic iron respiratory chain of both organisms. It is evident that the direct and accurate observation of absorbance changes *in situ* in intact organisms can be a useful complement to traditional reductionist approaches and to recent advances in proteomic and transcriptomic studies. In the case of *L. ferriphilum*, the ferrous iron-dependent reduction of the cytochrome 579 in the intact organism was complete within the 1 s mixing dead time of the instrument, even when the soluble ferrous concentration was as low as 50 μM (Blake and White, 2020). It was evident that the rate of the iron-dependent reduction of the cytochrome 579 *in situ* was far more rapid than was the corresponding rate of reduction of the purified protein *in vitro* under the same solution conditions. These contradictory observations constitute a cautionary example where a functional behavior that was monitored *in vitro* did not accurately reflect the analogous functional behavior that was monitored *in situ*.

DATA AVAILABILITY STATEMENT

The raw data supporting the conclusions of this article will be made available by the authors, without undue reservation.

AUTHOR CONTRIBUTIONS

RB wrote the manuscript and directed the project, and also collected and interpreted the stopped-flow kinetic data. JS directed the N-terminal amino acid sequencing and the electrospray mass spectrometry on the native cytochrome. RT conducted the alkaline pyridine hemochromogen studies. RW constructed the phylogenetic tree of the different homologs of cytochrome 579. All authors contributed to the article and approved the submitted version.

FUNDING

This work was supported by grant number 1830866 from the National Science Foundation.

ACKNOWLEDGMENTS

We thank Elizabeth Shute and Felicia Rusnak for expert technical assistance.

SUPPLEMENTARY MATERIAL

The Supplementary Material for this article can be found online at: https://www.frontiersin.org/articless/10.3389/fmicb.2021.673066/full#supplementary-material

REFERENCES

Bacher, G., Szymanski, W. W., Kaufman, S. L., Zollner, P., Blaas, D., and Allmaier, G. (2001). Charge-reduced nano electrospray ionization combined with differential mobility analysis of peptides, proteins, glycoproteins, noncovalent protein complexes and viruses. *J. Mass Spectrom.* 36, 1038–1052. doi: 10.1002/jms.208

Bartsch, R. G. (1971). Cytochromes: bacterial. *Methods Enzymol.* 23, 344–363. doi: 10.1016/S0076-6879(71)23110-4

Berry, E. A., and Trumpower, B. L. (1987). Simultaneous determination of hemes *a*, *b*, and *c* from pyridine hemochrome spectra. *Anal. Biochem.* 161, 1–15. doi: 10.1016/0003-2697(87)90643-9

Blake, R. C. II, Anthony, M. D., Bates, J. D., Hudson, T., Hunter, K. M., King, B. J., et al. (2016). *In situ* spectroscopy reveals that microorganisms in different phyla use different electron transfer biomolecules to respire aerobically on soluble iron. *Front. Microbiol.* 7:1963. doi: 10.3389/fmicb.2016.01963

Blake, R. C. II, and Blake, D. A. (2012). Electrospray ionization-ion mobility spectrometry identified monoclonal antibodies that bind exclusively to either the monomeric or a dimeric form of prostate specific antigen. *Anal. Chem.* 84, 6899–6906. doi: 10.1021/ac301527v

Blake, R. C. II, and Griff, M. N. (2012). *In situ* spectroscopy on intact *Leptospirillum ferrooxidans* reveals that reduced cytochrome 579 is an obligatory intermediate in the aerobic iron respiratory chain. *Front. Microbiol.* 3:136. doi: 10.3389/fmicb.2012.00136

Blake, R. C. II, Howard, G. T., and McGinness, S. (1994). Enhanced yields of iron-oxidizing bacteria by *in situ* electrochemical reduction of soluble iron

in the growth medium. *Appl. Environ. Microbiol.* 60, 2704–2710. doi: 10.1128/AEM.60.8.2704-2710.1994

Blake, R. C. II, and Shute, E. A. (1987). Respiratory enzymes of *Thiobacillus ferrooxidans*: a kinetic study of electron transfer between iron and rusticyanin in sulfate media. *J. Biol. Chem.* 262, 14983–14989. doi: 10.1016/S0021-9258(18)48126-4

Blake, R. C. II, and White, R. A. III (2020). *In situ* absorbance measurements: a new means to study respiratory electron transfer in chemolithotrophic microoganisms. *Adv. Microb. Physiol.* 76, 81–127. doi: 10.1016/bs.ampbs.2020.01.003

Blake, R. C. II, White, K. J., and Shute, E. A. (1991). Mixed ligand complexes of iron with cyanide and phenanthroline as new probes of metalloprotein electron transfer reactivity. *J. Biol. Chem.* 266, 19203–19211. doi: 10.1016/S0021-9258(18)54983-8

Carazzone, C., Rami, R., and Pergantis, S. A. (2008). Nanoelectrospray ion mobility spectrometry online with inductively coupled plasma-mass spectrometry for sizing large proteins, DNA, and nanoparticles. *Anal. Chem.* 80, 5812–5818. doi: 10.1021/ac7025578

Cardenas, J. P., Lazcano, M., Ossandon, F. J., Corbett, M., Holmes, D. S., and Watkin, E. (2014). Draft genome sequence of the iron-oxidizing acidophile *Leptospirillum ferriphilum* type strain DSM 14647. *Genome Announc.* 2:e01153–14. doi: 10.1128/genomeA.01153-14

Christel, S., Herold, M., Bellenberg, S., El Hajjami, M., Buett-Dihn, A., Pivkin, I. V., et al. (2018). Multi-omics reveals the lifestyle of the acidophilic, mineral-oxidizing model species *Leptospirillum ferriphilum*^{T}. *Appl. Environ. Microbiol.* 84:e02091–17. doi: 10.1128/AEM.02091-17

Claverie, J. M., and Notredame, C. (2007). *Bioinformatics for Dummies. 2nd Edn.* Indianapolis, IN: Wiley Publishing, Inc.

Coram, N. J., and Rawlings, D. E. (2002). Molecular relationship between two groups of the genus *Leptospirillum* and the finding that *Leptospirillum ferriphilum* sp. nov. dominates South African commercial biooxidation tanks that operate at 40°C. *Appl. Environ. Microbiol.* 68, 838–845. doi: 10.1128/AEM.68.2.838-845.2002

DeSa, R. J., and Matheson, I. B. C. (2004). A practical approach to interpretation of singular value decomposition results. *Methods Enzymol.* 384, 1–8. doi: 10.1016/S0076-6879(04)84001-1

Fee, J. A., Todaro, T. R., Luna, E., Sanders, D., Hunsicker-Wang, L. M., Patel, K. M., et al. (2004). Cytochrome rC_{552}, formed during expression of the truncated, *Thermus thermophilus* cytochrome c_{552} gene in the cytoplasm of *Escherichia coli*, reacts spontaneously to form protein-bound 2-formyl-4-vinyl (*Spirographis*) heme. *Biochemistry* 43, 12162–12176. doi: 10.1021/bi048968l

Ferrer, A., Bunk, B., Sproer, C., Biedendieck, R., Valdes, N., Jahn, M., et al. (2016). Complete genome sequence of the bioleaching bacterium *Leptospirillum* sp. group II strain CF-1. *J. Biotechnol.* 222, 21–22. doi: 10.1016/j.jbiotec.2016.02.008

Garcia-Moyano, A., Gonzalez-Toril, E., Moreno-Paz, M., Parro, V., and Amils, R. (2008). Evaluation of *Leptospirillum* spp. in the Rio Tinto, a model of interest to biohydrometallurgy. *Hydrometallurgy* 94, 155–161. doi: 10.1016/j.hydromet.2008.05.046

Golovacheva, R. S., Golyshina, O. V., Karavaiko, G. I., Dorofeev, A. G., Pivovarova, T. A., and Chernykh, N. A. (1992). A new iron-oxidizing bacterium, Leptospirillum thermoferrooxidans sp. nov. *Microbiology* 61, 744–750.

Goltsman, D. S. A., Dasari, M., Thomas, B. C., Shah, M. B., VerBerkmoes, N. C., Hettich, R. L., et al. (2013). New group in the *Leptospirillum* clade: cultivation-independent community genomics, proteomics, and transcriptomics of the new species "*Leptospirillum* group IV UBA BS". *Appl. Environ. Microbiol.* 79, 5384–5393. doi: 10.1128/AEM.00202-13

Goltsman, D. S. A., Denef, V. J., Singer, S. W., VerBerkmoes, N. C., Lefsrud, M., Mueller, R. S., et al. (2009). Community genomic and proteomic analyses of chemoautotrophic iron-oxidizing "*Leptospirillum rubarum*" (group II) and "*Leptospirillum ferrodiazotrophum*" (group III) bacteria in acid mine drainage biofilms. *Appl. Environ. Microbiol.* 75, 4599–4615. doi: 10.1128/AEM.02943-08

Gouy, M., Guindon, S., and Gascuel, O. (2009). SeaView version 4: a multiplatform graphical user interface for sequence alignment and phylogenetic tree building. *Mol. Biol. Evol.* 27, 221–224. doi: 10.1093/molbev/msp259

Hart, A. J., Murrell, J. C., Poole, P. K., and Norris, P. R. (1991). An acid-stable cytochrome in iron-oxidizing *Leptospirillum ferrooxidans*. *FEMS Microbiol. Lett.* 81, 89–94. doi: 10.1111/j.1574-6968.1991.tb04718.x

Hippe, H. (2000). *Leptospirillum* gen.nov. (ex Markosyan 1972), nom. rev., including *Leptospirillum ferrooxidans* sp. nov. (ex Markosyan 1972), nom. rev. and *Leptospirillum thermoferrooxidans* sp. nov. (Golovacheva et al., 1992). *Int. J. Syst. Evol. Microbiol.* 50, 501–503. doi: 10.1099/00207713-50-2-501

Hoang, D. T., Chernomor, O., von Haeseler, A., Minh, B. Q., and Vinh, L. S. (2017). UFBoot2: improving the ultrafast bootstrap approximation. *Mol. Biol. Evol.* 35, 518–522. doi: 10.1093/molbev/msx281

Issotta, F., Galleguillos, P. A., Moya-Beltran, A., Davis-Belmar, C. S., Rautenbach, G., Covarrubias, P. C., et al. (2016). Draft genome sequence of chloride-tolerant *Leptospirillum ferriphilum* Sp-Cl from industrial bioleaching operations in northern Chile. *Stand. Genomic Sci.* 11:19. doi: 10.1186/s40793-016-0142-1

Ivankov, D. N., Payne, S. H., Galperin, M. Y., Bonissone, S., Pevzner, P. A., and Frishman, D. (2013). How many signal peptides are there in bacteria? *Environ. Microbiol.* 15, 983–990. doi: 10.1111/1462-2920.12105

Jeans, C., Singer, S. W., Chan, C. S., VerBerkmoes, N. C., Shah, M., Hettich, R. L., et al. (2008). Cytochrome 572 is a conspicuous membrane protein with iron oxidation activity purified directly from a natural acidophilic microbial community. *ISME J.* 2, 542–550. doi: 10.1038/ismej.2008.17

Jiang, H., Liang, Y., Yin, H., Xiao, Y., Guo, X., Xu, Y., et al. (2015). Effects of arsenite resistance on the growth and functional gene expression of *Leptospirillum ferriphilum* and *Acidithiobacillus thiooxidans* in pure culture and coculture. *Biomed. Res. Int.* 2015:203197. doi: 10.1155/2015/203197

Kalyaanamoorthy, S., Minh, B. Q., Wong, T. K. F., von Haeseler, A., and Jermiin, L. S. (2017). ModelFinder: fast model selection for accurate phylogenetic estimates. *Nat. Methods* 14, 587–589. doi: 10.1038/nmeth.4285

Katoh, K., and Standley, D. M. (2013). MAFFT multiple sequence alignment software version 7: improvements in performance and usability. *Mol. Biol. Evol.* 30, 772–780. doi: 10.1093/molbev/mst010

Li, T. F., Painter, R. G., Ban, B., and Blake, R. C. II (2015). The multicenter aerobic iron respiratory chain of *Acidithiobacillus ferrooxidans* functions as an ensemble with a single macroscopic rate constant. *J. Biol. Chem.* 290, 18293–18303. doi: 10.1074/jbc.M115.657551

Lovley, D. R., Holmes, D. E., and Nevin, K. P. (2004). Dissimilatory Fe(III) and Mn(IV) reduction. *Adv. Microb. Physiol.* 49, 219–286. doi: 10.1016/S0065-2911(04)49005-5

Markosyan, G. E. (1972). A new iron-oxidizing bacterium – *Leptospirillum ferrooxidans* nov. gen. nov. sp. *Biol. J. Armenia* 25, 26–29.

Mi, S., Song, J., Lin, J., Che, Y., Zheng, H., and Lin, J. (2011). Complete genome of *Leptospirillum ferriphilum* ML-04 provides insight into its physiology and environmental adaptation. *J. Microbiol.* 49, 890–901. doi: 10.1007/s12275-011-1099-9

Murphy, M. J., and Siegel, L. M. (1973). Siroheme and sirohydrochlorin: the basis for a new type of porphyrin-related prosthetic group common to both assimilatory and dissimilatory sulfite reductases. *J. Biol. Chem.* 248, 6911–6919. doi: 10.1016/S0021-9258(19)43436-4

Nguyen, L. T., Schmidt, H. A., von Haeseler, A., and Minh, B. Q. (2014). IQ-TREE: a fast and effective stochastic algorithm for estimating maximum-likelihood phylogenies. *Mol. Biol. Evol.* 32, 268–274. doi: 10.1093/molbev/msu300

Ozols, J. (1990). Amino acid analysis. *Methods Enzymol.* 182, 587–601. doi: 10.1016/0076-6879(90)82046-5

Palmer, G., and Reedijk, J. (1992). Nomenclature of electron-transfer proteins. *J. Boil. Chem.* 267, 665–677.

Paquete, C. M., and Louro, R. O. (2010). Molecular details of multielectron transfer: the case of multiheme cytochromes from metal respiring organisms. *Dalton Trans.* 39, 4259–4266. doi: 10.1039/B917952F

Paquete, C. M., and Louro, R. O. (2014). Unveiling the details of electron transfer in multicenter redox proteins. *Acc. Chem. Res.* 47, 56–65. doi: 10.1021/ar4000696

Ram, R. J., VerBerkmoes, N. C., Thelen, M. P., Tyson, G. W., Baker, B. J., Blake, R. C. II, et al. (2005). Community proteomics of a natural microbial biofilm. *Science* 308, 1915–1920. doi: 10.1126/science.1109070

Rawlings, D. E., and Johnson, D. B. (2007). The microbiology of biomining: development and optimization of mineral-oxidizing microbial consortia. *Microbiology* 153, 315–324. doi: 10.1099/mic.0.2006/001206-0

Rawlings, D. E., Tributsch, H., and Hansford, G. S. (1999). Reasons why '*Leptospirillum*'-like species rather than *Thiobacillus ferrooxidans* are more dominant iron-oxidizing bacteria in many commercial processes for the biooxidation of pyrite and related ores. *Microbiology* 145, 5–13. doi: 10.1099/13500872-145-1-5

Ronk, M., Shively, J. E., Shute, E. A., and Blake, R. C. II (1991). Amino acid sequence of the blue copper protein rusticyanin from *Thiobacillus ferrooxidans*. *Biochemistry* 30, 9435–9442. doi: 10.1021/bi00103a007

Sand, W., Rhode, K., Sobotke, B., and Zenneck, C. (1992). Evaluation of *Leptospirillum ferrooxidans* for leaching. *Appl. Environ. Microbiol.* 58, 85–92. doi: 10.1128/AEM.58.1.85-92.1992

Scalf, M., Westphall, M. S., Krause, J., Kaufman, S. L., and Smith, L. M. (1999). Controlling charge states of large ions. *Science* 283, 194–197. doi: 10.1126/science.283.5399.194

Sharma, S., Cavallaro, G., and Rosato, A. (2010). A systematic investigation of multiheme *c*-type cytochromes in prokaryotes. *J. Biol. Inorg. Chem.* 15, 559–571. doi: 10.1007/s00775-010-0623-4

Singer, S. W., Chan, C. S., Zemla, A., VerBerkmoes, N. C., Hwang, M., Hettich, R. L., et al. (2008). Characterization of cytochrome 579, an unusual cytochrome isolated from an iron-oxidizing microbial community. *Appl. Environ. Microbiol.* 74, 4454–4462. doi: 10.1128/AEM.02799-07

Singer, S. W., Erickson, B. K., VerBrkmoes, N. C., Hwang, M., Shah, M. B., Hettich, R. L., et al. (2010). Posttranslational modification and sequence variation of redox-active proteins correlate with biofilm life cycle in natural microbial communities. *ISME J.* 4, 1398–1409. doi: 10.1038/ismej.2010.64

Smith, L. (1978). Bacterial cytochromes and their spectral characterization. *Methods Enzymol.* 53, 202–212. doi: 10.1016/S0076-6879(78)53025-5

Smith, P. K., Krohn, R. I., Hermanson, G. T., Mallia, A. K., Gartner, F. H., Provenzano, M. D., et al. (1985). Measurement of protein using bicinchoninic acid. *Anal. Biochem.* 150, 76–85. doi: 10.1016/0003-2697(85)90442-7

Tuovinen, O. H., and Kelly, D. P. (1973). Studies on the growth of *Thiobacillus ferrooxidans*. I. Use of membrane filters and ferrous iron agar to determine viable numbers, and comparison with $^{14}CO_2$-fixation and iron oxidation as measures of growth. *Arch. Microbiol.* 88, 285–296.

Tyson, G. W., Lo, I., Baker, B. J., Allen, E. E., Hugenholtz, P., and Banfield, J. F. (2005). Genome-directed isolation of the key nitrogen fixer *Leptospirillum ferrodiazotrophum* sp. nov. from an acidophilic microbial community. *Appl. Environ. Microbiol.* 71, 6319–6324. doi: 10.1128/AEM.71.10.6319-6324.2005

van den Heuvel, R. H., and Heck, A. J. (2004). Native protein mass spectrometry: from intact oligomers to functional machineries. *Curr. Opin. Chem. Biol.* 8, 519–526. doi: 10.1016/j.cbpa.2004.08.006

van Duijn, E., Bakkes, P. J., Heeren, R. M. A., van den Heuvel, R. H. H., van Heerikhuizen, H., van der Vies, S. M., et al. (2005). Monitoring macromolecular complexes involved in the chaperonin-assisted protein folding cycle by mass spectrometry. *Nat. Methods* 2, 371–376. doi: 10.1038/nmeth753

Weber, K. A., Achenbach, L. A., and Coates, J. D. (2006). Microorganisms pumping iron: anaerobic microbial iron oxidation and reduction. *Nat. Rev. Microbiol.* 4, 752–764. doi: 10.1038/nrmicro1490

Wyatt, P. J. (1993). Light scattering and the absolute characterization of macromolecules. *Anal. Chim. Acta* 272, 1–40. doi: 10.1016/0003-2670(93)80373-S

Zhang, X., Liu, X., Liang, Y., Xiao, Y., Ma, L., Guo, X., et al. (2017). Comparative genomics unravels the functional roles of co-occurring acidophilic bacteria in bioleaching heaps. *Front. Microbiol.* 8:790. doi: 10.3389/fmicb.2017.00790

Conflict of Interest: The authors declare that the research was conducted in the absence of any commercial or financial relationships that could be construed as a potential conflict of interest.

frontiers in Microbiology

ORIGINAL RESEARCH
published: 15 June 2021
doi: 10.3389/fmicb.2021.664216

Respiratory Heme A-Containing Oxidases Originated in the Ancestors of Iron-Oxidizing Bacteria

Mauro Degli Esposti[1], Ana Moya-Beltrán[2,3], Raquel Quatrini[2,3,4] and Lars Hederstedt[5]**

[1] Center for Genomic Sciences, Universidad Nacional Autónoma de México (UNAM), Cuernavaca, Mexico, [2] Fundación Ciencia & Vida, Santiago, Chile, [3] ANID–Millennium Science Initiative Program–Millennium Nucleus in the Biology of the Intestinal Microbiota, Santiago, Chile, [4] Facultad de Medicina y Ciencia, Universidad San Sebastian, Santiago, Chile, [5] The Microbiology Group, Department of Biology, Lund University, Lund, Sweden

Respiration is a major trait shaping the biology of many environments. Cytochrome oxidase containing heme A (COX) is a common terminal oxidase in aerobic bacteria and is the only one in mammalian mitochondria. The synthesis of heme A is catalyzed by heme A synthase (CtaA/Cox15), an enzyme that most likely coevolved with COX. The evolutionary origin of COX in bacteria has remained unknown. Using extensive sequence and phylogenetic analysis, we show that the ancestral type of heme A synthases is present in iron-oxidizing Proteobacteria such as *Acidithiobacillus* spp. These bacteria also contain a deep branching form of the major COX subunit (COX1) and an ancestral variant of CtaG, a protein that is specifically required for COX biogenesis. Our work thus suggests that the ancestors of extant iron-oxidizers were the first to evolve COX. Consistent with this conclusion, acidophilic iron-oxidizing prokaryotes lived on emerged land around the time for which there is the earliest geochemical evidence of aerobic respiration on earth. Hence, ecological niches of iron oxidation have apparently promoted the evolution of aerobic respiration.

Keywords: cytochrome oxidase, heme A synthase, CtaA, CtaG, bacterial evolution

OPEN ACCESS

Edited by:
Catarina M. Paquete, Universidade Nova de Lisboa, Portugal

Reviewed by:
Eva Nyvltova, University of Miami Health System, United States
Martin Warren, University of Kent, United Kingdom

****Correspondence:***
Mauro Degli Esposti
mauro1italia@gmail.com
Lars Hederstedt
Lars.Hederstedt@biol.lu.se

Specialty section:
This article was submitted to Microbial Physiology and Metabolism, a section of the journal Frontiers in Microbiology

Received: *04 February 2021*
Accepted: *12 May 2021*
Published: *15 June 2021*

Citation:
Degli Esposti M, Moya-Beltrán A, Quatrini R and Hederstedt L (2021) Respiratory Heme A-Containing Oxidases Originated in the Ancestors of Iron-Oxidizing Bacteria. Front. Microbiol. 12:664216. doi: 10.3389/fmicb.2021.664216

INTRODUCTION

Aerobic respiring organisms contain terminal oxygen reductases for energy metabolism at different oxygen levels in the environment. The evolutionary origin of these oxygen-consuming enzymes is unknown (Castresana and Saraste, 1995; Pereira et al., 2001; Han et al., 2011; Sharma and Wikström, 2014). A common class of terminal oxidases is heme A-containing proton pumping cytochrome oxidase (COX), which has a relatively low affinity for oxygen (Han et al., 2011; Degli Esposti et al., 2019) and consequently must have evolved during or after the Great Oxygenation Event (GOE), which produced stable levels of oxygen on earth (Konhauser et al., 2011). COX of the family A of Heme Copper Oxygen Reductases (HCO) is widespread in all kingdoms of life (Castresana and Saraste, 1995; Pereira et al., 2001; Han et al., 2011; Degli Esposti, 2020) due to extensive Lateral Gene Transfer (LGT) (Nelson-Sathi et al., 2015; Soo et al., 2017). Subsequently bacterial COX became the cytochrome *c* oxidase of mitochondrial organelles. The prokaryotes that initially evolved COX have remained elusive (Pereira et al., 2001; Soo et al., 2017; Degli Esposti et al., 2019; Matheus Carnevali et al., 2019) and, consequently, the origin of aerobic respiration is a major unresolved problem. To address the question of COX origin, we have studied the phylogeny of two proteins specifically required for COX biosynthesis and performed new and expanded analyses

on the phylogeny of the major protein subunit of COX. The latter analysis is focused on family A oxidases since the phylogenetic distribution of family B oxidases, which also have heme A, is rather patchy among bacteria. Indeed, it is possible that family B derived from some ancestral family A oxidase (Degli Esposti, 2020). Combined with other findings, our results suggest that family A COX has evolved in ancestors of extant acidophilic iron-oxidizing bacteria.

COX in mitochondria and aerobic bacteria is a multi-protein intrinsic membrane complex with several metal prosthetic groups. Subunit I, COX1, contains two heme A molecules (**Figures 1A,B**), denoted cytochrome *a* and a_3 in the assembled enzyme, and one copper atom, Cu_B. COX2 contains two copper atoms in a binuclear center, Cu_A (**Figure 1A**). The redox reaction of molecular oxygen reduction at the heme a_3-Cu_B center is coupled to the generation of an electrochemical gradient via conserved proton-conducting channels (Pereira et al., 2001; Ferguson and Ingledew, 2008; Han et al., 2011; Sharma and Wikström, 2014; Degli Esposti, 2020). This gradient drives ATP synthesis and various other energy-demanding functions in the cell.

Biosynthesis of COX requires multiple proteins that catalyze the formation of heme A, or are involved in the insertion of the metal cofactors and overall assembly of the enzyme in the membrane (**Figure 1A**). Heme A as a prosthetic group is only found in respiratory oxygen reductases (Hederstedt, 2012). The biosynthesis of heme A from protoheme IX (heme B) involves two enzymes (**Figure 1A**; Mogi et al., 1994; Hederstedt, 2012). First heme O synthase, CtaB/Cox10/CyoE, catalyzes formation of heme O and then heme A synthase, CtaA/Cox15, converts heme O into heme A. Synthesis of heme A **Figure 1B** requires ambient oxygen levels (Brown et al., 2002) that were attained in primordial earth only after the GOE. In bacteria, the genes for COX proteins and those for heme A synthesis and COX assembly factors show modularity, i.e., the genes are frequently clustered in the chromosome (**Figure 1C**). Based on the assumption that COX proteins and protein factors specifically required for COX biosynthesis have coevolved, we analyzed the phylogeny of bacterial CtaA to obtain insights on how COX has evolved. The results prompted us to establish a revised expanded classification of heme A synthases and develop a scheme for their evolution based upon phylogenetic data, which was compared to that of COX1 and the COX-specific assembly factor CtaG to define the likely origin of COX.

MATERIALS AND METHODS

Phylogenetic Analysis

Database searches and genome scanning were conducted by iterative BlastP (Basic Local Alignment Search Tool for Proteins) searches as detailed in the **Supplementary Material**. Briefly, wide searches expanded to 5000 hits were usually performed with the DELTABlast program using the BLOSUM62 substitution matrix (Boratyn et al., 2012). Integrated searches were expanded in granular detail to recognize established conserved domains of the (super) family to which it may belong (as shown in the NCBI protein website)[1] (Lu et al., 2020) preferentially using BlastP and PSI-BLAST searches restricted to 500 hits. Classification of HCO has been undertaken using the bioinformatic classifier available at http://www.evocell.org/hcoevocell.org (Sousa et al., 2011).

Maximum likelihood (ML) trees were initially produced with the MEGA5.2 program to elaborate BLAST outputs and preliminary phylogenetic frameworks (Degli Esposti et al., 2020), with a variety of substitution models (generally the WAG model for multitopic membrane proteins and the Dayhoff or BLOSUM62 substitution matrix for membrane-anchored, predominantly water-exposed proteins, and discrete gamma distribution of four categories to account for evolutionary rate differences among sites and lineages, allowing some sites to be evolutionarily invariable (Tamura et al., 2011). The MEGA program was also used to transform ML trees into ultrametricized trees similar to BEAST tree outputs using the condensed option, with a cut-off of 50% bootstrap support.

Phylogenetic inference was routinely undertaken using either Bayesian or ML probabilistic approaches. We reconstructed ML trees using the more sophisticated IQ-Tree program (Nguyen et al., 2015), normally from its server http://iqtree.cibiv.univie.ac.at/ (Trifinopoulos et al., 2016) with the ultrafast bootstrap option of 1000 replicates and the LG model as in previous publications (Degli Esposti et al., 2019; Spang et al., 2019). Additionally, we used mixture models of amino acid substitution, such as C20 (Le et al., 2008) and EX_EHO (Le and Gascuel, 2010). We found that the EX_EHO model tended to produce trees with stronger support than those obtained with the LG model for CtaA and COX1 proteins, but not with caa3_CtaG proteins, probably because of their limited conservation. ML trees were reconstructed also with the program PhyML 3.0 (Guindon et al., 2010), and generally run from the online platform http://www.phylogeny.fr/index.cgi using the WAG model and the Shimodaira–Hasegawa (SH)-like statistical support analysis. We used the program FigTree 1.4.4[2] for visualizing trees obtained with various methods.

We preferentially used the BEAST 2.6.2 package for Bayesian phylogenetic inference (Drummond et al., 2006) because of its information-rich outputs (Lee et al., 2013; Drummond and Bouckaert, 2015). Although predominantly utilized for divergence studies of animal species with genes including mitochondrial COX1-3 (Lee et al., 2013; Ratnasingham and Hebert, 2013), BEAST analysis has been applied also to study the molecular evolution of bacterial redox proteins (Khadka et al., 2018; Bouckaert et al., 2019). Manually curated alignments were first loaded into the BEAUti 2 app of the package to prepare.xml files containing the detailed settings for the phylogenetic analysis run with the BEAST program (Bouckaert et al., 2019). Routinely, such settings included: four gamma categories with shape 0.3 (or other empirically estimated values) and proportion of invariant sites from 0.01 to 0.1, depending on the protein and its taxonomic sampling; BLOSUM62 or WAG as substitution models; Relaxed Clock Log model and the gamma option for the Yule birth model (other priors were left in their default setting); at least 2

[1] https://www.ncbi.nlm.nih.gov/Structure/cdd/

[2] http://tree.bio.ed.ac.uk/software/figtree/

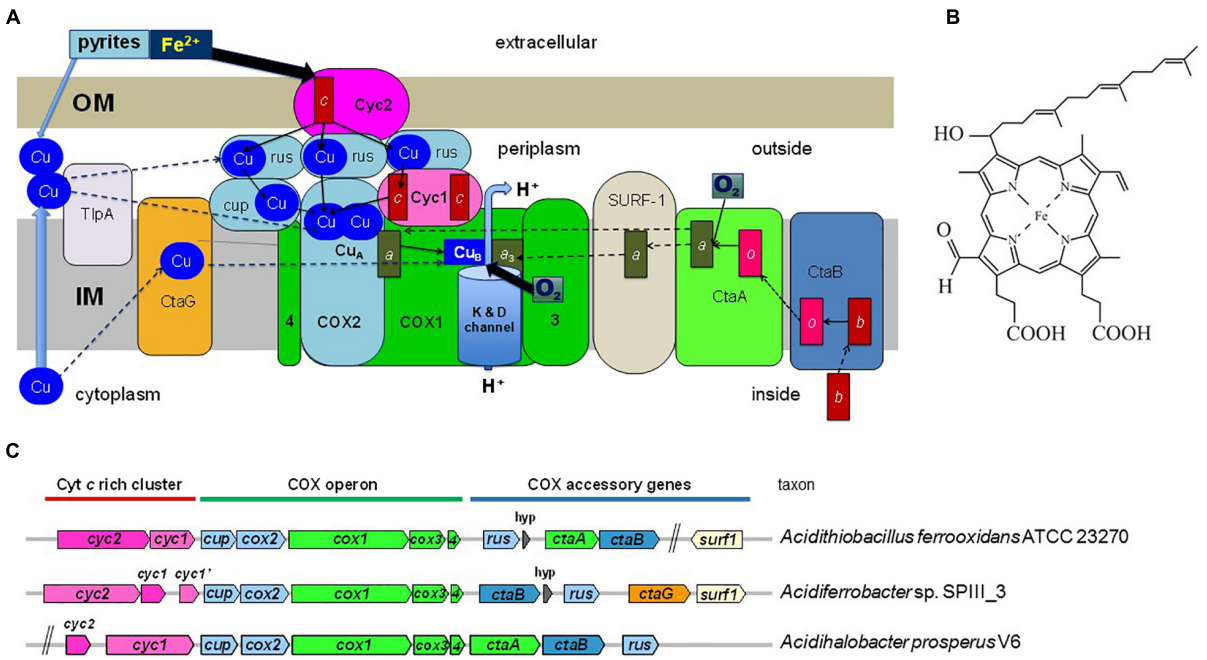

FIGURE 1 | Energy metabolism and COX gene clusters of iron-oxidizing bacteria. **(A)** The figure illustrates the electron transport system in the cytoplasmic membrane of iron-oxidizing bacteria and proteins that function in COX biogenesis. The two heme A molecules in the COX1 subunit are indicated by dark green rectangles labeled *a* and a_3. COX2 and other Cu-binding proteins are colored in pale blue, while proteins containing *c*-type cytochromes (heme C is indicated by the red rectangle) are in dark pink. COX3 and COX4 are abbreviated as 3 and 4, respectively, and are colored in bright green as subunit COX1. OM and IM indicate the outer and inner (cytoplasmic) membrane of the bacterium. Rusticyanin (rus) is shown in multiple copies because it is present in large excess with respect to the other redox proteins of the system (Blake et al., 2016). Cup refers to membrane-bound cupredoxin proteins (Degli Esposti, 2020). TlpA stands for thioredoxin-like protein A, a membrane-bound protein involved in Cu_A assembly. Thin arrows indicate electron transfer routes while dashed arrows indicate steps in COX biogenesis. The water enzyme product of COX is not shown. The overall scheme of electron transfer from extracellular donors to oxygen reduced in the cytoplasmic membrane applies to a variety of bacteria that have multiheme *c* cytochromes instead of rusticyanin mediators (Deng et al., 2018). **(B)** Structure of heme A. The difference of this variant of heme compared to heme B (protoheme IX) is the hydroxyethyl-farnesyl group and the formyl group. **(C)** Gene clusters for COX in bacteria often contain genes for heme A synthesis (*ctaA, ctaB*) and COX assembly (*ctaG, surf1*), as illustrated by representative gene clusters of iron-oxidizing Proteobacterial taxa. The size of the gene symbols is roughly proportional to gene length. hyp, gene for a short hypothetical protein.

million iterations for the Markov chain of Monte Carlo analysis with 5 pre-burnin. Trees were stored every 1000 iterations and then usually reduced by 10% burnin to generate Maximal Clade Credibility (MCC) output files with minimal posterior value of 0.1 using the TreeAnnotator app (Drummond and Bouckaert, 2015). MCC trees were graphically elaborated with the FigTree program, which produced a wealth of quantitative data for the various branches (Lee et al., 2013; Khadka et al., 2018), or visualized using the program DensiTree 2 (Bouckaert and Heled, 2014; Drummond and Bouckaert, 2015). In a few cases, we also used the program MrBayes v.3.0b4 as in reference (Degli Esposti et al., 2020).

Protein Sequence Analysis

Given that the quality of phylogenetic trees heavily depends upon the accuracy of the protein sequence alignments upon which they are reconstructed, we performed an in depth analysis of the sequence variation of each protein to guide its proper alignment. This analysis was undertaken by exploiting the versatility of the MEGA programs after importing whole sequences or alignments of multiple sequences downloaded directly from the BlastP searches. An initial alignment of the protein was built with a minimal set of 20 sequences using either the ClustalW or the MUSCLE algorithm within the MEGA5 program (Tamura et al., 2011). The alignments thus obtained contained several gaps that were often unnecessary to maximize for local sequence similarity, as verified by visual inspection; such gaps were then removed along manual refinements conducted with iterative rounds of implementation that were aided by the inclusion, whenever possible, of protein sequences for which 3D information is currently available. The alignments were then progressively enlarged to include sequences that were representative of different prokaryotic taxa in which the protein was found, with additional refinements to accommodate local sequence variations. Short residue gaps that were needed to properly align a single sequence were subsequently deleted along detailed manual refinements of local sequence similarity and congruent hydropathy profile.

The enlarged alignments thus refined were used to build phylogenetic trees encompassing most major molecular variants, as well as the overall taxonomic distribution of any protein studied. Some of the alignments are available upon request. Sequences that produced long branches or displayed high substitution rates were identified by statistical analysis as

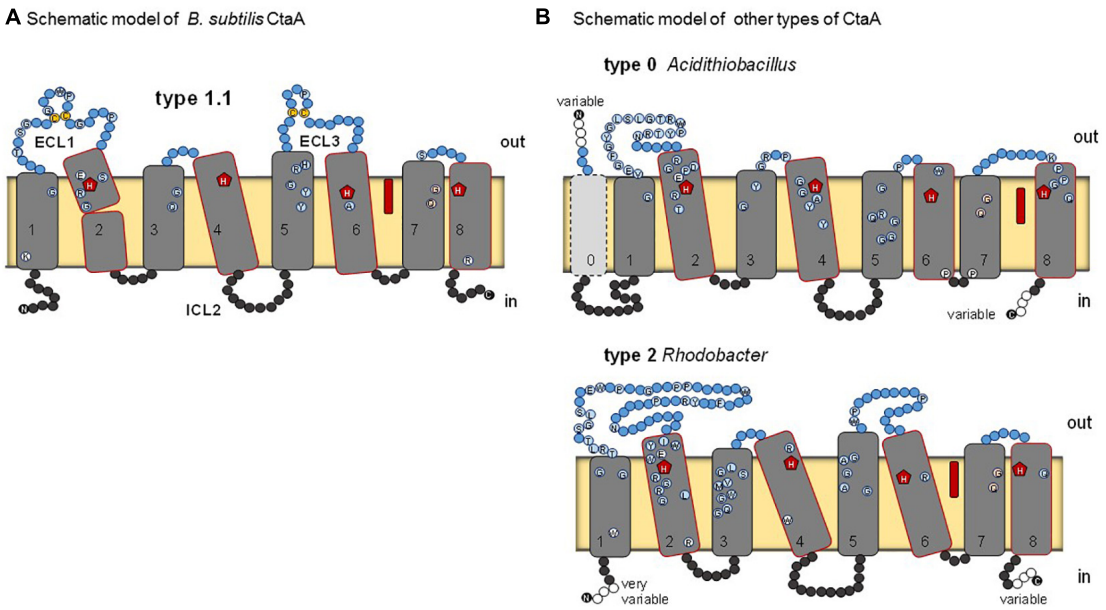

FIGURE 2 | Schematic models for various types of heme A synthase. **(A)** *B. subtilis* CtaA, based on the reported crystal structure of the protein (Niwa et al., 2018). Residues conserved among type 1.1 CtaA are shown by circles. ECL1 and ECL3 indicate extracellular loops on the periplasmic side (outer side) of the membrane. Heme B (red elongated symbol) occupies the cofactor domain. Disulfide linked cysteine residues in ECL1 and ECL3 are in yellow. **(B)** Models for type 0 and type 2 CtaA represented by the *Acidithiobacillus ferrooxidans* and *Rhodobacter capsulatus* enzymes, respectively. See **Table 1** for the classification of CtaA proteins. Residues that are conserved in the sequences of the represented types are shown by circles as in Panel **(A)**.

described in **Supplementary Material**. Such sequences were subsequently removed, often substituted by sequences clustering in the same subclade that did not display equivalent branch aberrations. Then the set of aligned sequences for a given protein was reduced to simplify tree presentation without altering the tree topology found with larger alignments.

The CtaA, caa3_CtaG and COX1 proteins studied here have multiple membrane-spanning segments (TM). Consequently, we have applied extensive hydropathy analysis to all proteins analyzed, using both the TMpred server https://embnet.vital-it.ch/software/TMPRED_form.html and the TMHMM Server v. 2.0 https://hsls.pitt.edu/obrc/index.php?page=URL1164644151. These programs utilize complementary methodologies that help define the ends of predicted TM (Möller et al., 2001). This sequence analysis was combined with the available 3D structural information for COX subunits (Iwata et al., 1995; Svensson-Ek et al., 2002), and CtaA (Niwa et al., 2018), to define the TM regions and other topological features in distant protein homologs, as in the case of proteins from iron-oxidizers. Membrane topology was graphically rendered with the program TOPO2[3] and then used as a platform for building the protein models.

Other Methods

Genome completeness was evaluated as described previously (Degli Esposti et al., 2019), or using information available in the GTNB database (Parks et al., 2018).

[3]http://www.sacs.ucsf.edu/TOPO2/

RESULTS AND DISCUSSION

Iron-Oxidizing Bacteria Appear to Have an Ancestral Form of Heme A Synthase

Heme A synthase is required for the biosynthesis of the characteristic heme prosthetic groups in COX. The heme A synthase enzyme protein belongs to the super-family of Cox15-CtaA, cl19388, members of which are widespread among prokaryotes (He et al., 2016). The 3D structure of *Bacillus subtilis* CtaA has been determined by X-ray diffraction crystallography (Niwa et al., 2018) and that of *Aquifex aeolicus* analyzed by cryogenic electron microscopy (Zeng et al., 2020). *B. subtilis* CtaA has 8 TM and two extended extracellular loops, ECL1 and ECL3, each of which contains a conserved pair of cysteine residues linked by a disulfide bond (Lewin and Hederstedt, 2016; Niwa et al., 2018; **Figure 2A**). Overall, the CtaA protein comprises two nearly superimposable 4-helical bundle domains, with the C-terminal domain binding a *b*-type heme group via two conserved histidine residues, while the N-terminal domain seems to contain the catalytic site for conversion of heme O into heme A (**Figure 2**).

Many members of the Cox15-CtaA superfamily lack cysteine pairs in extracellular loops, for example *Rhodobacter capsulatus* CtaA (**Figure 2B**) and the eukaryotic Cox15 homologs. These variants have been called type 2 to distinguish them from type 1 proteins represented by *B. subtilis* CtaA (He et al., 2016). In recent explorative work on CtaA sequences (Degli Esposti et al., 2020) we found more variants, as presented in the expanded classification system (**Table 1**) and in the unrooted phylogenetic

TABLE 1 | Classification of heme A synthase proteins.

Classification		Description					Taxonomic distribution
Class	**Type**	**ECL1 length**	**Cys pair 1**	**ECL3 length**	**Cys pair 2**	**Other features**	
D	0	Medium	No	Extremely short	No	Compact TM6&7	Acidithiobacilli, Fe-oxidizing gammaproteobacteria, *Nitrococcus, Metallibacterium*, *Salinisphaera*, *Defluviimonas*; thermoacidophilic Archaea: Thermoplasmatales, Sulfolobales and *Ca.* Marsarchaeota
C	1.0	Medium	Yes	Long	No	Long ICL2	Alicyclobacilli iron-oxidizers
C	1.0	Medium	Yes	Medium or short	No	Fused with ctaB or alone	Deinococus-Thermus, Chloroflexi MAG, Armatimonadetes, Verrucomicrobia, *Spirobacillus, Staphylococcus*, deltaproteobacteria, Euryarchaeaota MAGs
C	1.0	Long	Yes	Variable	No	Often substitution E57N *; many from metagenomes	Verrucomicrobia, CFB including *Ca.* Marinimicrobia, Balneolaeota, other phyla, unclassified bacteria
C	1.0	Medium or long	Yes	Medium or long	No	Cys pair 1 separated by 6 aa	Chloroflexi, Acetothermia (fused with CtaB)
C	1.0	Long	Yes	Very short	No	3D structure^, Cys pair 1 separated by 5 aa	Aquificae e.g., *Aquifex aeolicus* and *Hydrogenovirga*
B	1.1	Medium	Yes	Medium	Yes	3D structure~, Cys pair 1 separated by 6 aa	Bacillales, Cyanobacteria, Actinobacteria, Proteobacteria, *Ktenobacter* (fused with CtaB)
B	1.1	Medium	Yes	Short	Yes	Substitution E57K and H123N *	betaproteobacteria e.g., *Ca.* Accumulibacter, Acidiferrobacteraceae e.g., *Sulfurifustis*
B	1.1	Long	Yes	Long	Yes	Fused with ctaB, Cys pair 2 separated by 8-9 aa	*Bdellovibrio* & *Halobacteriovorax,* alphaproteobacteria MAG, other Proteobacteria
B	1.2	Long	Yes	Very short	Yes	Substitution H278D *	Aquificae e.g., *Thermocrinis*
C	1.3	Medium	Yes	Short	No	Substitution H60N *	Actinobacteria: Acidimicrobiaceae; Proteobacteria MAG
A	1.4	Medium	Yes			4TM, Cys pair separated by 6 aa	Archaea: TACK (*Aeropyrum pernix*), Euryarchaeota & Asgard
D	1.5	Medium to long	No	Long	No	Long ICL2	Verrucomicrobia, Acidobacteria, Chlorobi, *Ca.* Rokubacteria, *Ca.* Poribacteria, Omnitriophica, *Ca.* Division NC10, *Salinibacter*, *Ca.* Entotheonella, Planctomycetes
D	2.0	Extremely long	No	Long	No	Long ICL2	Gemmatimonadetes, Flavobacteria, *Ca.* Caldichraeota, Chloroflexi, Proteobacteria, mitochondria (Cox15)

The new classification of CtaA proteins here presented is expanded compared to that of reference (He et al., 2016) to include all the different types and subtypes that have been found in current versions of the NCBI database. The first column shows the alternative classification in classes A to D (Lewin and Hederstedt, 2016). ECL1 and ECL3 indicate major extracellular loops while ICL2 indicates intracellular loop 2. See ***Figure 2*** *for structural models of various types of CtaA. ~ (Niwa et al., 2018), ^ (Zeng et al., 2020), * (B. subtilis CtaA residue number; see* ***Figure 2A****).*

tree of **Supplementary Figure 1** (left). We also discovered a potential root for the phylogeny of CtaA in the Domain of Unknown Function 420 (DUF420) that has four TM. CtaM of *Staphylococcus aureus*, *Bacillus anthracis* and *B. subtilis* contain the DUF420 domain and are required for assembly of active COX, but dispensable for heme A synthesis (Hammer et al., 2016; von Wachenfeldt et al., 2021).

Our comprehensive new classification of heme A synthases (**Table 1**) is based upon the integration of the molecular features found in all variants present in current NCBI protein resources, including recently added metagenome data, and the consistent phylogenetic pattern of the variants that emerged from multiple approaches of phylogenetic analysis (detailed in the **Supplementary Material**). The Bayesian tree shown in **Figure 3A** represents a condensed view of the current phylogenetic distribution of CtaA proteins in prokaryotes, encompassing diverse representatives not only of type 1 and 2, but also members of two variants that we defined recently (Degli Esposti et al., 2020). One such variant is a derivative of type 1, called type 1.5. The other variant could not be fitted in either type 1 or type 2 and hence is called type 0 (**Table 1**). The type 0 CtaA proteins are very divergent in sequence but contain the invariant residues that are considered crucial for activity of heme A synthases (Hederstedt, 2012) (**Figure 2B**) and their genes are often present at the end of either the *rus* operon encoding COX subunits (**Figure 1C**) or the cytochrome bo_3 operon of acidophilic Fe^{2+}-oxidizers (Appia-Ayme et al., 1999; Quatrini et al., 2009; Issotta et al., 2018).

Type 0 CtaA consistently forms the basal branch in phylogenetic trees comprising all types of CtaA proteins

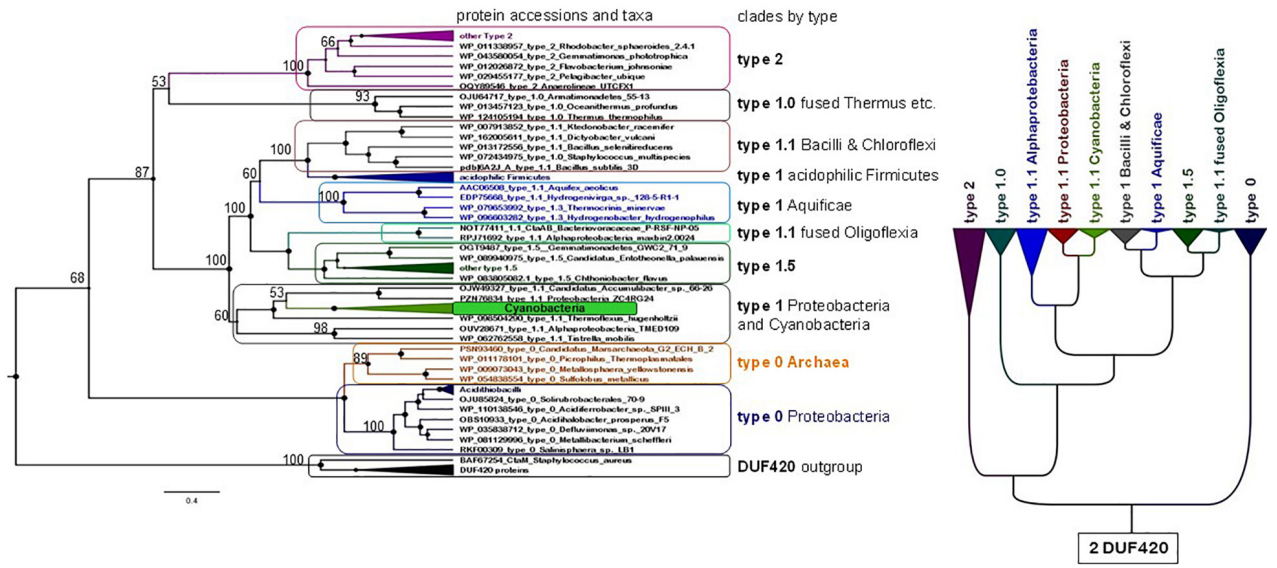

FIGURE 3 | Phylogeny and evolution of heme A synthase. **(A)** Bayesian Maximal Clade Credibility (MCC) tree obtained with the BEAST package using an alignment of 53 CtaA and 7 DUF420 protein sequences as the outgroup. A similar topology was seen in ML trees obtained with the same alignment and different methods (**Supplementary Figure 2** and results not shown). The alignment included 358 amino acid positions. Posterior support is expressed by the size of the dark circles on the nodes, the largest size representing 1 = 100%. Percentage values adjacent to various nodes are additionally shown. **(B)** Scheme for the molecular evolution of CtaA modelled on the silhouette of the Bayesian tree of bacterial CtaA proteins shown in **Supplementary Figure 3**. A primordial gene (presumed to encode a 4TM DUF420 protein) was duplicated and fused in tandem to give rise to a gene encoding a type 0-like CtaA protein. During subsequent evolution of CtaA, pairs of cysteine residues in ECL1 and ECL3 have been acquired and lost, depending on the lineage.

(**Figures 3A**, **4** and **Supplementary Figures 2–5**). This pattern suggests a scheme for the molecular evolution of CtaA proteins (**Figure 3B**), which fundamentally follows the branching order of Bayesian (ultrametric) trees obtained from comprehensive alignments of the bacterial variants of CtaA. We hypothesize that the gene for a four TM DUF420 protein might have been duplicated and fused to form the gene for the ancestor of all current CtaA proteins (**Figure 3B**). Type 0 CtaA may constitute the extant descendant of such an ancestral protein, from which the type 2 and type 1 CtaA branched off. This branching might have occurred simultaneously, forming the sister clades that are frequently observed in phylogenetic trees (**Figures 3**, **4** and **Supplementary Figure 3**; He et al., 2016; Degli Esposti et al., 2020), or in a rapid sequence of differentiation, in which the cysteine pairs of current type 1.1 CtaA might have been acquired gradually, as suggested by some Maximum Likelihood (ML) trees (**Supplementary Figure 4**). The latter possibility is sustained by the occurrence of type 1.0 CtaA proteins having only the first cysteine pair and a long ECL1 comparable to that of type 2 CtaA (**Table 1**). These proteins are clearly different from type 1.0 proteins such as that of *S. aureus*, which most likely derive from a recent loss of the cysteine pair in ECL3, since they retain the same extracellular loops and closely cluster with type 1.1 CtaA proteins of related taxa such as *B. subtilis* (**Table 1**, **Figures 3**, **4** and **Supplementary Figures 3–5**). Similarly, type 1.5 CtaA likely derives from secondary losses of both cysteine pairs from type 1.1 proteins of Proteobacteria. As known from experiments with *B. subtilis* CtaA, the two cysteine residues in ECL1, but not those in ECL3, are important for heme A synthase activity (Lewin and Hederstedt, 2016) and the size of ECL3 can be changed without loss of enzyme activity (Lewin and Hederstedt, 2008).

In summary, our detailed analysis [see **Supplementary Material** for the evaluation of potential problems arising from Long Branch Attraction, LBA (Brinkmann et al., 2005; Philippe et al., 2005; Bleidorn, 2017)] strongly suggests that type 0 CtaA constitutes the ancestral form of heme A synthase, or a relative thereof (**Figure 3B**). Next, we explored the current taxonomic distribution of these proteins that, following our rationale, would define extant taxa possessing early divergent forms of COX.

Taxonomic Distribution of Ancestral CtaA and Ecological Niches for Bacteria With This Type of CtaA

Blast searches with type 0 CtaA protein sequences against the entire nr database produced significant hits with closely related proteins and a few outgroup proteins. Currently there are about 100 recognized type 0 CtaA proteins, the majority of which is coded by the genomes of prokaryotes that share niches of acid soil or hydrothermal environments (Quatrini and Johnson, 2018; **Supplementary Figure 6**). The taxa of Proteobacteria with acidophilic iron- and sulfur-oxidizing physiology (*Acidithiobacillus*, *Acidiferrobacter* and *Acidihalobacter* spp.) contain the gene for type 0 CtaA as the sole

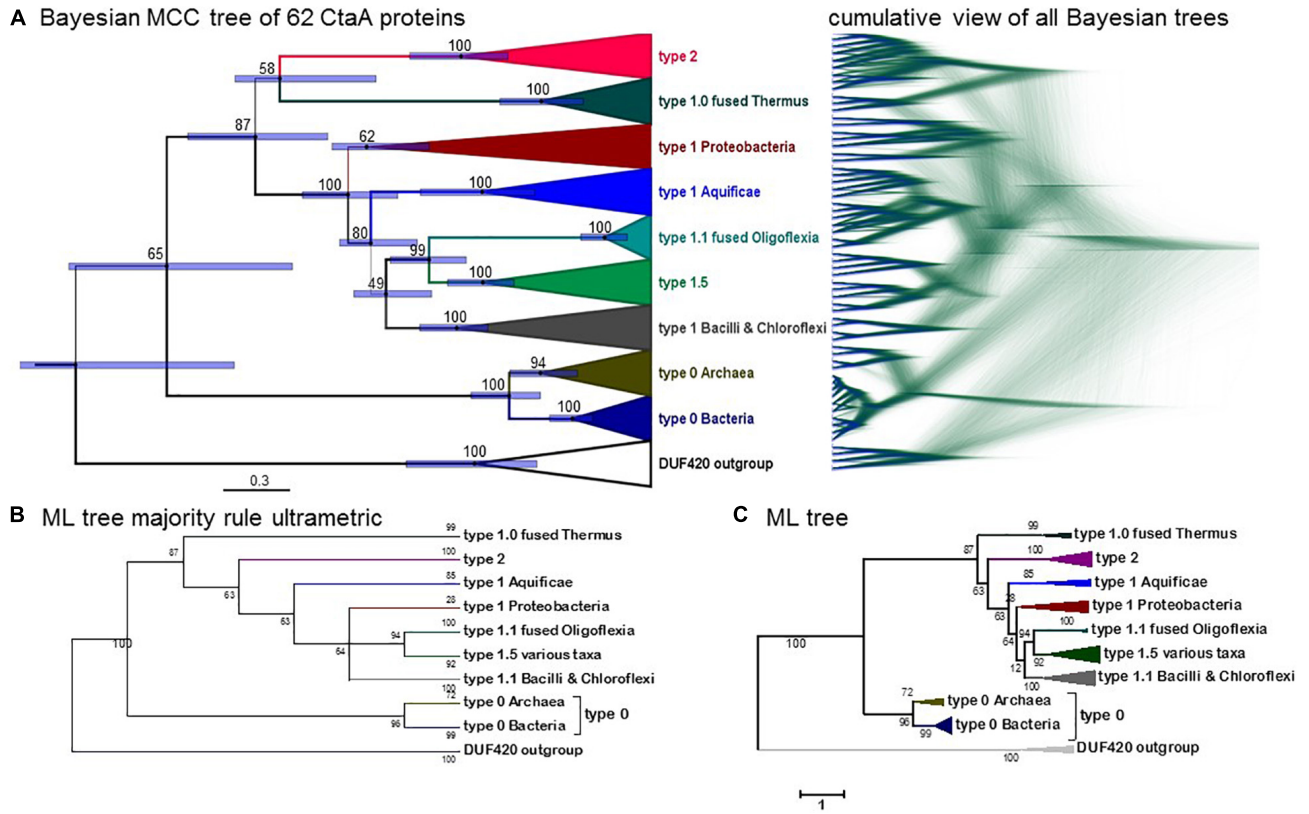

FIGURE 4 | Phylogeny of CtaA proteins from bacterial and archaeal taxa. **(A)** Bayesian MCC tree obtained from an alignment of 58 CtaA and 4 DUF420 sequences as in **Figure 3A** (for a total of 358 amino acid sites), with a chain length of 6.2 million iterations; left, BEAST MCC tree with posterior support in% and node bars expressing the 95%_HPD posterior probability, equivalent to confidence intervals (Lee et al., 2013); right, overlaid 5581 trees in mirror image with the DensiTree program. **(B)** Majority rule-like ML tree obtained with the same CtaA alignment as in Panel **(A)** using the MEGA5 program (1000 bootstraps) by collapsing clades with less than 50% support. **(C)** ML tree obtained with MEGA5 as in Panel **(B)** without further manipulation. Similar ML trees were obtained with other programs such as IQ-Tree.

heme A synthase. Intriguingly, several *Acidithiobacillus* species that lack the *rus* operon with COX genes also have type 0 CtaA orthologs (Acuña et al., 2013; Issotta et al., 2018). In these taxa, which include *At. caldus*, *At. sulfuriphilus* and *At. thiooxidans*, the gene for type 0 CtaA is usually found at the end of operons encoding orthologs of cytochrome bo_3 ubiquinol oxidases. Identification of cytochrome *a* in the membranes of *At. thiooxidans* and the isolation of a cytochrome aa_3 ubiquinol oxidase from the same bacterium (Sugio et al., 2006) suggest that these *Acidithiobacillus* spp. have heme A-containing quinol oxidases similar to *B. subtilis* cytochrome aa_3. The distribution of genes for type 0 CtaA is scattered on the chromosome of other Proteobacteria that are not strongly acidophilic.

Biochemical studies on COX have been reported for several thermoacidophilic archaea that often share the same acidic environments with *Acidithiobacillus* spp., i.e., *Sulfolobus* (Lübben and Morand, 1994; Castresana and Saraste, 1995; Yarzábal et al., 2004) and *Ferroplasma* (Yarzábal et al., 2004; Castelle et al., 2015; Blake et al., 2016). However, biochemical information is not currently available for the other prokaryotes that contain type 0 CtaA. Consequently, we had to apply deductive approaches of genomic and sequence analysis to rationalize the peculiar taxonomic distribution of type 0 CtaA and understand its possible relationship with the evolution of COX.

Archaea May Be Excluded From the Ancestry of Heme A-Containing Oxidases

Given the common ecophysiology of the organisms having type 0 CtaA, two alternative hypotheses can explain their current distribution (**Supplementary Figure 6**). The first hypothesis is that archaea first evolved CtaA and consequently heme A-containing oxidases and then passed the genes to bacteria. The second hypothesis is that ancestors of extant acidophilic bacteria evolved CtaA and COX first and their genes were transferred by LGT to archaeal lineages sharing their same environment. We examined the first hypothesis thoroughly, considering recent reports of Thermoplasmatales oxidases forming the basal branch in COX1 trees (Golyshina et al., 2016; Spang et al., 2019), which would strengthen the idea of archaeal ancestry for COX (Hemp and Gennis, 2008; Ducluzeau et al., 2014). Our phylogenetic analysis focused on archaeal COX proteins of family A. The COX1 proteins of the *phylum Ca.* Marsarchaeota (Jay et al., 2018)

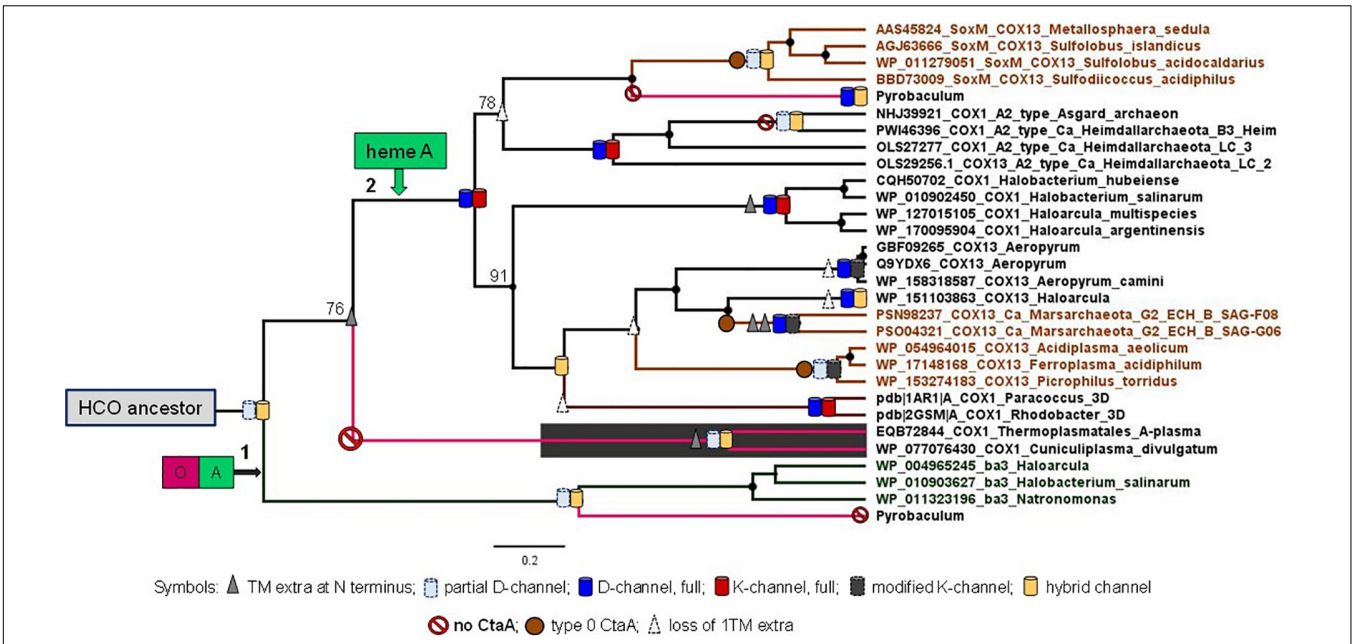

FIGURE 5 | Phylogeny of archaeal COX1. Bayesian MCC tree obtained with the BEAST package using an alignment of 28 archaeal COX1 sequences of both the family A and B and two bacterial COX1 from Rhodobacteraceae with known 3D structure as described in the **Supplementary Material**. The final alignment included 558 amino acid sites. Posterior branch support was 100% except for the three cases where numerals are shown adjacent to specific nodes. The distribution of an extra TM at the N terminal end and of the different variants of the K-channel classified in **Supplementary Figure 7**, as well as of the D-channel (Degli Esposti et al., 2020), were annotated onto the tree branches using the symbols shown at the bottom of the figure.

are fusion proteins with a highly divergent form of COX3 and contain two extra TM at the N-terminal end (**Supplementary Table 1**). This is an ancestral feature shared with diverse bacterial COX1 sequences (Degli Esposti, 2020), but not seen in other archaeal COX1 proteins such as SoxM, which also are COX1-3 fusion proteins (Pereira et al., 2001; Komorowski et al., 2002). Conversely, COX proteins of Cuniculiplasmataceae have been considered to be ancestral to the whole family A (Golyshina et al., 2016). We confirmed the basal position of these variants and found an extra TM at their N terminal end, but noted that genomes of Cuniculiplasmataceae spp. do not contain a gene for CtaA. Hence, their COX likely represents an intermediate in the transition between family A and B oxidases.

Once mapped upon a robust phylogenetic tree of family A and B oxidases (**Figure 5**), the distribution of an extra TM at the N terminal end and the variants of both the K- and D-channels for proton pumping (**Supplementary Figure 7**) indicate that the ancestor of archaeal heme A-containing oxidases diverged after the separation of Cuniculiplasmataceae from the ancestral lineage connecting to family B (node 2 in **Figure 5**). If this hypothetical proto-archaeal lineage contained the ancestor of all heme A-containing oxidases, then the feature of an extra TM at the N terminal end would have been lost at least five times along their evolution. The same ancestor must have possessed the proton conducting K-channel, because the canonical form of this channel is present in both major lineages departing from its node (**Figure 5** and **Supplementary Figure 7**). Consequently, the K-channel would have been independently lost seven times along the evolution of family A oxidases (**Figure 5**). Moreover, the presence of type 0 CtaA in organisms belonging to both major clades of archaeal family A oxidases implies multiple losses, if its gene were present in the archaeal ancestor (**Figure 5**). The appraisal of the predictions and implications applied to the tree and data in **Figure 5** indicates that the second hypothesis, namely that current archaeal genes for type 0 CtaA proteins have been acquired from bacteria via multiple LGT events, is much more plausible than the first hypothesis stating the opposite. Indeed, several works have suggested or reported LGT events from bacteria to archaea, especially for proteins associated with bioenergetics such as COX (Boucher et al., 2003; Blank, 2009, 2019; Nelson-Sathi et al., 2012, 2015; López-García et al., 2015; Wolfe and Fournier, 2018). Together with our integrated analysis (**Figure 5**), this evidence for LGT essentially excludes the first hypothesis.

Although Thermoplasmatales proteins appear to occupy the most basal branch of COX1 in phylogenetic trees (**Figure 6**, see also **Supplementary File** COX1refined100IQTreeEX_EHOFigTreefull.pdf), their clade exhibits a very long branch (**Figure 6** and **Supplementary Figure 8**). An equivalent long branch was observed in ML trees obtained with various methods and tended to cluster together with long branches of bacterial COX1-3 fusion proteins such as those of *Thermus* spp. (**Figure 6**, cf. **Supplementary Figure 8**). As mentioned earlier in connection with CtaA, attraction between protein clades with long branches is a recurrent artifact in phylogenetic analysis (Brinkmann et al., 2005; Philippe et al., 2005; Bleidorn, 2017). Our analysis suggests that the basal position of Thermoplasmatales COX1-3 proteins in trees

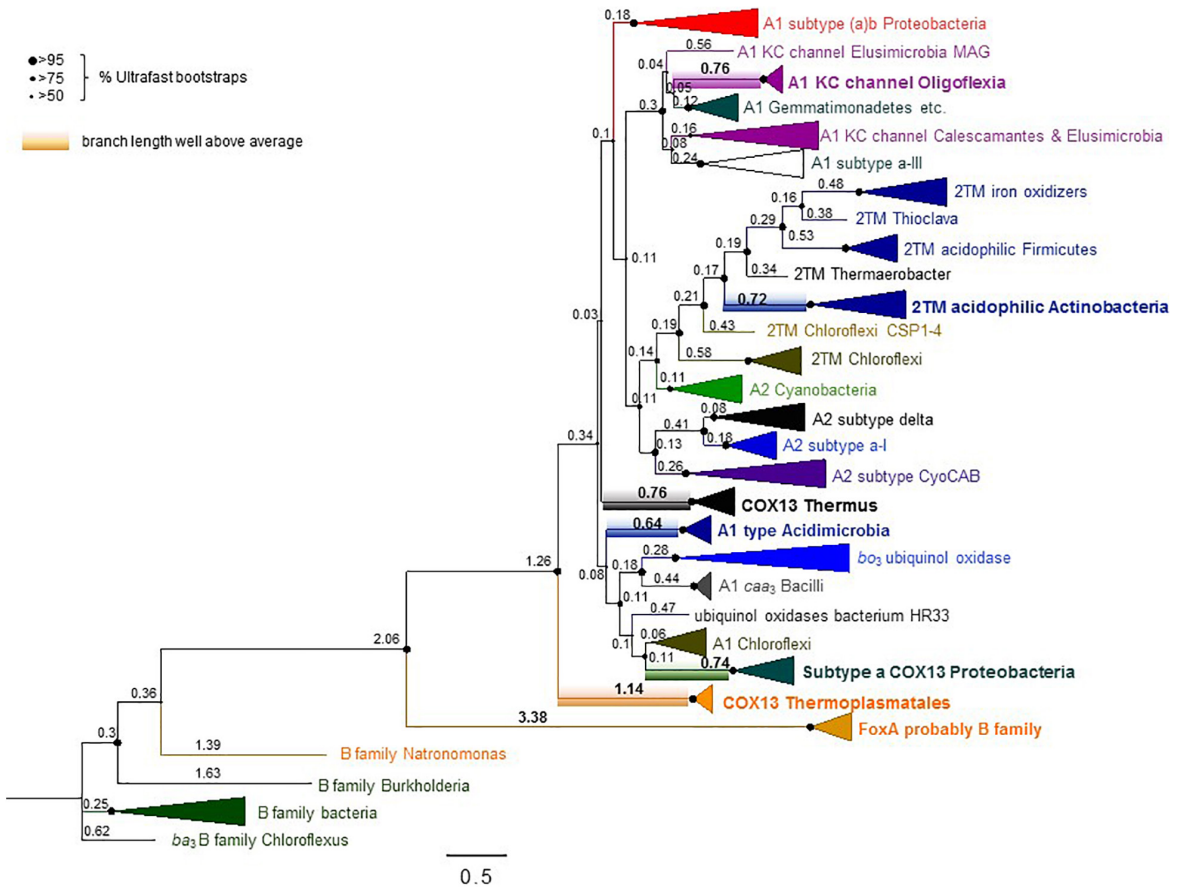

FIGURE 6 | Extended phylogenic tree of COX1 from many bacteria and Thermoplasmatales archaea. The ML tree was obtained with the program IQ-Tree using an alignment of 100 COX1 sequences from family A and B oxidases encompassing most subclades analyzed here (**Supplementary Table 1**). The alignment had 607 amino acid sites and was analyzed with the LG model. Similar trees were obtained with a slightly more trimmed version of the same alignment (**Supplementary Figure 8a** and separate supplementary file COX1refined100IQTreeEX_EHOFigTreefull.pdf), which had stronger values of%Ultrafast bootstraps support (indicated here by the size of the nodes shown on the left of the figure). The focus of this figure is to show the values for the relative branch length of the various subclades, annotated as raw values obtained from the FigTree program. See **Supplementary Figure 8b** for the statistical analysis of these values. Note the large values of branch length (highlighted in bold numerals) for the clades including the proteins from Thermoplasmatales and similarly COX1-3 fusion proteins from Proteobacteria and *Thermus* spp.

encompassing most COX subclades analyzed here (**Figure 6**), as well as in previously published phylogenetic trees (Spang et al., 2019), likely derives from LBA artifacts. Such problems probably arise from the different evolutionary rate of archaeal and bacterial proteins (Blank, 2009, 2019; Da Cunha et al., 2017; Cavalier-Smith and Chao, 2020). Moreover, the basal position of Thermoplasmatales COX1 in phylogenetic trees (**Figure 6** and **Supplementary Figure 8a**) does not reflect their phylogenetic position in species trees of archaea (Blank, 2009; Colman et al., 2018; Wolfe and Fournier, 2018), which is consistent with the relatively recent age of these thermoacidophilic prokaryotes (Blank, 2009; Colman et al., 2018).

Toward a Resolution of the Phylogeny of Bacterial COX1

Given that archaea can be excluded from the ancestry of COX, we next focused our work on bacterial COX to resolve its phylogeny, following the reductionist approaches presented in the **Supplementary Material**. We started from the observation that no bacterial genome could be found without the concomitant presence of CtaA and family A COX1 genes. We have analyzed all forms of heme A-containing oxidases in currently available genome sequences (**Supplementary Table 1**) but focus here on those belonging to family A for several reasons. This family is by far the most widespread of the HCO superfamily among living organisms and it encompasses the majority of prokaryotic lineages (see Degli Esposti, 2020 and references therein). In several bacterial taxa, the gene for heme A synthase is associated with the gene cluster of the COX subunits of family A HCO (Degli Esposti, 2020), while this is rarely the case for family B oxidases (Degli Esposti et al., 2019). Furthermore, prokaryotic genomes that encode a single terminal oxidase related to family B, as members of the Cuniculiplasmataceae, do not possess a gene for heme A synthase (**Figure 5**). Finally, and most importantly, family B oxidases do not present the ancestral features of an extra

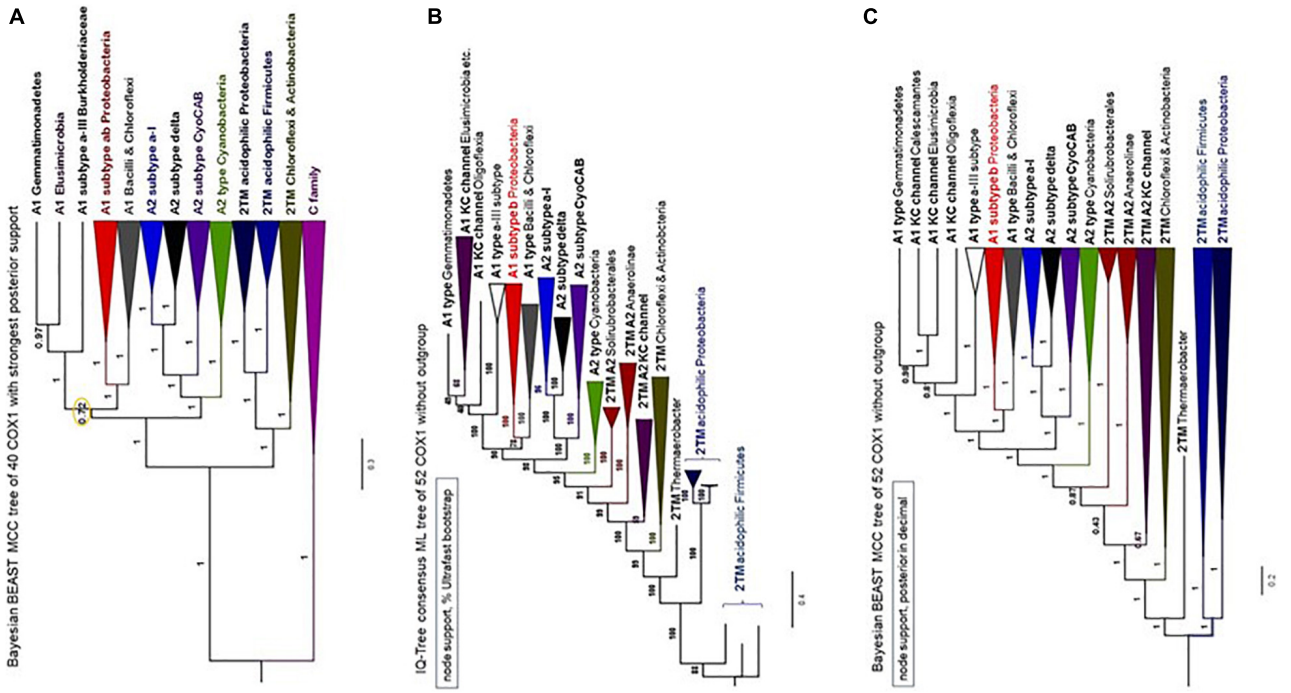

FIGURE 7 | Phylogeny of COX1 with and without family C outgroup. The illustration combines phylogenetic trees of COX1 obtained with similar alignments of COX1 sequences for a total of 647 amino acid sites. **(A)** MCC tree obtained with the BEAST program using a chain of 2 million iterations and the BLOSUM62 model applied to an alignment of 37 COX1 and three FixN protein sequences that was refined with the new approach presented in the **Supplementary Material** (in particular, **Supplementary Figures 11, 12**). The node indicated with the orange circle is the only one with posterior support below 0.97 (i.e., less than 97%) and was implemented from the tree shown in the related **Supplementary Figure 12a**. **(B,C)** Phylogenetic trees obtained with the IQ-Tree program in Panel B and the BEAST program in Panel **(C)** using the same WAG model as in Panel **(A)** and an alignment of 52 COX1 sequences without FixN paralogs as outgroup. The programs and node support systems are presented on the top left of each panel. Additional trees obtained with other programs and the same alignment (available upon request) are shown in **Supplementary Figures 12a,c**. The Bayesian tree in Panel **(C)** was re-rooted to the branch of acidophilic iron-oxidizers.

TM at the N-terminal end and residues typical of the K^C-channel that are shared by family A and C oxidases (Degli Esposti, 2020 – see also **Supplementary Figure 7**).

The phylogeny of bacterial COX1 is much more complicated than that of archaeal COX1, fundamentally because family A oxidases have a very broad phylogenetic distribution encompassing diverse bacterial lineages (Degli Esposti, 2020; Pereira et al., 2001). We have analyzed all COX1 variants found in available genome sequences and found that the great majority of the variants can be divided in about twenty bacterial subclades (**Supplementary Table 1**). Split gene clusters typically found in late diverging Actinobacteria, such as *Corynebacterium* spp., have been previously found to cluster with one of the subclades described in **Supplementary Table 1** (Degli Esposti, 2020), and were not analyzed here. After this initial selection, we progressively removed the subclades with long branches or fast substitution rate, that were present in phylogenetically broad trees such as that in **Figure 6**. This strategy was integrated with a novel approach to build COX1 alignments encompassing the N-terminal region so as to minimize LBA artifacts in assessing the phylogeny of bacterial COX1, as described in the dedicated section of **Supplementary Material**. Using multiple methods of phylogenetic inference, we ultimately concluded that the Bayesian tree shown in **Figure 7A** represents a most robust phylogeny of bacterial COX1. The tree presents an early separation of the A1 and the A2 type of COX1 from the basal clade containing COXI with 2 additional TM at the N-terminal end (these proteins are abbreviated 2TM) of various lineages, including iron-oxidizing bacteria. This phylogeny was confirmed in ML trees obtained with the same refined alignment (**Supplementary Figures 9–12**). Moreover, an equivalent topology emerged in phylogenetic trees obtained without family C paralogs as outgroup (**Figures 7B,C**). Hence, the choice of outgroup proteins used in previous phylogenetic trees does not affect the consistent basal position of the proteins with the ancestral 2TM extra feature, which include all those of iron-oxidizers that have type 0 CtaA.

Acidophilic Iron-Oxidizers Have an Ancestral Form of the COX Assembly Protein CtaG

CtaG is required for the assembly of Cu_B in COX1 (**Figure 1A**). It must be noted that there are two different types of proteins in bacteria that are called CtaG. One is a homolog of eukaryotic Cox11 and present in, for example, *P. denitrificans*. We present an analysis of this type of protein and its phylogenetic distribution in a dedicated section of the **Supplementary Material**. The other

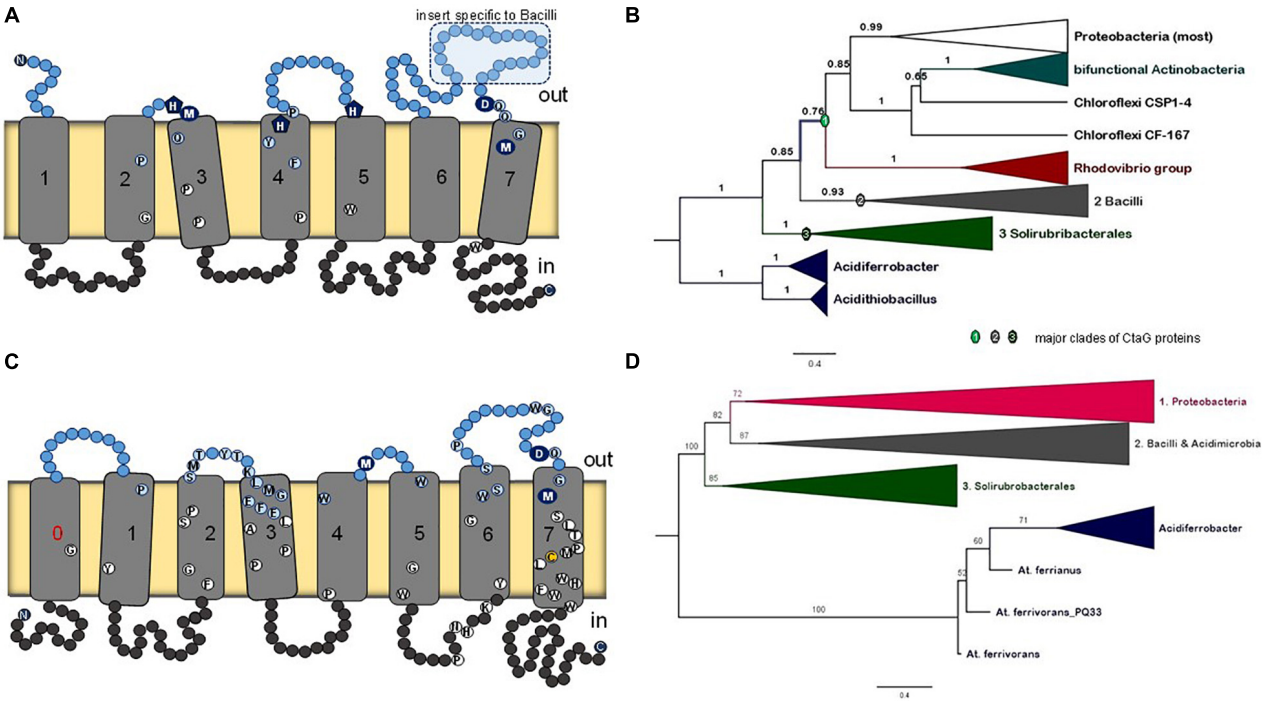

FIGURE 8 | Membrane structure and phylogeny of caa3_CtaG proteins. **(A)** Schematic model for the deduced transmembrane structure of *B. subtilis* caa3_CtaG, which was rendered with the same design as that used for CtaA (**Figure 2**). Residues potentially acting as Cu ion ligands are indicated with blue circles or pentagons including the invariant D249 (see text). Other highly conserved residues in caa3_CtaG proteins are depicted as in **Figure 2**. **(B)** Representative Bayesian tree obtained with the BEAST package using 40 caa3_CtaG sequences that were selected to represent the major clades previously found in wide phylogenetic analysis after removing proteins exhibiting long branches (**Supplementary Figures 13, 14a**). A similar tree was obtained with ML inference using the IQ-Tree program (**Supplementary Figure 14b**). The alignment contained a total of 242 amino acid sites. Posterior support of branches is expressed in decimals. **(C)** Schematic model for the structure of caa3_ctaG of acidophilic iron-oxidizing Proteobacteria, exemplified by that of *Acidithiobacillus ferrianus* (Norris et al., 2020). **(D)** The ML tree was obtained with the IQ-Tree program using an alignment of 42 caa3-CtaG sequences including their N terminal part [i.e., not trimmed as in Panel **(B)**]. The alignment contained a total of 337 amino acid residues and is made available upon request.

type is named caa3_CtaG and present in, for example, *B. subtilis* (Bengtsson et al., 2004). The caa3_CtaG constitutes the focus of our analysis for several reasons. It is a membrane protein with multiple TM (**Figure 8A**) and its function is intertwined with that of CtaA to form the heme a_3-Cu_B oxygen-reacting center in COX1. Moreover, the gene for caa3_CtaG often clusters with genes for COX in the chromosome (**Figure 1C**) of taxa that have the deep branching form of COX1 with the 2TM extra feature (**Supplementary Tables 1, 2**). Considering all these points, the molecular evolution of caa3_CtaG is likely connected with the early evolution of COX in bacteria, while that of Cox11 homologs may be more relevant to the bacterial ancestry of mitochondrial proteins (Degli Esposti et al., 2019).

There is no available structure for caa3_CtaG nor any paralog. The taxonomic distribution of caa3_CtaG is narrower than that of CtaA. To discern the molecular evolution of caa3_CtaG proteins, we undertook a systematic phylogenetic analysis of all the proteins that show the caa3_CtaG domain and have 6 to 9 TM (**Supplementary Table 2**). The most common structure is similar to that of *B. subtilis* caa3_CtaG, with 7 TM (**Figure 8A**). There are several conserved amino acid residues at the predicted positive (outer side) side of the membrane and which might function as Cu ligands (Degli Esposti et al., 2020), among which aspartate residue 249 appears to be invariant. The number of TM does not necessarily correlate with the phylogenetic position of caa3_CtaG proteins, which consistently cluster in three major clades (**Figure 8B** and **Supplementary Figures 13, 14**).

The possible phylogeny of caa3_CtaG proteins is shown by the tree of **Figure 8B** in its simplest and most robust form. This tree was reconstructed from an alignment of the sequences of 40 diverse proteins that represent the taxonomic breadth of the major clades of caa3_CtaG (**Supplementary Table 2**) while minimizing the presence of long branches, as described in the dedicated section of the **Supplementary Material**. The caa3_CtaG proteins of *Acidithiobacillus* spp. and *Acidiferrobacter* spp., which are predicted to have 8TM (one additional TM at the N-terminal end), show a different set of potential copper ion ligands than those in most other caa3_CtaG proteins (**Figure 8C**). However, these proteins maintain the invariant aspartate 249 (*B. subtilis* caa3_CtaG numbering) at the positive side of the membrane and are recognized as members of the caa3_CtaG superfamily. Using alignments that included also the N-terminal part of caa3_CtaG proteins, which has been routinely trimmed before (as in the alignment used to generate the tree in **Figure 8B**, cf. [Degli Esposti et al., 2020]), we obtained similar phylogenetic trees (**Figure 8D** and **Supplementary Figure 14**). Hence, the

basal position of caa3_CtaG of iron-oxidizing Proteobacteria such as *Acidithiobacillus* spp. was confirmed in multiple ways, consistent with the molecular evolution of CtaA (**Figure 3B**).

CONCLUSION

This work presents converging evidence suggesting that COX of extant acidophilic bacteria, in particular iron-oxidizing Proteobacteria such *Acidithiobacillus* and *Acidiferrobacter* spp., may be the closest to primitive heme A-containing respiratory oxidases. Protein factors specifically involved in biosynthesis of COX have presumably coevolved with COX1, as reflected by the clustering of their genes with those encoding COX proteins. The results of our in depth analysis of two proteins required for the assembly of the oxygen-reacting center in COX, CtaA for the biogenesis of heme A and caa3_CtaG for Cu_B, strongly support the inferred phylogeny of bacterial COX. Namely, CtaA and caa3_CtaG proteins of iron-oxidizing Proteobacteria form the basal branch in phylogenetic trees obtained with different inference methods and programs of phylogenetic analysis. Once invented, the advantageous bioenergetic capacity of respiration with molecular oxygen via heme A-containing oxidases evidently spread to various prokaryotes (Han et al., 2011; Wikström and Springett, 2020).

Geochemical and ecological evidence sustains the COX phylogeny that emerges from our data. Lithotrophic bacteria, such as *Acidithiobacillus* spp. and other acidophilic iron-oxidizers can release abundant levels of Cu ions by bioleaching of common crust rocks (Quatrini and Johnson, 2018; Degli Esposti et al., 2020). Cu bioavailability often limits COX biogenesis in aquatic environments, especially in oceans where Cu ion concentrations are normally low (Degli Esposti et al., 2019). The earliest geochemical evidence for bacterial respiration points to ancestral iron-oxidizing bacteria similar to extant *Acidithiobacillus* spp. as responsible for the acid leaching of soil crust rocks containing metals such as Cu, Cr and Co, which then were washed away from emerged land producing rich deposits in ocean sediments (Konhauser et al., 2011). Metal leaching driven by bacterial respiration lasted only a few hundred million years during and after the GOE (Konhauser et al., 2011). Once surface pyrite minerals were consumed by intense oxidation, COX genes had spread laterally to soil dwelling bacteria with faster growth capacity than the ancestors of extant iron oxidizers. To conclude, the early evolution of COX was apparently promoted by the availability of relatively high levels of oxygen produced locally by Cyanobacteria, combined with the availability of surface pyrite rock material in primordial earth environments.

DATA AVAILABILITY STATEMENT

The original contributions presented in the study are included in the article/**Supplementary Material**; further inquiries can be directed to the corresponding author/s.

AUTHOR CONTRIBUTIONS

MDE had the original idea for the study and initiated the writing of the manuscript, progressively involving the other co-authors who are experts in specific areas that are encompassed by this multi-disciplinary manuscript, structured most of the figures and tables. AM-B performed various phylogenetic analysis of COX assembly proteins. RQ is an expert on the family of Acidithiobacillaceae and contributed genomic and taxonomic data and did bioinformatic analyses. LH contributed expertise on heme A synthase and molecular microbiology information to frame and structure the manuscript. LH and MDE co-wrote the final manuscript. All authors contributed to the article and approved the submitted version.

FUNDING

Grant PAPIIT No. IN207718 to MDE was support for Esperanza Martínez-Romero. Work conducted in Chile was supported by ANID (under Grants FONDECYT 1181251 to RQ, Program de Apoyo a Centres con Financiamiento Basal AFB 170004 to RQ, and CONICYT-PFCHA/Doctorado Nacional 21171049 to AM-B), and the ANID-Millennium Science Initiative Program-NCN17_093 granted by the Ministry of Economy, Development and Tourism from Chile to RQ. LH was supported by the Swedish Research Council grant 2015-02547.

ACKNOWLEDGMENTS

We are indebted to Courtney Stairs (Lund University) and Diego Gonzalez-Halphen (UNAM University, Mexico City) for their critical insights to improve the manuscript and thank Simon Beard (Fundación Ciencia & Vida, Chile) for his help in building one figure.

SUPPLEMENTARY MATERIAL

The Supplementary Material for this article can be found online at: https://www.frontiersin.org/articles/10.3389/fmicb.2021.664216/full#supplementary-material

REFERENCES

Acuña, L. G., Cárdenas, J. P., Covarrubias, P. C., Haristoy, J. J., Flores, R., Nuñez, H., et al. (2013). Architecture and Gene Repertoire of the Flexible Genome of the Extreme Acidophile Acidithiobacillus caldus. *PLoS One* 8:e78237. doi: 10.1371/journal.pone.0078237

Appia-Ayme, C., Guiliani, N., Ratouchniak, J., and Bonnefoy, V. (1999). Characterization of an operon encoding two *c*-type cytochromes, an *aa*(3)-type cytochrome oxidase, and rusticyanin in Thiobacillus ferrooxidans ATCC 33020. *Appl. Environ. Microbiol.* 65, 4781–4787. doi: 10.1128/aem.65.11.4781-4787.1999

Bengtsson, J., von Wachenfeldt, C., Winstedt, L., Nygaard, P., and Hederstedt, L. (2004). CtaG is required for formation of active cytochrome *c* oxidase in Bacillus subtilis. *Microbiology* 150, 415–425. doi: 10.1099/mic.0.26691-0

Blake, I. R. C., Anthony, M. D., Bates, J. D., Hudson, T., Hunter, K. M., King, B. J., et al. (2016). In situ Spectroscopy Reveals that Microorganisms in Different

Phyla Use Different Electron Transfer Biomolecules to Respire Aerobically on Soluble Iron. *Front. Microbiol.* 7:1963.

Blank, C. E. (2009). Not so old Archaea - the antiquity of biogeochemical processes in the archaeal domain of life. *Geobiology* 7, 495–514. doi: 10.1111/j.1472-4669.2009.00219.x

Blank, C. E. (2019). Phylogenomic dating—a method of constraining the age of microbial taxa that lack a conventional fossil record. *Astrobiology* 9, 173–191. doi: 10.1089/ast.2008.0247

Bleidorn, C. (2017). *Phylogenomics*. Cham: Springer International Publishing, 173–193.

Boratyn, G. M., Schäffer, A., Agarwala, R., Altschul, S. F., Lipman, D. J., and Madden, T. L. (2012). Domain enhanced lookup time accelerated BLAST. *Biol. Direct.* 7:12. doi: 10.1186/1745-6150-7-12

Bouckaert, R. R., and Heled, J. (2014). DensiTree 2: Seeing trees through the forest. *BioRxiv* 2012:012401. doi: 10.1101/012401

Bouckaert, R., Vaughan, T. G., Barido-Sottani, J., Duchêne, S., Fourment, M., Gavryushkina, A., et al. (2019). BEAST 2.5: An advanced software platform for Bayesian evolutionary analysis. *PLoS Comput. Biol.* 15:e1006650.

Brinkmann, H., van der Giezen, M., Zhou, Y., De Raucourt, G. P., and Philippe, H. (2005). An empirical assessment of long-branch attraction artefacts in deep eukaryotic phylogenomics. *System. Biol.* 54, 743–757. doi: 10.1080/10635150500234609

Brown, K. R., Allan, B. M., Do, P., and Hegg, E. L. (2002). Identification of novel hemes generated by heme A synthase: evidence for two successive monooxygenase reactions. *Biochemistry* 41, 10906–10913. doi: 10.1021/bi0203536

Boucher, Y., Douady, C. J., Papke, R. T., Walsh, D. A., Boudreau, M. E., Nesbø, C. L., et al. (2003). Lateral gene transfer and the origins of prokaryotic groups. *Ann. Rev. Genet.* 37, 283–328. doi: 10.1146/annurev.genet.37.050503.084247

Castelle, C. J., Roger, M., Bauzan, M., Brugna, M., Lignon, S., Nimtz, M., et al. (2015). The aerobic respiratory chain of the acidophilic archaeon Ferroplasma acidiphilum: A membrane-bound complex oxidizing ferrous iron. *Biochim. Biophys. Acta* 1847, 717–728. doi: 10.1016/j.bbabio.2015.04.006

Castresana, J., and Saraste, M. (1995). Evolution of energetic metabolism: the respiration-early hypothesis. *Trends Biochem. Sci.* 20, 443–448. doi: 10.1016/s0968-0004(00)89098-2

Cavalier-Smith, T., and Chao, E. E. (2020). Multidomain ribosomal protein trees and the planctobacterial origin of neomura (eukaryotes, archaebacteria). *Protoplasma* 257, 621–753. doi: 10.1007/s00709-019-01442-7

Colman, D. R., Poudel, S., Hamilton, T. L., Havig, J. R., Selensky, M. J., Shock, E. L., et al. (2018). Geobiological feedbacks and the evolution of thermoacidophiles. *ISME J.* 12, 225–236. doi: 10.1038/ismej.2017.162

Da Cunha, V., Gaia, M., Gadelle, D., Nasir, A., and Forterre, P. (2017). Lokiarchaea are close relatives of Euryarchaeota, not bridging the gap between prokaryotes and eukaryotes. *PLoS Genet.* 13:e1006810. doi: 10.1371/journal.pgen.1006810

Degli Esposti, M. (2020). On the evolution of cytochrome oxidases consuming oxygen. *Biochim. Biophys. Acta Bioenerg.* 1861:148304. doi: 10.1016/j.bbabio.2020.148304

Degli Esposti, M., Garcia-Meza, V., Gomez, A. C., Moya-Beltran, A., Quatrini, R., and Hederstedt, L. (2020). Heme A-containing oxidases evolved in the ancestors of iron oxidizing bacteria. *BioRxiv* 2020:968255. doi: 10.1101/2020.03.01.968255v2

Degli Esposti, M., Mentel, M., Martin, W., and Sousa, F. L. (2019). Oxygen Reductases in Alphaproteobacterial Genomes: Physiological Evolution From Low to High Oxygen Environments. *Front. Microbiol.* 10:499.

Deng, X., Dohmae, N., Nealson, K. H., Hashimoto, K., and Okamoto, A. (2018). Multi-heme cytochromes provide a pathway for survival in energy-limited environments. *Sci. Adv.* 4:eaao5682. doi: 10.1126/sciadv.aao5682

Ducluzeau, A. L., Schoepp-Cothenet, B., van Lis, R., Baymann, F., Russell, M. J., and Nitschke, W. (2014). The evolution of respiratory O_2/NO reductases: an out-of-the-phylogenetic-box perspective. *J. R. Soc. Interface* 11:20140196. doi: 10.1098/rsif.2014.0196

Drummond, A. J., and Bouckaert, R. R. (2015). *Bayesian evolutionary analysis with BEAST*. Cambridge,: Cambridge University Press.

Drummond, A. J., Ho, S. Y., Phillips, M. J., and Rambaut, A. (2006). Relaxed phylogenetics and dating with confidence. *PLoS Biol.* 4:e88. doi: 10.1371/journal.pbio.0040088

Ferguson, S. J., and Ingledew, W. J. (2008). Energetic problems faced by micro-organisms growing or surviving on parsimonious energy sources and at acidic pH: I. Acidithiobacillus ferrooxidans as a paradigm. *Biochim. Biophys. Acta* 1777, 1471–1479. doi: 10.1016/j.bbabio.2008.08.012

Golyshina, O. V., Kublanov, I. V., Tran, H., Korzhenkov, A. A., Lünsdorf, H., Nechitaylo, T. Y., et al. (2016). Biology of archaea from a novel family Cuniculiplasmataceae (Thermoplasmata) ubiquitous in hyperacidic environments. *Sci. Rep.* 6:39034.

Guindon, S., Dufayard, J. F., Lefort, V., Anisimova, M., Hordijk, W., and Gascuel, O. (2010). New algorithms and methods to estimate maximum-likelihood phylogenies: assessing the performance of PhyML 3.0. *Syst. Biol.* 59, 307–321. doi: 10.1093/sysbio/syq010

Hammer, N. D., Schurig-Briccio, L. A., Gerdes, S. Y., Gennis, R. B., and Skaar, E. P. (2016). CtaM Is Required for Menaquinol Oxidase aa_3 Function in Staphylococcus aureus. *mBio* 7:4.

Han, H., Hemp, J., Pace, L. A., Ouyang, H., Ganesan, K., Roh, J. H., et al. (2011). Adaptation of aerobic respiration to low O_2 environments. *Proc. Natl. Acad. Sci. USA* 108, 14109–14114. doi: 10.1073/pnas.1018958108

He, D., Fu, C. J., and Baldauf, S. L. (2016). Multiple Origins of Eukaryotic cox15 Suggest Horizontal Gene Transfer from Bacteria to Jakobid Mitochondrial DNA. *Mol. Biol. Evol.* 33, 122–133. doi: 10.1093/molbev/msv201

Hederstedt, L. (2012). Heme A biosynthesis. *Biochim. Biophys. Acta Bioenerg.* 1817, 920–927.

Hemp, J., and Gennis, R. B. (2008). Diversity of the heme-copper superfamily in archaea: insights from genomics and structural modeling. *Results Prob. Cell Diff.* 45, 1–31. doi: 10.1007/400_2007_046

Issotta, F., Moya-Beltrán, A., Mena, C., Covarrubias, P. C., Thyssen, C., Bellenberg, S., et al. (2018). Insights into the biology of acidophilic members of the Acidiferrobacteraceae family derived from comparative genomic analyses. *Res. Microbiol.* 169, 608–617. doi: 10.1016/j.resmic.2018.08.001

Iwata, S., Ostermeier, C., Ludwig, B., and Michel, H. (1995). Structure at 2.8 A resolution of cytochrome *c* oxidase from Paracoccus denitrificans. *Nature* 376, 660–669. doi: 10.1038/376660a0

Jay, Z. J., Beam, J. P., Dlakić, M., Rusch, D. B., Kozubal, M. A., and Inskeep, W. P. (2018). Marsarchaeota are an aerobic archaeal lineage abundant in geothermal iron oxide microbial mats. *Nat. Microb.* 3, 732–740. doi: 10.1038/s41564-018-0163-1

Khadka, R., Clothier, L., Wang, L., Lim, C. K., Klotz, M. G., and Dunfield, P. F. (2018). Evolutionary History of Copper Membrane Monooxygenases. *Front. Microbiol.* 9:2493.

Komorowski, L., Verheyen, W., and Schäfer, G. (2002). The archaeal respiratory supercomplex SoxM from S. acidocaldarius combines features of quinole and cytochrome *c* oxidases. *J. Biol. Chem.* 383, 1791–1799.

Konhauser, K. O., Lalonde, S. V., Planavsky, N. J., Pecoits, E., Lyons, T. W., Mojzsis, S. J., et al. (2011). Aerobic bacterial pyrite oxidation and acid rock drainage during the Great Oxidation Event. *Nature* 478, 369–373. doi: 10.1038/nature10511

Le, S. Q., and Gascuel, O. (2010). Accounting for Solvent Accessibility and Secondary Structure in Protein Phylogenetics Is Clearly Beneficial. *Syst. Biol.* 59, 277–287. doi: 10.1093/sysbio/syq002

Le, S. Q., Lartillot, N., and Gascuel, O. (2008). Phylogenetic mixture models for proteins. *Phil. Trans. R. Soc. B* 363, 3965–3976. doi: 10.1098/rstb.2008.0180

Lee, M. S., Soubrier, J., and Edgecombe, G. D. (2013). Rates of phenotypic and genomic evolution during the Cambrian explosion. *Curr. Biol.* 23, 1889–1895. doi: 10.1016/j.cub.2013.07.055

Lewin, A., and Hederstedt, L. (2008). Promoted evolution of a shortened variant of heme A synthase in the membrane of Bacillus subtilis. *FEBS Lett.* 582, 1330–1334. doi: 10.1016/j.febslet.2008.03.015

Lewin, A., and Hederstedt, L. (2016). Heme A synthase in bacteria depends on one pair of cysteinyls for activity. *Biochim. Biophys. Acta Bioenerg.* 1857, 160–168. doi: 10.1016/j.bbabio.2015.11.008

López-García, P., Zivanovic, Y., Deschamps, P., and Moreira, D. (2015). Bacterial gene import and mesophilic adaptation in archaea. *Nat. Rev. Microbiol.* 13, 447–456. doi: 10.1038/nrmicro3485

Lu, S., Wang, J., Chitsaz, F., Derbyshire, M. K., Geer, R. C., Gonzales, N. R., et al. (2020). CDD/SPARCLE: the conserved domain database in 2020. *Nucleic Acids Res.* 48, D265–D268.

Lübben, M., and Morand, K. (1994). Novel prenylated hemes as cofactors of cytochrome oxidases. Archaea have modified hemes A and O. *J. Biol. Chem.* 269, 21473–21479. doi: 10.1016/s0021-9258(17)31828-8

Matheus Carnevali, P. B., Schulz, F., Castelle, C. J., Kantor, R. S., Shih, P. M., Sharon, I., et al. (2019). Hydrogen-based metabolism as an ancestral trait in lineages sibling to the Cyanobacteria. *Nat. Commun.* 10:463.

Möller, S., Croning, M. D., and Apweiler, R. (2001). Evaluation of methods for the prediction of membrane spanning regions. *Bioinformatics* 17, 646–653. doi: 10.1093/bioinformatics/17.7.646

Mogi, T., Saiki, K., and Anraku, Y. (1994). Biosynthesis and functional role of haem O and haem A. *Mol. Microbiol.* 14, 391–398. doi: 10.1111/j.1365-2958.1994.tb02174.x

Nelson-Sathi, S., Dagan, T., Landan, G., Janssen, A., Steel, M., McInerney, J. O., et al. (2012). Acquisition of 1,000 eubacterial genes physiologically transformed a methanogen at the origin of Haloarchaea. *Proc. Natl. Acad. Sci. USA* 109, 20537–20542. doi: 10.1073/pnas.1209119109

Nelson-Sathi, S., Sousa, F. L., Roettger, M., Lozada-Chávez, N., Thiergart, T., Janssen, A., et al. (2015). Origins of major archaeal clades correspond to gene acquisitions from bacteria. *Nature* 517, 77–80. doi: 10.1038/nature13805

Nguyen, L. T., Schmidt, H. A., von Haeseler, A., and Minh, B. (2015). Q. IQ-TREE: A fast and effective stochastic algorithm for estimating maximum likelihood phylogenies. *Mol. Biol. Evol.* 32, 268–274. doi: 10.1093/molbev/msu300

Niwa, S., Takeda, K., Kosugi, M., Tsutsumi, E., Mogi, T., and Miki, K. (2018). Crystal structure of heme A synthase from Bacillus subtilis. *Proc. Natl. Acad. Sci. USA* 115, 11953–11957.

Norris, P. R., Falagán, C., Moya-Beltrán, A., Castro, M., Quatrini, R., and Johnson, D. B. (2020). Acidithiobacillus ferrianus sp. nov.: an ancestral extremely acidophilic and facultatively anaerobic chemolithoautotroph. *Extremophiles* 24, 329–337. doi: 10.1007/s00792-020-01157-1

Parks, D. H., Chuvochina, M., Waite, D. W., Rinke, C., Skarshewski, A., Chaumeil, P. A., et al. (2018). A standardized bacterial taxonomy based on genome phylogeny substantially revises the tree of life. *Nat. Biotechnol.* 36, 996–1004. doi: 10.1038/nbt.4229

Pereira, M. M., Santana, M., and Teixeira, M. (2001). A novel scenario for the evolution of heme-copper oxygen reductases. *Biochim. Biophys. Acta* 1505, 185–208. doi: 10.1016/s0005-2728(01)00169-4

Philippe, H., Zhou, Y., Brinkmann, H., Rodrigue, N., and Delsuc, F. (2005). Heterotachy and long-branch attraction in phylogenetics. *BMC Evol. Bio* 5:50.

Quatrini, R., Appia-Ayme, C., Denis, Y., Jedlicki, E., Holmes, D. S., and Bonnefoy, V. (2009). Extending the models for iron and sulfur oxidation in the extreme acidophile Acidithiobacillus ferrooxidans. *BMC Genom.* 10:394. doi: 10.1186/1471-2164-10-394

Quatrini, R., and Johnson, D. B. (2018). Microbiomes in extremely acidic environments: functionalities and interactions that allow survival and growth of prokaryotes at low pH. *Curr. Opin. Microbiol.* 43, 139–147. doi: 10.1016/j.mib.2018.01.011

Ratnasingham, S., and Hebert, P. D. (2013). A DNA-based registry for all animal species: the Barcode Index Number (BIN) system. *PLoS One* 8:e66213. doi: 10.1371/journal.pone.0066213

Sharma, V., and Wikström, M. (2014). A structural and functional perspective on the evolution of the heme-copper oxidases. *FEBS Lett.* 588, 3787–3792. doi: 10.1016/j.febslet.2014.09.020

Soo, R. M., Hemp, J., Parks, D. H., Fische, W. W., and Hugenholtz, P. (2017). On the origins of oxygenic photosynthesis and aerobic respiration in cyanobacteria. *Science* 355, 1436–1440. doi: 10.1126/science.aal3794

Sousa, F. L., Alves, R. J., Pereira-Leal, J. B., Teixeira, M., and Pereira, M. M. (2011). A bioinformatics classifier and database for heme-copper oxygen reductases. *PLoS One* 6:e19117. doi: 10.1371/journal.pone.0019117

Spang, A., Stairs, C. W., Dombrowski, N., Eme, L., Lombard, J., Caceres, E. F., et al. (2019). Proposal of the reverse flow model for the origin of the eukaryotic cell based on comparative analyses of Asgard archaeal metabolism. *Nat. Microb.* 4, 1138–1148. doi: 10.1038/s41564-019-0406-9

Sugio, T., Hisazumi, T., Kanao, T., Kamimura, K., Takeuchi, F., and Negishi, A. (2006). Existence of aa_3-type ubiquinol oxidase as a terminal oxidase in sulfite oxidation of Acidithiobacillus thiooxidans. *Biosci. Biotech. Biochem.* 70, 1584–1591. doi: 10.1271/bbb.50623

Svensson-Ek, M., Abramson, J., Larsson, G., Törnroth, S., Brzezinski, P., and Iwata, S. (2002). The X-ray crystal structures of wild-type and EQ(I-286) mutant cytochrome *c* oxidases from Rhodobacter sphaeroides. *J. Mol. Biol.* 321, 329–339. doi: 10.1016/s0022-2836(02)00619-8

Tamura, K., Peterson, D., Peterson, N., Stecher, G., Nei, M., and Kumar, S. (2011). MEGA5: molecular evolutionary genetics analysis using maximum likelihood, evolutionary distance, and maximum parsimony methods. *Mol. Biol. Evol.* 28, 2731–2739. doi: 10.1093/molbev/msr121

Trifinopoulos, J., Nguyen, L. T., von Haeseler, A., and Minh, B. Q. (2016). W-IQ-TREE: a fast online phylogenetic tool for maximum likelihood analysis. *Nucleic Acid Res.* 44, W232–W235.

von Wachenfeldt, C., Hallgren, J., and Hederstedt, L. (2021). YtkA (CtaK) and YozB (CtaM) function in the biogenesis of cytochrome *c* oxidase in Bacillus subtilis. *Mol. Microbiol.* 2021:14701. doi: 10.1111/mmi.14701

Wikström, M., and Springett, R. (2020). Thermodynamic efficiency, reversibility, and degree of coupling in energy conservation by the mitochondrial respiratory chain. *Commun. Biol.* 3:451.

Wolfe, J. M., and Fournier, G. P. (2018). Horizontal gene transfer constrains the timing of methanogen evolution. *Nat. Ecol. Evol.* 2, 897–903. doi: 10.1038/s41559-018-0513-7

Yarzábal, A., Appia-Ayme, C., Ratouchniak, J., and Bonnefoy, V. (2004). Regulation of the expression of the Acidithiobacillus ferrooxidans rus operon encoding two cytochromes *c*, a cytochrome oxidase and rusticyanin. *Microbiology* 150, 2113–2123. doi: 10.1099/mic.0.26966-0

Zeng, H., Zhu, G., Zhang, S., Li, X., Martin, J., Morgner, N., et al. (2020). Isolated Heme A Synthase from Aquifex aeolicus Is a Trimer. *mBio* 11, e2615–e2619.

Conflict of Interest: The authors declare that the research was conducted in the absence of any commercial or financial relationships that could be construed as a potential conflict of interest.

frontiers in Microbiology

ORIGINAL RESEARCH
published: 25 June 2021
doi: 10.3389/fmicb.2021.683260

Genes Linking Copper Trafficking and Homeostasis to the Biogenesis and Activity of the *cbb*$_3$-Type Cytochrome *c* Oxidase in the Enteric Pathogen *Campylobacter jejuni*

*Nitanshu Garg, Aidan J. Taylor, Federica Pastorelli, Sarah E. Flannery, Phillip J. Jackson, Matthew P. Johnson and David J. Kelly**

Department of Molecular Biology and Biotechnology, The University of Sheffield, Sheffield, United Kingdom

OPEN ACCESS

Edited by:
Davide Zannoni, University of Bologna, Italy

Reviewed by:
Fevzi Daldal, University of Pennsylvania, United States
Soufian Ouchane, Centre National de la Recherche Scientifique, Center for the National Scientific Research (CNRS), France

***Correspondence:**
David J. Kelly
d.kelly@sheffield.ac.uk

Specialty section:
This article was submitted to Microbial Physiology and Metabolism, a section of the journal Frontiers in Microbiology

Received: *20 March 2021*
Accepted: *26 May 2021*
Published: *25 June 2021*

Citation:
Garg N, Taylor AJ, Pastorelli F, Flannery SE, Jackson PJ, Johnson MP and Kelly DJ (2021) Genes Linking Copper Trafficking and Homeostasis to the Biogenesis and Activity of the cbb$_3$-Type Cytochrome c Oxidase in the Enteric Pathogen Campylobacter jejuni. Front. Microbiol. 12:683260. doi: 10.3389/fmicb.2021.683260

Bacterial C-type haem-copper oxidases in the *cbb*$_3$ family are widespread in microaerophiles, which exploit their high oxygen-binding affinity for growth in microoxic niches. In microaerophilic pathogens, C-type oxidases can be essential for infection, yet little is known about their biogenesis compared to model bacteria. Here, we have identified genes involved in *cbb*$_3$-oxidase (Cco) assembly and activity in the Gram-negative pathogen *Campylobacter jejuni*, the commonest cause of human food-borne bacterial gastroenteritis. Several genes of unknown function downstream of the oxidase structural genes *ccoNOQP* were shown to be essential (*cj1483c* and *cj1486c*) or important (*cj1484c* and *cj1485c*) for Cco activity; Cj1483 is a CcoH homologue, but Cj1484 (designated CcoZ) has structural similarity to MSMEG_4692, involved in Qcr-oxidase supercomplex formation in *Mycobacterium smegmatis*. Blue-native polyacrylamide gel electrophoresis of detergent solubilised membranes revealed three major bands, one of which contained CcoZ along with Qcr and oxidase subunits. Deletion of putative copper trafficking genes *ccoI* (*cj1155c*) and *ccoS* (*cj1154c*) abolished Cco activity, which was partially restored by addition of copper during growth, while inactivation of *cj0369c* encoding a CcoG homologue led to a partial reduction in Cco activity. Deletion of an operon encoding PCu$_A$C (Cj0909) and Sco (Cj0911) periplasmic copper chaperone homologues reduced Cco activity, which was partially restored in the *cj0911* mutant by exogenous copper. Phenotypic analyses of gene deletions in the *cj1161c–1166c* cluster, encoding several genes involved in intracellular metal homeostasis, showed that inactivation of *copA* (*cj1161c*), or *copZ* (*cj1162c*) led to both elevated intracellular Cu and reduced Cco activity, effects exacerbated at high external Cu. Our work has therefore identified (i) additional Cco subunits, (ii) a previously uncharacterized set of genes linking copper trafficking and Cco activity, and (iii) connections with Cu homeostasis in this important pathogen.

Keywords: copper, homeostasis, periplasm, chaperone, supercomplex

INTRODUCTION

Haem-copper oxidases (HCOs) are proton-translocating respiratory complexes widely distributed in both prokaryotes and eukaryotes that contain a bi-nuclear haem-copper site at which oxygen reduction occurs. Three families of HCO can be distinguished based primarily on the sequence similarity of the core subunits. Type A include the cytochrome aa_3-type oxidases found in a range of aerobic bacteria and mitochondria, type B includes the ba_3 oxidases only found in bacteria, and type C contains the cbb_3-type oxidases, which have an integral c-type cytochrome subunit (Pereira et al., 2001). This type of enzyme has a high oxygen affinity and is typically found in a range of microaerophilic bacteria (Pitcher and Watmough, 2004).

Mechanistically, all HCOs operate using a redox loop mechanism for proton translocation across the membrane as well as pumping protons directly. However, while the A-type oxidases have two proton pathways (the D- and K-channels), which are used for water formation from oxygen and transmembrane proton pumping, respectively, the B- and C-types have a single proton pathway located in the same region as the K-channel of A-type oxidases (Buschmann et al., 2010). The stoichiometry of proton pumping by C-type oxidases has been controversial, and the best estimates indicate a H^+/e ratio of only 1, which is lower than other types of HCO's (Rauhamäki et al., 2012). However, working in combination with the quinol-cytochrome c reductase (Qcr) complex, the redox loop mechanism means that a higher overall H^+/e ratio can be achieved during electron transfer from quinol to oxygen.

The redox cofactors in the cbb_3 type of oxidase are bound to three subunits. CcoN contains a binuclear Cu_B–haem b_3 (high-spin) centre at which oxygen reduction occurs and an additional low-spin *b* haem. CcoO is a monohaem *c*-type cytochrome and CcoP is a dihaem *c*-type cytochrome. Electron transfer proceeds from the C-haems in CcoP to CcoO and then to oxygen via the redox centres in the CcoN subunit. Additional subunits have also been identified, with less clearly defined roles. CcoQ is a small protein needed for stabilising interactions of CcoP with the CcoNO core complex in some species (Peters et al., 2008) and which is commonly encoded in the same operon as the redox active subunits. Additional small subunits in addition to or in place of CcoQ are also found in complexes from different bacteria. The CcoH subunit is now known to be an integral protein in many, but not all purified complexes. Pawlik et al. (2010) demonstrated that biogenesis of CcoNOQP in *Rhodobacter capsulatus* proceeds via CcoQP and CcoNO sub-complexes, but in the absence of CcoH, neither the fully assembled CcoNOQP nor the CcoQP or CcoNO sub-complex were detectable. CcoH binds to CcoP via its transmembrane domain and stays tightly associated with the active, fully assembled complex. Type C oxidases from some *Pseudomonas* sp. can contain CcoM, a single transmembrane subunit required for complex stability but not activity (Kohlstaedt et al., 2016; Carvalheda and Pisliakov, 2017). CcoM and CcoQ share low sequence identity and it is thought they have different functions (Kohlstaedt et al., 2016; Carvalheda and Pisliakov, 2017).

A number of additional proteins have been found to be crucial for oxidase biogenesis and in particular for the export of copper to the periplasm and its insertion into the CcoN active site subunit. The *ccoG*, *ccoI*, and *ccoS* genes encode proteins involved in copper handling and export and their roles were first identified in *Bradyrhizobium japonicum* (Preisig et al., 1996) and further clarified in *R. capsulatus* (Koch et al., 2000). CcoG contains two cysteine-rich motifs that resemble those encountered in [4Fe–4S] cluster containing ferrodoxins, suggesting it has an oxidoreductase role (Preisig et al., 1996) and it has recently been shown to act as a cupric reductase (Marckmann et al., 2019). CcoI is a Cu-translocating P-type ATPase that transfers copper to the periplasm (Preisig et al., 1996; Koch et al., 2000). CcoS contains no characteristic motifs or homology to characterised proteins (Koch et al., 2000). Studies of the assembly of the cbb_3-type cytochrome *c* oxidase in *R. capsulatus* showed that in a *ccoI* deletion strain, the sub-complex CcoNOQ was absent, although monomeric CcoP was still detectable. In the absence of CcoS, the complex was assembled but with no enzymatic activity (Kulajta et al., 2006).

In eukaryotic cells, two key proteins Sco1 and Cox17 are required for the correct assembly of cytochrome *c* oxidase (Dickinson et al., 2000; Mattatall et al., 2000). The Cox17 protein is believed to be the specific copper donor to the mitochondrial inner membrane bound Sco1 (Horng et al., 2004). Mattatall et al. (2000) reported the discovery of YpmQ, a bacterial homolog of Sco1. Deletion of *ypmQ* in *Bacillus subtilis* reduced the expression of cytochrome *c* oxidase, the level of which was recovered on substituting the growth medium with additional copper. In *Deinococcus radiodurans* and *Caulobacter crescentus*, Banci et al. (2005) found a class of proteins of unknown function (referred to as PCu_AC) displaying a conserved gene neighbourhood to bacterial *sco1* genes, all sharing a potential metal binding motif $H(M)X_{10}MX_{21}HXM$, and potentially taking the role of Cox17 in bacteria, involving copper delivery to the Cu(A) center in the oxidase. Bacterial PCu_AC and Sco protein encoding genes are widespread and often found in the same operon (Abriata et al., 2008). For example in *R. capsulatus*, SenC, a Sco1-homologue and PccA, a PCu_AC-like periplasmic chaperone, have been identified. PccA has been demonstrated as a Cu-binding protein with a preference for Cu(I), which is required for efficient cbb_3-Cox assembly, in particular, at low Cu concentrations (Trasnea et al., 2016). Cu is transferred from PccA to SenC and vice versa at similar levels, constituting a Cu relay system that facilitates Cu delivery to cbb_3-type Cco (Trasnea et al., 2018). In the absence of PccA, SenC still obtains Cu that is exported by CcoI and facilitates Cco assembly, although with lower efficiency (Trasnea et al., 2018).

In contrast to the extensive information available for oxidase biogenesis and function in well studied model bacteria such as *R. capsulatus*, much less is known about the oxidases of divergent unrelated bacteria, such as those of the Campylobacterota (formerly Epsilonproteobacteria), containing well known human pathogens in the genera *Campylobacter*, *Helicobacter*, and *Arcobacter*. The microaerophilic *C. jejuni* is a normal commensal of birds, including poultry, where undercooked chicken is the main source of human infection. It is the most frequent cause

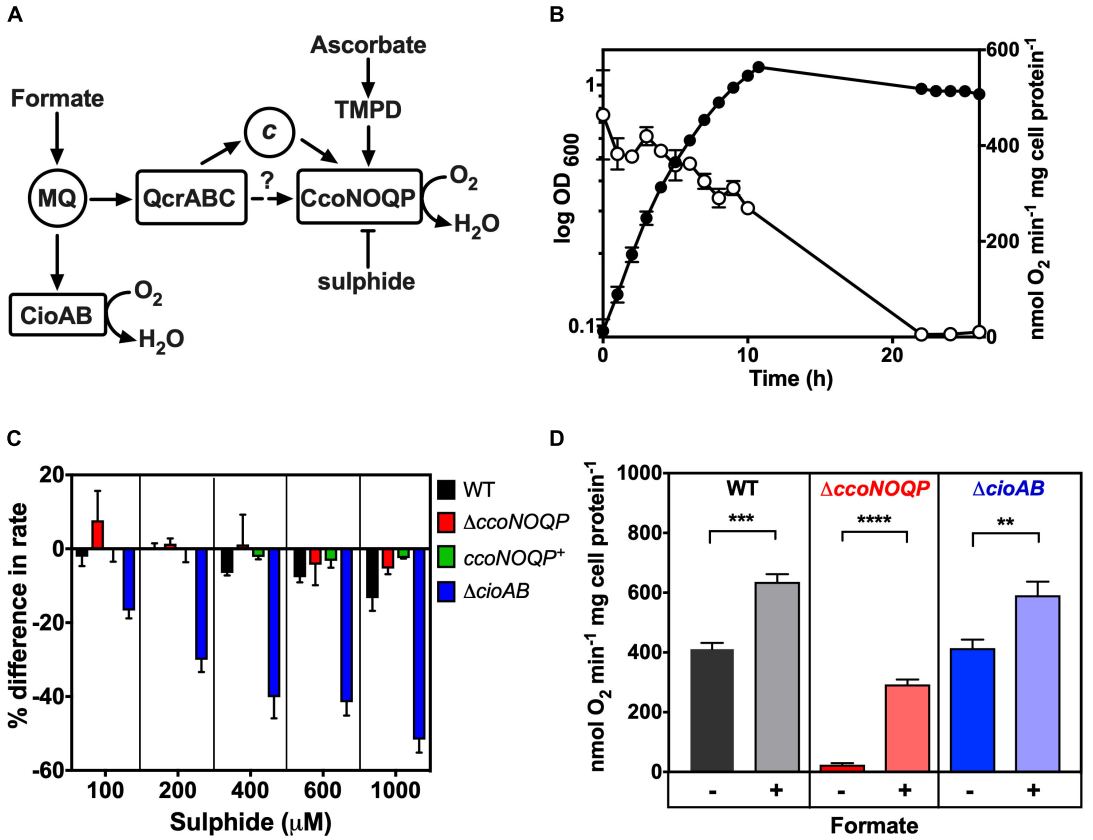

FIGURE 1 | Characterisation of cytochrome *c* oxidase activity in *Campylobacter jejuni*. **(A)** Simplified schematic of electron transport pathways to oxygen. Formate is a major physiological electron donor to the menaquinone (MQ) pool, where electrons can be directed either to the quinol oxidase CioAB or to the QcrABC complex and on to the cbb_3-type cytochrome *c* oxidase CcoNOQP. Ascorbate reduced TMPD specifically acts as a non-physiological electron donor to the CcoNOQP oxidase. Sulphide inhibits activity (—|) **(B)** Cco activity in wild-type cells grown in Mueller-Hinton medium at different stages of growth, measured as oxygen uptake in a Clark type electrode with ascorbate plus TMPD as electron donor. The data points show the mean rate of three independent experiments with the errors bars showing SD. In many cases the error bars are too small to be seen. Closed circles, OD measured at 600 nm; open circles, specific rate of ascorbate/TMPD driven oxygen uptake. **(C)** Effect of increasing sulphide concentrations on the rate of ascorbate/TMPD oxidase activity in wild-type (black bars), *ccoNOQP* deletion mutant (red bars), *ccoNOQP* complemented strain (*ccoNOQP*$^+$; green bars) and *cioAB* mutant (blue bars). The results are shown as the mean% difference in the rate compared to the rate without any sulphide addition. Error bars show SD from three independent experiments. **(D)** Cco activity measured with ascorbate/TMPD without (**–**) and with (**+**) 20 mM sodium formate in the assay. Wild type (black bars), Δ*ccoNOQP* (red bars) and Δ*cioAB* (blue bars) cells were grown to mid-exponential phase in Mueller-Hinton medium. The data are the average of triplicate cultures with error bars showing SD. Student's *t*-tests were performed to test significance ($0.01 > {**}p > 0.001$; $0.001 > {***}p > 0.0001$; $0.0001 > {****}p > 0.00001$). Raw data for **Figures 1–7** can be found in **Supplementary Tables 1, 2**.

of food-borne bacterial gastroenteritis worldwide, leading to an enormous disease buden and serious sequelae such as Guillain-Barré syndrome (O'Brien, 2017). Increasing antibiotic resistance is also a major problem and *C. jejuni* has been designated a WHO priority pathogen for study.

A cbb_3-type cytochrome c oxidase and a cytochrome bd-type quinol oxidase (**Figure 1A**) are present in the *C. jejuni* reference strain NCTC 11168 (Parkhill et al., 2000; Taylor and Kelly, 2019) and both oxidases are highly conserved in all other sequenced strains. The cytochrome c oxidase in *C. jejuni* is currently thought to be encoded by *ccoNOQP* genes (*cj1490c–cj1487c*; Parkhill et al., 2000) and has been shown to have a very high affinity for oxygen (Jackson et al., 2007). A *ccoN* mutant was constructed by Weingarten et al. (2008) and reported to be highly sensitive to oxygen and to exhibit a microaerobic growth defect. Importantly, this mutant was unable to colonise chicks (Weingarten et al., 2008) indicating a crucial role for the Cco enzyme in energy conservation *in vivo*. A *ccoNOQP* operon deletion mutant constructed by Liu and Kelly (2015) also had an aerobic growth defect but did not seem to be more sensitive to oxygen than the wild-type and measurements using a fluorescent probe did not show accumulation of reactive oxygen species (ROS). A study of gene expression in *C. jejuni* growing in the chick caecum also indicated the importance of this oxidase in host colonisation: the *cco* gene cluster was up-regulated about fourfold, suggesting the bacteria are present in a microaerobic niche (Woodall et al., 2005).

Only the *ccoNOQP* structural genes for the cbb_3-oxidase have thus far been identified in *C. jejuni* (Parkhill et al., 2000; Taylor and Kelly, 2019) and in particular it is unknown which additional genes/proteins are required for insertion of copper to form an active enzyme. In this work we have tested

TABLE 1 | Genes tested in this work for their role in oxidase assembly, activity and copper homeostasis.

Campylobacter jejuni locus tag	Gene name	Gene product function	Predicted cellular location
cj0369c	*ccoG*	Cupric reductase for cbb_3 oxidase biogenesis	Inner membrane anchored; cytoplasm facing
cj0908	–	Unknown	Inner membrane anchored; periplasm facing
cj0909	*pcuC*	Possible periplasmic Cu chaperone. Contains DUF461	Periplasm
cj0910	–	Unknown	Inner membrane anchored; periplasm facing
cj0911	*sco1*	Periplasmic Cu chaperone	Inner membrane anchored; Periplasm facing
cj1154c	*ccoS*	cbb_3-oxidase biogenesis protein	Inner membrane anchored
cj1155c	*ccoI*	cbb_3-oxidase biogenesis protein; Cu exporting ATPase	Inner membrane
cj1161c	*copA*	Cu exporting ATPase	Inner membrane
cj1162c	*copZ*	Cu chaperone	Cytoplasm
cj1163c	*czcD*	Zn exporting ATPase	Inner membrane
cj1164c	–	Unknown; Zn finger protein	Cytoplasm
cj1165c	–	Unknown; DUF1212, possible solute transporter	Inner membrane
cj1166c	–	Unknown; DUF1212, possible solute transporter	Inner membrane
cj1482c	–	Unknown; DUF386. Possible DNA helicase	Cytoplasm
cj1483c	*ccoH*	Oxidase subunit	Inner membrane
cj1484c	*ccoZ*	Unknown; DUF5130	Inner membrane
cj1485c	*ccoY*	Unknown	Inner membrane
cj1486c	*ccoX*	Unknown; DUF4006	Inner membrane
cj1487c	*ccoP*	Oxidase subunit; cytochrome c	Inner membrane; periplasm facing
cj1488c	*ccoQ*	Oxidase subunit	Inner membrane
cj1489c	*ccoO*	Oxidase subunit; cytochrome c	Inner membrane; periplasm facing
cj1490c	*ccoN*	Oxidase subunit; Cu-heam protein	Inner membrane

DUF, domain of unknown function.
Cellular location of gene products was inferred using sequence analysis and topology prediction by Signal P and TMHMM servers.

biogenesis gene function predictions based on homology and gene context by phenotypic analyses of deletion mutants in strain NCTC 11168. **Table 1** provides a list of the genes studied. In addition to characterizing the function of CcoG, H, I, S, Sco, and PcuC homologues by such mutant analyses, we also show that several novel genes are required for oxidase activity. The product of one of these (designated CcoZ) has structural similarity to actinobacterial proteins involved in oxidase-cytochrome *bc* supercomplex formation. Preliminary evidence such an association is presented.

MATERIALS AND METHODS

Strains and Culture Conditions

Campylobacter jejuni strains were routinely grown at 42°C under microaerobic conditions [10% (v/v) O_2, 5% (v/v) CO_2, and 85% (v/v) N_2] in a MACS growth cabinet (Don Whitley Scientific, Shipley, United Kingdom). Bacterial cells, from frozen stocks, were streaked on Columbia blood agar plates (with appropriate antibiotics) and incubated overnight in the MACS growth cabinet. Material from plates were used for inoculating 25–50 ml starter cultures in Mueller-Hinton broth supplemented with 20 mM L-serine and 10 μg ml^{-1} each of vancomycin and amphotericin B (MHS broth). Cultures were incubated on a shaker at 150 rpm in the MACS growth cabinet for 6–12 h followed by inoculation into growth cultures to an initial OD_{600} of ∼0.1. For mutant selection, kanamycin was used at 50 μg ml^{-1}. Minimum Essential Medium alpha (MeMα), (nucleosides added, no phenol red; Life Science technologies) was also used to grow *C. jejuni* for some experiments (see text). MeMα was supplemented with 40 μM $FeSO_4$, 20 mM Sodium Pyruvate and 20 mM L-Serine.

Copper Sensitivity Assay

Campylobacter jejuni starter cultures were grown as above. Cell pellets were washed by resuspending in 25 ml MeMα minimal media and centrifuged at 12,000×*g* for 4 min at 42°C. Cells were resuspended in MeMα minimal media and added to 5 ml MeMα (equilibrated for 4 h in a microaerobic environment at 42°C with shaking) in six well plates to make the starting OD_{600} ∼0.1. The media was supplemented with 0.1–5.0 mM copper sulphate ($CuSO_4$) (Sigma-Aldrich). The six well plates were incubated in a microaerobic environment at 42°C with shaking at 160 rpm until cells reached stationary phase at which point the OD_{600} was measured.

Cytochrome *c* Oxidase Activity

cbb_3-oxidase activity was measured as the rate of oxygen consumption of cell suspensions in a Clark-type oxygen electrode using 0.25 mM tetramethyl-*p*-phenylenediamine (TMPD) plus 1 mM sodium ascorbate as electron donor, calibrated using air-saturated 25 mM sodium phosphate buffer (pH 7.4) (220 nmol dissolved O_2 ml^{-1} at 42°C). For wild-type and mutant comparisons, 25 ml *C. jejuni* cultures were grown until exponential phase in MHS without additions or with 0.25 mM copper sulphate, as required. Cells were pelleted and re-suspended in ice cold 1 ml 20 mM sodium phosphate buffer (pH 7.4) and kept on ice. Total protein concentration of the cell suspension was determined by Lowry assay and the specific rate of oxidation was calculated as nmol oxygen consumed min^{-1} mg^{-1} total protein.

Inductively Coupled Plasma Mass Spectrometry of Cell Samples

Fractionation of *C. jejuni* cell compartments with minimal cross-contamination is challenging so we determined total intracellular metal contents using whole cell samples. Biological triplicate

TABLE 2 | Primers used in this work.

***Campylobacter jejuni* NCTC 11168 gene deletion ISA primers 5′–3′**	
Cj0908 ISA F1 F	GAGCTCGGTACCCGGGGATCCTCTAGAGTCACC TACTGGAGTTTTCAAATCTCC
Cj0908 ISA F1 KR	AAGCTGTCAAACATGAGAACCAAGGAGAATTATA GACAACCTTTTAAAACAAGCC
Cj0911 ISA F1 F	GAGCTCGGTACCCGGGGATCCTCTAGAGTCTTA ATAATCACAAAACCATAGAGTTAAAA
Cj0911 ISA F1 KR	AAGCTGTCAAACATGAGAACCAAGGAGAATTTT TTTAGCTCAAAATCAAAATAAAA
Cj0911 ISA F2 KF	GAATTGTTTTAGTACCTAGCCAAGGTGTGCTTA TACTTAAGCAAAAAGATCGGTT
Cj0911 ISA F2 R	AGAATACTCAAGCTTGCATGCCTGCAGGTCGTT TCTCAATTTGAAAATATTTCAAATA
CJ1154C ISA F1 F	GAGCTCGGTACCCGGGGATCCTCTAGAGTCAAG AGAAGGTGCAAAAGAGC
CJ1154C ISA F1 R	AAGCTGTCAAACATGAGAACCAAGGAGAATTCA TGATTATACTATTCATTCTT
CJ1154C ISA F2 F	GAATTGTTTTAGTACCTAGCCAAGGTGTGCTTC TTAAAAAGAAAAGCCTT
CJ1154C ISA F2 R	AGAATACTCAAGCTTGCATGCCTGCAGGTCCAC CGTCTCTATCTAAAAATA
CJ1155C ISA F1 F	GAGCTCGGTACCCGGGGATCCTCTAGAGTCATC GCTTCGATTTTTAAAAG
CJ1155C ISA F1 R	AAGCTGTCAAACATGAGAACCAAGGAGAATTGC AATGTTCACATTTCATA
CJ1155C ISA F2 F	GAATTGTTTTAGTACCTAGCCAAGGTGTGCAGG ATTAAAGAATGAATAGTATAA
CJ1155C ISA F2 R	AGAATACTCAAGCTTGCATGCCTGCAGGTCCAC CGTCTCTATCTAAAAATA
CJ0369C ISA F1 F	GAGCTCGGTACCCGGGGATCCTCTAGAGTCACC TATCATACCAATTTGAATGATT
CJ0369C ISA F1 R	AAGCTGTCAAACATGAGAACCAAGGAGAATGTG TCCTTGCATTTTTAGACC
CJ0369C ISA F2 F	GAATTGTTTTAGTACCTAGCCAAGGTGTGCAAA AATGAACTCAAATAGAACACCATCAC
CJ0369C ISA F2 R	AGAATACTCAAGCTTGCATGCCTGCAGGTCAGG AGCGTTAATTAAAACATTAAGAT
CJ1483C ISA F1 F	GAGCTCGGTACCCGGGGATCCTCTAGAGTCTTT TAATGAAAATATTTTAAGTCAAAAAGTAA
CJ1483C ISA F1 R	AAGCTGTCAAACATGAGAACCAAGGAGAATAAT TATAGCCAAAAGTGAAAGCA
CJ1483C ISA F2 F	GAATTGTTTTAGTACCTAGCCAAGGTGTGCGAA ACAGTGGGTTTTTTTAGCT
CJ1483C ISA F2 R	AGAATACTCAAGCTTGCATGCCTGCAGGTCTAC TTAAAAAACCTTGCAAATCATAA
CJ1486C ISA F1 F	GAGCTCGGTACCCGGGGATCCTCTAGAGTCCAA TGGGTCAAAATATCTTTTTAGT
CJ1486C ISA F1 R	AAGCTGTCAAACATGAGAACCAAGGAGAATTCA CCCCTTGAAAGAGAAAT
CJ1486C ISA F2 F	GAATTGTTTTAGTACCTAGCCAAGGTGTGCGTA AGGCTTTGGAATATTTAATTGTT
CJ1486C ISA F2 R	AGAATACTCAAGCTTGCATGCCTGCAGGTCGCA GCATTATAAATATCACCTTTATTTG
CJ1485C ISA F1 F	GAGCTCGGTACCCGGGGATCCTCTAGAGTCATG TAGCAAAAGATCTTTCAGCT
CJ1485C ISA F1 R	AAGCTGTCAAACATGAGAACCAAGGAGAATTGT GCTTCCTTTATACTTCTATGATC
CJ1485C ISA F2 F	GAATTGTTTTAGTACCTAGCCAAGGTGTGCAAA AAATATTACAAGATGGCTTTTTT
CJ1485C ISA F2 R	AGAATACTCAAGCTTGCATGCCTGCAGGTCTAT CACGATTTGCATTACCTATAGA

(Continued)

TABLE 2 | Continued

***Campylobacter jejuni* NCTC 11168 gene deletion ISA primers 5′–3′**	
CJ1484C ISA F1 F	GAGCTCGGTACCCGGGGATCCTCTAGAGTCCCA TGGAGAAGATGGAAAAG
CJ1484C ISA F1 R	AAGCTGTCAAACATGAGAACCAAGGAGAATCTA AAAAAAAGCCATCTTGTAATATTTT
CJ1484C ISA F2 F	GAATTGTTTTAGTACCTAGCCAAGGTGTGCACA AAGAAGAATAAAGAGGAAAAAAA
CJ1484C ISA F2 R	AGAATACTCAAGCTTGCATGCCTGCAGGTCGCC TTGAAGAGCTAAAAATTCTT
CJ1482C ISA F1 F	GAGCTCGGTACCCGGGGATCCTCTAGAGTCGAA ACTAAAAAAAGTTTTTGGCC
CJ1482C ISA F1 R	AAGCTGTCAAACATGAGAACCAAGGAGAATTGA AGAGCTAAAAATTCTTAATTTCA
CJ1482C ISA F2 F	GAATTGTTTTAGTACCTAGCCAAGGTGTGCATA AACTCATTTATAAAAAGGAATTAAAATG
CJ1482C ISA F2 R	AGAATACTCAAGCTTGCATGCCTGCAGGTCCAA GCTCGTTAAAAAAATTTTCTT
CJ1161C ISA F1 F	GAGCTCGGTACCCGGGGATCCTCTAGAGTCAGC TATTGTATTATCAATCTTGCTTTT
CJ1161C ISA F1 R	AAGCTGTCAAACATGAGAACCAAGGAGAATACG CAATTCTTCCATTATAAACG
CJ1161C ISA F2 F	GAATTGTTTTAGTACCTAGCCAAGGTGTGCAAG AATTTAAAAATTTAATTTTTA
CJ1161C ISA F2 R	AGAATACTCAAGCTTGCATGCCTGCAGGTCACA TTCCAAACCATTCTGCAA
CJ1162C ISA F1 F	GAGCTCGGTACCCGGGGATCCTCTAGAGTCCAT GATAATTGTAGCTATTTTGGG
CJ1162C ISA F1 R	AAGCTGTCAAACATGAGAACCAAGGAGAATCAA TTAACATTTTTTACTTTAAATTTCATTTT
CJ1162C ISA F2 F	GAATTGTTTTAGTACCTAGCCAAGGTGTGCTTT ATAATGGAAGAATTGCGTATAAA
CJ1162C ISA F2 R	AGAATACTCAAGCTTGCATGCCTGCAGGTCCTT CTTCTTTAAAAATTTGCAAATACA
CJ1163C ISA F1 F	GAGCTCGGTACCCGGGGATCCTCTAGAGTCTTT GGCTCTAGCTATAGGAGTGAG
CJ1163C ISA F1 R	AAGCTGTCAAACATGAGAACCAAGGAGAATATC TTATATCCTTTTTTGCTTGACAT
CJ1163C ISA F2 F	GAATTGTTTTAGTACCTAGCCAAGGTGTGCAAG GAGTGAAAATGAAATTTAAAGTAA
CJ1163C ISA F2 R	AGAATACTCAAGCTTGCATGCCTGCAGGTCAAA CATTTCAAAATACATAATAATCACACT
CJ1164C ISA F1 F	GAGCTCGGTACCCGGGGATCCTCTAGAGTCGAT TTGGCTTTGCTTATGCTT
CJ1164C ISA F1 R	AAGCTGTCAAACATGAGAACCAAGGAGAATAAT CTACATTACAAACTGGACATAACA
CJ1164C ISA F2 F	GAATTGTTTTAGTACCTAGCCAAGGTGTGCAGC TTTTTGACTTTTAATTTTTATAAAAAT
CJ1164C ISA F2 R	AGAATACTCAAGCTTGCATGCCTGCAGGTCGGT TTTAGCGTCAATTTCTTTT
CJ1165C ISA F1 F	GAGCTCGGTACCCGGGGATCCTCTAGAGTCGTG CTTTAAGCTGGGCTATATATG
CJ1165C ISA F1 R	AAGCTGTCAAACATGAGAACCAAGGAGAATTAA AATAAATTCAATCATCTTAAAATCCC
CJ1165C ISA F2 F	GAATTGTTTTAGTACCTAGCCAAGGTGTGCACT AGACATGCAAAAAAACATTAAAA
CJ1165C ISA F2 R	AGAATACTCAAGCTTGCATGCCTGCAGGTCTGG GAATGATGATGTTCATG
CJ1166C ISA F1 F	GAGCTCGGTACCCGGGGATCCTCTAGAGTCGAA CTATCCAAATTTGTTCCACTAC
CJ1166C ISA F1 R	AAGCTGTCAAACATGAGAACCAAGGAGAATTAT ATCAGGTTTTTCCATATTTTAATAATCT

(Continued)

TABLE 2 | Continued

***Campylobacter jejuni* NCTC 11168 gene deletion ISA primers 5′–3′**	
CJ1166C ISA F2 F	GAATTGTTTTAGTACCTAGCCAAGGTGTGCTTT TGGGATTTTAAGATGATTGA
CJ1166C ISA F2 R	AGAATACTCAAGCTTGCATGCCTGCAGGTCGTT TTAATGTTTTTTTGCATGTCTAG
***Campylobacter jejuni* NCTC 11168 mutant screening primers 5′–3′**	
Cj0908 F screening	TTCCTTGTACTTTATCAAGTAAATTTGG
Cj0911 F screening	AAGCACAGAGCTTAAATCTGG
Cj0911 R screening	ACACTCTTTGGCGCTAGGTT
Cj1154c F screening	CAAGAAAAGGGTATTGTGGC
Cj1154c R screening	GCAAATAATTTCTAGCCAAAAAA
Cj1155c F screening	CATTGCATCGTATTCGAGTT
Cj1155c R screening	GCAAATAATTTCTAGCCAAAAAA
Cj0369c F screening	TTCTTCGATAATTACAAAAGCTCC
Cj0369c R screening	GGCTAATTATATCTTAATTTTGGTTAATAAAA
Cj1483c F screening	CTTCATATAGGATGAAAAAAATATTACAAG
Cj1483c R screening	AATCAAGTTTTAAAAGATATTCAAGATTAAA
Cj1486c F screening	TTTTTCAAGTATAGGTCAATATAATGAAGA
Cj1486c R screening	ATAGTATCACGATTTGCATTACCTATAG
Cj1485c F screening	TTAAACATGGTTCAAAAGGTATGA
Cj1485c R screening	TTTAGTTTCTAACATTTTTTTTCCTCTT
Cj1484c F screening	TGCTGCTTATGTAGCAAAAGA
Cj1484c R screening	TGCTCAAACAAACTTTATCTAAAAAT
Cj1482c F screening	CTATAGGTAATGCAAATCGTGATACT
Cj1482c R screening	TGAGTAAGACCCAAACAATAACTTC
Cj1161c F screening	TGTCAATATGAAGTCCGCTTT
cj1161c R screening	AAAATTAATCATCATTTTTAAGAGAGAT
Cj1162c F screening	GGCTTTTATCAATGCTTTAACCA
cj1162c R screening	ATATTTTCTAAAATTCTTTGATAATCTTG
Cj1163c F screening	TATCTTATTTCTTTTATACGCAGTGA
cj1163c R screening	TTTTAAAGCCTAAAAAAGCATG
Cj1164c F screening	TTTTGATTTGTTGTATAGCACTTG
cj1164c R screening	AAGCGGACTTCATATTGACAT
Cj1165c F screening	ATCATATTACTTTAAATGTTGTAGATATGG
cj1165c R screening	AAAGAATTTGAAAGGATTGAATAAAT
Cj1166c F screening	GTGCTGCAAACTGAGAATCTC
cj1166c R screening	AACCAAATCTACATTACAAACTGGAC
KanR F	ATTCTCCTTGGTTCTCATGTTTGACAGCTTAT
KanR R	GCACACCTTGGCTAGGTACTAAAACAATTC
***Campylobacter jejuni* NCTC 11168 qRT-PCR primers 5′–3′**	
GyrA RT_F	ATGCTCTTTGCAGTAACCAAAAAA
GyrA RT_R	GGCCGATTTCACGCACTTTA
Cj1161c RT_F	TTATGTGAATTCTAGCGGGG
Cj1161c RT_R	CCCAAAGCTACAAGGGTATT
Cj1162c RT_F	TAGAAGTGGATTTGGAGCAA
Cj1162c RT_R	CGCTCTACAATCTCAAAACC
Cj1163c RT_F	TGGCACTTTTAAGCGATACT
Cj1163c RT_R	TGCACCCTTAAACATCATCA
Cj1164c RT_F	AGTGATAGGAGTGGAGTTGA
Cj1164c RT_R	GCCTAGCCAACTTTCTTTCT
Cj1165c RT_F	GGGATTTGGCTTTGCTTATG
Cj1165c RT_R	CTAGAGCCAAAGTCACAGAA
Cj1166c RT_F	ATGCGTAGGAAGAATAGCTG
Cj1166c RT_R	AAAAGCCGAATTTGCCATAG

Underlined bases are adaptor regions corresponding to the pGEM3zf vector (ISA F and R primers) or to the kanamycin resistance cassette (ISA KR and KF primers).

cultures of *C. jejuni* cells were grown in 500 ml MHS broth and cells were harvested at stationary phase by centrifuging at 17,700×*g* for 20 min at 4°C. Cell pellets were re-suspended in 10 ml wash buffer (10 mM HEPES, 0.5 M Sorbitol and 100 μM EDTA, pH 7.5) and centrifuged as above. The wash steps were repeated three times but in the third wash, EDTA was omitted from the wash buffer. After the final centrifugation the supernatants were discarded and cell pellets was resuspended in 1 ml concentrated HNO_3 (65% v/v) by vortexing. Samples were left in acid overnight and then analysed at the University of Sheffield Inductively Coupled Plasma Mass Spectrometry (ICP-MS) facility.

Isothermal Assembly Cloning and Allelic Exchange Mutagenesis

Isothermal assembly (ISA) cloning was used to generate mutant plasmids for transformation into *C. jejuni*, in order to delete specific genes by allelic exchange mutagenesis, replacing most of the coding region with a kanamycin resistance cassette derived from pJMK30 (van Vliet et al., 1998). The ISA reactions were performed by assembling 4 PCR amplified fragments; *Hin*cII digested pGEM3Zf(–) vector, two regions of ∼500 bp flanking the gene to be deleted, such that only the first few and last few codons of the gene were retained, and the kanamycin resistance cassette to be inserted between the two flanking regions. The kanamycin resistance cassette was amplified from pJMK30 using primers Kan F and Kan R (**Table 2**). The left flanking region of the gene to be deleted was amplified using primers F1 F and F1 KR (**Table 2**) and the right flanking region was amplified by F2 KF and F2 R. The F1 F and F2 R primers contain 30 bp adapters for the pGEM3zf(–) vector cut with *Hin*cII and the F1 R and F2 F primers contain 30 bp adapters for the kanamycin resistance cassette. All PCR amplifications were performed with Phusion polymerase (NEB). An ISA mastermix was prepared by mixing 40 μl 5 X ISA buffer, 0.125 μl T5 exonuclease (Cambio, United Kingdom), 2.5 μl Phusion polymerase (NEB) and 20 μl Taq ligase (NEB) and made to a total volume of 150 μl with dH_2O. 5 X ISA buffer consists of 25% (w/v) polyethylene glycol [PEG-8000], 500 mM *Tris*–HCl pH 7.5, 50 mM $MgCl_2$, 50 mM dithiothreitol [DTT], 1 mM of each dNTP, and 5 mM NAD. pGEM3Zf (–) was digested with *Hin*cII and phosphatase treated. The PCR fragments for the ISA reaction were combined in equimolar concentration with amounts ranging from 10 to 100 ng each, with the final volume of the mixture not exceeding 5 μl. A 15 μl ISA mastermix aliquot was thawed on ice and the mixture was added to it with the final volume made up to 20 μl with dH_2O. The reaction was incubated at 50°C for 1 h. The resulting DNA was immediately used to transform competent *Escherichia coli* DH5α cells, which were then grown on LB+ kanamycin agar plates. Colonies were screened by PCR using M13 primers and correct assembly of plasmids was confirmed by automated DNA sequencing (Core Genomic Facility, University of Sheffield Medical School, United Kingdom). Plasmids were electroporated into *C. jejuni*, cells plated out on non-selective Columbia agar plates and incubated overnight in microaerobic conditions at 42°C. The growth was harvested and transferred to selective

Columbia agar plates (with kanamycin) and incubated as above for 2–4 days. Colonies were checked by colony PCR with a combination of different screening and antibiotic cassette primers according to **Table 2**.

RT-PCR

The SV Total RNA Isolation System (Promega) was used to extract RNA from growing cells of *C. jejuni* in minimal media with or without added copper. Gene specific qRT-PCR primers (**Table 2**) were designed using PRIMER 3 software (Untergasser et al., 2007) to amplify 200–300 bp sequences within the gene of interest. The *C. jejuni gyrA* gene was used as the reference. All primers were diluted to 25 μM concentration in nuclease-free water and checked for specificity before use by performing a PCR reaction using *C. jejuni* genomic DNA as template. qRT-PCR reactions (20 μl volumes) were carried out in a MX3005P thermal cycler (Agilent) in a MicroAmp® 96-well optical reaction plate (ABI prism). Reactions were performed using either the Sensifast SYBR Lo-ROX one step kit or Sensifast SYBR Hi-ROX one step kit (Bioline, United Kingdom). Each reaction contained 10 μl Sensifast SYBR 2× buffer (Bioline, United Kingdom), 0.2 μl of each gene specific qRT-PCR primer, 0.2 μl reverse transcriptase (Bioline, United Kingdom), 0.4 μl RNAse inhibitor (Bioline, United Kingdom), 2 μl of matched RNA or DNA template and 7 μl nuclease free water (Bioline, United Kingdom). Each reaction using RNA was replicated in triplicate and reactions using genomic DNA were replicated in duplicate for the standard curve. In the thermal cycler, qRT-PCR reactions were carried out at 45°C for 10 min, 95°C for 2 min, followed by 40 cycles of 95°C for 20 s, 55°C for 30 s and 72°C for 20 s each. Data were collected with the associated MxPRO QPCR software (Agilent) and analyzed using Microsoft EXCEL. A standard curve for each gene was established using a series of *C. jejuni* genomic DNA dilutions to normalize for variation in primer annealing efficiency between different primer pairs. The relative expression levels of the target genes were calculated following the standard curve protocol described in the User Bulletin #2 (ABI Prism 7700 Sequence Detection System, Subject: Relative Quantification of Gene Expression) given by Applied Biosystems. Target gene expression was normalized to *gyrA* expression, which acted as an internal control. No-template reactions were included as negative controls for each primer set being used.

Haem Blotting

Cells were harvested during stationary phase by centrifuging at 17,700×*g* for 20 min at 4°C. Supernatant was discarded. Cell pellet was resuspended in 10 ml of ice-cold 10 mM HEPES buffer (pH 7.4) by gentle pipetting. The cell suspension was sonicated on ice for 6 × 15 s pulses at a frequency of 16 amplitude microns using a Soniprep 150 ultrasonic disintegrator (SANYO) and cell debris/unbroken cells were removed by centrifugation at 12,470×*g* for 20 min at 4°C. The supernatant was removed and centrifuged at 100,000×*g* at 4°C for 1 h in benchtop ultracentrifuge (Beckman). The pellet was washed by pouring off 10 mM HEPES buffer (pH 7.4) twice without disturbing the pellet, which was then re-suspended in 1 ml 25 mM phosphate buffer (pH 7.4) with gentle pipetting, transferred to a glass homogeniser and homogenised gently. Homogenised total membrane protein solution was stored at –80°C and concentration was measured by Lowry assay.

Haem blotting was performed with total membrane proteins according to Vargas et al. (1993) with some modifications. Samples were prepared in sample buffer (60 mM *Tris*–HCl pH 6.8, 2% [w/v] SDS, 0.005% [w/v] bromophenol blue, and 10% [w/v] glycerol) and mildly denatured at 37°C for 30–60 min. Proteins were separated by two separate SDS-PAGE gels. One was stained with Coomassie blue G250 and other was electroblotted onto nitrocellulose membrane (Hybond-C extra, GE Healthcare). SDS-PAGE and nitrocellulose membrane sandwich was made according to manufacturer's instructions and electroblotting was performed using Mini-Blot Electrophoretic Cell (Bio-Rad) in ice-cold transfer buffer (25 mM *Tris*, 190 mM glycine, 10% [v/v] methanol) for 1 h at constant 100 V. Then the membrane was washed with 20 mM Phosphate buffer for 5 min at RT to remove any residual SDS or methanol and covalently bound haem was detected as haem-associated peroxidase activity (Feissner et al., 2003), using the enhanced chemiluminesence (ECL) kit from GE Healthcare according to manufacturer's instructions. Membrane was covered with pre-mixed solutions A and B, incubated for 1 min at RT and developed by exposing for different times, as necessary, in ChemiDoc Imaging System (Bio-Rad).

Membrane Protein Isolation for Blue Native PAGE

Cells were harvested by centrifugation at 17,700×*g* for 20 min at 4°C. Supernatant was discarded and pellet was resuspended in 20 mM *Tris*–HCl pH 7.4, 50 mM NaCl, 1 mM ethylenediaminetetraacetic acid, 10% v/v glycerol, 2 mM dithiothreitol and 0.005% phenylmethylsulfonyl fluoride. Cells were lysed by two passes through a French press (20,000 psi) and cell debris were removed by centrifugation at 12,470×*g* for 20 min at 4°C. Soluble material was loaded onto 40/15% w/w sucrose step gradients and centrifuged at 107,400×*g* in a Beckman SW32 Ti for 10 h at 4°C. Membranes were harvested and protein concentration was measured using the BioRad DC protein assay.

BN-PAGE

Membranes containing 10 mg ml^{-1} protein were incubated in 2% (w/v) α-dodecylmaltoside (DDM) for 1 h at room temperature. Solubilized protein complexes were isolated and supplemented with a one-tenth volume of blue native sample buffer (100 mM Bis*Tris*–HCl pH 7.0, 0.5 M amino-*n*-caproic acid, 30% (w/v) sucrose, 50 mg ml^{-1} Coomassie Blue G250) and centrifuged for 20 min at 18,000×*g* at 4°C. Sample was loaded onto NativePAGE Bis*Tris* 4–16% gels (Novex) and run at 160 V for 2 h at 4°C in NativePAGE Running Buffer. The cathode chamber was supplemented with 2 ml of 50 mM Tricine, 15 mM Bis*Tris*–HCl pH 7.0, 0.01% Coomassie Blue G250. Imaging was performed using an Amersham Imager 600 in colour.

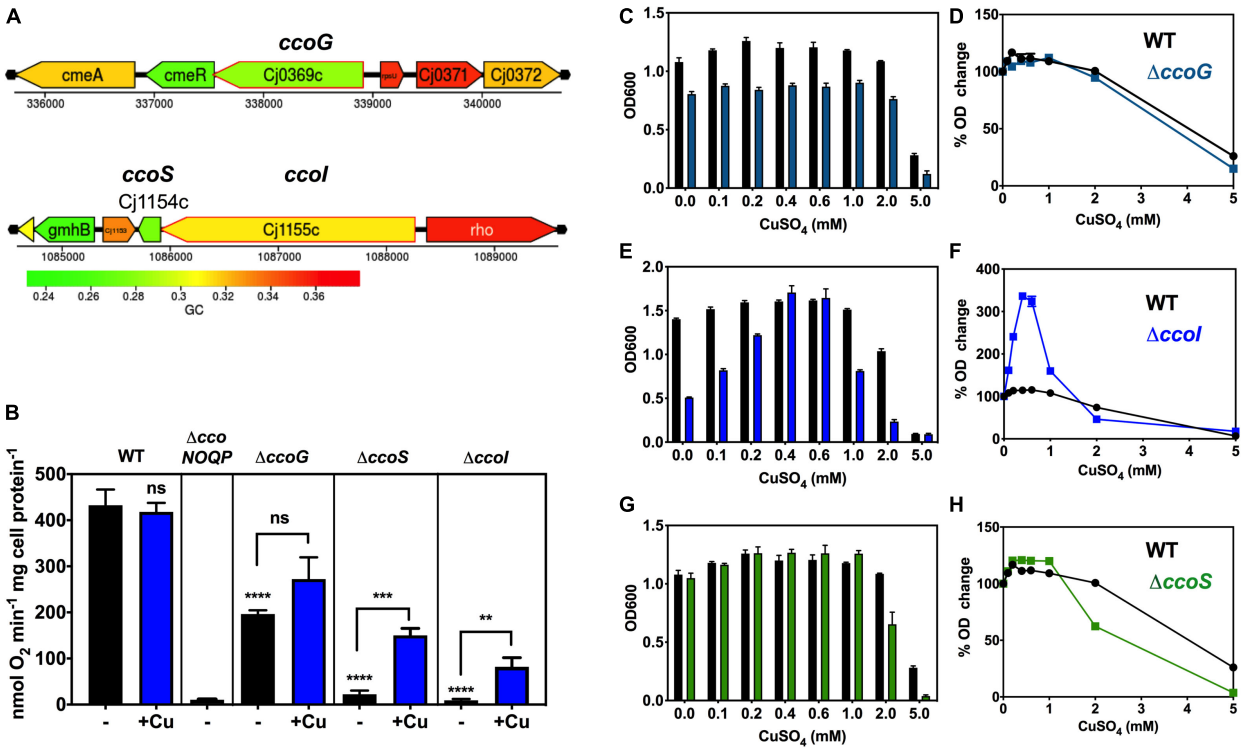

FIGURE 2 | Dependence of oxidase activity and growth on putative *ccoG*, *ccoI*, and *ccoS* genes and the effect of exogenous copper. **(A)** Genomic regions of NCTC 11168 encoding putative *ccoG* (*upper panel*), *ccoI* and *ccoS* (*lower panel*) genes. Images derived from campyDB (http://xbase.warwick.ac.uk/campydb/) and genes coloured by GC composition (see scale). **(B)** Cytochrome *c* oxidase activity measured with ascorbate/TMPD as electron donor. Wildtype, Δ*ccoNOQP*, Δ*ccoG*, Δ*ccoI*, and Δ*ccoS* cells were grown in unsupplemented Mueller-Hinton medium (approx. 0.05 μM copper) or with copper sulphate added to 0.6 mM (an excess but non-toxic level; see **Figure 3**). The data are the average of triplicate cultures with error bars showing SD. *t*-tests were performed to test significance ($p > 0.05$, ns; $0.01 > **p > 0.001$; $0.001 > ***p > 0.0001$; $****p > 0.0001$). The stars above the black bars represent the statistical significance of comparisons between the unsupplemented mutant and wild-type rates. Panels **(C–H)**, copper sensitivity of growth of wild-type and *ccoG*, *ccoI*, and *ccoS* mutants. WT, Δ*ccoG* **(C)**; Δ*ccoI* **(E)**; and Δ*ccoS* **(G)** cells were grown at different concentrations of $CuSO_4$ in Mueller-Hinton medium until stationary phase (24 h) and the final ODs were measured. The data are the average of triplicate cultures with error bars showing SD. In panels **(D,F,H)**, the corresponding raw data for each strain are normalised with respect to the final OD without Cu = 100%, to better visualise the degree of enhancement or inhibition of growth by copper.

Preparation of Peptides by In-Gel Tryptic Digestion and Analysis by Nano-Flow LC-MS/MS

Bands of interest were excised from the BN PAGE and subjected to trypsin digestion according to Pandey et al. (2000). Peptides dissolved in 0.5% (v/v) trifluoroacetic acid (TFA), 3% (v/v) acetonitrile were resolved in triplicate on an EASY-Spray PepMap RSLC C_{18} column (Thermo Scientific, 50 cm × 75 μm ID, 2 μm, 40°C). The gradient profile was delivered at 300 nl min^{-1} by a Dionex RSLCnano chromatography system (Thermo Scientific) as follows: 97% solvent A (0.1% formic acid in water) to 10% solvent B (0.08% formic acid in 80% acetonitrile) over 5 min, then 10–50% solvent B over 30 min. The mass spectrometer was a Q Exactive HF hybrid quadrupole-Orbitrap system (Thermo Scientific) programmed for data dependent acquisition with profile full MS scans at 120,000 resolution and a maximum of ten centroid product ion scans at 30,000 resolution per cycle. Proteins were identified using MaxQuant v. 1.6.10.43 (Cox and Mann, 2008) by searching the MS data files against the UniProtKB reference proteome database for *C. jejuni*[1] (downloaded on 6 February 2020). Search parameters were: carbamidomethyl-Cys (fixed modification), Met oxidation, protein N-terminal acetylation and Gln to pyro-Glu conversion (variable modifications) with a maximum of two missed cleavages. Proteins were quantified by intensity based absolute quantification (iBAQ; Schwanhäusser et al., 2011) and normalised between MS experiments to total iBAQ.

RESULTS

Characterisation of Cytochrome *c* Oxidase in Cells of *C. jejuni*: Cco Activity Is Growth Phase Dependent, Sulphide Sensitive and Not Inhibited by Formate

Campylobacter jejuni NCTC 11168 grown under standard microaerobic conditions in complex MHS broth showed high rates of Cco activity (measured as ascorbate/TMPD driven

[1]https://www.uniprot.org/proteomes/UP000249026

oxygen consumption) of ∼300–400 nmol oxygen consumed min^{-1} mg cell $protein^{-1}$ during the exponential phase of growth. However, the specific activity decreased rapidly as the cells entered stationary phase (**Figure 1B**). Thus, in all subsequent experiments, cells were harvested at mid-exponential phase to ensure maximal activity and valid comparisons between wild-type and mutant strains. Previously constructed deletion mutants in either the *ccoNOPQ* genes or *cioAB* genes encoding the major subunits of the two oxidases in *C. jejuni* (Liu and Kelly, 2015), were used as controls in subsequent experiments and to characterise the response of each oxidase to exogenous sulphide. With formate as a physiological electron donor, oxygen consumption by the *cioAB* mutant, where Cco is the only active oxidase, was severely inhibited by sulphide, whereas respiration in the *ccoNOQP* mutant was sulphide resistant up to 1 mM (**Figure 1C**). This agrees with studies in other bacteria where *bd*-type quinol oxidases are much more sulphide resistant than HCO's (Forte et al., 2016; Korshunov et al., 2016) and also correlates with the previously documented cyanide resistance of the *C. jejuni* quinol oxidase (Jackson et al., 2007). Finally, it has been reported that formate stimulates growth but actually inhibits the Cco activity in *C. jejuni* (Kassem et al., 2017). We found that addition of formate to cell suspensions in an oxygen electrode in the presence of ascorbate/TMPD, stimulated oxygen consumption compared to ascorbate/TMPD alone (**Figure 1D**). A stimulation was also seen in the *ccoNOQP* operon deletion mutant, where formate derived electrons reduce oxygen via the alternative quinol oxidase CioAB. Interestingly, stimulation was also observed in the *cioAB* deletion mutant, which is unexpected if we assume the Cco complex is operating at maximal rate with excess ascorbate/TMPD. Using higher concentrations of ascorbate or TMPD did not alter these rates, so the stimulation may be due to an unidentified oxidase independent oxygen consuming process. We conclude that formate does not inhibit oxidase activity.

Deletion of *ccoI* or *ccoS* Homologues Abolishes Cco Activity, Which Is Partially Rescued by Excess Copper

In *C. jejuni* NCTC 11168, the genes *cj1490c*, *cj1489c*, *cj1488c*, and *cj1487c* encode the known CcoNOQP subunits, respectively, of the cbb_3-type cytochrome *c* oxidase (Liu and Kelly, 2015), but the genes required for copper trafficking to the periplasm and insertion of copper into CcoN have not been identified. In many bacteria, a *ccoGHIS* operon is situated downstream of *ccoNOQP*, but in *C. jejuni*, candidate *ccoGHIS* genes are scattered throughout the genome and have not been functionally characterised previously. Genome annotation and BLAST searches showed that *cj0369* encodes a CcoG homologue, *cj1154c* encodes a CcoS homologue and *cj1155c* encodes a CcoI homologue, which may have a copper translocating function (**Figure 2A**). Kanamycin resistant deletion mutants of the cognate genes were made by replacing most of the coding regions with a kanamycin resistance cassette via homologous recombination (See "Materials and Methods"). This cassette carries a constitutive promoter and no terminator. Its insertion has been shown to result in expression of operonic downstream genes (Guccione et al., 2008, 2010) thus minimizing polar effects. The deletion mutants formed by transformation of *C. jejuni* cells with recombinant plasmids were checked for correct mutation by colony PCR with a combination of screening and kanamycin cassette primers (**Table 2**).

Figure 2B shows from ascorbate/TMPD driven oxygen consumption rates of wild-type and mutants strains that in the *ccoG* (*cj0369c*) deletion mutant, Cco activity was reduced by ∼50%. There was an indication of a stimulation of activity in the mutant by adding excess Cu, but this just failed to reach statistical significance ($P = 0.0524$). In contrast, in the *cj1155c* and *cj1154c* deletion mutants, lacking the *ccoI* and *ccoS* homologues, respectively, Cco activity was almost abolished but was rescued after growth with excess copper to similar extents (6.7-fold increase in activity for *ccoS* and 9.1-fold for *ccoI* mutants) (**Figure 2B**). These data are consistent with the involvement of CcoI and CcoS in copper supply to CcoNOQP.

Deletion of *ccoI* Causes a Severe Growth Defect That Is Fully Rescued by Excess Copper

Copper sensitivity of growth assays were performed with wild-type, Δ*ccoS* (*cj1154c*), Δ*ccoI* (*cj1155c*), and Δ*ccoG* (*cj0369c*) strains in complex MHS media by measuring final cell densities in triplicate cultures. ICP-MS analysis showed that the copper content of MHS was ∼0.05 μM; a small stimulation in growth on adding up to 0.2 mM of $CuSO_4$ to both wild-type and mutant strains was noted. More than 2 mM $CuSO_4$ was toxic for the bacterial cells but up to ∼1 mM had no significant toxicity in these media (**Figures 2C–H**).

The *ccoG* mutant showed a small growth defect that was insensitive to varying copper concentration compared to WT (**Figures 2C,D**). In contrast, cells lacking the CcoI homologue (Cj1155) were found to have a significant growth defect and were highly responsive to the external Cu concentration (**Figures 2E,F**). Increases in $CuSO_4$ concentration initially strongly stimulated growth and 0.4 mM completely complemented the absence of the *cj1155c* gene product. However, above 0.6 mM growth was inhibited more than the wild-type. Cells lacking the CcoS homologue (Cj1154) did not have a growth defect but growth was inhibited more than the wild-type at $CuSO_4$ concentrations above 1 mM (**Figures 2G,H**).

Role of the *cj0908–0911* Operon in Oxidase Assembly

We hypothesised that the operonic genes *cj0908–911* (**Figure 3A**) may encode proteins needed to transfer Cu from the periplasm to the CcoN subunit, as Cj0909 is a putative periplasmic Cu(I) binding protein homologous to bacterial PCu_AC and Cj0911 is a protein belonging to the Sco1 family. As described above, members of this family are required in other bacteria as a Cu chaperone for the proper assembly of cytochrome *c* oxidase. However, unlike Cj0909 and Cj0911, Cj0908 and Cj0910 are paralogous proteins (41% identical) that have no characterised counterparts in Cco assembly systems in other

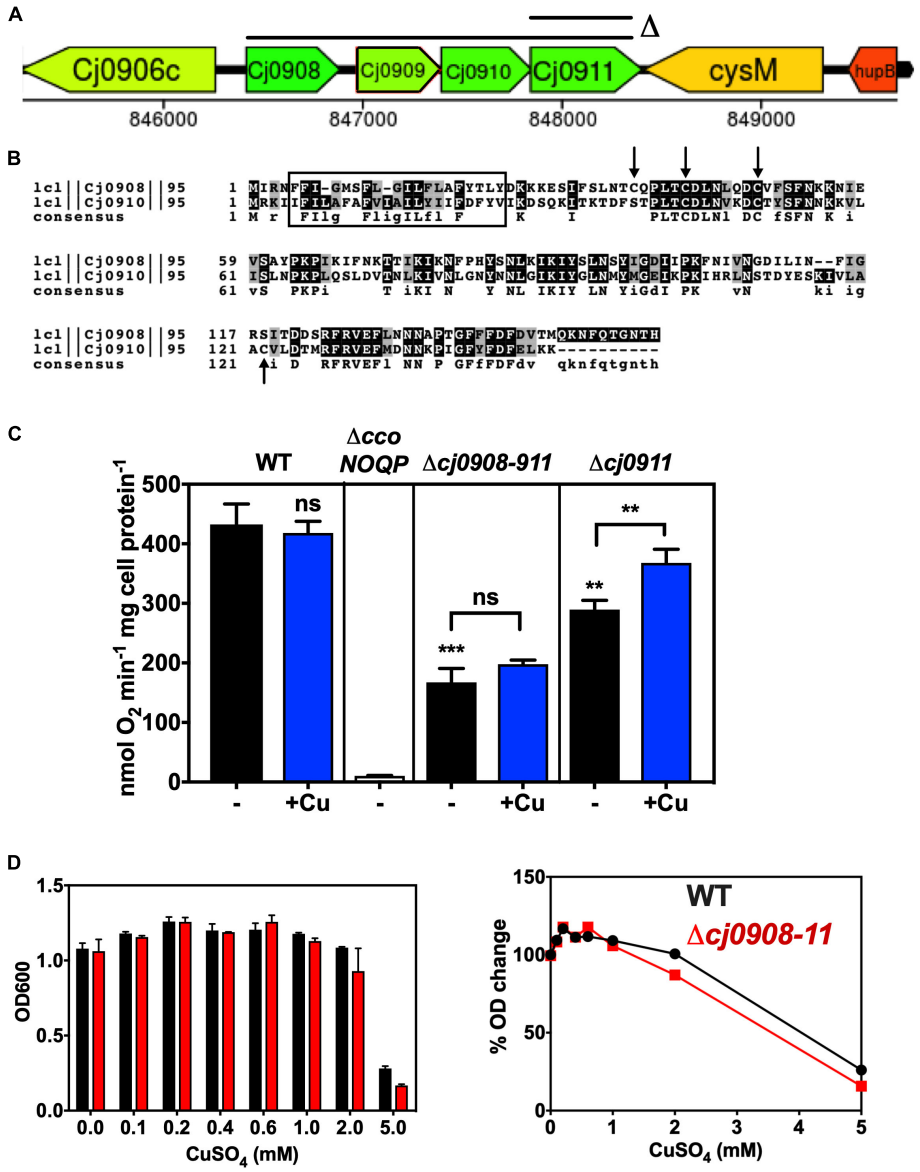

FIGURE 3 | Role of the *cj0908–911* genes in Cco activity. **(A)** Organisation of the genomic region surrounding *cj0908–911* and the extent of deletions made. An operon deletion plasmid in the pGEM3Zf vector was made using primers Cj0908 ISA F1 F, Cj0908 ISA F1 KR, Cj0911 ISA F2 KF and Cj0911 ISA F2 R (**Table 2**) to create the flanks between which the Kan cassette was inserted. Image derived from campyDB (http://xbase.warwick.ac.uk/campydb/) and genes coloured by GC composition as in the legend to **Figure 2**. **(B)** Alignment of Cj0908 and Cj0910 using T-COFFEE and BOXSHADE to show identical residues (Black boxes) and conservative substitutions (Grey boxes). The rectangular boxed area shows the single transmembrane helix predicted using TMHMM. Arrows highlight Cys residues in either or both proteins, which may have a redox function or bind Fe. **(C)** Cytochrome c oxidase activity measured with ascorbate/TMPD as electron donor. Wildtype, Δ*ccoNOQP*, Δ*cj0908-cj0911*, and Δ*cj0911* cells were grown in Mueller-Hinton medium without any added copper or with copper sulphate added to 0.6 mM. The data are the average of triplicate cultures with error bars showing SD. Students *t*-tests were performed to check significance ($p > 0.05$, ns; $0.01 > **p > 0.001$; $0.001 > ***p > 0.0001$). The stars above the black bars represent the statistical significance of comparisons between the unsupplemented mutant and wild-type rates. **(D)** Copper sensitivity of wild-type and *cj0908–911* mutant determined in the same way as described in the legend to **Figure 3**. *Left panel*; raw final cell density data; *Right panel*, data normalised to cell yield without copper = 100%.

bacteria. Interestingly, Cj0908 has a cysteine motif similar in part to thioredoxin–like [2Fe–2S] ferredoxins (Trx–like–Fd's) of C–X_4–C–X_6–C, while Cj0910 is missing the first Cys but has the C–X_6–C and an additional Cys at position 122 (**Figure 3B**). The SignalP and TMHMM servers predict no signal sequence but a single N-terminal transmembrane helix at the N-terminus of each protein, with the remainder of the protein likely to be periplasmic (**Figure 3B**).

A deletion mutant was constructed that removed the entire *cj0908–911* operon, which was replaced with a kanamycin cassette. In addition, an individual *cj0911* deletion mutant was made (**Figure 3A**). The data in **Figure 3C** shows that both of

these mutants were clearly affected in cytochrome c oxidase activity. In the Δ*cj0908–cj0911* strain activity was significantly reduced (over 50% lower) but was not abolished, suggesting that these gene products are involved in CcO assembly but are not essential for it. In the Δ*cj0911* mutant, lacking the Sco1 homologue, activity was also reduced but to a lesser extent compared to the entire operon mutant. A significant stimulation in activity on adding excess Cu is consistent with the involvement of Cj0911 in handling Cu, although this would need to be demonstrated biochemically. In contrast the operon mutant did not show stimulation of oxidase activity by copper (**Figure 3C**). In addition, growth experiments (**Figure 3D**) showed that the Δ*cj0908–cj0911* operon mutant was insensitive to varying amounts of Cu with respect to WT. Additional studies with individual mutants and analysis of the gene products will be needed to fully define the roles of *cj0908* and *cj0910*.

Deletion of the *cj0908–11* Operon, *cj1154c* or *cj1155c* Does Not Affect Biogenesis of the CcoO Subunit of Cytochrome *c* Oxidase

Total membrane preparations of wild-type, Δ*ccoNOQP*, Δ*ccoNOQP*$^{+}$, Δ*cj0908-cj0911*, Δ*ccoS*, and Δ*ccoI* cells were made as described in "Materials and Methods" and gently denatured in the absence of mercaptoethanol to preserve haem binding to *c*-type cytochromes. **Figure 4** shows the membrane cytochrome profiles after SDS-PAGE and protein blotting, with detection by haem-associated peroxidase activity. The two cytochrome *c* proteins associated with the oxidase complex, CcoO and CcoP have molecular masses of ∼25 and ∼31 kDa, respectively. CcoP could not be identified on these gels as it is about the same size as a very abundant cytochrome of a similar size but a band corresponding to the approximate size of CcoO is clearly absent in the *ccoNOQP* deletion mutant but present in both wild-type and complemented strains. This band is also present in membranes of the biogenesis mutants Δ*cj908–911*, Δ*ccoS*, and Δ*ccoI*. This suggests that CcoO can still be inserted into the membrane in the absence of biogenesis proteins that are needed for CcoN assembly (i.e., copper insertion).

Role of the *ccoH* Homologue *cj1483c* and Identification of *ccoX*, *ccoY*, and *ccoZ*; Novel Genes Downstream of *ccoP* That Are Required for Normal Oxidase Activity

cj1483c encodes a CcoH homologue, which in other bacteria is thought to be tightly associated with the oxidase. Intriguingly, although this *ccoH* homologue is just downstream of the structural gene *ccoP* (*cj1487c*), three intervening genes of unknown function (*cj1484c*, *cj1485c*, and *cj1486c*) are also present at this locus (**Figure 5A**). Given this gene organisation we constructed individual deletion mutants in each of these genes, in addition to a *cj1482c* mutant, to assess their Cco activity in comparison to isogenic wild-type and *ccoNOQP* deletion strains (**Figure 5B**). In both the *ccoH* (*cj1483c*) and *cj1486c* deletion mutants, oxidase activity was abolished and was not restored by adding excess copper, suggesting an absolutely essential role in the activity of the oxidase (**Figure 5B**). Both of these mutants showed a microaerobic growth defect (reduction in final cell density) and did not show any copper stimulation of growth compared to the wild-type (**Figure 5C**). Cj1486 is predicted by the TMHMM server to have a single transmembrane helix and is a member of a conserved family of small proteins of unknown function containing the DUF4006 domain. In the *cj1484c* and *cj1485c* mutants, in contrast to *cj1486c*, Cco activity was significantly decreased but not abolished. This phenotype could not be complemented by addition of exogenous copper (**Figure 5B**). Cj1485 consists of just 33 residues and is predicted by the TMHMM server to have a central transmembrane helix. Cj1484 (200 residues) contains a DUF5130 domain and a TPM_phosphatase domain. Finally, deletion of *cj1482c* had no effect on Cco activity compared to the wild-type, so we conclude that this gene is not involved in oxidase activity or biogenesis. In view of the abolished or compromised oxidase phenotypes of the *cj1486c*, *cj1485c*, and *cj1484c* mutants and the genomic linkage to both *ccoH* and *ccoNOQP*, we conclude that the proteins encoded by these genes are crucial for normal oxidase activity. We therefore designate these genes *ccoX* (*cj1486c*), *ccoY* (*cj1485c*), and *ccoZ* (*cj1484c*).

CcoH and CcoZ Are Associated With Oxidase and Cytochrome *bc* Complex Proteins in a High Molecular Weight Band After Detergent Solubilisation of Membranes

Modelling using the Phyre^{2} server (Kelley et al., 2015) showed that CcoZ (Cj1484) is structurally similar to Msmeg_4692, a protein that is part of an oxidase-cytochrome *bcc* supercomplex in the actinobacterium *Mycobacterium smegmatis* (Gong et al., 2018; Wiseman et al., 2018). Comparison of Cj1484 to Msmeg_4692 as the template (**Supplementary Figure 1**) shows the same mixed beta sheet/alpha helical fold with a TPM domain found in some phosphatases present in both proteins. This raised the possibility that such a supercomplex might exist in *C. jejuni*. The cytochrome *bc* complex (menaquinol:cytochrome c reductase) in *C. jejuni* is encoded by the *qcrABC* genes (preferred designation although annotated as *petABC*) and contains a dihaem cytochrome c_4 (QcrC) in place of cytochrome c_1 (Garg et al., 2018). We solubilised membrane preparations of wild-type cells with the detergent DDM and separated proteins by BN-PAGE (**Figure 6A**), which revealed the presence of several high molecular weight bands, the most prominent of which were designated band I (apparent molecular weight ∼730 kDa), band II (apparent molecular weight ∼600 kDa) and band III (apparent molecular weight ∼200 kDa). These bands were excised for trypsin digestion and the resultant peptides analysed by nanoflow LC-MS/MS as described in "Materials and Methods". The proteins contained in the bands were identified using the MS data-files as input for database searching and the complete results are shown in **Supplementary Table 2**. The number of proteins identified in bands I, II and III was 403, 622, and 717, respectively, and, in all cases, the highest

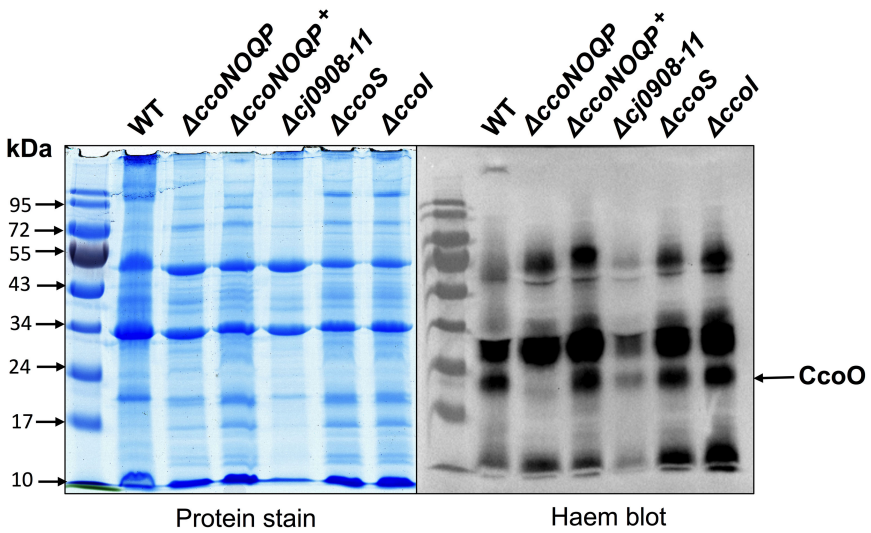

FIGURE 4 | Deletion of *cj0908–911*, *ccoS* or *ccoI* does not affect insertion of the CcoO cytochrome *c* into the cytoplasmic membrane. Samples of total membrane proteins of wild-type, Δ*ccoNOQP*, Δ*ccoNOQP*$^{+}$, Δ*cj0908-cj0911*, Δ*ccoS*, and Δ*ccoI*, were mildly denatured in the absence of mercaptoethanol to preserve attachment of C-haems to Cys residues and 20 μg protein in each lane was loaded on 10% SDS-PAGE gels. Gels were either stained with Coommassie brilliant blue (*left panel*) or for haem-associated peroxidase activity (*right panel*) using a standard enhanced chemiluminescence kit (See section "Materials and Methods"). The CcoO band (arrowed) is missing in Δ*ccoNOQP* only. CcoP is not visible because of intense c-type cytochrome bands of a similar size.

molecular mass represented was 168.8 kDa. Therefore, the bands contain populations of proteins co-migrating in both specific and non-specific complexes that are stable in the presence of DDM. The MS analysis identified nine protein components of the putative Qcr-oxidase supercomplex: CcoN, CcoO, CcoP, CcoH (Cj1483), CcoZ (Cj1484), CcoX (Cj1486), QcrA, QcrB, and QcrC. A quantitative comparison of these proteins, using mass spectral peak intensities normalised to approximate molar amount, revealed that band I contained very low levels of CcoO, CcoP, CcoH, CcoZ, QcrA, and QcrC (**Figure 6B**). Band II contained all nine proteins and, for the proteins also identified in band I, their quantification indicates an abundance of around 10-fold higher than in band I (**Figure 6C**, left panel). Expression of protein abundance relative to CcoO suggests a stoichiometry of 1:1:1 for CcoO, QcrA, and QcrC (**Figure 6C**, right panel). This correlation may reflect the occurrence of a complex *in vivo* that comprises both Cco and Qcr subunits. The sub-stoichiometric amounts of some subunits would therefore probably result from co-migrating populations of partially assembled precursor sub-complexes of a putative Qcr-oxidase complex, or from possible concealment of trypsin cleavage sites in transmembrane regions resulting in underrepresentation of those tryptic peptides in the mass spectra. The possible existence of intermediate sub-complexes in the formation of a functional Qcr-oxidase complex is supported by the quantification of CcoO and CcoP in a 1:1 ratio in band III (**Figure 6D**). While CcoH and CcoX were also quantified in band III at a similar stoichiometric ratio to band II, CcoZ was depleted 10-fold. This depletion was associated with an absence of QcrB and QcrC, and a substantial reduction in QcrA. Since absolute stoichiometry determinations by label-free MS may be indicative rather than decisive, particularly for membrane proteins where MS intensities may be underrepresented, further work will be needed to confirm the existence of a Qcr-oxidase complex and elucidate the mechanism of its assembly.

Characterisation of a Metal Homeostasis Gene Cluster and Relationships Between Copper Homeostasis and Cytochrome *c* Oxidase Activity

Cj1161 is homologous to bacterial CopA proteins (Hall et al., 2008), known to be P-type ATPases that have a copper efflux function related to maintaining intracellular Cu homeostasis (Rensing et al., 2000). Indeed, a previously constructed *cj1161c* mutant showed increased copper sensitivity consistent with this role (Hall et al., 2008). However, the *cj1161c* gene is encoded in a cluster (*cj1161c–cj1166c*) that may have related or additional functions in copper or metal homeostasis (**Figure 7A**). Cj1162 is a CopZ homologue; CopZ is a cytoplasmic copper chaperone that transfers copper to CopA (Singleton and Le Brun, 2007). Cj1163 is annotated as a Zn-Co-Ni P-type ATPase transporter (a CzcD homologue) and has recently been shown to be a thermoregulated Zn exporter (Barnawi et al., 2020). Cj1164 is homologous to Zn finger proteins. Cj1165 and Cj1166 are predicted to be integral membrane proteins with six transmembrane helices. They both have sequence similarity to serine/threonine efflux proteins, suggesting that they are not relevant for metal homeostasis. In order to assess the contribution of this gene cluster to Cco activity, deletion mutants were made in each of the *Cj1161c–cj1166c* genes individually and initially assayed for copper sensitivity, intracellular Cu content and the effect of Cu on gene expression.

Supplementary Figure 2 shows copper sensitivity profiles for these mutants in minimal media (based on MEM-alpha where the

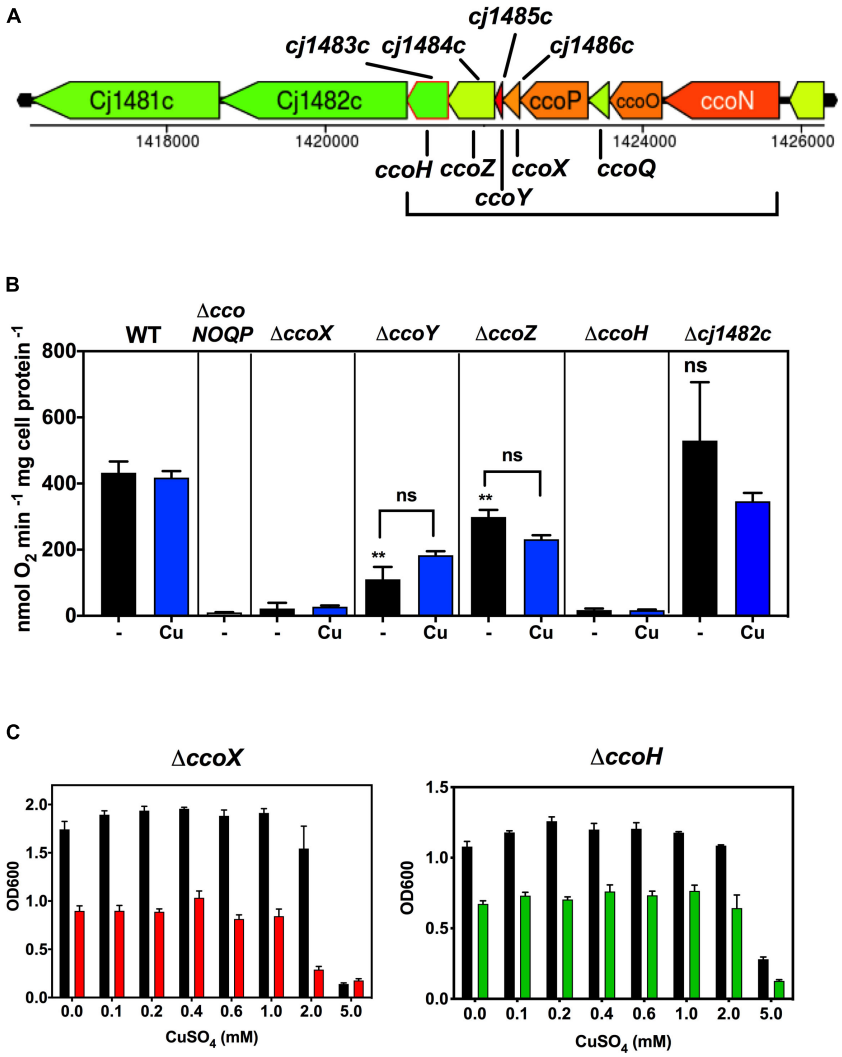

FIGURE 5 | Genes downstream of *ccoP* are required for Cco activity. **(A)** Gene organisation at the *ccoNOQP* locus. Image derived from campyDB (http://xbase.warwick.ac.uk/campydb/) and genes coloured by GC composition as in the legend to **Figure 2**. **(B)** Wildtype, Δ*ccoNOQP*, Δ*ccoX* (*cj1486c*), Δ*ccoY* (*cj1485c*), Δ*ccoZ* (*cj1484c*), Δ*ccoH* (*cj1483c*), and Δ*cj1482c* cells were grown in unsupplemented Mueller-Hinton medium or with copper sulphate added to 0.6 mM, as indicated. Cytochrome *c* oxidase activity was measured with ascorbate/TMPD as electron donor. Students *t*-tests were performed to check significance ($p > 0.05$, ns; $0.01 > **p > 0.001$). The stars above the black bars represent the statistical significance of comparisons between the unsupplemented mutant and wild-type rates. **(C)** Growth and copper sensitivity profiles of the Δ*ccoX* and Δ*ccoH* strains. In panels **(B,C)**, the data are the average of triplicate cultures with error bars showing SD.

unsupplemented copper concentration determined by ICP-MS was ∼0.02 μM). Exogenously added $CuSO_4$ stimulated growth up to a concentration of 0.1 mM in the wild type and all of the mutants, but Δ*copA*, Δ*copZ*, Δ*czcD*, and Δ*cj1164c* strains were significantly more sensitive to Cu than the wild type above this concentration. For each of these mutants, the profiles were broadly similar, with a concentration of ∼0.25 mM $CuSO_4$ resulting in a ∼50% reduction in final cell density compared to the wild type (**Supplementary Figure 2**). The results also showed that Δ*cj1165c* and Δ*cj1166c* were not differentially sensitive to Cu with respect to wild type (**Supplementary Figure 2**), consistent with these genes being uninvolved in copper homeostasis. Zinc sensitivity assays were performed on the *czcD* deletion strain (**Supplementary Figure 3**), which confirmed that it is indeed much more sensitive to Zn compared to the wild type or Δ*copA* strains (**Supplementary Figure 3A**). Comparison of the intracellular zinc levels in the wild-type and *czcD* mutant by ICP-MS revealed a significant accumulation of zinc in the mutant cells (**Supplementary Figure 3B**) supporting the results of Barnawi et al. (2020).

Inductively Coupled Plasma Mass Spectrometry was also used to measure total intracellular Cu in wild type and deletion mutant strains after growth in minimal media, with and without 0.25 mM excess $CuSO_4$. The results (**Figure 7B**) showed that when cells were grown in a Cu limiting environment, the intracellular Cu concentrations were very low and there was no significant

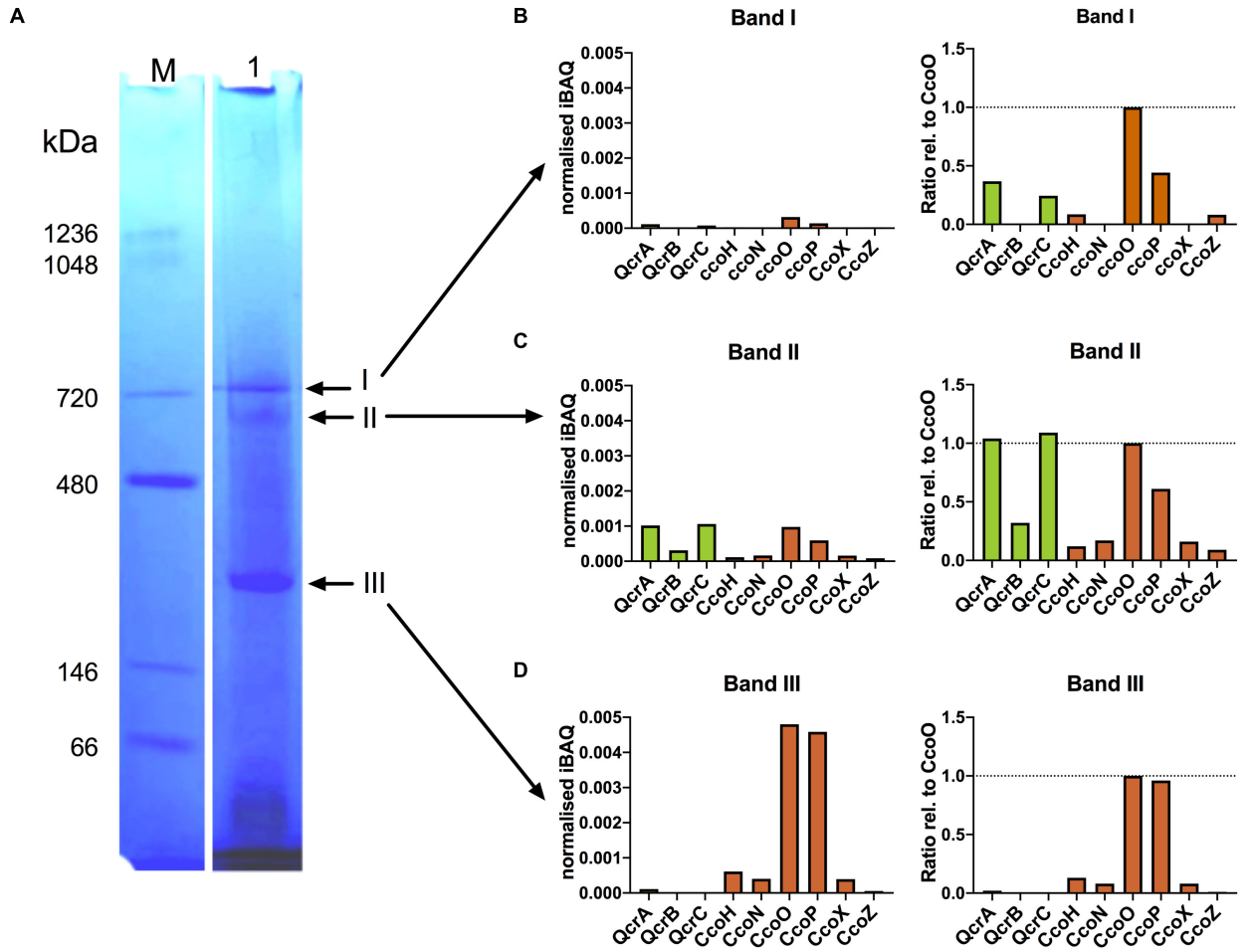

FIGURE 6 | Mass spectrometry reveals co-migration of putative Qcr-oxidase supercomplex components in blue-native PAGE. **(A)** BN-PAGE analysis of solubilised membrane fractions from *C. jejuni*. Membranes solubilised with 2% (w/v) αDDM were subjected to BN-PAGE separation as described in "Materials and Methods" (*Lane 1*). Arrows indicate bands (I–III) excised and subjected to in-gel tryptic digestion and analysed by mass spectrometry. *Lane M* contains molecular size markers. **(B–D)** Mass spectrometry-based quantification of Qcr (green) and Cco (brown) proteins by median iBAQ (*left panels*), and protein abundance ratios relative to CcoO (*right panels*), for excised gel bands I-III.

difference between wild type and any of the mutant strains. However, growth in the presence of 0.25 mM $CuSO_4$ resulted in higher intracellular Cu concentrations in Δ*copA* (∼7.5-fold), Δ*copZ* (∼2.4-fold), Δ*czcD* (∼2.8-fold), and Δ*cj1164c* (∼5.2-fold) knock out mutants compared to wild type cells grown with 0.25 mM $CuSO_4$. In contrast, Δ*cj1165c* showed only a ∼1.7-fold increase and Δ*cj1166c* showed no increase in intracellular copper compared to the wild-type. Overall, these results correlate well with the pattern of copper sensitivity shown by these mutants (**Supplementary Figure 2**). In order to examine patterns of copper dependent gene expression, qRT-PCR analysis was carried out on wild-type cells grown to mid-exponential phase in minimal media with or without 0.25 mM $CuSO_4$ (i.e., the same conditions used for the ICP-MS analysis above). **Figure 7C** shows that expression of *copA*, *copZ*, *and czcD* genes was increased ∼2–3 fold by exogenous Cu and *cj1164c* expression increased ∼1.5-fold. The expression of *cj1165c* and *cj1166c* was not increased by copper under these conditions.

From the above results and a consideration of the properties of the encoded proteins, only the *copA* and *copZ* genes are most clearly involved in Cu homeostasis in *C. jejuni*, while Cj1163 (and possibly Cj1164, though this was not further studied here) is involved in zinc homeostasis (Barnawi et al., 2020). Ascorbate/TMPD driven oxygen uptake assays for oxidase activity showed that the *copA* and *copZ* knock out mutants, but not the *czcD* mutant, have significantly lower Cco activity than wild type cells, when grown in the absence of any added copper (**Figure 7D**). Furthermore, addition of a concentration of $CuSO_4$ that is growth inhibitory in the minimal media used (0.25 mM) caused significant inhibition of Cco activity in the wild-type and this effect was exacerbated in both the *copA* and *copZ* mutants (**Figure 7D**). Overall, the data suggest that disruption in intracellular Cu homeostasis as well as the availability of Cu in the bacterial growth environment affects the activity of the cytochrome *c* oxidase.

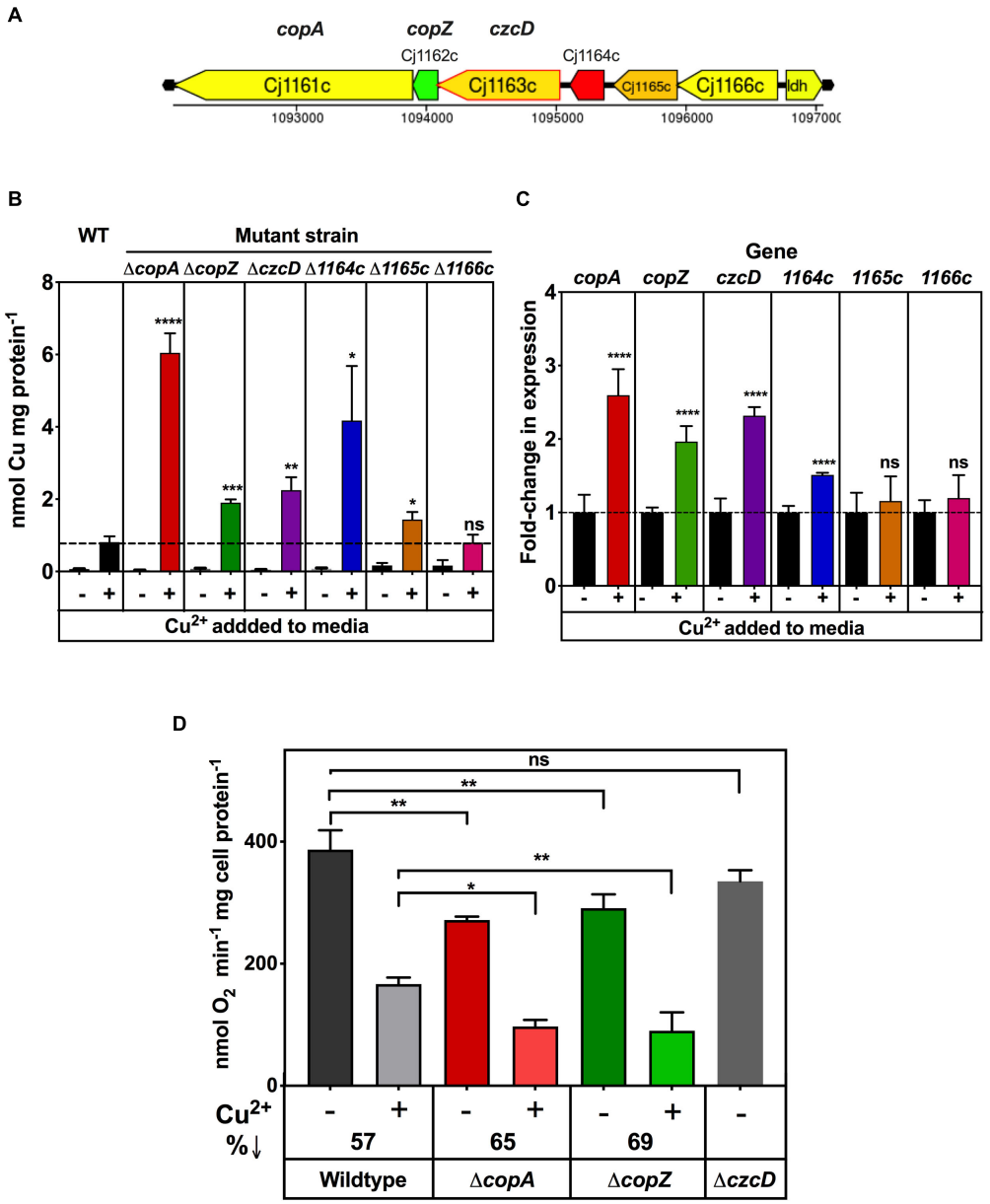

FIGURE 7 | Impairment of copper homeostasis negatively affects Cco activity. **(A)** Arrangement of genes encoding potential metal homeostasis proteins in *C. jejuni*. Genes are colour coded according GC content as in the legend to **Figure 2**. **(B)** Intracellular Cu accumulation in wild type, Δ*copA*, Δ*copZ*, Δ*czcD*, Δ*cj1164c*, Δ*cj1165c*, and Δ*cj1166c* cells grown either in unsupplemented MEMα minimal medium or with 0.25 mM copper sulphate added. Intracellular Cu content at stationary phase was measured by ICP-MS and normalised to total cell protein concentration as measured by Lowry assay. The data are the means of independent triplicate cultures with error bars showing SD. One-way ANOVA was performed to determine the significance of the difference between wild-type plus copper and the corresponding mutants plus copper ($p > 0.05$, ns; $0.05 > {}^{*}p > 0.01$; $0.01 > {}^{**}p > 0.001$; $0.001 > {}^{***}p > 0.0001$; $0.0001 > {}^{****}p$). **(C)** Effect of copper on gene expression, measured by qRT-PCR. *C. jejuni* wildtype cells were grown with or without 0.25 mM copper sulphate as in panel **(B)**. RNA was extracted (see "Materials and Methods") and qRT-PCR performed using primers shown in **Table 2** with the *gyrA* gene used as an internal control. The data are the means of independent triplicate cultures with error bars showing SD. For each gene, Students *t*-test was performed to determine the significance of the difference between expression measured without added copper (set to onefold in each case) and with added copper ($p > 0.05$, ns; $0.0001 > {}^{****}p$). **(D)** Cytochrome *c* oxidase activity in copper homeostasis mutants. *C. jejuni* wildtype, Δ*copA*, Δ*copZc*, and Δ*czcD* cells were grown in 5 ml MEMα minimal media in six-well plates, three wells with 0.25 mM copper sulphate and the other three wells without. Cytochrome *c* oxidase activity was measured by ascorbate/TMPD driven oxygen uptake normalised to total cell protein. The data are the average of independent triplicate cultures with error bars showing SD. One-way ANOVA was performed to determine the significance of the difference between wildtype and the mutants shown, either without or with added copper sulphate ($p > 0.05$, ns; $0.05 > {}^{*}p > 0.01$; $0.01 > {}^{**}p > 0.001$). The decrease in oxidase activity caused by growth with excess copper is indicated as%↓.

DISCUSSION

The Cco complex is a key proton-motive respiratory component in microaerobically grown *C. jejuni*. Its activity is high in actively growing cells, but declines during stationary phase. The intestine is a sulphide rich environment and we confirmed from the results of our mutant studies the sulphide sensitivity of the *C. jejuni* Cco complex and sulphide resistance of CioAB seen in other bacteria (Forte et al., 2016; Korshunov et al., 2016). However, it has been reported previously that a *ccoN* mutant is unable colonise the chicken host, while *cioAB* mutants were found to colonise normally (Weingarten et al., 2008) which is not consistent with this pattern of inhibition. Perhaps the niche occupied by *C. jejuni* is deep within the mucus layer overlying the intestinal epithelium where there is sufficient oxygen but low enough sulphide to enable continued Cco activity.

A continued supply of copper is clearly essential for Cco assembly and activity, but how copper is imported into *C. jejuni* is unknown. Unlike many bacteria, sequenced strains of *C. jejuni* do not seem to possess the CcoA transporter that has been shown to be important in uptake of copper for oxidase activity in *Rhodobacter* and many other genera (Ekici et al., 2014). In this work, we have therefore focused on identifying those genes that are involved in exporting copper from the cytoplasm to the periplasm for incorporation into the CcoN subunit via periplasmic chaperones.

Recent evidence suggests that the key transporter for copper export across the cytoplasmic membrane for oxidase assembly in Gram-negative bacteria is the P-type ATPase CcoI, assisted by CcoG, which is now known to act as a specific cupric reductase (Marckmann et al., 2019). Unlike some other cbb_3-type Cco containing bacteria, which have a *ccoGHIS* operon adjacent to *ccoNOQP*, we found that potential *ccoG*, *ccoI*, and *ccoS* genes are scattered throughout the genome in *C. jejuni* NCTC11168. Cj0369 is a membrane bound CcoG orthologue. The absence of Cj0369 reduced Cco activity substantially but this protein is clearly not essential for complex activity, suggesting other mechanisms of cupric reduction exist in the cytoplasm. In *R. capsulatus*, deletion of CcoG had more significant effects on the activity of the cbb_3-type Cco (Marckmann et al., 2019). The loss of activity was not rescued by growing cells with excess Cu in the medium suggesting Cj0369 is not involved directly in export, but does not rule out a redox role in copper handling.

Deletion of the *cj1155c* gene encoding a CcoI homologue completely abolished Cco activity but the activity was largely rescued on growing cells with excess copper. The mutant also showed a severe growth defect, which was completely rescued by $CuSO_4$ when added up to 0.6 mM, above which the Cu became inhibitory. Although this phenotype is consistent with the expected copper export role for CcoI, the ability of both the growth and oxidase phenotypes to be rescued by copper contrasts with the phenotype of a *ccoI* mutant in *R. capsulatus* (Koch et al., 2000) where exogenous copper does not rescue oxidase activity. The severity of the *ccoI* mutant growth defect in *C. jejuni* is also much greater than that of a *ccoNOQP* deletion mutant, suggesting an additional role. The phenotype is in fact more similar to that reported after deletion of a *ccoI* homologue called *ctpA* in *Rubrivivax gelatinosus* (Hassani et al., 2010). CtpA was shown to have a pleiotropic role in supplying copper not only for the cbb_3-type oxidase in *R. gelatinosus*, but also for the alternative aa_3-oxidase and the periplasmic nitrous oxide reductase, NosZ and the oxidase activity defect of a *ctpA* deletion mutant could be largely rescued by copper (Hassani et al., 2010). However, *C. jejuni* NCTC11168 does not possess these other copper containing respiratory complexes. The only other known periplasmic copper containing proteins in strain NCTC 11168 are the multi-copper oxidase CueO (Cj1516) involved in copper homeostasis (Hall et al., 2008) and the p19 protein, which is part of an iron uptake system (Chan et al., 2010; Liu et al., 2018). We found that CueO dependent phenoloxidase activity was unchanged in the *ccoI* mutant (unpublished observations) but further work will be required to investigate any connection with p19 or to identify other systems which may be dependent on CcoI. In *R. capsulatus*, the CcoNOQP complex was absent in a strain lacking *ccoI*, but CcoP itself was still detectable (Kulajta et al., 2006). However, a more recent study has shown that CcoN can be membrane inserted in the absence of CcoO or CcoP (Ekici et al., 2013), but the absence of CcoN (as would be expected in biogenesis mutants) usually results in loss of both of the c-type cytochromes in the complex. Although we could not visualise CcoP, haem blots did suggest the presence of CcoO in membranes of the *C. jejuni ccoI* mutant, possibly indicating independent assembly of the dihaem cytochrome c from the rest of the complex. This is also different to the situation in the absence of the CcoI homologue CtpA in *R. gelatinosus*, where both CcoO and CcoP were significantly reduced (Hassani et al., 2010). It would clearly be informative to know what the status of CcoN is in our biogenesis mutants but unfortunately we could not detect CcoN on immunoblots using *R. capsulatus* CcoN antibodies.

The Δ*cj1154c* strain lacking the CcoS homologue also completely lacked Cco activity. Koch et al. (2000) reported the necessity of CcoS in *R. capsulatus* for the presence of haem *b*, haem b_3, and Cu_B cofactors in the CcoN subunit. In *R. capsulatus* cells lacking CcoS, a CcoNOQP complex was detected but inactive (Kulajta et al., 2006). We found a copper sensitive phenotype for the Δ*cj1154c* strain and the addition of excess Cu to the growth medium partly rescued the Cco activity, but in contrast to the *ccoI* mutant, to only ∼20% of that in *C. jejuni* wild-type cells. This nevertheless suggests that Cj1154 might be required for copper handling for oxidase activity.

The periplasmic copper chaperones PCuC and Sco1 act as a relay system for insertion of Cu into CcoN (Trasnea et al., 2018). In *C. jejuni*, we identified Cj0909 as a PCuC homologue and Cj0911 as a Sco1 homologue. *cj0909* and *cj0911* form an operon with *cj0908* and *cj0910*, genes of unknown function. Both Δ*cj0908–cj0911* and Δ*cj0911* mutants showed significantly reduced Cco activity consistent with these gene products being involved in assembly of the oxidase. There was a greater reduction of Cco activity in Δ*cj0908–cj0911* (∼40% activity of WT) than in Δ*cj0911* (∼60% activity of WT), suggesting the additional importance of *cj0908*, *cj0909*, and *cj0910* gene products but single deletions in each of these genes will be required to dissect their individual contributions. Work in other bacteria has shown that the periplasmic copper chaperones are required under conditions

of low copper availability only and excess Cu in the medium often rescues the absence of either PCuC or Sco1 or both (Trasnea et al., 2016). When grown with excess Cu in the medium, Δ*cj0911* did show higher Cco activity but there was no difference in the Δ*cj0908–cj0911* strain. This suggests that it is not just the absence of both PCuC and Sco1 homologues in Δ*cj0908–cj0911* but also the absence of *cj0908* and/or *cj0910*, which is affecting the Cco activity. The paralogous Cj0908 and Cj910 proteins are predicted to be membrane anchored with a periplasmic domain containing Trx/Fd-like Cys motifs suggestive of a redox function. A possible role for these proteins could be to reduce Cu(II) to Cu(I), which is the form required for insertion into CcoN, prior to handling by the chaperones.

Cj1483 is a CcoH homologue based on BLAST searches. Δ*ccoH* has a growth defect and no Cco activity at all, irrespective of the amount of Cu in the medium. This observation is in accordance with the model suggested by Pawlik et al. (2010) in which biogenesis of cbb_3-type Cco proceeds via CcoQP and CcoNO subcomplexes in *R. capsulatus*, but neither the fully assembled cbb_3-type Cco nor the CcoQP or CcoNO subcomplex was detectable in cells lacking CcoH. They also showed that CcoH remains tightly associated with the active, fully assembled CcoNOQP complex.

We identified three novel genes located between *ccoH* (*cj1483c*) and *ccoP* (*cj1487c*), each of which was required for maximum oxidase activity. Mutant studies showed that CcoX (Cj1486) was essential for oxidase activity and maximum growth yield, while CcoY (Cj1485) and CcoZ (Cj1484) were important although not essential for oxidase activity. Fascinatingly, CcoZ has structural similarity (**Supplementary Figure 1**) to proteins that have been found to be associated with the cytochrome *bcc*-oxidase supercomplex in actinobacteria, e.g., *M. smegmatis* (Gong et al., 2018; Wiseman et al., 2018). Msmeg_4692 appears to mediate interactions of the oxidase with an extended C-terminal loop of the cytochrome *bcc* QcrB subunit (Wiseman et al., 2018). Examination of the QcrB sequence in *C. jejuni* does not show evidence of an unusually long C-terminal extension. However, one other unique aspect of the Qcr complex in the Campylobacterota in general and *C. jejuni* in particular, is that it contains a dihaem cytochrome *c* analogous to the situation in actinobacteria (Garg et al., 2018). Taken together, these observations raised the possibility that a Qcr-oxidase supercomplex might be present in *C. jejuni*, even though this bacterium contains multiple soluble periplasmic *c*-type cytochromes, two of which have been previously shown to be electron donors to the cbb_3-oxidase (Liu and Kelly, 2015). However, there is now evidence from *Rhodobacter* that Gram-negative cbb_3-type oxidases can form supercomplexes

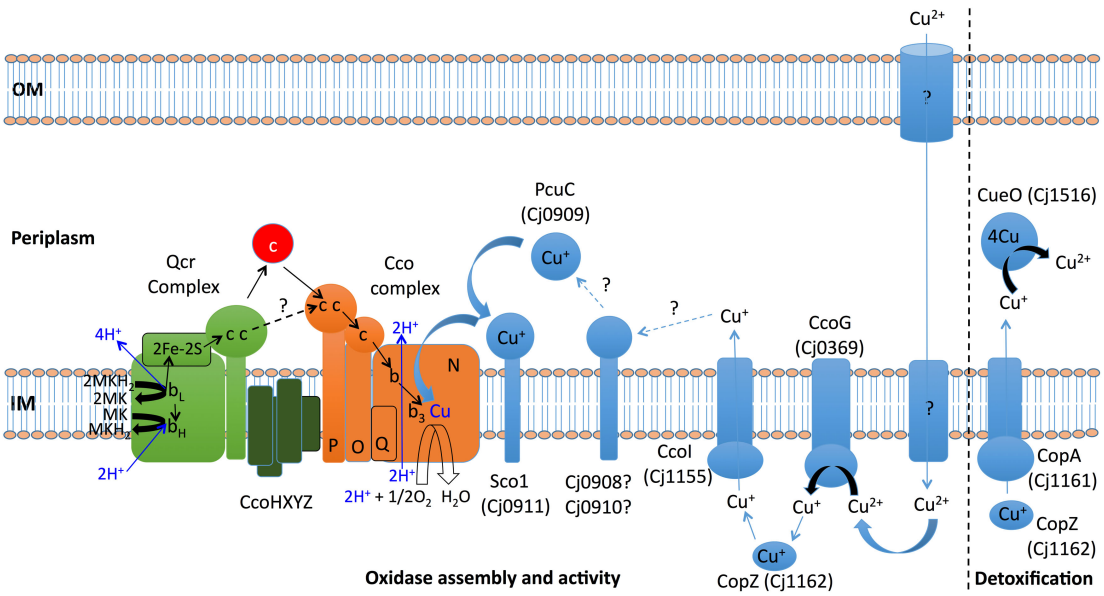

FIGURE 8 | Model for copper handling and homeostasis in *C. jejuni* NCTC 11168. Copper must be transported from the environment into the cell, but the mechanism is currently unknown as there is no CcoA importer in *C. jejuni*. Copper homeostasis/detoxification is achieved by the combined action of the CopA ATP-driven efflux pump, receiving copper from the cytoplasmic chaperone CopZ and the periplasmic multi-copper oxidase CueO (Cj1516) which oxidises toxic cupric ions to less toxic cuprous ions. CcoG (Cj0369) acts as a reductase that probably passes cuprous ions to CopZ. CpoZ is also thought to interact with CcoI, a specific efflux pump that is essential for copper delivery to the periplasm for transfer to the Cco enzyme complex, possibly via potential reductases Cj0908 and Cj0910 and copper chaperones PcuC (Cj0909) and Sco1 (Cj0911). Sco1 delivers cuprous copper to the CcoN subunit of the oxidase complex to form the bi-nuclear catalytic centre of the enzyme. Newly identified genes in this study encode three proteins (CcoXYZ) that might interact with both the Qcr and oxidase, perhaps forming a supercomplex. Direct copper handling proteins are shown in light blue, with light blue arrows depicting the transfer of copper ions. Electron transfers are shown as black arrows. Dark blue arrows show proton binding and release or direct proton translocation associated with electron transfer from Qcr to the oxidase complex. Soluble cytochromes *c* in the periplasm are shown as a red circle. The possibility of direct electron transfer between Qcr and oxidase is indicated by a dashed black line. OM, outer membrane; IM, inner (cytoplasmic) membrane.

(Steimle et al., 2021). The presence of CcoZ in the same high molecular weight band resolved by BN-PAGE as the subunits of both the CcoNOP and QcrABC proteins is consistent with such an association in *C. jejuni*, but clearly further work will be needed to confirm this. Such a complex may be unstable and difficult to isolate, as obtaining the cryo-EM structure of the *Rhodobacter* supercomplex required artificial linking of the constituent Qcr and oxidase complexes (Steimle et al., 2021). Unlike the obligate Qcr-Cco interaction in actinobacteria (where soluble c-type cytochromes are absent), in Gram-negative bacteria there may be regulation of the association of these complexes (e.g., under different growth conditions or oxygen supply) and it would be informative to examine how electron transfer from Qcr to the Cco complex in *C. jejuni* is altered in the absence of CcoXYZ as well as how Qcr-oxidase interactions are changed.

Finally, a link between oxidase activity and copper homeostasis in *C. jejuni* was suggested by the reduced oxidase activity in mutants in the *copA* (*cj1161c*) and *copZ* (*cj1162c*) genes. Metal homeostasis in the Campylobacterota has recently been reviewed (Kelley et al., 2021) but copper homeostasis is still incompletely understood. The copper sensitive phenotype of a *copA* mutant has been established previously (Hall et al., 2008) and such a mutant is also oxidative stress sensitive (Gardner and Olson, 2018). The function of the *cj1162c* gene has not been previously characterized but our results show that this *copZ* homologue also protects against copper toxicity; its expression is increased by exogenous copper and its deletion phenocopies that of a *copA* mutant; increased intracellular copper and copper sensitive growth. One explanation for the reduced oxidase activity in these mutants is that an inability to regulate intracellular Cu disturbs the correct copper trafficking though CcoI, necessary for oxidase assembly. Interestingly, in *R. capsulatus*, where deletion of *copZ* also results in lower cbb_3-oxidase activity, a membrane bound complex between CopZ and CcoI was detected, suggesting that the CopZ chaperone can supply CcoI with copper, as well as interacting with CopA for copper detoxification (Utz et al., 2019). However, in *C. jejuni*, the deletion of *ccoI* led to abolition of oxidase activity whereas deletion of *copZ* resulted in only a ∼30% reduction compared to wild-type in the absence of excess copper and ∼50% reduction in the presence of copper, so the phenotypes are not identical, as might be expected for an obligate CcoI-CopZ complex.

Based on the results obtained in this study, **Figure 8** shows a working model for the handling of copper in *C. jejuni* NCTC 11168, particularly in relation to the assembly and function of the Cco enzyme. The major unanswered questions concern the nature of the pathway for import of copper, the role of the Cj0908/Cj0910 and CcoXYZ proteins, and the possibility of Qcr-oxidase supercomplex formation.

DATA AVAILABILITY STATEMENT

The original contributions presented in the study are included in the article/**Supplementary Material**, further inquiries can be directed to the corresponding author.

AUTHOR CONTRIBUTIONS

DK designed the study and wrote the manuscript. NG, AT, FP, SF, and PJ performed the experiments and analysed the data. DK, PJ, and MJ supervised the work and edited the manuscript. All authors contributed to the article and approved the manuscript.

FUNDING

This work was supported a University of Sheffield Vice-Chancellors Ph.D. scholarship to NG and Biotechnology and Biological Research Council (BBSRC) Grant BB/S014497/1 to DK for AT. FP (BB/T007222/1) and SF (BB/M011151/1) were supported by BBSRC studentships via the White Rose DTP in Mechanistic Biology.

ACKNOWLEDGMENTS

We thank C.S. Raman (University of Maryland, United States) for discussions about possible additional oxidase subunits in *Campylobacter* and Mr. Callum Miller for help with the sulphide sensitivity assays shown in **Figure 1**.

SUPPLEMENTARY MATERIAL

The Supplementary Material for this article can be found online at: https://www.frontiersin.org/articles/10.3389/fmicb.2021.683260/full#supplementary-material

REFERENCES

Abriata, L. A., Banci, L., Bertini, I., Ciofi-Baffoni, S., Gkazonis, P., Spyroulias, G. A., et al. (2008). Mechanism of Cu(A) assembly. *Nat. Chem. Biol.* 4, 599–601.

Banci, L., Bertini, I., Cioffi-Baffoni, S., Katsari, E., Katsaros, N., Kubicek, K., et al. (2005). A copper(I) protein possibly involved in the assembly of CuA center of bacterial cytochrome c oxidase. *Proc. Natl. Acad. Sci. U. S. A.* 102, 3994–3999.

Barnawi, H., Masri, N., Hussain, N., Al-Lawati, B., Mayasari, E., Gulbicka, A., et al. (2020). RNA-based thermoregulation of a *Campylobacter jejuni* zinc resistance determinant. *PLoS Pathog.* 16:e1009008. doi: 10.1371/journal.ppat.1009008

Buschmann, S., Warkentin, E., Xie, H., Langer, J. D., Ermler, U., and Michel, H. (2010). The structure of cbb3 cytochrome oxidase provides insights into proton pumping. *Science* 329, 327–330. doi: 10.1126/science.1187303

Carvalheda, C. A., and Pisliakov, A. V. (2017). On the role of subunit M in cytochrome cbb_3 oxidase. *Biochem. Biophys. Res. Commun.* 491, 47–52. doi: 10.1016/j.bbrc.2017.07.031

Chan, A. C., Doukov, T. I., Scofield, M., Tom-Yew, S. A., Ramin, A. B., Mackichan, J. K., et al. (2010). Structure and function of P19, a high-affinity iron transporter of the human pathogen *Campylobacter jejuni*. *J. Mol. Biol.* 401, 590–604. doi: 10.1016/j.jmb.2010.06.038

Cox, J., and Mann, M. (2008). MaxQuant enables high peptide identification rates, individualized p.p.b.-range mass accuracies and proteome-wide protein quantification. *Nat. Biotechnol.* 26, 1367–1372. doi: 10.1038/nbt.1511

Dickinson, E. K., Adams, D. L., Schon, E. A., and Glerum, D. M. (2000). A human SCO2 mutation helps define the role of Sco1p in the cytochrome

oxidase assembly pathway. *J. Biol. Chem.* 275, 26780–26785. doi: 10.1016/s0021-9258(19)61443-2

Ekici, S., Jiang, X., Koch, H. G., and Daldal, F. (2013). Missense mutations in Cytochrome *c* maturation genes provide new insights into *Rhodobacter capsulatus* cbb_3-type cytochrome *c* oxidase biogenesis. *J. Bacteriol.* 195, 261–269. doi: 10.1128/jb.01415-12

Ekici, S., Turkarslan, S., Pawlik, G., Dancis, A., Baliga, N. S., Koch, H. G., et al. (2014). Intracytoplasmic copper homeostasis controls cytochrome *c* oxidase production. *mBio* 5:e01055-13.

Feissner, R., Xiang, Y., and Kranz, R. G. (2003). Chemiluminescent-based methods to detect subpicomole levels of c-type cytochromes. *Anal. Biochem.* 315, 90–94. doi: 10.1016/s0003-2697(02)00658-9

Forte, E., Borisov, V. B., Falabella, M., Colaço, H. G., Tinajero-Trejo, M., Poole, R. K., et al. (2016). The Terminal Oxidase Cytochrome *bd* Promotes Sulphide-resistant Bacterial Respiration and Growth. *Sci. Rep.* 6:23788.

Gardner, S. P., and Olson, J. W. (2018). Interaction of copper toxicity and oxidative stress in *Campylobacter jejuni*. *J. Bacteriol.* 200, e208–e218.

Garg, N., Taylor, A. J., and Kelly, D. J. (2018). Bacterial periplasmic nitrate and trimethylamine-N-oxide respiration coupled to menaquinol-cytochrome *c* reductase (Qcr): implications for electrogenic reduction of alternative electron acceptors. *Sci. Rep.* 8:15478.

Gong, H., Li, J., Xu, A., Tang, Y., Ji, W., Gao, R., et al. (2018). An electron transfer path connects subunits of a mycobacterial respiratory supercomplex. *Science* 362:eaat8923. doi: 10.1126/science.aat8923

Guccione, E., Hitchcock, A., Hall, S. J., Mulholland, F., Shearer, N., van Vliet, A. H., et al. (2010). Reduction of fumarate, mesaconate and crotonate by Mfr, a novel oxygen-regulated periplasmic reductase in *Campylobacter jejuni*. *Environ. Microbiol.* 12, 576–591. doi: 10.1111/j.1462-2920.2009.02096.x

Guccione, E., Leon-Kempis Mdel, R., Pearson, B. M., Hitchin, E., Mulholland, F., van Diemen, P. M., et al. (2008). Amino acid-dependent growth of *Campylobacter jejuni*: key roles for aspartase (AspA) under microaerobic and oxygen-limited conditions and identification of AspB (Cj0762), essential for growth on glutamate. *Mol. Microbiol.* 69, 77–93. doi: 10.1111/j.1365-2958.2008.06263.x

Hall, S. J., Hitchcock, A., Butler, C. S., and Kelly, D. J. (2008). A multicopper oxidase (Cj1516) and a CopA homologue (Cj1161) are major components of the copper homeostasis system of *Campylobacter jejuni*. *J. Bacteriol.* 190, 8075–8085. doi: 10.1128/jb.00821-08

Hassani, B. K., Astier, C., Nitschke, W., and Ouchane, S. (2010). CtpA, a copper-translocating P-type ATPase involved in the biogenesis of multiple copper-requiring enzymes. *J. Biol. Chem.* 285, 19330–19337. doi: 10.1074/jbc.m110.116020

Horng, Y. C., Cobine, P. A., Maxfield, A. B., Carr, H. S., and Winge, D. R. (2004). Specific copper transfer from the Cox17 metallochaperone to both Sco1 and Cox11 in the assembly of yeast cytochrome C oxidase. *J. Biol. Chem.* 279, 35334–35340.

Jackson, R. J., Elvers, K. T., Lee, L. J., Gidley, M. D., Wainwright, L. M., Lightfoot, J., et al. (2007). Oxygen reactivity of both respiratory oxidases in *Campylobacter jejuni*: the CydAB genes encode a cyanide-resistant, low-affinity oxidase that is not of the cytochrome *bd* type. *J. Bacteriol.* 18, 1604–1615. doi: 10.1128/jb.00897-06

Kassem, I. I., Candelero-Rueda, R. A., Esseili, K. A., and Rajashekara, G. (2017). Formate simultaneously reduces oxidase activity and enhances respiration in *Campylobacter jejuni*. *Sci. Rep.* 7:40117.

Kelley, B. R., Lu, J., Haley, K. P., Gaddy, J. A., and Johnson, J. G. (2021). Metal homeostasis in pathogenic Epsilonproteobacteria: mechanisms of acqusisition, efflux and regulation. *Metallomics* 13:mfaa0002.

Kelley, L. A., Mezulis, S., Yates, C. M., Wass, M. N., and Sternberg, M. J. E. (2015). The Phyre2 web portal for protein modeling, prediction and analysis. *Nat. Protoc.* 10, 845–858.

Koch, H. G., Winterstein, C., Saribas, A. S., Alben, J. O., and Daldal, F. (2000). Roles of the ccoGHIS gene products in the biogenesis of the cbb3-type cytochrome *c* oxidase. *J. Mol. Biol.* 297, 49–65. doi: 10.1006/jmbi.2000.3555

Kohlstaedt, M., Buschmann, S., Xie, H., Resemann, A., Warkentin, E., Langer, J. D., et al. (2016). Identification and Characterisation of the Novel Subunit CcoM in the cbb_3 Cytochrome *c* Oxidase from *Pseudomonas stutzeri* ZoBell. *mBio* 7:e01921-15.

Korshunov, S., Imlay, K. R., and Imlay, J. A. (2016). The cytochrome *bd* oxidase of *Escherichia coli* prevents respiratory inhibition by endogenous and exogenous hydrogen sulfide. *Mol. Microbiol.* 101, 62–77. doi: 10.1111/mmi.13372

Kulajta, C., Thumfart, J. O., Haid, S., Daldal, F., and Koch, H. G. (2006). Multi-step assembly pathway of the cbb_3-type cytochrome *c* oxidase complex. *J. Mol. Biol.* 355, 989–1004. doi: 10.1016/j.jmb.2005.11.039

Liu, M. M., Boinett, C. J., Chan, A. C. K., Parkhill, J., Murphy, M. E. P., and Gaynor, E. C. (2018). Investigating the *Campylobacter jejuni* transcriptional response to host intestinal extracts reveals the involvement of a widely conserved iron uptake system. *mBio* 9:e01347-18.

Liu, Y. W., and Kelly, D. J. (2015). Cytochrome *c* biogenesis in *Campylobacter jejuni* requires cytochrome c_6 (CccA; Cj1153) to maintain apocytochrome cysteine thiols in a reduced state for haem attachment. *Mol. Microbiol.* 96, 1298–1317.

Marckmann, D., Trasnea, P. I., Schimpf, J., Winterstein, C., Andrei, A., Schmollinger, S., et al. (2019). The cbb3-type cytochrome oxidase assembly factor CcoG is a widely distributed cupric reductase. *Proc. Natl. Acad. Sci. U.S.A.* 116, 21166–21175. doi: 10.1073/pnas.1913803116

Mattatall, N. R., Jazairi, J., and Hill, B. C. (2000). Characterisation of YpmQ, an accessory protein required for the expression of cytochrome *c* oxidase in *Bacillus subtilis*. *J. Biol. Chem.* 275, 28802–28809. doi: 10.1074/jbc.m002741200

O'Brien, S. J. (2017). The consequences of Campylobacter infection. *Curr. Opin. Gastroenterol.* 33, 14–20. doi: 10.1097/mog.0000000000000329

Pandey, A., Anderson, J. S., and Mann, M. (2000). Use of mass spectrometry to study signaling pathways. *Sci. STKE* 2000:pl1. doi: 10.1126/stke.2000.37.pl1

Parkhill, J., Wren, B. W., Mungall, K., Ketley, J. M., Churcher, C., Basham, D., et al. (2000). The genome sequence of the food-borne pathogen *Campylobacter jejuni* reveals hypervariable sequences. *Nature* 403, 665–668. doi: 10.1038/35001088

Pawlik, G., Kulajta, C., Sachelaru, I., Schröder, S., Waidner, B., Hellwig, P., et al. (2010). The putative assembly factor CcoH is stably associated with the cbb3-type cytochrome oxidase. *J. Bacteriol.* 192, 6378–6389. doi: 10.1128/jb.00988-10

Pereira, M. M., Santana, M., and Teixeira, M. (2001). A novel scenario for the evolution of haem-copper oxygen reductases. *Biochim. Biophys. Acta* 1505, 185–208. doi: 10.1016/s0005-2728(01)00169-4

Peters, A., Kulajta, C., Pawlik, G., Daldal, F., and Koch, H. G. (2008). Stability of the cbb_3-type cytochrome oxidase requires specific CcoQ-CcoP interactions. *J. Bacteriol.* 190, 5576–5586. doi: 10.1128/jb.00534-08

Pitcher, R. S., and Watmough, N. J. (2004). The bacterial cytochrome cbb_3 oxidases. *Biochim. Biophys. Acta.* 1655, 388–399.

Preisig, O., Zufferey, R., and Hennecke, H. (1996). The *Bradyrhizobium japonicum* fixGHIS genes are required for the formation of the high-affinity cbb3-type cytochrome oxidase. *Arch. Microbiol.* 165, 297–305. doi: 10.1007/s002030050330

Rauhamäki, V., Bloch, D. A., and Wikström, M. (2012). Mechanistic stoichiometry of proton translocation by cytochrome cbb_3. *Proc. Natl. Acad. Sci. U.S.A.* 109, 7286–7291. doi: 10.1073/pnas.1202151109

Rensing, C., Fan, B., Sharma, R., Mitra, B., and Rosen, B. P. (2000). CopA: an *Escherichia coli* Cu(I)-translocating P-type ATPase. *Proc. Natl. Acad. Sci. U.S.A.* 97, 652–656. doi: 10.1073/pnas.97.2.652

Schwanhäusser, B., Busse, D., Li, N., Dittmar, G., Schuchhardt, J., Wolf, J., et al. (2011). Global quantification of mammalian gene expression control. *Nature* 473, 337–342. doi: 10.1038/nature10098

Singleton, C., and Le Brun, N. E. (2007). Atx1-like chaperones and their cognate P-type ATPases: copper-binding and transfer. *Biometals* 20, 275–289. doi: 10.1007/s10534-006-9068-1

Steimle, S., van Eeuwen, T., Ozturk, Y., Kim, H. J., Braitbard, M., Selamoglu, N., et al. (2021). Cryo-EM structures of engineered active bc1-cbb3 type CIII2CIV super-complexes and electronic communication between the complexes. *Nat. Commun.* 12:929.

Taylor, A. J., and Kelly, D. J. (2019). The function, biogenesis and regulation of the electron transport chains in *Campylobacter jejuni*: new insights into the bioenergetics of a major food-borne pathogen. *Adv. Microb. Physiol.* 74, 239–329. doi: 10.1016/bs.ampbs.2019.02.003

Trasnea, P. I., Andrei, A., Marckmann, D., Utz, M., Khalfaoui-Hassani, B., Selamoglu, N., et al. (2018). A copper relay system involving two periplasmic

chaperones drives cbb_3-Type Cytochrome *c* oxidase biogenesis in *Rhodobacter capsulatus*. *ACS Chem. Biol.* 13, 1388–1397. doi: 10.1021/acschembio.8b00293

Trasnea, P. I., Utz, M., Khalfaoui-Hassani, B., Lagies, S., Daldal, F., and Koch, H. G. (2016). Cooperation between two periplasmic copper chaperones is required for full activity of the cbb_3 -type cytochrome *c* oxidase and copper homeostasis in *Rhodobacter capsulatus*. *Mol. Microbiol.* 100, 345–361. doi: 10.1111/mmi.13321

Untergasser, A., Nijveen, H., Rao, X., Bisseling, T., Geurts, R., and Leunissen, J. A. (2007). Primer3Plus, an enhanced web interface to Primer3. *Nucleic Acids Res.* 35, W71–W74.

Utz, M., Andrei, A., Milanov, M., Trasnea, P. I., Marckmann, D., Daldal, F., et al. (2019). The Cu chaperone CopZ is required for Cu homeostasis in *Rhodobacter capsulatus* and influences cytochrome cbb_3 oxidase assembly. *Mol. Microbiol.* 111, 764–783. doi: 10.1111/mmi.14190

van Vliet, A. H., Wooldridge, K. G., and Ketley, J. M. (1998). Iron-responsive gene regulation in a *Campylobacter jejuni* fur mutant. *J. Bacteriol.* 180, 5291–5298. doi: 10.1128/jb.180.20.5291-5298.1998

Vargas, C., McEwan, A. G., and Downie, J. A. (1993). Detection of c-type cytochromes using enhanced chemiluminescence. *Anal. Biochem.* 209, 323–326. doi: 10.1006/abio.1993.1127

Weingarten, R. A., Grimes, J. L., and Olson, J. W. (2008). Role of *Campylobacter jejuni* respiratory oxidases and reductases in host colonization. *Appl. Environ. Microbiol.* 74, 1367–1375. doi: 10.1128/aem.02261-07

Wiseman, B., Nitharwal, R. G., Fedotovskaya, O., Schäfer, J., Guo, H., Kuang, Q., et al. (2018). Structure of a functional obligate complex III2IV2 respiratory supercomplex from *Mycobacterium smegmatis*. *Nat. Struct. Mol. Biol.* 25, 1128–1136. doi: 10.1038/s41594-018-0160-3

Woodall, C. A., Jones, M. A., Barrow, P. A., Hinds, J., Marsden, G. L., Kelly, D. J., et al. (2005). *Campylobacter jejuni* gene expression in the chick cecum: evidence for adaptation to a low-oxygen environment. *Infect. Immun.* 73, 5278–5285. doi: 10.1128/iai.73.8.5278-5285.2005

Conflict of Interest: The authors declare that the research was conducted in the absence of any commercial or financial relationships that could be construed as a potential conflict of interest.

frontiers in Microbiology

ORIGINAL RESEARCH
published: 16 August 2021
doi: 10.3389/fmicb.2021.714508

Bespoke Biomolecular Wires for Transmembrane Electron Transfer: Spontaneous Assembly of a Functionalized Multiheme Electron Conduit

Samuel E. H. Piper[1], Marcus J. Edwards[1†], Jessica H. van Wonderen[1], Carla Casadevall[2], Anne Martel[3], Lars J. C. Jeuken[4], Erwin Reisner[2], Thomas A. Clarke[1] and Julea N. Butt[1]**

[1] School of Chemistry and School of Biological Sciences, University of East Anglia, Norwich, United Kingdom, [2] Yusuf Hamied Department of Chemistry, University of Cambridge, Cambridge, United Kingdom, [3] Institut Laue-Langevin, Grenoble, France, [4] School of Biomedical Sciences, University of Leeds, Leeds, United Kingdom

OPEN ACCESS

Edited by:
Davide Zannoni,
University of Bologna, Italy

Reviewed by:
Benjamin K. Keitz,
University of Texas at Austin,
United States
Okamoto Akihiro,
International Center for Materials Nanoarchitectonics (WPI-MANA),
Japan

***Correspondence:**
Thomas A. Clarke
tom.clarke@uea.ac.uk
Julea N. Butt
j.butt@uea.ac.uk

†Present address:
Marcus J. Edwards,
School of Life Sciences, University of Essex, Colchester, United Kingdom

Specialty section:
This article was submitted to Microbial Physiology and Metabolism, a section of the journal Frontiers in Microbiology

Received: 25 May 2021
Accepted: 12 July 2021
Published: 16 August 2021

Citation:
Piper SEH, Edwards MJ, van Wonderen JH, Casadevall C, Martel A, Jeuken LJC, Reisner E, Clarke TA and Butt JN (2021) Bespoke Biomolecular Wires for Transmembrane Electron Transfer: Spontaneous Assembly of a Functionalized Multiheme Electron Conduit. Front. Microbiol. 12:714508. doi: 10.3389/fmicb.2021.714508

Shewanella oneidensis exchanges electrons between cellular metabolism and external redox partners in a process that attracts much attention for production of green electricity (microbial fuel cells) and chemicals (microbial electrosynthesis). A critical component of this pathway is the outer membrane spanning MTR complex, a biomolecular wire formed of the MtrA, MtrB, and MtrC proteins. MtrA and MtrC are decaheme cytochromes that form a chain of close-packed hemes to define an electron transfer pathway of 185 Å. MtrA is wrapped inside MtrB for solubility across the outer membrane lipid bilayer; MtrC sits outside the cell for electron exchange with external redox partners. Here, we demonstrate tight and spontaneous *in vitro* association of MtrAB with separately purified MtrC. The resulting complex is comparable with the MTR complex naturally assembled by *Shewanella* in terms of both its structure and rates of electron transfer across a lipid bilayer. Our findings reveal the potential for building bespoke electron conduits where MtrAB combines with chemically modified MtrC, in this case, labeled with a Ru-dye that enables light-triggered electron injection into the MtrC heme chain.

Keywords: cytochrome, electron transfer, microbial fuel cell, microbial electrosynthesis, photosensitizer, biomolecular wire, SANS, *Shewanella*

INTRODUCTION

Dissimilatory metal-reducing bacteria (DMRB) are able to gain energy for growth by coupling the oxidation of organic compounds to the reduction of iron- and manganese-containing minerals. These terminal respiratory electron acceptors are insoluble. They cannot enter the bacterial cell and DMRB have evolved mechanisms to transport electrons out of the cell across otherwise electrically insulating lipid membranes (White et al., 2016; Santoro et al., 2017). The same mechanisms allow respiration on numerous extracellular electron acceptors including suitably poised electrodes. Thus, DMRB attract much attention for their abilities to deliver clean energy and chemicals

(Kato, 2015; Schroder et al., 2015; Nealson, 2017; Santoro et al., 2017) in addition to their fascinating microbiology.

Shewanella oneidensis MR-1 is a model organism for fundamental and applied studies of DMRB (Fredrickson et al., 2008; Shi et al., 2012; Breuer et al., 2015; Bursac et al., 2017). The primary mechanism of electron release from *S. oneidensis* MR-1 is relatively simple (**Figure 1A**) and at the molecular level is arguably the best understood of the DMRB. Electrons from the oxidation of organic compounds are transferred *via* menaquinol to the inner membrane quinol dehydrogenase CymA (McMillan et al., 2012). Periplasmic cytochromes STC and FccA then transfer electrons from CymA to the outer membrane-associated MTR complex (Sturm et al., 2015). At the cell surface, electrons are transferred from the MTR complex to terminal respiratory acceptors either directly or *via* flavin mediators (von Canstein et al., 2008; Marsili et al., 2008). Alongside transmembrane electron transfer, the MTR complex is proposed to transport protons across outer membranes as the rate-limiting event (Okamoto et al., 2017) during electron transfer from biofilms of *S. oneidensis* to electrodes.

The MTR complex (Edwards et al., 2020) is composed of three proteins (**Figure 1B**). Two of these proteins form an outer membrane spanning complex, MtrAB, which assembles as a naturally insulated biomolecular wire with both a structure and function that are analogous to those of an electrical cable. MtrA binds an approximately linear chain of 10 *c*-type hemes which spans the lipid bilayer. Those hemes are insulated from the membrane by embedding within a 26 strand beta-barrel formed by MtrB. Electrons enter MtrAB at Heme A1 in the periplasm. At the external face of MtrAB, Heme A10 is positioned close to Heme C5 in the decaheme cytochrome MtrC (heme edge-to-heme edge distance of 8 Å) (Edwards et al., 2020). By this means, electrons can transfer from MtrA to MtrC for distribution across 10 hemes and a large surface area of MtrC that can be accessed by extracellular electron acceptors. MtrC may also pass electrons to a homologous extracellular decaheme cytochrome OmcA (Shi et al., 2006).

Previously, we reported (Lockwood et al., 2018) that *in vitro* mixing of purified MtrAB and soluble forms of MtrC results in the spontaneous formation of a stable high-affinity complex. Formation of the complex was evidenced by native PAGE and analytical ultracentrifugation with both techniques describing a complex of approximately 210 kDa that is indicative of a 1:1 association of soluble MtrC (approximately 80 kDa) and MtrAB (approximately 120 kDa). However, at that time, no information was available on the structure or electron transfer properties of the *in vitro* assembled complex. We address those gaps in knowledge in this report. Utilizing small-angle neutron scattering (SANS), the complex formed spontaneously *in vitro* is shown to have a similar structure to the MTR complex purified directly from *S. oneidensis* and revealed to be equally effective in the transfer of electrons across lipid bilayers. Our results pave the way for novel synthetic biology approaches to assemble functional MtrC:MtrAB complexes in homologous and heterologous hosts, with the potential to utilize chemically modified MtrC subunits to impart non-native functionality.

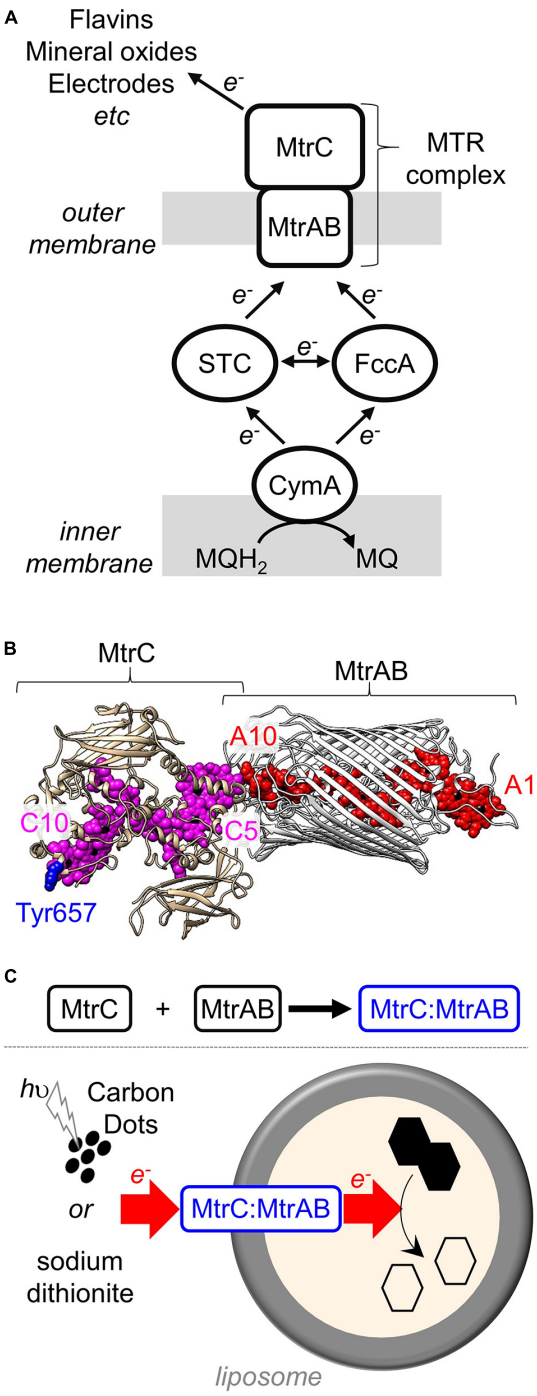

FIGURE 1 | The MTR complex of *Shewanella*. **(A)** Schematic of the electron transfer pathway in *S. oneidensis* MR-1 from menaquinol (MQH_2) to external terminal respiratory electron acceptors. **(B)** Model for the MTR complex of *S. oneidensis* MR-1 based on the crystal structure (Edwards et al., 2020) of *S. baltica* MTR complex. MtrAB (gray) showing the hemes (red). MtrC (tan) illustrating the location of the hemes (purple) and Tyr657 (blue). Hemes numbered according to their order of attachment to the primary sequence. Image rendered with Chimera. **(C)** Schematic of the *in vitro* association of MtrC and MtrAB (above) and trans-membrane electron transfer (below) through the resultant MtrC:MtrAB complex in proteoliposomes carrying the azo-dye cargo (black hexagons).

MATERIALS AND METHODS

Protein Purification and Biochemical Analyses

Y657C MtrC, lacking the lipid attachment site of wild-type MtrC and carrying a C-terminal Strep II affinity tag, and MtrAB were purified as previously described (Edwards et al., 2018; Lockwood et al., 2018; van Wonderen et al., under review) after overexpression from pBAD202D/TOPO vectors carried by a strain of *Shewanella oneidensis* MR-1 lacking the *mtr* operon. Cys-directed labeling of Y657C MtrC with [Ru(4-bromomethyl-4′-methylbipyridine)(2,2′-bipyridine)$_2$](PF$_6$)$_2$ (HetCat, Switzerland) was performed as described previously (van Wonderen et al., 2018, under review). The labeling efficiency was close to 100% as judged by LC-MS and UV-visible absorbance spectroscopy. The Ru-dye-labeled protein is termed Ru-MtrC (**Supplementary Figure 2**). For LC-MS, performed as described in van Wonderen et al. (2018), protein (typically $>$2 mg ml^{-1}) was diluted with formic acid (0.1%, *v*/*v*) and acetonitrile (2%, *v*/*v*) prior to analysis.

Protein concentrations were quantified by absorbance spectroscopy of the fully oxidized, air-equilibrated proteins with all hemes in the Fe(III) state; for MtrAB using $\varepsilon_{408\ nm}$ = 1,238,000 M^{-1} cm^{-1} and for Ru-MtrC (van Wonderen et al., under review) using $\varepsilon_{408\ nm}$ = 1,389,000 M^{-1} cm^{-1}. Extinction coefficients were experimentally determined by the pyridine hemochromagen method (Barr and Guo, 2015). Photoluminescence was measured for anaerobic protein solutions with 50 mM sodium phosphate, 50 mM NaCl, 5 mM lauryldimethylamine oxide (LDAO) (Sigma-Aldrich), pH 7.5 in sealed 1 ml quartz fluorescence cuvettes. Emission spectra were recorded using an excitation wavelength of 460 nm. Measurements were made with a Cary Eclipse Fluorescence Spectrophotometer: excitation slit width, 20 nm; emission slit width, 10 nm; and PMT detector voltage, medium.

Gel filtration chromatography was carried out at 4°C using a Superose 6 Increase 10/300 column (Cytiva) operated by an Äkta Pure chromatography system. The column was equilibrated with 50 mM sodium phosphate, 50 mM NaCl, 5 mM LDAO, pH 7.5 before loading 0.5 ml of protein sample in the same buffer. The sample was eluted at a flow rate of 0.25 ml min^{-1}, eluent was monitored by optical spectroscopy at 410 nm to detect the presence of heme.

Analytical Ultracentrifugation

Sedimentation equilibrium analytical ultracentrifugation (SE-AUC) experiments were performed using a Beckman Optima XLA-I analytical ultracentrifuge equipped with scanning absorbance optics. Measurements were performed in 50 mM sodium phosphate, 50 mM NaCl, 0.1% (*v*/*v*) Triton X-100 (Acros Organics), pH 7.5 for which the density (ρ) was calculated as 1.007 g ml^{-1} using utility software in Ultrascan II (Demeler, 2005). Ultrascan II was also used to calculate the partial specific volume ($\overline{\upsilon}$) of each protein: 0.721 ml g^{-1} for Ru-MtrC, 0.716 ml g^{-1} for MtrAB, and 0.718 ml g^{-1} for the Ru-MtrC:MtrAB complex. SE-AUC was performed at 20°C using speeds of 8,000, 10,000, and 12,000 rpm with absorbance profiles recorded at 410 nm. The program Ultrascan II was used to analyze the sedimentation equilibrium profiles and to fit the data to those predicted for single non-interacting species. Data are presented as $R^2 - R^2_{ref}$ against Ln($A_{410\ nm}$); the gradient of this plot can be used to determine the molecular weight (M_W) of the species by the equation:

$$M_W = \frac{2RT}{(1-\overline{\upsilon}\rho)\,\omega^2} \times \frac{d\ln(C_r)}{d(R^2 - R^2_{ref})}$$

where R is the gas constant, T is the temperature, C_r is the sample concentration at radial distance R, R_{ref} is the radial distance of the sample meniscus, and ω is the angular velocity. Radial distance is measured from the axis of rotation.

SANS Data Collection and Analysis

Ru-MtrC:MtrAB was prepared by combining Ru-MtrC with a slight excess of MtrAB and performing gel filtration chromatography as described above. Ru-MtrC:MtrAB eluting from the Superose 6 Increase 10/300 column with V_e < 16.5 ml, i.e., separated from free MtrAB, was pooled and loaded onto a 5-ml HiTrap Q FF column (Cytiva) equilibrated with 50 mM sodium phosphate, 50 mM NaCl, 5 mM LDAO, pH 7.5. Bound protein was washed with 50 ml of 20 mM HEPES, 100 mM NaCl, 2.8 mM Fos-choline 12 (Anatrace), pH 7.8 at 1 ml min^{-1} to exchange the detergent before elution with 20 mM HEPES, 0.5 M NaCl, 2.8 mM Fos-choline 12, pH 7.8. A 100-kDa molecular weight cutoff spin concentrator (Millipore) was then used to lower the NaCl concentration to 100 mM and concentrate the protein to 10 mg ml^{-1}. Immediately prior to SANS data collection, the protein sample was dialyzed overnight in a sealed DURAN bottle containing 20 mM HEPES, 100 mM NaCl, 2.8 mM Fos-choline 12, 13% D_2O, pH 7.8 using a 50-kDa molecular weight cut-off Dispo-Biodialyzer (Merck). Inclusion of 13% D_2O ensured that the neutron scattering length density of the buffer matched that of Fos-choline 12 micelles. This match point was previously determined by a SANS study of MtrAB and the MTR complex (Edwards et al., 2018). Protein samples at concentrations of 6.3 and 3.1 mg ml^{-1} were prepared by appropriate dilution using dialysis buffer to ensure precise buffer matching. Samples of 200 microliters were centrifuged at 13,000 × *g* for 10 min at 4°C to remove any potentially aggregated material, although no visible pellet was observed, before being sealed in 0.1 cm path-length suprasil quartz cuvettes (Hellma). An aliquot of dialysis buffer was also prepared in the same manner and was measured alongside the protein sample for downstream buffer subtraction.

SANS data were collected on the D22 diffractometer (Institut Laue-Langevin, France) using a neutron beam (λ = 6 Å ± 10%) at three configurations of collimation, 17.6, 8.0, and 2.8 m, and respective detector distances of 17.6, 8.0, and 1.4 m covering Q ranging from 0.003 to 0.6 Å^{-1}. The collimation cross-section was 40 × 55 mm, and the sample aperture was 7 × 10 mm. Exposure times ranged from 60 s to 2 h depending on sample concentration, contrast, and instrument configuration. Data reduction was performed using GRASP

including blocked beam and empty cell background subtraction, sample thickness and transmission scaling, and calibration to absolute intensity using incident neutron flux at sample position. As the final step azimuthal averaging was performed to output the scattering intensity I(Q).

Data were processed as previously described (Edwards et al., 2018) for the MTR complex. Briefly, curves were merged and buffer subtraction was carried out utilizing IGOR Pro (Wavemetrics) with the NCNR macros installed (Kline, 2006). The ATSAS software suite (Manalastas-Cantos et al., 2021) was used to analyze the I(Q) curves in order to perform a Guinier analysis to estimate the radius of gyration (R_g) at low Q ($Q_{max} \times R_g < 1.3$) and to produce Kratky plots to evaluate the overall compactness of the protein complexes. GNOM (Svergun, 1992) was used to calculate the pair distance distribution function [$P(r)$], i.e., the Fourier inversion of the scattering intensity [$I(Q)$], which provides an independent estimation of R_g as well as the maximum dimension of the scattering particle D_{max}. Using DAMMIF (Franke and Svergun, 2009), 20 bead models of the molecule were refined to fit the experimental $P(r)$. The DAMAVER suite of software (Volkov and Svergun, 2003) was then used to create pairwise alignments of all 20 models, identify and remove outliers among the models, 2 of the 20 models in this case, and create an average from the remaining 18 models. Reported molecular envelopes were produced by refinement of the averaged model using DAMMIN (Svergun, 1999). A homology model for the MTR complex of *S. oneidensis* (**Figure 1B**) was prepared by using Phyre2 to generate a model for MtrAB and combining that with the crystal structure of *S. oneidensis* MtrC (PDB ID: 4LM8) docked in the same position as MtrC of the *S. baltica* MTR complex (PDB ID: 6R2Q). This homology model was aligned to the SANS molecular envelopes using SUPCOMB (Kozin and Svergun, 2001). SANS data collection and processing statistics are reported in **Supplementary Table 3**.

Photoreduction of Ru-MtrC and Ru-MtrC:MtrAB Suspensions

Experiments were performed in anaerobic 50 mM Tris:HCl, 10 mM KCl, 100 mM EDTA, and 0.2% (*v*/*v*) Triton X-100, pH 8.5. Spectra were recorded in 1 ml SOG cuvettes (Hellma) in a Biochrom WPA Biowave II Diode-array spectrophotometer placed in a N_2-filled chamber (Belle Technology, atmospheric O_2 < 5 ppm). An Omega Optical 475RB Notch filter was used to prevent photoexcitation by the spectrophotometer. The light source for photoreduction was a Thorlabs mounted LED (λ_{max} = 450 nm) (**Supplementary Figure 1**) equipped with a collimator adapter. The excitation intensity at the sample was 110 W m^{-2} (0.42 mE m^{-2} s^{-1}) as determined by potassium ferrioxalate actinometry (Hatchard and Parker, 1956; Pitre et al., 2015). Samples were irradiated continuously from above and spectra taken at the desired time intervals. The percentage of reduced hemes was quantified using the baseline-corrected absorbance of the heme Soret band at 420 nm. The absorbance prior to irradiation was taken to be of the fully oxidized protein (0% reduced heme). The absorbance of fully reduced protein (100% reduced heme) was obtained at the end of the experiment by addition of an excess of the chemical reductant sodium dithionite.

Preparation of Liposomes and Proteoliposomes

Liposomes were prepared following an adaptation of the method reported by Stikane et al. (2019). Twenty milligrams of Polar lipid extract (Avanti Polar Lipids) was suspended in 750 μl of 50 mM Tris:HCl, 10 mM KCl, and 10 mM reactive red 120 (RR120, Sigma-Aldrich), pH 8.5 by vigorous vortexing for 20 min. The suspended lipid was then solubilized by addition of 500 μl of 250 mM octyl glucoside (Anatrace). Proteins were then incorporated by addition of 100 μl of 25 μM protein complex in 50 mM sodium phosphate, 50 mM NaCl, and 5 mM LDAO, pH 7.5. Ru-MtrC and MtrAB were mixed to form the Ru-MtrC:MtrAB complex prior to incorporation of this complex into proteoliposomes. For control experiments without proteins, liposomes were prepared by addition (100 μl) of 50 mM sodium phosphate, 50 mM NaCl, and 5 mM LDAO, pH 7.5. The resulting mixture was incubated on ice for 20 min before gradual addition, over 2 min, to ice-cold 50 mM Tris:HCl, 10 mM KCl, and 10 mM RR120, pH 8.5 to give a final volume of 50 ml. This dilution lowered the octyl glucoside concentration below its critical micelle concentration resulting in liposome formation with spontaneous protein integration and RR120 encapsulation.

The dilute liposome suspension was subjected to ultracentrifugation at 205,000 × *g* for 1 h to pellet the liposomes. After removal of the supernatant, pellets were transferred to a N_2-filled chamber and resuspended in 50 ml of anaerobic 50 mM Tris:HCl and 10 mM KCl, pH 8.5. The liposome pellets recovered after a second ultracentrifugation, as above, were then resuspended to a final volume of 1 ml in anaerobic 50 mM Tris:HCl and 10 mM KCl, pH 8.5 and allowed to equilibrate overnight at room temperature in the anaerobic chamber. The liposome concentration of these samples was approximately 300 nM, estimated on the basis of the liposome dimensions (see below) and lipid composition as described in **Supplementary Material**.

Dynamic light scattering was used to assess the dimensions of the liposomes in samples containing approximately 6 nM liposome in 50 mM Tris:HCl and 10 mM KCl, pH 8.5. Measurements used a Zetasizer Nano with DTS1070-folded capillary cells (Malvern Panalytical, Malvern, United Kingdom), and zeta potentials were measured using the same equipment. Samples were equilibrated at 25°C for 2 min prior to measurement, and the solvent viscosity was considered to be that of water. The identity of proteins in each of the samples was confirmed using SDS-PAGE with proteins visualized by heme (Thomas et al., 1976) or Coomassie stain.

Transmembrane Electron Transfer in (Proteo-) Liposomes

Bleaching of encapsulated RR120 was used to monitor transmembrane electron transfer with (proteo-) liposomes as illustrated schematically in **Figure 1C**. All experiments

were performed inside a N_2-filled chamber (Belle Technology, Weymouth, United Kingdom; atmospheric $O_2 < 5$ ppm). For experiments with sodium dithionite as the electron donor, a stock solution (20 mg ml^{-1}) was prepared by dissolving the required mass in anaerobic 50 mM Tris:HCl and 10 mM KCl, pH 8.5. Sodium dithionite was then added (approximately 0.1 mM final concentration) to anaerobic suspensions of (proteo-) liposomes (approximately 6 nM) containing RR120 in anaerobic 50 mM Tris:HCl and 10 mM KCl, pH 8.5 in 1 ml SOG cuvettes. Absorbance spectra were measured over 30 min. Finally, Triton X-100 was added to 0.2% (*v*/*v*) to lyse the liposomes. In all cases, this final step led to rapid bleaching of all RR120 present and demonstrated the presence of excess reductant.

Photochemically driven transmembrane electron transfer was monitored by a similar method using graphitic N-doped carbon dots as described in Martindale et al. (2017) and **Supplementary Figure 3**. Prior to use, the graphitic N-doped carbon dots were suspended to 1 mg ml^{-1} in anaerobic 50 mM Tris:HCl and 10 mM KCl, pH 8.5. For photoreduction, anaerobic samples in 1 ml SOG cuvettes contained approximately 6 nM (proteo-) liposomes with encapsulated RR120, 10 μg ml^{-1} of graphitic-N-doped carbon dots, and 25 mM EDTA in 50 mM Tris:HCl and 10 mM KCl, pH 8.5. Samples were irradiated by visible-light ($\lambda > 400$ nm) from the side using a Krüss cold light source (**Supplementary Figure 1**) with a fiber optic light pipe as described in Rowe et al. (2017) Light intensity was measured at 2.5 kW m^{-2} using an Amprobe Solar-100 solar power meter.

Absorbance spectra were measured at desired times with a Biochrom WPA Biowave II diode array spectrophotometer. Scattering due to the liposomes was calculated using the equation:

$$Scattering\ intensity = A + B/\lambda^4$$

and subtracted from the measured data. For each series of experiments, the variables A and B were adjusted to give a good fit to the measured data where absorbance from protein and dye were minimal, below 260 and above 640 nm (e.g., **Supplementary Figure 4**). Dye absorbance was then quantified at 539 nm, a wavelength which is isosbestic with respect to heme oxidation state (Stikane et al., 2019).

RESULTS AND DISCUSSION

MtrAB when purified and resuspended in detergent micelles was previously (Lockwood et al., 2018) shown to bind to separately purified soluble forms of MtrC but not OmcA, which is an extracellular decaheme cytochrome of *S. oneidensis* homologous to MtrC. This selective binding led us to anticipate that the MtrC:MtrAB complex would have a structure similar to that of the MTR complex. MtrC Heme C5 would be positioned close to MtrAB Heme A10 (**Figure 1B**), and the environment of MtrC Heme C10 would be the same in purified MtrC as in the MTR complex. Labeling the surface of MtrC near Heme C10 with a luminescent dye would provide the opportunity to report on that local environment. If, in addition, that dye could transfer photo-energized electrons to the MtrC hemes, there might be opportunities to probe MtrC to MtrAB electron transfer within the MtrC:MtrAB complex following light-triggered electron injection into MtrC Heme C10.

The thiol-reactive dye [Ru(4-bromomethyl-4′-methylbipyridine)(2,2′-bipyridine)$_2$]$(PF_6)_2$ (Geren et al., 1991; Millett and Durham, 2002) has been successfully attached to cysteine residues on the surfaces of a number of redox proteins. This dye has a well-characterized luminescence that is sensitive to local environment (van Wonderen et al., 2018). Furthermore, the photoexcited dye is capable of injecting photo-energized electrons into multiheme cytochromes including *S. oneidensis* STC (van Wonderen et al., 2019) and of PpcA of *Geobacter sulfurreducens* (Kokhan et al., 2015). Thus, we prepared (van Wonderen et al., under review) a soluble MtrC variant with Tyr657 replaced by Cys on the surface of MtrC at a site close to Heme C10 (**Figure 1B**). Cys657 was then labeled by reaction with [Ru(4-bromomethyl-4′-methylbipyridine)(2,2′-bipyridine)$_2$]$(PF_6)_2$ to form a protein, here termed Ru-MtrC, that retains the spectral and redox properties of the hemes in the native protein (van Wonderen et al., under review).

As described below, Ru-MtrC forms a 1:1 complex when mixed with MtrAB. The structure of the resultant complex, termed Ru-MtrC:MtrAB, was assessed by analytical ultracentrifugation, gel-filtration chromatography, SANS, and luminescence spectroscopy. Electron transfer was probed by optical spectroscopy of the complex in detergent micelles and incorporated in lipid bilayers.

Oligomeric State and Solution Structure of the Ru-MtrC:MtrAB Complex

SE-AUC provides a direct measure of the average mass of proteins in solution (Lebowitz et al., 2002). As a consequence, their oligomeric state can be readily defined and SE-AUC was the method of choice for initial characterization of samples containing Ru-MtrC, MtrAB, and 1:1 mixtures of Ru-MtrC with MtrAB. Data were collected at three rotation speeds for each sample. In each case, the absorbance profile indicative of protein concentration across the sample, e.g., **Figure 2A**, was well-described by the behavior predicted for a single, non-interacting species. For Ru-MtrC (0.4 μM), the apparent mass was 82,400 Da, and for MtrAB (0.4 μM), it was 120,000 Da. These values are in good agreement with those of 76,788 and 114,047 Da calculated for Ru-MtrC and MtrAB, respectively, on the basis of primary sequence, covalent modification by 10 *c*-type hemes, and labeling of the former protein with the Ru-dye. It was concluded that Ru-MtrC and MtrAB are monomer and heterodimer, respectively, under the experimental conditions.

Analysis of the absorbance profiles for samples containing MtrAB (0.25 μM) and an equal concentration of Ru-MtrC revealed a single homogeneous species with an apparent molecular mass of approximately 204,000 Da. This mass is comparable with the sum (190,835 Da) of those for Ru-MtrC and MtrAB. Thus, Ru-MtrC combines with MtrAB to form a heterotrimer having a 1:1 ratio of Ru-MtrC and MtrAB. We note that all samples contained 0.1% (*v*/*v*) of the detergent Triton X-100, to maintain solubility of the membrane proteins, and that

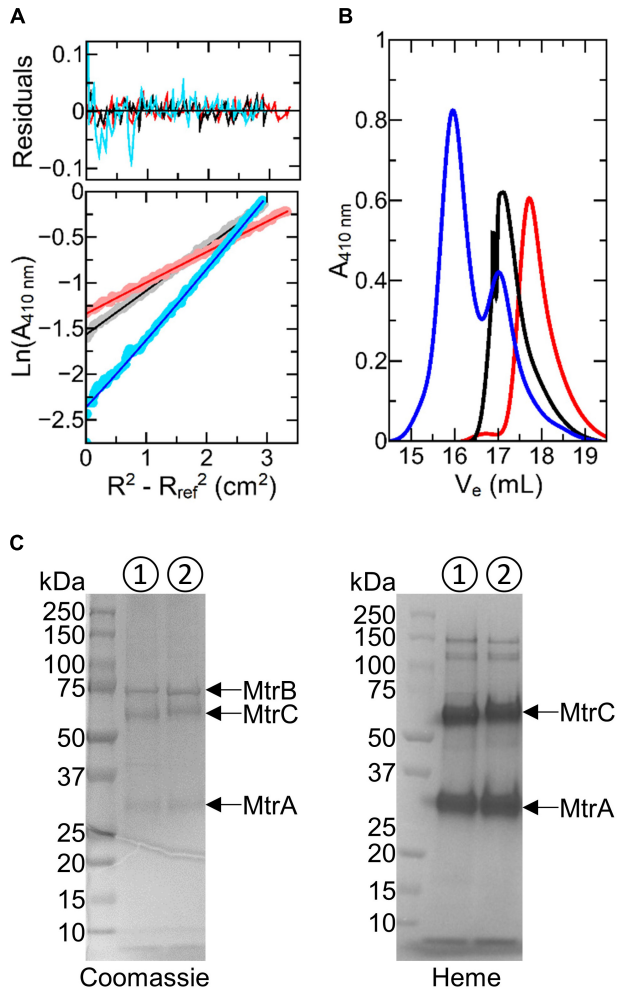

FIGURE 2 | Biophysical characterization of Ru-MtrC:MtrAB. **(A)** Sedimentation equilibrium analytical ultracentrifugation traces for 0.4 μM MtrAB (black), 0.4 μM Ru-MtrC (red), and a mixture of 0.25 μM Ru-MtrC equilibrated with 0.25 μM MtrAB (blue). Samples were centrifuged at 8,000 rpm for 20 h at 20°C in 50 mM sodium phosphate, 50 mM NaCl, and 0.1% (*v/v*) Triton X-100, pH 7.5 to reach equilibrium. Lower panel: data (circles) and fits (lines) to the behavior for a single non-interacting species; see text for details. Upper panel: residuals. **(B)** Gel filtration chromatograms for samples of 40 μM MtrAB (black), 40 μM Ru-MtrC (red), and a mixture of 32 μM Ru-MtrC equilibrated with 48 μM MtrAB (blue). A Superose 6 Increase 10/300 column was equilibrated in 50 mM sodium phosphate, 50 mM NaCl, and 5 mM LDAO, pH 7.5. Elution was at 0.25 ml min^{-1}. **(C)** SDS-PAGE analysis of the MTR complex (①) and Ru-MtrC:MtrAB (②) (V_e < 16.5 ml from gel filtration shown in **(B)**). Proteins visualized by Coomassie and Heme stain as indicated.

the approximate micellar weight for Triton X-100 is 80 kDa. However, there is negligible micellar contribution to the overall mass for proteins of the size studied here. This is because the partial specific volume of Triton X-100 (0.91 ml g^{-1}) (Paradies, 1980) is close to that of the buffer-electrolyte (0.99 ml g^{-1}) such that the micelle is only weakly affected by the centrifugal force. The proteins, by comparison, have partial specific volumes of approximately 0.72 ml g^{-1}.

Further evidence for spontaneous formation of a tight, stable complex between Ru-MtrC and MtrAB was provided by analytical gel filtration chromatography (**Figure 2B**). Resolution was afforded by a Superose 6 Increase column for samples having a concentration approximately 100× greater than used for SE-AUC analysis. Ru-MtrC eluted as a single peak centered on an elution volume (V_e) of approximately 17.8 ml and samples of the higher mass MtrAB complex eluted as a single peak centered on V_e approximately 17.1 ml. A sample containing Ru-MtrC (32 μM) equilibrated with an excess of MtrAB (48 μM) eluted as two peaks. The smaller peak, centered on V_e approximately 17.1 ml, is assigned to excess MtrAB. The larger peak, centered on V_e approximately 15.5 ml, is assigned to a species of higher molecular mass that we consider to be the Ru-MtrC:MtrAB complex. This interpretation was supported by SDS-PAGE (**Figure 2C**) of material with V_e approximately 15.5 ml where bands with the expected mass of Ru-MtrC, MtrA, and MtrB were observed.

Previously (Edwards et al., 2018), we used SANS to resolve the molecular envelopes of MtrAB and the MTR complex purified from *S. oneidensis*. For those experiments, proteins were suspended in a buffer containing Fos-choline 12 detergent and 13% D_2O in order to match the neutron scattering length density of both detergent micelles and bulk buffer solution. Upon buffer subtraction, the scattering intensity profile of the detergent micelles is also subtracted revealing the neutron scattering intensity profile from the protein complexes alone. We used the same approach here to resolve the molecular envelope of Ru-MtrC:MtrAB. We note that our ability to prepare Ru-MtrC:MtrAB in Triton X-100 (SE-AUC), LDAO (gel filtration), and Fos-choline 12 (SANS) highlights the stability of the complex in a range of detergents.

Neutron scattering data were collected for Ru-MtrC:MtrAB at concentrations of 6.3 and 3.1 mg ml^{-1}. The scattering intensity profiles scaled linearly with protein concentration indicating an absence of concentration-dependent interparticle interactions (**Supplementary Figure 5**). The scattering profiles were merged, providing a curve (**Figure 3A**) with high reliability and signal to noise. Guinier analysis (**Figure 3B**) produced a linear plot indicating that the samples of Ru-MtrC:MtrAB were not aggregated and had an approximate radius of gyration (R_g) of 46.9 ± 0.6 Å. A Kratky plot [$I(Q) \times Q^2$ vs. Q, where $I(Q)$ is the intensity at a given scattering distance and Q is momentum transfer] (**Figure 3C**) indicated Ru-MtrC:MtrAB was globular. $P(r)$ distance distribution curves were generated using the GNOM program based on inverse Fourier transform of the data to a maximum Q-value of 0.161 $Å^{-1}$. The scattering intensity decreased significantly beyond this value, so data were truncated before calculation of $P(r)$ distribution curves. The $P(r)$ curve shape (**Figure 3D**) was suggestive of a globular protein with a maximum distance in the molecule, D_{max}, of 166 Å and an R_g of 48.2 Å. The latter is in good agreement with the value determined by Guinier analysis (see above). The theoretical scattering produced by this $P(r)$ curve fits well to the experimental scattering data (**Figure 3A**) with a χ^2 of 0.764 as determined by GNOM.

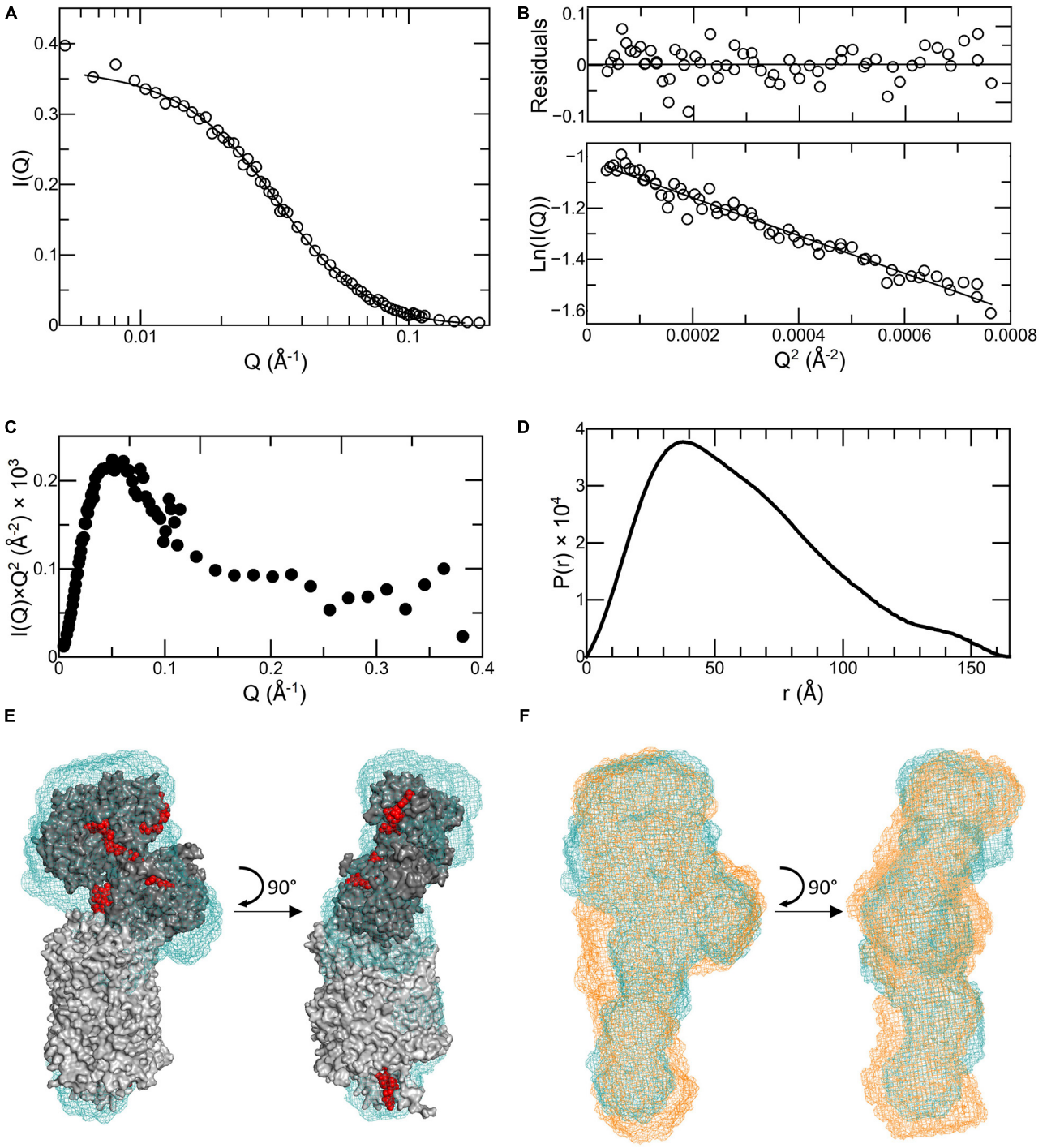

FIGURE 3 | Analysis of SANS data for Ru-MtrC:MtrAB. **(A)** Scattering data (truncated to Q = 0.161 Å^{-1}) shown as circles with the fit to the $P(r)$ curve generated by GNOM shown as a line. **(B)** Guinier region of scattering curve, lower panel shows data as circles and a linear fit as a line. Upper panel shows residuals from fitting. **(C)** Kratky plot. **(D)** $P(r)$ distance distribution curve. **(E)** Molecular envelope of Ru-MtrC:MtrAB (blue mesh) generated by DAMMIN aligned with the homology model of the MTR complex from *S. oneidensis* (gray with red hemes). **(F)** Molecular envelope of Ru-MtrC:MtrAB (blue mesh) aligned with that of the MTR complex (orange mesh). Source data for latter as reported in Edwards et al. (2018), see text for details.

The $P(r)$ curve was used to produce *ab initio* structural models for Ru-MtrC:MtrAB using DAMMIF (Franke and Svergun, 2009); these were then processed with DAMAVER (Volkov and Svergun, 2003) as previously described (Edwards et al., 2018). Final refinement using DAMMIN (Svergun, 1999) produced a molecular envelope which is shown in **Figure 3E**. It has been

aligned, using SUPCOMB (Kozin and Svergun, 2001) to the homology model for the *S. oneidensis* MTR complex (**Figure 1B**) generated based upon the crystal structure of the MTR complex from *S. baltica* OS185 (Edwards et al., 2020) and the structure of MtrC from *S. oneidensis* MR-1 (Edwards et al., 2015). The theoretical scattering profile produced by this molecular envelope had a χ^2-value of 2.748 (determined by DAMMIN) against the original scattering curve (**Supplementary Figure 6F**), indicating a good fit to the data, and the alignment had a normalized spatial discrepancy (NSD) of 2.05. The data reveal agreement between the Ru-MtrC:MtrAB molecular envelope from SANS and the homology model for the MTR complex at the level of resolution afforded by SANS.

The scattering data obtained previously (Edwards et al., 2018) for the MTR complex was subject to the same analysis and modeling comparable with that described above for Ru-MtrC:MtrAB (**Supplementary Figure 6**). The final molecular envelope for the MTR complex had a χ^2-value of 1.972 (determined by DAMMIN) against the scattering data (**Supplementary Figure 6F**) and alignment to the homology model for *S. oneidensis* MTR complex gave a NSD of 2.72 (**Supplementary Figure 6E**). The DAMMIN models of the Ru-MtrC:MtrAB and MTR complexes are compared in **Figure 3F** and reveal very similar global structures at the resolution provided by SANS. Both models align similarly well with the homology model for the MTR complex generated from the crystal structure (Edwards et al., 2020) of the complex from *S. baltica*. This finding gives confidence in the homology model generated to describe the structure of the *S. oneidensis* MTR complex. In addition, it reveals that the MTR solution structure is not significantly different to that resolved in a crystalline state.

SANS analysis of Ru-MtrC:MtrAB lacks the resolution required to locate the Ru-dye attached to MtrC Cys657. To confirm the dye is positioned away from the interface between MtrC and MtrAB, as expected from the structure of the MTR complex (**Figure 1B**), the spectral properties of the dye attached to MtrC were investigated in the absence and presence of MtrAB. If MtrC Heme C10 is located near the interface with MtrAB, we can expect this to impact the photoluminescence intensity or spectral profile of the Ru-dye. However, there was negligible change to the emission spectrum of 1 μM Ru-MtrC after incubation with 0.5, 1, or 2 μM MtrAB over a 5-h period (**Supplementary Figure 7**). These observations are consistent with a "correct" relative orientation of Ru-MtrC and MtrAB such that Heme C10 is positioned some distance from MtrAB (**Figure 1B**).

Electron Transfer Through the Ru-MtrC:MtrAB Complex

SANS analysis suggests Ru-MtrC:MtrAB assembles in either the same or a highly similar manner to the wild-type MTR complex assembled in the outer membrane of *Shewanella*. To further investigate the *in vitro*-assembled Ru-MtrC:MtrAB complex, a series of experiments explored its electron transfer properties. Initial investigations took advantage of the Ru-dye attached to MtrC. The photoexcited triplet state of this dye, generated by absorption of photons at blue wavelengths, is a strong reductant (E_m approximately -830 mV vs. SHE) with a lifetime of approximately 600 ns that is capable of transferring its photoenergized electron to a nearby protein cofactor (e.g., Geren et al., 1991; Millett and Durham, 2002; van Wonderen et al., 2018, 2019, under review). The photoenergized electron becomes trapped in the protein if the oxidized dye is reduced by a sacrificial electron donor and provided there are no sacrificial acceptors present. For cytochromes with multiple hemes, such photoreduction is cumulative (van Wonderen et al., 2018) and readily quantified by changes in absorbance of the Soret band as illustrated for Ru-MtrC (e.g., **Figure 4A**). Initially, the protein is fully oxidized with all hemes in the Fe(III) state as indicated by the Soret band with maximum absorbance at 410 nm (**Figure 4A**, thick red line). Upon irradiation (λ = 450 nm) in the presence of EDTA as sacrificial electron donor, the Soret band was red shifted and gained intensity (**Figure 4A**, thin red lines). These changes revealed the formation of reduced Fe(II)-containing hemes. Fully reduced Ru-MtrC with 10 Fe(II) hemes produced on equilibration with an excess of the chemical reductant sodium

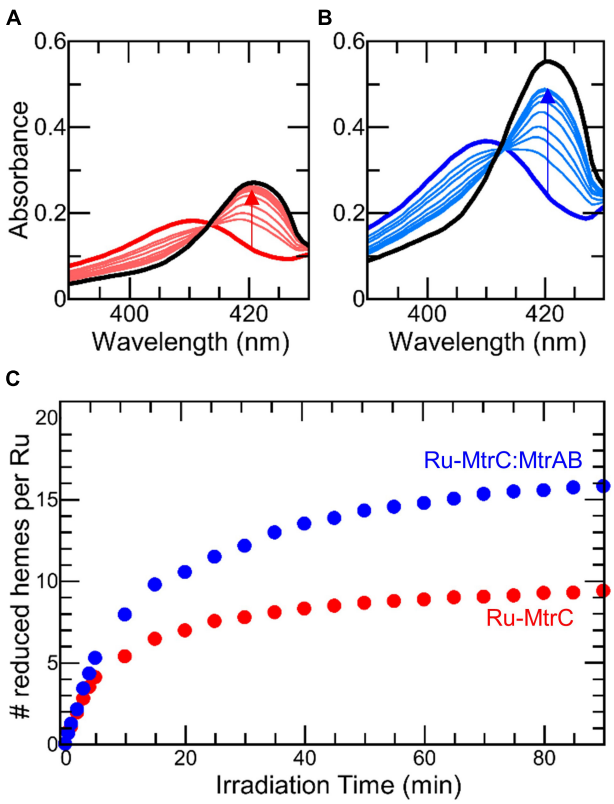

FIGURE 4 | Photoreduction of Ru-MtrC and Ru-MtrC:MtrAB Suspensions. Spectra of oxidized protein (thick colored line), over 90 min irradiation (thin colored lines), and after addition of dithionite (black line) for **(A)** Ru-MtrC and **(B)** Ru-MtrC:MtrAB. Samples of Ru-MtrC (0.12 μM) and Ru-MtrC:MtrAB (0.14 μM) in anaerobic 50 mM Tris, 10 mM KCl, 100 mM EDTA, and 0.2% (*v/v*) Triton X-100, pH 8.5. Irradiation at 450 nm, intensity 110 W m^{-2}. **(C)** Time course of photoreduction for Ru-MtrC (red) and Ru-MtrC:MtrAB (blue). Number of reduced hemes defined by $\Delta A_{420\ nm}$; see text for details.

dithionite has an intense Soret band with maximum absorbance at 420 nm (**Figure 4A**, black line).

Cumulative photoreduction of Ru-MtrC:MtrAB was observed during equivalent experiments (e.g., **Figure 4B**). Of significance was the finding that for this complex, approximately 20 min irradiation was sufficient to drive the reduction of > 10 hemes per molecule of Ru-dye (**Figure 4C**). It can be concluded that Ru-MtrC transfers electrons to MtrAB. Reduction was not detected in the absence of EDTA, without irradiation, and without the Ru-dye allowing us to propose a likely mechanism for the cumulative photoreduction (**Scheme 1**). In Scheme 1, the excited state Ru-dye is presented as $^*Ru^{2+}$, the box represents MtrC (or MtrC:MtrAB), D is the sacrificial electron donor EDTA, and only productive steps for cumulative photoreduction are illustrated.

A striking feature of the time courses for photoreduction of MtrC and MtrC:MtrAB is that the maximum (i.e., initial) rates are of the order of 1 heme min^{-1} despite predicted (Jiang et al., 2019, 2020) and measured (van Wonderen et al., under review) heme-to-heme electron transfer rates > μs^{-1}. Similar behavior was described (van Wonderen et al., 2019) for the tetraheme cytochrome STC of *S. oneidensis* labeled in a manner comparable with that for Ru-MtrC described here. This situation points toward rate-limiting events that involve the Ru-dye, e.g., photoexcitation, EDTA oxidation, and/or charge separation (recombination). However, further investigation of these possibilities falls beyond the scope of this present study.

The timescale of cumulative photoreduction reported in this study makes it difficult to confidently distinguish the contribution of electron transfer within Ru-MtrC:MtrAB from that due to electron transfer between such complexes. To overcome this difficulty and provide a description of electron transfer through Ru-MtrC:MtrAB, we incorporated the complex into liposome bilayers. The proteoliposomes, illustrated schematically in **Figure 1C**, contained RR120 an azo-dye that undergoes reductive bleaching (E_m = -0.4 V vs. SHE) to provide a readily quantifiable spectroscopic indicator of electron transfer into the proteoliposomes (Stikane et al., 2019).

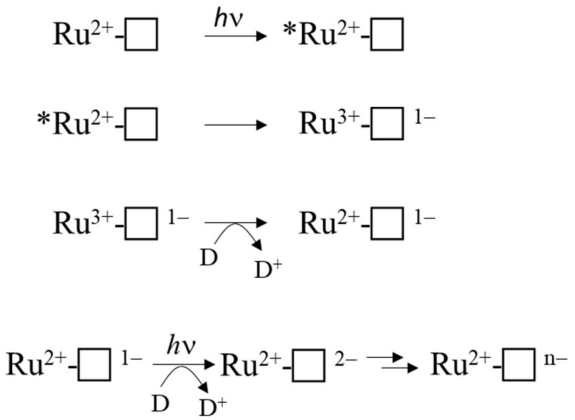

SCHEME 1 | Proposed mechanism of cumulative photoreduction showing only productive steps.

Proteoliposomes loaded with RR120 were prepared as described in section "Materials and Methods." SDS-PAGE confirmed that the proteins added during liposome formation were retained in the samples used to study electron transfer (**Figure 5**, inset). The presence of encapsulated RR120 was confirmed by a large peak from 460 to 570 nm in the absorbance spectra (**Figures 6A,B**) alongside a smaller Soret peak at 410 nm from Fe(III) heme. Deconvolution of these spectral features allowed the concentrations of dye and Mtr proteins to be calculated (**Supplementary Figure 4** and **Supplementary Table 2**) and demonstrated that the ratio of complex to dye in both types of proteoliposome were similar (approximately 1:270). Dynamic light scattering revealed the size distributions of the proteoliposomes were independent of the incorporated protein (**Figure 5**). Zeta potential measurements gave values between -40 and -45 mV with no discernable dependence on the presence or absence of Mtr proteins. This finding is consistent with our estimate of < 5 complexes per liposome (**Supplementary Table 2**) with the complex having a footprint of approximately 40 nm^2 in comparison with a proteoliposome surface area of approximately 30,000 nm^2.

The 8 electrons necessary to reduce RR120 and its small extinction coefficient ($\varepsilon_{539\ nm}$ = 32.3 $mM^{-1}\ cm^{-1}$) combined with the slow cumulative photoreduction rates for Ru-dye irradiation described above made it necessary for us to use different electron delivery systems with the (proteo-) liposomes. We chose the reductants for their previously described (Stikane et al., 2019) ability to produce rapid (<10 min) bleaching of internalized RR120 in MTR containing proteoliposomes. Addition of sodium dithionite to proteoliposomes containing Ru-MtrC:MtrAB or the MTR complex resulted in a rapid bleaching of the internalized RR120 (**Figures 6A,B,D**). In the absence of Mtr proteins, there was very little bleaching of

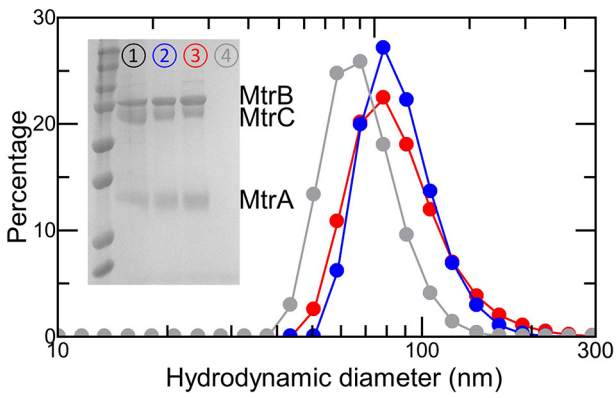

FIGURE 5 | Characterization of (proteo-) liposomes. Size analysis by dynamic light scattering of RR120-containing liposomes with Ru-MtrC:MtrAB (blue), the MTR complex (red), or no proteins (gray). Proteoliposome concentrations estimated at 6 nM in 50 mM Tris:HCl and 10 mM KCl, pH 8.5. Inset shows Coomassie-stained SDS-PAGE gel loaded with the MTR complex (①); RR120-containing proteoliposomes with the MTR complex (②) or Ru-MtrC:MtrAB (③); and RR120-containing liposomes (④). Prestained protein ladder as in **Figure 2C**.

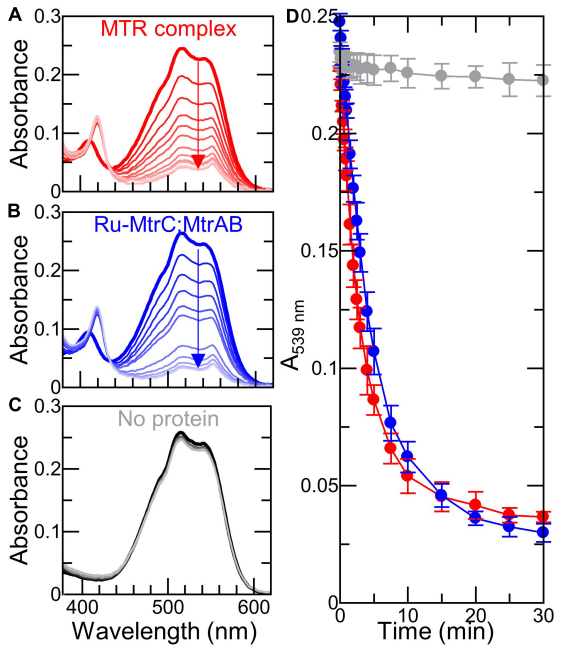

FIGURE 6 | Dithionite-driven electron transfer across (proteo-)liposome bilayers **(A–C)** Spectra of 6 nM (proteo-) liposomes containing RR120 with indicated proteins before (thick line) and over 30 min following addition of 0.1 mM dithionite (thin lines); arrows indicate bleaching of RR120. Samples in 50 mM Tris:HCl and 10 mM KCl, pH 8.5. Scattering due to liposomes has been subtracted; see text for details. **(D)** Time course for bleaching of encapsulated RR120 from **(A–C)** with data points connected for clarity. Data are the average of $n = 3$ datasets and error bars show standard deviation.

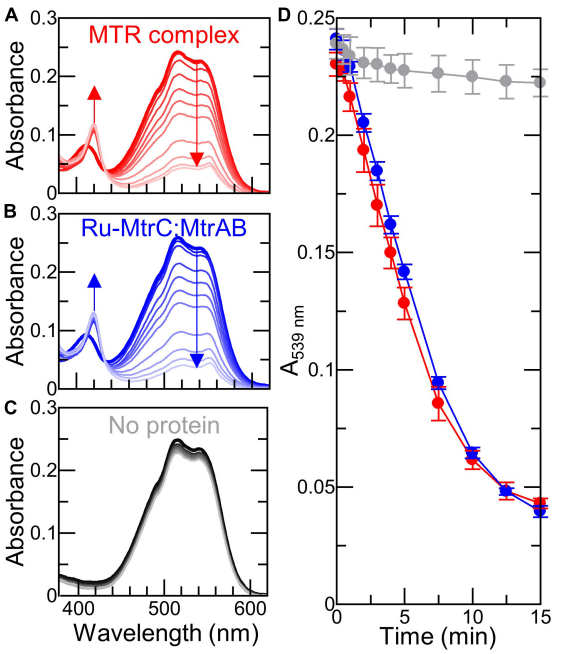

FIGURE 7 | Light-driven electron transfer across (proteo-)liposome bilayers with graphitic N-doped carbon dots. **(A–C)** Spectra of 6 nM (proteo-) liposomes containing RR120 with indicated proteins before (thick line) and over 15 min irradiation (thin lines) with visible light (2.5 kW m^{-2}); arrows indicate reduction of hemes and bleaching of RR120. Samples in 50 mM Tris:HCl, 10 mM KCl, 25 mM EDTA, AND 10 μg ml^{-1} graphitic N-doped carbon dots, pH 8.5. Scattering contributions from carbon dots and liposomes have been subtracted; see text for details. **(D)** Time course showing bleaching of encapsulated RR120 in (proteo-) liposomes from **(A–C)** with data points connected for clarity. Data are the average of $n = 3$ datasets, and error bars show standard deviation.

the dye over the same time period (**Figures 6C,D**). Thus, Ru-MtrC:MtrAB is an effective conduit for electron transfer across the lipid bilayer. Furthermore, the rate of electron transfer through Ru-MtrC:MtrAB is comparable with that of the MTR complex (**Figure 6D**).

A final series of experiments explored the ability of graphitic N-doped carbon dots to support light-driven transmembrane electron transfer. These nanoparticles support rapid photoreduction when irradiated with white light ($\lambda > 400$ nm) in the presence of EDTA as sacrificial electron donor (Martindale et al., 2017). When our RR120 proteoliposomes containing Ru-MtrC:MtrAB or MTR complex were irradiated in the presence of EDTA, the rapid bleaching of RR120 was observed (**Figures 7A,B**). The complexes supported comparable rates of bleaching indicative of equivalent rates of electron transfer through Ru-MtrC:MtrAB and the MTR complex. Photoreduction of the Mtr hemes was also apparent through changes in the Soret band, specifically the red shift and increase of intensity. Almost all hemes appeared to be reduced in the first minute, indicating that electron transfer between (Ru-)MtrC and MtrAB is fast compared with the reduction of RR120. In the absence of Mtr proteins, liposomes containing RR120 showed very little evidence for dye bleaching over the same time period (**Figure 7C**). Thus, bleaching of the dye is dependent on electron transfer through the Mtr biomolecular wires.

Equivalent experiments performed in the absence of carbon dots or EDTA showed negligible reduction of heme and no bleaching of the encapsulated RR120 (**Supplementary Figure 8**). Furthermore, there was no detectable increase in the rate of RR120 bleaching in Ru-MtrC:MtrAB liposomes compared with MTR liposomes (**Figure 7D**). We conclude that Ru-MtrC makes very little contribution to photochemical electron production in these experiments and that carbon dots are the primary driver of the observed photochemistry.

By two methods of analysis, we find that transmembrane electron transfer by the Ru-MtrC:MtrAB complex is comparable with that by the MTR complex. This supports Ru-MtrC:MtrAB having a structure comparable with that of the MTR complex of *S. baltica* (**Figure 1B**), where MtrA Heme A10 and MtrC Heme C5 lie in close proximity to facilitate electron transfer across the interface between the two decaheme cytochromes. We note that the orientation(s) of the complexes in the proteoliposome membranes is not known. However, this is unlikely to affect our conclusions. Given the demonstrated similarity in structure of the MTR complex and Ru-MtrC:MtrAB, we expect that the

populations of "inside-out" and "right-side-out" complex are similar for each type of proteoliposome. Both orientations are likely to occur as the protein complexes are present during formation of the liposome bilayers.

DISCUSSION

An increasing number and diversity of organisms are recognized to naturally transfer electrons between internal enzymes and external redox partners (Bose et al., 2014; White et al., 2016). The electron transfer pathways, evolved to allow survival in the absence of cell permeable electron acceptors, now inspire biotechnology to produce green energy and/or chemicals from material typically considered waste. Examples include the remediation of water-borne organic "waste" molecules coupled to electricity production in microbial fuel cells, and the microbial electrosynthesis of valued chemicals from CO_2 and N_2 driven by electricity from renewable sources (Chiranjeevi and Patil, 2020). These strategies rely on electron exchange between bacteria and electrodes. However, until recently, there has been very little molecular understanding of the proteins essential for electron exchange across bacterial outer membranes. It is now apparent that outer membrane-spanning complexes with a *c*-type cytochrome inside a beta-barrel porin protein play a major role in such electron transfer for numerous and phylogenetically diverse Gram-negative bacteria (Hartshorne et al., 2009; White et al., 2016; Edwards et al., 2020). Biochemical details are beginning to emerge for the porin-cytochrome fusion exemplified by CYC2 of *Acidithiobacillus ferroxidans* (Yarzabal et al., 2002; Castelle et al., 2008) the PioAB proteins of *Rhodopseudomonas palustris* TIE-1 (Gupta et al., 2019; Li et al., 2020) and the PCA complexes of *Geobacter sulfurreducens* (Liu et al., 2014). However, it is for *Shewanella* species that trans-outer membrane electron transfer is perhaps best described at the molecular level (e.g., **Figures 1A,B**). Notably, the MTR complex provides the primary, and bidirectional, route for electron transfer across the bacterial outer membrane (Ross et al., 2011; Shi et al., 2012).

Recent resolution of the molecular structure of an MTR complex (Edwards et al., 2020) paves the way for its rational engineering to facilitate electrical interfacing of *Shewanella*, or heterologous hosts, with external redox partners. The present study was informed by that structure. We have engineered MtrC for photoreduction by labeling the external surface with a Ru(II)-dye photosensitizer adjacent to the terminal Heme C10. Photo-energized electrons transfer from the dye to MtrC, and subsequently to MtrAB. Furthermore, the bespoke biomolecular wire created by mixing water-soluble Ru-MtrC with the lipid-soluble MtrAB porin:cytochrome complex is indistinguishable from purified MTR in both its structure and ability to transfer electrons across lipid bilayers. Our results can now inform the engineering of bacteria for inclusion in novel biohybrid materials with bespoke transmembrane biomolecular wires. Not only do they provide insight into the cellular pathway for MTR assembly, they suggest bespoke MTR complexes may be assembled in a modular fashion on the surface of live bacteria. We consider both topics below.

Precise details of the cellular MTR assembly pathway are lacking at the present time. In MR-1, the *mtrC*, *mtrB*, and *mtrA* genes encoding for the components of the MTR complex are co-transcribed. The translated peptides are transported in an unfolded state, through the Sec pathway, into the periplasm. The *Shewanella* cytochrome *c* maturation pathway folds MtrA and MtrC and attaches 10 hemes to each protein (Jin et al., 2013). MtrB is then combined with periplasmic MtrA to form the MtrAB complex through a process that may be initiated in the periplasm (Schicklberger et al., 2011). By contrast the type II secretion pathway secretes folded MtrC (Shi et al., 2008) to the external cell surface where it resides as a lipoprotein (Myers and Myers, 2001). The MTR complex forms when the lipoprotein MtrC, anchored to the external cell surface, associates with MtrAB in the outer membrane. By demonstrating that soluble MtrC, lacking the N-terminal lipid attachment site (Lockwood et al., 2018) associates with MtrAB to form a complex indistinguishable from MTR, this study reveals that the interfacial contacts between MtrC and MtrAB are sufficient to define and stabilize a functional complex. The lipid anchor carried by genomically encoded MtrC appears to have no structural role. That anchor may ensure that secreted MtrC, synthesized in a process requiring significant investment of cellular resources, diffuses only across the cell surface, essentially in 2D, until it encounters and associates with the MtrAB complex to then perform its role in anaerobic respiration.

With regard to developing novel biotechnology for greener chemical synthesis, much inspiration is provided by bacteria, such as *S. oneidensis* MR-1, which naturally couple internal and external redox processes. Electrons, for example, derived from lactate oxidation by *S. oneidensis* MR-1 (**Figure 1A**) have been delivered (Fan et al., 2018) to an exogenous extracellular catalyst for atom-transfer radical polymerization (**Figure 8A**). Separately, genetic engineering of *S. oneidensis* introduced new metabolism and demonstrated the production of value-added substances more oxidized than the substrates (**Figure 8B**) when glycerol was converted to ethanol (Flynn et al., 2010) and acetoin produced from glucose (Bursac et al., 2017). Both studies benefited from electrode-assisted fermentation with the liberated electrons passed to anodes. In the future, we envisage value-adding half-reactions inside the bacteria will be coupled to value-adding half-reactions that occur outside the cells such that the concepts above are integrated in a single biotechnology. In such a scenario, the performance may be enhanced if MtrC is functionalized with an external electrocatalyst to facilitate electron exchange with the cells. Furthermore, using external photoelectrocatalysts will have the additional advantage of allowing reactions to be driven by the energy of sunlight to achieve semiartificial photosynthesis in a living organism (**Figure 8C**).

While such opportunities are exciting, the direct labeling of bacteria with (photo-)electrocatalysts is likely to provide a challenge, not least the possibility that labeling reactions might compromise cell viability. By demonstrating spontaneous formation of a stable and functional complex able to transfer electrons across a lipid bilayer, this work suggests an alternative route to assembling such biohybrids (**Figure 8C**). In the first step, selective *in vitro* functionalization of purified, soluble

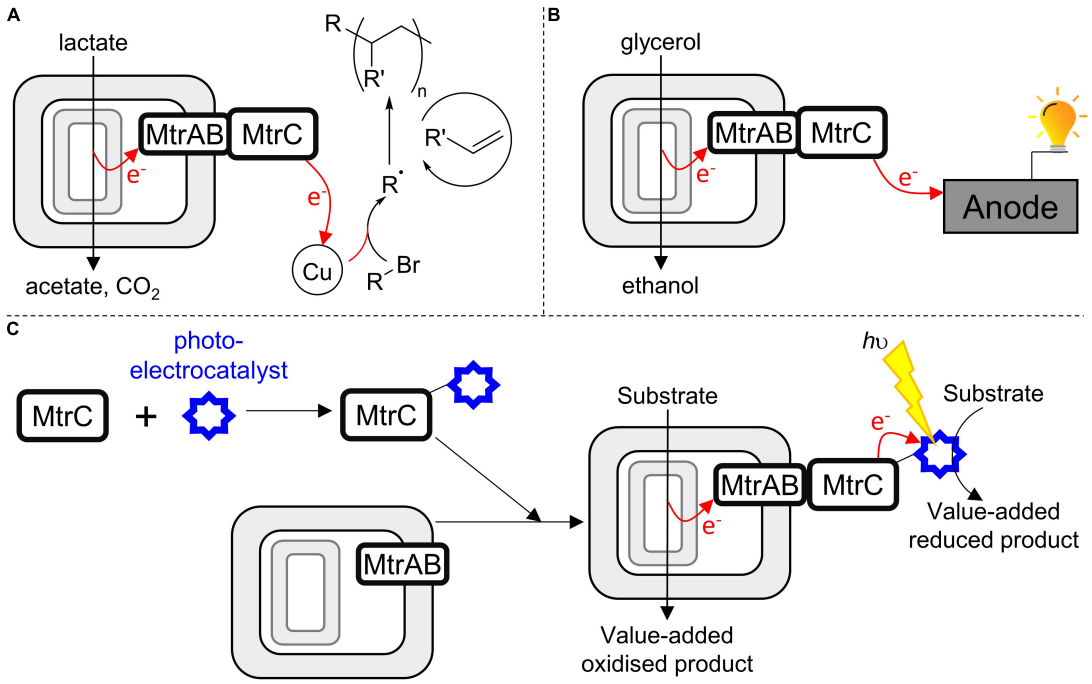

FIGURE 8 | Harnessing the MTR complex to couple internal (biological) and external (synthetic) catalysts in a closed redox cycle. **(A)** *S. oneidensis* as a living electrode driving an exogenous copper-based catalyst to produce radicals, these initiate olefin polymerization (Fan et al., 2018). **(B)** *S. oneidensis* performing electrode-assisted glycerol oxidation (Flynn et al., 2010). **(C)** A strategy to engineer bacteria for semiartificial photosynthesis motivated by this work; soluble MtrC is functionalized with a photoelectrocatalyst and then assembles spontaneously with bacteria presenting MtrAB in their outer membrane; allowing intracellular substrate oxidation to be coupled to extracellular photoelectrocatalysis.

MtrC would be carried out under optimal conditions. Then, spontaneous association of functionalized MtrC with cells presenting MtrAB in their outer membrane would afford assembly of the desired biohybrid materials through a strategy that makes a virtue of the intrinsic modularity of the MTR complex. With regard to this strategy, do conditions exist whereby functional MtrC:MtrAB complexes can be assembled by combining soluble, functionalized MtrC with bacteria presenting MtrAB in their outer membranes? Experiments to assess this possibility are ongoing in our laboratories. We also aim to engineer the coupling of MtrC to photosensitizers more sustainable than Ru(II)-dyes, and that support faster light-driven electron accumulation in the protein.

In conclusion, we have demonstrated photoreduction of MtrC photosensitized by covalent linkage to an inorganic dye. We have also established that the structure and electron transfer properties of the complex formed when functionalized MtrC associates with MtrAB *in vitro* are comparable with those of the native MTR complex. Together, these observations lay the foundations for rational engineering of the MtrC:MtrAB complex for novel synthetic biology for enhanced biotechnology of *Shewanella* and heterologous hosts such as *Escherichia coli* (Schuergers et al., 2017; Su and Ajo-Franklin, 2019).

DATA AVAILABILITY STATEMENT

The datasets presented in this study can be found in online repositories. The names of the repository/repositories and accession number(s) can be found below: http://www.sasbdb.org/, SASDL97, SASDLA7; https://research-portal.uea.ac.uk/en/persons/julea-butt, no accession number.

AUTHOR CONTRIBUTIONS

JB, TC, SP, LJ, and ER designed research. SP, ME, JW, and AM performed the research. CC provided carbon dots. SP, JW, ME, AM, and TC analyzed data. JB, SP, ME, and TC wrote the manuscript. All authors provided critical feedback on the results and manuscript.

FUNDING

Funding was from the UK Biotechnology and Biological Sciences Research Council (BB/S002499/1, BB/S00159X/1, BB/S000704, and BB/P01819X/1 and a Doctoral Training Partnership Ph.D. studentship to SEHP) and Engineering and Physical Sciences Research Council (EP/M001989/1). Beamtime 8-03-986 was awarded for work at ILL (Grenoble, France). Access to transmission electron microscopy was provided through the EPSRC Multi-User Equipment Call (EP/P030467/1). Open access funding was provided by EP/W523288/1.

ACKNOWLEDGMENTS

We thank Dr. Simone Payne for assistance with protein purification and Dr. Sam Rowe for spectral characterization of the lights used for irradiation.

SUPPLEMENTARY MATERIAL

The Supplementary Material for this article can be found online at: https://www.frontiersin.org/articles/10.3389/fmicb.2021.714508/full#supplementary-material

REFERENCES

Barr, I., and Guo, F. (2015). Pyridine hemochromagen assay for determining the concentration of heme in purified protein solutions. *Bio Protoc.* 5:e1594.

Bose, A., Gardel, E. J., Vidoudez, C., Parra, E. A., and Girguis, P. R. (2014). Electron uptake by iron-oxidizing phototrophic bacteria. *Nat. Commun.* 5:3391.

Breuer, M., Rosso, K. M., Blumberger, J., and Butt, J. N. (2015). Multi-haem cytochromes in *Shewanella oneidensis* MR-1: structures, functions and opportunities. *J. R. Soc. Interface* 12:20141117. doi: 10.1098/rsif.2014.1117

Bursac, T., Gralnick, J. A., and Gescher, J. (2017). Acetoin production via unbalanced fermentation in *Shewanella oneidensis*. *Biotechnol. Bioeng.* 114, 1283–1289. doi: 10.1002/bit.26243

Castelle, C., Guiral, M., Malarte, G., Ledgham, F., Leroy, G., Brugna, M., et al. (2008). A new iron-oxidizing/O2-reducing supercomplex spanning both inner and outer membranes, isolated from the extreme acidophile *Acidithiobacillus ferrooxidans*. *J. Biol. Chem.* 283, 25803–25811. doi: 10.1074/jbc.m802496200

Chiranjeevi, P., and Patil, S. A. (2020). Strategies for improving the electroactivity and specific metabolic functionality of microorganisms for various microbial electrochemical technologies. *Biotechnol. Adv.* 39:107468. doi: 10.1016/j.biotechadv.2019.107468

Demeler, B. (2005). "UltraScan–a comprehensive data analysis software package for analytical ultracentrifugation experiments," in *Analytical Ultracentrifugation: Techniques and Methods*, eds D. J. Scott, S. E. Harding, and A. J. Rowe (Cambridge: Royal Society of Chemistry).

Edwards, M. J., White, G. F., Butt, J. N., Richardson, D. J., and Clarke, T. A. (2020). The crystal structure of a biological insulated transmembrane molecular wire. *Cell* 181, 665–673. doi: 10.1016/j.cell.2020.03.032

Edwards, M. J., White, G. F., Lockwood, C. W., Lawes, M. C., Martel, A., Harris, G., et al. (2018). Structural modeling of an outer membrane electron conduit from a metal-reducing bacterium suggests electron transfer via periplasmic redox partners. *J. Biol. Chem.* 293, 8103–8112. doi: 10.1074/jbc.ra118.001850

Edwards, M. J., White, G. F., Norman, M., Tome-Fernandez, A., Ainsworth, E., Shi, L., et al. (2015). Redox linked flavin sites in extracellular decaheme proteins involved in microbe-mineral electron transfer. *Sci. Rep.* 5:11677.

Fan, G., Dundas, C. M., Graham, A. J., Lynd, N. A., and Keitz, B. K. (2018). *Shewanella oneidensis* as a living electrode for controlled radical polymerization. *Proc. Natl. Acad. Sci. U.S.A.* 115, 4559–4564. doi: 10.1073/pnas.1800869115

Flynn, J. M., Ross, D. E., Hunt, K. A., Bond, D. R., and Gralnick, J. A. (2010). Enabling unbalanced fermentations by using engineered electrode-interfaced bacteria. *mBio* 1:e00190-10.

Franke, D., and Svergun, D. I. (2009). DAMMIF, a program for rapid ab-initio shape determination in small-angle scattering. *J. Appl. Crystallogr.* 42, 342–346. doi: 10.1107/s0021889809000338

Fredrickson, J. K., Romine, M. F., Beliaev, A. S., Auchtung, J. M., Driscoll, M. E., Gardner, T. S., et al. (2008). Towards environmental systems biology of *Shewanella*. *Nat. Rev. Microbiol.* 6, 592–603.

Geren, L., Hahm, S., Durham, B., and Millett, F. (1991). Photoinduced electron-transfer between cytochrome c peroxidase and yeast cytochrome c labeled at Cys-102 with (4-bromomethyl-4'-methylbipyridine)[bis(bipyridine)]Ruthenium2+. *Biochemistry* 30, 9450–9457. doi: 10.1021/bi00103a009

Gupta, D., Sutherland, M. C., Rengasamy, K., Meacham, J. M., Kranz, R. G., and Bose, A. (2019). Photoferrotrophs produce a PioAB electron conduit for extracellular electron uptake. *mBio* 10:e02668-19.

Hartshorne, R. S., Reardon, C. L., Ross, D., Nuester, J., Clarke, T. A., Gates, A. J., et al. (2009). Characterization of an electron conduit between bacteria and the extracellular environment. *Proc. Natl. Acad. Sci. U.S.A.* 106, 22169–22174. doi: 10.1073/pnas.0900086106

Hatchard, C. G., and Parker, C. A. (1956). A new sensitive chemical actinometer .2. Potassium ferrioxalate as a standard chemical actinometer. *Proc. R. Soc. Lond. A Math. Phys. Sci.* 235, 518–536. doi: 10.1098/rspa.1956.0102

Jiang, X. Y., Burger, B., Gajdos, F., Bortolotti, C., Futera, Z., Breuer, M., et al. (2019). Kinetics of trifurcated electron flow in the decaheme bacterial proteins MtrC and MtrF. *Proc. Natl. Acad. Sci. U.S.A.* 116, 3425–3430. doi: 10.1073/pnas.1818003116

Jiang, X. Y., van Wonderen, J. H., Butt, J. N., Edwards, M. J., Clarke, T. A., and Blumberger, J. (2020). Which multi-heme protein complex transfers electrons more efficiently? Comparing MtrCAB from *Shewanella* with OmcS from Geobacter. *J. Phys. Chem. Lett.* 11, 9421–9425. doi: 10.1021/acs.jpclett.0c02842

Jin, M., Jiang, Y. M., Sun, L. L., Yin, J. H., Fu, H. H., Wu, G. F., et al. (2013). Unique organizational and functional features of the cytochrome c maturation system in *Shewanella oneidensis*. *PLoS One* 8:e75610. doi: 10.1371/journal.pone.0075610

Kato, S. (2015). Biotechnological aspects of microbial extracellular electron transfer. *Microbes Environ.* 30, 133–139. doi: 10.1264/jsme2.me15028

Kline, S. R. (2006). Reduction and analysis of SANS and USANS data using IGOR Pro. *J. Appl. Crystallogr.* 39, 895–900. doi: 10.1107/s0021889806035059

Kokhan, O., Ponomarenko, N. S., Pokkuluri, P. R., Schiffer, M., Mulfort, K. L., and Tiede, D. M. (2015). Bidirectional photoinduced electron transfer in Ruthenium(II)-tris-bipyridyl-modified PpcA, a multi-heme c-type cytochrome from *Geobacter sulfurreducens*. *J. Phys. Chem. B* 119, 7612–7624. doi: 10.1021/jp511558f

Kozin, M. B., and Svergun, D. I. (2001). Automated matching of high- and low-resolution structural models. *J. Appl. Crystallogr.* 34, 33–41. doi: 10.1107/s0021889800014126

Lebowitz, J., Lewis, M. S., and Schuck, P. (2002). Modern analytical ultracentrifugation in protein science: a tutorial review. *Protein Sci.* 11, 2067–2079. doi: 10.1110/ps.0207702

Li, D. B., Edwards, M. J., Blake, A. W., Newton-Payne, S. E., Piper, S. E. H., Jenner, L. P., et al. (2020). His/Met heme ligation in the PioA outer membrane cytochrome enabling light-driven extracellular electron transfer by *Rhodopseudomonas palustris* TIE-1. *Nanotechnology* 31:354002. doi: 10.1088/1361-6528/ab92c7

Liu, Y. M., Wang, Z. M., Liu, J., Levar, C., Edwards, M. J., Babauta, J. T., et al. (2014). A trans-outer membrane porin-cytochrome protein complex for extracellular electron transfer by *Geobacter sulfurreducens* PCA. *Environ. Microbiol. Rep.* 6, 776–785. doi: 10.1111/1758-2229.12204

Lockwood, C. W. J., van Wonderen, J. H., Edwards, M. J., Piper, S. E. H., White, G. F., Newton-Payne, S., et al. (2018). Membrane-spanning electron transfer proteins from electrogenic bacteria: production and investigation. *Methods Enzymol.* 613, 257–275. doi: 10.1016/bs.mie.2018.10.011

Manalastas-Cantos, K., Konarev, P. V., Hajizadeh, N. R., Kikhney, A. G., Petoukhov, M. V., Molodenskiy, D. S., et al. (2021). ATSAS 3.0: expanded functionality and new tools for small-angle scattering data analysis. *J. Appl. Crystallogr.* 54, 343–355. doi: 10.1107/s1600576720013412

Marsili, E., Baron, D. B., Shikhare, I. D., Coursolle, D., Gralnick, J. A., and Bond, D. R. (2008). *Shewanella* secretes flavins that mediate extracellular electron transfer. *Proc. Natl. Acad. Sci. U.S.A.* 105, 3968–3973. doi: 10.1073/pnas.0710525105

Martindale, B. C. M., Hutton, G. A. M., Caputo, C. A., Prantl, S., Godin, R., Durrant, J. R., et al. (2017). Enhancing light absorption and charge transfer efficiency in carbon dots through graphitization and core nitrogen doping. *Angew. Chem.* 56, 6459–6463. doi: 10.1002/anie.201700949

McMillan, D. G. G., Marritt, S. J., Butt, J. N., and Jeuken, L. J. C. (2012). Menaquinone-7 is specific cofactor in tetraheme quinol dehydrogenase CymA. *J. Biol. Chem.* 287, 14215–14225. doi: 10.1074/jbc.m112.348813

Millett, F., and Durham, B. (2002). Design of photoactive ruthenium complexes to study interprotein electron transfer. *Biochemistry* 41, 11315–11324. doi: 10.1021/bi0262956

Myers, J. M., and Myers, C. R. (2001). Role for outer membrane cytochromes OmcA and OmcB of *Shewanella putrefaciens* MR-1 in reduction of manganese dioxide. *Appl. Environ. Microb.* 67, 260–269. doi: 10.1128/aem.67.1.260-269.2001

Nealson, K. H. (2017). Bioelectricity (electromicrobiology) and sustainability. *Microb. Biotechnol.* 10, 1114–1119. doi: 10.1111/1751-7915.12834

Okamoto, A., Tokunou, Y., Kalathil, S., and Hashimoto, K. (2017). Proton transport in the outer-membrane flavocytochrome complex limits the rate of extracellular electron transport. *Angew. Chem.* 56, 9082–9086. doi: 10.1002/anie.201704241

Paradies, H. H. (1980). Shape and size of a non-ionic surfactant micelle. Triton X-100 in aqueous solution. *J. Phys. Chem.* 84, 599–607. doi: 10.1021/j100443a008

Pitre, S. P., McTiernan, C. D., Vine, W., DiPucchio, R., Grenier, M., and Scaiano, J. C. (2015). Visible-light actinometry and intermittent illumination as convenient tools to study Ru(bpy)3Cl2 mediated photoredox transformations. *Sci. Rep.* 5:16397.

Ross, D. E., Flynn, J. M., Baron, D. B., Gralnick, J. A., and Bond, D. R. (2011). Towards electrosynthesis in *Shewanella*: energetics of reversing the Mtr pathway for reductive metabolism. *PLoS One* 6:e16649. doi: 10.1371/journal.pone.0016649

Rowe, S. F., Le Gall, G., Ainsworth, E. V., Davies, J. A., Lockwood, C. W. J., Shi, L., et al. (2017). Light-driven H2 wvolution and C=C or C=O bond hydrogenation by *Shewanella oneidensis*: a versatile strategy for photocatalysis by nonphotosynthetic microorganisms. *ACS Catal.* 7, 7558–7566. doi: 10.1021/acscatal.7b02736

Santoro, C., Arbizzani, C., Erable, B., and Ieropoulos, I. (2017). Microbial fuel cells: from fundamentals to applications. A review. *J. Power Sources* 356, 225–244. doi: 10.1016/j.jpowsour.2017.03.109

Schicklberger, M., Bucking, C., Schuetz, B., Heide, H., and Gescher, J. (2011). Involvement of the *Shewanella oneidensis* decaheme cytochrome MtrA in the periplasmic stability of the beta-barrel protein MtrB. *Appl. Environ. Microb.* 77, 1520–1523. doi: 10.1128/aem.01201-10

Schroder, U., Harnisch, F., and Angenent, L. T. (2015). Microbial electrochemistry and technology: terminology and classification. *Energy Environ. Sci.* 8, 513–519. doi: 10.1039/c4ee03359k

Schuergers, N., Werlang, C., Ajo-Franklin, C. M., and Boghossian, A. A. (2017). A synthetic biology approach to engineering living photovoltaics. *Energy Environ. Sci.* 10, 1102–1115. doi: 10.1039/c7ee00282c

Shi, L., Chen, B. W., Wang, Z. M., Elias, D. A., Mayer, M. U., Gorby, Y. A., et al. (2006). Isolation of a high-affinity functional protein complex between OmcA and MtrC: two outer membrane decaheme c-type cytochromes of *Shewanella oneidensis* MR-1. *J. Bacteriol.* 188, 4705–4714. doi: 10.1128/jb.01966-05

Shi, L., Deng, S., Marshall, M. J., Wang, Z. M., Kennedy, D. W., Dohnalkova, A. C., et al. (2008). Direct involvement of type II secretion system in extracellular translocation of *Shewanella oneidensis* outer membrane cytochromes MtrC and OmcA. *J. Bacteriol.* 190, 5512–5516. doi: 10.1128/jb.00514-08

Shi, L., Rosso, K. M., Clarke, T. A., Richardson, D. J., Zachara, J. M., and Fredrickson, J. K. (2012). Molecular underpinnings of Fe(III) oxide reduction by *Shewanella oneidensis* MR-1. *Front. Microbiol.* 3:50. doi: 10.3389/fmicb.2012.00050

Stikane, A., Hwang, E. T., Ainsworth, E. V., Piper, S. E. H., Critchley, K., Butt, J. N., et al. (2019). Towards compartmentalized photocatalysis: multihaem proteins as transmembrane molecular electron conduits. *Faraday Discuss.* 215, 26–38. doi: 10.1039/c8fd00163d

Sturm, G., Richter, K., Doetsch, A., Heide, H., Louro, R. O., and Gescher, J. (2015). A dynamic periplasmic electron transfer network enables respiratory flexibility beyond a thermodynamic regulatory regime. *ISME J.* 9, 1802–1811. doi: 10.1038/ismej.2014.264

Su, L., and Ajo-Franklin, C. M. (2019). Reaching full potential: bioelectrochemical systems for storing renewable energy in chemical bonds. *Curr. Opin. Biotech.* 57, 66–72. doi: 10.1016/j.copbio.2019.01.018

Svergun, D. I. (1992). Determination of the regularization parameter in indirect-transform methods using perceptual criteria. *J. Appl. Crystallogr.* 25, 495–503. doi: 10.1107/s0021889892001663

Svergun, D. I. (1999). Restoring low resolution structure of biological macromolecules from solution scattering using simulated annealing. *Biophys. J.* 76, 2879–2886. doi: 10.1016/s0006-3495(99)77443-6

Thomas, P. E., Ryan, D., and Levin, W. (1976). Improved staining procedure for detection of peroxidase-activity of cytochrome P-450 on sodium dodecyl-sulfate polyacrylamide gels. *Anal. Biochem.* 75, 168–176. doi: 10.1016/0003-2697(76)90067-1

van Wonderen, J. H., Hall, C. R., Jiang, X. Y., Adamczyk, K., Carof, A., Heisler, I., et al. (2019). Ultrafast light-driven electron transfer in a Ru(II)tris(bipyridine)-labeled multiheme cytochrome. *J. Am. Chem. Soc.* 141, 15190–15200. doi: 10.1021/jacs.9b06858

van Wonderen, J. H., Li, D. B., Piper, S. E. H., Lau, C. Y., Jenner, L. P., Hall, C. R., et al. (2018). Photosensitised multiheme cytochromes as light-driven molecular wires and resistors. *ChemBioChem* 19, 2206–2215. doi: 10.1002/cbic.201800313

Volkov, V. V., and Svergun, D. I. (2003). Uniqueness of ab initio shape determination in small-angle scattering. *J. Appl. Crystallogr.* 36, 860–864.

von Canstein, H., Ogawa, J., Shimizu, S., and Lloyd, J. R. (2008). Secretion of flavins by *Shewanella* species and their role in extracellular electron transfer. *Appl. Environ. Microb.* 74, 615–623. doi: 10.1128/aem.01387-07

White, G. F., Edwards, M. J., Gomez-Perez, L., Richardson, D. J., Butt, J. N., and Clarke, T. A. (2016). Mechanisms of bacterial extracellular electron exchange. *Adv. Microb. Physiol.* 68, 87–138. doi: 10.1016/bs.ampbs.2016.02.002

Yarzabal, A., Brasseur, G., Ratouchniak, J., Lund, K., Lemesle-Meunier, D., DeMoss, J. A., et al. (2002). The high-molecular-weight cytochrome c Cyc2 of *Acidithiobacillus ferrooxidans* is an outer membrane protein. *J. Bacteriol.* 184, 313–317. doi: 10.1128/jb.184.1.313-317.2002

Conflict of Interest: The authors declare that the research was conducted in the absence of any commercial or financial relationships that could be construed as a potential conflict of interest.

Publisher's Note: All claims expressed in this article are solely those of the authors and do not necessarily represent those of their affiliated organizations, or those of the publisher, the editors and the reviewers. Any product that may be evaluated in this article, or claim that may be made by its manufacturer, is not guaranteed or endorsed by the publisher.

frontiers in Microbiology

ORIGINAL RESEARCH
published: 01 September 2021
doi: 10.3389/fmicb.2021.722229

Understanding Metabolic Remodeling in *Mycobacterium smegmatis* to Overcome Energy Exigency and Reductive Stress Under Energy-Compromised State

*Varsha Patil and Vikas Jain**

Microbiology and Molecular Biology Laboratory, Department of Biological Sciences, Indian Institute of Science Education and Research, Bhopal, India

OPEN ACCESS

Edited by:
Davide Zannoni, University of Bologna, Italy

Reviewed by:
Jianping Xie, Southwest University, China
Hugo Gramajo, CONICET Instituto de Biología Molecular y Celular de Rosario (IBR), Argentina

***Correspondence:**
Vikas Jain
vikas@iiserb.ac.in

Specialty section:
This article was submitted to Microbial Physiology and Metabolism, a section of the journal Frontiers in Microbiology

Received: *08 June 2021*
Accepted: *11 August 2021*
Published: *01 September 2021*

Citation:
Patil V and Jain V (2021) Understanding Metabolic Remodeling in Mycobacterium smegmatis to Overcome Energy Exigency and Reductive Stress Under Energy-Compromised State. Front. Microbiol. 12:722229. doi: 10.3389/fmicb.2021.722229

Mycobacteria such as *Mycobacterium tuberculosis*, the causative agent of tuberculosis that annually kills several million people worldwide, and *Mycobacterium smegmatis*, the non-pathogenic fast-growing mycobacteria, require oxidative phosphorylation to meet their energy requirements. We have previously shown that deletion of one of the two copies of *atpD* gene that codes for the ATP synthase β-subunit establishes an energy-compromised state in *M. smegmatis*. Here we report that upon such deletion, a major routing of electron flux occurs through the less energy-efficient complexes of its respiratory chain. Δ*atpD* bacterium also shows an increased reduced state which is further confirmed by the overexpression of WhiB3, a major redox sensor. We show a substantial modulation of the biosynthesis of cell wall associated lipids and triacylglycerol (TAG). An accumulation of TAG-containing lipid bodies is further confirmed by using ^{14}C oleate incorporation. Interestingly, the mutant also shows an overexpression of TAG-degrading lipase genes, and the intracellular lipolytic enzymes mediate TAG hydrolysis for their utilization as energy source. We believe that our *in vitro* energy-depleted model will allow us to explore the critical link between energy metabolism, redox homeostasis, and lipid biosynthesis during ATP-depleted state, which will enhance our understanding of the bacterial adaptation, and will allow us to identify novel drug targets to counter mycobacterial infections.

Keywords: mycobacteria, lipid metabolism, triacylglycerol, ATP synthase, lipid bodies, redox regulation

INTRODUCTION

Tuberculosis, caused by the bacterium *Mycobacterium tuberculosis*, is one of the serious public health concerns globally (Eisinger et al., 2020). *M. tuberculosis* is known to reside in a dormant state for prolonged period, and targeting such dormant *M. tuberculosis* is a big challenge for the current chemotherapeutic approaches (Gengenbacher and Kaufmann, 2012). Thus, a continuous arms race between human and mycobacteria is leading to the discovery and development of novel drug targets and therapeutics against *M. tuberculosis*.

Oxidative phosphorylation (OXPHOS) is an efficient pathway to sustain bacterial growth and survival (Bald et al., 2017). During this process, electrons obtained through the donors of central metabolic pathways are transferred from the respiratory complexes to O_2 *via* electron transport chain (ETC) (Matsoso et al., 2005). This highly flexible respiratory chain in mycobacteria consist of various membrane-embedded electron carrier molecules and enzymes that mediate the transfer of electron, which is coupled with the generation of proton motive force (PMF) that drives ATP synthesis (Cook et al., 2014). The electron travels from complex-I (NADH dehydrogenase) to complex-II (succinate dehydrogenase) with the help of electron carrier molecule menaquinone. The chain is terminated *via* two terminal oxidases namely *aa3*-type cytochrome *c* oxidase (supercomplex along with cytochrome *bc1* and cytochrome *c*) and cytochrome *bd* oxidase which eventually catalyzes the reduction of O_2 to water molecule by using the electrons from menaquinone and cytochrome *c*, respectively (Kana et al., 2001; Matsoso et al., 2005). Previous studies suggest that in *Mycobacterium smegmatis* during low growth rate and low air saturation (0.6%), the cytochrome *bd* oxidase complex is upregulated >50-fold, which exemplifies the importance of cytochrome *bd* at low O_2 rates (Berney and Cook, 2010). Moreover during hypoxia under the inhibitory conditions of cytochrome *bc1-aa3* oxidase complex, cytochrome *bd* has been shown to play an important role in cell survival (Kana et al., 2001; Cook et al., 2014). Furthermore, the involvement of cytochrome *bd* in adaptation of *M. tuberculosis* toward adverse environmental conditions is very well known (Giuffre et al., 2012; Forte et al., 2016). Hence, respiration plays a very important role in mycobacterial survival in order to respond and adapt toward different environmental niche and stress conditions.

The inhibition of respiratory chain may occur either by suppression of the respiratory complexes (Lamprecht et al., 2016; Moosa et al., 2017) or due to an exposure to external stress factors such as hypoxia, nutrient deficiency, acid, NO, CO, etc., which eventually influence the redox environment of the cell by making the electron carriers more reduced (Cook et al., 2014; Iqbal et al., 2018; Akela and Kumar, 2021). Hypoxia is known to induce reactive oxygen species (ROS) (Brunelle et al., 2005), whereas NO acts as one of the major antimicrobial stress agents generating reactive nitrogen species (RNS) in the cell, thereby leading to the fluctuations in redox state (Mehta and Singh, 2019). This necessitates mycobacteria to respond toward the environmental variations to maintain homeostasis. In order to defend from the internal oxidants and reductants, mycobacteria has evolved with specific mechanisms that assist in maintaining an appropriate redox balance within the cell (Zhai et al., 2019). In *M. tuberculosis*, for example, it has been suggested that during reduced O_2 conditions, WhiB3 senses the changes in the intracellular redox environment leading to metabolic switchover to fatty acids as the preferred nutrient source for the cell (Mehta and Singh, 2019). The presence of 4Fe–4S cluster in WhiB3 helps in maintaining redox homeostasis *via* regulating the metabolism and polyketide biosynthesis in the cell, thereby assisting in the persistence of the pathogen within the host (Mehta and Singh, 2019). The metabolic dependency of *M. tuberculosis* upon host fatty acids and cholesterol ensures a long-term survival during the persistence phase of infection (Gomez and McKinney, 2004; Pandey and Sassetti, 2008). Nevertheless, how these fatty acids are acquired, stored, and further utilized is still unclear in mycobacteria.

We have previously shown that the deletion of one of the two copies of *atpD* gene that codes for the β-subunit of the ATP synthase machinery renders *M. smegmatis* in an energy-compromised state (Patil and Jain, 2019). In the present work, we investigated in detail the mechanism involved in this adaptation and report that in *M. smegmatis*, deletion of *atpD* results in the remodeling of the ETC with utilizing less efficient proton non-translocating complexes. This results in the establishment of a reductive stress in the cell, which is dissipated by a major redox sensor, WhiB3-mediated modulation of the biosynthesis of storage lipids (triacylglycerol). We have previously shown that in Δ*atpD*, β-oxidation is enhanced for the generation of energy (Patil and Jain, 2019). It, therefore, appears that *M. smegmatis* follows two distinctive and seemingly opposite pathways in order to adapt to a low-energy state. Our work here thus reveals a distinct relationship between lipid accumulation and its utilization in *M. smegmatis* under energy-compromised state, and that a respiratory shift drives the global cellular changes leading to redox imbalance and metabolic dependency on fatty acid. We believe that understanding these cellular characteristics and their modulation to stress is vital for the identification and development of novel therapeutic drug targets to treat mycobacterial infections.

RESULTS

We have previously shown that *M. smegmatis atpD* gene (MSMEG_4936), which codes for the β-subunit of F_0F_1 ATP synthase, is important for mycobacterial physiology and metabolism (Patil and Jain, 2019), and that the deletion of one of the two copies of *atpD* renders the bacterium in an energy-compromised state. In this manuscript, we explore the impact of this deletion on the physiology of *M. smegmatis* and address how cell adapts to this physiological state and survives.

Deletion of *atpD* Results in Altered Expression of the Respiratory Chain Complexes

To understand in detail how *M. smegmatis* adapts to and survive in the depleted energy state, we first looked into the highly flexible mycobacterial ETC and its complexes that facilitate mycobacterial survival by coordinating with the central metabolism under variety of environmental conditions. *M. smegmatis* consists of energy efficient type-I NADH dehydrogenase complex (NDH1), which is proton pumping in nature, encoded by *nuo* operon, and a proton non-pumping type-II NADH dehydrogenase complex (NDH2) encoded by *ndh* gene (MSMEG_3621). The two terminal oxidases utilized by mycobacterial ETC for reduction of oxygen include the energy-efficient cytochrome bc_1-aa_3 supercomplex

and the energetically less efficient cytochrome *bd* oxidase (Cook et al., 2014; Iqbal et al., 2018). The transfer of electron from these terminal oxidases generates a PMF, which is then subsequently utilized for ATP synthesis *via* F_0F_1 ATP synthase. Transcriptional analysis shows that while the genes belonging to type-I NADH dehydrogenase are downregulated (**Figure 1A**), the proton non-pumping type-II NADH dehydrogenase is upregulated (**Figure 1B**) in the Δ*atpD* strain as compared to the wild-type and the complemented strain. Similarly, the energy efficient terminal electron acceptor cytochrome bc_1-aa_3 complex is found to be transcriptionally repressed (**Figure 1C**), whereas the energetically less efficient cytochrome *bd* oxidase genes are found to be induced (**Figure 1D**). This shift in the mycobacterial respiration machinery observed here suggests a modification in the respiration from proton translocating to non-proton-translocating state in Δ*atpD*. Similar observations were also seen when *M. tuberculosis* was grown under hypoxia conditions (Shi et al., 2005), suggesting a conserved respiratory adaptation in both pathogenic *M. tuberculosis* and non-pathogenic *M. smegmatis*.

We next hypothesized that such a broad change in the ETC machinery will affect the intracellular concentration of H^+, which will result in an acidic pH in the cytoplasm and alter cellular membrane polarization. Hence we measured the changes in the membrane polarization by using a fluorescent dye $DiBAC_4(3)$ [Bis (1,3-dibutylbarbituric acid) trimethine oxonol], which readily diffuses across a depolarized membrane. Interestingly, the Δ*atpD* bacterium displayed increased fluorescence suggesting alteration in the membrane polarization as compared to the wild-type and the complemented strain (**Figure 1E**). Overall our data suggest that due to the deletion of single copy of *atpD*, the respiratory functions and energy production factors are maintained at a low level and result in altered membrane polarization.

Altered Membrane Polarization Disrupts Redox Homeostasis in Δ*atpD*, and Is Balanced by Lipid Biosynthesis

Membrane potential plays an important role in energy storage during OXPHOS (Zorova et al., 2018). Previous studies suggest that bacteria possess a remarkable ability to maintain their membrane polarized, even during external stress (Prindle et al., 2015; Blee et al., 2020). A sharp decline in the membrane potential is considered dangerous to the cell, due to its inefficiency to produce ATP and leading to the generation of reductive stress in the cell (Zorova et al., 2018), which leads to slow down of respiratory complexes (Akela and Kumar, 2021). Furthermore, we have previously shown that Msm Δ*atpD* has reduced levels of ATP with increased ROS and high $NADH/NAD^+$ ratio, indicating an imbalanced redox state within the cell (Patil and Jain, 2019). We, therefore, asked how cell manages this intracellular redox imbalance in order to replenish the depleted NAD^+ levels for survival. It has been suggested that *dosS/dosR* system functions as a prominent sensor for the extracellular redox signals such as reduced oxygen and NO levels (Kumar et al., 2007). WhiB3, on the other hand, is known as a major intracellular redox sensor in *M. tuberculosis*, which acts by maintaining the redox balance in the cell thereby regulating the central metabolism (Singh et al., 2009). *M. smegmatis* WhiB3 (MSMEG_1597) shares 79.8% identity with *M. tuberculosis* WhiB3 (Rv3416) (**Supplementary Figure 1**). Hence we hypothesized that in *M. smegmatis* under an energy-compromised state, WhiB3 acts as the major redox regulator involved in the dissipation of the reductive stress *via* synthesis of storage lipid. Therefore, we determined the expression level of WhiB3 in *M. smegmatis*, and found a threefold upregulation in its expression in *atpD* knock-out strain as compared to the wild-type and the *atpD*-complemented ($atpD^C$) strain (**Figure 2A**). An upregulation in WhiB3 here clearly suggests that a redox state persists in *M. smegmatis* under energy-compromised state, which further corroborates with our previous study (Patil and Jain, 2019).

Furthermore, since WhiB3 in *M. tuberculosis* is known to be a positive transcriptional regulator for lipid biosynthesis genes such as those involved in polyketide biosynthesis (*pks*) and complex cell wall-associated lipids (Singh et al., 2009), we determined the mRNA expression level of MSMEG_4727 (*pks5*), which is a homolog of *M. tuberculosis pks2* with 65% identity (**Supplementary Figure 2**), MSMEG_0408 (*pks1*) (**Figure 2B**), trehalose di-mycolate (TDM) (mycolyltransferases) genes in *M. smegmatis* (Ojha et al., 2010) such as MSMEG_6398 and MSMEG_2078 (**Figure 2C**), MSMEG_4731, involved in the synthesis of polymethyl-branched fatty acids (Tran et al., 2019) in *M. smegmatis* (**Figure 2D**), and the polyketide synthase-associated protein (Pap) gene such as MSMEG_4728 (Onwueme et al., 2004; Tran et al., 2019), and *mmpL*, MSMEG_4741 (**Figure 2E**), which is posited to encode the enzymes involved in the synthesis and transport of glycolipids such as GPL, lipo-oligosaccharide (LOS), and sulfolipid-1 (Tran et al., 2019). Interestingly, we found an upregulation of all the cell wall-associated genes. During hypoxia, since the respiratory chain is down-regulated, *M. tuberculosis* is known to regenerate NAD^+ from NADH *via* WhiB3, thereby sensing the intracellular redox alterations and causing the metabolic switchover to fatty acids as the preferred carbon source (Singh et al., 2009). Such metabolic shift induced by WhiB3 is known to regulate the production of methyl branched polyketides (PAT/DAT, SL-1, and PDIM) and TAG (Singh et al., 2009). Hence the observed overexpression of WhiB3 and its role in modulating polyketide biosynthesis in *M. smegmatis* Δ*atpD* immediately suggest an important function played by WhiB3 in homeostasis maintenance *via* lipid biosynthesis and as a physiological redox regulator in *M. smegmatis* under energy-compromised state.

Loss of *atpD* Severely Affects the Cardiolipin Content in *M. smegmatis* Cell Membrane and Altered Mycolic Acid Levels Leading to Loss of Acid Fastness

Since in Msm Δ*atpD*, an upregulation in WhiB3 suggests dissipation of reductive stress *via* lipid biosynthesis, at this juncture, an analysis of the lipid content of the cell becomes extremely important. Cell membrane lipids are known to play

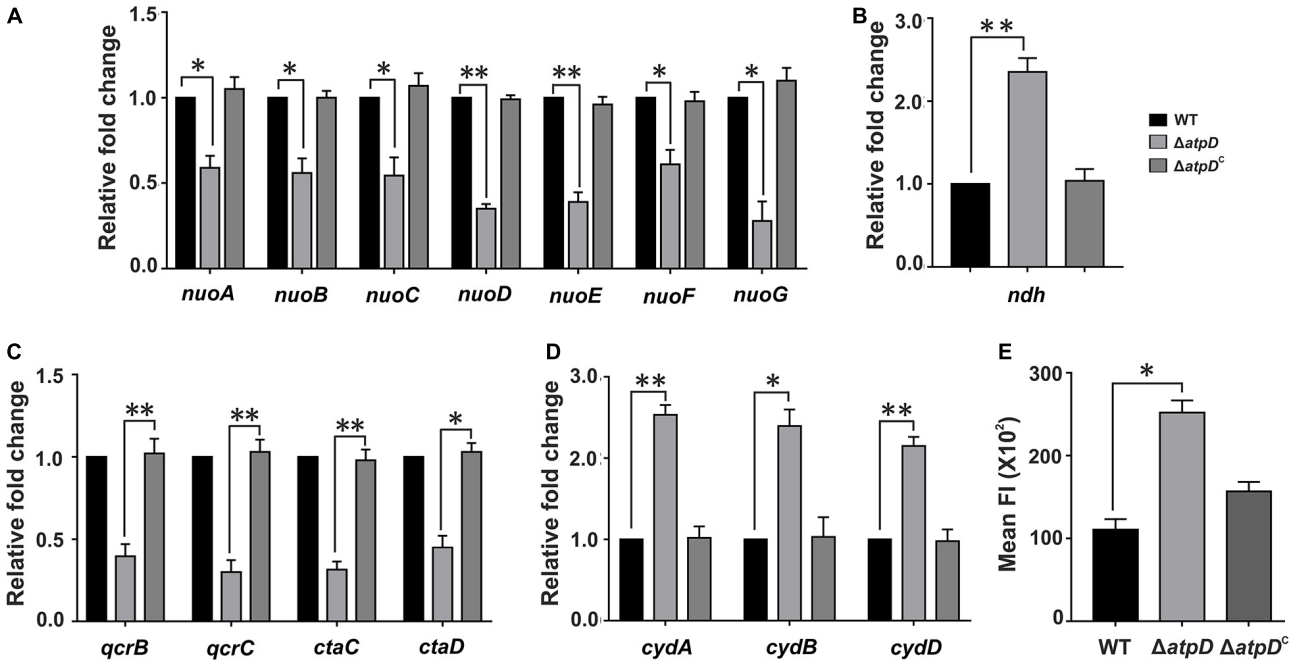

FIGURE 1 | Transcriptional changes in the respiratory chain complexes and an altered membrane polarization in *M. smegmatis* Δ*atpD*. Plots show the expression profiles for genes belonging to NDH1 complex (*nuo* operon, **A**), NDH2 complex (*ndh*, **B**), cytochrome *bc1-aa3* complex (*qcr* and *cta*, **C**), and cytochrome-*bd* oxidase complex (*cyd*, **D**) in *M. smegmatis* wild-type (WT), *atpD* knock out (Δ*atpD*), and *atpD*-complemented (Δ*atpD*^{C}) strains. Panel **(E)** shows the membrane polarization in all the three strains as monitored by $DiBAC_4(3)$ dye. In panels **(A–D)**, the transcript level in each case is compared with that of *M. smegmatis* WT, which is taken as 1. In all the panels, data represent an average of at least three independent experiments with error bars representing standard deviation. **P*-value < 0.05; ***P*-value < 0.01.

a crucial role in the membrane dynamics during growth and stress (Stallings and Glickman, 2010; Queiroz and Riley, 2017). Mycobacterial cell membrane consists of a plethora of lipids, which function as the structural components and storage bodies for the cell (Queiroz and Riley, 2017). A general pathway for the biosynthesis of these lipids in mycobacteria is depicted in **Figure 3A**. Major structural and storage mycobacterial lipids include phospholipids such as the cardiolipin (CL), phosphatidylethanolamine (PE), phosphatidylinositol (PI), glycosylated PIs, phosphatidylserine (PS), phosphatidylglycerol (PG; a minor species in mycobacteria), and triacylglycerol (TAG), which is a neutral storage lipid for the cell (Crellin et al., 2013). Furthermore, out of the major phospholipids, CL accounts for the maximum amount (37%) of the total phospholipids in mycobacterial plasma membrane followed by PE (32%) and PI/PIMs (28%) (Crellin et al., 2013). We, therefore, first determined the levels of CL in all the three strains. CL is known to form aggregates within the membrane and is determined using Nonyl Acridine orange (NAO) fluorescent dye, which specifically binds to it (Mileykovskaya et al., 2001). Interestingly, the Δ*atpD* bacterium shows reduced fluorescence as compared to that of the wild-type and the complemented strain (**Figure 3B**), which is further corroborated well by the FACS analysis (**Figure 3C**). To gain further insight into the reduction in the cardiolipin levels in knock-out strain, we analyzed the mRNA expression level of plasma membrane biogenesis genes (depicted in **Figure 3D**) by reverse transcription-quantitative PCR (RT-qPCR). We observe several folds reduction in the expression of all the plasma membrane biogenesis genes (*pgsA1*, *pgsA2*, which is a putative cardiolipin synthase gene, and *pgsA3*) in the knock-out strain as compared to the wild-type and the complemented strain (**Figure 3E**). Overall, this significantly reduced fluorescence and the gene expression levels in the knock-out strain are together suggestive of low amounts of cardiolipin (CL) content in the Δ*atpD* strain as compared to the wild-type and the complemented strain. This also manifests a compromised cell envelope in *M. smegmatis* Δ*atpD* as shown in our previous study (Patil and Jain, 2019). Next we examined the levels of other major phospholipids in the cell such as Phosphatidylethanolamine or PE (*MSMEG_6851*), Phosphatidylserine or PS (*MSMEG_0860*), and Phosphatidylinositol or PI (*MSMEG_2933*) by RT-PCR as well as by monitoring the incorporation of ^{14}C oleic acid into phospholipids of all the three strains. Interestingly, our data show that the levels of these phospholipids remain almost unchanged in both wild-type and mutant strains (**Figure 3F** and **Supplementary Figure 3**). Taken together, these results suggest that the mycobacterial cell under energy-compromised state might depend on some other lipids in order to maintain survival.

Since mycolic acid acts as the major component of the mycobacterial cell wall, we next asked if the levels of mycolic acid are affected in *M. smegmatis* Δ*atpD*. To investigate this, we first examined the transcription level of the genes belonging

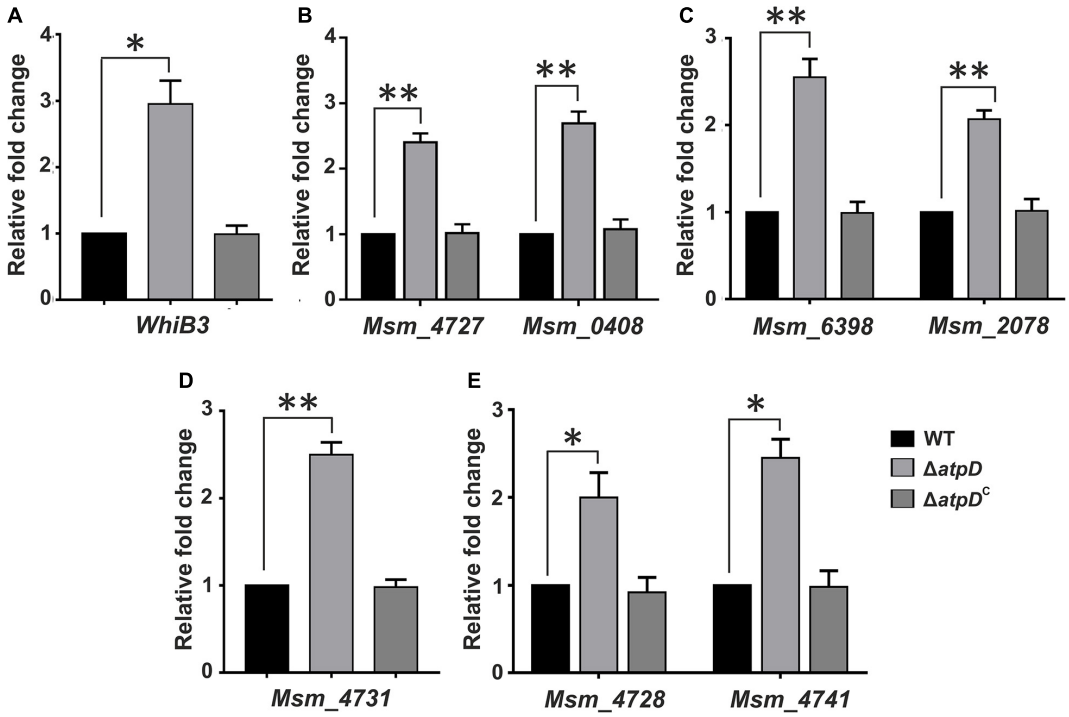

FIGURE 2 | *Mycobacterium smegmatis* Δ*atpD* shows redox homeostasis under energy-deprived state. Shown are the relative mRNA transcript levels of redox sensor gene WhiB3 **(A)**, polyketide biosynthesis genes **(B)**, trehalose di-mycolate (TDM) biosynthesis genes **(C)**, polymethyl-branched fatty acid gene **(D)**, and polyketide synthase-associated protein (Pap) and *mmpL* genes **(E)** in *M. smegmatis* wild-type (WT), *atpD* knock out (Δ*atpD*), and *atpD*-complemented (Δ*atpD*^{C}) strains. In all the panels, the transcript level in each case is compared with that of *M. smegmatis* WT, which is taken as 1. Data represent an average of at least three independent experiments with error bars representing standard deviation. **P*-value < 0.05; ***P*-value < 0.01.

to the FAS-I and FAS-II pathway involved in the biosynthesis of mycolic acid. Surprisingly, several-fold downregulation in the expression level of the genes belonging to the FAS-II and FAS-I pathway such as *fabD* (MSMEG_4325), *kasA* (MSMEG_4327), *kasB* (MSMEG_4328), *mabA* (MSMEG_3150), *accA3* (acetyl-CoA carboxylase; MSMEG_1807), *accD4* (MSMEG_6391), *accD6* (MSMEG_4329), and *fas* (MSMEG_4757) is observed in the *atpD* knock-out strain as compared to the wild-type and the complemented strain (**Figure 4A**). The observed downregulation in the FAS-I and FAS-II pathway genes suggests an alteration in mycolic acid levels (Shi et al., 2010) in the mutant as compared to the wild-type strain. Taken together, this indicates that the deletion of *atpD* gene negatively influences the *de novo* lipid biosynthesis. Further it is well known that alteration in the mycolic acid biosynthesis within the cell leads to loss of acid-fastness in mycobacteria (Daniel et al., 2011, 2016). Therefore, we investigated whether such phenotype is also shown by Δ*atpD*. Therefore, the cells were stained with Auramine-O (acid-fast staining green fluorescent dye), which stains mycolic acids present in the cell envelope of mycobacteria and has been widely used to determine the acid-fastness property of the cells. Here, the *atpD* knock-out strain shows reduced Auramine-O fluorescence indicating loss of acid fastness (**Figure 4B**). On the other hand, both the wild-type and the complemented bacteria (Δ*atpD*^{C}) are acid-fast positive as judged by the retention of Auramine-O fluorescence (**Figure 4B**). Additionally, the mutant shows increased Nile red fluorescence, which is indicative of neutral lipid accumulation, as compared to the wild-type and the complemented strain (**Figure 4B**). Further, in order to obtain a quantitative estimation, we analyzed Auramine-O and Nile red fluorescence *via* FACS analysis and also measured the fluorescence on a SpectraMax multimode plate reader. Our results clearly show a significant reduction in the Auramine-O fluorescence and a drastic increase in the Nile red fluorescence in Δ*atpD* strain as compared to the wild-type and the complemented strain (**Figures 4C,D**). It is worth mentioning here that loss of acid-fastness is a feature reported for dormant mycobacteria (Daniel et al., 2011, 2016). Altogether, this remarkable alteration in the cardiolipin, other phospholipids, and mycolic acid levels in Δ*atpD* strongly points toward a significant rerouting of the lipid metabolism to other form in the mutant strain under energy-compromised state.

Upregulation of WhiB3 Promotes Physiological and Metabolic Adaptations by Increasing TAG Accumulation in *M. smegmatis* Under Energy-Compromised State

In *M. tuberculosis*, WhiB3 is suggested to modulate the differential production of cell wall associated and storage lipids

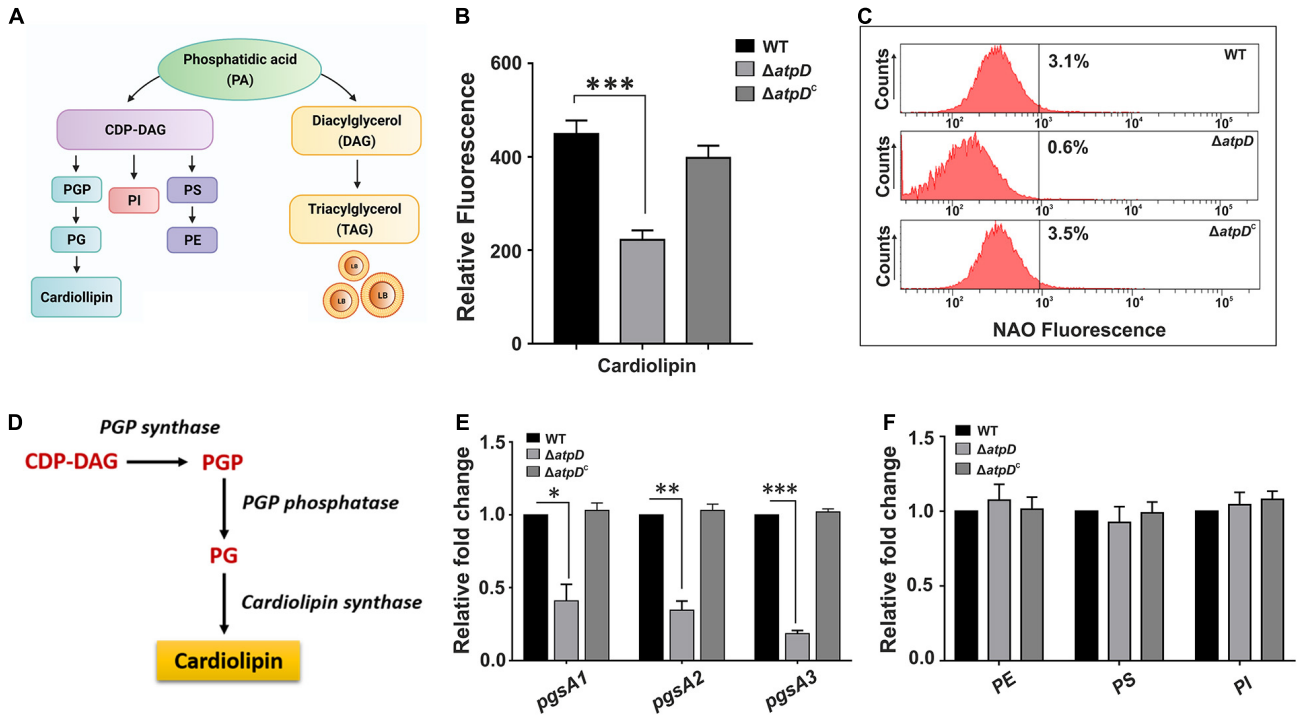

FIGURE 3 | *Mycobacterium smegmatis* Δ*atpD* shows reduced cardiolipin content. Panel **(A)** shows various mycobacterial membrane lipids along with the flow of key phospholipid biosynthesis pathways. PGP, phosphatidylglycerol phosphate; PG, phosphatidylglycerol; PI, phosphatidylinositol; PS, phosphatidylserine; PE, phosphatidylethanolamine; CDP-DAG, cytidine-diphosphate diacylglycerol. Panel **(B)** shows the Nonyl Acridine orange (NAO) dye fluorescence measured for *M. smegmatis* wild-type (WT), *atpD* knock-out (Δ*atpD*), and *atpD*-complemented (Δ*atpD*^{C}) strains. Panel **(C)** shows the flow cytometric analysis of all the three strains after staining the cells with NAO dye. The percentage value represents the fraction of cells that are positive for that fluorescence. Flow cytometry experiments were repeated at least thrice; the graph shows only one representative data. Panel **(D)** shows the cardiolipin biosynthesis pathway in mycobacteria. Panel **(E)** shows the gene expression analysis for plasma membrane biosynthesis genes *pgsA1, pgsA2*, and *pgsA3* by RT-qPCR in *M. smegmatis* wild-type, Δ*atpD*, and Δ*atpD*^{C} strains. Panel **(F)** shows the relative expression level of major structural genes – *MSMEG_6851* (phosphatidylethanolamine or PE), *MSMEG_0860* (phosphatidylserine or PS), and *MSMEG_2933* (phosphatidylinositol or PI) in *M. smegmatis* wild-type, Δ*atpD*, and Δ*atpD*^{C} strains. In both panels **(E,F)**, the transcript level in each case is compared with that of *M. smegmatis* WT, which is taken as 1. In panels **(B,E,F)**, data represent an average of at least three independent experiments with standard deviation shown as error bars. **P*-value < 0.05; ***P*-value < 0.01; ****P*-value < 0.005. Panel **(A)** is created with www.BioRender.com.

via redox-dependent switching mechanism (Singh et al., 2009); our data also suggest a significant rerouting to some other form of lipid in Msm Δ*atpD*. Since TAG is the major storage lipid in mycobacteria (Daniel et al., 2011), we next explored the genetic basis of this phenomenon in Δ*atpD*, and examined the differential expression of the genes involved in TAG biosynthesis pathway, which is also known as Kennedy pathway in *M. smegmatis* (Maarsingh and Haydel, 2018). Interestingly, we find that the transcription profile of the genes coding for the enzymes catalyzing the TAG biosynthesis such as glycerol kinase (*glpK*, MSMEG_6759), glycerol-3-phosphate acyl transferase (GPAT, MSMEG_4703), acylglycerol phosphate acyltransferase (AGPAT, MSMEG_4284), and the two wax ester synthase/acyl-CoA:diacylglycerol acyltransferase (WSDGAT, MSMEG_1882, and MSMEG_4705), which catalyzes the final step of TAG biosynthesis, is upregulated in the Δ*atpD* mutant as compared to the wild-type and the complemented strain (**Figure 5A**). In *M. tuberculosis*, *tgs1* is known to be the major TAG synthase gene (Daniel et al., 2004), and we found the two homologs of *tgs1* genes in *M. smegmatis*, MSMEG_5242 and MSMEG_3948, which bear significant similarity (69%) with the *M. tuberculosis tgs1* (**Supplementary Figure 4**). Interestingly, the transcript levels of these genes are also found to be higher (**Figure 5A**), which strongly suggests that this phenomenon may be conserved in *M. tuberculosis* as well. We additionally noticed that in *M. tuberculosis*, *tgs1* gene is under direct control of *dosS/dosR* operon, and is highly overexpressed under stress conditions such as hypoxia, acidic environment, and under dormancy conditions (Daniel et al., 2011). Our previous report also showed an overexpression of dormancy regulon genes *dosS* and *dosR* that are the known mediators of *tgs1*-dependent TAG accumulation (Patil and Jain, 2019). Thus, an overexpression of TAG synthase genes in *M. smegmatis* Δ*atpD* (under an energy-compromised state) points toward the dormancy related metabolic state in the cell.

The upregulation of the Kennedy pathway in the Δ*atpD* mutant strongly supports our hypothesis that the mutant retains TAG as the major storage lipid. To further confirm this finding, the mutant cells were stained with Nile red dye that specifically stains neutral lipids within the cell. Our confocal microscopy

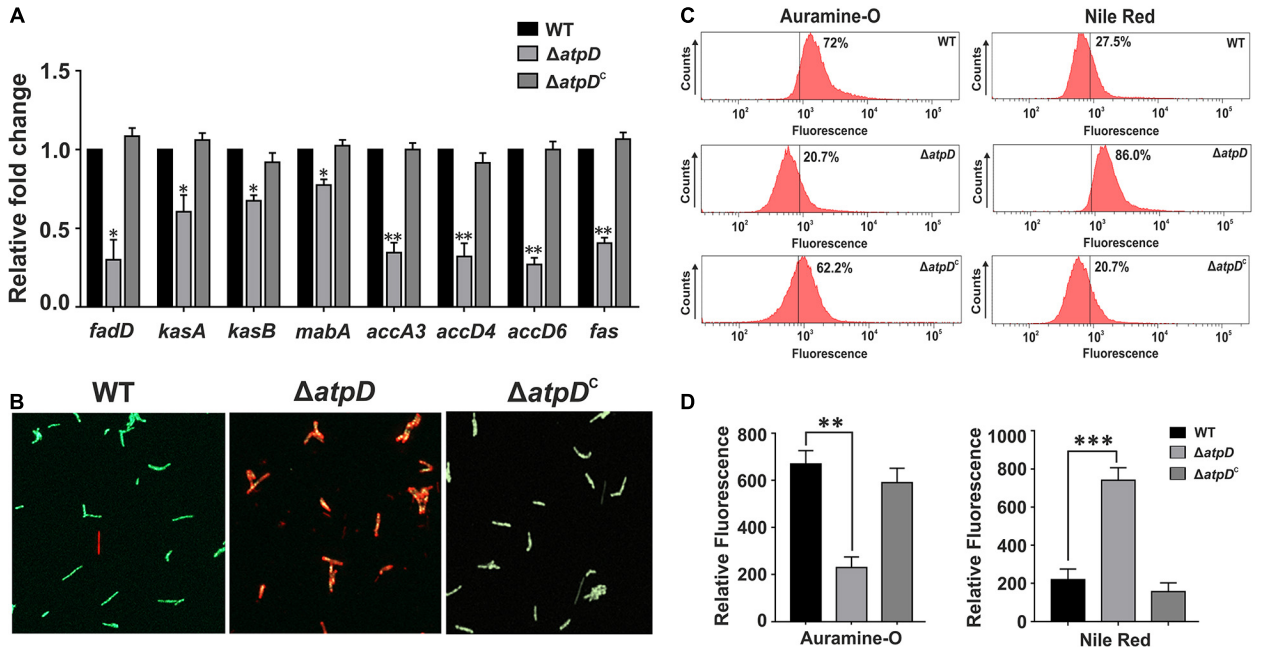

FIGURE 4 | *Mycobacterium smegmatis* shows reduced mycolic acid levels leading to loss of acid-fastness under energy-compromised state. Panel **(A)** shows the relative mRNA transcript levels of the genes belonging to the FAS-II and FAS-I lipid biosynthesis pathway genes such as *fabD* (MSMEG_4325), *kasA* (MSMEG_4327), *kasB* (MSMEG_4328), *mabA* (MSMEG_3150), *accA3* (acetyl-CoA carboxylase; MSMEG_1807), *accD4* (MSMEG_6391), *accD6* (MSMEG_4329), and *fas* (MSMEG_4757) in *M. smegmatis* wild-type (WT), *atpD* knock-out (Δ*atpD*), and *atpD*-complemented (Δ*atpD*^{C}) strains. The transcript level in each case is compared with that of *M. smegmatis* wild-type, which is taken as 1. Panel **(B)** shows the fluorescence microscopy images for the *M. smegmatis* WT, Δ*atpD*, and Δ*atpD*^{C} strains after staining the cells with Auramine-O and Nile red. Panel **(C)** shows the flow cytometric analysis of all the three strains after staining the cells with Auramine-O and Nile red dye, as mentioned. The percentage value represents the fraction of cells that are positive for that fluorescence. Flow cytometry experiments were repeated at least thrice. Panel **(D)** shows the quantification by measuring the fluorescence of Auramine-O and Nile red dyes as mentioned on fluorescence plate reader for *M. smegmatis* WT, Δ*atpD*, and Δ*atpD*^{C} strains. In all the panels, the experiments were repeated at least thrice. In both panels **(B,C)**, only one representative image is shown. In panels **(A,D)**, error bars represent standard deviation. **P*-value < 0.05; ***P*-value < 0.01; ****P*-value < 0.005.

data clearly shows the presence of large number of brightly stained lipid bodies (LBs) in the knockout strain (**Figure 5B**). Transmission electron microscopy (TEM) analysis of the clinical strains of *M. tuberculosis* carried out by Vijay and coworkers clearly demonstrated a distinct accumulation of LBs containing TAG (Vijay et al., 2017). Therefore, in order to visualize the LBs in *M. smegmatis*, we performed its ultrastructural analysis using TEM. Our data clearly show the presence of large amount of LBs in the Δ*atpD* bacterium as compared to the wild-type and the complemented strain (**Figures 5C,D**). We additionally examined the levels of TAG in the mycobacterial cells using thin layer chromatography (TLC) wherein the knock-out strain shows a clear accumulation of TAG as an intense band compared to that obtained in the wild-type and the complemented strain (**Figure 5E**). Furthermore, in order to confirm that the free fatty acids (FFAs) incorporated within the knockout cells are mainly stored as TAG rather that simple FFA or phospholipids (McCarthy, 1971; Weir et al., 1972; Nakagawa et al., 1976; Barksdale and Kim, 1977), we used ^{14}C oleic acid as a radiolabelled substrate and monitored the incorporation of ^{14}C oleic acid as it acts as the major component of TAG. All the three bacteria *viz.* wild-type, Δ*atpD*, and Δ*atpD*^{C} were grown in the presence ^{14}C-Oleic acid, and the radiolabeled lipids were extracted and analyzed by silica-based TLC. We observe that in the knock-out strain, the incorporation of ^{14}C-Oleic acid in TAG is significantly higher as compared to wild-type and complemented strain (**Supplementary Figure 5**). This further strengthens our observation that the *atpD* mutant retains TAG as the storage lipid.

TAG Hydrolysis Is Mediated by Intracellular Lipase Enzymes and the Consumption Can Be Blocked by Lipase Inhibitor

During dormancy, *M. tuberculosis* is known to utilize accumulated TAGs as energy source (Daniel et al., 2011), wherein FFAs are released *via* lipase-mediated hydrolysis, which further participate in β-oxidation. Therefore, in order to understand if *M. smegmatis* Δ*atpD* preferentially utilizes TAG as an energy source, we examined the expression profile of various intracellular lipase genes in *M. smegmatis*. Interestingly, we observe at least two- to threefold higher expression of several lipase (*lip*) genes such as *lipG*, *lipJ*, *lipI*, *lipN*, *lipO*, *lipT*, and *lipZ* in *M. smegmatis* Δ*atpD* as compared to the wild-type and the complemented bacterium (**Figure 6A**), indicating the possibility of enhanced TAG hydrolysis. In *M. tuberculosis*, lipase activity has been suggested to be regulated

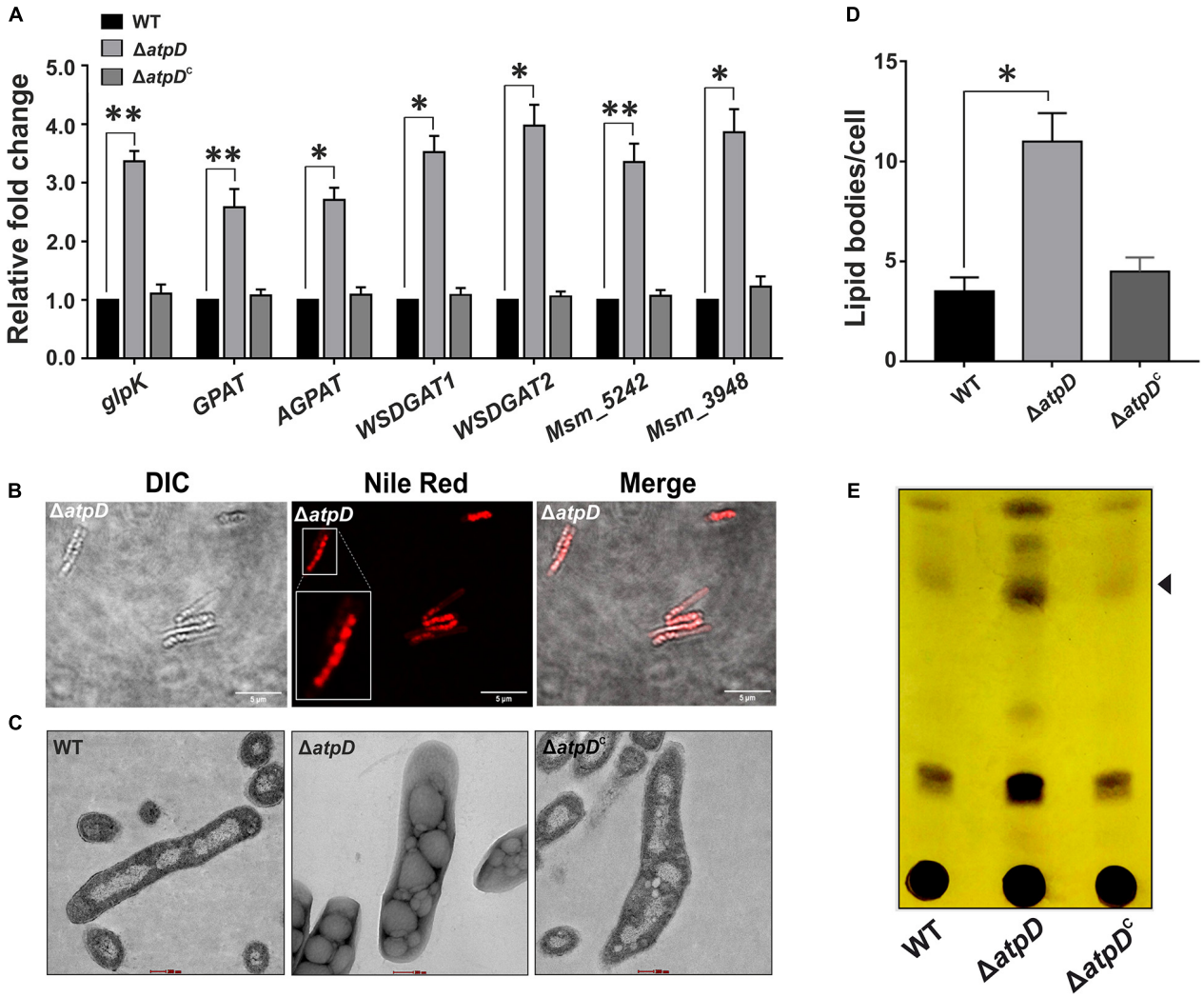

FIGURE 5 | Increased TAG accumulation in *M. smegmatis* under energy-compromised state. Panel **(A)** shows the relative mRNA transcript levels of genes belonging to Kennedy pathway such as glycerol kinase (*glpK*), glycerol-3 phosphate acyl transferase (*GPAT*), acylglycerol phosphate acyltransferase (*AGPAT*), two wax ester synthase/acyl-CoA: diacylglycerol acyltransferase (*WSDGAT*) and the TAG synthase genes (*MSMEG_3948* and *MSMEG_5242*; these are homologues of *tgs1* in *M. tuberculosis*) in *M. smegmatis* wild-type (WT), *atpD* knock-out (Δ*atpD*), and *atpD*-complemented (Δ*atpD*^{C}) strains. The transcript level in each case is compared with that of *M. smegmatis* WT, which is taken as 1. Panel **(B)** shows the confocal microscopy images after staining the cells with the Nile red dye. A single zoomed-in image in the Nile red panel is presented as inset for clarity. Panel **(C)** shows the transmission electron microscopy (TEM)-based ultrastructural analysis of all the three strains for the presence of lipid bodies (LBs). The scale bar in each image corresponds to 200 nm. Panel **(D)** shows the quantification of the LBs (n = 23) for the images obtained in panel **(C)**. Panel **(E)** depicts the TLC image presenting the TAG accumulation in *M. smegmatis* WT, *atpD* knock out (Δ*atpD*), and Δ*atpD*^{C} strains. Spot corresponding to the TAG is marked with an arrowhead. In panels **(A,D)**, data show an average of at least three independent experiments with error bars representing standard deviation. **P*-value < 0.05; ***P*-value < 0.01. In panels **(B,C,E)**, only one representative image is shown.

at post-translational level (Ravindran et al., 2014). Hence to confirm that enhanced lipase gene expression also results in enhanced lipase production, we measured the lipase activity in *M. smegmatis* Δ*atpD* in the presence and absence of a pathway-independent lipase inhibitor, tetrahydrolipstatin (THL). Lipase inhibitors are well-known to interfere with the lipid metabolism by impairing the activity of cellular lipolytic enzymes (Lass et al., 2011; Zechner et al., 2012). These lipid inhibitors are used to detect the molecular basis of TAG accumulation and its metabolism (Lass et al., 2011; Zechner et al., 2012). Our data show that in *M. smegmatis* Δ*atpD*, higher lipase expression coincides well with higher lipase activity that is reduced in the presence of inhibitor (**Figure 6B**). Overall our results suggest the importance of both accumulation and possible hydrolysis of TAGs for the energy production under an energy-compromised state.

In order to further confirm if Δ*atpD* preferentially utilizes TAG as an energy source, we monitored the TAG consumption in Δ*atpD*. We first grew the mutant strain for 24 h to allow for the accumulation of TAG. The cells were then transferred to a fresh medium without any carbon source and the TAG utilization was monitored for 48 h. Our results clearly show a linear decrease in

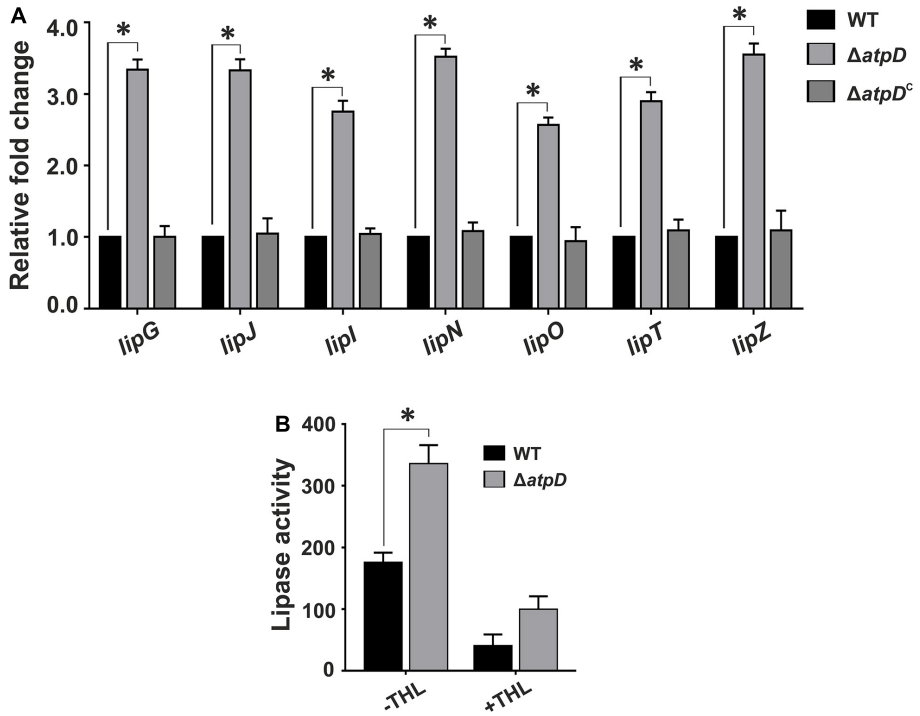

FIGURE 6 | *Mycobacterium smegmatis* Δ*atpD* shows higher lipase gene expression coupled with an increased lipase activity. Panel **(A)** shows the relative mRNA transcript levels of the lipase genes (*lipG, lipJ, lipI, lipN, lipO, lipT*, and *lipZ*) in *M. smegmatis* wild-type (WT), *atpD* knock out (Δ*atpD*), and *atpD*-complemented (Δ*atpD*^{C}) strains. The transcript level in each case is compared with that of *M. smegmatis* wild-type, which is taken as 1. Panel **(B)** shows the lipase activity in *M. smegmatis* WT and its *atpD* knock-out (Δ*atpD*) variant measured in the absence (–THL) and in the presence (+THL) of lipase inhibitor tetrahydrolipstatin (THL). In both the panels, data represent an average of at least three independent experiments with error bars depicting standard deviation. **P*-value < 0.05.

the relative TAG content as a function of time, which suggests TAG hydrolysis in the mutant strain (**Figures 7A,B**). To further confirm that mycobacterial lipases hydrolyze TAG, the mutant bacteria were treated with an increasing concentration of THL for 2 h. Thereafter, the cells were washed and resuspended in fresh medium containing increasing concentrations of THL (5, 50, and 100 μg/ml) and were further incubated for 24 h. The samples were collected and TAG content was analyzed by TLC. The data show no significant difference in the TAG levels at 2 h time point in the presence or absence of the inhibitor (**Figure 7C**). However, interestingly, after 24 h of incubation, while the untreated cells show a significant disappearance of TAG, the cells exposed to increasing concentration of THL show the presence of TAG (**Figures 7D,E**). Taken together, our data suggest that *M. smegmatis* utilizes stored LBs containing TAG during energy depletion state by means of hydrolyzing neutral lipids. We wish to add here that the TAG consumption in Δ*atpD* also depends upon the expression of endogenous lipase enzymes, which further leads to the release of FFA. These FFAs are then utilized by the cell fueling the lipid oxidation pathways such as β-oxidation supporting the cell survival. The end product of the β-oxidation pathway is acetyl-CoA, which is directly channeled into the glyoxylate shunt to acquire cellular energy, thereby utilizing fatty acid as the major carbon source (Serafini et al., 2019). Indeed an upregulation of the β-oxidation pathway and glyoxylate shunt in *M. smegmatis* Δ*atpD*, as shown previously (Patil and Jain, 2019), corroborates well with these observations.

Bedaquiline-Treated Wild-Type *M. smegmatis* Also Shows Increased WhiB3 Expression Coupled With TAG Accumulation and Lipase Gene Upregulation

Bedaquiline (BDQ) is known as the first-in-class ATP synthase inhibitor, having an extremely high selectivity for mycobacterial ATP synthase (Lakshmanan and Xavier, 2013). Upon BDQ exposure, *M. tuberculosis* has been shown to undergo significant metabolic remodeling along with reduced ATP/ADP levels (Koul et al., 2014; Akela and Kumar, 2021). BDQ inhibits bacterium's ability to utilize OXPHOS and forces the cell to rely upon substrate-level phosphorylation, thereby continuing with ATP generation (Smith et al., 2020). Although an adequate amount of energy is provided by substrate-level phosphorylation for the cell survival, mycobacteria majorly depend upon OXPHOS to sustain their basic energy requirements (Foo et al., 2020). Hence, BDQ treatment in mycobacteria is thought to disturb the cellular environment forcing the cell to reroute its metabolism to overcome the stressful condition.

An earlier work suggested that bactericidal antibiotics induce ROS formation in *M. tuberculosis* leading to alterations in

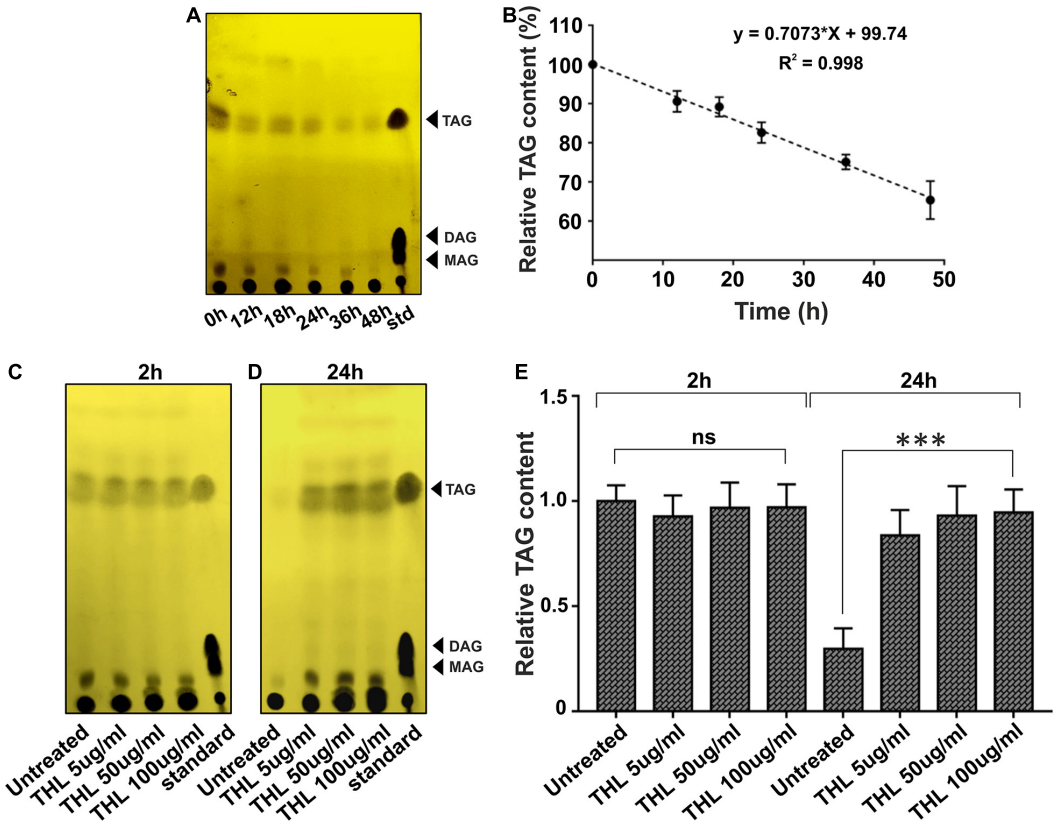

FIGURE 7 | Intracellular lipolytic enzymes mediate TAG hydrolysis in *M. smegmatis* Δ*atpD*. Panel **(A)** shows the TLC image for the triacylglycerol (TAG) accumulation and its disappearance in *M. smegmatis* Δ*atpD* upon starvation with time (in hours). TAG mobility was compared with standard (std). Spot corresponding to the TAG, diacylglycerol (DAG), and monoacylglycerol (MAG) is marked with an arrowhead. Panel **(B)** shows the relative quantification of TAG by densitometric analysis of the TLC with time (in hours). Here, 100% corresponds to the 0 h time point. Panels **(C,D)** depict the TLC image showing the TAG accumulation and disappearance after the treatment of cells with a lipase inhibitor tetrahydrolipstatin (THL) at 2 h **(C)** and 24 h **(D)** time period. "Untreated" represents cells without THL treatment. "standard" is similar to "std" in panel **(A)**. Panel **(E)** shows the relative TAG content as assessed by densitometric analysis of the TLC image, obtained before and after treating the cells with the increasing concentration of THL. The experiments were repeated at least thrice. In panels **(A,C,D)**, only one representative image is shown. In panels **(B,E)**, error bars represent standard deviation. ***P-value < 0.005; "ns," not significant.

cellular redox state (Dwyer et al., 2014). Additionally, BDQ in combination with other antibiotics such as clofazimine and telacebec is very well known to induce oxidative stress and ROS formation with increased cellular reductive stress in *M. tuberculosis* (Lamprecht et al., 2016). Furthermore, since *M. smegmatis* Δ*atpD* balances the cellular reductive stress *via* WhiB3 overexpression, we asked if this mechanism persists in *M. smegmatis* upon BDQ treatment also. Hence we determined the WhiB3 expression under BDQ-treated condition. Interestingly, BDQ-treated wild-type *M. smegmatis* shows ∼3.5-fold upregulation of the WhiB3 expression (**Figure 8A**). Moreover, since our previous report also suggests that *M. smegmatis* Δ*atpD* strain largely mimics BDQ-treated wild-type *M. smegmatis* (Patil and Jain, 2019), at this juncture, we asked if WhiB3 overexpression in BDQ-treated wild-type *M. smegmatis* also accumulates TAG, thereby dissipating the reductive stress and utilizing TAG as an energy source for the cell survival. Our results clearly show that BDQ-treated wild-type *M. smegmatis* also overexpresses TAG biosynthesis pathway genes (*glpK*, GPAT, AGPAT, WSDGAT1, WSDGAT2, MSMEG_3948, and MSMEG_5242) similar to the untreated Δ*atpD* strain (**Figure 8B**). Additionally, BDQ treatment also results in overexpression of lipase genes (**Figure 8C**), suggesting the possibility of increased TAG hydrolysis upon treatment with BDQ. These results strongly indicate that upon BDQ treatment, wild-type *M. smegmatis* stores as well as consumes TAG to meet its energy requirements, which mimics the Δ*atpD* strain in the absence of BDQ. This observation has a significant impact, since it is widely accepted that *M. tuberculosis* switches from carbohydrate to host fatty acids in the phagosome, and balances the reductive stress (Singh et al., 2009). Taken together, our data indicate a critical role of redox sensitive WhiB3 in regulating crucial aspects in mycobacterial physiology and survival during BDQ-treatment.

DISCUSSION

Mycobacterium tuberculosis exhibits a remarkable metabolic flexibility and robust ETC to survive under various stress

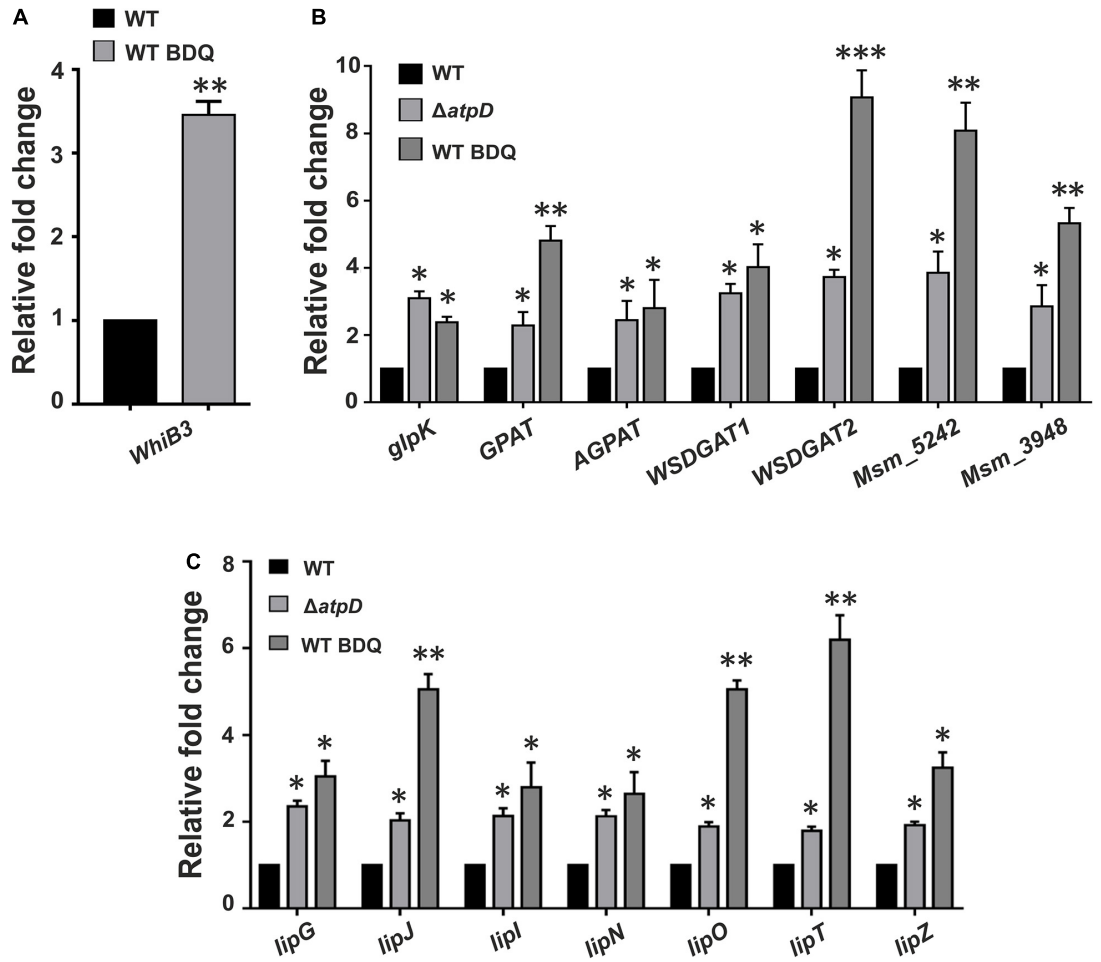

FIGURE 8 | Bedaquiline-treated wild-type *M. smegmatis* shows increased WhiB3 expression coupled with TAG accumulation and lipase gene upregulation. Panel **(A)** shows the mRNA transcript level of redox sensor WhiB3 in wild-type *M. smegmatis* cell either without (WT) or with bedaquiline (BDQ)-treatment (WT BDQ); for comparison with the *M. smegmatis atpD* knock-out strain, refer to **Figure 2A**. Panel **(B)** shows the relative mRNA transcript levels of genes belonging to Kennedy pathway such as glycerol kinase (*glpK*), glycerol-3 phosphate acyl transferase (*GPAT*), acylglycerol phosphate acyltransferase (*AGPAT*), two wax ester synthase/acyl-CoA: diacylglycerol acyltransferase (*WSDGAT*) and the TAG synthase genes (*MSMEG_3948* and *MSMEG_5242*; these are homologues of *tgs1* in *M. tuberculosis*) in *M. smegmatis* WT, its *atpD* knock-out variant (Δ*atpD*), and the bedaquiline (BDQ)-treated wild-type *M. smegmatis* (WT BDQ). Panel **(C)** shows the relative mRNA transcript levels of the lipase genes (*lipG, lipJ, lipI, lipN, lipO, lipT*, and *lipZ*) in *M. smegmatis* WT, *atpD* knock-out (Δ*atpD*), and the bedaquiline (BDQ)-treated wild-type *M. smegmatis* (WT BDQ). In all of the panels, the mRNA transcript in the case of untreated WT is taken as 1 for comparison. In each panel, the data represent an average of at least three independent experiments. Error bars represent standard deviation. **P*-value < 0.05; ***P*-value < 0.01; ****P*-value < 0.005.

conditions (Iqbal et al., 2018). Thus OXPHOS in mycobacteria is a tightly regulated process. However, the restricted respiration due to O_2 depletion or by inhibition of ETC complexes induces changes in the mycobacterial respiratory machinery making the electron carriers to be more reduced thereby leading to alteration in the redox homeostasis (Bhat et al., 2012). Bacteria utilize a large number of dehydrogenases and redox sensors in order to dissipate reductive stress caused by an excessive accumulation of NADH and to replenish the cellular NAD^+ levels (Bhat et al., 2012). For example, the Rex repressors in the Gram-positive bacteria are known to regulate the gene expression changes in response to altered NADH/NAD^+ ratios (Gyan et al., 2006). The Fnr regulators also sense the intracellular O_2 levels *via* (4Fe-4S) cluster and thereby regulate the cellular response (Kiley and Beinert, 1998). Similarly, the RegB histidine kinase (HK) of the *Rhodobacter capsulatus* two component system (TCS) RegBA, and the AcrB HK of *E*scherichia *coli* TCS AcrBA were also suggested to be upregulated under anaerobic conditions (Bekker et al., 2010). However, homologs of none of these genes are present in *M. smegmatis*.

The DosSR TCS in mycobacteria consists of two heme-based HK, DosS, and DosT, that directly sense the intracellular concentration of O_2 in the cell, and relays the signal to a response regulator DosR, which upregulates the target responsive dormancy regulon genes under reduced oxygen conditions (Kim et al., 2010; Tan et al., 2010). Some major dormancy regulon genes upregulated during reduced oxygen include

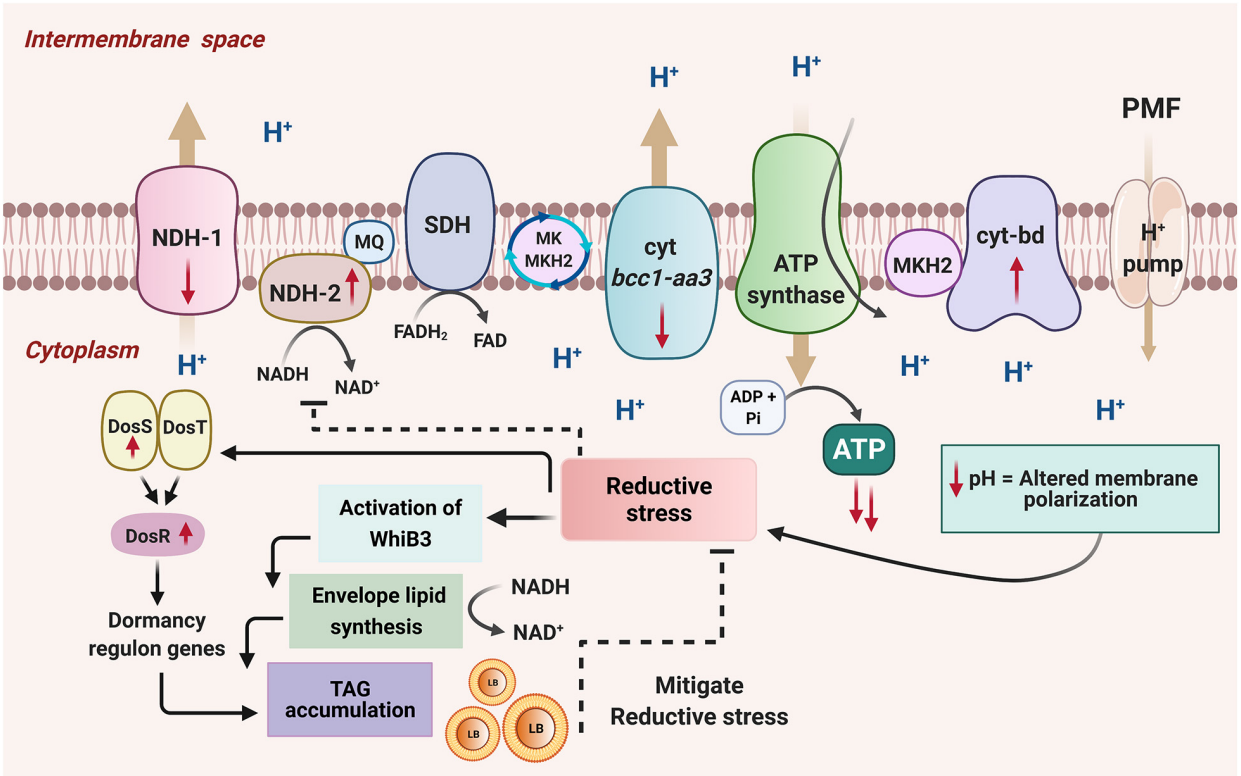

FIGURE 9 | A model depicting the adaptation of *M. smegmatis* under energy-compromised state. Disruption of one copy of *atpD* in *M. smegmatis* drives the transcriptional changes in the mycobacterial ETC. The energy efficient complexes (NDH1 and cyt bc_1-aa_3) are down-regulated while the energy less efficient complexes (NDH2 and cyt *bd* oxidase) are upregulated as shown by the direction of the red arrows. This leads to the remodeling of the respiration chain, and, as a result, the protons get trapped in the cytoplasmic region as they are now unable to translocate to the periplasmic region, resulting in the decrease in cellular pH. This causes a change in the membrane polarization, and leads to the reductive stress in the cell. This activates a redox sensor, WhiB3, which dissipates the reductive stress by promoting biosynthesis of cell wall associated lipids and by increasing TAG accumulation. WhiB3-mediated lipid biosynthesis helps in the regeneration of NAD^+ from NADH, which helps in mitigating the reductive stress. The accumulated TAG forms lipid bodies (LB). Mycobacteria also possess another sensing mechanism DosSRT dormancy regulon, which detects changes in cellular redox state through the heme proteins of its two sensor kinases, DosS and DosT. This transfers the signal to the response regulator DosR, which mediates the upregulation of dormancy regulon genes. An essential gene of this regulon that gets activated during stress is the *tgs1*, which is the major TAG regulator gene, mediating production and accumulation of lipid bodies (LB) containing TAG, thereby dissipating the reducing equivalents and facilitating mycobacterial survival under energy-compromised state. Hence these combined effects of WhiB3 and Dos regulon mediated signaling pathways function to overcome the energy demand and maintain the redox homeostasis in *M. smegmatis* under energy-compromised state. Figure is created with www.BioRender.com.

nitrate reductase (*narK2* and *narX*), fumarate reductase (Frd, *frdABCD*), ferredoxin (*fdxA*), DNA repair genes (*nrdZ*) and TAG biosynthesis genes (*tgs1*) (Tan et al., 2010). In addition, upon exposure to variety of stress (reduced O_2, NO, and CO), the DosSR TCS gets activated leading to an increase in the cellular NADH pools, thus playing an important role during reductive stress in mycobacteria (Kumar et al., 2007; Honaker et al., 2010). Another major redox regulator in mycobacteria is WhiB3 that senses the intracellular redox state, and helps in the dissipation of the reductive stress generated due to accumulated NADH cofactor *via* lipid biosynthesis (Singh et al., 2009). The metabolic shift induced by WhiB3 regulates the production of methyl branched polyketides (PAT/DAT, SL-1, and PDIM) and TAG (Singh et al., 2009). Synthesis of these lipids by WhiB3 consumes NADH, replenishing the cellular NAD^+ levels and relieving the cell from reductive stress (Singh et al., 2009). Interestingly, the TAG synthase *tgs1* gene is under the direct control of DosSR operon (Kumari et al., 2017). Lipid inclusions are highly prevalent amongst various prokaryotic organisms such as *Rhodococcus*, *Streptomyces*, *Nocardia*, and *Pseudomonas aeruginosa* and in eukaryotic organisms like *Saccharomyces cerevisiae*. In mycobacteria, TAG accumulation has recently received renewed interest. The W-Beijing lineage of *M. tuberculosis* also shows an upregulation of DosR/S operon with an overproduction of TAG levels. LB containing TAG are the most prominent storage fuel in mycobacteria that not only are essential for prolonged survival, infection, dormancy, and persistence, but are also required for the reactivation of growth following dormancy (Daniel et al., 2011). Similarly, the sputum analysis of pulmonary TB patients and MDR strains of *M. tuberculosis* also show the presence of TAG containing LB, suggesting importance of TAG accumulation in TB pathogenesis and infection (Vijay et al., 2017). Hence TAG acts as a major redox sink to dissipate reductive stress in the cell.

In the present work, we report a critical outcome of the deletion of one of the two copies of *atpD* gene in *M. smegmatis*. We have previously shown that deletion of one copy of *atpD* gene in *M. smegmatis* renders the cell in an energy-compromised state (Patil and Jain, 2019). Here we investigated the adaptive mechanisms undertaken by the bacterium during such condition. We show that *M. smegmatis* under energy compromised state exhibits restricted respiration by downregulating the energy efficient ETC complexes *viz.* NDH1 and cyt *bc1-aa3* complex and upregulating energetically less efficient ETC complexes *viz.* NDH2 and cyt-*bd* oxidase complex. This broad shift in the respiratory machinery results in the trapping of protons in the cytoplasmic region, resulting in the acidification of cellular pH. This change alters the membrane polarization as seen by an increase in $DiBAC_4(3)$ fluorescence in the knockout cells as compared to the wild-type. Moreover, a higher $NADH/NAD^+$ ratio and an increased ROS levels induces an altered redox state. Finally, in order to dissipate these reducing equivalents and to maintain intracellular redox balance, WhiB3, a major redox sensor, is upregulated and it maintains the redox homeostasis *via* modulating the biosynthesis of cell wall-associated lipids and TAG resulting in an accumulation of LBs. Our results show that Δ*atpD* bacterium tends to accumulate more LBs than the wild-type bacterium, indicating that TAG accumulation is a prominent metabolic adaptation in Δ*atpD* under energy-compromised state. Additionally, by using ^{14}C oleic acid, we further show that the FFAs incorporated within the knockout cells are mainly stored as TAG rather that simple FFA or phospholipids. Furthermore, the *atpD* bacterium also shows loss of acid fastness and significantly down-regulated cardiolipin biosynthesis gene expression which is most likely the result of an upregulated TAG biosynthesis pathway in Δ*atpD*. With an upregulation of TAG pathway, we also observed a concomitant overexpression of intracellular lipases genes, suggesting that the accumulated TAG is hydrolyzed for its utilization. Furthermore, an overproduction of lipases along with the previously reported enhanced β-oxidation (Patil and Jain, 2019) together indicates that the stored lipids are used for energy production (**Figure 9**). This likely happens because the Δ*atpD* bacterium is unable to meet its energy requirements by OXPHOS due to lesser availability of functional ATP synthase. It is worth adding here that the catabolism of the fatty acids under such energy-depleted state leads to the production of acetyl CoA, which is then metabolized *via* glyoxylate shunt in order to avoid carbon loss *via* TCA oxidation. Hence the lipids are acted upon by the lipases to release FFAs, which are then metabolized *via* β-oxidation generating a pool of acetyl CoA, which thereafter enters the glyoxylate cycle producing energy for cell survival (Patil and Jain, 2019).

Interestingly, wild-type *M. smegmatis* upon BDQ treatment also shows an upregulation in WhiB3 expression, suggesting an important role of WhiB3 mediated redox sensing in mycobacterial virulence under BDQ-treated conditions. Additionally, a predominance of TAG biosynthesis coupled with an increased lipase production is also observed similar to Δ*atpD*. This phenomenon appears to be conserved in *M. tuberculosis*; indeed, proteomic analysis of *M. tuberculosis* treated with BDQ showed an upregulation of TAG biosynthesis gene products at 6 and 24 h time (Koul et al., 2014). This strongly indicates that the survival response of bacterium to BDQ treatment is identical to what we observe upon creating an energy-compromised state by disrupting ATP synthase machinery.

The observed physiological changes presented in this manuscript depict a significant outcome of the metabolic dependency of mycobacteria on fatty acids as an energy source under energy-deprived state and a highly evolved mechanism of dissipating reducing equivalents in the cell *via* TAG metabolism. We thus conclude that mycobacteria exhibit a robust and flexible system that allows rerouting of its central metabolic pathways under an energy-compromised state. Further, since TAG accumulation provides metabolic energy to the dormant cell, we believe that our work will also contributes toward the exploration of newer possible drug targets in eliminating the dormant and persistent pathogenic mycobacteria.

Experimental Procedures

Bacterial Strains, Plasmids, Reagents, Media, and Growth Conditions

Wild-type *M. smegmatis* mc^2155, *atpD* knock-out (Δ*atpD*), and the complemented strain ($\Delta atpD^C$) were grown in Middlebrook 7H9 (MB7H9 broth; Difco) containing 2% glucose and 0.05% tyloxapol surfactant (Sigma-Aldrich, MO, United States) as indicated, at 37°C with constant shaking at 200 rpm. *M. smegmatis* Δ*atpD* and $\Delta atpD^C$ were taken from the laboratory stock (Patil and Jain, 2019). The cultures were supplemented with 50 μg ml^{-1} kanamycin (Sigma) or 100 μg ml^{-1} hygromycin (MP Biomedical), wherever required. Protein expression was induced by the addition of 2% acetamide (wherever required).

Lipid Extraction and Analysis by Thin Layer Chromatography

Triacylglycerol was extracted following the chloroform:methanol (2:1 v/v) method. Briefly, the bacteria were grown in MB7H9 medium supplemented with 2% glucose and 0.05% tyloxapol till 24 h. The cells were then lyophilized and 300 mg of cells in each case were further used for TAG extraction by chloroform:methanol (2:1 v/v). The lower organic layer was collected, and the lipids were dried and re-suspended in chloroform:methanol (1:1 v/v). Lipids were further separated by TLC using hexane:diethylether:formic acid (40:10:1 v/v) as the mobile phase. The plates were allowed to dry, and stained using 5% phosphomolybdic acid in 95% ethanol followed by charring at 140°C for 5 min.

For TAG hydrolysis experiments, bacteria were grown in MB7H9 medium supplemented with 2% glucose and 0.05% tyloxapol for 24 h. The cells were then harvested by centrifugation at 5000 rpm for 15 min and washed with 1X-PBS buffer. The cells were further resuspended in the media without any carbon source in order to induce starvation. The cells were then incubated at 37°C with constant shaking at 200 rpm, and samples were collected at specific time points. For lipase inhibition experiments, the cells were pre-incubated with lipase inhibitor THL for 2 h. A portion of these cells was then harvested and washed with 1X-PBS buffer, while the remaining cells were further incubated for 24 h, with appropriate THL concentrations

(5, 50, and 100 μg/ml^{-1}). Cells were then harvested at specific time points and their lipid content was analyzed by TLC. Densitometric analysis was performed using ImageJ software to determine the relative TAG content in the samples.

Ultrastructure Analysis by Transmission Electron Microscopy

Transmission electron microscopy was carried out with *M. smegmatis* cells essentially as described previously (Gupta et al., 2015; Patil and Jain, 2019) with some modifications. Briefly, the bacterial cell pellet was obtained from 24 h grown culture. The cells were fixed in 0.15 M sodium cacodylate buffer containing 2% osmium tetraoxide for 2 h at RT. The cells were then washed with cacodylate buffer followed by fixation for 3 h at RT in 0.15 M sodium cacodylate buffer containing 2% tannic acid and 2% glutaraldehyde solution. The cells were then washed again with cacodylate buffer, and re-fixed with 2% osmium tetraoxide overnight. Samples were then washed with Milli-Q water and embedded in 2% molten agarose. The finely cut agar block pieces were then subjected to sequential acetone dehydration at increasing concentrations for 30 min each (30, 50, 70, 90, and 100%), followed by infiltration and embedding in Spurr's resin. After ultra-sectioning, the samples were stained with uranyl acetate and phosphotungstic acid, imaged on FEI Talos 200S system, equipped with a 200 kV Field Emission Gun, and the LBs were counted manually.

Auramine-O and Nile Red Microscopy and Fluorescence Measurements

For fluorescence microscopy, the fluorescent acid-fast staining dye Auramine-O was used along with a neutral lipid staining dye Nile red (9-diethylamino-5H-benzo-a-phenoxazine-5-one) using the protocol as described previously (Deb et al., 2009) with some modifications. Briefly, the log phase cultures (OD_{600} ∼0.6) of wild-type *M. smegmatis* mc^{2}155, Δ*atpD*, and Δ*atpD*^{C} were harvested and washed with 1X-PBST (0.137 M NaCl, 0.0027 M KCl, 0.01 M Na_2HPO_4, 0.0018 M KH_2PO_4, 0.05% Tween-20). Thereafter, the cultures were evenly spread to make a smear on a glass slide, heat fixed, covered with Auramine-O (10 mg ml^{-1}), and incubated for 20 min. The cells were then washed briefly with water and treated with the decolorizer (acid alcohol) for 30 s. Further, the specimen was washed and covered with Nile red solution (10 mg ml^{-1} in ethanol) and incubated for 15 min. The cells were then washed and covered with potassium permanganate solution for 1 min, washed thoroughly with water, air dried, and imaged on using ApoTome Fluorescence Microscope (Carl Zeiss) using an 100× objective lens.

For Nile red confocal microscopy experiments, the Δ*atpD* cells were grown for 24 h. The cells were then harvested and washed with 1X-PBS buffer and further resuspended in it. Nile red dye (10 mg/ml in ethanol) was added to the cell suspension. Cells were further incubated for 30 min in dark at 37°C. The stained cells were then harvested and washed twice with 1X-PBST buffer and finally resuspended in it. A total of 2 μl of bacterial suspension was spotted on 1% agarose pad. Bacteria were then analyzed by capturing the images on Olympus FV3000 confocal microscope with 100× oil-objective.

The flow cytometry based FACS measurements were performed using BD-FACS Aria III equipped with CELL QUEST software (South San Francisco, CA, United States). For measuring the Auramine-O and Nile red fluorescence, log phase cultures of all the strains were harvested, and washed with 1X-PBST. Both Auramine-O and Nile red dyes were added to the samples at a final concentration of 10 mg/ml. Samples were incubated at room temperature in dark for 1 h, washed twice and re-suspended in 1X-PBST buffer. Flow cytometry was performed using FITC and Texas Red filter for Auramine and Nile red, respectively. Alternatively, fluorescence was measured on SpectraMax M5 plate reader with Ex/Em wavelengths set at 438/505 nm for Auramine-O and at 550/640 nm for Nile red.

Assessment of the Presence of Cardiolipin by Staining With Nonyl Acridine Orange

The flow cytometry based FACS measurements were performed using BD-FACS Aria III equipped with cell quest software (South San Francisco, CA, United States). The total cardiolipin levels were measured using NAO (10-Nonyl Acridine orange). Briefly log phase cultures (OD_{600} ∼0.6) of all the strains were harvested, and washed with 1X-PBST. The cells were then incubated with 10 μM NAO for 30 min at room temperature, washed twice and re-suspended in 1X-PBST buffer. Fluorescence was then measured using FITC filter for flow cytometry, and, alternatively, on Spectramax M5 plate reader with Ex/Em wavelengths set at 495/519 nm.

Metabolic Incorporation of Radiolabeled Oleic Acid by *Mycobacterium smegmatis*

Wild-type *M. smegmatis* and its variants were grown in MB7H9 medium supplemented with 2% glucose and 0.05% tyloxapol till log phase (OD_{600} ∼0.6) at 37°C with constant shaking at 200 rpm. ^{14}C-oleate (50 μCi mol^{-1}; 5 μCi per 10 ml of culture; Perkin Elmer, Waltham, MA, United States) was then added in each culture for 30 min. Thereafter, the lipid extraction, TLC, and phosphor imaging procedures were performed as described previously with some modifications (Daniel et al., 2016). Briefly, the cells were harvested by centrifugation at 8000 rpm at 4°C and were washed with 1X-PBST buffer to remove the unincorporated radioactive material. The lipids were then extracted using chloroform:methanol (2:1 v/v). The organic layer was recovered and dried completely. The dried lipids were further dissolved in chloroform:methanol (1:1 v/v) and were subjected to TLC using hexane:ethyl ether:formic acid (40:10:1 v/v) as the mobile phase. For each sample, the amount of radioactivity present was measured on a scintillation counter, and the equal amount of radioactivity was loaded on TLC. The TLC plate was then dried and imaged on a phosphor imager (FLA 9000; GE Healthcare). For phospholipid analysis, ^{14}C-oleate (54.3 μCi mmol^{-1}; 5 μCi per 10 ml of culture) was added in each culture for 6 h, followed by lipid extraction as stated above. Dried lipids were further dissolved in chloroform:methanol (1:1 v/v).

Equal cpm was spotted on TLC, and the lipids were separated using $CHCl_3$:CH_3OH:H_2O (65:25:4 v/v) as the mobile phase, followed by phosphor imaging procedure as mentioned above.

Lipase Assay

Lipase activity was assessed using Lipase Assay Kit (Sigma Aldrich, MAK048) following the manufacturer's instructions with some modifications. Briefly, the log phase cultures were harvested and washed with 1X-PBST. The cells were then resuspended in lipase buffer followed by the addition of lipase inhibitor (tetrahydrolipstatin or THL), wherever required, to a final concentration of 80 μM. The cells were then sonicated and were further processed for lipase assay. Fluorescence was recorded on SpectraMax M5 plate reader with Ex/Em wavelengths set at 529/600 nm.

RNA Extraction, cDNA Synthesis, and RT-qPCR

Differential gene expression profile was obtained by RT-qPCR for bacteria essentially as described previously (Patil and Jain, 2019). Briefly, the cells were grown till $OD_{600} \sim 0.8$. The cells were then harvested, and processed for RNA isolation using RNeasy Mini kit (QIAGEN) by following manufacturer's instructions. cDNA was synthesized using i-script cDNA synthesis kit (Bio-Rad) as per the manufacturer's instructions. The obtained cDNA was then used for qPCR experiments, carried out on StepOnePlus real-time PCR system (Applied Biosystems) using iTaq universal SYBR green mix (Bio-Rad) as per the manufacturer's instructions. *rpoB* gene was used as an internal control. Data were analyzed as per $2^{-\Delta\Delta Ct}$ method. Primers used for these PCR reactions are listed in **Supplementary Table 1**.

Statistical Analysis

Data are represented as arithmetic means in the results that are obtained from at least three independent experiments with standard deviations shown as error bar. Statistical significance was calculated using unpaired *t*-test for data analysis as mentioned in the respective figure legends.

DATA AVAILABILITY STATEMENT

The original contributions presented in the study are included in the article/**Supplementary Material**, further inquiries can be directed to the corresponding author/s.

AUTHOR CONTRIBUTIONS

VJ and VP designed the research, analyzed the data, and wrote the manuscript. VP performed the research. Both authors contributed to the article and approved the submitted version.

FUNDING

This work was supported by intramural funds from IISER Bhopal to VJ.

ACKNOWLEDGMENTS

VP acknowledges the receipt of DST INSPIRE-Senior Research Fellowship from the Department of Science and Technology (DST), Government of India. We thank DST-FIST facility at IISER Bhopal for the Confocal and TEM imaging.

SUPPLEMENTARY MATERIAL

The Supplementary Material for this article can be found online at: https://www.frontiersin.org/articles/10.3389/fmicb.2021.722229/full#supplementary-material

Supplementary Figure 1 | Pairwise sequence alignment of WhiB3 protein of *M. tuberculosis* and *M. smegmatis*. Pairwise sequence alignment of WhiB3 protein from *M. tuberculosis* (Rv3416) and *MSMEG_1597* from *M. smegmatis* is shown. "*" represents conserved residue.

Supplementary Figure 2 | Sequence alignment of polyketide biosynthesis protein of *M. tuberculosis* and *M. smegmatis*. Pairwise sequence alignment of Rv3825c protein (*pks2*) from *M. tuberculosis* and MSMEG_4724 (*pks5*) from *M. smegmatis* is shown. "*" represents conserved residue.

Supplementary Figure 3 | Phospholipid analysis by thin layer chromatography. Panel shows the TLC image depicting the phospholipids in *M. smegmatis* wild-type (WT), *atpD* knock out (Δ*atpD*), and *atpD*-complemented ($\Delta atpD^C$) strains. Spot corresponding to PE, PI, and PS (top to bottom) is marked with arrowhead. Experiments were repeated at least thrice; only one representative image is shown.

Supplementary Figure 4 | Sequence alignment of TAG synthase enzymes of *M. tuberculosis* and *M. smegmatis*. Multiple sequence alignment of Rv3130c protein (*tgs1*) from *M. tuberculosis* and its homologs MSMEG_3948 and MSMEG_5242 from *M. smegmatis* is shown. "*" represents conserved residue in all three cases.

Supplementary Figure 5 | TAG accumulation examination in *M. smegmatis* by thin layer chromatography. Panel shows the autoradiogram of the TLC demonstrating the incorporation of radiolabeled ^{14}C-oleic acid in TAG in wild-type (WT), *atpD* knock-out (Δ*atpD*), and *atpD*-complemented ($\Delta atpD^C$) strains of *M. smegmatis*. Arrowhead points to the various species obtained on TLC such as triacylglycerol (TAG), diacylglycerol (DAG), and monoacylglycerol (MAG). Lane 4 has the free ^{14}C-oleic acid. Experiments were repeated at least thrice; only one representative image is shown.

Supplementary Table 1 | List of primers used in this study. Primers and their sequences used in the RT-qPCR experiments, and the genes that they target are given.

REFERENCES

Akela, A. K., and Kumar, A. (2021). Bioenergetic heterogeneity in *Mycobacterium tuberculosis* residing in different subcellular niches. *mbio* 12:e0108821.

Bald, D., Villellas, C., Lu, P., and Koul, A. (2017). Targeting energy metabolism in mycobacterium tuberculosis, a new paradigm in antimycobacterial drug discovery. *mBio* 8:e00272-17.

Barksdale, L., and Kim, K. S. (1977). Mycobacterium. *Bacteriol. Rev.* 41, 217–372.

Bekker, M., Alexeeva, S., Laan, W., Sawers, G., Teixeira de Mattos, J., and Hellingwerf, K. (2010). The ArcBA two-component system of *Escherichia coli* is regulated by the redox state of both the ubiquinone and the menaquinone pool. *J. Bacteriol.* 192, 746–754. doi: 10.1128/jb.01156-09

Berney, M., and Cook, G. M. (2010). Unique flexibility in energy metabolism allows mycobacteria to combat starvation and hypoxia. *PLoS One* 5:e8614. doi: 10.1371/journal.pone.0008614

Bhat, S. A., Singh, N., Trivedi, A., Kansal, P., Gupta, P., and Kumar, A. (2012). The mechanism of redox sensing in *Mycobacterium tuberculosis*. *Free Radic. Biol. Med.* 53, 1625–1641. doi: 10.1016/j.freeradbiomed.2012.08.008

Blee, J. A., Roberts, I. S., and Waigh, T. A. (2020). Membrane potentials, oxidative stress and the dispersal response of bacterial biofilms to 405 nm light. *Phys. Biol.* 17:036001. doi: 10.1088/1478-3975/ab759a

Brunelle, J. K., Bell, E. L., Quesada, N. M., Vercauteren, K., Tiranti, V., Zeviani, M., et al. (2005). Oxygen sensing requires mitochondrial ROS but not oxidative phosphorylation. *Cell Metab.* 1, 409–414. doi: 10.1016/j.cmet.2005.05.002

Cook, G. M., Hards, K., Vilchèze, C., Hartman, T., and Berney, M. (2014). Energetics of respiration and oxidative phosphorylation in mycobacteria. *Microbiol. Spectr.* 2:10.1128/microbiolspec.MGM2-0015-2013.

Crellin, P. K., Luo, C. Y., and Morita, Y. S. (2013). Metabolism of plasma membrane lipids in mycobacteria and corynebacteria, lipid metabolism, rodrigo valenzuela baez. *IntechOpen* 6, 119–148.

Daniel, J., Deb, C., Dubey, V. S., Sirakova, T. D., Abomoelak, B., Morbidoni, H. R., et al. (2004). Induction of a novel class of diacylglycerol acyltransferases and triacylglycerol accumulation in *Mycobacterium tuberculosis* as it goes into a dormancy-like state in culture. *J. Bacteriol.* 186, 5017–5030. doi: 10.1128/jb.186.15.5017-5030.2004

Daniel, J., Kapoor, N., Sirakova, T., Sinha, R., and Kolattukudy, P. (2016). The perilipin-like PPE15 protein in *Mycobacterium tuberculosis* is required for triacylglycerol accumulation under dormancy-inducing conditions. *Mol. Microbiol.* 101, 784–794. doi: 10.1111/mmi.13422

Daniel, J., Maamar, H., Deb, C., Sirakova, T. D., and Kolattukudy, P. E. (2011). Mycobacterium tuberculosis uses host triacylglycerol to accumulate lipid droplets and acquires a dormancy-like phenotype in lipid-loaded macrophages. *PLoS Pathog.* 7:e1002093. doi: 10.1371/journal.ppat.1002093

Deb, C., Lee, C. M., Dubey, V. S., Daniel, J., Abomoelak, B., Sirakova, T. D., et al. (2009). A novel in vitro multiple-stress dormancy model for *Mycobacterium tuberculosis* generates a lipid-loaded, drug-tolerant, dormant pathogen. *PLoS One* 4:e6077. doi: 10.1371/journal.pone.0006077

Dwyer, D. J., Belenky, P. A., Yang, J. H., MacDonald, I. C., Martell, J. D., Takahashi, N., et al. (2014). Antibiotics induce redox-related physiological alterations as part of their lethality. *Proc. Natl. Acad. Sci. U.S.A.* 111, E2100–E2109.

Eisinger, R. W., Embry, A. C., Read, S. W., and Fauci, A. S. (2020). 2019: a banner year for tuberculosis research. *J. Infect. Dis.* 222, 1768–1771. doi: 10.1093/infdis/jiaa051

Foo, C.-Y., Pethe, K., and Lupien, A. (2020). Oxidative phosphorylation—an update on a new, essential target space for drug discovery in *Mycobacterium tuberculosis*. *Appl. Sci.* 10:2339. doi: 10.3390/app10072339

Forte, E., Borisov, V. B., Falabella, M., Colaco, H. G., Tinajero-Trejo, M., Poole, R. K., et al. (2016). The terminal oxidase cytochrome bd promotes sulfide-resistant bacterial respiration and growth. *Sci. Rep.* 6:23788.

Gengenbacher, M., and Kaufmann, S. H. (2012). *Mycobacterium tuberculosis*: success through dormancy. *FEMS Microbiol. Rev.* 36, 514–532. doi: 10.1111/j.1574-6976.2012.00331.x

Giuffre, A., Borisov, V. B., Mastronicola, D., Sarti, P., and Forte, E. (2012). Cytochrome bd oxidase and nitric oxide: from reaction mechanisms to bacterial physiology. *FEBS Lett.* 586, 622–629. doi: 10.1016/j.febslet.2011.07.035

Gomez, J. E., and McKinney, J. D. (2004). *M. tuberculosis* persistence, latency, and drug tolerance. *Tuberculosis (Edinb.)* 84, 29–44. doi: 10.1016/j.tube.2003.08.003

Gupta, K. R., Kasetty, S., and Chatterji, D. (2015). Novel functions of (p)ppGpp and Cyclic di-GMP in mycobacterial physiology revealed by phenotype microarray analysis of wild-type and isogenic strains of *Mycobacterium smegmatis*. *Appl. Environ. Microbiol.* 81, 2571–2578. doi: 10.1128/aem.03999-14

Gyan, S., Shiohira, Y., Sato, I., Takeuchi, M., and Sato, T. (2006). Regulatory loop between redox sensing of the NADH/NAD(+) ratio by Rex (YdiH) and oxidation of NADH by NADH dehydrogenase Ndh in *Bacillus subtilis*. *J. Bacteriol.* 188, 7062–7071. doi: 10.1128/jb.00601-06

Honaker, R. W., Dhiman, R. K., Narayanasamy, P., Crick, D. C., and Voskuil, M. I. (2010). DosS responds to a reduced electron transport system to induce the *Mycobacterium tuberculosis* DosR regulon. *J. Bacteriol.* 192, 6447–6455. doi: 10.1128/jb.00978-10

Iqbal, I. K., Bajeli, S., Akela, A. K., and Kumar, A. (2018). Bioenergetics of Mycobacterium: An Emerging Landscape for Drug Discovery. *Pathogens* 7:24. doi: 10.3390/pathogens7010024

Kana, B. D., Weinstein, E. A., Avarbock, D., Dawes, S. S., Rubin, H., and Mizrahi, V. (2001). Characterization of the cydAB-encoded cytochrome bd oxidase from *Mycobacterium smegmatis*. *J. Bacteriol.* 183, 7076–7086. doi: 10.1128/jb.183.24.7076-7086.2001

Kiley, P. J., and Beinert, H. (1998). Oxygen sensing by the global regulator, FNR: the role of the iron-sulfur cluster. *FEMS Microbiol. Rev.* 22, 341–352. doi: 10.1111/j.1574-6976.1998.tb00375.x

Kim, M. J., Park, K. J., Ko, I. J., Kim, Y. M., and Oh, J. I. (2010). Different roles of DosS and DosT in the hypoxic adaptation of mycobacteria. *J. Bacteriol.* 192, 4868–4875. doi: 10.1128/jb.00550-10

Koul, A., Vranckx, L., Dhar, N., Göhlmann, H. W. H., Özdemir, E., Neefs, J.-M., et al. (2014). Delayed bactericidal response of *Mycobacterium tuberculosis* to bedaquiline involves remodelling of bacterial metabolism. *Nat. Commun.* 5, 3369–3369.

Kumar, A., Toledo, J. C., Patel, R. P., Lancaster, J. R. Jr., and Steyn, A. J. (2007). *Mycobacterium tuberculosis* DosS is a redox sensor and DosT is a hypoxia sensor. *Proc. Natl. Acad. Sci. U.S.A.* 104, 11568–11573. doi: 10.1073/pnas.0705054104

Kumari, P., Sikri, K., Kaur, K., Gupta, U. D., and Tyagi, J. S. (2017). Sustained expression of DevR/DosR during long-term hypoxic culture of *Mycobacterium tuberculosis*. *Tuberculosis (Edinb.)* 106, 33–37. doi: 10.1016/j.tube.2017.06.003

Lakshmanan, M., and Xavier, A. S. (2013). Bedaquiline–the first ATP synthase inhibitor against multi drug resistant tuberculosis. *J. Young Pharm.* 5, 112–115. doi: 10.1016/j.jyp.2013.12.002

Lamprecht, D. A., Finin, P. M., Rahman, M. A., Cumming, B. M., Russell, S. L., Jonnala, S. R., et al. (2016). Turning the respiratory flexibility of *Mycobacterium tuberculosis* against itself. *Nat. Commun.* 7:12393.

Lass, A., Zimmermann, R., Oberer, M., and Zechner, R. (2011). Lipolysis–a highly regulated multi-enzyme complex mediates the catabolism of cellular fat stores. *Prog. Lipid Res.* 50, 14–27. doi: 10.1016/j.plipres.2010.10.004

Maarsingh, J. D., and Haydel, S. E. (2018). *Mycobacterium smegmatis* PrrAB two-component system influences triacylglycerol accumulation during ammonium stress. *Microbiology* 164, 1276–1288. doi: 10.1099/mic.0.000705

Matsoso, L. G., Kana, B. D., Crellin, P. K., Lea-Smith, D. J., Pelosi, A., Powell, D., et al. (2005). Function of the cytochrome bc1-aa3 branch of the respiratory network in mycobacteria and network adaptation occurring in response to its disruption. *J. Bacteriol.* 187, 6300–6308. doi: 10.1128/jb.187.18.6300-6308.2005

McCarthy, C. (1971). Utilization of palmitic acid by *Mycobacterium avium*. *Infect. Immun.* 4, 199–204. doi: 10.1128/iai.4.3.199-204.1971

Mehta, M., and Singh, A. (2019). *Mycobacterium tuberculosis* WhiB3 maintains redox homeostasis and survival in response to reactive oxygen and nitrogen species. *Free Radic. Biol. Med.* 131, 50–58. doi: 10.1016/j.freeradbiomed.2018.11.032

Mileykovskaya, E., Dowhan, W., Birke, R. L., Zheng, D., Lutterodt, L., and Haines, T. H. (2001). Cardiolipin binds nonyl acridine orange by aggregating the dye at exposed hydrophobic domains on bilayer surfaces. *FEBS Lett.* 507, 187–190. doi: 10.1016/s0014-5793(01)02948-9

Moosa, A., Lamprecht, D. A., Arora, K., Barry, C. E. III, Boshoff, H. I. M., Ioerger, T. R., et al. (2017). Susceptibility of *Mycobacterium tuberculosis* cytochrome bd oxidase mutants to compounds targeting the terminal respiratory oxidase, cytochrome c. *Antimicrob. Agents Chemother.* 61:e01338-17.

Nakagawa, H., Kashiwabara, Y., and Matsuki, G. (1976). Metabolism of triacylglycerol in *Mycobacterium smegmatis*. *J. Biochem.* 80, 923–928. doi: 10.1093/oxfordjournals.jbchem.a131378

Ojha, A. K., Trivelli, X., Guerardel, Y., Kremer, L., and Hatfull, G. F. (2010). Enzymatic hydrolysis of trehalose dimycolate releases free mycolic acids during mycobacterial growth in biofilms. *J. Biol. Chem.* 285, 17380–17389. doi: 10.1074/jbc.m110.112813

Onwueme, K. C., Ferreras, J. A., Buglino, J., Lima, C. D., and Quadri, L. E. (2004). Mycobacterial polyketide-associated proteins are acyltransferases: proof

of principle with *Mycobacterium tuberculosis* PapA5. *Proc. Natl. Acad. Sci. U.S.A.* 101, 4608–4613. doi: 10.1073/pnas.0306928101

Pandey, A. K., and Sassetti, C. M. (2008). Mycobacterial persistence requires the utilization of host cholesterol. *Proc. Natl. Acad. Sci. U.S.A.* 105, 4376–4380. doi: 10.1073/pnas.0711159105

Patil, V., and Jain, V. (2019). Insights into the physiology and metabolism of a mycobacterial cell in an energy-compromised state. *J. Bacteriol.* 201:e00210-19.

Prindle, A., Liu, J., Asally, M., Ly, S., Garcia-Ojalvo, J., and Süel, G. M. (2015). Ion channels enable electrical communication in bacterial communities. *Nature* 527, 59–63. doi: 10.1038/nature15709

Queiroz, A., and Riley, L. W. (2017). Bacterial immunostat: *Mycobacterium tuberculosis* lipids and their role in the host immune response. *Rev. Soc. Bras. Med. Trop.* 50, 9–18. doi: 10.1590/0037-8682-0230-2016

Ravindran, M. S., Rao, S. P., Cheng, X., Shukla, A., Cazenave-Gassiot, A., Yao, S. Q., et al. (2014). Targeting lipid esterases in mycobacteria grown under different physiological conditions using activity-based profiling with tetrahydrolipstatin (THL). *Mol. Cell Proteomics* 13, 435–448. doi: 10.1074/mcp.m113.029942

Serafini, A., Tan, L., Horswell, S., Howell, S., Greenwood, D. J., Hunt, D. M., et al. (2019). *Mycobacterium tuberculosis* requires glyoxylate shunt and reverse methylcitrate cycle for lactate and pyruvate metabolism. *Mol. Microbiol.* 112, 1284–1307. doi: 10.1111/mmi.14362

Shi, L., Sohaskey, C. D., Kana, B. D., Dawes, S., North, R. J., Mizrahi, V., et al. (2005). Changes in energy metabolism of *Mycobacterium tuberculosis* in mouse lung and under in vitro conditions affecting aerobic respiration. *Proc. Natl. Acad. Sci. U.S.A.* 102, 15629–15634. doi: 10.1073/pnas.0507850102

Shi, L., Sohaskey, C. D., Pheiffer, C., Datta, P., Parks, M., McFadden, J., et al. (2010). Carbon flux rerouting during *Mycobacterium tuberculosis* growth arrest. *Mol. Microbiol.* 78, 1199–1215. doi: 10.1111/j.1365-2958.2010.07399.x

Singh, A., Crossman, D. K., Mai, D., Guidry, L., Voskuil, M. I., Renfrow, M. B., et al. (2009). *Mycobacterium tuberculosis* WhiB3 maintains redox homeostasis by regulating virulence lipid anabolism to modulate macrophage response. *PLoS Pathog.* 5:e1000545. doi: 10.1371/journal.ppat.1000545

Smith, T. C. II, Pullen, K. M., Olson, M. C., McNellis, M. E., Richardson, I., Hu, S., et al. (2020). Morphological profiling of tubercle bacilli identifies drug pathways of action. *Proc. Natl. Acad. Sci. U.S.A.* 117, 18744–18753. doi: 10.1073/pnas.2002738117

Stallings, C. L., and Glickman, M. S. (2010). Is *Mycobacterium tuberculosis* stressed out? A critical assessment of the genetic evidence. *Microbes Infect.* 12, 1091–1101. doi: 10.1016/j.micinf.2010.07.014

Tan, M. P., Sequeira, P., Lin, W. W., Phong, W. Y., Cliff, P., Ng, S. H., et al. (2010). Nitrate respiration protects hypoxic *Mycobacterium tuberculosis* against acid- and reactive nitrogen species stresses. *PLoS One* 5:e13356. doi: 10.1371/journal.pone.0013356

Tran, T., Bonham, A. J., Chan, E. D., and Honda, J. R. (2019). A paucity of knowledge regarding nontuberculous mycobacterial lipids compared to the tubercle bacillus. *Tuberculosis (Edinb.)* 115, 96–107. doi: 10.1016/j.tube.2019.02.008

Vijay, S., Hai, H. T., Thu, D. D. A., Johnson, E., Pielach, A., Phu, N. H., et al. (2017). Ultrastructural analysis of cell envelope and accumulation of lipid inclusions in clinical *Mycobacterium tuberculosis* isolates from sputum, oxidative stress, and iron deficiency. *Front. Microbiol.* 8:2681.

Weir, M. P., Langridge, W. H. III, and Walker, R. W. (1972). Relationships between oleic acid uptake and lipid metabolism in *Mycobacterium smegmatis*. *Am. Rev. Respir. Dis.* 106, 450–457. doi: 10.1164/arrd.1972.106.3.450

Zechner, R., Zimmermann, R., Eichmann, T. O., Kohlwein, S. D., Haemmerle, G., Lass, A., et al. (2012). FAT SIGNALS–lipases and lipolysis in lipid metabolism and signaling. *Cell Metab.* 15, 279–291. doi: 10.1016/j.cmet.2011.12.018

Zhai, W., Wu, F., Zhang, Y., Fu, Y., and Liu, Z. (2019). The immune escape mechanisms of *Mycobacterium tuberculosis*. *Int. J. Mol. Sci.* 20:340. doi: 10.3390/ijms20020340

Zorova, L. D., Popkov, V. A., Plotnikov, E. Y., Silachev, D. N., Pevzner, I. B., Jankauskas, S. S., et al. (2018). Mitochondrial membrane potential. *Anal. Biochem.* 552, 50–59.

Conflict of Interest: The authors declare that the research was conducted in the absence of any commercial or financial relationships that could be construed as a potential conflict of interest.

Publisher's Note: All claims expressed in this article are solely those of the authors and do not necessarily represent those of their affiliated organizations, or those of the publisher, the editors and the reviewers. Any product that may be evaluated in this article, or claim that may be made by its manufacturer, is not guaranteed or endorsed by the publisher.

frontiers in Microbiology

ORIGINAL RESEARCH
published: 08 September 2021
doi: 10.3389/fmicb.2021.720644

Maturation of *Rhodobacter capsulatus* Multicopper Oxidase CutO Depends on the CopA Copper Efflux Pathway and Requires the *cutF* Product

Yavuz Öztürk[1,2], Crysten E. Blaby-Haas[3,4], Noel Daum[1], Andreea Andrei[1,5], Juna Rauch[1], Fevzi Daldal[2] and Hans-Georg Koch[1]**

[1] Institut für Biochemie und Molekularbiologie, ZBMZ, Faculty of Medicine, Albert-Ludwigs-Universität Freiburg, Freiburg, Germany, [2] Department of Biology, University of Pennsylvania, Philadelphia, PA, United States, [3] Biology Department, Brookhaven National Laboratory, Upton, NY, United States, [4] Department of Biochemistry and Cell Biology, Stony Brook University, Stony Brook, NY, United States, [5] Fakultät für Biologie, Albert-Ludwigs-Universität Freiburg, Freiburg, Germany

OPEN ACCESS

Edited by:
Nicole Buan,
University of Nebraska-Lincoln,
United States

Reviewed by:
Lorena Novoa-Aponte,
National Institute of Diabetes and Digestive and Kidney Diseases, National Institutes of Health (NIH), United States
Ulrike Kappler,
The University of Queensland, Australia

***Correspondence:**
Fevzi Daldal
fdaldal@sas.upenn.edu
Hans-Georg Koch
Hans-Georg.Koch@biochemie.uni-freiburg.de

Specialty section:
This article was submitted to Microbial Physiology and Metabolism, a section of the journal Frontiers in Microbiology

Received: 04 June 2021
Accepted: 18 August 2021
Published: 08 September 2021

Citation:
Öztürk Y, Blaby-Haas CE, Daum N, Andrei A, Rauch J, Daldal F and Koch H-G (2021) Maturation of Rhodobacter capsulatus Multicopper Oxidase CutO Depends on the CopA Copper Efflux Pathway and Requires the cutF Product. Front. Microbiol. 12:720644. doi: 10.3389/fmicb.2021.720644

Copper (Cu) is an essential cofactor required for redox enzymes in all domains of life. Because of its toxicity, tightly controlled mechanisms ensure Cu delivery for cuproenzyme biogenesis and simultaneously protect cells against toxic Cu. Many Gram-negative bacteria contain extracytoplasmic multicopper oxidases (MCOs), which are involved in periplasmic Cu detoxification. MCOs are unique cuproenzymes because their catalytic center contains multiple Cu atoms, which are required for the oxidation of Cu^{1+} to the less toxic Cu^{2+}. Hence, Cu is both substrate and essential cofactor of MCOs. Here, we investigated the maturation of *Rhodobacter capsulatus* MCO CutO and its role in periplasmic Cu detoxification. A survey of CutO activity of *R. capsulatus* mutants with known defects in Cu homeostasis and in the maturation of the cuproprotein cbb_3-type cytochrome oxidase (cbb_3-Cox) was performed. This revealed that CutO activity is largely independent of the Cu-delivery pathway for cbb_3-Cox biogenesis, except for the cupric reductase CcoG, which is required for full CutO activity. The most pronounced decrease of CutO activity was observed with strains lacking the cytoplasmic Cu chaperone CopZ, or the Cu-exporting ATPase CopA, indicating that CutO maturation is linked to the CopZ-CopA mediated Cu-detoxification pathway. Our data demonstrate that CutO is important for cellular Cu resistance under both aerobic and anaerobic growth conditions. CutO is encoded in the *cutFOG* operon, but only CutF, and not CutG, is essential for CutO activity. No CutO activity is detectable when *cutF* or its putative Cu-binding motif are mutated, suggesting that the *cutF* product serves as a Cu-binding component required for active CutO production. Bioinformatic analyses of CutF-like proteins support their widespread roles as putative Cu-binding proteins for several Cu-relay pathways. Our overall findings show that the cytoplasmic CopZ-CopA dependent Cu detoxification pathway contributes to providing Cu to CutO maturation, a process that strictly relies on *cutF*.

Keywords: *Rhodobacter capsulatus*, copper homeostasis, multicopper oxidase, respiratory and photosynthetic growth, copper chaperones, cuproenzyme biogenesis

INTRODUCTION

The redox properties of copper (Cu) make it a suitable cofactor for cuproenzymes that are involved in vital metabolic reactions (Festa and Thiele, 2011; Andrei et al., 2020). However, this inherent property of Cu makes it also very reactive and toxic even at low concentrations by facilitating the production of hydroxyl radicals that attack primarily Fe-S clusters, and by interfering with major biosynthetic pathways, including chlorophyll and *c*-type cytochrome maturation processes (Gaetke and Chow, 2003; Durand et al., 2015; Steunou et al., 2020). Hence, cells have developed sophisticated mechanisms for Cu homeostasis, maintaining the availability of Cu for cuproprotein biosynthesis, while simultaneously preventing Cu toxicity (Osman and Cavet, 2008; Boal and Rosenzweig, 2009; Quintana et al., 2017). During the last decade, the cbb_3-type cytochrome oxidase (cbb_3-Cox) of the facultative phototrophic bacterium *Rhodobacter capsulatus* has been developed into an excellent model for studying cuproprotein biogenesis, and the pathways for Cu detoxification and cuproprotein maturation have been delineated (Ekici et al., 2014; Utz et al., 2019; Andrei et al., 2020). The maturation of the binuclear heme b_3-Cu_B catalytic center in subunit CcoN of cbb_3-Cox is a multi-step process that requires the coordinated action of Cu transporters and Cu chaperones to supply Cu^{1+} to cbb_3-Cox (Khalfaoui-Hassani et al., 2016). It begins with the uptake of Cu^{2+} by the major facilitator superfamily (MFS) protein CcoA (Ekici et al., 2012; Zhang et al., 2019). Next, intracellular Cu^{2+} is reduced to Cu^{1+} by the Cu reductase CcoG (Marckmann et al., 2019) and then conveyed via the cytoplasmic chaperone CopZ to the P_{1B}-type ATPase CcoI for Cu^{1+} translocation into the periplasm (Utz et al., 2019). Especially under low Cu availability, Cu is inserted into cbb_3-Cox by sequential interactions of the periplasmic Cu chaperones SenC and PccA (Lohmeyer et al., 2012; Trasnea et al., 2018).

In many bacteria, excess Cu is sensed by CueR-like transcription factors, which regulate the expression of Cu tolerance genes including *copA*, *copZ,* and *cueO* (Outten et al., 2000; Stoyanov et al., 2001; Changela et al., 2003; Peuser et al., 2011; Philips et al., 2015). Cu-exporting P_{1B}-type ATPases such as CopA represent the central component of the Cu-efflux pathway in most Gram-negative bacteria (Petersen and Moller, 2000; Rensing et al., 2000; Argüello et al., 2013). Like CcoI, CopA receives Cu from the cytoplasmic chaperone CopZ and exports it in an ATP-dependent step to the periplasm (Gonzalez-Guerrero and Arguello, 2008; Utz et al., 2019). In the periplasm, laccase-like multicopper oxidases (MCOs), such as CueO of *Escherichia coli* and CutO of *R. capsulatus*, play a crucial role in Cu detoxification by oxidizing Cu^{1+} to the less toxic Cu^{2+} (Cha and Cooksey, 1991; Grass and Rensing, 2001; Outten et al., 2001; Wiethaus et al., 2006; Achard et al., 2010; Rowland and Niederweis, 2013; Granja-Travez and Bugg, 2018).

Laccase-like MCOs are unique enzymes because they require Cu ions in their catalytic centers for Cu^{1+} oxidation, hence Cu serves as a cofactor and a substrate for these enzymes. These Cu oxidases are typically monomeric proteins that consist of three cupredoxin domains and contain four Cu atoms in the catalytic site. These Cu ions are discriminated by distinct spectroscopic properties and referred to as T1 Cu, T2 Cu and the binuclear T3 Cu (Bello et al., 2012). Substrates bind to the T1 Cu, also referred to as blue Cu, which shuttles electrons to a trinuclear Cu site (TNC), composed of the T2 Cu and the two T3 Cu ions (Bello et al., 2012). In addition to the four Cu ions in the catalytic site, MCOs can also bind additional Cu via their methionine-rich segments (MRS), and at least three additional Cu are bound to the MRS in *E. coli* CueO (Singh et al., 2011). However, the length and sequence of MRS are variable between MCOs from different species (Fernandes et al., 2007; Djoko et al., 2008; Sakuraba et al., 2011). *R. capsulatus* CutO exhibits similarity (25% identity) to CueO of *E. coli*, and in particular, all Cu binding motifs are completely conserved (Wiethaus et al., 2006). CutO is encoded in the tricistronic *cutFOG* operon (*rcc02111*, *rcc02110*, and *rcc02109*) (**Figure 1A**), and all three genes (initially called *orf635-cutO-cutR*) are required for Cu tolerance (Wiethaus et al., 2006). The transcription of *cutO* strictly depends on the promoter upstream of *cutF* (Wiethaus et al., 2006), and the expression of *cutO* and *cutG* is affected by Cu availability, unlike *cutF* expression (Rademacher et al., 2012; Selamoglu et al., 2020). However, the mechanisms of this Cu-dependent transcriptional regulation are largely unknown. Initially, it has been suggested that CutG acts as a transcriptional repressor in the absence of Cu (Wiethaus et al., 2006). The product of *cutG* is homologous to the Cu-thiol oxidoreductase CopG of *Pseudomonas aeruginosa* (42% identity and 68% similarity) and is widely distributed among Gram-negative bacteria. It is frequently present in Cu resistance-conferring gene clusters encoding CueO, CopA, and CusCBA (Monchy et al., 2006; Wiethaus et al., 2006; Behlau et al., 2011; Marrero et al., 2012). *P. aeruginosa* CopG contains a cysteine-bridged tetranuclear Cu cluster and contributes to Cu resistance under anaerobic conditions via its Cu oxidoreductase activity (Hausrath et al., 2020). In addition to its enzymatic activity, CopG is proposed to be involved in Cu transfer reactions (Hausrath et al., 2020).

Unlike CutG, CutF-like proteins are detected by BLASTp in only a small subset of bacterial genomes. Searching with CutF against the non-redundant protein sequence database with default parameters identifies similar proteins in only 10 genomes, all from *Rhodobacteraceae* (see section "Results"). CutF from *R. capsulatus* encodes a predicted small protein of 118 amino acids, and has a putative Sec signal sequence, suggesting that CutF is translocated to the periplasm. Sequence alignment of CutF homologs shows a conserved CXXXC motif in its central part that could ligate Cu. *cutF* expression does not seem to be regulated by Cu (Rademacher et al., 2012), and a *cutF* translation product was not detected in comparative cuproproteome analyses of *R. capsulatus*, despite large differential variations of CutO- and CutG-levels under Cu-supplemented or Cu-depleted growth conditions (Selamoglu et al., 2020). These observations suggest that CutF might be a low abundance protein of unknown function, potentially required for the production of active CutO. Furthermore, in the light of the dual role of Cu as an essential cofactor and also as a substrate of MCOs, it is unclear whether the Cu cofactor required for forming the catalytic center and the substrate Cu^{1+} that is converted to Cu^{2+} by the catalytic center,

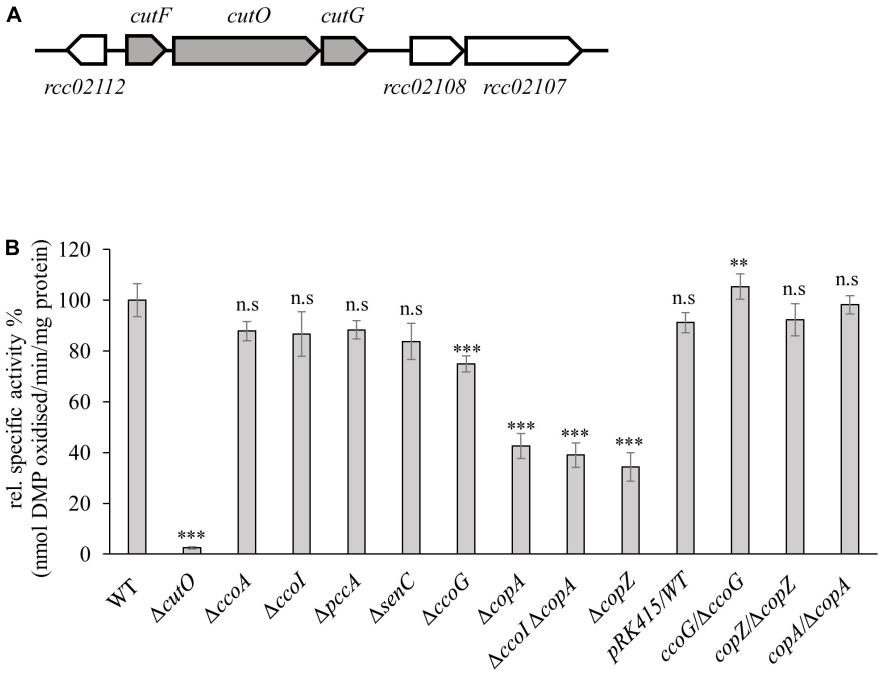

FIGURE 1 | Genetic organization and activity of the multi-copper oxidase (MCOs) CutO in *Rhodobacter capsulatus*. **(A)** Genetic organization of the *cutFOG* operon in *R. capsulatus*. *CutO* codes for the multicopper oxidase (*rcc02110*), and *cutF* (*rcc02111*) and *cutG* (*rcc02109*) for largely uncharacterized proteins. The open reading frame *rcc02112* encodes a putative glyoxalase/bleomycin resistance protein/dioxygenase. The open reading frames *rcc02108* and *rcc02107* encode hypothetical proteins with unknown function. **(B)** CutO activity of different *R. capsulatus* mutants deficient in cbb_3-Cox assembly and Cu homeostasis. Periplasmic fractions were isolated from the indicated strains, grown in magnesium–calcium, peptone, yeast extract (MPYE) medium supplemented with 10 μM $CuSO_4$. 50 μg periplasmic soluble protein was used in the 2,6-DMP assay and absorbance was measured at 468 nm. The activity of wild-type (WT) was set to 100% and the relative activities of the indicated strains were calculated. The activities of mutant strains that showed significantly reduced CutO activity were also tested after complementation with pRK415-borne copies of the respective genes. WT containing the pRK415 vector served as a control. Three independent experiments were performed with three technical replicates and the error bars reflect the standard deviation (n = 9). Statistical analyses were performed with the Satterthwaite corrected two-sided Student t-test, using the activity of the WT as reference. (*) refers to p-values ≤ 0.05; (**) to p-values ≤ 0.01, and (***) to p-values ≤ 0.001.

are provided by the same Cu-delivery pathway. In the current study, we performed a rule-based bioinformatic search combined with profile hidden Markov Models (HMMs) to identify CutF-like proteins encoded by available proteobacterial genomes and tested the role of CutF for CutO activity, and the source of catalytic Cu and substrate Cu for CutO assembly and activity were investigated.

MATERIALS AND METHODS

Bacterial Strains and Growth Conditions

The bacterial strains and plasmids used in this study are described in **Supplementary Table 1**. *R. capsulatus* strains were grown under respiratory (Res) or photosynthetic (PS) conditions on magnesium–calcium, peptone, yeast extract (MPYE) enriched medium (Daldal et al., 1986), or Sistrom's minimal medium A (Med A; Sistrom, 1960), supplemented with kanamycin, spectinomycin, gentamycin or tetracycline as appropriate (10, 10, 1 or 2.5 μg per mL, respectively) at 35°C. For PS growth, cultures were incubated under saturating light intensity in anaerobic jars containing H_2 and CO_2 generating gas packs (Becton Dickinson and Co.) (Jenney and Daldal, 1993). For protein production of arabinose-inducible genes in *R. capsulatus*, liquid media were supplemented with 0.5% L-arabinose (L-ara) at OD_{685} of 0.5–0.6 and further growth for 6 h. *E. coli* strains were grown on lysogeny broth medium (LB; Bertani, 1951), containing ampicillin, kanamycin, or tetracycline (at 100, 50, or 12.5 μg per mL, respectively) as appropriate.

Copper-Sensitivity Assays and NADI Staining on Plates

The growth of *R. capsulatus* strains in the presence of different $CuSO_4$ concentrations was monitored using spot assays (Utz et al., 2019). Strains were grown semi aerobically overnight to an OD_{685} of ∼ 0.9 and cell counts were determined based on OD_{685} of 1.0 = 7.5 × 10^8 cells/mL. For each strain, 1 × 10^8 cells were resuspended in 400 μL medium and subsequently serially diluted in a 96-well plate. Dilutions ranging from 10^0 to 10^{-7} were spotted on MPYE plates containing different concentrations of $CuSO_4$ by a 48 pin replica plater. The plates were incubated under the Res and Ps conditions for approx. 2 and 3 days, respectively, before scoring the data.

The *in vivo* cbb_3-Cox activity of *R. capsulatus* colonies was visualized qualitatively using the "NADI" staining solution made by mixing 1:1 (v/v) ratio of 35 mM α-naphtol and 30 mM *N*,

N, *N*′, *N*′ –dimethyl-*p*-phenylene diamine (DMPD) dissolved in ethanol and water, respectively (Koch et al., 1998b).

Molecular Genetic Techniques

Chromosomal Inactivation of *cutFOG* and *copA* in a Δ*ccoI* (CW2) Strain

Chromosomal knock-out alleles of *cutG* and *cutF* genes were obtained by interposon mutagenesis using the Gene Transfer Agent (GTA; Yen et al., 1979; Daldal et al., 1986) and in-frame markerless chromosomal deletion method, respectively (Brimacombe et al., 2013). A Δ(*cutG*:*Gm*) deletion-insertion allele, carried by the conjugative plasmid pRK415 (Ditta et al., 1985) in the *R. capsulatus* GTA overproducer strain Y262 was used to inactivate the chromosomal copy of *cutG* in Δ*cutO* and Δ*cutFO* (YO-ΔcutFO) strains (Selamoglu et al., 2020) to obtain the Δ*cutOG* double (Δ*cutO*Δ*cutG*) and the Δ*cutFOG* (Δ*cutF*Δ*cutO*Δ*cutG*) triple mutants (**Supplementary Table 1**). The in-frame, markerless chromosomal deletion method was used for creating a Δ*cutF* in-frame deletion allele, containing only its first four and last four codons, carried by the suicide plasmid pZDJ (pYO-Δ02111Su) in *E. coli* strain S17-1 (Selamoglu et al., 2020). This plasmid was conjugated into the Δ*cutO* strain to obtain the Δ*cutFO* double mutant. The transconjugants were selected for Gm^r and counter-selected using sucrose, which is toxic in the presence of *sacB* carried by the pYO-Δ02111Su plasmid. After two passages in non-selective liquid MedA, colonies carrying a chromosomal deletion of *cutF* were selected for their ability to grow under Res conditions in the presence of 10% sucrose due to second homologous recombination eliminating the chromosome-integrated copy of pYO-Δ02111Su (Brimacombe et al., 2013; Kuchinski et al., 2016). A few of these sucrose-resistant and Gm^s colonies were screened by colony PCR to detect the in-frame deletions, and amplified fragments were confirmed by DNA sequencing. The Δ*ccoI*Δ*copA* double mutant was obtained by using the pRK-CopA2:Kan plasmid (Ekici et al., 2014) carrying the Δ(*copA:kan*) allele in the GTA overproducer Y262 strain. GTA particles isolated from this strain were used with the Δ*ccoI* strain for GTA-mediated interposon mutagenesis as above (Yen et al., 1979; Daldal et al., 1986).

Cloning of *cutFOG* Operon With Its Native Promoter and Construction of Epitope-Tagged Protein Variants

Standard molecular genetic techniques were performed as described previously (Koch et al., 1998a; Sambrook and Russel, 2001). The tagged version of *cutFOG* genes ($cutF_{Strep}O_{Flag}G_{MycHis}$ or $cutF_{Flag}O_{Flag}G_{MycHis}$) were cloned while maintaining the integrity of the operon, including its 526 bp upstream (promoter) and 466 bp downstream (transcriptional terminator) DNA regions using appropriate primers (**Supplementary Table 2**). The DNA fragments encoding the N-terminally or C-terminally tagged version of the corresponding proteins were amplified by PCR using the wild-type (WT) MT1131 genomic DNA as a template. The PCR primers used for the NEBuilder^R HiFi assembly cloning method (NEB Lab, United States) contained 20 bp long 5′ overlapping regions between the vector arms and the gene fragments, and after amplifications, the PCR products were purified by Qiagen PCR purification kit (Qiagen, Hilden, Germany). The quantity and quality of the amplified DNA fragments were checked via a nanodrop spectrophotometer and agarose gel electrophoresis, respectively, and used in the assembly reactions. HiFi assembly master mix (NEBuilder^R) was used in a single step reaction to assemble the 526 bp upstream fragment, $cutF_{Strep}$ (or $cutF_{Flag}$), $cutO_{Flag}$, $cutG_{MycHis}$, 466 bp downstream fragment, and the conjugative plasmid pRK415 digested with *Kpn*I and *Xba*I restriction enzymes, according to the NEB protocol. In each case, the total amount of DNA fragments used was ∼ 0.4 – 0.5 pmoles, and the vector to insert ratio was ∼ 1:2 to 1:3. The samples were incubated in a thermocycler at 50°C for 60 min, and 4 μL of the assembly reaction was transformed to a chemically competent *E. coli* HB101 strain. Two versions of $cutF_{Strep}$ were constructed, one containing the tag at its C-terminus with a Gly-Gly-Ser-Ala (GGSA) linker, and the other containing the tag at its N-terminus after its signal peptide cleavage site with a GGSA linker. A similar N-terminally tagged version of *cutF*, replacing its Strep tag with a Flag tag was also constructed to yield $cutF_{N-Flag}$.The $cutO_{Flag}$ and $cutG_{MycHis}$ were cloned by adding their tags at the C-termini of all constructs. The constructed conjugative plasmids pRK-cutFOG1 ($cutF_{C-Strep}O_{Flag}G_{MycHis}$) pRK-cutFOG2 ($cutF_{N-Strep}O_{Flag}G_{MycHis}$) and pRK-cutFOG3 ($cutF_{N-Flag}O_{Flag}G_{MycHis}$) were confirmed by DNA sequencing. The correct clones were conjugated into the *R. capsulatus* Δ*cutFOG* strain via triparental crosses (**Supplementary Table 1**).

Construction of CutO, CutF, and CutG Mutant Derivatives

Two mutant versions of CutO were constructed by substituting Cys473 to Ala ($CutO_{C473A}$, leading to the loss of the T1 Cu site), and by deleting the 41 amino acid long methionine rich MDHGAMDHSATPMQGMDGMADMMSLPGMAEMHAAME GGLSM sequence between the domains 1 and 2 of CutO ($CutO_{\Delta MRS}$) using the mutagenic primers cutF(EP)-F, cutO(C473A)-R, cutGopr-F, and cutTer-R for $CutO_{C473A}$, cutF(EP)-F, cutOdelMRS-R, cutOdelMRS-F, cutOopr-R, cutGopr-F and cutTer-R for $CutO_{\Delta MRS}$ (**Supplemetary Table 2**), using the *cutFOG* operon with its native promoter and terminator regions. The amplified fragments were assembled into the *Kpn*I-*Xba*I digested pRK415 vector as above. For these mutations, pRK-cutFO_{Flag}G plasmid carrying the CutFO_{Flag}G variant was used as a template. This plasmid was constructed by using the primers cutF(EP)-F, cutOopr-R, cutOopr-F, and cutTer-R (**Supplementary Tables 1, 2**) as described above.

Substitution of two conserved Cys residues in CutF by Ala ($C_{69}XXXC_{73}$ to $A_{69}XXXA_{73}$) and truncation of C-terminal Proline-rich region ($\Delta P_{109}EPEGPPPRL_{118}$) were constructed on pRK-cutFOG3 ($cutF_{N-Flag}O_{Flag}G_{MycHis}$) by using the mutagenic primers cutF(EP)-F, cutF(C-A)-R, cutF(C-A)-F and cutTer-R for $CutF_{C-A}$, cutF(EP)-F, cutF(del-Cter)-R, cutF(del-Cter)-F and cutTer-R for $CutF_{\Delta C-ter}$ (**Supplementary Table 2**). The amplified fragments were assembled into the *Kpn*I-*Xba*I digested pRK415 vector as above.

Substitution of three conserved Cys residues of CutG to Ala ($C_{40}XC_{42}C_{43}$ to $A_{40}XA_{42}A_{43}$) and three Met residues to Ala

($M_{120}X_{(6)}M_{127}$ to $A_{120}X_{(6)}A_{127}$ of CutG) were constructed on pRK-cutFOG3 ($cutF_{N-Flag}O_{Flag}G_{MycHis}$) by using the mutagenic primers cutF(EP)-F, cutG(C-A)-R, cutG(C-A)-F and cutTer-R for $CutG_{C-A}$, cutF(EP)-F, cutG(M-A)-R, cutG(M-A)-F and cutTer-R for $CutG_{M-A}$ (**Supplementary Table 2**). Assembly of the fragments was performed as described above.

Cloning of pRS1-*cutF* for *in vivo* and *in vitro* Expression

The ORF of *cutF* was cloned into the plasmid pRS1 (Jauss et al., 2019) for *in vivo* and *in vitro* expression. The vector pRS1 was linearized by using the pRS1-F and pRS1-R primers at the start codon ATG. The amplification mixture containing the linear form of pRS1 was digested with *Dpn*I to remove its circular form used as a PCR template. The $cutF_{N-Flag}$ including a 20 bp overlapping sequence of pRS1 vector was amplified from pRK-cutFOG3 by using the primers pRS1cutF-F and pRS1cutF-R (**Supplementary Table 2**) and Q5® High-Fidelity DNA Polymerase (NEB Lab, MA, United States). The HiFi assembly (NEBuilderR) and transformation procedures similar to those described above were used for this construction, except that the 4 μL of the assembly reaction mixture was transformed to chemically competent *E. coli* NEB® 5-alpha and C43(DE3) strain, selecting for Amp^r colonies. The resulting plasmid pRS1-cutF was confirmed by DNA sequencing.

Total RNA Isolation and Transcription Analysis by RT-PCR

Semi-aerobic (Res grown) cultures of *R. capsulatus* in MPYE medium with (10 μM $CuSO_4$) and without Cu addition were grown to mid-log phase (OD_{685} 0.5–0.8). Total RNA was isolated from $\sim 1 \times 10^9$ cells thus obtained using the Qiagen RNeasy mini kit (Qiagen, Hilden, Germany), and digested with DNase I for 30 min at 25°C in the presence of RNase inhibitor RNasin. ∼120–180 ng of total RNA was used in RT-PCR reactions with the One-Step RT-PCR kit (Qiagen, Hilden, Germany). Transcriptional features of the *cutFOG* operon were analyzed using the cutFO(rtPCR)-F/cutFO(rtPCR)-R primer pairs covering 400 bp of *cutFO*, and the cutOG(rtPCR)-F/cutOG(rtPCR)-R primer pairs covering 500 bp of *cutOG*, and the 16SrRNA-F and 16SrRNA-R primers provided an internal control for amplification of a 450-bp region of *R. capsulatus* 16S rRNA gene (**Supplementary Table 2**; Ekici et al., 2014). Control reactions omitted the RNA template from the reaction mixture and the amplified RT-PCR products were separated using 2% agarose gels.

Biochemical and Biophysical Techniques

Membrane Preparation for SDS-PAGE and TMBZ Staining

Cytoplasmic membrane fractions and supernatant fractions (soluble cytoplasmic and periplasmic proteins) were prepared by using 50 or 250 mL of *R. capsulatus* cultures grown overnight under Res conditions in MPYE. Cells were broken by using either a French pressure cell at 18,000 lb/inch^2 or an Emulsiflex C3 homogenizer (Avestin, Ottawa, ON, Canada) at 10,000 lb/inch^2 as described earlier (Gray et al., 1994; Knupffer et al., 2019). Membranes were resuspended in 400 μL of 50 mM triethanolamine acetate (pH 7.5), 0.5 mM phenylmethylsulfonyl fluoride (PMSF), 1 mM EDTA, and 1 mM dithiothreitol, and the protein concentrations were determined by using a modified Lowry assay (Noble and Bailey, 2009).

Multicopper Oxidase Activity

The oxidation of 2,6-dimethoxyphenol (2,6-DMP) by the periplasmic fraction (20 or 50 μg total protein) of *R. capsulatus* cells was monitored either continuously with a TIDAS 100 spectrophotometer for 15 min or with Ultrospec 3,100 pro reader for endpoint measurement at 468 nm. The molar concentration of oxidized 2,6-DMP was calculated using $\varepsilon = 14{,}800\ M^{-1}\ cm^{-1}$ of oxidized 2,6-DMP (Solano et al., 2001).

The periplasmic fraction was isolated following published protocols (McEwan et al., 1984; Trasnea et al., 2016). In brief, bacterial cultures (50 mL) were grown overnight on MPYE under Res or PS conditions in the presence or absence of supplementary $CuSO_4$, as specified in the legends to the figures. The entire culture was harvested and washed at 4°C with 12 mL of 50 mM Tris–HC1 pH 8.0, the final pellet resuspended to a concentration of 10 mL/g of wet weight in the SET buffer (0.5 M sucrose, 1.3 mM EDTA, 50 mM Tris–HC1 pH 8.0), incubated with 600 μg lysozyme/mL at 30°C for 60 min, and spheroplasts formation was monitored by microscopy (**Supplementary Figure 1**). The suspension was sedimented at 4°C by centrifugation at 13.000 rpm for 30 min. The supernatant (periplasmic fraction) was stored on ice while the pellet was resuspended in a total volume of 1.5 mL of SET buffer in 2 mL eppendorf tubes. This suspension was sonicated on ice with a Dawe Soniprobe (United Kingdom) four times with 15 s sonication and 30 s break at 150 W and then centrifuged at 5.000 rpm for 10 min. The pellet was discarded and the supernatant was further centrifuged at 45.000 rpm for 90 min. The supernatant (cytoplasmic fraction) together with the last pellet resuspended in 100 μL of ICM buffer (membrane fraction) were stored at −80°C.

Immune Detection and Heme Staining

For immune-detection following SDS- or BN-PAGE, proteins were electro-blotted onto nitrocellulose (GE Healthcare, Germany) or PVDF Immobilon-P (GE Healthcare, Germany) membranes, respectively, and antibodies against the Flag-, His- or Myc-tags (clone 9E10) were purchased from either Sigma or Millipore (Temecula, CA, United States). Heme staining was performed as described earlier (Koch et al., 1998a). For this purpose, 16.5% Tris–Tricine SDS-PAGE were used (Schagger and Von Jagow, 1987). Samples were denatured in SDS-loading buffer for 10 min at 95°C for soluble proteins, 20 min at 37°C for membrane-bound proteins, and following electrophoresis, the *c*-type cyts revealed by their peroxidase activities using 3,3′, 5, 5′ tetramethylbenzidine (TMBZ) and H_2O_2 (Thomas et al., 1976).

In vitro Synthesis of CutF

An *in vitro* coupled transcription-translation system was used to synthesize CutF. Cytosolic translation factors (CTF) and high-salt washed ribosomes were used in 25 μL aliquots, as described before (Hoffschulte et al., 1994; Koch et al., 1999).

A final concentration of 11 mM MgAc was used in all samples, a control sample lacking ribosomes was included, and the radioactive labeling mix containing ^{35}S-Methionine/^{35}S-Cysteine was purchased from Hartmann Analytic (Braunschweig, Germany). The reaction mixture was prepared on ice and then incubated for 30 min at 35°C with gentle shaking. At the end of the synthesis, the *in vitro* reaction was mixed with 1:1 10% TCA, precipitated for 40 min on ice, the samples were pelleted in a precooled table-top centrifuge at 13,700 × *g* for 18 min. The pellet was further resuspended in 30 μL TCA, mixed with a loading dye prepared as described earlier (Steinberg et al., 2020), and subsequently denatured at 37°C for 20 min. The samples were subjected to a 5–15% SDS-PAGE, and the separated proteins were visualized by phosphorimaging.

Phylogenomic Analyses

Identification of CutF-Like Proteins

Because of the relatively small size (118 amino acid residues) and poor sequence conservation, a rule-based approach was used to identify CutF-like protein sequences. Genes within a 10-gene window surrounding CutO-encoding homologs (defined as containing either PF00394 or PF07731 or both) from publicly available proteobacterial genomes were collected using the genomic context tool EFI-GNT (Gerlt, 2017; Zallot et al., 2019). Gene neighbors were then filtered based on the following criteria: the encoded protein is smaller than 170 amino acids, does not match to a known Pfam domain, contains a predicted signal peptide, a CXXXC sequence motif (where X is any amino acid), and the PP sequence motif. The resulting protein sequences were aligned with MUSCLE (Madeira et al., 2019), viewed with Jalview (Waterhouse et al., 2009), and sequences were removed based on manual inspection of the CXXXC motif alignment. The multiple sequence alignment thus obtained was used to search for similar proteins via jackhammer (Potter et al., 2018) against the Proteobacterial Reference Proteome set in the UniProt database (The UniProt Consortium, 2019) with 11 iterations at which point no additional sequences were identified. Any sequence matching to a Pfam domain was removed, resulting in a total of 2,938 sequences that we refer to as CutF-like proteins.

Copper-Oxidase Sequence Similarity Network

Bacterial reference proteomes from the UniProt database were searched for proteins that contained the three Cu-oxidase domains PF00394, PF07731, and PF07732, resulting in 4,040 sequences. The EFI-Enzyme Similarity Tool (EFI-EST[1]; Gerlt et al., 2015) was used to build the similarity network with an alignment score of 100, and nodes were collapsed at a similarity of 90%. The network thus built was visualized with Cytoscape (Shannon et al., 2003) and nodes were clustered using the yFiles organic layout.

Copper Oxidase Phylogenetic Reconstruction

Proteobacterial Cu oxidase-like proteins from the sequence similarity network were extracted and mapped to UniRef90 in the UniProt database (Suzek et al., 2015). Phylogenetic analysis was performed using the CIPRES web portal (Miller et al., 2010) with MAFFT on XSEDE (v. 7.305) for the sequence alignment (Katoh and Standley, 2013) and FastTree with 1,000 bootstrap replicates (Price et al., 2010). Branches with less than 50% bootstrap support were deleted.

[1]http://efi.igb.illinois.edu/efi-est/

RESULTS

CutO Activity Is Largely Independent of the Cu Supply System for *cbb*$_3$-Cox Assembly, but Partly Relies on the CopZ-CopA Cu Export Pathway

Maturation of the cuproprotein *cbb*$_3$-Cox depends on a complex Cu delivery chain that involves at least six proteins, which shuttle Cu from the extracellular space into the cytosol and back to the periplasm prior to Cu insertion into the catalytic subunit CcoN (Andrei et al., 2020). The complexity of this Cu supply chain raises the question of whether it is dedicated solely to *cbb*$_3$-Cox assembly or also used at least partly for the maturation of other extracytoplasmic cuproproteins, such as the periplasmic CutO protein. CutO activities of mutant strains (Δ*ccoA*, Δ*ccoG*, Δ*copZ,* Δ*ccoI*, Δ*senC,* and Δ*pccA*) that are deficient in known proteins required for Cu delivery to *cbb*$_3$-Cox were determined using the 2,6-DMP assay with periplasmic extracts of the mutant strains (Solano et al., 2001). The specific activity of the wild-type (15 nanomoles of 2,6-DMP oxidized/min/mg of protein) was set to 100% and the specific activity in the mutants was determined (**Figure 1B**). The single Δ*cutO* mutant served as a control and showed no 2,6-DMP oxidation, indicating that this assay monitors exclusively CutO mediated multi copper oxidase activity in *R. capsulatus* periplasmic extracts. In comparison to the wild-type activity, no significant difference in the Δ*ccoA* strain that lacks the MFS-type Cu importer was seen. Mutant strains lacking the two periplasmic chaperones SenC and PccA, which are required for *cbb*$_3$-Cox assembly at low Cu concentrations, or CcoI, the Cu-exporting P_{1B}-type ATPase that is essential for *cbb*$_3$-Cox biogenesis (Kulajta et al., 2006; Lohmeyer et al., 2012; Trasnea et al., 2018), also showed no detectable reduction of CutO activity. A small but reproducible reduction of CutO activity (approx. 25%) was observed in the absence of the cupric reductase CcoG (Marckmann et al., 2019), which was fully restored to wild type activity by a plasmid-borne copy of *ccoG* (**Figure 1B**). CcoG reduces Cu^{2+} to Cu^{1+}, which is then bound by the chaperone CopZ or the P_{1B}-type ATPases CcoI and CopA (Gonzalez-Guerrero and Arguello, 2008; Utz et al., 2019). In contrast to CcoI, CopA is dispensible for *cbb*$_3$-Cox biogenesis, but is required for Cu detoxification (Ekici et al., 2014), which in *R. capsulatus* also involves CcoG and CopZ (Marckmann et al., 2019; Utz et al., 2019). Therefore, the CutO activities of Δ*copA* and Δ*copZ* single, as well as a Δ*copA*Δ*ccoI* double mutants were tested. These assays showed similar residual activities (about 60% reduction compared to wild-type) for both the single and double Δ*copA* mutants, and the single *copZ* mutant (**Figure 1B**). The reduced MCO activities in the Δ*copA* and Δ*copZ* single

mutants were fully restored by providing the respective genes in *trans* (**Figure 1B**). Considering that all strains grew well in the presence of 10 μM Cu, overall data showed that CutO production is independent of the cbb_3-Cox maturation machinery, except for CcoG and CopZ, and relies partly on the CopZ-CopA dependent Cu detoxification pathway. As none of the deletion mutants examined resulted in a complete loss of CutO activity, part of the Cu supply to CutO may be provided by other proteins, or may come directly from the periplasm.

Genes of the Multicopper Oxidase Operon *cutFOG* Are Important Determinants of Cu Resistance Under Aerobic and Anaerobic Growth Conditions

The physiological roles of the *cutFOG* gene products were analyzed by creating individual Δ*cutF*, Δ*cutO*, and Δ*cutG* knock-out mutants and by measuring their growth at different Cu concentrations under both respiratory (Res) and anaerobic-photosynthetic (Ps) conditions. Supplemental Cu concentrations ranging from 5 to 600 μM and 5 to 75 μM $CuSO_4$ were used for Res- and Ps-growth, respectively (**Supplementary Figures 2, 3**). As controls, the Δ*copA* and Δ*copZ* strains were included, and their Cu sensitivity profiles matched previously reported observations (Utz et al., 2019; **Supplementary Figure 2**). Under Res-condition the wild type grew up to 500 μM Cu, but growth impairment of the Δ*cutO* mutant started already at 250 μM $CuSO_4$ (**Figure 2A**) and complete inhibition was observed at 400 μM $CuSO_4$ (**Supplementary Figure 2**). The Δ*cutF* strain showed a similar Cu sensitivity, although slightly less pronounced than in the Δ*cutO* mutant (**Figure 2A**). In contrast, the Δ*cutG* strain was less Cu sensitive than the Δ*cutO* and Δ*cutF* strains (**Figure 2A**), and complete growth inhibition was only observed at 500 μM $CuSO_4$ (**Supplementary Figure 2**). Despite the widespread distribution of CutG-like Cu resistance proteins and the more limited occurrence of CutF-like proteins (see below), *R. capsulatus* CutF appears to be as crucial for Cu detoxification as the multicopper oxidase CutO. However, the Δ*cutO* and Δ*cutF* mutants tolerated higher Cu concentrations than the Δ*copA* strain under Res growth condition (**Figure 2A**). This observation is likely due to the accumulation of cytosolic Cu^{1+} in the *R. capsulatus* Δ*copA* strain (Ekici et al., 2014; Utz et al., 2019), which might be more toxic than the accumulation of Cu^{1+} in the periplasm when CutO or CutF are absent.

One of the major targets of excess Cu in the periplasm is the cytochrome c maturation (Ccm) pathway (Sanders et al., 2005; Durand et al., 2015; Verissimo et al., 2017). Due to the presence of a quinol oxidase, the Ccm pathway is not essential for growth of *R. capsulatus* under Res conditions (Koch et al., 1998a; Swem and Bauer, 2002). However, the Ccm pathway is required for Ps-growth, and the Δ*cutF*, Δ*cutO*, and Δ*cutG* knock-out strains were therefore also tested under PS conditions. In agreement with the inhibitory effect on *c*-type cytochrome biogenesis (Durand et al., 2015), the *cutO* and *cutF* deletions strains were highly Cu sensitive under PS conditions (**Figure 2A** and **Supplementary Figure 3**). In comparision to the wild type, which grew up to 75 μM Cu, the Δ*cutG* and Δ*copA* strains were also more Cu sensitive, but still showed partial growth at 10 μM Cu (**Figure 2A** and **Supplementary Figure 3**). Although the Ccm pathway is not essential under Res condition, it is required for the activity of cbb_3-Cox, as this enzyme contains two membrane-bound *c*-type cytochrome subunits (Gray et al., 1994; Koch et al., 1998a). Hence, the inhibition of the Ccm pathway by Cu accumulation in the periplasm was further probed by determining the cbb_3-Cox activity using the NADI staining under Res conditions. All three mutant strains showed a NADI-positive response on plates without Cu supplementation, indicating that the absence of the *cutFOG* genes *per se* did not influence cbb_3-Cox activity. However, in the presence of 250 μM Cu, the Δ*cutO* strain did not turn blue when the NADI-reagent was applied, indicating the lack of cbb_3-Cox activity (**Figure 2B**). A reduced blue coloring was also observed in the Δ*cutF* strain, unlike the Δ*cutG* strain that was comparable to the wild-type in response to NADI staining (**Figure 2B**). This was further validated by performing tetramethylbenzidine (TMBZ)-mediated heme staining on membranes isolated from the deletion strains grown by respiration in the presence or absence of 250 μM Cu (**Figure 2C** and **Supplementary Figure 4**). Membranes of the Cu-supplemented wild-type strain showed reduced amounts of the membrane-bound electron donor cytochrome c_y and cytochrome *c* peroxidase (29 and 37 kDa, respectively), but no major difference was observed in the amounts of CcoO and CcoP, the two *c*-type cytochrome subunits of cbb_3-Cox. There was also no difference in the amounts of the cytochrome c_1 subunit of the bc_1 complex and the soluble electron donor cytochrome c_2. In contrast, membranes of the Cu supplemented Δ*cutO* and Δ*cutF* mutants exhibited a different cytochrome profile than the wild type and the Δ*cutG* mutant. In the absence of CutO or CutF, only cytochrome c_1 was detectable and the cytochrome subunits CcoO and CcoP of cbb_3-Cox were absent, while in the absence of CutG a cytochrome *c* profile similar to that of wild-type cells was observed (**Figure 2C**).

In summary, these data demonstrated that the multicopper oxidase CutO and the functionally uncharacterized putative protein CutF are important determinants for preventing Cu toxicity and inhibition of cytochrome biogenesis in the bacterial periplasm. In contrast, although widely conserved among bacteria, CutG does not seem to play a major role in Cu detoxification in *R. capsulatus*, suggesting that its function is dispensable or redundant with other *R. capsulatus* proteins.

CutO Activity Is Strictly Dependent on CutF, While CutG Is Partially Dispensable for Its Activity

To correlate the observed Cu sensitivity phenotypes of the Δ*cutF*, Δ*cutO,* and Δ*cutG* mutants with their CutO activities, periplasmic fractions of the individual mutants were prepared and their CutO activities were measured spectrophotometrically using 2,6-DMP as a substrate (**Figure 3A**). In the absence of CutG, CutO activity was reduced to about 50% of the wild-type activity, whereas in the absence of CutF only very low CutO activity was observed (**Figure 3A**), demonstrating that

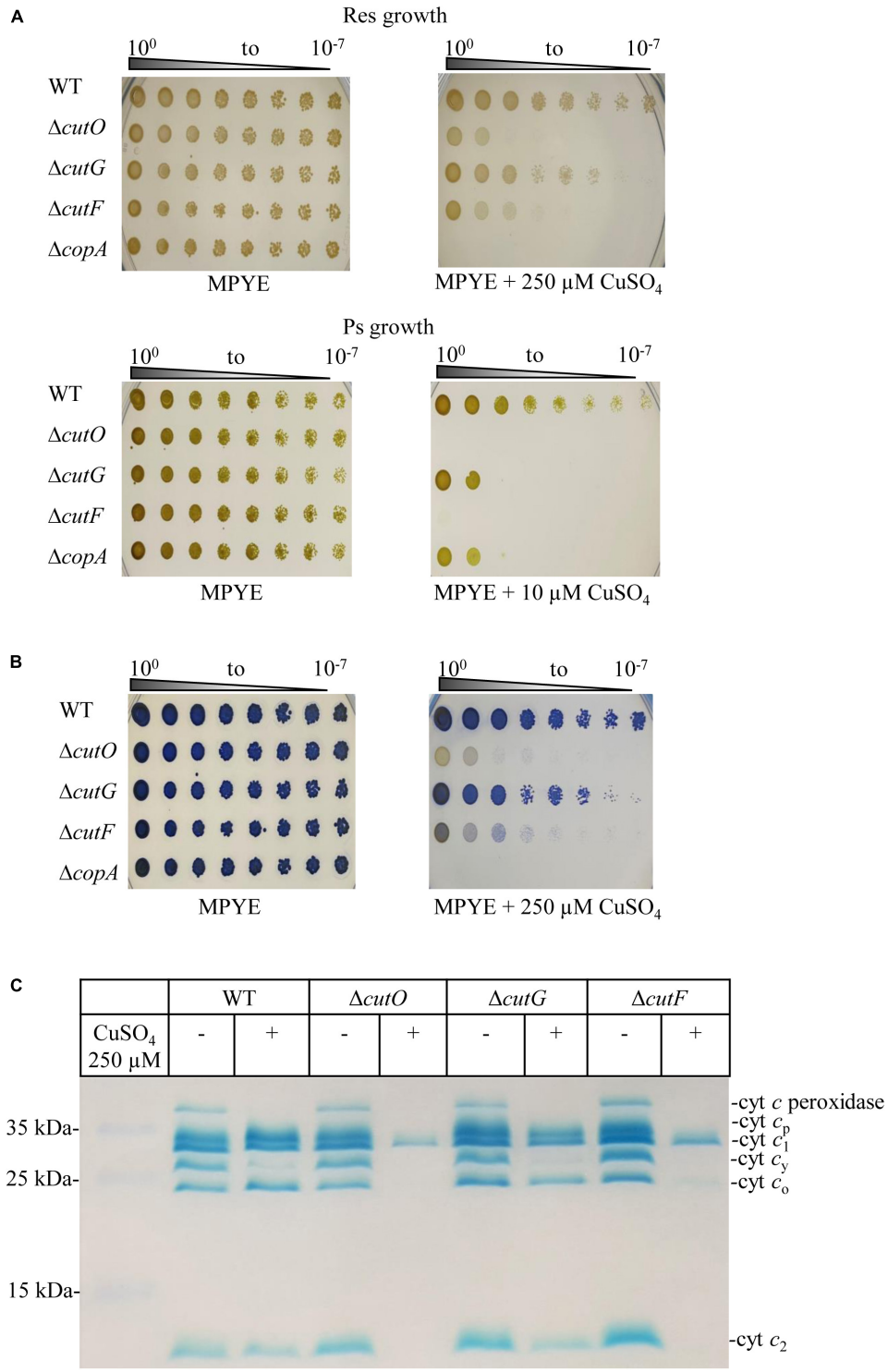

FIGURE 2 | Copper (Cu) sensitivity assay and cytochrome *c* profiles of the *cutF*, *cutO*, *and cutG* knockout strains of *R. capsulatus*. **(A)** WT and the indicated knockout strains were serially diluted and growth was tested on MPYE agar plates supplemented with 10 or 250 μM $CuSO_4$ for photosynthetic and respiratory growth, respectively, and incubated under appropriate growth conditions for 2–3 days. As a control, the Δ*cop*A strain lacking the Cu-exporting P_{1B}-type ATPase CopA was included. **(B)** The cbb_3-Cox activities of the indicated strains grown under respiratory conditions on MPYE + 250 μM $CuSO_4$ were determined by the NADI reaction. The blue dye indophenol blue is formed within 45 s in the presence of active cbb_3-Cox. No or very low cytochrome *c* oxidase activities were observed for the Δ*cutO* and Δ*cutF* strains in the presence of 250 μM Cu. **(C)** The *c*-type cytochrome profiles of mutant strains grown in the presence and absence of supplemented $CuSO_4$ were determined by heme-staining of isolated membranes and after separation on 16.5% SDS-PAGE. Cyt c_p and cyt c_o correspond to the subunits of cbb_3-Cox, cyt c_1 is the subunit of cyt bc_1 complex, and cyt c_y and cyt c_2, correspond to membrane-bound and soluble electron carriers, respectively.

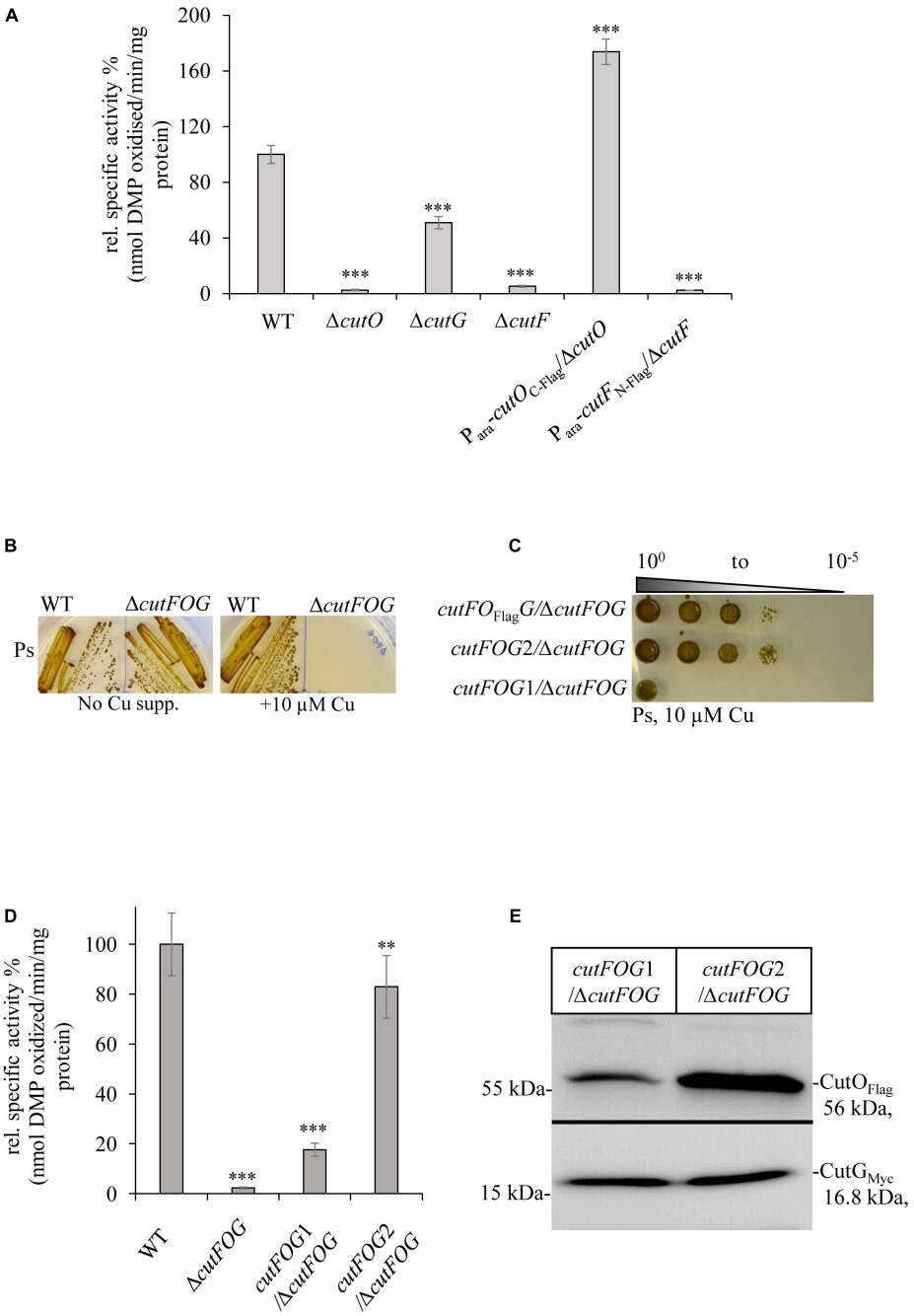

FIGURE 3 | CutF but not CutG is essential for CutO activity. **(A)** CutO activity of WT and the Δ*cutO,* Δ*cutF,* and Δ*cutG* single mutant strains of *R. capsulatus*. The CutO activity was determined as described in the legend to **Figure 1B**. Epitope-tagged versions of *cutO* and *cutF* were expressed from an arabinose-inducible promoter from plasmid pRK415. The activity of WT was set to 100% and the relative activities of the indicated strains were calculated. Three independent experiments were performed with three technical replicates and the error bars reflect the standard deviation ($n = 9$). Statistical analyses were performed as described in **Figure 1**. (*) refers to p- values ≤ 0.05; (**) to p-values ≤ 0.01, and (***) to p-values ≤ 0.001. **(B)** Cu sensitivity of the WT and the Δ*cutFOG* triple knock-out strain, grown under PS conditions and in the presence or absence of 10 µM $CuSO_4$. **(C)** Spot assay for Cu sensitivity of the Δ*cutFOG* strain expressing differently tagged plasmid-borne copies of the *cutFOG*-operon. In $cutFO_{Flag}G$, CutO was C-terminally Flag-tagged. In *cutFOG1* ($cutF_{C-Strep}O_{Flag}G_{MycHis}$) and *cutFOG2* ($cutF_{N-strep}O_{Flag}G_{MycHis}$), all three genes were tagged, but contained the Strep-tag either at the C-terminus (*cutFOG1*) or at the N-terminus (*cutFOG2*) of *cutF*. **(D)** CutO activities of the strains shown in panel **(C)**. Periplasmic fractions were isolated from the indicated strains, grown in MPYE medium supplemented with 10 µM $CuSO_4$. 50 µg protein of the periplasmic fractions were used in the assay. Three independent experiments were performed with three technical repetitions and the error bars reflect the standard deviation ($n = 9$). The activity of WT was set to 100% and the relative activities of the other strains were calculated. Statistical analyses were as in **Figure 1**. (*) refers to p-values ≤ 0.05; (**) to p-values ≤ 0.01, and (***) to p-values ≤ 0.001. **(E)** Immunoblot analyses of the Δ*cutFOG* strain harboring either the *cutFOG1* or *cutFOG2* constructs. 50 µg of soluble protein and α-Flag antibodies were used for the detection of CutO (upper panel) and 75 µg protein and α-Myc antibodies were used for detection of CutG (lower panel). Although Strep-tagged, CutF could not be detected in immunoblots in either construct, although the *cutFOG2* construct fully complemented the Δ*cutFOG* strain.

while CutG is important, CutF is essential for CutO activity. The observed CutO activities in the Δ*cutF* and Δ*cutG* strains also correlated well with the observed Cu sensitivity phenotypes, suggesting that Cu resistance is directly linked to CutO activity.

Epitope tagged versions of *cutF*, *cutG* and *cutO* genes were cloned into an arabinose inducible plasmid and introduced into the respective mutants. A C-terminally Flag-tagged CutO variant fully rescued CutO activity in the Δ*cutO* strain, but an N-terminally Flag-tagged CutF variant did not rescue the Δ*cutF* mutant (**Figure 3A**). The Δ*cutF* strain was generated by an in-frame, markerless chromosomal deletion for avoiding any potential polar effect on *cutO* expression. Thus, the lack of complementation by an ectopic *cutF* copy, suggested that either the presence of the tag on CutF interfered with its activity, or that stable production of CutF required the integrity of the *cutFOG* operon.

This was analyzed by constructing a Δ*cutFOG* triple knock-out strain and testing its complementation by different *cutFOG*-encoding plasmids. As predicted from the phenotypes of the single mutants, the Δ*cutFOG* strain was highly sensitive to Cu (**Figure 3B**), but Cu sensitivity was rescued by the plasmid pRK-cutFO$_{Flag}$G, which encoded the *cutFOG*-operon under control of its native promoter and a C-terminally Flag-tagged CutO variant (**Figure 3C**).

Subsequently, each gene within the operon was individually tagged to allow immunological identification of the corresponding gene products. For CutF, two variants were constructed, containing a Strep-tag either at the C-terminus (pRK-cutFOG1, $cutF_{\underline{C}-Strep}O_{Flag}G_{MycHis}$) or at the N-terminus after the signal sequence cleavage site (pRK-cutFOG2 $cutF_{\underline{N}-Strep}O_{Flag}G_{MycHis}$). Plasmid pRK-cutFOG2 fully rescued the Cu sensitive phenotype of the Δ*cutFOG* strain, while pRK-cutFOG1 did so only partially (**Figure 3C**). Analyses of the CutO activities of these strains showed that CutO activity was not detectable in the Δ*cutFOG* strain, but activity was fully restored by the presence of pRK-cutFOG2 (**Figure 3D**). In contrast, in the presence of pRK-cutFOG1 only about 15% of wild type activity was detected (**Figure 3D**).

Immune detection of the periplasmic fractions isolated from the Δ*cutFOG* strain carrying pRK-cutFOG1 or pRK-cutFOG2 revealed lower CutO levels in pRK-cutFOG1 containing cells, while the CutG levels were comparable (**Figure 3E** and **Supplementary Figure 5**). Thus, the addition of a Strep-tag to the conserved C-terminus of CutF apparently impaired its function, reducing the steady-state amounts of CutO and its activity. Despite the availability of N-terminally or C-terminally tagged variants, immune detection of CutF was not possible in strains expressing pRK-cutFOG1 or pRK-cutFOG2, in line with earlier unsuccessful attempts (Rademacher et al., 2012; Selamoglu et al., 2020).

For exploring the molecular basis of this lack of CutF detection, an *E. coli in vitro* coupled transcription-translation system was used to confirm that CutF can be produced, as inferred by the genetic complementation assays using constructs maintaining the *cutFOG* operon integrity (**Figure 3C**). Indeed, *in vitro* translation confirmed the production of a protein of correct molecular mass corresponding to $cutF_{N-Flag}$ ORF (**Figure 4A**), further suggesting that the *cutF* product is either produced at very low levels or undergoes rapid degradation *in vivo*. A possible degradation of CutF would also explain the presence of the weaker approx. 10 kDa product that is detected after *in vitro* translation (**Figure 4A**). Next, appropriate RT-PCR experiments were performed to assess if the low level of CutF originates from its poor transcription, using total RNA extracted from pRK-cutFOG2/Δ*cutFOG* cells grown in the absence, or presence of 10 μM $CuSO_4$ supplementation. Appropriate primer pairs (**Supplementary Table 2**) for the fragments overlapping the gene borders of either *cutFO* (400 bp) or *cutOG* (550 bp) were used for RT-PCR. Quantification of the amplified fragments by *ImageJ* revealed that the 3′ *cutOG* border region was amplified approx. six times more than the 5′ *cutFO* border region in the presence of Cu (**Figure 4B**). Internal controls using genomic DNA confirmed the specificity and efficiency of the selected primer pairs (**Supplementary Figure 6**). Assuming that *cutFOG* genes form a single transcription unit (Wiethaus et al., 2006), this result suggested that the stability of the 5′ end of the

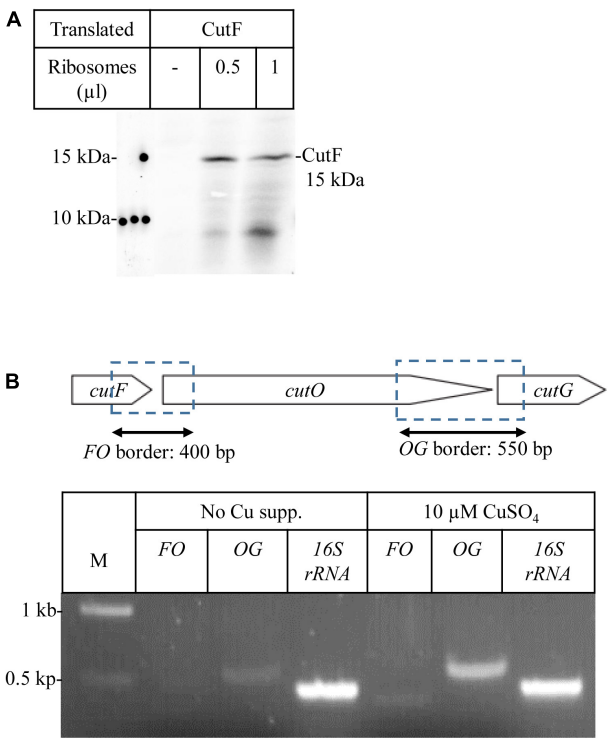

FIGURE 4 | CutF is translated into protein **(A)** *In vitro* protein synthesis of CutF. After *in vitro* synthesis, samples were separated by SDS-PAGE, and the radioactively labeled bands were detected by phosphorimaging. Different volumes (μl) of purified *Escherichia coli* ribosomes were used for *in vitro* synthesis **(B)** Transcriptional analysis of the *cutFOG* operon. Physical map of the *cutFOG* operon (upper cartoon representation) indicating the DNA fragments emerging from RT-PCR (double arrow). RT-PCR analyses of *cutFOG* mRNA levels in *cutFOG2*/Δ*cutFOG* cells grown on MPYE without and with 10 μM Cu^{2+} supplementation. The 16S ribosomal RNA (450 bp) was used as an internal control. The intensities of the bands were determined by the *ImageJ* software. A negative control PCR omitting templates was performed in each case to check for DNA contamination (data not shown).

produced mRNA encompassing *cutF* is much lower than its 3′ end corresponding to *cutO* and *cutG*, in agreement with the low-level production of *cutF* translation product. It was previously shown that the *cutF–cutO* intergenic region contains a stem-loop structure that affects the stability of the *cutFOG* mRNA, playing a role in its post-transcriptional Cu response (Rademacher et al., 2012).

The Conserved Putative Cu Binding Motif and the Proline Residues at the C-Terminus of CutF Are Essential for Its Function

The highly conserved putative Cu binding CXXXC motif in the central part of CutF, and the unusual proline-rich sequence surrounded with charged residues at its C-terminal end (**Figure 5A**), were probed by mutagenesis for their plausible functions using the pRK-cutFOG3 ($cutF_{N-\mathrm{Flag}}O_{\mathrm{Flag}}G_{\mathrm{MycHis}}$) construct which maintains the *cutFOG* operon integrity. The $C_{69}XXH_{72}C_{73}$ motif was changed to AXXHA, and the ten C-terminal amino acids (P_{109}EPEGPPPRL$_{118}$) of CutF were deleted, yielding the plasmids pRK-CutF_{C-A}OG and pRK-Cut$F_{\Delta C-ter}$OG, respectively. Expression of these CutF variants in the Δ*cutFOG* strain showed that both mutations significantly reduced the CutO levels (**Figure 5B** and **Supplementary Figure 7**), resulting in a ∼ 90% decrease of CutO activity, comparable to the CutO activity in the Δ*cutF* strain (**Figure 5C**). These data suggested that the conserved CXXXC motif, usually found in Cu chaperones, and the proline-rich sequence are essential for the function of CutF for CutO maturation and activity. Whether or not these CutO defects originate from a lack of proper Cu binding to CutF or a productive CutF-CutO interaction, remains to be further analyzed.

The availability of the mutant CutF variants allowed us to further assess the need for the structural integrity of the *cutFOG* operon by testing the CutO activity in the Δ*cutOG* strain carrying the pRK-cutF_{C-A}OG plasmid. In this strain a functional *cutF* is expressed from the chromosome and functional *cutOG* are located on a plasmid. Similarly, the CutO activity of the Δ*cutFG* mutant carrying the pRK-cutFO_{C473A}G plasmid with an inactive CutO copy (see below section "CutO Confers Cu Resistance by O2-Dependent and O2-Independent Mechanisms") and intact copies of *cutFG* on the plasmid was analyzed. The latter strain contained an intact copy of *cutO* on the chromosome. The CutO activities in both strains were as low as in the Δ*cutO* or Δ*cutF* single mutants (**Supplementary Figure 8**), again supporting the need for the integrity of the *cutFOG* operon for CutO production, suggesting that transcription, translation or secretion of the *cutFOG* genes or their products are coupled.

The Conserved Putative Cu Binding Motifs of CutG Are Not Required for CutO Activity

Mutagenesis was also performed on CutG by alanine replacements of the conserved Cys and Met residues of its $C_{40}XC_{42}C_{43}$ and $M_{120}X(6)M_{127}$ motifs, respectively, using the pRK-cutFOG3 ($cutF_{N-\mathrm{Flag}}O_{\mathrm{Flag}}G_{\mathrm{MycHis}}$) construct to yield the CutG_{C-A} and CutG_{M-A} variants (**Figure 6A**). Unlike the CutF mutations, neither of these CutG mutations significantly affected CutO activity (**Figure 6B**), in agreement with its dispensable role for CutO activity and maturation as well as for Cu tolerance, as already seen with a Δ*cutG* strain (**Figure 2** and **Supplementary Figures 2, 3**). The higher CutO activities of the CutG mutants in comparison to the Δ*cutG* mutant suggests that either the putative Cu-binding motifs of CutG are dispensable for its function in CutO maturation or that possible maturation defects are compensated for by the increased production of the plasmid-encoded CutG variants.

Bioinformatic Analysis of CutF-Like Proteins and Their Co-occurrence With Other Cu- Related Genes

Bioinformatic analyses were initiated to determine the distribution of CutF homologs in bacterial genomes. Likely due to the relatively small size of CutF (118 amino acids) and the low sequence conservation across homologs, searches for sequence-similarity using BLASTp against the UniProt database resulted in only a few significant hits. However, we observed that the proteobacterial *cutO* homologs are often located next to a gene encoding a small protein roughly the same length as CutF, containing a CXXXC motif, a putative signal peptide, and a C-terminal PP motif, similar to *R. capsulatus* CutF. Based on these features, we performed a rule-based approach to generate an initial set of CutF-like proteins encoded by genes neighboring copper oxidase genes. This initial set was then used to initiate a less-restrictive search for CutF-like proteins using iteratively built profile-HMMs. We reasoned that CutF-like proteins may also be in gene neighborhoods that lack MCO genes or may have some sequence divergence not represented by the initial set.

Using this approach, we identified nearly 3,000 CutF-like sequences in reference proteomes (The UniProt Consortium, 2019) from proteobacteria, including five CutF-like sequences of *R. capsulatus* and two of *Rhodobacter sphaeroides* species (**Figure 7**). As exemplified by these seven proteins, the iterative nature of our analysis captured proteins that do not have the CXXXC motif found in CutF, but do have a conserved cysteine-containing variation of this motif located in roughly the same region of the protein. The C-terminal PP motif is highly conserved among these proteins. The closest annotated HMM in the PFam database to the identified CutF-like proteins is DUF2946 (PF11162), which enclose small proteins with a C-terminal PP motif and a CXXC motif instead of the CXXXC motif in the central region. Intriguingly, DUF2946 was previously associated with Cu homeostasis through gene neighborhood analysis (Kenney and Rosenzweig, 2018). CutF-like proteins, as identified here in proteobacteria, are found in all classes of proteobacteria. There is an apparent enrichment for CutF-like proteins in alpha-proteobacteria (58%), but when taking into account the number of reference proteomes available for each class, there are roughly an equal amount of CutF-like proteins in alpha- and beta-proteobacteria, half as many in gamma-proteobacteria and a quarter as many in delta-proteobacteria (**Figure 8**).

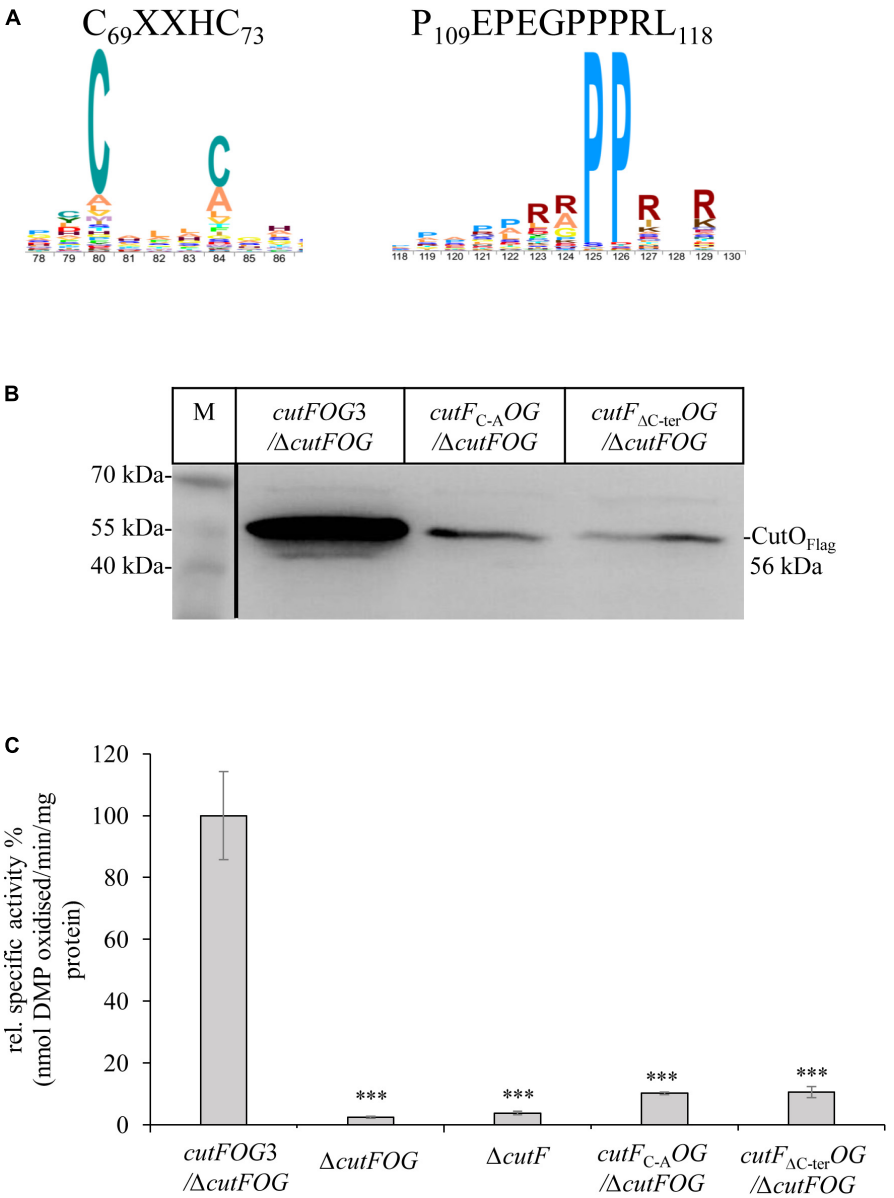

FIGURE 5 | The conserved cysteine motif and the proline-rich C-terminus of CutF are essential for its function. **(A)** Sequence logo of the conserved CutF motifs. **(B)** Immunoblot analysis of the CutO proteins from the strains carrying the *cutF*$_{C-A}$*OG* (Substitution of putative Cu binding $C_{69}XXXC_{73}$ motif by $A_{69}XXXA_{73}$) and *cutF*$_{\Delta C-ter}$*OG* (truncation of C-terminal proline-rich region, $P_{109}EPEGPPPRL_{118}$) plasmids producing the CutF$_{C-A}$ and CutF$_{\Delta C-ter}$ mutant proteins, respectively. In both plasmids CutO was C-terminally Flag-tagged. 200 μg of soluble protein and α-Flag antibodies were used for the detection of CutO. 15% SDS-PAGE was used for separation. **(C)** CutO activities in the Δ*cutFOG* strain expressing either *cutFOG3* (*cutF*$_{N-Flag}$*O*$_{Flag}$*G*$_{MycHis}$) or the mutated *cutF*$_{C-A}$*OG* or *cutF*$_{\Delta C-ter}$*OG* variants. In all cases, CutO was C-terminally Flag-tagged. The Δ*cutFOG* and the single Δ*cutF* mutants served as an additional control. Strains were grown on MPYE medium in the presence of 10 μM $CuSO_4$. 50 μg of the same soluble protein from the periplasmic fractions were used in the assay. Three independent experiments were performed with three technical repetitions and the error bars reflect the standard deviation (n = 9). Statistical analyses were performed as in **Figure 1**, using the *cutFOG3*/Δ*cutFOG* strain as reference. (*) refers to p- values ≤ 0.05; (**) to p-values ≤ 0.01, and (***) to p-values ≤ 0.001.

Having identified a set of proteins with sequence characteristic analogous to CutF, we next asked to what extent are these proteins associated with homologs of CutO. To differentiate CutO proteins from other Cu oxidases, we built a sequence similarity network (**Figure 8**). We found that 40% of the genes corresponding to proteins from the CutO cluster are neighboring a gene encoding a CutF-like protein, and roughly 71% of proteins belonging to the CutO cluster are encoded by genomes that also encode a CutF-like protein. The high degree of genomic co-occurrence illustrated by these proteins, suggested that a functional link between CutO and CutF is not limited to *Rhodobacter*. In addition to *Rhodobacterales* (where there were 41 cases), gene proximity was also observed in *Rhizobiales* (31 cases) and *Rhodospirillales* (5 cases). Moreover,

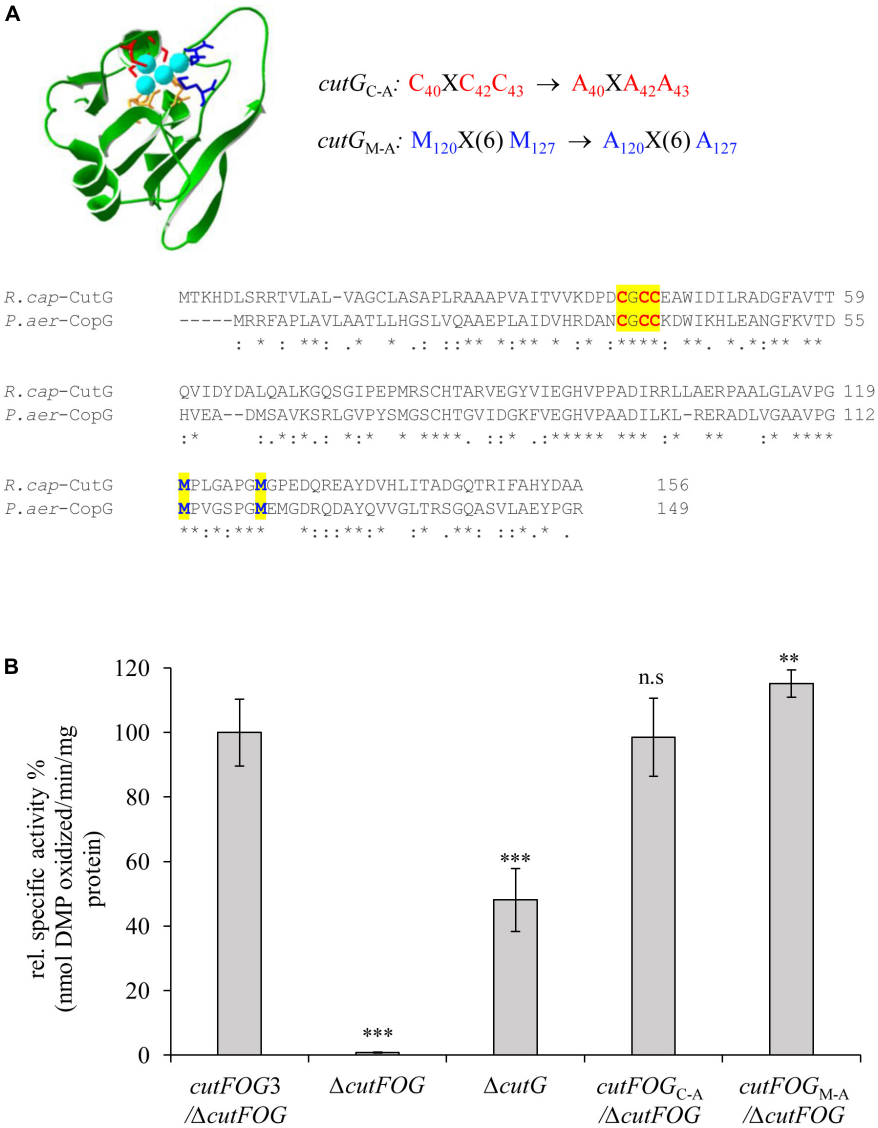

FIGURE 6 | CutG is not essential for CutO activity **(A)** Model for the *R. capsulatus* CutG built on the X-ray structure of CopG from *Pseudomonas aeruginosa* (PDB ID: 6WIS) by the Swiss-Model software. The upper panel shows the conserved motifs and their substitutions. The lower panel shows the amino acid alignment between the *R. capsulatus* (*R. cap*) CutG and *P. aeruginosa* (*P. aer*) CopG. The conserved Cysteines and Methionines are highlighted in red and blue letters, respectively. **(B)** CutO activities of the indicated strains expressing $cutG_{C-A}$ and $cutG_{M-A}$. The periplasmic fractions were isolated from the strains grown on MPYE medium in the presence of 10 μM $CuSO_4$. 50 μg total protein was used in the 2,6-DMP assay. The activity of the Δ*cutFOG* strain carrying the plasmid pRK-*cutFOG3* ($cutF_{N-Flag}O_{Flag}G_{MycHis}$) strain was set to 100% and the relative activities of the other strains were calculated. Three independent experiments were performed with three technical repetitions and the error bars reflect the standard deviation ($n = 9$). Statistical analyses were performed as in **Figure 1**, using the activity of the *cutFOG3*/Δ*cutFOG* strain as reference. (*) refers to *p*- values ≤ 0.05; (**) to *p*-values ≤ 0.01, and (***) to *p*-values ≤ 0.001.

55% of CutO-like proteins are encoded by genomes that contain genes for both the CutF and CutG proteins. In comparison, co-occurrence between CutF-like proteins and clusters containing CueO- (the *E. coli* multicopper oxidase) and FtsP- (cell division protein with a multicopper oxidase-like structure) like proteins is low, being only 8% and 2%, respectively (**Figure 8** and **Supplementary Figure 9**). However, we did observe gene proximity with a CutF-like protein and Cu oxidase proteins from outside the CutO cluster in the alpha-proteobacterial lineages Caulobacterales (2), Parvularculales (1), and Sphingomonadales (43), the beta-proteobacterial lineages Burkholderiales (10), Neisseriales (1), and Nitrosomonadales (1), and the gamma-proteobacterial lienages Acidiferrobacterales (2), Alteromonadales (11), Cellvibrionales (9), Chromatiales (4), Enterobacterales (2), Oceanospirillales (11), Pseudomonadales (11), Thiotrichales (3), and Xanthomonadales (29).

Next, we focused our gene neighborhood analysis on the CutF-like proteins. Only 23% of CutF-like proteins are associated with Cu oxidase genes, suggesting that our analysis captured CutF-like proteins that could be involved in processes independent of a

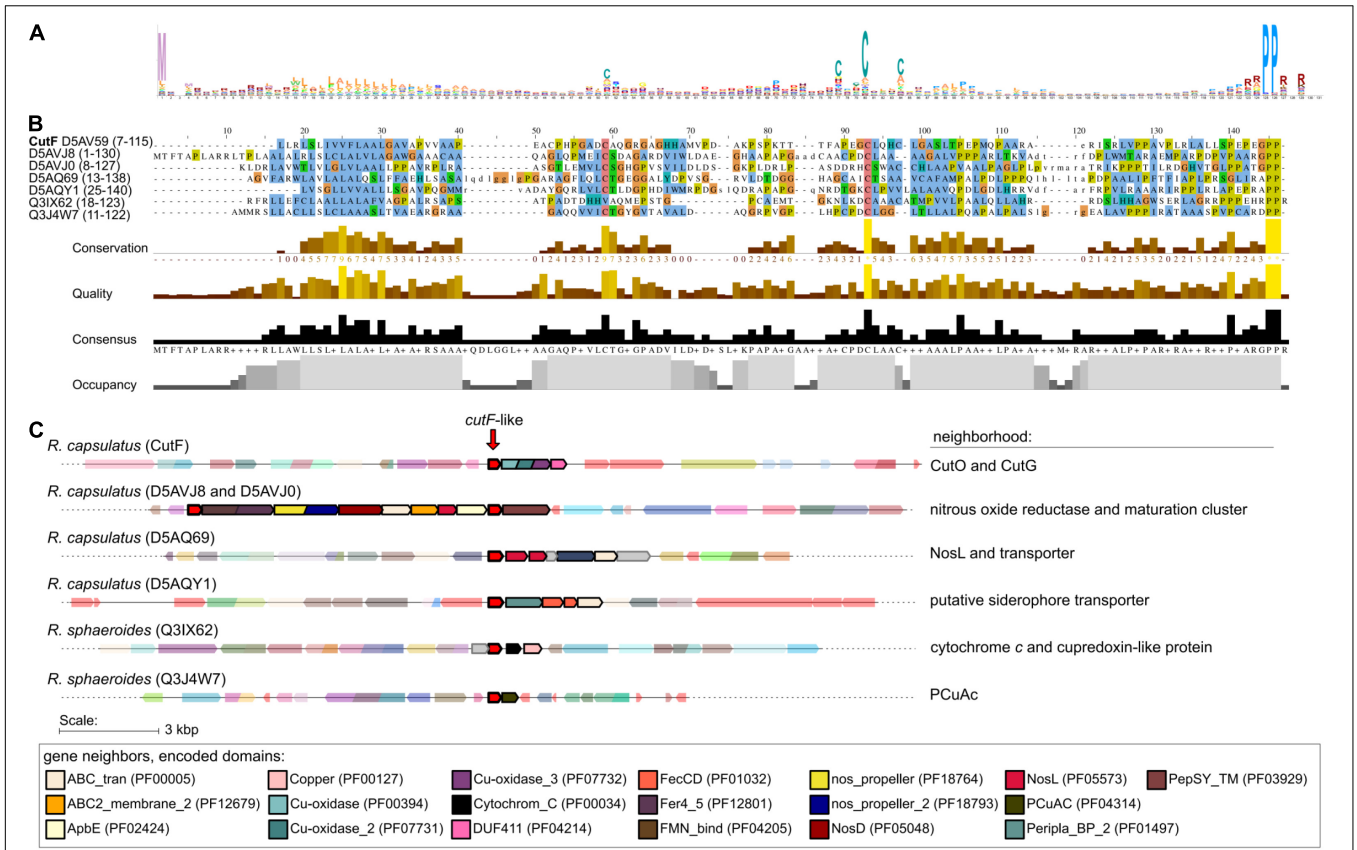

FIGURE 7 | Identification of CutF-like proteins in publicly available sequenced genomes. **(A)** Sequence logo representing profile hidden Markov model (from the 10th iteration of jackhammer) used to identify CutF-like sequences. **(B)** Multiple sequence alignment as viewed with Jalview (Waterhouse et al., 2009) of identified CutF-like sequences from *R. capsulatus* and *Rhodobacter sphaeroides*. The color scheme used is that of clustalx, and the UniProt protein IDs are indicated as labels. The quantitative alignment annotations below the alignment displayed as histograms are automatically calculated by Jalview for each column. **(C)** Genomic context of identified CutF-like sequences from *R. capsulatus* and *R. sphaeroides*. "Neighborhood" refers to genes likely in an operon with the gene encoding the CutF-like protein. Genes are colored according to identified Pfam domains shown at the bottom of the figure.

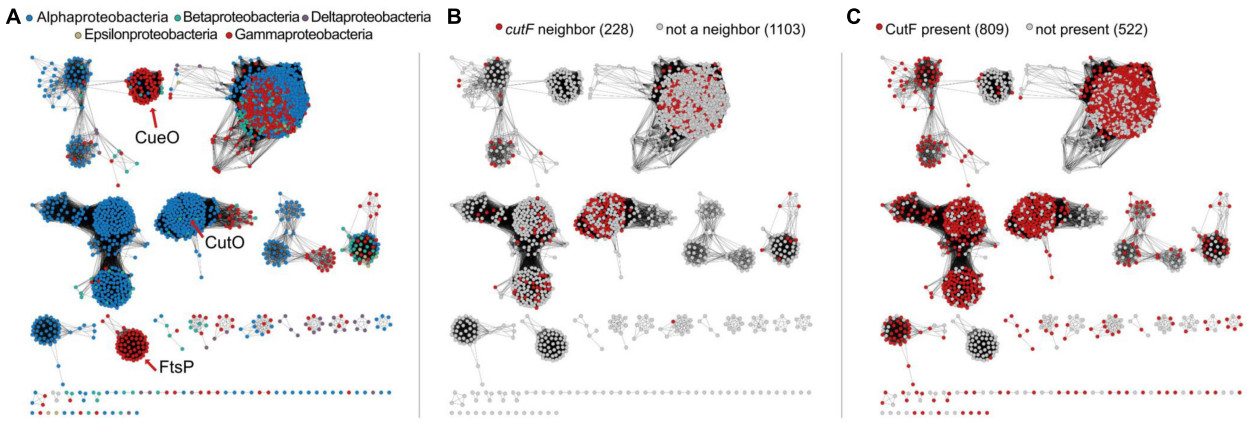

FIGURE 8 | Sequence similarity networks of Cu-oxidase-like proteins. **(A)** network representing sequences containing Pfam domains PF00394, PF07731, and PF07732 from Uniprot-designated reference proteomes in the proteobacterial lineage. Nodes are colored according to the legend shown in each panel. The location of nodes representing CueO and FtsP from *E. coli* and CutO from *R. capsulatus* are indicated with red arrows. **(B)** Nodes are colored as to whether *cutF* is a neighbor of the Cu-oxidase-encoding gene. **(C)** Nodes are colored based on whether CutF is encoded in the genome or not. For panels **(B,C)**, numbers in parentheses on top of each panel represent the number of nodes in the network.

Cu oxidase. Based on the putative Cu-binding proteins identified by Andreini et al. (2008), 88% of the neighborhoods contained at least one gene encoding for a putative Cu-binding protein (**Supplementary Table 3**), such as nitrous oxide reductase, the Cu chaperones NosL, CopC, SenC, and PccA, as well as the Cu transporters CopB, CopD, and the Cus efflux system (**Supplementary Table 3**). These associations plus the presence of cysteine motifs suggest that CutF-like proteins are involved in Cu homeostasis, and that there are likely different subgroups interacting with different proteins.

CutO Confers Cu Resistance by O_2-Dependent and O_2-Independent Mechanisms

An additional plasmid-borne $CutFO_{Flag}G$ variant was constructed in which the *cutFOG* expression is controlled by its native promoter to probe if the steady-state amounts and activities of CutO are influenced by the Cu concentration in the medium. This plasmid fully complemented the Δ*cutFOG* triple knock-out strain, and periplasmic extracts of these cells grown in the presence of different Cu concentrations were analyzed. The data showed a Cu-concentration dependent increase of the CutO activity (**Figure 9A**) that coincided with increased CutO protein levels (**Figure 9B** and **Supplementary Figure 10A**). This is in line with the Cu-induced increase of the CutO levels observed by cuproproteome analyses of *R. capsulatus* (Selamoglu et al., 2020) and with studies using in-frame *cutO*-lacZ fusions (Rademacher et al., 2012).

Multicopper oxidases like CutO use O_2 as an electron acceptor and thus are catalytically active only in the presence of O_2 (Solomon et al., 2008). Therefore, it was surprising that the Δ*cutO* strain was highly Cu sensitive even under anaerobic conditions (**Figure 2**). This suggested that CutO might confer Cu resistance not just by the O_2-dependent oxidation of Cu^{1+} to the less toxic Cu^{2+}, but also by another O_2-independent mechanism. Two CutO variants, $CutO_{C473A}$ and $CutO_{\Delta MRS}$, produced from the plasmid pRK-$cutFO_{Flag}G$ were constructed to further analyze this finding. In the $CutO_{C473A}$ variant, the Cys473 ligand of the T1 Cu center was replaced by alanine, which is expected to inactivate CutO. In the $CutO_{\Delta MRS}$ variant, the MRS, which accommodates the Cu ions Cu5, Cu6, and Cu7 in the *E. coli* homolog CueO was deleted, which is expected to reduce the ability of CutO to bind Cu (Kataoka et al., 2007;

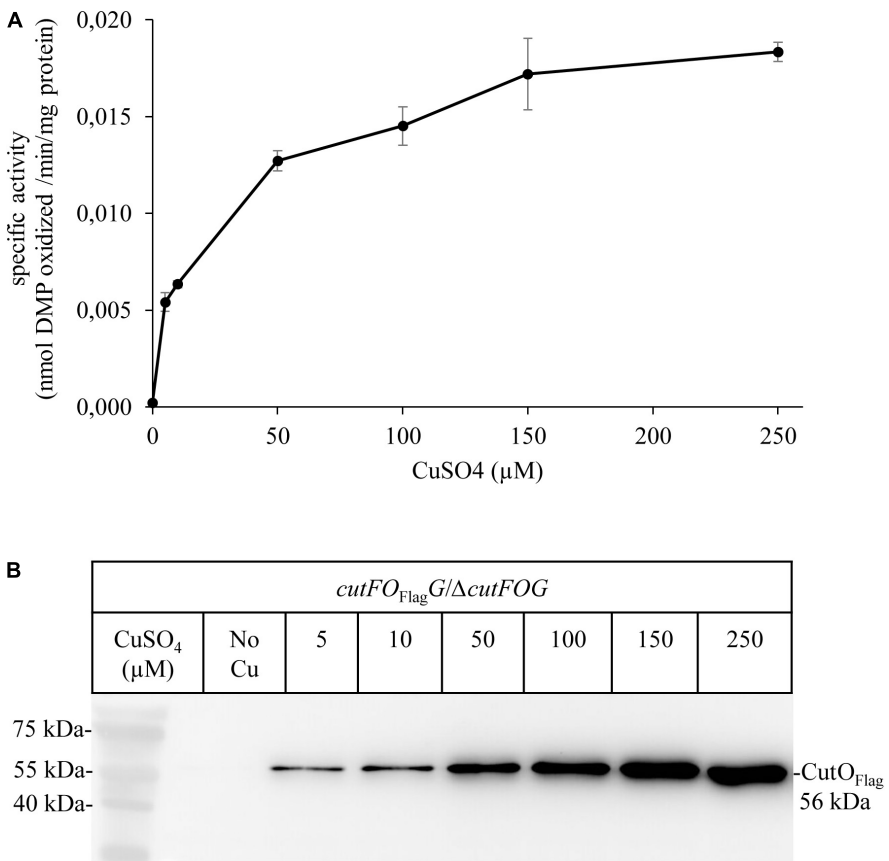

FIGURE 9 | Activity and steady-state levels of CutO are Cu-dependent. **(A)** The activity of plasmid-encoded Flag-tagged CutO (*cutFO*$_{Flag}$*G*) expressed in the Δ*cutFOG* strain, grown in MPYE medium supplemented with different $CuSO_4$ concentrations. 50 μg protein of the periplasmic fractions were used for the assay. Shown are the mean values of three independent assays with three technical repetitions and the error bars reflect the standard deviation (*n* = 9). **(B)** For immunoblot analysis of the $CutO_{Flag}$, approximately 40 μg of periplasmic proteins were separated on 15% SDS-PAGE and treated with anti-Flag antibodies.

Singh et al., 2011). Both plasmids were individually transferred into the Δ*cutFOG* strain, and cells were tested for CutO activity, CutO levels, and Cu sensitivity (**Figure 10**).

The $CutO_{C473A}$ mutant had no detectable CutO activity just like the Δ*cutFOG* strain, but in the $CutO_{\Delta MRS}$ mutant, the CutO activity was approx. 2-fold higher than wild-type activity (**Figure 10A**). This is likely due to the increased accumulation of this CutO variant as indicated by immuno-detection using anti-Flag antibodies (**Figure 10B** and **Supplementary Figure 10B**). In addition, the absence of the MRS might favor access of bulky organic substrates to the catalytic site of CutO. This was shown for *E. coli* CueO, where the deletion of the MRS led to a 10% reduction of the cuprous oxidase activity, while it increased the oxidation of alternative substrates, like phenolic components such as 2,2'-Azino-bis (3-ethylbenzothiazoline-6-sulfonic acid) or 2,6-DMP (Kataoka et al., 2007). The MRS was therefore proposed to provide a specificity filter to ensure preferentially Cu^{1+} oxidation (Roberts et al., 2003). When testing the Cu sensitivity profile on enriched medium supplemented with 250 μM $CuSO_4$ under similar Res growth conditions, both mutant variants showed Cu resistance levels comparable to those conferred by the plasmid-borne wild-type CutO (**Figure 10C**), while the Δ*cutFOG* strain failed to form single colonies. When the Cu concentration was increased to 400 μM, the Δ*cutFOG* strain was completely unable to grow, while cells expressing either the $CutO_{C473A}$ variant or the $CutO_{\Delta MRS}$ variant still grew, although growth was reduced in comparison to wild-type CutO (**Figure 10C**). Moreover, when the same experiment was repeated under anaerobic-PS conditions, the Δ*cutFOG* strain was significantly growth-impaired already at 5 μM Cu and did not grow at 10 μM Cu. In contrast, both of the two CutO variants grew almost like the MT1131 wild-type strain with native CutO, or a Δ*cutFOG* strain complemented with endogenous CutFOG levels (**Figure 10D**). The observation that the $CutO_{C473A}$ variant, which has no O_2-dependent Cu oxidase activity, also confers Cu resistance further indicated that CutO-mediated Cu resistance also involves an O_2-independent step. The O_2-dependent and O_2-independent Cu resistance mechanisms of CutO seem to be set apart in the catalytically inactive $CutO_{C473A}$ mutant variant, as this mutant still provides Cu tolerance even in the absence of O_2. Hence, a dual function of CutO in Cu resistance emerges: (1) O_2-dependent enzymatic reduction of Cu^{1+} to the less toxic Cu^{2+}, and (2) protein-mediated sequestration of Cu, reducing the total Cu concentration. The latter possibility is supported by the presence of additional Cu sites in the MRS of *E. coli* CueO (Singh et al., 2011) and by the observation that neither the inactivation of the T1 site nor the deletion of the MRS abolishes Cu resistance (**Figure 10D**).

DISCUSSION

In Gram-negative bacteria, P_{1B}-type ATPases CopA and the CopZ-like chaperones have been identified as major determinants for Cu detoxification of the cytoplasm (Gonzalez-Guerrero and Arguello, 2008; Argüello et al., 2013; Utz et al., 2019). The multicopper oxidase CueO (CutO) provides a similar function for the periplasm by oxidizing Cu^{1+} to the less toxic Cu^{2+} and likely by sequestering excess Cu via the MRS (Petersen and Moller, 2000; Grass and Rensing, 2001; Fernandes et al., 2007; Singh et al., 2011; Novoa-Aponte et al., 2019). In many, but not all bacteria, the expression of genes determining cytoplasmic and periplasmic Cu tolerance, like *copA*, *copZ,* and *cueO*, are coordinated by the transcriptional regulator CueR (Outten et al., 2000; Stoyanov et al., 2001; Peuser et al., 2011). In the current study, we investigated the maturation of the cuproenzyme CutO with respect to its assembly and the mechanism by which it provides Cu resistance. The better-known multi-step machinery for Cu insertion into cbb_3-Cox directed us to inquire if any known component(s) of this machinery is also used for the assembly of CutO. The results indicated that CutO activity is not affected significantly by the lack of the known cbb_3-Cox assembly factors CcoA, SenC, and PccA. The latter components are critical under low Cu availability whereas Cu detoxification, including CutO induction, requires higher Cu concentration, in line with these findings. Among the remaining components, a small but reproducible decrease (∼25% of wild-type activity) was seen in the Δ*ccoG* strain. Mutant strains lacking the Cu^{2+} reductase CcoG are defective in cbb_3-Cox assembly and also exhibit Cu sensitivity (Marckmann et al., 2019), possibly due to the decreased CutO activity in a Δ*ccoG* strain as seen here. Under aerobic conditions, Cu is present primarily as Cu^{2+}, while most Cu chaperones and P_{1B}-type ATPases involved in exporting Cu to the periplasm only bind Cu^{+}. Hence, the elimination of CcoG might result in reduced cytoplasmic Cu^{1+} quota, leading to less Cu^{1+} loaded CopZ and subsequently to reduced Cu^{1+} supply to both the CopA and CcoI P_{1B}-type ATPases (Utz et al., 2019; **Figure 11**). The Cu^{2+}-reducing activity of CcoG and the Cu-transfer activity of CopZ are the only so far identified nexuses between Cu resistance and cbb_3-Cox assembly in *R. capsulatus*.

The deletion of *copZ* and *copA* decreased the periplasmic CutO activity significantly (65 and 60% of wild-type, respectively), indicating that the CopZ-CopA dependent cytoplasmic detoxification system provides at least a portion of Cu^{1+} required for CutO maturation. However, the residual CutO activity in the absence of CopZ or CopA also indicates that alternate pathway(s) for supplying Cu to CutO exists in *R. capsulatus*, which need to be further explored. In Gram-negative bacteria, outer membrane proteins, like OmpC or ComC, contribute to Cu tolerance by so far unknown mechanisms (Kershaw et al., 2005; Mermod et al., 2012; Giachino and Waldron, 2020) and it is possible that Cu for CutO maturation in *R. capsulatus* can also be provided by Cu uptake from the environment. In any event, partial dependency of CutO activity on the cytoplasmic CopZ-CopA Cu detoxification pathway implies that compartmental Cu detoxification processes are coordinated to ensure efficient Cu homeostasis (Outten et al., 2001; Peuser et al., 2011; Rademacher et al., 2012; Pezza et al., 2016; **Figure 11**). Intriguingly, although the effects of CopA and CopZ on CutO activity were similar, their effects on Cu tolerance (inhibitory concentration ∼20 μM for Δ*copA* and ∼200 μM $CuSO_4$ for Δ*copZ*) were about tenfold different (Utz et al., 2019). This suggests that in this species an alternative

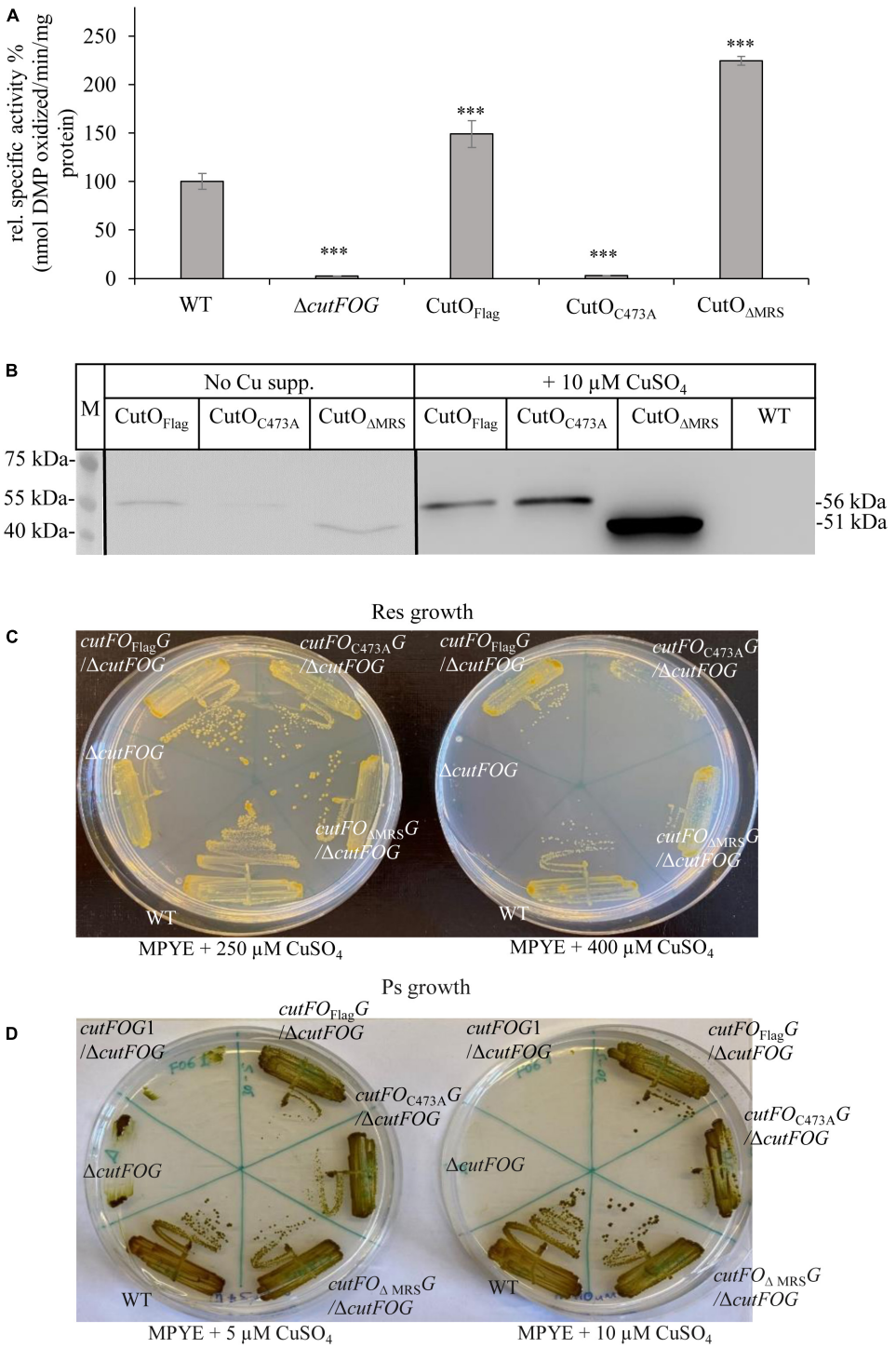

FIGURE 10 | Activity, steady-state levels, and Cu sensitivity of different CutO mutants. **(A)** CutO activity of the CutO mutant variants CutO$_{C473A,}$ carrying a mutation in the T1Cu binding motif, and CutO$_{ΔMRS}$, in which the methionine-rich segment (MRS) was deleted, was determined by using 50 µg protein of the periplasmic fraction isolated from strains grown on MPYE medium in the presence of 10 µM CuSO$_4$. Three independent experiments were performed with three technical repetitions and the error bars reflect the standard deviation (n = 9). The activity of the WT strain was set to 100% and the relative activities of the other strains were calculated. Statistical analyses were performed as in **Figure 1**, using the activity of the WT strain as reference. (*) refers to p- values ≤ 0.05; (**) to p-values ≤ 0.01, and (***) to p-values ≤ 0.001. **(B)** Immunoblot analysis of Flag-tagged wild type CutO and its mutant variants grown in the presence and absence of CuSO$_4$ supplement. After isolation of the periplasmic fraction, 50 µg protein were separated on 12% SDS PAGE and treated with anti-Flag antibodies. **(C)** Respiratory (Res) and **(D)** photosynthetic (PS) growth of *R. capsulatus* strains carrying a plasmid born copy of CutO$_{Flag}$ or its mutant variants (CutO$_{C473A}$ and CutO$_{ΔMRS}$) on MPYE medium supplemented with different amounts of CuSO$_4$. The *cutFOG*1/Δ*cutFOG* strain carrying the *cutF*$_{C-Strep}$*O*$_{Flag}$*G*$_{MycHis}$ construct was used as an additional control for Ps growth.

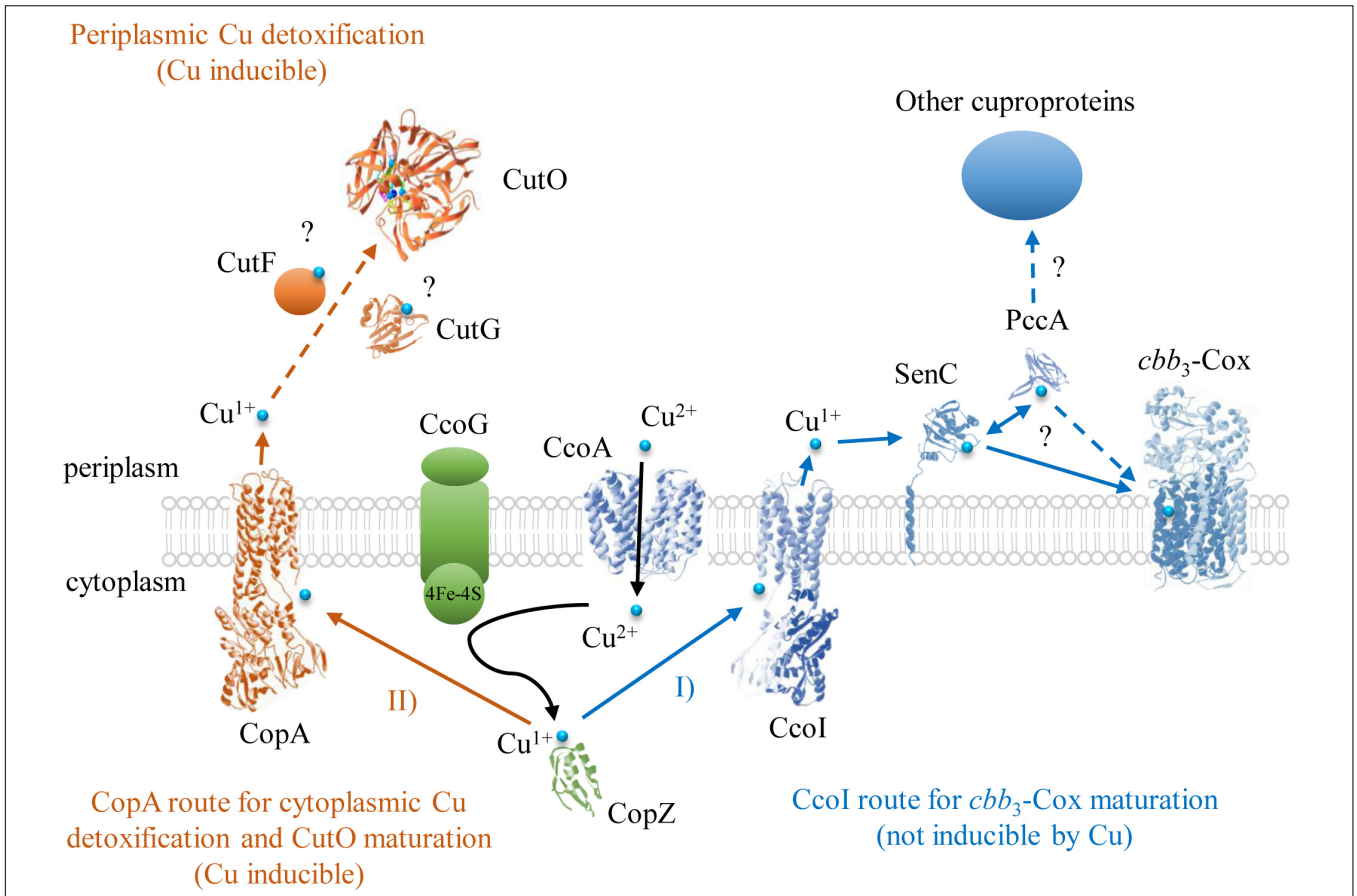

FIGURE 11 | The Cu detoxification and cuproenzyme biogenesis pathways for cbb_3-Cox and CutO in *R. capsulatus*. Two Cu export routes to the periplasm have been identified so far in *R. capsulatus*. One of them is through the P_{1B}-type ATPase CcoI that exports Cu^{1+} to the periplasm for cbb_3-Cox assembly. In the periplasm, Cu is bound to SenC (or alternatively to PccA) and subsequently inserted into the catalytic subunit CcoN of cbb_3-Cox. The other route is via the P_{1B}-type ATPase CopA, which has a lower affinity/higher turnover rate for Cu, and exports excess cytosolic Cu^{1+} to the periplasm for CutO maturation and subsequent oxidation to Cu^{+2}. In addition to the CopZ-CopA Cu delivery pathway for CutO maturation, alternative Cu supply pathways for CutO likely exist in *R. capsulatus*, but have not been characterized yet. Structures were retrieved from the protein database with the following IDs: 3RFU (CopA and CcoI), 6WIS (CopG for CutG), 3OD3 (CueO for CutO), 1K0V (CopZ), 3WDO (YajR for CcoA), 4WBR (ScoI/SenC), 2K70(PCuAC/PccA), 5DJQ (cbb_3-Cox), and depicted using Swiss-PdbViewer.

CopZ-independent pathway is able to convey Cu to CopA, which delivers Cu to the periplasm for CutO maturation. In contrast to *P. aeruginosa*, which contains two CopZ paralogs (CopZ1 and CopZ2) (Novoa-Aponte et al., 2019), a second *copZ* is not detectable in the *R. capsulatus* genome and the CopZ-independent Cu delivery pathway to CopA remains to be characterized.

Under both aerobic and anaerobic Ps conditions, the catalytically inactive $CutO_{C473A}$ variant still provided Cu resistance, although to a lesser extent than the native CutO. This is intriguing because the strictly conserved T1 Cu site is absent in this mutant due to the mutation of the C-terminal HCH motif (Roberts et al., 2002; Augustine et al., 2010). In addition, under anaerobic conditions, CutO is assumed to be inactive due to the absence of O_2 as an electron acceptor. How CutO supports Cu resistance in the absence of the T1 Cu and O_2 is not obvious. Considering that additional Cu binding sites have been identified in the MRS region of MCOs (Fernandes et al., 2007; Singh et al., 2011), a likely possibility is that CutO contributes to Cu resistance not only by Cu(I) oxidation but also by sequestering Cu via its secondary Cu binding sites, including MRS. This is also supported by the observation that deleting the MRS of CutO attenuated Cu resistance as compared to wild type or the $CutO_{C473A}$ variant of CutO. The high cellular content of the inactive Cut_{C473A} variant also indicates that the T1Cu, although essential for activity, is not required for CutO stability.

The precursor of CutO has, like its *E. coli* homolog CueO, a Tat signal peptide, which is often found in proteins that are transported across the membrane in a folded and inactive state (Kudva et al., 2013). In the case of *E. coli* CueO, it has been shown that a signal peptide-deficient CueO variant produced in the cytoplasm contained no bound Cu (even under Cu supplemented conditions) and that externally added Cu can be readily inserted *in vitro* to yield an active protein (Stolle et al., 2016). These findings together with the observed dependence of CutO maturation on the CopZ-CopA Cu export pathway and the co-localization of CutO with the two putative periplasmic Cu binding proteins CutF and CutG within the

cutFOG operon suggest that maturation of active CutO likely occurs in the periplasm.

The experimental results of *cutFOG* knockout strains and the mutant variants of CutF and CutG proteins showed that CutF, but not CutG, is essential for CutO assembly. Indeed, mutating the conserved Cys residues of CutG, which ligate the two Cu ions, or mutating the two Met residues, which constitute the ligands for another Cu atom (Hausrath et al., 2020), showed that this protein is dispensable for CutO maturation. This could be due to the presence of a functionally redundant protein in the *R. capsulatus* periplasm. Alternatively, it has been suggested that *P. aeruginosa* CopG, which is homologous to CutG, might act as a Cu oxidoreductase that balances the Cu^{1+}/Cu^{2+} equilibrium, and thereby contributes to Cu tolerance (Hausrath et al., 2020). Thus, CutG might be primarily required as a back-up Cu defense system.

In general, due to the toxicity of Cu, cells use chaperones with very high Cu affinity to prevent the availability of free Cu in cell compartments (Banci et al., 2010; Novoa-Aponte et al., 2019, 2020), and to convey Cu to its destination using specific protein-protein interactions (Banci et al., 2009). Biogenesis of membrane-integral and periplasmic cuproenzymes involves a large variety of specialized periplasmic Cu chaperones, in comparison to the limited variety of cytoplasmic chaperones. Clearly, a need for direct and specific protein-protein interactions emerges between the Cu donor chaperones and Cu accepting cuproproteins (e.g., SenC and PccA for cbb_3-Cox, NosL for NosZ, and CueP for superoxide dismutase), which drive the biogenesis of a multitude of extracytoplasmic cuproproteins (Andrei et al., 2020). Although our data clearly demonstrate the essential role of CutF in CutO maturation, its exact function is currently unknown. It could act as a Cu chaperone that takes part in the Cu^{1+} transfer from CopA to CutO, in line with its essential CXXXC motif that could ligate Cu^{1+} with a trigonal planar geometry, similar to the Cu binding motif of SenC (**Figure 11**). A periplasmic function of CutF is also supported by its predicted cleavable signal sequence, which suggests a post-translational translocation into the periplasm. In *E. coli*, the periplasmic chaperone CusF accepts Cu^{1+} directly from the Cu-bound form of CopA by specific interaction upon ATP hydrolysis (Padilla-Benavides et al., 2014). A decrease in Cu^{1+} transfer efficiency was observed upon mutating the extracellular loops of CopA, or the electropositive surface of CusF (Padilla-Benavides et al., 2014). Similarly, CutF with its Cu chaperone-like Cu-binding motif and its genome-wide co-localization with other genes encoding cuproproteins as indicated by bioinformatic analyses may function as a periplasmic Cu^{1+} chaperone for CutO maturation. At the C-terminus, CutF contains a conserved proline-rich region. These regions preferentially adopt a type II helical conformation that facilitates protein-protein interactions, as shown e.g., for TonB or OmpA (Williamson, 1994). In CutF, this region may provide a structural domain for interactions with CutO and/or CopA.

Remarkably, bioinformatic analyses documented a more general role for CutF and CutF-like proteins as important members of the Cu homeostasis networks and cuproprotein biogenesis. CutF-like proteins seem widespread in proteobacteria and are more often found in alpha-proteobacterial species. On average, two CutF-like genes were found per genome, and typically in distinct gene neighborhoods, suggesting that these paralogs may have evolved to function in different Cu-trafficking processes. The corresponding genes are often found in gene neighborhoods with Cu chaperones, such as NosL, CopC, CusF, SenC, and PccA, suggesting that in those organisms, CutF-like proteins are involved in Cu homeostasis.

However, different to other periplasmic Cu chaperones, which are easily detectable and present in μM concentrations in *Rhodobacter* cells (Trasnea et al., 2018), CutF appears to be of very low abundance and is basically undetectable in *Rhodobacter* (Rademacher et al., 2012; Selamoglu et al., 2020). Still, the extremely low amount of CutF is both necessary and sufficient for full CutO activity, provided that *cutF* is located in *cis*, next to *cutO* conserving the structural integrity of *cutFOG* operon. Examination of *cutF* expression using a coupled *in vitro* transcription-translation system showed that its ORF can indeed be translated if transcribed, and related RT-PCR results indicated that its low cellular level may stem from its mRNA stability. Although *cutFOG* comprises a single transcription unit (Wiethaus et al., 2006), the 5′ end of this mRNA corresponding to *cutF* seems less abundant than the remainder covering *cutO* and *cutG*, in agreement with the higher steady-state levels of CutO and CutG in cells. The 40 bp long *cutF–cutO* intergenic region contains a stem-loop structure that possibly affects the stability of this mRNA. Mutagenesis of the *cutF–cutO* intergenic region indicated that it encodes for a Cu-responsive mRNA element that is essential for the Cu-dependent expression of *cutO* and *cutG* (Rademacher et al., 2012). Future studies addressing the exact function of CutF would require detecting CutF and monitoring its cellular localization.

DATA AVAILABILITY STATEMENT

The original contributions presented in the study are included in the article/**Supplementary Material**, further inquiries can be directed to the corresponding author/s.

AUTHOR CONTRIBUTIONS

YÖ, CB-H, ND, AA, JR, FD, and H-GK contributed to the design of the study, the acquisition, analysis, and interpretations of the data. All authors contributed to writing the article and approved the submitted version.

FUNDING

This work was supported by the German Research Foundation (DFG grants DFG GRK2202 – 235777276/RTG and Project-ID 403222702 – SFB 1381 to H-GK); and by grants from the Division of Chemical Sciences, Geosciences, and Biosciences, Office of Basic Energy Sciences of Department of Energy [DOE DE-FG02-91ER20052] and National Institute of Health [NIH GM 38237] to FD. CB-H is supported by the U.S. Department of Energy, Office

of Science, Office of Biological and Environmental Research, as part of the Quantitative Plant Science Initiative at Brookhaven National Laboratory.

ACKNOWLEDGMENTS

YÖ gratefully acknowledges support by Philipp-Schwartz-Initiative of the Alexander von Humboldt Foundation. Work included in this study has also been performed in partial fulfillment of the requirements for the doctoral thesis of AA.

SUPPLEMENTARY MATERIAL

The Supplementary Material for this article can be found online at: https://www.frontiersin.org/articles/10.3389/fmicb.2021.720644/full#supplementary-material

REFERENCES

Achard, M. E. S., Tree, J. J., Holden, J. A., Simpfendorfer, K. R., Wijburg, O. L. C., Strugnell, R. A., et al. (2010). The multi-copper-ion oxidase CueO of *Salmonella enterica* serovar typhimurium is required for systemic virulence. *Infect. Immun.* 78, 2312–2319. doi: 10.1128/iai.01208-09

Andrei, A., Öztürk, Y., Khalfaoui-Hassani, B., Rauch, J., Marckmann, D., Trasnea, P. I., et al. (2020). Cu homeostasis in bacteria: the ins and outs. *Membranes* 10:242. doi: 10.3390/membranes10090242

Andreini, C., Banci, L., Bertini, I., and Rosato, A. (2008). Occurrence of copper proteins through the three domains of life: a bioinformatic approach. *J. Proteome Res.* 7, 209–216. doi: 10.1021/pr070480u

Argüello, J. M., Raimunda, D., and Padilla-Benavides, T. (2013). Mechanisms of copper homeostasis in bacteria. *Front. Cell. Infect. Microbiol.* 3:73. doi: 10.3389/fcimb.2013.00073

Augustine, A. J., Kjaergaard, C., Qayyum, M., Ziegler, L., Kosman, D. J., Hodgson, K. O., et al. (2010). Systematic perturbation of the trinuclear copper cluster in the multicopper oxidases: the role of active site asymmetry in its reduction of O2 to H2O. *J. Am. Chem. Soc.* 132, 6057–6067. doi: 10.1021/ja909143d

Banci, L., Bertini, I., Calderone, V., Della-Malva, N., Felli, I. C., Neri, S., et al. (2009). Copper(I)-mediated protein-protein interactions result from suboptimal interaction surfaces. *Biochem. J.* 422, 37–42. doi: 10.1042/bj20090422

Banci, L., Bertini, I., Ciofi-Baffoni, S., Kozyreva, T., Zovo, K., and Palumaa, P. (2010). Affinity gradients drive copper to cellular destinations. *Nature* 465, 645–648. doi: 10.1038/nature09018

Behlau, F., Canteros, B. I., Minsavage, G. V., Jones, J. B., and Graham, J. H. (2011). Molecular characterization of copper resistance genes from *Xanthomonas citri* subsp. citri and *Xanthomonas alfalfae* subsp. citrumelonis. *Appl. Environ. Microbiol.* 77, 4089–4096. doi: 10.1128/aem.03043-10

Bello, M., Valderrama, B., Serrano-Posada, H., and Rudiño-Piñera, E. (2012). Molecular dynamics of a thermostable multicopper oxidase from thermus thermophilus HB27: structural differences between the apo and holo forms. *PLoS One* 7:e40700. doi: 10.1371/journal.pone.0040700

Bertani, G. (1951). Studies on lysogenesis. I. the mode of phage liberation by lysogenic *Escherichia coli*. *J. Bacteriol.* 62, 293–300. doi: 10.1128/jb.62.3.293-300.1951

Boal, A. K., and Rosenzweig, A. C. (2009). Structural biology of copper trafficking. *Chem. Rev.* 109, 4760–4779. doi: 10.1021/cr900104z

Brimacombe, C. A., Stevens, A., Jun, D., Mercer, R., Lang, A. S., and Beatty, J. T. (2013). Quorum-sensing regulation of a capsular polysaccharide receptor for the *Rhodobacter capsulatus* gene transfer agent (RcGTA). *Mol. Microbiol.* 87, 802–817. doi: 10.1111/mmi.12132

Cha, J. S., and Cooksey, D. A. (1991). Copper resistance in *Pseudomonas* syringae mediated by periplasmic and outer membrane proteins. *Proc. Natl. Acad. Sci. U.S.A.* 88, 8915–8919.

Changela, A., Chen, K., Xue, Y., Holschen, J., Outten, C. E., O'halloran, T. V., et al. (2003). Molecular basis of metal-ion selectivity and zeptomolar sensitivity by CueR. *Science* 301, 1383–1387. doi: 10.1126/science.1085950

Daldal, F., Cheng, S., Applebaum, J., Davidson, E., and Prince, R. C. (1986). Cytochrome c2 is not essential for phototrophic growth of *Rhodopseudomonas capsulata*. *Proc. Natl. Acad. Sci U.S.A.* 83, 2012–2016. doi: 10.1073/pnas.83.7.2012

Ditta, G., Schmidhauser, T., Yacobson, E., Lu, P., Liang, X.-W., Finlay, D. R., et al. (1985). Plasmids related to the broad host range vectro, pRK290, useful for cloning and for monitoring gene expression. *Plasmid* 13, 149–153. doi: 10.1016/0147-619x(85)90068-x

Djoko, K. Y., Xiao, Z., and Wedd, A. G. (2008). Copper resistance in *E. coli*: the multicopper oxidase PcoA catalyzes oxidation of copper(I) in CuICuII-PcoC. *ChemBioChem* 9, 1579–1582. doi: 10.1002/cbic.200800100

Durand, A., Azzouzi, A., Bourbon, M.-L., Steunou, A.-S., Liotenberg, S., Maeshima, A., et al. (2015). c-Type cytochrome assembly is a key target of copper toxicity within the bacterial periplasm. *mBio* 6:e01007-15.

Ekici, S., Turkarslan, S., Pawlik, G., Dancis, A., Baliga, N. S., Koch, H.-G., et al. (2014). Intracytoplasmic copper homeostasis controls cytochrome c oxidase production. *mBio* 5:e01055-13.

Ekici, S., Yang, H. H., Koch, H. G., and Daldal, F. (2012). Novel transporter required for biogenesis of cbb(3)-type cytochrome c oxidase in *Rhodobacter capsulatus*. *Mbio* 3:e00293-11.

Fernandes, A. T., Soares, C. M., Pereira, M. M., Huber, R., Grass, G., and Martins, L. O. (2007). A robust metallo-oxidase from the hyperthermophilic bacterium *Aquifex aeolicus*. *FEBS J.* 274, 2683–2694. doi: 10.1111/j.1742-4658.2007.05803.x

Festa, R. A., and Thiele, D. J. (2011). Copper: an essential metal in biology. *Curr. Biol.* 21, R877–R883.

Gaetke, L. M., and Chow, C. K. (2003). Copper toxicity, oxidative stress, and antioxidant nutrients. *Toxicology* 189, 147–163. doi: 10.1016/s0300-483x(03)00159-8

Gerlt, J. A. (2017). Genomic enzymology: web tools for leveraging protein family sequence-function space and genome context to discover novel functions. *Biochemistry* 56, 4293–4308. doi: 10.1021/acs.biochem.7b00614

Gerlt, J. A., Bouvier, J. T., Davidson, D. B., Imker, H. J., Sadkhin, B., Slater, D. R., et al. (2015). Enzyme function initiative-enzyme similarity tool (EFI-EST): a web tool for generating protein sequence similarity networks. *Biochim. Biophys. Acta Proteins Proteom.* 1854, 1019–1037. doi: 10.1016/j.bbapap.2015.04.015

Giachino, A., and Waldron, K. J. (2020). Copper tolerance in bacteria requires the activation of multiple accessory pathways. *Mol. Microbiol.* 114, 377–390. doi: 10.1111/mmi.14522

Gonzalez-Guerrero, M., and Arguello, J. M. (2008). Mechanism of Cu+-transporting ATPases: soluble Cu+ chaperones directly transfer Cu+ to transmembrane transport sites. *Proc. Natl. Acad. Sci. U.S.A.* 105, 5992–5997. doi: 10.1073/pnas.0711446105

Granja-Travez, R. S., and Bugg, T. D. H. (2018). Characterization of multicopper oxidase CopA from *Pseudomonas* putida KT2440 and *Pseudomonas* fluorescens Pf-5: involvement in bacterial lignin oxidation. *Arch. Biochem. Biophys.* 660, 97–107. doi: 10.1016/j.abb.2018.10.012

Grass, G., and Rensing, C. (2001). CueO is a multi-copper oxidase that confers copper tolerance in *Escherichia coli*. *Biochem. Biophys. Res. Commun.* 286, 902–908. doi: 10.1006/bbrc.2001.5474

Gray, K. A., Grooms, M., Myllykallio, H., Moomaw, C., Slaughter, C., and Daldal, F. (1994). *Rhodobacter capsulatus* contains a novel cb-type cytochrome c oxidase without a CuA center. *Biochemistry* 33, 3120–3127. doi: 10.1021/bi00176a047

Hausrath, A. C., Ramirez, N. A., Ly, A. T., and Mcevoy, M. M. (2020). The bacterial copper resistance protein CopG contains a cysteine-bridged tetranuclear copper cluster. *J. Biol. Chem.* 295, 11364–11376. doi: 10.1074/jbc.ra120.013907

Hoffschulte, H. K., Drees, B., and Muller, M. (1994). Identification of a soluble SecA/SecB complex by means of a subfractionated cell-free export system. *J. Biol. Chem.* 269, 12833–12839. doi: 10.1016/s0021-9258(18)99951-5

Jauss, B., Petriman, N. A., Drepper, F., Franz, L., Sachelaru, I., Welte, T., et al. (2019). Noncompetitive binding of PpiD and YidC to the SecYEG translocon

expands the global view on the SecYEG interactome in *Escherichia coli*. *J. Biol. Chem.* 294, 19167–19183. doi: 10.1074/jbc.ra119.010686

Jenney, F. E. Jr., and Daldal, F. (1993). A novel membrane-associated c-type cytochrome, cyt cy, can mediate the photosynthetic growth of *Rhodobacter capsulatus* and *Rhodobacter sphaeroides*. *EMBO J.* 12, 1283–1292. doi: 10.1002/j.1460-2075.1993.tb05773.x

Kataoka, K., Komori, H., Ueki, Y., Konno, Y., Kamitaka, Y., Kurose, S., et al. (2007). Structure and function of the engineered multicopper oxidase CueO from *Escherichia coli*-deletion of the methionine-rich helical region covering the substrate-binding site. *J. Mol. Biol.* 373, 141–152. doi: 10.1016/j.jmb.2007.07.041

Katoh, K., and Standley, D. M. (2013). MAFFT multiple sequence alignment software version 7: improvements in performance and usability. *Mol. Biol. Evol.* 30, 772–780. doi: 10.1093/molbev/mst010

Kenney, G., and Rosenzweig, A. C. (2018). Chalkophores. *Ann. Rev. Biochem.* 87, 645–676. doi: 10.1146/annurev-biochem-062917-012300

Kershaw, C. J., Brown, N. L., Constantinidou, C., Patel, M. D., and Hobman, J. L. (2005). The expression profile of *Escherichia coli* K-12 in response to minimal, optimal and excess copper concentrations. *Microbiology* 151, 1187–1198. doi: 10.1099/mic.0.27650-0

Khalfaoui-Hassani, B., Verissimo, A. F., Shroff, N. P., Ekici, S., Trasnea, P.-I., Utz, M., et al. (2016). "Biogenesis of cytochrome c complexes: from insertion of redox cofactors to assembly of different subunits," in *Cytochrome Complexes: Evolution, Structures, Energy Transduction, and Signaling*, eds W. A. Cramer and T. Kallas (Dordrecht: Springer Netherlands), 527–554. doi: 10.1007/978-94-017-7481-9_27

Knupffer, L., Fehrenbach, C., Denks, K., Erichsen, V., Petriman, N. A., and Koch, H. G. (2019). Molecular mimicry of SecA and signal recognition particle binding to the bacterial ribosome. *MBio* 10:e01317-19.

Koch, H. G., Hengelage, T., Neumann-Haefelin, C., Macfarlane, J., Hoffschulte, H. K., Schimz, K. L., et al. (1999). In vitro studies with purified components reveal signal recognition particle (SRP) and SecA/SecB as constituents of two independent protein-targeting pathways of *Escherichia coli*. *Mol. Biol. Cell* 10, 2163–2173. doi: 10.1091/mbc.10.7.2163

Koch, H. G., Hwang, O., and Daldal, F. (1998a). Isolation and characterization of *Rhodobacter capsulatus* mutants affected in cytochrome cbb3 oxidase activity. *J. Bacteriol.* 180, 969–978. doi: 10.1128/jb.180.4.969-978.1998

Koch, H. G., Myllykallio, H., and Daldal, F. (1998b). Using genetics to explore cytochrome function and structure in *Rhodobacter*. *Methods Enzymol.* 297, 81–94. doi: 10.1016/s0076-6879(98)97008-2

Kuchinski, K. S., Brimacombe, C. A., Westbye, A. B., Ding, H., and Beatty, J. T. (2016). The SOS response master regulator LexA regulates the gene transfer agent of *Rhodobacter capsulatus* and represses transcription of the signal transduction protein CckA. *J. Bacteriol.* 198, 1137–1148. doi: 10.1128/jb.00839-15

Kudva, R., Denks, K., Kuhn, P., Vogt, A., Muller, M., and Koch, H. G. (2013). Protein translocation across the inner membrane of Gram-negative bacteria: the Sec and Tat dependent protein transport pathways. *Res. Microbiol.* 164, 505–534. doi: 10.1016/j.resmic.2013.03.016

Kulajta, C., Thumfart, J. O., Haid, S., Daldal, F., and Koch, H. G. (2006). Multi-step assembly pathway of the cbb3-type cytochrome c oxidase complex. *J. Mol. Biol.* 355, 989–1004. doi: 10.1016/j.jmb.2005.11.039

Lohmeyer, E., Schröder, S., Pawlik, G., Trasnea, P.-I., Peters, A., Daldal, F., et al. (2012). The ScoI homologue SenC is a copper binding protein that interacts directly with the cbb3-type cytochrome oxidase in *Rhodobacter capsulatus*. *Biochim. Biophys. Acta* 1817, 2005–2015. doi: 10.1016/j.bbabio.2012.06.621

Madeira, F., Park, Y. M., Lee, J., Buso, N., Gur, T., Madhusoodanan, N., et al. (2019). The EMBL-EBI search and sequence analysis tools APIs in 2019. *Nucleic Acids Res.* 47, W636–W641.

Marckmann, D., Trasnea, P. I., Schimpf, J., Winterstein, C., Andrei, A., Schmollinger, S., et al. (2019). The cbb 3-type cytochrome oxidase assembly factor CcoG is a widely distributed cupric reductase. *Proc. Natl. Acad. Sci. U.S.A.* 116, 21166–21175. doi: 10.1073/pnas.1913803116

Marrero, K., Sánchez, A., González, L. J., Ledón, T., Rodríguez-Ulloa, A., Castellanos-Serra, L., et al. (2012). Periplasmic proteins encoded by VCA0261-0260 and VC2216 genes together with copA and cueR products are required for copper tolerance but not for virulence in *Vibrio cholerae*. *Microbiology* 158, 2005–2016. doi: 10.1099/mic.0.059345-0

McEwan, A. G., Jackson, J. B., and Ferguson, S. J. (1984). Rationalization of properties of nitrate reductases in *Rhodopseudomonas-capsulata*. *Arch. Microbiol.* 137, 344–349. doi: 10.1007/bf00410732

Mermod, M., Magnani, D., Solioz, M., and Stoyanov, J. V. (2012). The copper-inducible ComR (YcfQ) repressor regulates expression of ComC (YcfR), which affects copper permeability of the outer membrane of *Escherichia coli*. *BioMetals* 25, 33–43. doi: 10.1007/s10534-011-9510-x

Miller, M., Pfeiffer, W., and Schwartz, T. (2010). "Creating the CIPRES science gateway for inference of large phylogenetic trees," in *Proceedings of the Gateway Computing Environments Workshop (GCE)*, New Orleans, LA, 11572–11578.

Monchy, S., Benotmane, M. A., Wattiez, R., Van Aelst, S., Auquier, V., Borremans, B., et al. (2006). Transcriptomic and proteomic analyses of the pMOL30-encoded copper resistance in *Cupriavidus metallidurans* strain CH34. *Microbiology* 152, 1765–1776. doi: 10.1099/mic.0.28593-0

Noble, J. E., and Bailey, M. J. A. (2009). "Chapter 8 Quantitation of protein," in *Methods in Enzymology*, eds R. R. Burgess and M. P. Deutscher (Cambridge, MA: Academic Press), 73–95. doi: 10.1016/s0076-6879(09)63008-1

Novoa-Aponte, L., Ramírez, D., and Argüello, J. M. (2019). The interplay of the metallosensor CueR with two distinct CopZ chaperones defines copper homeostasis in *Pseudomonas aeruginosa*. *J. Biol. Chem.* 294, 4934–4945. doi: 10.1074/jbc.ra118.006316

Novoa-Aponte, L., Xu, C., Soncini, F. C., and Arguello, J. M. (2020). The two-component system CopRS maintains subfemtomolar levels of free copper in the periplasm of *Pseudomonas aeruginosa* using a phosphatase-based mechanism. *mSphere* 5:e01193-20.

Osman, D., and Cavet, J. S. (2008). Copper homeostasis in bacteria. *Adv. Appl. Microbiol.* 65, 217–247. doi: 10.1016/s0065-2164(08)00608-4

Outten, F. W., Huffman, D. L., Hale, J. A., and O'halloran, T. V. (2001). The independent cue and cus systems confer copper tolerance during aerobic and anaerobic growth in *Escherichia coli*. *J. Biol. Chem.* 276, 30670–30677. doi: 10.1074/jbc.m104122200

Outten, F. W., Outten, C. E., Hale, J., and O'halloran, T. V. (2000). Transcriptional activation of an *Escherichia coli* copper efflux regulon by the chromosomal MerR homologue, CueR. *J. Biol. Chem.* 275, 31024–31029. doi: 10.1074/jbc.m006508200

Padilla-Benavides, T., Thompson, A. M. G., Mcevoy, M. M., and Argüello, J. M. (2014). Mechanism of ATPase-mediated Cu+ export and delivery to periplasmic chaperones: the interaction of *Escherichia coli* CopA and CusF. *J. Biol. Chem.* 289, 20492–20501. doi: 10.1074/jbc.m114.577668

Petersen, C., and Moller, L. B. (2000). Control of copper homeostasis in *Escherichia coli* by a P-type ATPase, CopA, and a MerR-like transcriptional activator, CopR. *Gene* 261, 289–298. doi: 10.1016/s0378-1119(00)00509-6

Peuser, V., Glaeser, J., and Klug, G. (2011). The RSP_2889 gene product of *Rhodobacter sphaeroides* is a CueR homologue controlling copper-responsive genes. *Microbiology* 157, 3306–3313. doi: 10.1099/mic.0.051607-0

Pezza, A., Pontel, L. B., López, C., and Soncini, F. C. (2016). Compartment and signal-specific codependence in the transcriptional control of *Salmonella* periplasmic copper homeostasis. *Proc. Natl. Acad. Sci. U.S.A.* 113, 11573–11578. doi: 10.1073/pnas.1603192113

Philips, S. J., Canalizo-Hernandez, M., Yildirim, I., Schatz, G. C., Mondragón, A., and O'halloran, T. V. (2015). Allosteric transcriptional regulation via changes in the overall topology of the core promoter. *Science* 349, 877–881. doi: 10.1126/science.aaa9809

Potter, S. C., Luciani, A., Eddy, S. R., Park, Y., Lopez, R., and Finn, R. D. (2018). HMMER web server: 2018 update. *Nucleic Acids Res.* 46, W200–W204.

Price, M. N., Dehal, P. S., and Arkin, A. P. (2010). FastTree 2 – approximately maximum-likelihood trees for large alignments. *PLoS One* 5:e9490. doi: 10.1371/journal.pone.0009490

Quintana, J., Novoa-Aponte, L., and Arguello, J. M. (2017). Copper homeostasis networks in the bacterium *Pseudomonas aeruginosa*. *J. Biol. Chem.* 292, 15691–15704. doi: 10.1074/jbc.m117.804492

Rademacher, C., Moser, R., Lackmann, J. W., Klinkert, B., Narberhaus, F., and Masepohl, B. (2012). Transcriptional and posttranscriptional events control copper-responsive expression of a *Rhodobacter capsulatus* multicopper oxidase. *J. Bacteriol.* 194, 1849–1859. doi: 10.1128/jb.06274-11

Rensing, C., Fan, B., Sharma, R., Mitra, B., and Rosen, B. P. (2000). CopA: an *Escherichia coli* Cu(I)-translocating P-type ATPase. *Proc. Natl. Acad. Sci. U.S.A.* 97, 652–656. doi: 10.1073/pnas.97.2.652

Roberts, S. A., Weichsel, A., Grass, G., Thakali, K., Hazzard, J. T., Tollin, G., et al. (2002). Crystal structure and electron transfer kinetics of CueO, a multicopper oxidase required for copper homeostasis in *Escherichia coli*. *Proc. Natl. Acad. Sci. U.S.A.* 99, 2766–2771. doi: 10.1073/pnas.052710499

Roberts, S. A., Wildner, G. F., Grass, G., Weichsel, A., Ambrus, A., Rensing, C., et al. (2003). A labile regulatory copper ion lies near the T1 copper site in the multicopper oxidase CueO. *J. Biol. Chem.* 278, 31958–31963. doi: 10.1074/jbc.m302963200

Rowland, J. L., and Niederweis, M. (2013). A multicopper oxidase is required for copper resistance in *Mycobacterium tuberculosis*. *J. Bacteriol.* 195, 3724–3733. doi: 10.1128/jb.00546-13

Sakuraba, H., Koga, K., Yoneda, K., Kashima, Y., and Ohshima, T. (2011). Structure of a multicopper oxidase from the hyperthermophilic archaeon *Pyrobaculum aerophilum*. *Acta Crystallogr. Sect. F Struct. Biol. Cryst. Commun.* 67, 753–757.

Sambrook, J., and Russel, D. W. (2001). *Molecular Cloning*. Cold Spring Harbor, NY: Cold Spring Harbor Laboratory.

Sanders, C., Deshmukh, M., Astor, D., Kranz, R. G., and Daldal, F. (2005). Overproduction of CcmG and CcmFH(Rc) fully suppresses the c-type cytochrome biogenesis defect of *Rhodobacter capsulatus* CcmI-null mutants. *J. Bacteriol.* 187, 4245–4256. doi: 10.1128/jb.187.12.4245-4256.2005

Schagger, H., and Von Jagow, G. (1987). Tricine sodium dodecyl-sulfate polyacrylamide-gel electrophoresis for the separation of proteins in the range from 1-kda to 100-kda. *Anal. Biochem.* 166, 368–379. doi: 10.1016/0003-2697(87)90587-2

Selamoglu, N., Önder, Ö, Öztürk, Y., Khalfaoui-Hassani, B., Blaby-Haas, C. E., Garcia, B. A., et al. (2020). Comparative differential cuproproteomes of *Rhodobacter capsulatus* reveal novel copper homeostasis related proteins. *Metallomics* 12, 572–591. doi: 10.1039/c9mt00314b

Shannon, P., Markiel, A., Ozier, O., Baliga, N. S., Wang, J. T., Ramage, D., et al. (2003). Cytoscape: a software environment for integrated models of biomolecular interaction networks. *Genome Res.* 13, 2498–2504. doi: 10.1101/gr.1239303

Singh, S. K., Roberts, S. A., Mcdevitt, S. F., Weichsel, A., Wildner, G. F., Grass, G. B., et al. (2011). Crystal structures of multicopper oxidase CueO bound to copper(I) and silver(I): functional role of a methionine-rich sequence. *J. Biol. Chem.* 286, 37849–37857. doi: 10.1074/jbc.m111.293589

Sistrom, W. R. (1960). A requirement for sodium in the growth of *Rhodopseudomonas-spheroides*. *J. Gen. Microbiol.* 22, 778–785. doi: 10.1099/00221287-22-3-778

Solano, F., Lucas-Elio, P., Lopez-Serrano, D., Fernandez, E., and Sanchez-Amat, A. (2001). Dimethoxyphenol oxidase activity of different microbial blue multicopper proteins. *FEMS Microbiol. Lett.* 204, 175–181. doi: 10.1111/j.1574-6968.2001.tb10882.x

Solomon, E. I., Augustine, A. J., and Yoon, J. (2008). O(2) reduction to H(2)O by the multicopper oxidases. *Dalton Trans.* 30, 3921–3932. doi: 10.1039/b800799c

Steinberg, R., Origi, A., Natriashvili, A., Sarmah, P., Licheva, M., Walker, P. M., et al. (2020). Posttranslational insertion of small membrane proteins by the bacterial signal recognition particle. *PLoS Biol.* 18:e3000874. doi: 10.1371/journal.pbio.3000874

Steunou, A. S., Durand, A., Bourbon, M. L., Babot, M., Tambosi, R., Liotenberg, S., et al. (2020). Cadmium and copper cross-tolerance. Cu(+) Alleviates Cd(2 +) toxicity, and both cations target heme and chlorophyll biosynthesis pathway in *Rubrivivax gelatinosus*. *Front. Microbiol.* 11:893. doi: 10.3389/fmicb.2020.00893

Stolle, P., Hou, B., and Brüser, T. (2016). The Tat substrate CueO is transported in an incomplete folding state. *J. Biol. Chem.* 291, 13520–13528. doi: 10.1074/jbc.m116.729103

Stoyanov, J. V., Hobman, J. L., and Brown, N. L. (2001). CueR (YbbI) of *Escherichia coli* is a MerR family regulator controlling expression of the copper exporter CopA. *Mol. Microbiol.* 39, 502–511. doi: 10.1046/j.1365-2958.2001.02264.x

Suzek, B. E., Wang, Y., Huang, H., Mcgarvey, P. B., and Wu, C. H. (2015). UniRef clusters: a comprehensive and scalable alternative for improving sequence similarity searches. *Bioinformatics* 31, 926–932. doi: 10.1093/bioinformatics/btu739

Swem, D. L., and Bauer, C. E. (2002). Coordination of ubiquinol oxidase and cytochrome cbb(3) oxidase expression by multiple regulators in *Rhodobacter capsulatus*. *J. Bacteriol.* 184, 2815–2820. doi: 10.1128/jb.184.10.2815-2820.2002

The UniProt Consortium (2019). UniProt: a worldwide hub of protein knowledge. *Nucleic Acids Res.* 47, D506–D515.

Thomas, P. E., Ryan, D., and Levin, W. (1976). An improved staining procedure for the detection of the peroxidase activity of cytochrome P-450 on sodium dodecyl sulfat polyacrylamide gels. *Anal. Biochem.* 75, 168–176. doi: 10.1016/0003-2697(76)90067-1

Trasnea, P. I., Andrei, A., Marckmann, D., Utz, M., Khalfaoui-Hassani, B., Selamoglu, N., et al. (2018). A copper relay system involving two periplasmic chaperones drives cbb3-type cytochrome c oxidase biogenesis in *Rhodobacter capsulatus*. *ACS Chem. Biol.* 13, 1388–1396. doi: 10.1021/acschembio.8b00293

Trasnea, P.-I., Marckmann, D., Utz, M., and Koch, H.-G. (2016). Measurement of cellular copper in *Rhodobacter capsulatus* by atomic absorption spectroscopy. *Bioprotocol* 6:e1948.

Utz, M., Andrei, A., Milanov, M., Trasnea, P. I., Marckmann, D., Daldal, F., et al. (2019). The Cu chaperone CopZ is required for Cu homeostasis in *Rhodobacter capsulatus* and influences cytochrome cbb3 oxidase assembly. *Mol. Microbiol.* 111, 764–783. doi: 10.1111/mmi.14190

Verissimo, A. F., Khalfaoui-Hassani, B., Hwang, J., Steimle, S., Selamoglu, N., Sanders, C., et al. (2017). The thioreduction component CcmG confers efficiency and the heme ligation component CcmH ensures stereo-specificity during cytochrome c maturation. *J. Biol. Chem.* 292, 13154–13167. doi: 10.1074/jbc.m117.794586

Waterhouse, A. M., Procter, J. B., Martin, D. M. A., Clamp, M., and Barton, G. J. (2009). Jalview version 2-a multiple sequence alignment editor and analysis workbench. *Bioinformatics* 25, 1189–1191. doi: 10.1093/bioinformatics/btp033

Wiethaus, J., Wildner, G. F., and Masepohl, B. (2006). The multicopper oxidase CutO confers copper tolerance to *Rhodobacter capsulatus*. *FEMS Microbiol. Lett.* 256, 67–74. doi: 10.1111/j.1574-6968.2005.00094.x

Williamson, M. P. (1994). The structure and function of proline-rich regions in proteins. *Biochem J.* 297(Pt 2), 249–260. doi: 10.1042/bj2970249

Yen, H. C., Yhu, N. T., and Marrs, B. L. (1979). Characterization of the gene transfer agent made by an overproducer mutant of *Rhodopseudomonas capsulata*. *J. Mol. Biol.* 131, 157–168. doi: 10.1016/0022-2836(79)90071-8

Zallot, R., Oberg, N., and Gerlt, J. A. (2019). The EFI web resource for genomic enzymology tools: leveraging protein, genome, and metagenome databases to discover novel enzymes and metabolic pathways. *Biochemistry* 58, 4169–4182. doi: 10.1021/acs.biochem.9b00735

Zhang, Y., Blaby-Haas, C. E., Steimle, S., Verissimo, A. F., Garcia-Angulo, V. A., Koch, H.-G., et al. (2019). Cu transport by the extended family of CcoA-like transporters (CalT) in *Proteobacteria*. *Sci. Rep.* 9:1208.

Conflict of Interest: The authors declare that the research was conducted in the absence of any commercial or financial relationships that could be construed as a potential conflict of interest.

Publisher's Note: All claims expressed in this article are solely those of the authors and do not necessarily represent those of their affiliated organizations, or those of the publisher, the editors and the reviewers. Any product that may be evaluated in this article, or claim that may be made by its manufacturer, is not guaranteed or endorsed by the publisher.

frontiers in Microbiology

ORIGINAL RESEARCH
published: 09 September 2021
doi: 10.3389/fmicb.2021.723835

Aerobic Respiration and Its Regulation in the Metal Reducer *Shewanella oneidensis*

*Kristen Bertling†, Areen Banerjee†‡ and Daad Saffarini**

Department of Biological Sciences, University of Wisconsin-Milwaukee, Milwaukee, WI, United States

Shewanella oneidensis MR-1 is a facultative anaerobe known for its ability to reduce metal oxides. Anaerobic respiration, especially metal reduction, has been the subject of extensive research. In contrast, *S. oneidensis* aerobic respiration has received less attention. *S. oneidensis* expresses *cbb3*- and *aa3*-type cytochrome *c* oxidases and a *bd*-type quinol oxidase. The *aa3*-type oxidase, which in other bacteria is the major oxygen reductase under oxygen replete conditions, does not appear to contribute to aerobic respiration and growth in *S. oneidensis*. Our results indicated that although the *aa3*-type oxidase does not play a role in aerobic growth on lactate, the preferred carbon source for *S. oneidensis*, it is involved in growth on pyruvate or acetate. These results highlight the importance of testing multiple carbon and energy sources when attempting to identify enzyme activities and mutant phenotypes. Several regulatory proteins contribute to the regulation of aerobic growth in *S. oneidensis* including CRP and ArcA. The 3',5'-cAMP phosphodiesterase (CpdA) appears to play a more significant role in aerobic growth than either CRP or ArcA, yet the deficiency does not appear to be the result of reduced oxidase genes expression. Interestingly, the Δ*cpdA* mutant was more deficient in aerobic respiration with several carbon sources tested compared to Δ*crp*, which was moderately deficient only in the presence of lactate. To identify the reason for Δ*cpdA* aerobic growth deficiency, we isolated a suppressor mutant with transposon insertion in SO_3550. Inactivation of this gene, which encodes an anti-sigma factor, restored aerobic growth in the *cpdA* mutant to wild-type levels. Inactivation of SO_3550 in wild-type cells, however, did not affect aerobic growth. The *S. oneidensis* genome encodes two additional CRP-like proteins that we designated CrpB and CrpC. Mutants that lack *crpB* and *crpC* were deficient in aerobic growth, but this deficiency was not due to the loss of oxidase gene expression.

Keywords: aerobic respiration, *Shewanella oneidensis* MR1, crp, cAMP phosphodiesterase, anti-sigma factor, cytochrome oxidase

OPEN ACCESS

Edited by:
Davide Zannoni,
University of Bologna, Italy

Reviewed by:
Myriam Brugna,
Aix-Marseille Université, France
Johannes Gescher,
Karlsruhe Institute of Technology (KIT), Germany

****Correspondence:***
Daad Saffarini,
daads@uwm.edu

†These authors have contributed equally to this work

‡Present address:
Areen Banerjee,
GreenLight Biosciences,
Medford, MA, United States

Specialty section:
This article was submitted to Microbial Physiology and Metabolism, a section of the journal Frontiers in Microbiology

Received: *11 June 2021*
Accepted: *26 July 2021*
Published: *09 September 2021*

Citation:
Bertling K, Banerjee A and Saffarini D (2021) Aerobic Respiration and Its Regulation in the Metal Reducer Shewanella oneidensis. Front. Microbiol. 12:723835. doi: 10.3389/fmicb.2021.723835

INTRODUCTION

Shewanella oneidensis MR-1 is a Gram-negative facultative anaerobe found mostly at the oxic/anoxic interface in freshwater environments. The ability of *S. oneidensis* to thrive in such environments is attributed to its extreme respiratory versatility with regard to electron acceptors, which include oxygen, radionuclides, elemental sulfur, and metal oxides

(Fredrickson et al., 2008). The ability to use metals as terminal electron acceptors has spurred research into electricity generation by *S. oneidensis*. The location of *c*-type cytochromes, such as MtrC, on the outer cell surface (Beliaev et al., 2001) and the ability to reduce metal oxides made *S. oneidensis* and other metal reducing bacteria attractive candidates to study electricity production in microbial fuel cells (Bouhenni et al., 2010; Bretschger et al., 2010).

In addition to the anaerobic reductases, *S. oneidensis* expresses three terminal aerobic oxidases. These are encoded by the *cco* operon (SO_2364–2357), the *cox* genes (SO_4606–4609), and *cydABX* (SO_3286–3284). The *cco* and *cox* operons encode the cbb_3- and aa_3-type enzymes that belong to the heme-copper oxidase (HCO) family, while *cydAB* encodes a *bd*-type quinol oxidase (Borisov et al., 2011; Sousa et al., 2012; Le Laz et al., 2014).

Type A HCO or aa_3-type cytochrome *c* oxidases have low oxygen affinity, and in many organisms, they are the primary enzymes used when oxygen is readily available (Ludwig, 1987; García-Horsman et al., 1994). In contrast, the cbb_3-type cytochrome *c* oxidase has high affinity for oxygen, and it is the primary enzyme used under microaerobic conditions (Pitcher and Watmough, 2004; Buschmann et al., 2010). The *bd*-type enzymes are quinol oxidases that have a high affinity for oxygen, and as such, function under microaerobic conditions (Borisov et al., 2011).

The *S. oneidensis* aerobic oxidases do not appear to function under the same environmental conditions as their counterparts in other bacteria. The *cbb3*-type cytochrome oxidase, in addition to the *bd* quinol oxidase, appears to play a major role in aerobic respiration. Mutants deficient in *cbb3*-type cytochrome oxidase grew slower than the wild type, while loss of *bd* quinol oxidase did not have an effect on aerobic growth, suggesting that the *cbb3*-type enzyme is the major oxidase under aerobic conditions (Gao et al., 2010; Kouzuma et al., 2012; Le Laz et al., 2014). Mutants that lack aa_3-type cytochrome *c* oxidase had no effect on aerobic growth and the lack of detectable enzyme activity in wild-type cells suggested that it may not be expressed (Le Laz et al., 2014). A recent report, however, showed that the *S. oneidensis* aa_3-type cytochrome *c* oxidase is expressed under highly aerobic conditions and carbon starvation (Le Laz et al., 2016).

The cAMP-receptor protein CRP is a global regulatory protein that controls the expression of many of the anaerobic reductase genes (Pitcher and Watmough, 2004; Charania et al., 2009). Δ*crp* mutant is completely deficient in anaerobic growth with several electron acceptors and is slightly impaired in aerobic growth (Saffarini et al., 2003; Kasai et al., 2017). Three adenylate cyclases and one phosphodiesterase (CpdA) regulate cellular cAMP levels (Charania et al., 2009; Yin et al., 2016). Interestingly, mutants deficient in adenylate cyclase activity are deficient in anaerobic respiration, while a mutant that lacks CpdA is deficient in aerobic respiration (Charania et al., 2009; Yin et al., 2016). The work presented in this paper suggests that the *aa3*-type and *cbb3*-type cytochrome oxidases are involved in aerobic respiration when pyruvate and acetate are used as carbon sources. Furthermore, our results suggest that the aerobic growth deficiency observed in Δ*cpdA* is not due to the loss of cytochrome *c* oxidases, and this deficiency can be suppressed by a mutation in a putative anti-sigma factor.

MATERIALS AND METHODS

Bacterial Strains and Growth Conditions

The bacterial strains and plasmids used in this study are listed in **Table 1**. *S. oneidensis* MR-1 and *Escherichia coli* cells were cultured aerobically in lysogeny broth (LB) at 30 and 37°C, respectively. Antibiotics (20 mg/ml chloramphenicol, 25 mg/ml kanamycin, and 25 mg/ml gentamycin) were added as needed. For anaerobic growth, *S. oneidensis* cells were grown in basal medium supplemented with 50 mM lactate, 0.02% casamino acids, and 10 mM of either fumarate or DMSO (Saffarini et al., 2003). Anaerobic growth was performed in Hungate tubes and monitored at A_{600}. To test aerobic growth, the mutants and the wild type were grown with vigorous shaking in 500 ml flasks containing 50 ml basal medium supplemented with 0.01% casamino acids, and 30 or 50 mM of the indicated carbon source. For some experiments, growth was carried out in 24 well plates containing 600 µl basal medium supplemented as above. Optical density was measured using the Tecan Infinite® m200 PRO plate reader.

TABLE 1 | List of strains and plasmids used in this study.

Strain/Plasmids	Description	References
S. oneidensis		
MR-1	Wild-type *S. oneidensis*	Fredrickson et al., 2008
SR-694	MR-1Δ*crp*	Charania et al., 2009
SR-722	MR-1Δ*cpdA*	This work
SR-1507	MR-1 ΔSO_2364–2,357 (Δ*cco*)	This work
SR-1648	MR-1 ΔSO_4,606–4,609 (Δ*cox*)	This work
SR-1649	MR-1 Δ*cco*Δ*cox*	This work
SR-1699	MR-1 with pER21 insertion inSO_3,550	This work
SR-1700	Δ*cpdA* with pER21 insertion inSO_3,550	This work
SR-1716	MR-1 Δ*cydAB* (Δ*cyd*)	This work
SR-1717	MR-1 ΔSO-2551	This work
SR-1718	MR-1 ΔSO_2550–2,551	This work
E. coli		
EC100D+	*E. coli* EC100 derivative, *pir*+	Epicenter Technologies
β2155	*pir*::RP4, Km^r	Dehio and Meyer, 1997
Plasmids		
pJBC1	Cloning and sequencing vector, Cm^R	Bouhenni et al., 2010
pER21	R6K *ori*, Gm^R, *sacB*, *lacZ* a-fragment	Bouhenni et al., 2005
pMC10	Promoter probe vector, *lacZ*, Cm^R	Shroff et al., 2010
pAB1	*cpdA* in pJB3Cm6	This work
RB1	mini*Himar* Transposon	Bouhenni et al., 2005

Generation of Chromosomal Deletion Mutants

Chromosomal gene deletions were performed as described previously (Shirodkar et al., 2011). 1 kb fragments flanking the gene(s) of interest were amplified using Phusion polymerase (New England Biolabs) and the primers listed in **Supplementary Table S1**. The fragments were amplified, digested, and then ligated before cloning into the SmaI site of the suicide vector pER21 (**Table 1**). Plasmids carrying the insert of interest were used to transform *E. coli* β2155 cells (Dehio and Meyer, 1997) by electroporation and then transferred to *S. oneidensis* MR-1 strains by conjugation. Mutants with chromosomal deletions were selected on 5% sucrose plates then screened by PCR to verify deletion of the target gene.

Promoter-Activity Assays

DNA fragments directly upstream of the genes of interest were amplified from genomic DNA by PCR using Phusion polymerase and the primers listed in **Supplementary Table S1**. HindIII and BamHI restriction sites were included in the primer design. The amplified fragments were digested and cloned into pMC10 (Shroff et al., 2010). Following transformation of *E. coli* β2155 (Dehio and Meyer, 1997), the plasmids were transferred into wild-type and mutant strains by conjugation. Cultures were assayed for β-galactosidase activity essentially as previously described (Miller, 1972).

cAMP Detection Assay

Shewanella oneidensis strains grown in LB overnight were diluted 1:8 with basal medium supplemented with 50 mM lactate and 0.02% casamino acids and used to grow cultures aerobically and anaerobically. For anaerobic growth, cultures were supplemented with 10 mM fumarate or 10 mM DMSO and incubated anaerobically in sealed serum vials for 3 h. For aerobic growth, 50 ml cultures in 2 liter flasks were grown for 3 h with vigorous shaking. Cells were then pelleted and lysed by boiling in phosphate buffered saline. The supernatants from the boiled samples were used to measure intracellular cAMP using the Fluorescent HitHunter cAMP detection kit (GE-Healthcare). Protein concentrations in equivalent culture samples were determined using the BCA assay reagents (Thermo Scientific). Spent media from both aerobic and anaerobic cultures were filtered with a 0.22 μm filter then used to measure extracellular cAMP levels.

Generation of Δ*cpdA* Suppressor Mutant

Transposon mutants in a Δ*cpdA* background were generated using pmini*Himar* RB1 (Bouhenni et al., 2005). The plasmid was transferred into *S. oneidensis* by conjugation. Mutants were selected on basal medium agar supplemented with 30 mM lactate, 0.01% casamino acids, and 25 μg/ml kanamycin. Chromosomal DNA was isolated, digested with BamHI, re-ligated, and used to transform *E. coli* EC100D$^+$. Plasmid DNA was sequenced by Eurofins Scientific using the primer 615 (**Supplementary Table S1**). The resulting sequences were analyzed, and mutants of interest were selected for further study. Insertional inactivation of the gene of interest was achieved by cloning an internal fragment of 500 bp into the suicide plasmid pER21 (Bouhenni et al., 2010). The resulting plasmid was transferred into wild-type MR-1 and Δ*cpdA* by conjugation. Mutants were selected on LB agar plates supplemented with 25 mg/ml gentamycin.

RESULTS

The Effect of Carbon Source on Growth of *S. oneidensis* Oxidase Mutants

To understand the role of the *S. oneidensis* oxidases, we generated mutants that lack the *cco*, *cox*, and *cyd* operons that encode the cbb_3-type oxidase, aa_3-type oxidase, and *bd* quinol oxidase, respectively. The mutants were tested for growth using lactate, pyruvate, or acetate as carbon and energy sources. In the absence of oxygen, with either fumarate or DMSO as electron acceptors, all mutants grew similar to the wild type when lactate was used as the carbon source (**Figure 1**). The Δ*cco* mutant was slightly deficient in anaerobic growth with DMSO and fumarate when pyruvate was the sole carbon source and electron donor. Growth of the other oxidase mutants tested was indistinguishable from that of the wild type (**Figure 2** and data not shown).

Single and double oxidase mutants were tested for aerobic growth using different carbon sources. In the presence of lactate, deletion of *cco* genes slowed growth of the mutant, whereas deletion of the other oxidase genes had no effect (**Figure 3A**). The estimated doubling time of Δ*cco* mutant was 6.7 h. The doubling time of Δ*cyd*, Δ*cox,* and wild-type strains ranged between 5.0 and 5.4 h. In contrast, significant growth deficiencies were observed in *cco* and *cox* single and double mutants when grown with acetate or pyruvate (**Figures 3B**,**C**). Overall, growth is slower when acetate or pyruvate are used as sole carbon sources, likely exacerbating the deficiency phenotype. In the presence of acetate, the doubling time of Δ*cco*, Δ*cox*, and Δ*cco*Δ*cox* mutants was 1.35, 1.3, and 1.5 times that of the wild type, respectively. A similar growth pattern was seen when the mutants were grown aerobically with pyruvate. It is noteworthy that the deficiency of the double Δ*cco*Δ*cox* was more pronounced with a doubling time almost twice that of the wild type. Introduction of *cox* genes into the double mutant restored its ability to grow similar to the single Δ*cco* mutant (**Figure 3C**). These results suggest that the aa_3-type oxidase is functional in *S. oneidensis*, but its activity and contribution to aerobic growth may depend on the energy and carbon source that the bacterium uses.

The Role of CRP and CpdA in Aerobic Growth

The function of CpdA (SO_3901) as a cAMP phosphodiesterase has been previously described (Yin et al., 2016; Kasai et al., 2018). We generated a Δ*cpdA* mutant and tested for cAMP levels and growth phenotypes. In aerobically grown cells, intracellular cAMP increased from 28.9 ± 3.1 pmoles/mg protein in the wild type to 106.2 ± 20.3 pmoles/mg protein in Δ*cpdA*. Similarly,

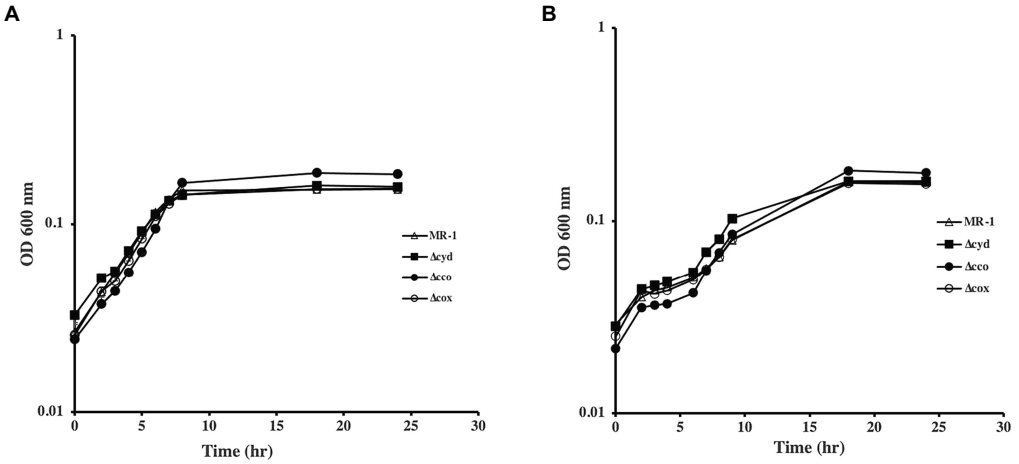

FIGURE 1 | Anaerobic growth of oxidase mutants in lactate-minimal medium with fumarate **(A)** and DMSO **(B)**. None of the mutants exhibited growth deficiencies under the conditions tested. The data are the means and standard deviations of three independent experiments.

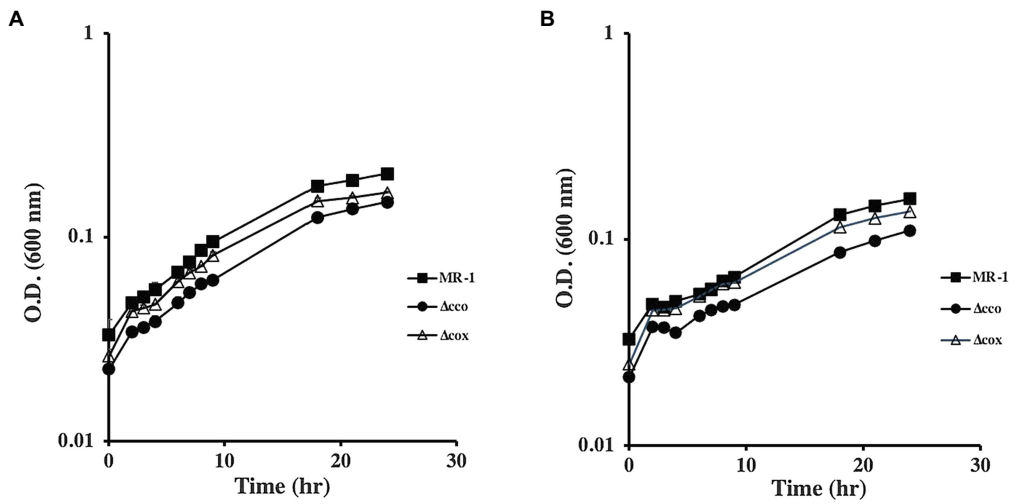

FIGURE 2 | Anaerobic growth of oxidase mutants with fumarate **(A)** and DMSO **(B)** as electron acceptors and pyruvate as the carbon source. Δ*cox* grew similar to the wild type, while Δ*cco* had a moderate growth deficiency with both electron acceptors. Δ*cyd* mutant grew similar to the wild type but is not shown for clarity. The data are the means and standard deviations of three independent experiments.

higher extracellular cAMP concentrations were consistently detected in the Δ*cpdA* mutant than in the wild type (26.5 ± 3.3 and 13.8 ± 2.5 nmoles/mg protein, respectively). These results are in agreement with the previously reported role of CpdA as a cAMP phosphodiesterase (Yin et al., 2016; Kasai et al., 2018). Because cAMP is required for CRP activation, we reasoned that a *cpdA* mutation will affect anaerobic respiration. Growth of Δ*cpdA* in lactate-basal medium with fumarate or DMSO was similar to the wild type but appeared to reach stationary phase at a lower cell density than the wild type (**Supplementary Figure S1** and data not shown). Growth of Δ*cpdA* was also tested aerobically in rich and minimal media. We did not detect a growth deficiency when the mutant was grown aerobically in LB (data not shown). However, the mutant grew poorly in minimal medium supplemented with lactate (**Figure 4**). These results are in agreement with the findings of Kasai et al. (2018). We further tested aerobic growth of Δ*cpdA* and complemented mutant in the presence of pyruvate and acetate (**Figure 4** and **Supplementary Figure S2**). The mutant was deficient in aerobic growth in the presence of these carbon sources and complementation restored its ability to grow similar to the wild type (**Figure 4** and data not shown).

Although *S. oneidensis* CRP is best known for its role in the regulation of anaerobic respiration, it appears to have an effect on aerobic respiration. To further investigate the role of CRP in this process, we monitored aerobic growth of wild type and Δ*crp* mutant in the presence of different carbon sources. In the presence of lactate, the Δ*crp* mutant exhibited

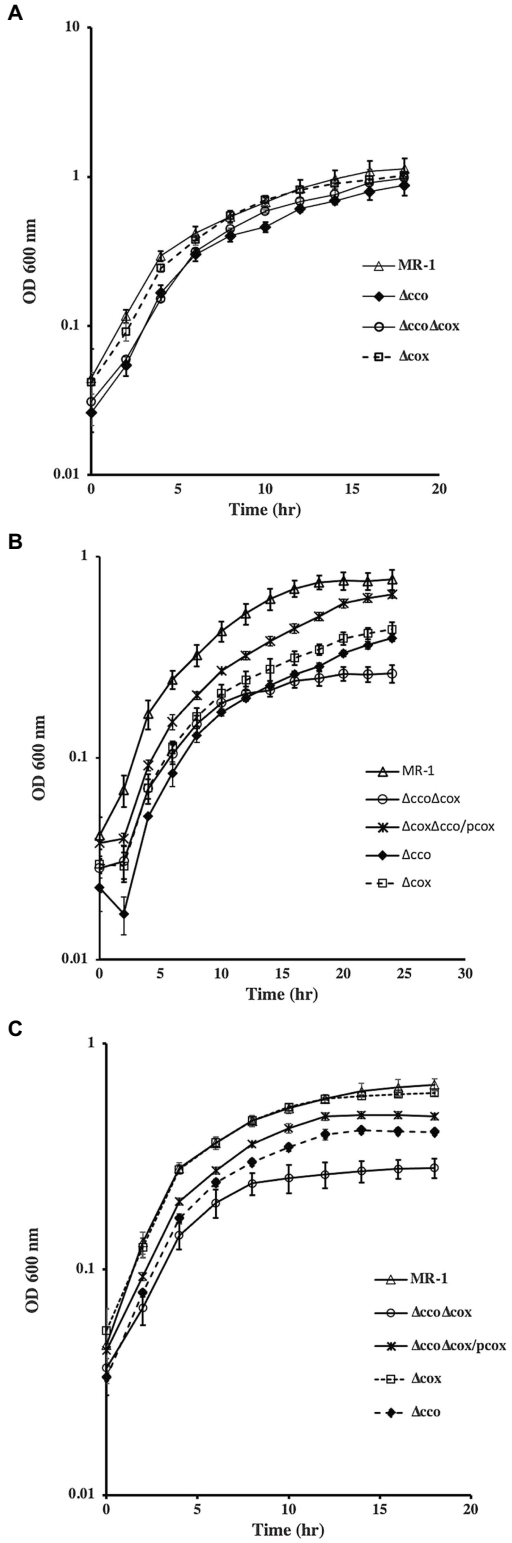

FIGURE 3 | Aerobic growth of *S. oneidensis* wild-type and oxidase mutants with lactate **(A)**, acetate **(B)**, and pyruvate **(C)**. Both Δ*cco* and Δ*cco*Δ*cox* mutants were more deficient in growth with acetate and pyruvate than with lactate. Δ*cyd* mutant grew similar to the wild type but is not shown for clarity. The data are the means and standard deviations of three independent experiments.

a slight deficiency in growth compared to the wild type (**Supplementary Figure S2**). This deficiency was not observed when acetate or pyruvate was used as carbon sources or when the mutant was grown in rich medium, such as LB (**Supplementary Figure S2** and data not shown). This result was surprising, and it is not clear why the *crp* mutant exhibits growth deficiencies with lactate but not with other carbon sources.

Previous reports suggested the positive regulation of *cco* and *cyd* genes by CRP and CpdA (Yin et al., 2016). A more recent microarray analysis suggested that CpdA does not an effect expression of these two oxidases (Kasai et al., 2018). Using *lacZ*-promoter fusions, we tested the expression of *cco* and *cyd* genes in Δ*crp* and Δ*cpdA*. Our results indicate that CpdA and CRP do not affect the expression of the *cco* operon (**Figure 5**). Furthermore, loss of CRP, but not CpdA, led to reduced expression of *cydAB* indicating that this operon is positively regulated by CRP (**Figure 5**).

Isolation of a Δ*cpdA* Suppressor Mutant

To identify the reason for Δ*cpdA* growth deficiency under aerobic but not anaerobic conditions, we isolated a transposon mutant in a Δ*cpdA* background that grew in basal medium under aerobic conditions similar to the wild type (**Figure 6**). Sequence analysis identified a transposon insertion in SO_3550, which is predicted to encode an anti-sigma factor and is in an operon with SO_3551 that encodes a putative extracytoplasmic function (ECF) sigma factor. To confirm that the ability of Δ*cpdA* SO-3550::*himar* to grow in minimal medium aerobically was due to inactivation of SO_3550, we generated an insertional mutation in this gene in a Δ*cpdA* background. Inactivation of SO_3550 in Δ*cpdA* restored the mutant's ability to grow aerobically in minimal medium (**Figure 6**). Insertional inactivation of SO_3550 was also performed in wild-type MR-1 in an attempt to identify SO_3550 function. However, analysis of the resulting mutant did not reveal any growth deficiencies under the conditions we tested (**Figure 6**).

Identification of Putative cAMP-Binding Proteins Involved in Aerobic Respiration

In addition to CRP, the *S. oneidensis* genome contains two genes, SO_2550 and SO_2551, that we designated *crpB* and *crpC, respectively.* These genes are separated by 125 nucleotides. Sequence analysis identified putative nucleotide and DNA-binding domains with similarity to CRP-like proteins. Single and double chromosomal deletion mutants were generated and tested for aerobic growth with different electron acceptors. Δ*crpC* grew aerobically with all carbon sources tested. Similarly, a mutant that lacks *cprB* did not exhibit any aerobic growth deficiency. In contrast, a strain that lacked both genes was deficient in aerobic growth with lactate, pyruvate, and acetate. These results suggest that *crpB* and *crpC* may be redundant and both play a role in aerobic growth. Complementation of the mutants restored their ability to grow with all carbon sources tested (**Figure 7**). Since the double Δ*crpB* Δ*crpC* mutant was deficient in aerobic growth, we tested it for expression of *cco* and *cyd* genes using promoter-*lacZ* fusions. There was no detectable

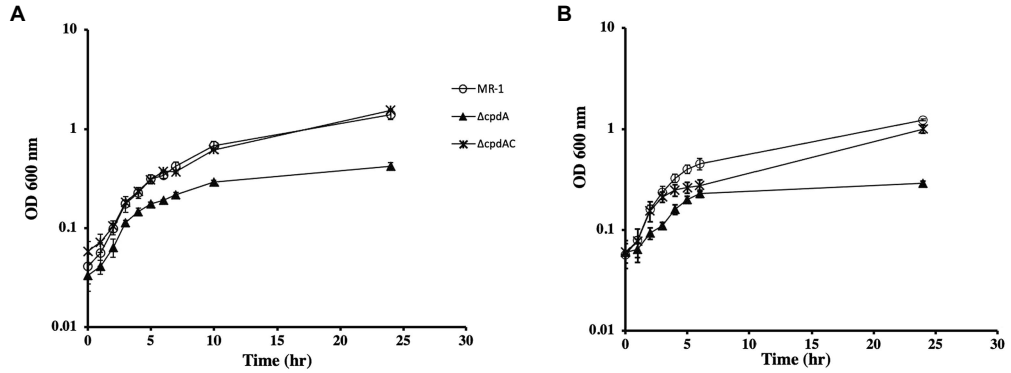

FIGURE 4 | Aerobic growth of wild type, Δ*cpdA*, and complemented mutant (Δ*cpdA*C) in basal medium supplemented with lactate **(A)** or pyruvate **(B)**. Complementation of Δ*cpdA* restored its ability to grow with both carbon sources. Legend applies to **A** and **B**. The data are the means and standard deviations of three independent experiments.

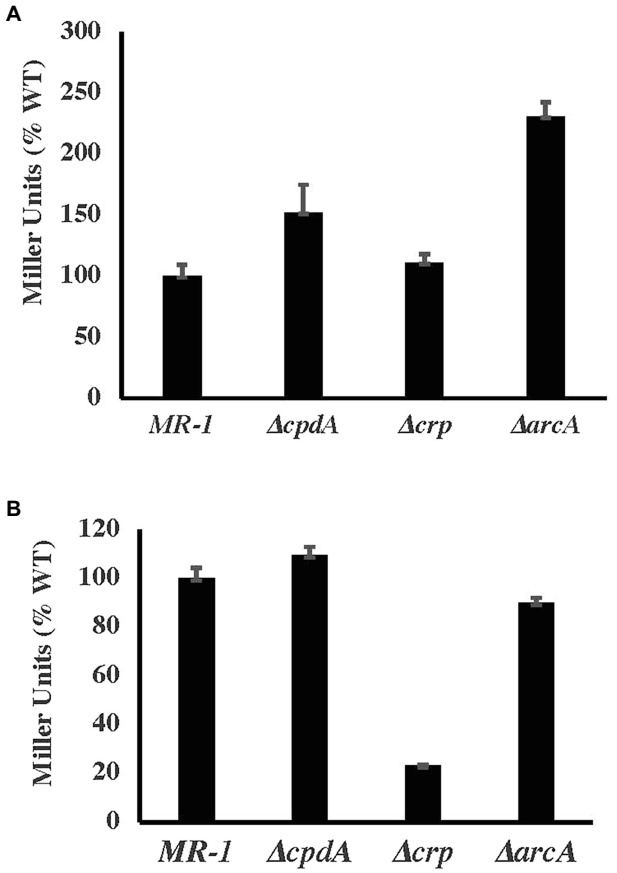

FIGURE 5 | ß-galactosidase activity (in Miller relative to WT) of *cco* **(A)** and *cyd* **(B)** promoter-*lacZ* fusions under aerobic conditions in basal medium supplemented with 30 mM lactate and 0.01% casamino acids.

difference in ß-galactosidase activity in the mutant compared to the wild type, suggesting that neither CrpB nor CrpC regulate the expression of the *cco* and *cyd* genes (**Supplementary Figure S3**).

DISCUSSION

Shewanella oneidensis exhibits amazing respiratory versatility that allows it to survive in the changing oxic/anoxic interface of aquatic environments. At least 14 terminal electron acceptors have been identified and many anaerobic terminal reductases and reduction pathways have been elucidated (Beliaev et al., 2002; Fredrickson et al., 2008; Gao et al., 2009; Shirodkar et al., 2011; Brockman et al., 2020). For aerobic respiration, three terminal oxidases have been identified. The cbb_3-type is active under oxygen replete conditions and appears to be the major oxidase (Le Laz et al., 2014) while the *bd*-type quinol oxidase, encoded by *cydAB*, functions under microaerobic conditions and early stationary phase (Zhou et al., 2013; Le Laz et al., 2014). The function of the *aa3*-type was more difficult to identify. Earlier reports suggested this cytochrome *c* oxidase does not play a role in aerobic respiration and may not be expressed (Zhou et al., 2013). Biochemical analysis failed to detect *aa3*-type oxidase in aerobic cells grown in rich media (Le Laz et al., 2014), but the enzyme was detectable in cells grown in minimal medium but starved for nutrients similar to the *Pseudomonas aeruginosa* aa_3-type oxidase (Kawakami et al., 2010; Le Laz et al., 2016; Osamura et al., 2017). Kouzuma et al. (2012) isolated a mutant deficient in the aa_3- and cbb_3-type oxidases that grew slower than the wild type or the single mutants on lactate (Kouzuma et al., 2012) suggesting that the aa_3-type cytochrome *c* oxidase activity is not confined to conditions of extreme nutrient stress. Our results support this prediction. In defined minimal media supplemented with lactate, little difference was observed between the wild-type and the single oxidase mutants (**Figure 3**). However, the growth patterns of these mutants appear to change dramatically in the presence of other carbon courses. The Δ*cco* mutant was clearly deficient in aerobic growth with pyruvate and acetate. The Δ*cox* mutant had a significant deficiency when grown with acetate, and the double Δ*cco*Δcox was noticeably deficient in growth in the presence of both carbon sources (**Figure 3**). Lactate is the preferred carbon source for *S. oneidensis* and in its presence, acetate metabolism is inhibited

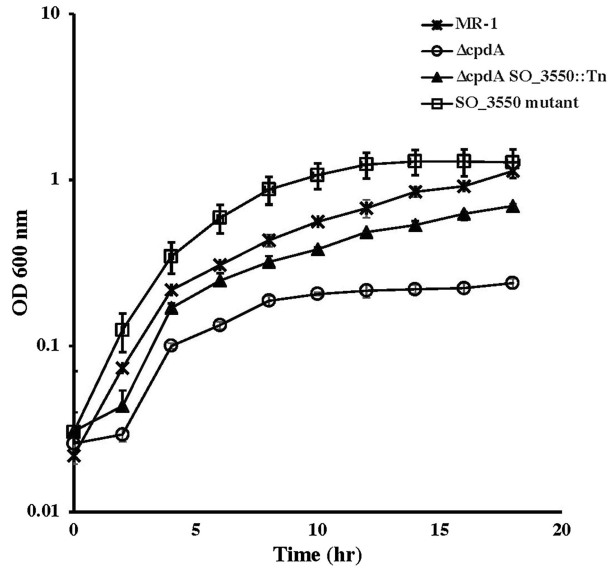

FIGURE 6 | Aerobic growth of wild-type *Shewanella oneidensis* and Δ*cpdA* strains in basal medium supplemented with 30 mM lactate and 0.01% casamino acids. Insertional inactivation of SO_3550 in Δ*cpdA* allowed the phosphodiesterase mutant to recover its ability to grow aerobically in minimal media. Inactivation of SO_3550 in wild-type MR-1 did not affect the ability of the mutant to grow aerobically. The data are the means and standard deviations of three independent experiments.

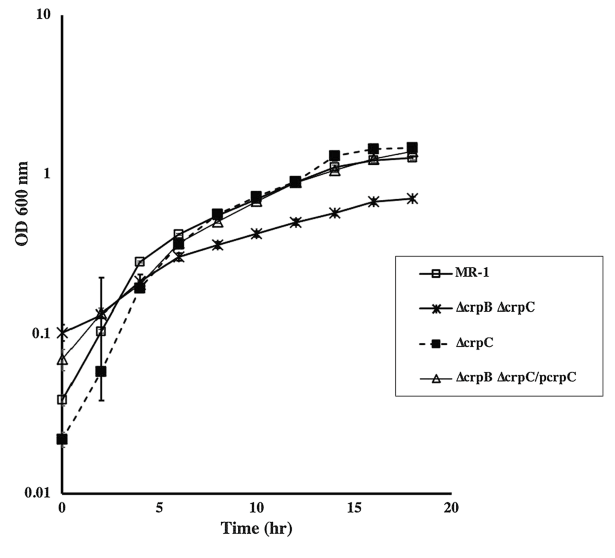

FIGURE 7 | Aerobic growth of wild type, Δ*crpB* and Δ*crpC* with lactate as the carbon source. Loss of both genes resulted in slow growth compared to the wild type. Growth was restored to wild-type levels by the introduction of *crpC*. Complementation was also achieved by the introduction of *crpB* and *crpC* on a plasmid (data not shown). The data are the means and standard deviations of three independent experiments.

(Tang et al., 2007). Based on the results presented in this paper and work from others, we propose that the *S. oneidensis* aa_3-type cytochrome oxidase is active under nutrient stress in the absence of its preferred carbon source. It may be that expression of aa_3-type cytochrome oxidase constitutes part of a stress response to nutrient or oxidative stress conditions. We also observed that the Δ*cco* strain was mildly deficient in anaerobic growth with fumarate & DMSO as electron acceptors (**Figure 2**). This result backs the findings of Gao et al. (2010) who observed that the Δ*cco* mutant was deficient in Uranium reduction.

Carbon metabolism in *E. coli* and other bacteria is regulated by the cAMP-receptor protein CRP (Guest, 1992). In *S. oneidensis* and its close relative *Shewanella* ANA-3, CRP regulates anaerobic respiration (Saffarini et al., 2003). *S. oneidensis* Δ*crp* mutants were deficient in aerobic growth with lactate but were not significantly deficient with acetate or pyruvate (Kasai et al., 2017 and **Supplementary Figure S2**). The aerobic growth deficiency in Δ*crp* does not appear to be due to loss of oxidase genes since expression of the *cco* operon is not affected by loss of CRP (**Figure 5**). *cydAB* expression was downregulated in Δ*crp*, but because loss of *cydAB* does not significantly affect aerobic growth, we do not expect this regulation to be the reason for the *crp* mutant deficiency. In addition to CRP, ArcA, which regulates anaerobic DMSO reduction in *S. oneidensis*, appears to be involved in aerobic growth. *arcA* mutants grow slower than the wild type under aerobic conditions (Gralnick et al., 2005; Shroff et al., 2010). These results are surprising because ArcA appears to negatively regulate *cco* gene expression under both aerobic and anaerobic conditions (**Figure 5** and Shroff et al., 2010).

cAMP phosphodiesterases regulate gene expression by controlling intracellular cAMP levels. These enzymes are involved in colony size, virulence, regulation of carbon metabolism, and biofilm formation among others (for review see Matange, 2015). Their function can be dependent or independent from the cAMP-receptor protein and may include hydrolysis of other cyclic nuclides, such as cGMP (Matange, 2015). *S. oneidensis* CpdA hydrolyzes cAMP and cyclic di-GMP (This work; Yin et al., 2016; Kasai et al., 2018). Although *S. oneidensis* CpdA is involved in the regulation of cAMP levels under both aerobic and anaerobic conditions, it does not appear to play a significant role in anaerobic growth, unlike CRP (**Supplementary Figure S1**). In contrast, *S. oneidensis cpdA* mutants are deficient in aerobic growth. This deficiency was observed in minimal (**Figure 4**) but not in rich media (Kasai et al., 2018). Although previous reports suggested that CpdA positively regulates the expression of aerobic oxidase genes, our results (**Figure 5**) and those of Kasai et al. (2018) indicated that expression of the oxidase genes was not affected in Δ*cpdA*. In fact, the aerobic growth deficiency in *cpdA* mutant can be complemented by the addition of casamino acids (**Supplementary Figure S4** and Kasai et al., 2018). It is interesting to note that growth of Δ*cpdA* with 0.2% casamino acids was similar to growth of the wild type with 0.05% casamino acids. This suggests that the mutant, although it can be complemented with casamino acids, is still deficient compared to the wild type (**Supplementary Figure S4**).

To further understand the role of CpdA in aerobic respiration, we isolated a suppressor mutant of *cpdA* with an insertion in

SO_3550 that is predicted to encode an anti-sigma factor. This gene is located downstream of SO_3551, which is predicted to encode an ECF sigma factor. The two genes appear to be arranged in an operon with another ORF (SO_3552). Since SO_3550 is the last gene in the presumptive operon, its disruption is not expected to affect the expression of the two other ORFs, suggesting that loss of only the anti-sigma factor is sufficient to restore aerobic growth to the *cpdA* mutant to almost wild-type levels (**Figure 6**). The function of SO_3550 is not clear. We attempted to identify its function by inactivating this gene in the wild-type strain, but we did not detect a deficiency in growth when compared to the wild type. It is intriguing that SO_3550 is adjacent to an ECF sigma factor gene and that sequence analysis predicts possible regulation of this operon by CRP. The microarray data presented by Kasai et al. (2018) do not indicate up- or downregulation of any of the five MR-1 ECF sigma factors or their cognate anti-sigma factors in the Δ*cpd*A mutant (Kasai et al., 2018). Therefore, the action of this anti-sigma factor and its cognate sigma may not be directly affected by *cpd*A. ECF sigma factors are typically activated in response to stress. In view of the fact that Δ*cpd*A growth deficiency can be ameliorated by either the addition of amino acids (**Supplementary Figure S4** and Kasai et al., 2018) or inactivation of SO_3550, we suggest that the growth deficiency may be due to energy stress and lack of sufficient ATP. This may be reflected in the downregulation of amino acid biosynthesis genes in Δ*cpdA* (Kasai et al., 2018). In the absence of a cAMP phosphodiesterase, the cell accumulates cAMP and may deplete ATP normally used for biosynthesis and growth. Inactivation of SO_3550 is predicted to activate the ECF sigma factor SO_3551. SO_3551 may modulate the function of a subset of adenylate cyclases under stress conditions or play a role in the regulating of amino acid metabolism. Clearly, additional work is needed to elucidate the function of SO_3550 and its putative cognate sigma factor SO_3551.

Many *S. oneidensis* genes exhibit redundancy. Genes involved in metal reduction, for example, have multiple homologs in the genome. There are three adenylate cyclases whose functions appear to be partially redundant. There is also redundancy in the function of terminal oxidases, such as the cbb_3- and *bd*-type oxidases. CRP is no exception. The *S. oneidensis* genome encodes two putative cAMP-receptor-like proteins. Similar to CRP and ArcA, CrpB and CrpC play a role in aerobic growth (**Figure 7**) but do not appear to have an effect on the expression of terminal aerobic oxidase genes (**Supplementary Figure S3**). We suggest that these CRP-like proteins have a role in carbon metabolism similar to CRP (Kasai et al., 2017). The results presented here add to our knowledge of the mechanisms of aerobic respiration in *S. oneidensis*, but also add new elements to the complexity of the process. Clearly additional work is needed to understand how *S. oneidensis* regulates growth and respiration in its environment.

DATA AVAILABILITY STATEMENT

The original contributions presented in the study are included in the article/**Supplementary Material**, and further inquiries can be directed to the corresponding author.

AUTHOR CONTRIBUTIONS

KB generated oxidase mutants and analyzed the mutant's phenotypes and gene expression. AB generated cpdA mutant, measured cAMP level in aerobic and anaerobic cells, and analyzed the mutant's phenotypes. DS conceived the project, performed growth experiments, and wrote the manuscript. All authors contributed to the article and approved the submitted version

ACKNOWLEDGMENTS

The authors acknowledge the support of the Department of Energy (DE-FG02-07ER64382) and thank Marwan McBride for experimental assistance.

SUPPLEMENTARY MATERIAL

The Supplementary Material for this article can be found online at https://www.frontiersin.org/articles/10.3389/fmicb.2021.723835/full#supplementary-material

REFERENCES

Beliaev, A. S., Saffarini, D. A., McLaughlin, J. L., and Hunnicutt, D. (2001). MtrC, an outer membrane decahaem c cytochrome required for metal reduction in Shewanella putrefaciens MR-1. *Mol. Microbiol.* 39, 722–730. doi: 10.1046/j.1365-2958.2001.02257.x

Beliaev, A. S., Thompson, D. K., Khare, T., Lim, H., Brandt, C. C., Li, G., et al. (2002). Gene and protein expression profiles of *Shewanella oneidensis* during anaerobic growth with different electron acceptors. *Omics J. Integr. Biol.* 6, 39–60. doi: 10.1089/15362310252780834

Borisov, V. B., Gennis, R. B., Hemp, J., and Verkhovsky, M. I. (2011). The cytochrome bd respiratory oxygen reductases. *Biochim. Biophys. Acta BBA-Bioenerg.* 1807, 1398–1413. doi: 10.1016/j.bbabio.2011.06.016

Bouhenni, R., Gehrke, A., and Saffarini, D. (2005). Identification of genes involved in cytochrome c biogenesis in *Shewanella oneidensis*, using a modified mariner transposon. *Appl. Environ. Microbiol.* 71, 4935–4937. doi: 10.1128/AEM.71.8.4935-4937.2005

Bouhenni, R. A., Vora, G. J., Biffinger, J. C., Shirodkar, S., Brockman, K., Ray, R., et al. (2010). The role of *Shewanella oneidensis* MR-1 outer surface structures in extracellular electron transfer. *Electroanal. Int. J. Devoted Fundam. Pract. Asp. Electroanal.* 22, 856–864. doi: 10.1002/elan.200880006

Bretschger, O., Cheung, A. C., Mansfeld, F., and Nealson, K. H. (2010). Comparative microbial fuel cell evaluations of Shewanella spp. *Electroanal. Int. J. Devoted Fundam. Pract. Asp. Electroanal.* 22, 883–894. doi: 10.1002/elan.200800016

Brockman, K. L., Shirodkar, S., Croft, T. J., Banerjee, R., and Saffarini, D. A. (2020). Regulation and maturation of the *Shewanella oneidensis* Sulfite reductase SirA. *Sci. Rep.* 10, 1–12. doi: 10.1038/s41598-020-57587-6

Buschmann, S., Warkentin, E., Xie, H., Langer, J. D., Ermler, U., and Michel, H. (2010). The structure of cbb3 cytochrome oxidase provides insights into proton pumping. *Science* 329, 327–330. doi: 10.1126/science.1187303

Charania, M. A., Brockman, K. L., Zhang, Y., Banerjee, A., Pinchuk, G. E., Fredrickson, J. K., et al. (2009). Involvement of a membrane-bound class III adenylate cyclase in regulation of anaerobic respiration in *Shewanella oneidensis* MR-1. *J. Bacteriol.* 191, 4298–4306. doi: 10.1128/JB.01829-08

Dehio, C., and Meyer, M. (1997). Maintenance of broad-host-range incompatibility group P and group Q plasmids and transposition of Tn5 in Bartonella henselae following conjugal plasmid transfer from *Escherichia coli*. *J. Bacteriol.* 179, 538–540. doi: 10.1128/jb.179.2.538-540.1997

Fredrickson, J. K., Romine, M. F., Beliaev, A. S., Auchtung, J. M., Driscoll, M. E., Gardner, T. S., et al. (2008). Towards environmental systems biology of Shewanella. *Nat. Rev. Microbiol.* 6, 592–603. doi: 10.1038/nrmicro1947

Gao, H., Barua, S., Liang, Y., Wu, L., Dong, Y., Reed, S., et al. (2010). Impacts of *Shewanella oneidensis* c-type cytochromes on aerobic and anaerobic respiration. *Microb. Biotechnol.* 3, 455–466. doi: 10.1111/j.1751-7915.2010.00181.x

Gao, H., Yang, Z. K., Barua, S., Reed, S. B., Romine, M. F., Nealson, K. H., et al. (2009). Reduction of nitrate in *Shewanella oneidensis* depends on atypical NAP and NRF systems with NapB as a preferred electron transport protein from CymA to NapA. *ISME J.* 3, 966–976. doi: 10.1038/ismej.2009.40

García-Horsman, J. A., Barquera, B., Rumbley, J., Ma, J., and Gennis, R. B. (1994). The superfamily of heme-copper respiratory oxidases. *J. Bacteriol.* 176:5587. doi: 10.1128/jb.176.18.5587-5600.1994

Gralnick, J. A., Brown, C. T., and Newman, D. K. (2005). Anaerobic regulation by an atypical arc system in *Shewanella oneidensis*. *Mol. Microbiol.* 56, 1347–1357. doi: 10.1111/j.1365-2958.2005.04628.x

Guest, J. R. (1992). Oxygen-regulated gene expression in *Escherichia coli*. *J. Gen. Microbiol.* 138, 2253–2263. doi: 10.1099/00221287-138-11-2253

Kasai, T., Kouzuma, A., and Watanabe, K. (2017). CRP regulates D-lactate oxidation in *Shewanella oneidensis* MR-1. *Front. Microbiol.* 8:869. doi: 10.3389/fmicb.2017.00869

Kasai, T., Kouzuma, A., and Watanabe, K. (2018). CpdA is involved in amino acid metabolism in *Shewanella oneidensis* MR-1. *Biosci. Biotechnol. Biochem.* 82, 166–172. doi: 10.1080/09168451.2017.1413326

Kawakami, T., Kuroki, M., Ishii, M., Igarashi, Y., and Arai, H. (2010). Differential expression of multiple terminal oxidases for aerobic respiration in *Pseudomonas aeruginosa*. *Environ. Microbiol.* 12, 1399–1412. doi: 10.1111/j.1462-2920.2009.02109.x

Kouzuma, A., Hashimoto, K., and Watanabe, K. (2012). Influences of aerobic respiration on current generation by *Shewanella oneidensis* MR-1 in single-chamber microbial fuel cells. *Biosci. Biotechnol. Biochem.* 76, 270–275. doi: 10.1271/bbb.110633

Le Laz, S., Kpebe, A., Bauzan, M., Lignon, S., Rousset, M., and Brugna, M. (2014). A biochemical approach to study the role of the terminal oxidases in aerobic respiration in *Shewanella oneidensis* MR-1. *PLoS One* 9:e86343. doi: 10.1371/journal.pone.0086343

Le Laz, S., Kpebe, A., Bauzan, M., Lignon, S., Rousset, M., and Brugna, M. (2016). Expression of terminal oxidases under nutrient-starved conditions in *Shewanella oneidensis*: detection of the A-type cytochrome c oxidase. *Sci. Rep.* 6:19726. doi: 10.1038/srep19726

Ludwig, B. (1987). Cytochrome c oxidase in prokaryotes. *FEMS Microbiol. Rev.* 3, 41–56. doi: 10.1111/j.1574-6968.1987.tb02451.x

Matange, N. (2015). Revisiting bacterial cyclic nucleotide phosphodiesterases: cyclic AMP hydrolysis and beyond. *FEMS Microbiol. Lett.* 362:fnv183. doi: 10.1093/femsle/fnv183

Miller, J. (1972). "Assay of β-galactosidase," in *Experiments in Molecular Genetics* Cold Spring Harbor, NY, 352–355.

Osamura, T., Kawakami, T., Kido, R., Ishii, M., and Arai, H. (2017). Specific expression and function of the A-type cytochrome c oxidase under starvation conditions in *Pseudomonas aeruginosa*. *PLoS One* 12:e0177957. doi: 10.1371/journal.pone.0177957

Pitcher, R. S., and Watmough, N. J. (2004). The bacterial cytochrome cbb3 oxidases. *Biochim. Biophys. Acta BBA-Bioenerg.* 1655, 388–399. doi: 10.1016/j.bbabio.2003.09.017

Saffarini, D. A., Schultz, R., and Beliaev, A. (2003). Involvement of cyclic AMP (cAMP) and cAMP receptor protein in anaerobic respiration of *Shewanella oneidensis*. *J. Bacteriol.* 185:3668. doi: 10.1128/JB.185.12.3668-3671.2003

Shirodkar, S., Reed, S., Romine, M., and Saffarini, D. (2011). The octahaem SirA catalyses dissimilatory sulfite reduction in *Shewanella oneidensis* MR-1. *Environ. Microbiol.* 13, 108–115. doi: 10.1111/j.1462-2920.2010.02313.x

Shroff, N. P., Charania, M. A., and Saffarini, D. A. (2010). ArcB1, a homolog of *Escherichia coli* ArcB, regulates dimethyl sulfoxide reduction in *Shewanella oneidensis* MR-1. *J. Bacteriol.* 192, 3227–3230. doi: 10.1128/JB.01695-09

Sousa, F. L., Alves, R. J., Ribeiro, M. A., Pereira-Leal, J. B., Teixeira, M., and Pereira, M. M. (2012). The superfamily of heme–copper oxygen reductases: types and evolutionary considerations. *Biochim. Biophys. Acta BBA-Bioenerg.* 1817, 629–637. doi: 10.1016/j.bbabio.2011.09.020

Tang, Y. J., Meadows, A. L., and Keasling, J. D. (2007). A kinetic model describing *Shewanella oneidensis* MR-1 growth, substrate consumption, and product secretion. *Biotechnol. Bioeng.* 96, 125–133. doi: 10.1002/bit.21101

Yin, J., Meng, Q., Fu, H., and Gao, H. (2016). Reduced expression of cytochrome oxidases largely explains cAMP inhibition of aerobic growth in *Shewanella oneidensis*. *Sci. Rep.* 6:24449. doi: 10.1038/srep24449

Zhou, G., Yin, J., Chen, H., Hua, Y., Sun, L., and Gao, H. (2013). Combined effect of loss of the caa3 oxidase and Crp regulation drives Shewanella to thrive in redox-stratified environments. *ISME J.* 7, 1752–1763. doi: 10.1038/ismej.2013.62

Conflict of Interest: The authors declare that the research was conducted in the absence of any commercial or financial relationships that could be construed as a potential conflict of interest.

Publisher's Note: All claims expressed in this article are solely those of the authors and do not necessarily represent those of their affiliated organizations, or those of the publisher, the editors and the reviewers. Any product that may be evaluated in this article, or claim that may be made by its manufacturer, is not guaranteed or endorsed by the publisher.

frontiers in Microbiology

REVIEW
published: 13 September 2021
doi: 10.3389/fmicb.2021.703525

Energy Conservation in Fermentations of Anaerobic Bacteria

*Wolfgang Buckel**

Laboratorium für Mikrobiologie, Fachbereich Biologie, Philipps-Universität Marburg, Marburg, Germany

Anaerobic bacteria ferment carbohydrates and amino acids to obtain energy for growth. Due to the absence of oxygen and other inorganic electron acceptors, the substrate of a fermentation has to serve as electron donor as well as acceptor, which results in low free energies as compared to that of aerobic oxidations. Until about 10 years ago, anaerobes were thought to exclusively use substrate level phosphorylation (SLP), by which only part of the available energy could be conserved. Therefore, anaerobes were regarded as unproductive and inefficient energy conservers. The discovery of electrochemical Na^+ gradients generated by biotin-dependent decarboxylations or by reduction of NAD^+ with ferredoxin changed this view. Reduced ferredoxin is provided by oxidative decarboxylation of 2-oxoacids and the recently discovered flavin based electron bifurcation (FBEB). In this review, the two different fermentation pathways of glutamate to ammonia, CO_2, acetate, butyrate and H_2 via 3-methylaspartate or via 2-hydroxyglutarate by members of the *Firmicutes* are discussed as prototypical examples in which all processes characteristic for fermentations occur. Though the fermentations proceed on two entirely different pathways, the maximum theoretical amount of ATP is conserved in each pathway. The occurrence of the 3-methylaspartate pathway in clostridia from soil and the 2-hydroxyglutarate pathway in the human microbiome of the large intestine is traced back to the oxygen-sensitivity of the radical enzymes. The coenzyme B_{12}-dependent glutamate mutase in the 3-methylaspartate pathway tolerates oxygen, whereas 2-hydroxyglutaryl-CoA dehydratase is extremely oxygen-sensitive and can only survive in the gut, where the combustion of butyrate produced by the microbiome consumes the oxygen and provides a strict anaerobic environment. Examples of coenzyme B_{12}-dependent eliminases are given, which in the gut are replaced by simpler extremely oxygen sensitive glycyl radical enzymes.

Keywords: $\Delta\mu Na^+$, decarboxylation, ferredoxin, Rnf, electron bifurcation, coenzyme B_{12}, glycyl radical enzymes, oxygen sensitivity

OPEN ACCESS

Edited by:
Wolfgang Nitschke, Centre National de la Recherche Scientifique (CNRS), France

Reviewed by:
William Martin, University of Düsseldorf Medical School, Germany
Matthias Boll, University of Freiburg, Germany

***Correspondence:**
Wolfgang Buckel
buckel@staff.uni-marburg.de

Specialty section:
This article was submitted to Microbial Physiology and Metabolism, a section of the journal Frontiers in Microbiology

Received: *30 April 2021*
Accepted: *30 July 2021*
Published: *13 September 2021*

Citation:
Buckel W (2021) Energy Conservation in Fermentations of Anaerobic Bacteria. Front. Microbiol. 12:703525. doi: 10.3389/fmicb.2021.703525

INTRODUCTION

Fermentation is a chemical reaction catalyzed by living cells with two different meanings. In biotechnology the bacterial production of a certain compound mainly from glucose under aerobic conditions is called fermentation, e.g., L-lysine fermentation. In this review, however, fermentation is defined as an anaerobic bacterial redox process of an organic substrate leading to different products, e.g., fermentation of glutamate to ammonia, CO_2, acetate, butyrate and hydrogen. Thereby glutamate is oxidized to CO_2 and acetate; the resulting reducing equivalents are used to

Abbreviations: $FAD^{\bullet-}$, FAD anionic semiquinone; $FADH^-$, FAD hydroquinone; Fd, ferredoxin; Fd^- reduced ferredoxin.

synthesize butyrate and H_2 to establish a balanced chemical equation. Inorganic electron acceptors such as nitrate, sulfate or Fe(III) are not involved; otherwise the process would be called respiration rather than fermentation. Thermodynamically, a fermentation is an exergonic process with a free energy of $\Delta G^{\circ\prime} < -20$ kJ/mol. ΔG° is defined for 1 M substrates and products, 10^5 Pa for gasses and at a temperature of 298 K. Under biological conditions, in dilute aqueous solutions (55.5 M H_2O) and at pH 7.0, $\Delta G^{\circ\prime}$ is used. In this review, the $\Delta G^{\circ\prime}$ values have been calculated from the data given by Thauer et al. (1977).

A well-established fermentation is the conversion of glucose by lactic acid bacteria to lactate at pH 7.0 with $\Delta G^{\circ\prime} = -185$ kJ/mol (eq. 1). In contrast, the aerobic oxidation of glucose in mammalian cells with O_2 to CO_2 and H_2O yields $\Delta G^{\circ\prime} = -2{,}872$ kJ/mol (eq. 2).

$$C_6H_{12}O_6 \rightarrow 2\,CH_3{-}CHOH{-}COO^- + 2\,H^+;$$

$$\Delta G^{\circ\prime} = -185\,kJ/mol \quad (1)$$

$$C_6H_{12}O_6 + 6\,O_2 \rightarrow 6\,CO_2 + 6\,H_2O;$$

$$\Delta G^{\circ\prime} = -2{,}872\,kJ/mol \quad (2)$$

Glucose oxidation via glycolysis, pyruvate dehydrogenase, Krebs' (citric acid) cycle and mitochondrial respiratory chain are very well analyzed processes leading to about 38 mol ATP/mol glucose; (−2,872 kJ/mol glucose): (38 mol ATP/mol glucose) = −76 kJ/mol ATP. Hence in a catabolic reaction with one or more irreversible steps, a free energy change of −76 kJ is required to generate 1 mol ATP, whereas under equilibrium conditions only about −50 kJ are necessary (Thauer et al., 1977; Buckel and Thauer, 2013). If this value is applied to the fermentation of glucose to 2 lactate, the ATP yield should be (−185 kJ/mol): (−76 kJ/mol ATP) = 2.4 ATP, which is 20% higher than 2.0 ATP via substrate level phosphorylation in glycolysis. This examples tells why energy conservation in fermentative anaerobic bacteria has been considered as inefficient. The discovery that anaerobic bacteria are able use in addition electrochemical ion gradients for ATP synthesis, catalyzed by ubiquitous H^+ or Na^+ dependent F_1F_0-ATP-synthases (von Ballmoos et al., 2009), changed this view. Work by Konings and colleagues showed that in the glucose fermenting *Streptococcus cremoris*, the export of a formed lactic acid molecule is accompanied by a proton, which establishes an electrochemical proton gradient (Otto et al., 1980). Since 2 lactic acids are produced from glucose, two additional protons are exported which can give rise to 0.5 ATP catalyzed by ATP synthase. Thus the involvement of electrochemical ion gradients allows bacteria to use energy increments that are smaller than that of 1 ATP, which makes anaerobes even more efficient than aerobes. Therefore, the amount of energy to synthesize 1 ATP in anaerobes is now considered as about −66 kJ rather than −76 kJ in aerobes; see section "Fermentation of Glutamate: 2-Hydroxyglutarate or 3-Methylaspartate Pathway?"

In this review, I will show that also anaerobes have enzymes which are able to generate a Na^+/H^+ motive force, the biotin-containing decarboxylases (see section "Biotin-Containing Decarboxylases as Sodium Ion Pumps") and the NAD:ferredoxin oxidoreductase (Rnf, see section "The Na+/H+ Pump Ferredoxin:NAD Oxidoreductase Also Called Rnf"). Sections "Flavin Based Electron Bifurcation" and "On the Mechanism of Electron Bifurcation Catalyzed by EtfAB-Bcd" will give an introduction to flavin based electron bifurcation, by which "energy rich" reduced ferredoxin and flavodoxin are obtained. In section "Fermentation of Glutamate: 2-Hydroxyglutarate or 3-Methylaspartate Pathway?" the 2-hydroxyglutarate and the 3-methylaspartate pathway of the fermentation of glutamate are introduced, which apply the biotin-containing decarboxylases and Rnf together with substrate level phosphorylation (SLP) to obtain the maximum theoretical yield of ATP. Section "Oxygen-Tolerant and -Intolerant Radical Enzymes" tackles the question why nature evolved two different pathways of glutamate fermentation. Finally, section "Butyrate Provides Anaerobiosis in the Gut" shows how butyrate converts the human gut to an extremely oxygen-free environment and an ideal environment for strict anaerobic bacteria.

BIOTIN-CONTAINING DECARBOXYLASES AS SODIUM ION PUMPS

Concomitant with the discovery of Konings, bacterial Na^+ pumps were detected and isolated, driven by decarboxylation (Buckel, 2001a). The first decarboxylase of this type was detected by Dimroth (1980) in *Klebsiella pneumoniae* and characterized in the following years as biotin containing integral membrane enzyme catalyzing the decarboxylation of oxaloacetate to pyruvate, $\Delta G^{\circ\prime} \approx -30$ kJ/mol coupled to the translocation of 2 Na^+. This breakthrough was followed by methylmalonyl-CoA decarboxylase from *Veillonella aerogenes* (Hilpert and Dimroth, 1982) and glutaconyl-CoA decarboxylases from *Acidaminococcus fermentans, Peptostreptococcus asaccharolyticus* (formerly called *Peptococcus aerogenes;* Ezaki et al., 1983) and *Clostridium symbiosum* (Buckel and Semmler, 1982, 1983). These enzymes share a common two step mechanism: the carboxyl group of the substrate is transferred to enzyme bound biotin. Addition of a proton to the carbonyl group of the formed N-carboxybiotin causes decarboxylation, which drives the translocation of Na^+ ions from the cytoplasm through the membrane to the outside of the bacterium. These biotin containing decarboxylases are composed of 3–5 subunits. The largest and hydrophilic α-subunit catalyzes the carboxy transfer from substrate to biotin and the extremely hydrophobic β-subunit is responsible for the decarboxylation of carboxybiotin and Na^+ transport. Biotin is covalently attached to a conserved lysine residue of the γ-subunit and the small δ-subunit connects the α-subunit in the cytoplasm with the β-subunit in the membrane (Vitt et al., 2020). Variations are observed with the γ-subunit. In oxaloacetate decarboxylase from *K. aerogenes*, a small domain

of the α-subunit serves as γ-subunit (Schwarz et al., 1988; Xu et al., 2020), whereas glutaconyl-CoA decarboxylase from *C. symbiosum* contains two slightly different γ-subunits (Kress et al., 2009). The amount of Na^+ ions transported by these pumps could be determined for oxaloacetate decarboxylase from *K. pneumoniae* as up to 2 Na^+ per decarboxylation (Dimroth and Thomer, 1993). This is supported by the recent cryo-EM structure (4.5 Å resolution) of the trimeric βγ-subunit complex of oxaloacetate decarboxylase from *Salmonella typhimurium*, where two Na^+ binding sites in one β-subunit were detected. Unfortunately, the coupling between decarboxylation of carboxybiotin and Na^+-transport could not be elucidated (Xu et al., 2020).

Oxaloacetate decarboxylase from *K. pneumoniae* is involved in the fermentation of citrate to 2 acetates, 1.2 CO_2 and 0.5 formate. The pathway involves citrate cleavage to acetate and oxaloacetate, decarboxylation of the latter to CO_2, pyruvate and $\Delta\mu Na^+$, cleavage of pyruvate with CoA to acetyl-CoA and formate, substrate level phosphorylation (SLP) with acetyl-CoA to acetate, CoA and ATP. Generation of $\Delta\mu Na^+$ is used for citrate transport and for driving the endergonic reduction of NAD^+ for anabolic purposes by formate via ubiquinol (Pfenninger-Li and Dimroth, 1992). A balanced stoichiometry of citrate fermentation would give $\Delta G^{\circ\prime} = -78.7$ kJ/mol, which is the amount of energy required for the synthesis of about 1.2 ATP (eq. 3).

$$Citrate^{3-} + H_2O \rightarrow CO_2 + formate^- + 2\ acetate^-;\ \Delta G^{\circ\prime} = -78.7\ kJ/mol \quad (3)$$

Propionigenium modestum thrives from an apparently very simple chemical reaction, the decarboxylation of succinate to propionate (eq. 4) (Hilpert et al., 1984). Propionate CoA-transferase converts succinate to succinyl-CoA, which is rearranged to (*R*)-methylmalonyl-CoA in a coenzyme B_{12}-dependent manner. Epimerization affords (*S*)-methylmalonyl-CoA, which is decarboxylated to propionyl-CoA, whereby $\Delta\mu Na^+$ is generated (Hilpert and Dimroth, 1982). At the low succinate concentrations in the Canale Grande in Venice, Italy (ca. 1 mM), from which the organism was isolated (Schink, 1982), the free energy is sufficient for about ½ ATP (eq. 4). $\Delta\mu Na^+$ directly drives the Na^+-dependent F_1F_o-ATP synthase (Laubinger and Dimroth, 1988).

$$Succinate^{2-} + H^+ \rightarrow propionate^- + CO_2;\ \Delta G^{\circ\prime} = -24.4\ kJ/mol;\ at\ 1\ mM\ concentrations\ \Delta G^{*\prime} = -43.5\ kJ/mol \quad (4)$$

THE Na^+/H^+ PUMP FERREDOXIN:NAD OXIDOREDUCTASE ALSO CALLED RNF

The genes coding for Rnf have been known from *Rhodobacter capsulatus,* where it is involved in nitrogen fixation and named Rnf (for *Rhodobacter* nitrogen fixation) (Schmehl et al., 1993). Similar genes were detected in the genome of *C. tetani*, a close relative of *C. tetanomorphum*, whose membranes catalyzed the oxidation of NADH with ferricyanide [hexacyanoferrate(III)] (Brüggemann et al., 2003; Imkamp et al., 2007). The enzyme complex in membranes from *C. tetanomorphum*, which contained the highest activity, could be solubilized with dodecylmaltoside and purified (Boiangiu et al., 2005; Jayamani, 2008). SDS-PAGE indicated that the complex was composed of six different subunits RnfCDGEAB (**Figure 1**), RnfCDGE are related to four subunits of the sodium pumping NADH:quinone oxidoreductase (Nqr) from *Vibrio cholerae* (Steuber et al., 2014a,b). The yellow-brownish native enzyme complex contained covalently bound flavin, non-covalently bound FMN, riboflavin and 23 ± 1 mol Fe per mol protein, most likely in six iron-sulfur clusters (Boiangiu et al., 2005).

The oxidation of NADH with ferricyanide catalyzed by Rnf in membrane vesicles from *C. tetanomorphum* showed no Na^+-dependence; probably the electrons did not pass through all six subunits due to a short cut. Therefore, the reaction was performed in reverse. The reduction of NAD^+ was measured in an assay, in which 1 mM Ti(III)citrate was used to keep ferredoxin in the reduced state. Controls showed that Ti(III)citrate reduced NAD^+ without ferredoxin and membranes at pH ≥ 7.0. But at pH 6.8 again no Na^+-dependence could be observed (Imkamp et al., 2007; Jayamani, 2008). The first Na^+-transport with an Rnf was demonstrated with membrane vesicles from *Acetobacterium woodii*, NAD^+, Ti(III)citrate and $^{22}Na^+$ by Biegel and Müller (2010). The electrogenic transport was stimulated by valinomycin in the presence of K^+ and inhibited by 100 μM Na^+-ionophore N,N,N',N'-tetracyclohexyl-1,2-phenylendioxydiacetamide (ETH 2120). Later Ti(III)citrate was replaced by purified carbon monoxide dehydrogenase/acetyl-CoA synthase and CO as reductant for ferredoxin, which resulted in much more reliable dependencies on Na^+ (Hess et al., 2013). In a similar manner reduced ferredoxin and flavodoxin quinol were generated with the electron bifurcating electron transfer flavoprotein (EtfAB) and butyryl-CoA dehydrogenase (Bcd) both from *A. fermentans* (see also next chapter, eq. 5). With membranes from *A. fermentans* it was shown that Rnf activity was Na^+-dependent with apparent K_m = 120 ± 20 μM Na^+ and K_m = 280 ± 50 μM Li^+ at pH 6.8; in addition, K_m = 2.0 ± 0.4 μM flavodoxin and 1.4 ± 0.1 μM ferredoxin were measured (Chowdhury et al., 2016). The values for Rnf from *A. woodii* were: K_m = 201 ± 30 μM Na^+ at pH 6 and K_m = 155 ± 39 μM Na^+ at pH 7.7 (Hess et al., 2013). Surprisingly, the K_m values for Na^+ and Li^+ are much lower than those of the biotin-containing Na^+ pumps glutaconyl-CoA decarboxylase from A. *fermentans* (Buckel and Semmler, 1982) or oxaloacetate decarboxylase from *K. pneumoniae* (Dimroth and Thomer, 1986), which exhibit apparent K_m values of 1.0–1.5 mM Na^+ and 25–100 mM Li^+. Recently a survey showed that not all anaerobic bacteria contain Rnfs and not all Rnfs are Na^+-dependent. Thus the Rnf activity is absent in *R. capsulatus* and *Escherichia coli*, but present also in *Bacteroides fragilis*, *Clostridium ljungdahlii*, *V. cholerae,* and *Clostridium kluyveri.* Besides *C. tetanomorphum*, *A. fermentans,* and *A. woodii*, a

Na^+-dependence could be only detected in Rnf from *B. fragilis* (Hess et al., 2016).

FLAVIN BASED ELECTRON BIFURCATION

Ferredoxin-dependent electron bifurcation represents an important additional process to generate the energy rich molecule. Only a few enzymes, such as pyruvate ferredoxin: oxidoreductases (PFOR), reduce ferredoxin, the substrate of Rnf. A search for a reductant other than PFOR, took the butyryl-CoA dehydrogenases (Bcd) into consideration, because the difference between the reduction potentials of NAD/NADH, E_0' = −320 mV, and crotonyl-CoA/butyryl-CoA, E_0' = −10 mV, amounts to +310 mV, equal to $\Delta G^{\circ\prime} = -n \times F \times \Delta E_o' = -2 \times 96.5 \times 0.310$ Volt = −59.8 kJ mol^{-1}. Probably Bcd also reduces ferredoxin or pumps Na^+ driven by this large ΔG°'. The hypothesis of a membrane bound butyryl-CoA dehydrogenase (Bcd) could be refuted by the already known isolation of a soluble green homotetrameric Bcd from *A. fermentans* which could be separated from the yellow heterodimeric electron transferring flavoprotein (EtfAB) (Buckel, 1990). A very similar green soluble Bcd has been known from *Megasphaera elsdenii* (formerly called *Peptostreptococcus elsdenii*) (Engel and Massey, 1971), which like *A. fermentans* belongs to the *Negativicutes*, a class with a Gram-negative cell wall of the, predominantly, Gram-positive phylum *Firmicutes* (Latin: cutis firma = strong outer skin) (Marchandin et al., 2010). In contrast, butyryl-CoA dehydrogenase from the Gram-positive *C. tetanomorphum* forms a tight complex with the heterodimeric EtfAB (EtfAB-Bcd). But immunogold labeling and electron microscopy clearly showed that this EtfAB-Bcd complex was also not associated with the membrane (Herrmann, 2008). Nevertheless, a hypothesis arose from these negative results that the reduction of crotonyl-CoA with NADH catalyzed by Bcd from *C. tetanomorphum* was somehow involved in the reduction of ferredoxin (E_o' = −420 mV). Furthermore, since 1969 it was known that cell extracts of *Clostridium kluyveri* catalyzed an acetyl-CoA dependent reduction of ferredoxin with NADH (Thauer et al., 1969). Since the cell extract contained all enzymes for the synthesis of butyrate (Seedorf et al., 2008) as did *C. tetanomorphum* cells, it was ferredoxin that indeed should be reduced by NADH. Similar to complex III of the mitochondrial respiratory chain, it was postulated that NADH reduced EtfAB, which bifurcated one electron exergonically to δ-FAD of Bcd and the other endergonically to ferredoxin (eq. 5) (Herrmann et al., 2008). To reduce crotonyl-CoA with two electrons, repetition of the reaction is required:

$$2\,NADH + Crotonyl - CoA + 2\,Fd \rightarrow 2\,NAD^+ + Butyryl\text{-}CoA$$

$$+2Fd^-;\ \Delta E_o' = +210\,mV;\ \Delta G^{\circ\prime} = -40.5\,kJ/mol \quad (5)$$

This hypothesis was verified first with the purified Etf-Bcd complex from *C. kluyveri* (Li et al., 2008). The catalytic amounts of purified ferredoxin from *Clostridium pasteurianum* were regenerated with purified [FeFe]hydrogenase also from *C. pasteurianum*. If one of the components of this assay (NADH, crotonyl-CoA, Fd, hydrogenase or EtfAB-Bcd) was omitted, no reaction could be observed. Hence the electron bifurcation system is tightly coupled. The purified Etf-Bcd complex from *C. tetanomorphum* catalyzed exactly the same reaction as in eq. 5, as did the combination of Bcd and EtfAB from *A. fermentans* or *M. elsdenii* (Chowdhury et al., 2014, 2015).

ON THE MECHANISM OF ELECTRON BIFURCATION CATALYZED BY EtfAB-Bcd

To study the mechanism of electron bifurcation, EtfAB-Bcd was chosen, because it contains no iron-sulfur cluster and in the resting state, it is state stable under air; for other bifurcating systems see: Buckel and Thauer (2018a,b) and Kayastha et al. (2021). EtfAB-Bcd harbors three differently bound FAD molecules, α- and β-FAD in EtfAB, and δ-FAD, one in each subunit of the tetrameric Bcd (**Figure 1**). As source for EtfABs, *A. fermentans* (Chowdhury et al., 2014) and *M. elsdenii* (Chowdhury et al., 2015; Vigil et al., 2021) are the most suitable organisms, because their EtfABs form no tight complexes with their Bcds and can be studied separately. The crystal structure EtfAB from *A. fermentans* (*Af*-EtfAB) revealed its composition of 3 domains, similar to those of Etfs involved in fatty acid and anaerobic toluene oxidations (**Figure 2**, Bifurcation-like state) (Chowdhury et al., 2014; Vogt et al., 2019). Domains I and II form subunit A and domain III subunit B. α-FAD is located in domain II (subunit A) with its isoalloxazine ring at the interface to domain III (subunit B). β-FAD sits on domain III with its isoalloxazine ring at the interface between domains III and I. β-FAD is only present in bifurcating Etfs, whereas in non-bifurcating Etfs, e.g., those acting as electron acceptors of acyl-CoA dehydrogenases, AMP alone occupies the place of the AMP part of β-FAD; the place for the isoalloxazine part is empty (Roberts et al., 1996). In *Af*-EtfAB, the distance between α- and β-FAD is 18 Å; the possible rotation of α-FAD on the flexible domain II toward β-FAD by about 10° shortens the distance between the two FADs to 14 Å, the longest distance of fast electron tunneling (Moser et al., 1992). NADH is located close to β-FAD. Since the already known structure of Bcd from *M. elsdenii* did not tell anything about the interaction with Etf (Djordjevic et al., 1995), the structure of the tight EtfAB-Bcd complex from *Clostridium difficile* was solved (**Figure 2**, Dehydrogenase state) (Demmer et al., 2017). The structure revealed the homotetrameric Bcd with one EtfAB at each subunit, $(EtfAB)_4(Bcd)_4$. Furthermore, α-FAD on the flexible domain II has rotated by about 80° in the opposite direction toward δ-FAD of Bcd, until 8 Å distance. Thus the two structures represent two states of the bifurcating system. The structure of EtfAB alone is close to the bifurcating state with a distance between α-FAD and β-FAD of 18 Å. In complex with Bcd, α-FAD swings into the dehydratase D-state, which brings it 34 Å apart from β-FAD (**Figure 2**).

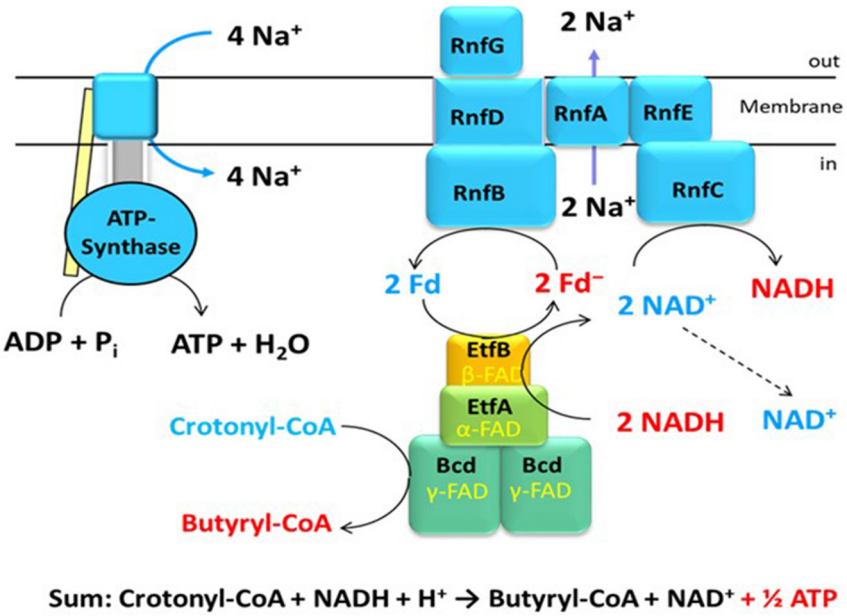

FIGURE 1 | An example of energy conservation in butyrate producing anaerobic bacteria via the generation of an ion motif force. The bifurcating EtfAB-Bcd complex reduces 2 Fd with NADH driven by the exergonic reduction of crotonyl-CoA to butyryl-CoA with a second NADH. The Rnf complex in the membrane produces 2 $\Delta\mu Na^+$ from the exergonic reduction of NAD^+ by 2 Fd^-. The ATPase generates 1 ATP from 4 $\Delta\mu Na^+$.

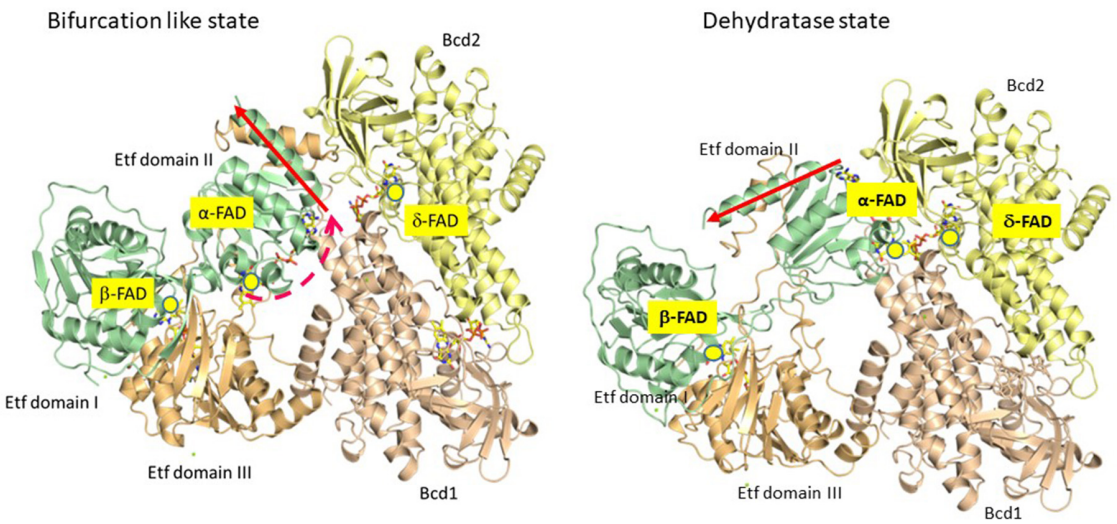

FIGURE 2 | Partial crystal structures of the recombinant Etf-Bcd complex from *C. difficile* produced in *E. coli;* EtfAB and 2 subunits of the tetrameric Bcd are displayed. The dehydratase state shows the structure as solved. In the bifurcation state domain II of Etf rotated CW by 80° as found in Etf from *A. fermentans* (see red arrow)*;* Etf, domains I + II (subunit A) in green, domain III (subunit B) in light brown, Bcd1 in yellow and Bcd2 in pinkish-brown. In the dehydratase state, α-FAD and δ-FAD are located close together (8 Å distance), ready for ET. In the bifurcation-like state, α-FAD and β-FAD are 18 Å apart; further rotation by 10° CW would bring them closer together by 4 Å, ready for electron bifurcation (taken from Buckel and Thauer, 2018a).

Potentiometric titrations with dithionite under anaerobic conditions followed by UV/vis spectroscopy revealed the reduction potentials E_0' for EtfAB, α-FAD/α-$FAD^{\bullet-}$ = +134 mV, α-$FAD^{\bullet-}$/α-$FADH^-$ = −36 mV, β-FAD/β-$FADH^{\bullet-}$ = −271 mV; for Bcd, δ-FAD/δ-$FAD^{\bullet-}$ = −42 mV, δ-FAD^-/δ-$FADH^-$ = −64 mV (**Figure 3**; Sucharitakul et al., 2021b). The one-electron reduction potentials of β-FAD could not be measured by the applied method, because the half-life of the semiquinone is expected to be extremely short, $T_{1/2}$ ca. 10 ps (Lubner et al., 2017). In analogy to the long-known Q-cycle in the mitochondrial complex III, a reactive β-$FAD^{\bullet-}$ with an extremely low stability constant (log K_s << 0) is necessary for

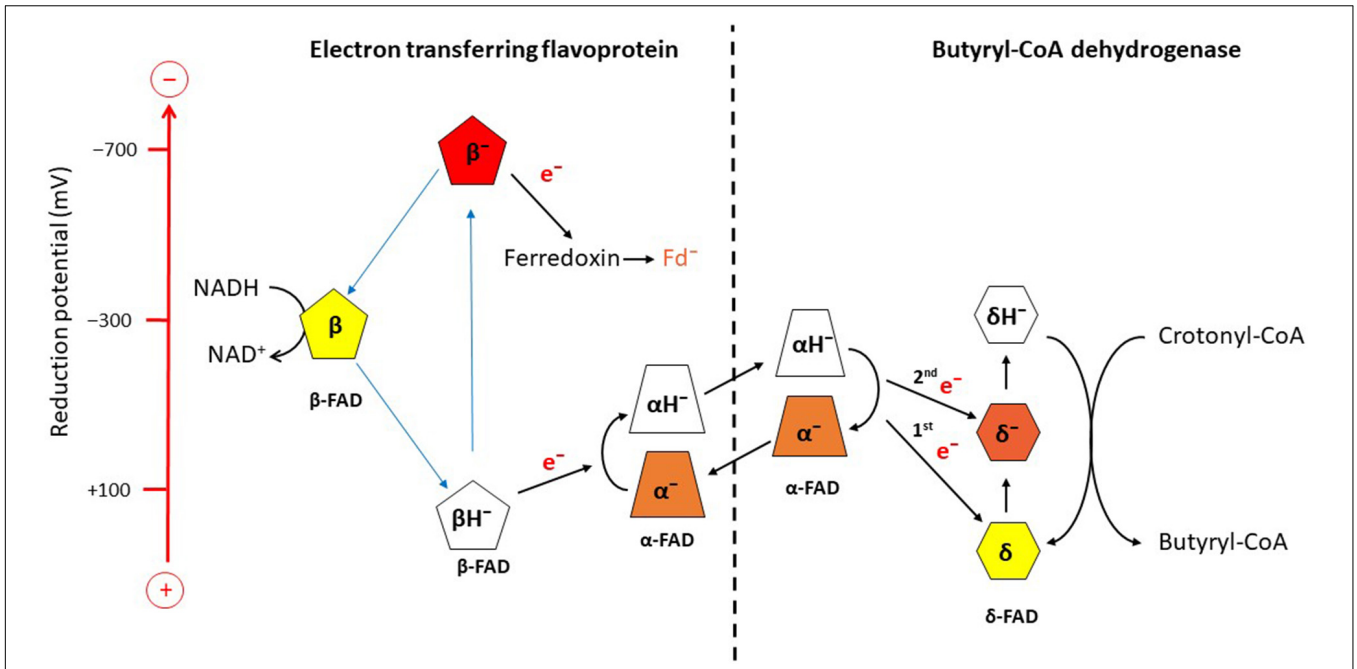

FIGURE 3 | Scheme of electron bifurcation in the EtfAB-Bcd complex. The different FADs are placed according to their approximate reduction potential. NADH reduces β-FAD to β-FADH$^-$, which bifurcates. One electron goes to α-FAD$^-$ and the formed semiquinone, β-FAD$^{\bullet-}$, reduces ferredoxin (Fd) to Fd$^-$. The formed hydroquinone (α-FADH$^-$) swings over to Bcd and transfers one electron to δ-FAD. Note the decrase of the reduction potential of α-FAD$^{\bullet-}$ due to the change in location from Etf to Bcd. Repetition of this process yields δ-FADH$^-$, which reduces crotonyl-CoA to butyryl-CoA. The FAD semiquinones are red, the quinones yellow and the hydroquinones colorless (Sucharitakul et al., 2021a,b).

electron bifurcation (eq. 6) (Bergdoll et al., 2016). Therefore, the β-FAD/β-FAD$^{\bullet-}$ reduction potential must be much more negative than that of β-FAD$^{\bullet-}$/β-FADH$^-$, whereas in flavoproteins with stable semiquinones the opposite is the case (log $K_s > 0$), e.g., flavodoxin from *A. fermentans* with reduction potentials for FAD/FAD$^-$ = −60 mV are much higher than that for FAD$^-$/FADH$^-$ = −420 mV (Hans et al., 2002).

$$K_s = \frac{[\mathrm{FAD}^{\bullet-}]^2}{[\mathrm{FAD}] \times [\mathrm{FADH}^-]} \leq 10^{-14} \geq 10^{-21} \qquad (6)$$

To convert K_s to the one-electron reduction potentials of the bifurcating cofactor with a reduction potential of E_0', the relationship of eq. 7 is used. A graphical plot of E' versus log K_s gives two straight lines which cross at $E' = E_o'$ and log K_s = 0. At log $K_s > 0$, the potentials are normal and at log $K_s < 0$ the potentials are inverse or called "crossed" (Nitschke and Russell, 2012).

$$E' = \pm (2.3\, RT\, {}^1\!/_2\, F^{-1} \times \log K_s) + E_o' \qquad (7)$$

$$E' = \pm (0.0295 \times \log K_s) + E_o'; \; at\; T = 298\; K$$

Two values of K_s were determined experimentally, 10^{-14} to 10^{-15} with the cytochrome bc_1 complex III (Zhang et al., 2007) and 10^{-21} with the bifurcating archaeal enzyme NAD$^+$ ferredoxin-NADP reductase (Nfn), which reversibly bifurcates the electrons from NADPH to ferredoxin and NAD$^+$ (eq. 8) (Lubner et al., 2017).

$$2\,NADPH + NAD^+ + 2\,Fd = 2\,NADP^+ + NADH + 2\,Fd^- + H^+ \qquad (8)$$

Besides from the Archaeon *Pyrococcus furiosus* (Lubner et al., 2017), Nfn has also been characterized from the bacteria *C. kluyveri* (Wang et al., 2010), *Thermotoga maritima* (Demmer et al., 2015) and *Sporomusa ovata* (Kremp et al., 2020). The enzyme acts as transhydrogenase and in the reverse direction ensures with the "energy rich" Fd$^-$ that the NAD$^+$/NADPH ratio is kept low at E' = −380 mV and the NAD$^+$/NADH ratio high at E' = −280 mV. Hence *in vivo* NADPH is a better reductant and NAD$^+$ a better oxidant.

According to Eq. 7, the one-electron reduction potentials of β-FADH$^-$ are calculated with an assumed log K_s = −15.2 to ± 0.0295 × (−15.2) + (−0.271) = ± 0.448−0.271 = +0.177 and −0.719 Volt (**Figure 3**; Buckel and Thauer, 2018a). The electron with the higher potential goes endergonically from +177 mV to α-FAD$^-$ (−36 mV) and the lower potential electron goes exergonically from −719 mV to ferredoxin (−390 mV) sitting about 6 Å apart from β-FAD. Thus the two one-electron transfers are coupled; the first electron moves uphill only if the second electron falls downhill to ferredoxin and vice versa (**Figure 3**). Now the formed α-FADH$^-$ rotates by 90° toward Bcd and transfers one electron to δ-FAD of Bcd and the regenerated α-FAD$^-$ returns to β-FAD. Surprisingly, in the presence of

Bcd, the reduction potential of the formed α-FADH$^-$ changes to close to the two-electron reduction potential of α-FAD/α-FADH$^-$ = −228 mV, which enables much better electron transfer to the potential of δ-FAD/δ-FAD$^-$ = +162 mV. The next electron bifurcation transfers one electron via α-FADH$^-$ to δ-FAD$^-$ (−63 mV) and the formed δ-FADH$^-$ changes to the two-electron reduction potential of −100 mV, which easily reduces crotonyl-CoA to butyryl-CoA (−10 mV; **Figure 3**).

Probably the reader wonders why during electron bifurcation, α-FAD$^{\bullet-}$ rather than α-FAD acts as high potential acceptor. There are three reasons, firstly the reduction potential of α-FAD with +134 mV is too high, whereas that of α-FAD$^{\bullet-}$ is more in the right range of −36 mV. In electron bifurcation, the potential difference between β-FADH$^-$ and α-FAD$^{\bullet-}$ with + 179−(−36) = +215 mV should be similar to the negative difference between the potentials of β-FADH$^-$ and Fd with −719−(−390) = −329 mV, to ensure tight coupling. With α-FAD as acceptor, the difference of + 179−(+134) = +45 mV would be much too low. Secondly, the change of the one-electron reduction potential of α-FADH$^-$ to the two-electron reduction potential cannot occur at the state of α-FAD$^{\bullet-}$. Thirdly, as soon as EtfAB encounters NADH, either in vitro or in vivo, α-FAD is reduced to the semiquinone (Sucharitakul et al., 2021a). Finally, stopped flow measurements by Jeerus Sucharitakul directly showed that Etf with α-FADH$^-$ indeed transferred one electron to Bcd, whereas with α-FAD$^{\bullet-}$ no electron transfer was observed (Sucharitakul et al., 2021b, unpublished).

FERMENTATION OF GLUTAMATE: 2-HYDROXYGLUTARATE OR 3-METHYLASPARTATE PATHWAY?

The previous chapters described enzymatic systems which are able to establish electrochemical Na^+ or H^+ gradients for energy conservation in anaerobic bacteria. In addition, electron bifurcation as a major source of reduced ferredoxin has been presented. This chapter shows how the two pathways of glutamate fermentation apply these systems to obtain the theoretical yield of ATP/glutamate (eq. 9). −314 kJ/5 glutamate: −66 kJ/ATP = 4.8 ATP/5 glutamate; 0.96 ATP/glutamate.

$$5\ Glutamate^- + 6\ H_2O + 2\ H^+ \rightarrow 5\ NH_4^+ + 5\ CO_2 + 6\ acetate^- + 2\ butyrate^- + H_2 \quad (9)$$

(Buckel, 2001b).

In the 2-hydroxyglutarate pathway (**Figure 4**), which has been found in *A. fermentans*, *C. symbiosum*, *P. asaccharolyticus,* and *F. nucleatum* (Buckel and Barker, 1974), NAD^+ oxidizes glutamate to 2-oxoglutarate and ammonia (Hornby and Engel,

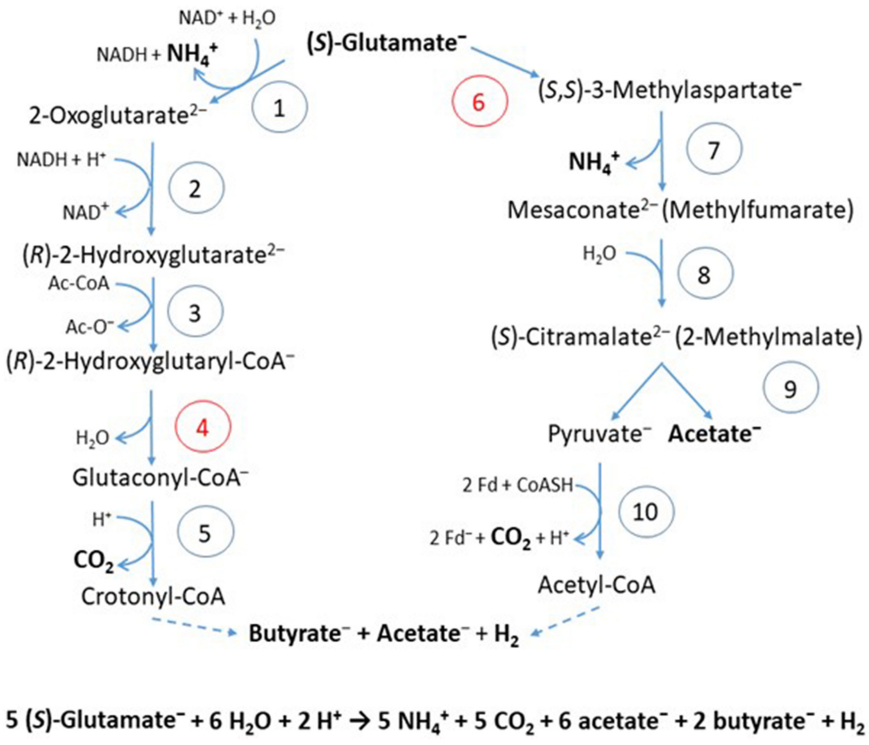

FIGURE 4 | Fermentation of glutamate via 2-hydroxyglutarate or via 3-methylaspartate. The numbers in the circles represent the corresponding enzymes; red numbers denote radical enzymes: 1, (*S*)-glutamate dehydrogenase; 2, (*R*)-2-hydroxyglutarate dehydrogenase; 3, glutaconate CoA-transferase; 4, (*R*)-2-hydroxyglutaryl-CoA dehydratase; 5, glutaconyl-CoA decarboxylase, Na^+-pumping; 6, glutamate mutase, coenzyme B_{12}-dependent; 7, methylaspartase; 8, mesaconase; 9, (*S*)-citramalate lyase; 10, pyruvate:ferredoxin oxidoreductase (PFOR). Ac-CoA, acetyl or glutaconyl-CoA; Fd, ferredoxin; Fd$^-$, reduced ferredoxin. The formation of butyrate and acetate are shown in **Figure 5**. Hydrogen, H_2 is formed from 2 H^+ and 2 Fd$^-$, catalyzed by a [FeFe]-hydrogenase.

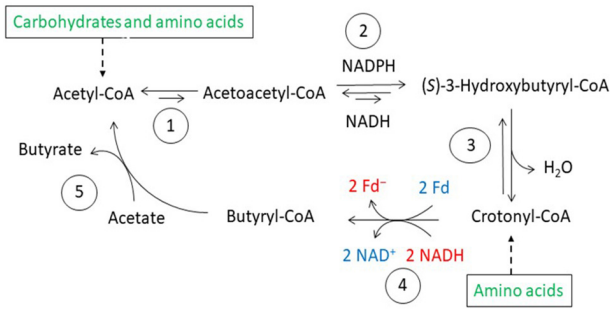

FIGURE 5 | Butyrate synthesis in anaerobic bacteria. 1, Thiolase; 2, (*S*)-3-hydroxybutyryl-CoA dehydrogenases, NADH and NADPH specific; 3, (*S*)-3-hydroxybutyryl-CoA dehydratase; 4, electron bifurcating EtfAB-butyryl-CoA dehydrogease complex; 5, butyrate CoA-transferase.

1984). The formed NADH reduces 2-oxoglutarate to (*R*)-2-hydroxyglutarate (Yu et al., 2012), which is converted to the thioester by acetyl-CoA (Buckel et al., 1981) and dehydrated to glutaconyl-CoA; for a review see Buckel (2019). Glutaconyl-CoA is the substrate of the third group of biotin-containing and Na^+-dependent decarboxylases (Buckel and Semmler, 1983). Glutaconyl-CoA is a vinylogous malonyl-CoA, in which the δ-carboxylate is equally activated as the β-carboxylates in malonyl-CoA and methylmalonyl-CoA. Decarboxylation of 5 glutaconyl-CoA yields 5 × 2 $\Delta\mu Na^+$ and 5 crotonyl-CoA (2-butenoyl-CoA), three of which disproportionate oxidatively to 6 acetyl-CoA and 3 NADH (**Figure 5**). Four NADH reduce 2 crotonyl-CoA to 2 butyryl-CoA and 4 ferredoxin (Fd) to 4 Fd^- via electron bifurcation. Two Fd^- give rise to H_2 catalyzed by a [FeFe]hydrogenase and the other two Fd^- to 2 $\Delta\mu Na^+$ + 1 NADH via Rnf. In summary, the 5 $\Delta\mu Na^+$ used for the transport of 5 glutamates into the cell have to be considered (Brüggemann et al., 2003). The net conserved energy amounts to 5 × 2 + 2 − 5 = 7 $\Delta\mu Na^+$ and 2 butyryl-CoA + 6 acetyl-CoA, 5 of which are required for the activation of 5 × 2-hydroxyglutarates. The remaining 3 thioesters are equivalent to 3 ATP by SLP (**Table 1**). If 4 $\Delta\mu Na^+$ give 1 ATP, then the yield is 7/4 + 3 = 4.75 (≈ 4.8) ATP/5 glutamate, as expected.

Several clostridia, *Clostridium tetanomorphum*, *C. cochlearium,* and *C. tetani*, use a completely different pathway of glutamate fermentation, but with the same stoichiometry as that via 2-hydroxyglutarate (eq. 9) (Buckel and Barker, 1974). This 3-methylaspartate pathway is initiated by the coenzyme B_{12}-dependent carbon skeleton rearrangement of (*S*)-glutamate to (2*S*,3*S*)-3-methylaspartate (Barker et al., 1964), from which ammonia is readily eliminated affording mesaconate (methylfumarate) (Barker et al., 1959). Addition of water yields (*S*)-citramalate (2-methylmalate) (Blair and Barker, 1966), which is cleaved to acetate and pyruvate (Buckel and Bobi, 1976). Oxidation of 5 pyruvate to 5 acetyl-CoA, 5 CO_2 and 10 Fd^- is catalyzed by pyruvate:ferredoxin oxidoreductase (PFOR) (**Figure 4**). 4 Acetyl-CoA condense to 2 acetoacetyl-CoA, which are reduced with 2 NADH to 2 (*S*)-3-hydroxybutyryl-CoA, dehydrated to 2 crotonyl-CoA and further reduced with 4 NADH to 2 butyryl-CoA and 4 reduced ferredoxin via electron bifurcation (**Figure 5**). For the reduction of 6 NAD^+ by Rnf, 12 Fd^- are consumed and give rise to 12 $\Delta\mu Na^+$. The remaining 2 Fd^- are used to produce 1 H_2. The import of 5 glutamate consumes 5 $\Delta\mu Na^+$. In summary, 3 ATP are obtained via SLP from 1 acetyl-CoA and 2 butyryl-CoA and 7/4 ATP from the remaining 12–5 = 7 $\Delta\mu Na^+$, altogether 4.75 ATP/5 glutamate, the same as in the 2-hydroxyglutarate pathway (**Table 1**).

The fermentations of glutamate via methylaspartate or 2-hydroxyglutarate lead to identical products and to identical amounts of conserved ATP. Therefore, the question arises why bacteria exclusively use one of these pathways. One would expect that bacteria prefer the 2-hydroxyglutarate pathway because the 3-methylaspartate pathway requires about 30 additional enzymes for the anaerobic biosynthesis of the coenzyme B_{12} (Moore and Warren, 2012), whereas in the 2-hydroxyglutarate pathway only the ubiquitous cofactors NAD, FAD, CoA, pyridoxal-5′-phosphate and biotin are involved. These cofactors are not pathway specific, because they are also necessary for anabolism. In absence of vitamin B_{12}, *Fusobacterium varium* uses the 2-hydroxyglutarate pathway, whereas after addition of 1 μM vitamin B_{12} or just 1 μM $CoCl_2$ to the medium, the organism ferments glutamate via 3-methylaspartate (Ramezani et al., 2011). Hence, *F. varium* is able to synthesize coenzyme B_{12} when Co^{2+} is present and the argument that the expression of 30 additional genes for B_{12} synthesis favors the 2-hydroxyglutarate pathway does not apply. Therefore, the reason for the existence of this pathway must be found somewhere else.

The organisms using the 2-hydroxyglutarate pathway, *A. fermentans, P. asaccharolyticus, C. symbiosum, F. nucleatum, and F. varium* were isolated from anaerobic niches of the human host, preferentially from the human large intestine. In contrast, the members of the 3-methylaspartate pathway *C. tetanomorphum, C. tetani, C. cochlearium, C. lentoputrescens, C. limosum, C. malenominatum* have been detected outside the gut on places like soil, where organic matter decomposes anaerobically (Buckel, 2001b). The employment of the 2-hydroxyglutarate pathway in the human gut could be due to the much lower oxygen concentration as compared to soil which encounters often exposures to air through plant roots, earthworms, moles, etc. Probably, the oxygen sensitivity of enzymes of an important pathway might be responsible for the ecology of the organism.

Both glutamate fermenting pathways contain oxygen sensitive radical enzymes. Whereas coenzyme B_{12}-dependent glutamate mutase in the 3-methylaspartate pathway is only moderately oxygen sensitive, 2-hydroxyglutaryl-CoA dehydratase in the 2-hydroxyglutarate pathway immediately becomes inactive after exposure to air. Coenzyme B_{12}-dependent mutases catalyze the reversible radical rearrangement of a methine radical to a methylene radical. The process is initiated by homolysis of the carbon-cobalt bond of coenzyme B_{12}. The formed 5′-deoxyadenosyl radical abstracts the *Si*-hydrogen atom from the methylene group at C3 of (*S*)-glutamate and after rearrangement adds it back to the formed methylene radical yielding the methyl group of (2*S*,3*S*)-3-methylaspartate.

TABLE 1 | Energy conservation in the two pathways of glutamate fermentation.

Path-way	$\Delta\mu Na^+$ consumed	$\Delta\mu Na^+$ generated	Thioester (TE) consumed	TE generated	Fd reduced to Fd^-	Fd^- oxidized to Fd	Sum (generated)
HG	5 × 1 Transport	5 × 2 by DC 2 by Rnf	5 AcCoA	6 AcCoA 2 BuCoA	4 by EB	2 by Rnf 2 by Hase	7 $\Delta\mu Na^+$ 3 TE
MA	5 × 1 Transport	6 × 2 by Rnf	4 AcCoA	5 AcCoA 2 BuCoA	10 by PFOR 4 by EB	12 by Rnf 2 by Hase	7 $\Delta\mu Na^+$ 3 TE

HG, 2-hydroxyglutarate pathway; MA, 3-methylaspartate pathway; DC, Na^+ pumping decarboxylase; AcCoA, acetyl-CoA; BuCoA, butyryl-CoA; Fd and Fd^-, oxidized and reduced ferredoxin; EB, electron bifurcation; PFOR, pyruvate ferredoxin oxidoreductase; Hase, [FeFe]hydrogenase.

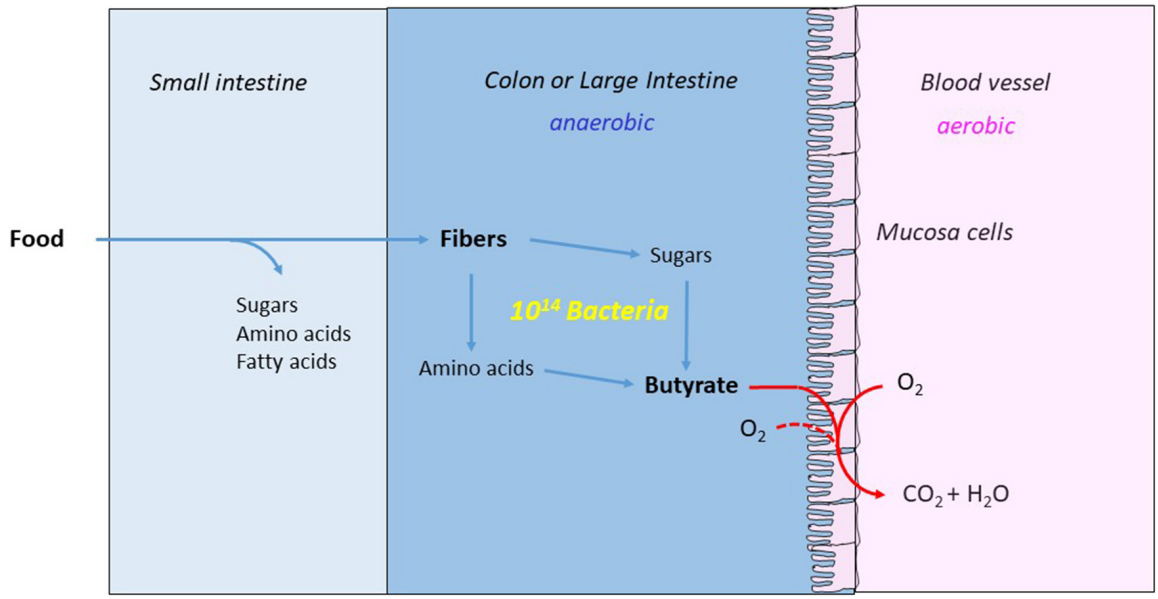

FIGURE 6 | Butyrate nourishes the mucosa cells and makes the colon anaerobic. The major part of the food is digested and absorbed in the small intestine. The remaining fibers are hydrolyzed to monosaccharides and amino acids by the anaerobic bacteria and fermented the large intestine or colon to acetate, propionate and butyrate. The mucosa cells combust the produced butyrate with oxygen from blood and colon, whereby the colon becomes strictly anaerobic.

After each turnover, the radical disappears by reformation of the carbon-cobalt bond of the coenzyme, for a review see Buckel and Golding (1996). Thus, in the presence of air, the radicals are only transiently exposed to oxygen as the coenzyme B_{12}-dependent methylmalonyl-CoA mutase in human mitochondria.

In contrast, 2-hydroxyglutaryl-CoA dehydratase acts with a completely different radical mechanism (Buckel and Keese, 1995), for a review see Buckel (2019). The enzyme system is composed of two proteins. The homodimeric activator contains one ADP in each subunit and one [4Fe-4S] cluster coordinated by four cysteines, two from each subunit, similar to the iron protein (NifH) of nitrogenase (Locher et al., 2001). The heterodimeric dehydratase holds one [4Fe-4S] cluster in each subunit. Each cluster is coordinated by three cysteines; the fourth coordination is occupied in subunit A by a sulfur atom and in subunit B by water, which can be replaced by the thioester carbonyl of the substrate. The dehydration is initiated by ATP/ADP exchange of the activator and reduction of its $[4Fe\text{-}4S]^{2+}$ cluster by reduced ferredoxin (Fd^-). Driven by ATP hydrolysis, the extra electron is transferred to or "shot into" the [4Fe-4S] cluster of subunit A and further shifted to cluster B, where 2-hydroxyglutaryl-CoA is bound. The electron in cluster B reduces the thioester carbonyl to a ketyl radical, which due to its lower basicity is replaced from the iron by the hydroxyl group at C-2, a process called ligand swapping. Aided by the iron of cluster B, the nucleophilic ketyl eliminates the hydroxyl group to form an enoxy radical. The hydroxyl group at the iron of the cluster acts as base to remove the now acidic β-proton at C-3. The resulting allylic ketyl replaces the formed water by a second ligand swapping and returns the electron via cluster B to cluster A. The formed product glutaconyl-CoA is released and cluster B is able to accept the next substrate together with the electron form cluster A. The dehydratase is able to catalyze at least 1000 turnovers before another ATP molecule has to be hydrolyzed to continue catalysis (Kim et al., 2005). Proof of this mechanism was obtained by detection of the corresponding allylic ketyl radical of (*R*)-2-hydroxyisocaproyl-CoA dehydratase from *C. difficile* (Kim et al., 2008).

It has been shown experimentally that (*R*)-2-hydroxyacyl-CoA dehydratases are indeed much more oxygen sensitive than coenzyme B_{12}-dependent carbon skeleton mutases. Whereas

2-hydroxyglutarate dehydratases had to be purified and assayed under strict exclusion of oxygen (Kim et al., 2005), glutamate mutase could be purified under air. During catalysis, however, after about 1 min a significant effect of air on the rate of 3-methylaspartate formation from glutamate was observed (Leutbecher et al., 1992). In the dehydratases, the electron never disappears during the catalytic cycle and the iron-sulfur cluster of the activator is solvent accessible, which makes it extremely oxygen sensitive. The question arises why the gut, where (*R*)-2-hydroxyacyl-CoA dehydratases are active, contains such low oxygen concentrations despite its ample supply with oxygen-rich blood (see section "Butyrate Provides Anaerobiosis in the Gut").

OXYGEN-TOLERANT AND -INTOLERANT RADICAL ENZYMES

In the previous chapters it has been shown that the 3-methylaspartate pathway tolerates oxygen because after each turnover of glutamate mutase, the cobalt-carbon bond between the 5′-deoxyadenosyl radical and cob(II)alamin is reformed. Thus, only during catalysis the radical is exposed to oxygen. In contrast, in (*R*)-2-hydroxyglutaryl-CoA dehydratase of the alternative glutamate fermenting pathway, the radical is always present and exposed to the medium. In addition, the iron-sulfur clusters of the dehydratase and its activator are very oxygen-sensitive. Most likely, this is the reason, why organisms of the 2-hydroxyglutarate pathway are only found in the gut or in strictly anaerobic marine sediments. Furthermore, B_{12}-dependent carbon skeleton mutases and eliminases as well as thiamin diphosphate dependent enzymes are substituted in the gut by glycyl radical enzymes (**Table 2**). Similar to (*R*)-2-hydroxyacyl-CoA dehydratases, glycyl radical enzymes also require specific activating enzymes. These activases belong to the large family of radical SAM enzymes, which catalyze the one electron-reduction of S-adenosylmethionine (SAM) to methionine and the 5′-deoxyadenosyl radical. This radical irreversibly abstracts one hydrogen from a conserved glycine residue of the enzyme to give a stable protein-bound radical. Upon binding of substrate, the glycyl radical abstracts the sulfhydryl hydrogen form a nearby cysteine residue, which in turn removes the hydrogen atom from the substrate. After the rearrangement, the radical returns to the glycine residue and remains stable until the next turnover, unless it is attacked by oxygen (Knappe and Sawers, 1990; Shisler and Broderick, 2014).

Many organisms including humans are able to degrade propionate via carboxylation of propionyl-CoA to (*S*)-methylmalonyl-CoA and racemization to (*R*)-methylmalonyl-CoA, which is rearranged to succinyl-CoA mediated by coenzyme B_{12}. The Krebs cycle converts succinyl-CoA to oxaloacetate, which enters gluconeogenesis or is degraded via pyruvate to acetyl-CoA. Propionibacteria use the reverse pathway to produce propionate from succinate. *Veillonella alcalescens* and *P. modestum* conserve energy with the biotin-dependent Na^+-pump (*S*)-methylmalonyl-CoA decarboxylase (Hilpert and Dimroth, 1982; Schink, 1982). In contrast, *Clostridium propionicum*, isolated from marine mud (Cardon and Barker, 1946), converts alanine, cysteine and serine via pyruvate (Hofmeister et al., 1993) to (*R*)-lactate, which is dehydrated via (*R*)-lactyl-CoA to acrylyl-CoA (Schweiger and Buckel, 1984; Hofmeister and Buckel, 1992) and reduced to propionyl-CoA (Hetzel et al., 2003). Like 2-hydroxyglutaryl-CoA dehydratase, lactyl-CoA dehydratase is an extremely oxygen sensitive radical enzyme (Parthasarathy et al., 2010). The rumen micro-organism *Megasphaera elsdenii* reduces about half of the consumed lactate in the same way as *C. propionicum*; the other half is oxidized to acetyl-CoA, from which butyrate (C2 + C2), valerate (C2 + C3) and caproate (3 × C2) are formed (Lewis and Elsden, 1955).

The pyridoxal-5′-phosphate dependent elimination of water from threonine leads to 2-oxobutyrate and ammonia (Hofmeister et al., 1993). Homocysteine, derived from methionine, suffers a similar elimination to 2-oxobutyrate, ammonia and sulfide. Some anaerobic bacteria oxidize 2-oxobutyrate with ferredoxin to propionyl-CoA catalyzed by a thiamin diphosphate (TDP)-dependent enzyme and excrete propionate. *C. propionicum* reduces 2-oxobutyrate to (*R*)-2-hydroxybutyrate and dehydrates (*R*)-2-hydroxybutyryl-CoA to crotonyl-CoA, catalyzed by (*R*)-lactyl-CoA dehydratase (Hofmeister and Buckel, 1992).

Three eliminations of water from 1,2-diols are known, each of which is catalyzed by two different enzymes, either coenzyme B_{12}-dependent or by the much more oxygen-sensitive glycyl radical enzymes (**Table 2**). The coenzyme B_{12}-dependent glycerol dehydratase catalyzes the removal of the central hydroxyl group of glycerol yielding 3-hydroxypropanal (Forage and Foster, 1982), which can be reduced to 1,3-propanediol, a building block for polyesters. The discovery of the glycyl radical dehydratase from *Clostridium butyricum* (O'Brien et al., 2004) though extremely oxygen-sensitive, paved the road to a more economic fermentation of 1,3-propanediol from glycerol, because the already established procedure with the coenzyme B_{12}-dependent enzyme required feeding with the precious vitamin B_{12}. The mechanism of coenzyme B_{12}-dependent eliminations was first studied with propane-1,2-diol dehydratase from *Aerobacter aerogenes* by Janós Rétey and Dulio Arigoni in Switzerland (Rétey et al., 1966) as well as Robert H. Abeles (Zagalak et al., 1966) in the United States. In the human gut, degradation of L-fucose (6-deoxygalactose) and L-rhamnose (6-deoxymannose) affords propane-1,2-diol, which is dehydrated to propanal, catalyzed by the glycyl radical enzyme propane-1,2-diol dehydratase (Levin and Balskus, 2018). The third pair of coenzyme B_{12} and glycyl radical enzymes catalyzing the same reaction are classes II and III of ribonucleotide reductase (Greene et al., 2020). The formation of the conserved thiyl radical in this enzyme is performed in class II by the 5′-deoxyadenosyl radical from coenzyme B_{12} and in class III by the glycyl radical. Abstraction of the 3′-hydrogen of the ribonucleotide by the thiyl radical and deprotonation of the 3′-hydroxyl group affords a nucleophilic ketyl (radical anion), which eliminates the adjacent 2′-hydroxyl group (Buckel, 2019). The reduction of the formed enoxy radical differs between the classes. In class II the reductants are two cysteine residues which form a disulfide, whereas class III uses formate for this purpose.

TABLE 2 | Pairs of oxygen-tolerant and intolerant enzymes which catalyze the same reaction or are key enzymes of alternative pathways leading to the same products.

Pathway/Enzymes	Oxygen-tolerant	Oxygen-intolerant
Glutamate fermentation	Glutamate mutase B_{12}	(*R*)-2-Hydroxyglutaryl-CoA dehydratase
Lactate, pyruvate, alanine, cysteine and serine fermentation to propionate	Methylmalonyl-CoA mutase B_{12}	(*R*)-Lactyl-CoA dehydratase
Glycerol dehydratase	B_{12}-dependent eliminase	Glycyl radical enzyme
Propane-1,2-diol dehydratase	B_{12}-dependent eliminase	Glycyl radical enzyme
Ribonucleotide reductase	Class II: B_{12}-dependent eliminase and reductase	Class III: Glycyl radical eliminase and reductase
Ethanolamine ammonia lyase	B_{12}-dependent eliminase	–
Choline-trimethylamine lyase	–	Glycyl radical enzyme
Threonine and methionine fermentation to propionate and butyrate	TDP-dependent oxidation of 2-oxobutyrate to propionyl-CoA	Dehydration of (*R*)-2-hydroxybutyryl-CoA by (*R*)-lactyl-CoA dehydratase
Oxidation of 2-oxoacids to acyl-CoA	TDP-dependent enzymes: Pyruvate ferredoxin oxidoreductase; pyruvate dehydrogenase (NAD)	Glycyl radical enzyme: pyruvate:formate lyase (PFL)
Taurine fermentation	TDP-dependent enzyme: Sulfoacetaldehyde desulfonase	Glycyl radical enzyme: Isethionate lyase

In the eliminations of ammonia from ethanolamine or trimethylamine from choline, carbon nitrogen bonds are broken. Interestingly, for the deamination of ethanolamine only a coenzyme B_{12}-dependent enzyme is known (Shibata et al., 2010), whereas the elimination of trimethylamine from choline is exclusively catalyzed by a glycyl radical enzyme (Craciun et al., 2014). Perhaps the different elimination mechanisms, but not the oxygen sensitivity, are responsible for the kind of radical enzyme applied. It has been proposed theoretically (Buckel, 1996; Feliks and Ullmann, 2012; Kovacevic et al., 2018) and demonstrated experimentally (Levin and Balskus, 2018) that in the dehydration of propane-1,2-diol catalyzed by the glycyl radical enzyme, the hydroxyl group at C2 is eliminated. Coenzyme B_{12}-dependent propane-1,2-diol dehydratase and glycerol dehydratase, however, shift the hydroxyl group at C2 to C1, forming propane-1,1-diol or 3-hydroxypropane-1,1-diol which dehydrate to the aldehydes. Because trimethylamine is a better leaving group than ammonia, chemistry might compel choline lyase to use the glycyl radical mechanism. Trimethylamine (TMA) is of medical importance, because in the liver it is oxidized to the N-oxide (TMAO), which may cause cancer and other diseases (Gatarek and Kaluzna-Czaplinska, 2021).

The oxidation of pyruvate to acetyl-CoA is a complex reaction for which nature has developed thiamin diphosphate, which causes Umpolung of the carbonyl group of the 2-oxo acid to enable decarboxylation. Most likely a concealed radical is involved in the reaction (Chen et al., 2018). The oxidant is either NAD^+ or ferredoxin. In aerobes with NAD^+ the reaction is irreversible, but reversible with ferredoxin in anaerobes (Eqs. 10, 11). Thus this reaction is an example of anaerobes being more efficient energy converters than aerobes.

$$Pyruvate^- + NAD^+ + CoASH \rightarrow Acetyl\text{-}SCoA + NADH$$

$$+CO_2;\ \Delta G^{\circ\prime} = -32\ kJ/mol \tag{10}$$

$$Pyruvate^- + 2\ Fd + CoASH = Acetyl\text{-}SCoA + 2\ Fd^- + CO_2$$

$$+H^+;\ \Delta G^{\circ\prime} = -13\ kJ/mol \tag{11}$$

Under strict anaerobic conditions, pyruvate dehydrogenase of *E. coli* (Eq. 10) is replaced by the glycyl radical enzyme, pyruvate formate lyase (PFL), which catalyzes the reversible cleavage of pyruvate to acetyl-CoA and formate (Eq. 12). The enzyme is also present in other enterobacteria and several clostridia.

$$Pyruvate^- + CoASH = Acetyl\text{-}SCoA + formate^-;$$

$$\Delta G^{\circ\prime} = -19\ kJ/mol \tag{12}$$

The degradation of taurine (2-aminoethylsulfonate) in aerobes and facultative anaerobes affords sulfoacetaldehyde by amino transfer to pyruvate. The aldehyde is converted by

the TDP-dependent sulfoacetaldehyde acetyltransferase Xsc to acetyl phosphate and sulfite (Ruff et al., 2003). Under the strict anaerobic conditions in the gut, the Bacillus *Bilophila wadsworthia* bypasses Xcs with an aldehyde reductase and the glycyl radical enzyme isethionate lyase. This enzyme catalyzes the radical diol dehydratase-like elimination of isethionate (2-sulfoethanol) yielding acetaldehyde and sulfite which is reduced to H_2S (Peck et al., 2019). AdhE catalyzes the oxidation of acetaldehyde to acetyl-CoA, which as well as acetyl phosphate yields ATP by SLP. The genes *iseG* and *iseH* coding for isethionate lyase and its activating enzyme were also detected in several well-known sulfate reducing organisms (Dawson et al., 2021). The genes from *Desulfovibrio vulgaris* str. Hildenborough were expressed in *E. coli* and the produced proteins characterized as active isethionate lyase (Xing et al., 2019; Wei and Zhang, 2021).

In this review it has become apparent that radical reactions play an important part in the metabolism of anaerobes and most likely already in prebiotic chemistry (Dragicevic et al., 2015). **Table 2** summarizes the pairs of oxygen-tolerant and intolerant enzymes which catalyze radical reactions leading to the same product or are key enzymes of alternative pathways. Whereas the oxygen-intolerant 2-hydroxyacyl-CoA dehydratases and glycyl radical enzymes have simple cofactors, the oxygen-tolerant coenzyme B_{12} and TDP-dependent enzymes use the most complex cofactors known in biochemistry (Jurgenson et al., 2009; Moore and Warren, 2012). Apparently, the oxygen-intolerant radical enzymes evolved first and prevailed under the primeval atmosphere until the oxygen concentration raised, which forced nature to develop the oxygen tolerant and much more complex cofactors coenzyme B_{12} and TDP. The oxygen-intolerant radical enzymes survived only in strictly anaerobic places such as the human gut and marine sediments. Probably, these coenzyme B_{12} and TDP dependent fermentations were not present at the origin of life, but emerged just before or during the Great Oxidation event at 2.1 billion years ago (Anbar et al., 2007).

BUTYRATE PROVIDES ANAEROBIOSIS IN THE GUT

Many obligate anaerobic bacteria in the human gut produce butyrate. The most common pathway is the condensation of two acetyl-CoA to acetoacetyl-CoA, followed by the first reduction to (*S*)-3-hydroxybutyryl-CoA, dehydration to crotonyl-CoA and the second reduction to butyryl-CoA as shown in the fermentation of glutamate via 3-methylaspartate. The first reductants are NADH or at low acetyl-CoA concentrations NADPH as found in *Clostridium kluyveri*. The stronger reductant NADPH helps to shift the unfavorable equilibrium of acetyl-CoA condensation to acetoacetyl-CoA toward (*S*)-3-hydroxybutyryl-CoA (**Figure 5**). The second reduction by NADH is coupled to the reduction of ferredoxin via electron bifurcation (Buckel and Thauer, 2013). Butyrate is released either by a CoA-transferase with acetate or by SLP via butyryl-phosphate (Louis and Flint, 2017). This pathway is used by most organisms fermenting carbohydrates, as are bacteria related to *Roseburia intestinalis*, *Faecalibacterium prausnitzii*, and *Eubacterium hallii* (all belong to Firmicutes). They are among the most abundant known butyrate-producing bacteria in human feces, comprising about 8% of the total flora (Hold et al., 2003). The majority of the bacteria in the human gut belong to Bacteroidetes (Gevers et al., 2012; Huttenhower and Gevers, 2012), which produce acetate and succinate rather than butyrate. As mentioned above *A. fermentans*, *M. elsdenii,* and *C. difficile* also use electron bifurcation for butyrate synthesis.

To the author's knowledge, electron bifurcation with crotonyl-CoA appears to be the only pathway to butyrate in anaerobes. Probably no anaerobe wants to abandon the large energy released during butyrate synthesis by taking another route. Some acetate assimilating aerobes, however, reduce crotonyl-CoA with NADH directly to butyryl-CoA without proceeding via Etf. Actually the enzyme acts as crotonyl-CoA carboxylase yielding ethylmalonyl-CoA. Only at low CO_2 concentrations the product is butyryl-CoA (Erb et al., 2007).

Fermentations of amino acids, which give rise to butyrate, are degraded to acetyl-CoA or directly to crotonyl-CoA as shown by the fermentation of glutamate via 2-hydroxyglutarate. *Clostridium propionicum* oxidizes threonine and methionine to (*R*)-2-hydroxybutyrate which is converted to crotonyl-CoA by a mechanism similar to that shown for (*R*)-2-hydroxyglutarate (Barker and Wiken, 1948). The complex anaerobic degradation of lysine in *Clostridium subterminale* SB4 (Barker, 1981) and *Fusobacterium nucleatum* (Barker et al., 1982) involves the radical SAM-dependent 2,3-shift and the coenzyme B_{12}-dependent 6,5-shift of the amino groups to 3,5-diaminohexanoate (Ruzicka et al., 2000). The latter is deaminated to 3-oxo-5-aminohexanoate and cleaved with acetyl-CoA to acetoacetate and 3-aminobutyryl-CoA followed by deamination to crotonyl-CoA (Jeng and Barker, 1974) and reduction to butyryl-CoA, which forms butyrate and acetoacetyl-CoA with acetoacetate. Histidine is degraded to butyrate via glutamate either by *C. tetanomorphum* via the 3-methylaspartate pathway or by *C. symbiosum* via the 2-hydroxyglutarate pathway (Barker, 1981). In a Stickland type fermentation, proline is reduced to 5-aminovalerate by *Clostridium sporogenes* (Stickland, 1935), which is deaminated to 5-hydroxyvalerate and further converted via homocrotonyl-CoA to valerate (homobutyrate) by *Clostridium viride* (Eikmanns and Buckel, 1991; Buckel et al., 1994).

In the human gut, butyrate is the preferred nutrient of the mucosa cells, which form the inner wall of the large intestine, also called colonic epithelia cells. Butyrate activates the nuclear peroxisome proliferator-activated receptor-γ (PPAR-γ), a transcription factor, which in turn stimulates mitochondrial β-oxidation. The very active β-oxidation of butyrate is fueled by oxygen from the blood and consumes any remaining oxygen inside of the intestine resulting in an oxygen-free medium, where anaerobes optimally thrive. PPAR-γ also inhibits expression of the *NO2* gene, which codes for an enzyme that catalyzes the

oxidation of arginine with oxygen to nitric oxide (NO). NO is further oxidized to nitrate, an electron acceptor for potentially pathogenic enterobacteria. For example, *E. coli*, the best known bacterium of the human gut, is well adapted to the strict anaerobic environment as demonstrated by its glycyl radical enzymes class III ribonucleotide reductase and pyruvate:formate lyase (PFL, eq. 11). However, in the presence of oxygen or nitrate the facultative anaerobe forms pyruvate dehydrogenase (eq. 10) and multiplies very fast, from about 1% of the anaerobic microbiome to a major inhabitant of the gut. In case, the quickly spreading *E. coli* strain is pathogenic, severe diseases can occur. To prevent such events, butyrate nourishes colonic epithelia cells, which provides an oxygen-free medium for the microbiome in the large intestine and protects the host from harmful bacteria (Cani, 2017). For a constant butyrate production, the microbiome must be well fed with carbohydrates and amino acids. However, glucose, lactose, starch, glycogen and most proteins are digested and resorbed already in the small intestine, and nothing is left for the microbiome in the gut. Therefore, the human diet must contain indigestible carbohydrate and protein fibers for the mircrobiome, which is able to hydrolyze almost every glycosidic and peptide bond. Hence, fibers for the human diet are necessary for a healthy gut. The microbiologists Erica and Justin Sonnenburg remind their children to eat enough fibers by saying "Feed your bugs!" (Sonnenburg and Sonnenburg, 2015).

AUTHOR CONTRIBUTIONS

The author confirms being the sole contributor of this work and has approved it for publication.

ACKNOWLEDGMENTS

The author thank Tobias Erb, Max Planck Institute for Terrestrial Microbiology, Marburg, Germany for generous support, Bernard T. Golding, University of Newcastle upon Tyne, United Kingdom, and Rudolf K. Thauer, Max Planck Institute for Terrestrial Microbiology, for helpful discussions.

REFERENCES

Anbar, A. D., Duan, Y., Lyons, T. W., Arnold, G. L., Kendall, B., Creaser, R. A., et al. (2007). A whiff of oxygen before the great oxidation event? *Science* 317, 1903–1906. doi: 10.1126/science.1140325

Barker, H. A. (1981). Amino acid degradation by anaerobic bacteria. *Annu. Rev. Biochem.* 50, 23–40. doi: 10.1146/annurev.bi.50.070181.000323

Barker, H. A., Kahn, J. M., and Hedrick, L. (1982). Pathway of lysine degradation in *Fusobacterium nucleatum*. *J. Bacteriol.* 152, 201–207. doi: 10.1128/jb.152.1.201-207.1982

Barker, H. A., Smyth, R. D., Wilson, R. M., and Weissbach, H. (1959). The purification and properties of beta-methylaspartase. *J. Biol. Chem.* 234, 320–328. doi: 10.1016/s0021-9258(18)70297-4

Barker, H. A., Suzuki, F., Iodice, A., and Rooze, V. (1964). Glutamate mutase reaction. *Ann. N. Y. Acad. Sci.* 112, 644–654. doi: 10.1111/j.1749-6632.1964.tb45041.x

Barker, H. A., and Wiken, T. (1948). The origin of butyric acid in the fermentation of threonine by *Clostridium propionicum*. *Arch. Biochem.* 17, 149–151.

Bergdoll, L., Ten Brink, F., Nitschke, W., Picot, D., and Baymann, F. (2016). From low- to high-potential bioenergetic chains: thermodynamic constraints of Q-cycle function. *Biochim. Biophys. Acta* 1857, 1569–1579. doi: 10.1016/j.bbabio.2016.06.006

Biegel, E., and Müller, V. (2010). Bacterial Na^+-translocating ferredoxin:NAD^+ oxidoreductase. *Proc. Natl. Acad. Sci. U.S.A.* 107, 18138–18142. doi: 10.1073/pnas.1010318107

Blair, A. H., and Barker, H. A. (1966). Assay and purification of (+)-citramalate hydro-lyase components from *Clostridium tetanomorphum*. *J. Biol. Chem.* 241, 400–408. doi: 10.1016/s0021-9258(18)96931-0

Boiangiu, C. D., Jayamani, E., Brügel, D., Herrmann, G., Kim, J., Forzi, L., et al. (2005). Sodium ion pumps and hydrogen production in glutamate fermenting anaerobic bacteria. *J. Mol. Microbiol. Biotechnol.* 10, 105–119. doi: 10.1159/000091558

Brüggemann, H., Baumer, S., Fricke, W. F., Wiezer, A., Liesegang, H., Decker, I., et al. (2003). The genome sequence of *Clostridium tetani*, the causative agent of tetanus disease. *Proc. Natl. Acad. Sci. U.S.A.* 100, 1316–1321. doi: 10.1073/pnas.0335853100

Buckel, W. (1990). "Amino acid fermentation: coenzyme B_{12}-dependent and -independent pathways," in *The Molecular Basis of Bacterial Metabolism 41. Colloquium - Mosbach 1990*, eds G. Hauska and R. Thauer (Heidelberg: Springer Verlag), 21–30. doi: 10.1007/978-3-642-75969-7_3

Buckel, W. (1996). Unusual dehydrations in anaerobic bacteria: considering ketyls (radical anions) as reactive intermediates in enzymatic reactions. *FEBS Lett.* 389, 20–24. doi: 10.1016/0014-5793(96)00530-3

Buckel, W. (2001a). Sodium ion-translocating decarboxylases. *Biochim. Biophys. Acta* 1505, 15–27. doi: 10.1016/s0005-2728(00)00273-5

Buckel, W. (2001b). Unusual enzymes involved in five pathways of glutamate fermentation. *Appl. Microbiol. Biotechnol.* 57, 263–273. doi: 10.1007/s002530100773

Buckel, W. (2019). Enzymatic reactions involving ketyls: from a chemical curiosity to a general biochemical mechanism. *Biochemistry* 58, 5221–5233. doi: 10.1021/acs.biochem.9b00171

Buckel, W., and Barker, H. A. (1974). Two pathways of glutamate fermentation by anaerobic bacteria. *J. Bacteriol.* 117, 1248–1260. doi: 10.1128/jb.117.3.1248-1260.1974

Buckel, W., and Bobi, A. (1976). The enzyme complex citramalate lyase from *Clostridium tetanomorphum*. *Eur. J. Biochem.* 64, 255–262. doi: 10.1111/j.1432-1033.1976.tb10295.x

Buckel, W., Dorn, U., and Semmler, R. (1981). Glutaconate CoA-transferase from *Acidaminococcus fermentans*. *Eur. J. Biochem.* 118, 315–321. doi: 10.1111/j.1432-1033.1981.tb06404.x

Buckel, W., and Golding, B. (1996). Glutamate and 2-methyleneglutarate mutase: from microbial curiosities to paradigms for coenzyme B_{12}-dependent enzymes. *Chem. Soc. Rev.* 25, 329–337. doi: 10.1039/cs9962500329

Buckel, W., Janssen, P. H., Schuhmann, A., Eikmanns, U., Messner, P., Sleytr, U., et al. (1994). *Clostridium viride* sp. nov., a strictly anaerobic bacterium using 5-aminovalerate as growth substrate, previously assigned to *Clostridium aminovalericum*. *Arch. Microbiol.* 162, 387–394.

Buckel, W., and Keese, R. (1995). One-electron redox reactions of CoASH esters in anaerobic bacteria – a mechanistic proposal. *Angew. Chem.* 34, 1502–1506. doi: 10.1002/anie.199515021

Buckel, W., and Semmler, R. (1982). A biotin-dependent sodium pump: glutaconyl-CoA decarboxylase from *Acidaminococcus fermentans*. *FEBS Lett.* 148, 35–38. doi: 10.1016/0014-5793(82)81237-4

Buckel, W., and Semmler, R. (1983). Purification, characterisation and reconstitution of glutaconyl-CoA decarboxylase, a biotin-dependent sodium pump from anaerobic bacteria. *Eur. J. Biochem.* 136, 427–434. doi: 10.1111/j.1432-1033.1983.tb07760.x

Buckel, W., and Thauer, R. K. (2013). Energy conservation via electron bifurcating ferredoxin reduction and proton/Na^+ translocating ferredoxin oxidation. *Biochim. Biophys. Acta* 1827, 94–113. doi: 10.1016/j.bbabio.2012.07.002

Buckel, W., and Thauer, R. K. (2018a). Flavin-based electron bifurcation, a new mechanism of biological energy coupling. *Chem. Rev.* 118, 3862–3886. doi: 10.1021/acs.chemrev.7b00707

Buckel, W., and Thauer, R. K. (2018b). Flavin-based electron bifurcation, ferredoxin, flavodoxin, and anaerobic respiration with protons (Ech) or NAD^+ (Rnf) as electron acceptors: a historical review. *Front. Microbiol.* 9:401. doi: 10.3389/fmicb.2018.00401

Cani, P. D. (2017). Gut cell metabolism shapes the microbiome. *Science* 357, 548–549. doi: 10.1126/science.aao2202

Cardon, B. P., and Barker, H. A. (1946). Two new amino-acid-fermenting bacteria, *Clostridium propionicum* and *Diplococcus glycinophilus*. *J. Bacteriol.* 52, 629–634. doi: 10.1128/jb.52.6.629-634.1946

Chen, P. Y., Aman, H., Can, M., Ragsdale, S. W., and Drennan, C. L. (2018). Binding site for coenzyme a revealed in the structure of pyruvate:ferredoxin oxidoreductase from *Moorella thermoacetica*. *Proc. Natl. Acad. Sci. U.S.A.* 115, 3846–3851. doi: 10.1073/pnas.1722329115

Chowdhury, N. P., Kahnt, J., and Buckel, W. (2015). Reduction of ferredoxin or oxygen by flavin-based electron bifurcation in *Megasphaera elsdenii*. *FEBS J.* 282, 3149–3160. doi: 10.1111/febs.13308

Chowdhury, N. P., Klomann, K., Seubert, A., and Buckel, W. (2016). Reduction of flavodoxin by electron bifurcation and sodium ion-dependent reoxidation by NAD^+ catalyzed by ferredoxin-NAD^+ reductase (Rnf). *J. Biol. Chem.* 291, 11993–12002. doi: 10.1074/jbc.m116.726299

Chowdhury, N. P., Mowafy, A. M., Demmer, J. K., Upadhyay, V., Koelzer, S., Jayamani, E., et al. (2014). Studies on the mechanism of electron bifurcation catalyzed by electron transferring flavoprotein (Etf) and butyryl-CoA dehydrogenase (Bcd) of *Acidaminococcus fermentans*. *J. Biol. Chem.* 289, 5145–5157. doi: 10.1074/jbc.m113.521013

Craciun, S., Marks, J. A., and Balskus, E. P. (2014). Characterization of choline trimethylamine-lyase expands the chemistry of glycyl radical enzymes. *ACS Chem. Biol.* 9, 1408–1413. doi: 10.1021/cb500113p

Dawson, C. D., Irwin, S. M., Backman, L. R. F., Le, C., Wang, J. X., Vennelakanti, V., et al. (2021). Molecular basis of C-S bond cleavage in the glycyl radical enzyme isethionate sulfite-lyase. *Cell Chem. Biol.* 28, 1–14. doi: 10.1016/j.chembiol.2021.03.001

Demmer, J. K., Huang, H., Wang, S., Demmer, U., Thauer, R. K., and Ermler, U. (2015). Insights into flavin-based electron bifurcation via the NADH-dependent reduced ferredoxin:NADP oxidoreductase structure. *J. Biol. Chem.* 290, 21985–21995. doi: 10.1074/jbc.m115.656520

Demmer, J. K., Pal Chowdhury, N., Selmer, T., Ermler, U., and Buckel, W. (2017). The semiquinone swing in the bifurcating electron transferring flavoprotein/butyryl-CoA dehydrogenase complex from *Clostridium difficile*. *Nat. Commun.* 8:1577.

Dimroth, P. (1980). A new sodium-transport system energized by the decarboxylation of oxaloacetate. *FEBS Lett.* 122, 234–236. doi: 10.1016/0014-5793(80)80446-7

Dimroth, P., and Thomer, A. (1986). Kinetic analysis of the reaction mechanism of oxaloacetate decarboxylase from *Klebsiella aerogenes*. *Eur. J. Biochem.* 156, 157–162. doi: 10.1111/j.1432-1033.1986.tb09561.x

Dimroth, P., and Thomer, A. (1993). On the mechanism of sodium ion translocation by oxaloacetate decarboxylase of *Klebsiella pneumoniae*. *Biochemistry* 32, 1734–1739. doi: 10.1021/bi00058a006

Djordjevic, S., Pace, C. P., Stankovich, M. T., and Kim, J. J. (1995). Three-dimensional structure of butyryl-CoA dehydrogenase from *Megasphaera elsdenii*. *Biochemistry* 34, 2163–2171. doi: 10.1021/bi00007a009

Dragicevic, I., Baric, D., Kovacevic, B., Golding, B. T., and Smith, D. M. (2015). Non-enzymatic ribonucleotide reduction in the prebiotic context. *Chemistry* 21, 6132–6143. doi: 10.1002/chem.201405741

Eikmanns, U., and Buckel, W. (1991). Crystalline green 5-hydroxyvaleryl-CoA dehydratase from *Clostridium aminovalericum*. *Eur. J. Biochem.* 197, 661–668. doi: 10.1111/j.1432-1033.1991.tb15956.x

Engel, P. C., and Massey, V. (1971). Green butyryl-coenzyme a dehydrogenase. an enzyme-acyl-coenzyme a complex. *Biochem. J.* 125, 889–902. doi: 10.1042/bj1250889

Erb, T. J., Berg, I. A., Brecht, V., Müller, M., Fuchs, G., and Alber, B. E. (2007). Synthesis of C5-dicarboxylic acids from C2-units involving crotonyl-CoA carboxylase/reductase: the ethylmalonyl-CoA pathway. *Proc. Natl. Acad. Sci. U.S.A.* 44, 31496–31502.

Ezaki, T., Yamamoto, N., Ninomiya, K., Suzuki, S., and Yabuuchi, E. (1983). Transfer of *Peptococcus indolicus, Peptococcus asaccharolyticus, Peptococeus prevotii and Peptococcus magnus* to the genus Peptostreptococcus and proposal of *Peptostreptococcus tetardius* sp. nov. *Int. J. Syst. Bacteriol.* 33, 683–689. doi: 10.1099/00207713-33-4-683

Feliks, M., and Ullmann, G. M. (2012). Glycerol dehydratation by the B_{12}-independent enzyme may not involve the migration of a hydroxyl group: a computational study. *J. Phys. Chem. B* 116, 7076–7087. doi: 10.1021/jp301165b

Forage, R. G., and Foster, M. A. (1982). Glycerol fermentation in *Klebsiella pneumoniae*: functions of the coenzyme B_{12}-dependent glycerol and diol dehydratases. *J. Bacteriol.* 149, 413–419. doi: 10.1128/jb.149.2.413-419.1982

Gatarek, P., and Kaluzna-Czaplinska, J. (2021). Trimethylamine N-oxide (TMAO) in human health. *EXCLI J.* 20, 301–319.

Gevers, D., Pop, M., Schloss, P. D., and Huttenhower, C. (2012). Bioinformatics for the human microbiome project. *PLoS Comput. Biol.* 8:e1002779. doi: 10.1371/journal.pcbi.1002779

Greene, B. L., Kang, G., Cui, C., Bennati, M., Nocera, D. G., Drennan, C. L., et al. (2020). Ribonucleotide reductases: structure, chemistry, and metabolism suggest new therapeutic targets. *Annu. Rev. Biochem.* 98, 45–75. doi: 10.1146/annurev-biochem-013118-111843

Hans, M., Bill, E., Cirpus, I., Pierik, A. J., Hetzel, M., Alber, D., et al. (2002). Adenosine triphosphate-induced electron transfer in 2-hydroxyglutaryl-CoA dehydratase from *Acidaminococcus fermentans*. *Biochemistry* 41, 5873–5882. doi: 10.1021/bi020033m

Herrmann, G. (2008). *Enzymes of Two Clostridial Amino-Acid Fermentation Pathways*. Ph. D. thesis. Germany: Philipps Universität Marburg.

Herrmann, G., Jayamani, E., Mai, G., and Buckel, W. (2008). Energy conservation via electron-transferring flavoprotein in anaerobic bacteria. *J. Bacteriol.* 190, 784–791. doi: 10.1128/jb.01422-07

Hess, V., Gallegos, R., Jones, J. A., Barquera, B., Malamy, M. H., and Müller, V. (2016). Occurrence of ferredoxin:NAD(+) oxidoreductase activity and its ion specificity in several Gram-positive and Gram-negative bacteria. *PeerJ* 4:e1515. doi: 10.7717/peerj.1515

Hess, V., Schuchmann, K., and Müller, V. (2013). The ferredoxin:NAD^+ oxidoreductase (Rnf) from the acetogen *Acetobacterium woodii* requires Na^+ and is reversibly coupled to the membrane potential. *J. Biol. Chem.* 288, 31496–31502. doi: 10.1074/jbc.m113.510255

Hetzel, M., Brock, M., Selmer, T., Pierik, A. J., Golding, B. T., and Buckel, W. (2003). Acryloyl-CoA reductase from *Clostridium propionicum*. an enzyme complex of propionyl-CoA dehydrogenase and electron-transferring flavoprotein. *Eur. J. Biochem.* 270, 902–910. doi: 10.1046/j.1432-1033.2003.03450.x

Hilpert, W., and Dimroth, P. (1982). Conversion of the chemical energy of methylmalonyl-CoA decarboxylation into a Na^+ gradient. *Nature* 296, 584–585. doi: 10.1038/296584a0

Hilpert, W., Schink, B., and Dimroth, P. (1984). Life by a new decarboxylation-dependent energy conservation mechanism with Na^+ as coupling ion. *EMBO J.* 3, 1665–1670. doi: 10.1002/j.1460-2075.1984.tb02030.x

Hofmeister, A. E., and Buckel, W. (1992). (*R*)-lactyl-CoA dehydratase from *Clostridium propionicum*. Stereochemistry of the dehydration of (*R*)-2-hydroxybutyryl-CoA to crotonyl-CoA. *Eur. J. Biochem.* 206, 547–552. doi: 10.1111/j.1432-1033.1992.tb16958.x

Hofmeister, A. E., Grabowski, R., Linder, D., and Buckel, W. (1993). L-serine and L-threonine dehydratase from *Clostridium propionicum*. two enzymes with different prosthetic groups. *Eur. J. Biochem.* 215, 341–349. doi: 10.1111/j.1432-1033.1993.tb18040.x

Hold, G. L., Schwiertz, A., Aminov, R. I., Blaut, M., and Flint, H. J. (2003). Oligonucleotide probes that detect quantitatively significant groups of butyrate-producing bacteria in human feces. *Appl. Environ. Microbiol.* 69, 4320–4324. doi: 10.1128/aem.69.7.4320-4324.2003

Hornby, D. P., and Engel, P. C. (1984). Characterization of *Peptostreptococcus asaccharolyticus* glutamate dehydrogenase purified by dye-ligand chromatography. *J. Gen. Microbiol.* 130, 2385–2394. doi: 10.1099/00221287-130-9-2385

Huttenhower, C., and Gevers, D. (2012). Structure, function and diversity of the healthy human microbiome. *Nature* 486, 207–214. doi: 10.1038/nature11234

Imkamp, F., Biegel, E., Jayamani, E., Buckel, W., and Müller, V. (2007). Dissection of the caffeate respiratory chain in the acetogen *Acetobacterium woodii*:

Identification of an Rnf-type NADH dehydrogenase as a potential coupling site. *J. Bacteriol.* 189, 8145–8153. doi: 10.1128/jb.01017-07

Jayamani, E. (2008). *A Unique Way of Energy Conservation in Glutamate Fermenting Clostridia* Ph D dissertation. Germany: Philipps-University Marburg.

Jeng, I., and Barker, H. A. (1974). Purification and properties of l-3-aminobutyryl coenzyme a deaminase from a lysine-fermenting *Clostridium*. *J. Biol. Chem.* 249, 6578–6584. doi: 10.1016/s0021-9258(19)42195-9

Jurgenson, C. T., Begley, T. P., and Ealick, S. E. (2009). The structural and biochemical foundations of thiamin biosynthesis. *Annu. Rev. Biochem.* 78, 569–603. doi: 10.1146/annurev.biochem.78.072407.102340

Kayastha, K., Vitt, S., Buckel, W., and Ermler, U. (2021). Flavins in the electron bifurcation process. *Arch. Biochem. Biophys.* 701:108796. doi: 10.1016/j.abb.2021.108796

Kim, J., Darley, D., and Buckel, W. (2005). 2-Hydroxyisocaproyl-CoA dehydratase and its activator from *Clostridium difficile*. *FEBS J.* 272, 550–561. doi: 10.1111/j.1742-4658.2004.04498.x

Kim, J., Darley, D. J., Buckel, W., and Pierik, A. J. (2008). An allylic ketyl radical intermediate in clostridial amino-acid fermentation. *Nature* 452, 239–242. doi: 10.1038/nature06637

Knappe, J., and Sawers, G. (1990). A radical-chemical route to acetyl-CoA: the anaerobically induced pyruvate formate-lyase system of *Escherichia coli*. *FEMS Microbiol. Rev.* 6, 383–398. doi: 10.1111/j.1574-6968.1990.tb04108.x

Kovacevic, B., Baric, D., Babic, D., Bilic, L., Hanzevacki, M., Sandala, G. M., et al. (2018). Computational tale of two enzymes: glycerol dehydration with or without B_{12}. *J. Am. Chem. Soc.* 140, 8487–8496. doi: 10.1021/jacs.8b03109

Kremp, F., Roth, J., and Müller, V. (2020). The *Sporomusa* type Nfn is a novel type of electron-bifurcating transhydrogenase that links the redox pools in acetogenic bacteria. *Sci. Rep.* 10:14872.

Kress, D., Brügel, D., Schall, I., Linder, D., Buckel, W., and Essen, L. O. (2009). An asymmetric model for Na^+-translocating glutaconyl-CoA decarboxylases. *J. Biol. Chem.* 284, 28401–28409. doi: 10.1074/jbc.m109.037762

Laubinger, W., and Dimroth, P. (1988). Characterization of the ATP synthase of *Propionigenium modestum* as a primary sodium pump. *Biochemistry* 27, 7531–7537. doi: 10.1021/bi00419a053

Leutbecher, U., Böcher, R., Linder, D., and Buckel, W. (1992). Glutamate mutase from *Clostridium cochlearium*. purification, cobamide content and stereospecific inhibitors. *Eur. J. Biochem.* 205, 759–765. doi: 10.1111/j.1432-1033.1992.tb16840.x

Levin, B. J., and Balskus, E. P. (2018). Characterization of 1,2-propanediol dehydratases reveals distinct mechanisms for B_{12}-dependent and glycyl radical enzymes. *Biochemistry* 57, 3222–3226. doi: 10.1021/acs.biochem.8b00164

Lewis, D., and Elsden, S. R. (1955). The fermentation of L-threonine, L-serine, L-cysteine and acrylic acid by a gram-negative coccus. *Biochem. J.* 60, 683–692. doi: 10.1042/bj0600683

Li, F., Hinderberger, J., Seedorf, H., Zhang, J., Buckel, W., and Thauer, R. K. (2008). Coupled ferredoxin and crotonyl coenzyme A (CoA) reduction with NADH catalyzed by the butyryl-CoA dehydrogenase/ Etf complex from *Clostridium kluyveri*. *J. Bacteriol.* 190, 843–850. doi: 10.1128/jb.01417-07

Locher, K. P., Hans, M., Yeh, A. P., Schmid, B., Buckel, W., and Rees, D. C. (2001). Crystal structure of the *Acidaminococcus fermentans* 2-hydroxyglutaryl-CoA dehydratase component A. *J. Mol. Biol.* 307, 297–308. doi: 10.1006/jmbi.2000.4496

Louis, P., and Flint, H. J. (2017). Formation of propionate and butyrate by the human colonic microbiota. *Environ. Microbiol.* 19, 29–41. doi: 10.1111/1462-2920.13589

Lubner, C. E., Jennings, D. P., Mulder, D. W., Schut, G. J., Zadvornyy, O. A., Hoben, J. P., et al. (2017). Mechanistic insights into energy conservation by flavin-based electron bifurcation. *Nat. Chem. Biol.* 13, 655–659. doi: 10.1038/nchembio.2348

Marchandin, H., Teyssier, C., Campos, J., Jean-Pierre, H., Roger, F., Gay, B., et al. (2010). *Negativicoccus succinicivorans* gen. nov., sp. nov., isolated from human clinical samples, emended description of the family *Veillonellaceae* and description of *Negativicutes* classis nov., *Selenomonadales* ord. nov. and fam. nov. in the bacterial phylum Firmicutes. *Int. J. Syst. Evol. Microbiol.* 60, 1271–1279. doi: 10.1099/ijs.0.013102-0

Moore, S. J., and Warren, M. J. (2012). The anaerobic biosynthesis of vitamin B_{12}. *Biochem. Soc. Trans.* 40, 581–586. doi: 10.1042/bst20120066

Moser, C. C., Keske, J. M., Warncke, K., Farid, R. S., and Dutton, P. L. (1992). Nature of biological electron transfer. *Nature* 355, 796–802. doi: 10.1038/355796a0

Nitschke, W., and Russell, M. J. (2012). Redox bifurcations: mechanisms and importance to life now, and at its origin: a widespread means of energy conversion in biology unfolds. *Bioessays* 34, 106–109. doi: 10.1002/bies.201100134

O'Brien, J. R., Raynaud, C., Croux, C., Girbal, L., Soucaille, P., and Lanzilotta, W. N. (2004). Insight into the mechanism of the B_{12}-independent glycerol dehydratase from *Clostridium butyricum*: preliminary biochemical and structural characterization. *Biochemisty* 43, 4635–4645. doi: 10.1021/bi035930k

Otto, R., Sonnenberg, A. S. M., Veldkamp, H., and Konings, W. N. (1980). Generation of an electrochemical proton gradient in *Streptococcus cremoris* by lactate efflux. *Proc. Natl. Acad. Sci. U.S.A.* 77, 5502–5506. doi: 10.1073/pnas.77.9.5502

Parthasarathy, A., Buckel, W., and Smith, D. M. (2010). On the thermodynamic equilibrium between (*R*)-2-hydroxyacyl-CoA and 2-enoyl-CoA. *FEBS J.* 277, 1738–1746. doi: 10.1111/j.1742-4658.2010.07597.x

Peck, S. C., Denger, K., Burrichter, A., Irwin, S. M., Balskus, E. P., and Schleheck, D. (2019). A glycyl radical enzyme enables hydrogen sulfide production by the human intestinal bacterium *Bilophila wadsworthia*. *Proc. Natl. Acad. Sci U.S.A.* 116, 3171–3176. doi: 10.1073/pnas.1815661116

Pfenninger-Li, X. D., and Dimroth, P. (1992). NADH formation by Na^+-coupled reversed electron transfer in *Klebsiella pneumoniae*. *Mol. Microbiol.* 6, 1943–1948. doi: 10.1111/j.1365-2958.1992.tb01367.x

Ramezani, M., Resmer, K. L., and White, R. L. (2011). Glutamate racemization and catabolism in *Fusobacterium varium*. *FEBS J.* 278, 2540–2551. doi: 10.1111/j.1742-4658.2011.08179.x

Rétey, J., Umani-Ronchi, A., Seibl, J., and Arigoni, D. (1966). Zum mechanismus der propandioldehydrase-reaktion. *Experientia* 22, 502–503. doi: 10.1007/bf01898652

Roberts, D. L., Frerman, F. E., and Kim, J. J. (1996). Three-dimensional structure of human electron transfer flavoprotein to 2.1-Å resolution. *Proc. Natl. Acad. Sci. U.S.A.* 93, 14355–14360. doi: 10.1073/pnas.93.25.14355

Ruff, J., Denger, K., and Cook, A. M. (2003). Sulphoacetaldehyde acetyltransferase yields acetyl phosphate: purification from *Alcaligenes defragrans* and gene clusters in taurine degradation. *Biochem. J.* 369, 275–285. doi: 10.1042/bj20021455

Ruzicka, F. J., Lieder, K. W., and Frey, P. A. (2000). Lysine 2,3-aminomutase from *Clostridium subterminale* SB4: mass spectral characterization of cyanogen bromide-treated peptides and cloning, sequencing, and expression of the gene kamA in *Escherichia coli*. *J. Bacteriol.* 182, 469–476. doi: 10.1128/jb.182.2.469-476.2000

Schink, B. (1982). *Propionigenium modestum* gen. nov. sp. nov. a new strictly anaerobic, nonsporing bacterium growing on succinate. *Arch. Microbiol.* 133, 209–216. doi: 10.1007/bf00415003

Schmehl, M., Jahn, A., Meyer zu Vilsendorf, A., Hennecke, S., Masepohl, B., Schuppler, M., et al. (1993). Identification of a new class of nitrogen fixation genes in *Rhodobacter capsulatus*: a putative membrane complex involved in electron transport to nitrogenase. *Mol. Gen. Genet.* 241, 602–615. doi: 10.1007/bf00279903

Schwarz, E., Oesterhelt, D., Reinke, H., Beyreuther, K., and Dimroth, P. (1988). The sodium ion translocating oxalacetate decarboxylase of *Klebsiella pneumoniae*. sequence of the biotin-containing alpha-subunit and relationship to other biotin-containing enzymes. *J. Biol. Chem.* 263, 9640–9645. doi: 10.1016/s0021-9258(19)81564-8

Schweiger, G., and Buckel, W. (1984). On the dehydration of (*R*)-lactate in the fermentation of alanine to propionate by *Clostridium propionicum*. *FEBS Lett.* 171, 79–84. doi: 10.1016/0014-5793(84)80463-9

Seedorf, H., Fricke, W. F., Veith, B., Brüggemann, H., Liesegang, H., Strittmatter, A., et al. (2008). The genome of *Clostridium kluyveri*, a strict anaerobe with unique metabolic features. *Proc. Natl. Acad. Sci. U.S.A.* 105, 2128–2133. doi: 10.1073/pnas.0711093105

Shibata, N., Tamagaki, H., Hieda, N., Akita, K., Komori, H., Shomura, Y., et al. (2010). Crystal structures of ethanolamine ammonia-lyase complexed with coenzyme B_{12} analogs and substrates. *J. Biol. Chem.* 285, 26484–26493. doi: 10.1074/jbc.m110.125112

Shisler, K. A., and Broderick, J. B. (2014). Glycyl radical activating enzymes: structure, mechanism, and substrate interactions. *Arch. Biochem. Biophys.* 546, 64–71. doi: 10.1016/j.abb.2014.01.020

Sonnenburg, J., and Sonnenburg, E. (2015). *The Good Gut*. London: Bantam Press.

Steuber, J., Halang, P., Vorburger, T., Steffen, W., Vohl, G., and Fritz, G. (2014a). Central role of the Na(+)-translocating NADH:quinone oxidoreductase (Na(+)-NQR) in sodium bioenergetics of *Vibrio cholerae*. *Biol. Chem.* 295, 1389–1399. doi: 10.1515/hsz-2014-0204

Steuber, J., Vohl, G., Casutt, M. S., Vorburger, T., Diederichs, K., and Fritz, G. (2014b). Structure of the *V. cholerae* Na^+-pumping NADH:quinone oxidoreductase. *Nature* 516, 62–67. doi: 10.1038/nature14003

Stickland, L. H. (1935). Studies in the metabolism of the strict anaerobes (Genus *Clostridium*): the reduction of proline by *Cl. sporogenes*. *Biochem. J.* 29, 288–290. doi: 10.1042/bj0290288

Sucharitakul, J., Buckel, W., and Chaiyen, P. (2021a). Rapid kinetics reveal surprising flavin chemistry in the bifurcating electron transfer flavoprotein from *Acidaminococcus fermentans*. *J. Biol. Chem.* 296:100124. doi: 10.1074/jbc.RA120.016017

Sucharitakul, J., Buttranon, S., Wongnate, T., Chowdhury, N. P., Prongjit, M., Buckel, W., et al. (2021b). Modulations of the reduction potentials of flavin-based electron bifurcation complexes and semiquinone stabilities are key to control directional electron flow. *FEBS J.* 288, 1008–1026. doi: 10.1111/febs.15343

Thauer, R. K., Jungermann, K., Rupprecht, E., and Decker, K. (1969). Hydrogen formation from NADH in cell-free extracts of *Clostridium kluyveri*. acetyl coenzyme a requirement and ferredoxin dependence. *FEBS Lett.* 4, 108–112. doi: 10.1016/0014-5793(69)80208-5

Thauer, R. K., Jungermann, R., and Decker, K. (1977). Energy conservation in chemotrophic anaerobic bacteria. *Bacteriol. Rev.* 41, 100–180. doi: 10.1128/br.41.1.100-180.1977

Vigil, W. Jr., Niks, D., Franz-Badur, S., Chowdhury, N., Buckel, W., and Hille, R. (2021). Spectral deconvolution of redox species in the crotonyl-CoA-dependent NADH:ferredoxin oxidoreductase from *Megasphaera elsdenii*. a flavin-dependent bifurcating enzyme. *Arch. Biochem. Biophys.* 701:108793. doi: 10.1016/j.abb.2021.108793

Vitt, S., Prinz, S., Hellwig, N., Morgner, N., Ermler, U., and Buckel, W. (2020). Molecular and low-resolution structural characterization of the Na^+-translocating glutaconyl-CoA decarboxylase from *Clostridium symbiosum*. *Front. Microbiol.* 11:48011. doi: 10.3389/fmicb.2020.00480

Vogt, M. S., Schühle, K., Koelzer, S., Peschke, P., Chowdhury, N. P., Kleinsorge, D., et al. (2019). Structural and functional characterization of an electron transfer flavoprotein involved in toluene degradation in strictly anaerobic bacteria. *J. Bacteriol.* 201, e00326. doi: 10.1128/JB.00326-19

von Ballmoos, C., Wiedenmann, A., and Dimroth, P. (2009). Essentials for ATP synthesis by F_1F_0 ATP synthases. *Annu. Rev. Biochem.* 78, 649–672. doi: 10.1146/annurev.biochem.78.081307.104803

Wang, S., Huang, H., Moll, J., and Thauer, R. K. (2010). $NADP^+$ reduction with reduced ferredoxin and $NADP^+$ reduction with NADH are coupled via an electron-bifurcating enzyme complex in *Clostridium kluyveri*. *J. Bacteriol.* 192, 5115–5123. doi: 10.1128/jb.00612-10

Wei, Y., and Zhang, Y. (2021). Glycyl radical enzymes and sulfonate metabolism in the microbiome. *Annu. Rev. Biochem.* 90, 817–846. doi: 10.1146/annurev-biochem-080120-024103

Xing, M., Wei, Y., Zhou, Y., Zhang, J., Lin, L., Hu, Y., et al. (2019). Radical-mediated C-S bond cleavage in C2 sulfonate degradation by anaerobic bacteria. *Nat. Commun.* 10:1609.

Xu, X., Shi, H., Gong, X., Chen, P., Gao, Y., Zhang, X., et al. (2020). Structural insights into sodium transport by the oxaloacetate decarboxylase sodium pump. *Elife* 9:e53853. doi: 10.7554/eLife.53853

Yu, X., Bresser, J., Schall, I., Djurdjevic, I., Buckel, W., Wang, X., et al. (2012). Development of a satisfactory and general continuous assay for aminotransferases by coupling with (*R*)-2-hydroxyglutarate dehydrogenase. *Anal. Biochem.* 432, 127–131. doi: 10.1016/j.ab.2012.09.009

Zagalak, B., Frey, P. A., Karabatsos, G. L., and Abeles, R. H. (1966). The stereochemistry of the conversion of D and L 1,2-propanediols to propionaldehyde. *J. Biol. Chem.* 241, 3028–3035. doi: 10.1016/s0021-9258(18)96492-6

Zhang, H., Dutton, P. L., and Moser, C. C. (2007). Exposing the complex III Q_o semiquinone radical. *Biochim. Biophys. Acta* 1767, 883–887. doi: 10.1016/j.bbabio.2007.04.004

Conflict of Interest: The author declares that the research was conducted in the absence of any commercial or financial relationships that could be construed as a potential conflict of interest.

Publisher's Note: All claims expressed in this article are solely those of the authors and do not necessarily represent those of their affiliated organizations, or those of the publisher, the editors and the reviewers. Any product that may be evaluated in this article, or claim that may be made by its manufacturer, is not guaranteed or endorsed by the publisher.

frontiers in Microbiology

ORIGINAL RESEARCH
published: 13 September 2021
doi: 10.3389/fmicb.2021.712465

The CopA2-Type P_{1B}-Type ATPase CcoI Serves as Central Hub for *cbb*$_3$-Type Cytochrome Oxidase Biogenesis

*Andreea Andrei[1,2], Maria Agostina Di Renzo[3,4,5], Yavuz Öztürk[1], Alexandra Meisner[1], Noel Daum[1], Fabian Frank[3], Juna Rauch[1], Fevzi Daldal[6], Susana L. A. Andrade[3] and Hans-Georg Koch[1]**

[1]Institut für Biochemie und Molekularbiologie, ZBMZ, Faculty of Medicine, Albert-Ludwigs-Universität Freiburg, Freiburg, Germany, [2]Faculty of Biology, Albert-Ludwigs-Universität Freiburg, Freiburg, Germany, [3]Institute for Biochemistry, Faculty of Chemistry and Pharmacy, Albert-Ludwigs-University Freiburg, Freiburg, Germany, [4]Spemann Graduate School of Biology and Medicine (SGBM), University of Freiburg, Freiburg, Germany, [5]Faculty of Chemistry and Pharmacy, Albert-Ludwigs-Universität Freiburg, Freiburg, Germany, [6]Department of Biology, University of Pennsylvania, Philadelphia, PA, United States

OPEN ACCESS

Edited by:
Zhaomin Yang,
Virginia Tech, United States

Reviewed by:
Teresita Padilla-Benavides,
Wesleyan University, United States
Mathias Lübben,
Ruhr University Bochum, Germany

***Correspondence:**
Hans-Georg Koch
Hans-Georg.Koch@biochemie.uni-freiburg.de

Specialty section:
This article was submitted to Microbial Physiology and Metabolism, a section of the journal Frontiers in Microbiology

Received: *20 May 2021*
Accepted: *12 July 2021*
Published: *13 September 2021*

Citation:
*Andrei A, Di Renzo MA, Öztürk Y, Meisner A , Daum N, Frank F, Rauch J, Daldal F, Andrade SLA and Koch H-G (2021) The CopA2-Type P_{1B}-Type ATPase CcoI Serves as Central Hub for **cbb**$_3$-Type Cytochrome Oxidase Biogenesis. Front. Microbiol. 12:712465. doi: 10.3389/fmicb.2021.712465*

Copper (Cu)-transporting P_{1B}-type ATPases are ubiquitous metal transporters and crucial for maintaining Cu homeostasis in all domains of life. In bacteria, the P_{1B}-type ATPase CopA is required for Cu-detoxification and exports excess Cu(I) in an ATP-dependent reaction from the cytosol into the periplasm. CopA is a member of the CopA1-type ATPase family and has been biochemically and structurally characterized in detail. In contrast, less is known about members of the CopA2-type ATPase family, which are predicted to transport Cu(I) into the periplasm for cuproprotein maturation. One example is CcoI, which is required for the maturation of *cbb*$_3$-type cytochrome oxidase (*cbb*$_3$-Cox) in different species. Here, we reconstituted purified CcoI of *Rhodobacter capsulatus* into liposomes and determined Cu transport using solid-supported membrane electrophysiology. The data demonstrate ATP-dependent Cu(I) translocation by CcoI, while no transport is observed in the presence of a non-hydrolysable ATP analog. CcoI contains two cytosolically exposed N-terminal metal binding sites (N-MBSs), which are both important, but not essential for Cu delivery to *cbb*$_3$-Cox. CcoI and *cbb*$_3$-Cox activity assays in the presence of different Cu concentrations suggest that the glutaredoxin-like N-MBS1 is primarily involved in regulating the ATPase activity of CcoI, while the CopZ-like N-MBS2 is involved in Cu(I) acquisition. The interaction of CcoI with periplasmic Cu chaperones was analyzed by genetically fusing CcoI to the chaperone SenC. The CcoI-SenC fusion protein was fully functional *in vivo* and sufficient to provide Cu for *cbb*$_3$-Cox maturation. In summary, our data demonstrate that CcoI provides the link between the cytosolic and periplasmic Cu chaperone networks during *cbb*$_3$-Cox assembly.

Keywords: P_{1B}-type ATPases, CcoI, *cbb*$_3$-type cytochrome *c* oxidase biogenesis, SenC, *Rhodobacter capsulatus*, solid-supported membrane electrophysiology, CopZ

INTRODUCTION

Copper is an essential, yet potentially toxic micronutrient, which is required for the catalytic activity of many important enzymes, like cytochrome oxidases (Cox) or Cu-Zn superoxide dismutases. The redox properties of Cu are especially crucial for the oxygen-linked activities of these enzymes, but they also favor cytotoxic effects that can lead to the formation of hydroxyl radicals (Argüello et al., 2013; Andrei et al., 2020). Cu homeostasis is therefore tightly controlled by the coordinated action of Cu transporters and Cu chaperones to maintain a sufficient Cu quota for cuproprotein biogenesis while preventing accumulation of excess Cu in the cytosol (Rosenzweig and O'Halloran, 2000; Rensing and Grass, 2003; Banci et al., 2010a; Arguello et al., 2016). Central to this coordination are P_{1B}-type ATPases, a ubiquitous class of transition metal exporters, located in the cytoplasmic membrane of bacteria, the basolateral membrane of enterocytes or the trans-Golgi network of hepatocytes and brain cells (Crisponi et al., 2010; Smith et al., 2014; Andrei et al., 2020).

Despite sequence variations, the overall structure of Cu-transporting P_{1B}-type ATPases is largely conserved between the family members from different species. They usually consist of eight transmembrane helices (TM) and three cytoplasmic domains (Arguello et al., 2007). The transmembrane module contains two invariable metal binding sites (MBSs), TM-MBS1 and TM-MBS2, characterized by the presence of conserved Cys-Pro-Cys and Asp-Met-Ser motifs, respectively (Wu et al., 2008). Inactivation of any of these sites leads to the inhibition of Cu transport, and reduced ATPase activity (Gonzalez-Guerrero et al., 2008, 2009). In the cytoplasmic module, the nucleotide-binding domain (N-domain) binds ATP for the transient phosphorylation of an invariant Asp residue located in the phosphorylation domain (P-domain). The third cytoplasmic domain, the actuator domain (A-domain), is suggested to relay conformational changes from the N- and P-domains to the transmembrane module and to control the dephosphorylation of the P-domain. The ATP-dependent Cu translocation by P_{1B}-ATPases largely follows the Post-Albers cycle, first described for Na^+, K^+-ATPases (Post et al., 1972; Palmgren and Nissen, 2011). However, due to the potential toxicity of Cu and the virtual absence of free Cu in the bacterial cytosol, the catalytic activity of P_{1B}-type ATPases is thought to be further influenced by Cu transfer reactions from cytosolic Cu chaperones to their MBSs (Arguello et al., 2016).

Typically, bacteria contain more than one Cu-exporting P_{1B}-type ATPase. While CopA1-type ATPases export excess Cu and primarily mediate Cu detoxification, CopA2-type ATPases provide Cu for cuproprotein biogenesis (Preisig et al., 1996; Koch et al., 2000; Gonzalez-Guerrero et al., 2010; Smith et al., 2014). This functional diversity is also reflected by distinct catalytic activities: CopA1-type ATPases have a high turnover rate and low affinity for Cu(I), while the opposite applies to CopA2-type ATPases, in line with the general concept that affinity gradients are important determinants for the cellular Cu metabolism (Banci et al., 2010c).

In addition to their different catalytic properties, CopA1- and CopA2-type ATPases also show variations in their soluble MBSs (**Figure 1**), which can be located at the N-terminus (N-MBSs) or at the C-terminus (C-MBSs; Mandal and Arguello, 2003; Drees et al., 2015). In most CopA1-type ATPases, the N-MBSs are not essential for Cu-transport, but rather function as Cu-sensing domains to regulate Cu translocation rates, potentially *via* interaction with the ATP-binding N-domain and A-domain (Wu et al., 2008). The most common Cu-binding motif in N-MBSs is a Met-x-Cys-x-x-Cys motif that adopts a ferredoxin-like *βαββαβ* fold, also found in cytosolic CopZ-like Cu chaperones (Banci et al., 2003; Rodriguez-Granillo and Wittung-Stafshede, 2008; Agarwal et al., 2010). Matching Cu-binding motifs in CopA1-ATPases and their cognate chaperones appears to be important for their activity, as illustrated by the less common cupredoxin-like Cys-x-Cys-x-Met-x-Met motif of *Streptococcus pneumoniae* CopA, which is also present in its cognate chaperone CupA (Fu et al., 2013).

Little is known about the function of the N-MBSs in CopA2-type ATPases, which like CcoI, are relevant for the export of Cu required for the cbb_3-type Cox in bacteria. This type of Cox is widely distributed in bacteria, but absent in eukaryotes (Ekici et al., 2012). The cbb_3-type Cox of the facultative phototrophic bacterium *Rhodobacter capsulatus* has developed into a well-studied model system for dissecting bacterial Cu homeostasis, because cbb_3-Cox is the only Cox present in this organism and contains only one Cu ion in its catalytic heme *b*-Cu_B center of subunit CcoN (Gray et al., 1994; Steimle et al., 2021). This is different from the universally conserved aa_3-type Cox, which contains a second Cu center in the electron-accepting subunit II (Thompson et al., 2012). In cbb_3-Cox, this subunit is replaced by the two membrane-bound *c*-type cytochromes, CcoO and CcoP (Ekici et al., 2012). The absence of CcoI in *R. capsulatus* cells prevents the formation of an active cbb_3-Cox, but has no major effect on Cu sensitivity, in agreement with its dedicated function in cuproprotein biogenesis (Utz et al., 2019). CcoI is part of a complex Cu supply chain identified in *R. capsulatus* (Koch et al., 2000), which starts with Cu(II)-uptake by the major facilitator super family member CcoA (Ekici et al., 2014). Once in the cytosol, Cu(II) is reduced to Cu(I) by the membrane-bound ferredoxin-like protein CcoG. CcoG represents the first bacterial cupric reductase that reduces Cu(II) in the cytosol, and this activity is important for efficient cbb_3-type Cox assembly (Marckmann et al., 2019). Cu(I) is then likely bound to the Cu chaperone CopZ. *R. capsulatus* CopZ was found to interact with both CopA and CcoI and this interaction is likely guided by the Cu concentration in the cytosol. At high Cu concentrations, CopZ primarily transfers Cu to CopA for extrusion, while at low Cu concentrations, CopZ mediates Cu transfer to CcoI for cbb_3-Cox assembly (Utz et al., 2019). Interestingly, the absence of CopZ markedly increases Cu sensitivity in *R. capsulatus*, but only slightly reduces cbb_3-Cox activity, indicating that Cu detoxification is the primary role of CopZ. In addition, at low Cu availability, two periplasmic Cu chaperones are involved in conveying Cu to cbb_3-Cox. The membrane-bound SenC is homologous to the ScoI-family of Cu chaperones, also involved in the assembly of the Cu_A-center in subunit II of aa_3-Cox (Canonica et al., 2019a,b). SenC cooperates with the soluble, periplasmic Cu chaperone PccA and Cu transfer between both proteins has been confirmed experimentally

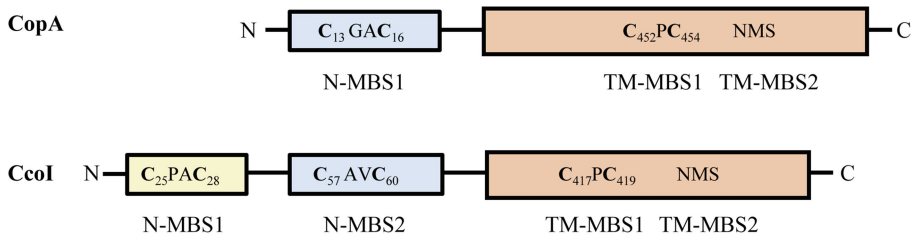

FIGURE 1 | Comparison of *Rhodobacter capsulatus* CopA and CcoI. The CopZ-like CxxC Cu binding site (N-MBS1 in CopA and N-MBS2 in CcoI) is depicted in pale blue. CcoI contains an additional glutaredoxin-like MBS (CPAC, N-MBS1) at the very N-terminus, depicted in yellow. The core cytoplasmic and transmembrane domains of CcoI and CopA are depicted in orange, with the two transmembrane Cu binding sites indicated (TM-MBS1 & 2). Numbers in subscript refer to the amino acid positions in the respective protein.

(Trasnea et al., 2018). *In vitro* studies showed that Cu transfer between SenC and PccA works in both directions (Trasnea et al., 2018), leaving unknown whether SenC, PccA or a so far unknown protein is the primary acceptor of translocated Cu(I) in the periplasm. In the absence of PccA, cbb_3-type Cox activity is reduced to approx. 30%, but when *senC* is deleted basically no cbb_3-type Cox activity is present under low Cu availability (Lohmeyer et al., 2012; Trasnea et al., 2016), indicating that PccA is not essential for cbb_3-Cox assembly, even at Cu-limiting conditions.

In *R. capsulatus*, CcoI is considered to be a central player in the Cu supply pathway to cbb_3-Cox, yet experimental proof that it indeed transports Cu is lacking. In addition, the unusual presence of two distinct N-MBSs in CcoI raises questions about their role(s) in CcoI-mediated Cu delivery to cbb_3-Cox. Finally, how CcoI cooperates with periplasmic Cu chaperones for cbb_3-Cox assembly is largely unknown. In the current study, we used solid-supported membrane electrophysiology (SSM) to demonstrate the ATP-dependent Cu(I) translocation by CcoI. This method allows to monitor the ability of transporter proteins to translocate charged ions across the membrane. Furthermore, we analyzed the role of the two N-MBSs in CcoI and provide evidence that a CcoI-SenC complex is required for cbb_3-Cox assembly.

MATERIALS AND METHODS

Bacterial Strains and Growth Conditions

Escherichia coli C43(DE3) cells were grown aerobically in lysogeny broth (LB) at 37°C. When indicated, the medium was supplemented with 50 μg/ml ampicillin or 12.5 μg/ml tetracycline. *R. capsulatus* wild type and mutant strains were grown semi-aerobically on enriched yeast-peptone medium (MPYE) or Sistrom's minimal medium (Sistrom, 1960) at 35°C, with 110 rpm shaking and supplemented with appropriate antibiotics (**Supplementary Table S1**). For protein production, solid and liquid media were supplemented with 0.2% or 0.5% *L*-arabinose (*L*-ara), respectively. All strains and plasmids are listed in **Supplementary Tables S1, S2**.

Molecular Genetic Techniques

For mutating the CcoI MBSs, the plasmid pBAD-*ccoI*-Myc/HisA, which contains *ccoI* under the control of the P_{ara} promoter (Utz et al., 2019), was used as template for PCR-mutagenesis. All primers are listed in **Supplementary Table S3**. This generated the plasmids pBAD-*ccoI*($C_{25}A/C_{28}A$)-Myc/His, pBAD-*ccoI*($C_{57}A/C_{60}A$)-Myc/His and pBAD-*ccoI*($C_{417}A/C_{419}A$)-Myc/His, which were confirmed by sequencing. The constructs were transformed into *E. coli* C43(DE3) for protein purification. For expression in *R. capsulatus* strains, the constructs were inserted into the broad host range plasmid pRK415. First, the pBAD-*ccoI*-Myc/HisA derivatives were linearized using the pBAD-specific 4a and 4b primers (**Supplementary Table S2**) with 20 bp 5' overlapping regions containing the BamHI restriction site and then integrated into BamHI digested pRK415 by the HiFi Gibson assembly method, as described by the manufacturer (NEB Lab, MA). The constructs were first transformed into chemically competent *E. coli* DH5-α cells, and thereafter to HB101 cells for heterologous conjugation. The pRK-*ccoI*($C_{25}A/C_{28}A$), pRK-*ccoI*($C_{57}A/C_{60}A$), and pRK-*ccoI*($C_{417}A/C_{419}A$) constructs were confirmed by sequencing and then conjugated into *R. capsulatus* strains by triparental conjugation. CcoI production was monitored after induction with 0.5% *L*-ara and visualized by immune blotting using antibodies against the Myc and His tags.

For the chromosomal inactivation of *copZ* and *copA* genes in the *R. capsulatus* Δ*ccoI* strain, the pRK415-Δ*copZ* plasmid carrying the Δ(*copZ::Gm*) allele was introduced into *R. capsulatus* Gene Transfer Agent (GTA) overproducer strain Y262, as described before (Koch et al., 1998; Utz et al., 2019). The GTA particles carrying the Δ(*copZ::Gm*) allele were mixed with the Δ*ccoI* strain for GTA mediated interposon mutagenesis (Yen et al., 1979; Daldal et al., 1986), yielding the Δ*ccoI*Δ*copZ* double mutant. The Δ*ccoI*Δ*copA* double mutant was generated as described (Öztürk et al., Submitted). The pRK-*copA*::Kan plasmid carrying the Δ(*copA::kan*) allele (RCAP_rcc01180) in *R. capsulatus* Y262 strain (Ekici et al., 2014) provided the GTA particles used with the Δ*ccoI* strain to generate the Δ*ccoI*Δ*copA* double mutant (**Supplementary Table S1**).

The *ccoI-senC* fusion and its inactive variants *ccoI*($C_{417}A/C_{419}A$)*-senC* and *ccoI-senC*($C_{83}A/C_{87}A$) were cloned into the *L*-ara inducible expression vector pBAD-Myc/HisA. The plasmid pBAD was linearized by using the primer 5a and 5b (**Supplementary Table S3**) and the PCR product thus obtained was digested with DpnI to remove the template plasmid. The *ccoI* coding sequence without its stop codon was genetically

fused to the *senC* coding sequence starting at Gly_2 as its first amino acid, *via* an overlapping sequence encoding GGSG-*FLAG*-GGSG as a linker, and amplified by using the pair of primers 6a and 6b, 7a and 7b (**Supplementary Table S3**). Genomic DNA of *R. capsulatus* MT1131 was used as a template. For the mutated versions of *ccoI* and *senC,* the pair of primers 8a and 8b, 9a and 9b (**Supplementary Table S3**) were used, respectively. HiFi Gibson assembly method (NEB) was used as described above to yield pBAD-*ccoI-senC*, pBAD-*ccoI*($C_{417}A/C_{419}A$)*-senC*, and pBAD-*ccoI-senC*($C_{83}A/C_{87}A$) plasmids, which were confirmed by sequencing. These plasmids were then integrated into the broad host range plasmid pRK415, generating pRK-*ccoI-senC*, pRK-*ccoI(M)-senC*, and pRK-*ccoI-senC(M)* (*M* designating the respective mutants), which were confirmed by sequencing and transformed into chemically competent *E. coli* HB101 cells for subsequent triparental conjugation into *R. capsulatus* strains.

CcoI Purification

E. coli C43(DE3) cells producing wild-type and appropriate variants of CcoI for downstream purification purposes were grown to an optical density (OD_{600}) of 0.6, cooled down for 20 min at 4°C and supplemented with 0.2% *L*-ara. Cultures were incubated at 30° C, 180 rpm for 90 min., and all downstream steps were performed on ice. Cells were harvested at 7,460 *x g* for 12 min in a JLA 9.100 rotor. The pellet was washed in 50 ml 50 mM TeaAc buffer and recentrifuged. 10 ml of resuspension buffer (50 mM TeaAc, pH 7.5, 1 mM EDTA, pH 8, 0.4 mM aminohexanoic acid) per 10 g of cells was used to resuspend the pellet. Prior to cell disruption, 2 mM Pefabloc, 2 mM DTT and 5 Complete Protease Inhibitor tablets (Roche, Germany) were added per 100 ml of cell suspension, which was passed three times through the Emulsiflex-c3 (Avestin, Ontario, Canada) with an applied pressure of 10,000 psi. After cell disruption, cell debris were removed by centrifugation for 20 min in a F21 rotor at 27,000 *x g*. The supernatant was then further centrifuged at 192,800 *x g* in a Ti 50.2 rotor for 2 h, to isolate the membrane fraction. Subsequently, the membranes were resuspended with a loose Dounce homogenizer pestle in 10 ml dilution buffer (25 mM Tris, pH 7.5, 500 mM NaCl, 10 mM $MgCl_2$, 10% Glycerol, 2 mM Pefabloc, 2 mM DTT, 1 tablet of Complete Protease Inhibitor/50 ml buffer) per each gram of membrane fraction. Membrane proteins were solubilized using 1% (*w/v*) DDM (ThermoFisher Scientific, Germany) in the presence of 2 mM Pefabloc, 2 mM DTT, and 1 tablet of complete protease Inhibitor/50 ml suspension and incubated, under gentle rotation for 1 h at 4°C. Solubilized proteins were separated from the insoluble material by centrifugation at 192,800 *x g*, for 45 min, 4° C, using a 50.2 Ti rotor. Finally, the supernatant was spiked with imidazole pH 7.5 to reach a final concentration of 25 mM and filtered through a 0.4 µm sterile filter immediately before injecting it onto a 5 ml HisTrap HP (High Purity) affinity column (VWR International), previously charged with Ni and equilibrated in Buffer A (dilution buffer enriched with 0.03% (*w/v*) DDM and 25 mM imidazole pH 8.0). After three washing steps with increasing imidazole concentrations (25 mM, 50 mM, and 100 mM imidazole, respectively) and removing impurities, CcoI was selectively eluted with Buffer A enriched with 0.03% (*w/v*) DDM and 300 mM imidazole. The pooled CcoI fractions were then concentrated using an Amicon filter with 50 kDa cut-off size (Milipore, Germany) and injected onto a size exclusion Superdex 200 16/600 column (GE Healthcare, Germany) pre-equilibrated in Buffer B (25 mM Tris pH 7.5, 10 mM $MgCl_2$, 300 mM NaCl, 5% Glycerol, 2 mM DTT, 0.03% DDM). The monomeric protein peak was pooled, concentrated to 10 mg/ml, as determined using the BCA assay kit (ThermoFisher Scientific, Germany) and directly used for proteoliposome reconstitutions or ATPase assays. All steps described were performed at 4°C.

Liposome Preparation and Proteoliposome Reconstitution

Three lipid mixtures were used to prepare liposomes for CcoI reconstitution: (a) 1 ml *E. coli* polar lipids (Polar), (b) 15 mg/ml *E. coli* polar lipids supplemented with 4 mg/ml phosphatidylcholine (Polar + PC) and (c) a 1 ml mixture of pure lipids (3.5 mg/ml DSPC (18:0 1,2-distearoyl-sn-glycero-3-phosphatidyl-choline), 3.5 mg/ml PE (16,1 1,2-dipalmitoleoyl-sn-glycero-3-phosphatidyl-ethanolamine), 2 mg/ml PG (18:0–18:1 1-stearoyl-2-oleoyl-sn-glycero-3-phospho-(1'-rac-glycerol), 1 mg/ml DGTS (1,2-dipalmitoyl-sn-glycero-3-O-4'-(N,N,N-trimethyl)-homoserine); all obtained from Avanti Polar Lipids, Alabaster, United States). The pure lipid mixture was designed to better mimic the native *R. capsulatus* membrane lipid composition (Imhoff, 1991; Aygun-Sunar et al., 2006). The lipids were dissolved in chloroform and mixed in a round flask. The chloroform was then evaporated using a rotary evaporator operating under a 100–150 mbar vacuum for 1 h, at room temperature. The resulting dried lipid film was hydrated using 2.5 ml liposome buffer (25 mM Tris-HCl pH 7.5, 300 mM KCl) to a final lipid concentration of 10 mg/ml and resuspended for 90 min in the rotary evaporator by rotation, without vacuum. To obtain large unilamellar vesicles, the lipid suspensions were extruded 21 times through a 0.4 µm polycarbonate membrane (Whatman®; Merck, Germany) using a mini-extruder (Avanti Polar Lipids, Alabaster, Unied States). 250 µl aliquots of the different liposomes were flash frozen in liquid nitrogen and stored at −80°C until further use.

For CcoI reconstitution, 250 µl of a chosen liposome suspension were slowly thawed and destabilized by the addition of 50 µl of 10% (*v/v*) Triton X-100, for 1 h at room temperature, prior to protein incorporation. To prepare proteoliposomes with a lipid-to-protein ratio (LPR) of 5:1, 60 µl of pure CcoI (10 mg/ml) were added to detergent-destabilized liposomes. The suspension was incubated for 30 min at room temperature and the detergent was removed using bio-beads (Bio-Rad Laboratories, Germany) and proteoliposome buffer (25 mM Tris–HCl pH 7.5, 300 mM KCl, 5 mM $MgCl_2$), following the supplier instructions. The 2× 1 h incubation with activated bio-beads were performed at room temperature on a rocking platform, while the third incubation step was carried out at 4°C, overnight. The final proteoliposome suspensions were aliquoted and, if not immediately used, flash frozen in liquid N_2 and stored at −80°C.

Solid Supported Membrane Electrophysiology

To determine the ability of CcoI to transport Cu(I), solid-supported membrane (SSM) electrophysiology was employed (Schulz et al., 2008; Grewer et al., 2013; Wacker et al., 2014; Rycovska-Blume et al., 2015; Bazzone et al., 2017; Tadini-Buoninsegni, 2020). All measurements were performed on a SURFE^{2}R-N1 instrument (Nanion Technologies, Munich, Germany). For these experiments, 3 mM diameter gold electrodes were coated with 50 µl of 0.5 mM 1-octadecanethiol in isopropanol, for 45 min at room temperature. Then, 1.5 µl of a lipid suspension (16.5 mg/ml diphytanoyl phosphatidylcholine and 0.28 mg/ml octadecylamine, in *n*-decane; Avanti Lipids) was added and covered in 50 µl of proteoliposome buffer (25 mM Tris-HCl pH 7.5, 300 mM KCl, 5 mM $MgCl_2$). Finally, to establish the sensor unit, 10 µl of liposomes (negative control) or proteoliposomes were added to adsorb onto the hybrid bilayer-coated electrodes by 1 h incubation at room temperature, followed by a 30 min centrifugation step at 2,500 *x g*, 20 °C. Once inside the instrument, the sensor is subject to a rapid flux (100 µl/s) and exchange of solutions (Bazzone et al., 2013, 2017; Wacker et al., 2014). Typically, exchange cycles between a non-activating (NA), activating (A), and again NA-solutions, lasting 2 s each, are applied. The two solutions are ionically equivalent, but the molecular species thought to trigger the electrogenic event is only present in the A-solution while the NA-solution should minimize solution exchange and lipid interaction artifacts, and also brings the system back to baseline (Toyoshima, 2009; Mattle et al., 2015; Smith et al., 2015; Bazzone et al., 2017; Gantner, 2017). In our case, on top of containing a stabilizing buffer for the protein and enough salts to reduce artifacts (Bazzone et al., 2013, 2017), the NA- and A-solutions also contained $MgCl_2$ (to stabilize ATP), cysteine (to maintain the Cu(I) oxidation state and deliver it to the ATPase; Yang et al., 2007) and ascorbic acid to reduce Cu(II) to Cu(I).

In SSM-electrophysiology, the establishment of a compound membrane between the adsorbed vesicles and the hybrid bilayer on the gold electrode surface (the measuring electrode) allows recording transient currents *via* capacitive coupling (Bazzone et al., 2017). In brief, the rapid exchange of solutions establishes a membrane potential across the vesicle membrane that acts as driving force for protein-mediated electrogenic events. Typically, the analysis of such transient currents is done upon perfusion of the system from a NA- to A-solution. The peak of the transient reflects the number of charges that participate in the electrogenic event and its decay in a function of the electrogenic event itself and the amount of protein that is present in the system (Bazzone et al., 2017; Gantner, 2017). The transient currents were initially analyzed using the SURFE2R-N1 instrument specific analysis software (Nanion) and further processed in OriginPro 2020 and Excel.

ATPase Assay

The ATPase activity of CcoI was determined by using ^{33}P-ATP (Hartmann Analytic, Braunschweig, Germany) as substrate (Wenk et al., 2012). Purified CcoI or its variants were incubated with 10–100 µm ^{33}P-ATP solution in a final volume of 20 µl reaction buffer (50 mM Tris pH 7.5, 300 mM NaCl, 10 mM MgCl2, 0.03% DDM, 10% glycerol). The amount of protein to be used was determined by titration of 1–16 µM final protein concentration in the reaction mixture. To measure the effect of Cu(I) on the ATPase activity of CcoI, Cu(II) was reduced to Cu(I) with 10 mM ascorbic acid and titrated to the reaction mixture. The reaction was incubated for 15 min at 35° C, with gentle shaking. The released inorganic phosphate was separated from the reaction mixture by mixing with 800 µl charcoal solution (20 mM phosphoric acid, 5% charcoal). After 10 min incubation on ice, the charcoal was pelleted in a precooled table-top centrifuge for 12 min at 17,130 *x g* maximum speed. To determine the amount of hydrolyzed $^{33}PO_4$, 200 µl of the supernatant was mixed with 3 ml scintillation liquid and measured with a scintillation counter (PerkinElmer Life Sciences, Waltham, United states). As controls, blank measurements were performed without protein and subtracted from the experimental values.

Preparation of ICM and Blue Native PAGE Analyses

For preparation of inverted cytoplasmic membranes (ICMs) of *R. capsulatus* strains, previously published protocols were used (Koch et al., 1998; Pawlik et al., 2010). Native complexes were investigated on Blue Native (BN) PAGE as described in (Utz et al., 2019) and antibodies against c-Myc (clone 9E10, Sigma Aldrich) and polyclonal antibodies against CcoN (Koch et al., 1998) were used.

cbb_3-Cox Activity Assays (DMPD and TMPD)

For dimethyl-*p*-phenylendiamine (DMPD) oxidation (Marckmann et al., 2019), 10^8 cells with an OD_{685} 0.8–1 were collected from each strain and mixed with 1 mM DMPD in Buffer D (25 mM Tris pH 7.5, 150 mM NaCl) to a final volume of 1 ml. DMPD oxidation was monitored photometrically at 554 nm for at least 4 min. The DMPD oxidation in wild type MT1131 was set to 100% cbb_3-Cox activity. The TMPD (*N, N, N, N*-tetramethyl-*p*-phenylendiamine) oxidation assay for determining cbb_3-Cox activity was performed using ICMs. 10 µg of total protein in ICMs were mixed with 1 mM TMPD and adjusted to a final volume of 1 ml with Buffer D. TMPD oxidation was monitored photometrically for at least 30 s at 611 nm. Cox-independent TMPD oxidation was monitored in the presence of 200 µM sodium-cyanide, a specific inhibitor of cbb_3-Cox, and subtracted from the cyanide-free sample. Data processing was performed as described for the DMPD assay.

Reproducibility Statement

All experiments were performed multiple times with independent biological and technical replicates as indicated in the legends to the figures. The mean values and standard deviations (SD) were calculated using the *Excel* and *Graphpad prism* softwares. For statistical analyses, a Student unpaired two-way t-test with the Satterthwaite correction was performed (Welch-test).[1]

[1]https://matheguru.com/

Probability values (values of p) are indicated in the legends to the Figures. A value of $p > 0.05$ was generally considered to be not significant (n.s.). To obtain statistically meaningful SSM data, a minimum of five sensors were analyzed per proteoliposome batch and at least two proteoliposome preparations for a given protein/variant were used. Reported peak current values represent the average of a minimum of three measurements per sensor and the error bars represent the standard deviation of the mean. At the end of a given set of experiments, the stability of the protein used was confirmed by comparing the final electrogenic signal obtained to that recorded under the initial conditions. Only signal losses less than 20% were accepted.

RESULTS

The P_{1B}-Type ATPase CcoI Drives Electrogenic Cu(I) Efflux For cbb_3-Cox Maturation

CcoI shares high sequence similarity with P_{1B}-type ATPases, which constitute a conserved family of ATP-dependent Cu(I) export proteins (Arguello et al., 2007; Smith et al., 2014). CcoI contains four putative MBSs (**Figure 1; Supplementary Figure S1**). The cytosolically exposed N-terminus contains two MBSs: the glutaredoxin-like CPAC motif (N-MBS1; Hatori and Lutsenko, 2016) is present in CcoI-like P_{1B}-type ATPases, but absent in CopA-like P_{1B}-type ATPases (**Figure 1**), whereas the CAVC motif (N-MBS2) is conserved in both CopA- and CcoI-like ATPases and is homologous to the Cu-binding motif of the CopZ-like copper chaperones (Utz et al., 2019; Andrei et al., 2020). Two other MBSs are present in the membrane-integral domain of CcoI (**Figure 1**). The CPC motif (TM-MBS1) is located in the transmembrane helix (TM) 4 and the NMS motif (TM-MBS2) is formed by an asparagine residue from TM5 together with methionine and serine residues from TM8. Both TM-MBSs are conserved among Cu-transporting P_{1B}-ATPases (Arguello et al., 2007; Smith et al., 2014) and are necessary to drive the outward transport of copper (Mandal et al., 2004).

Cu transport by CopA-like P_{1B}-type ATPases has been extensively studied using different methods (Gonzalez-Guerrero et al., 2010; Völlmecke et al., 2012; Drees et al., 2015; Abeyrathna et al., 2020; Tadini-Buoninsegni, 2020), but similar information on CcoI-type ATPases is limited. Cu transport by CopA1 and CopA2 of *Pseudomonas aeruginosa* has been determined by using *E. coli* expressed proteins and monitoring ^{64}Cu accumulation in membrane vesicles (Gonzalez-Guerrero et al., 2010). This allowed for identifying important kinetic differences between the two types of Cu transporting ATPases (Raimunda et al., 2011). Yet, the activity of a CopA2-type ATPase has not been studied so far using a reconstituted system devoid of any other transporter, which might interfere with data interpretation.

Earlier work demonstrated that the absence of CcoI results in an inactive and unstable cbb_3-Cox (Koch et al., 2000; Utz et al., 2019). The cbb_3-Cox deficiency in the Δ*ccoI* strain could not be complemented by increasing the external Cu concentration in the medium, or by expressing a plasmid-borne copy of *copA*, encoding for the second Cu-exporting P_{1B}-type ATPase present in the *R. capsulatus* membrane (Ekici et al., 2014; Utz et al., 2019). In order to validate the hypothesis that CcoI is involved in the transport of Cu for cbb_3-Cox maturation, we employed solid-supported membrane electrophysiology. This technique allows monitoring protein-mediated electrogenic events in a controlled *in vitro* setup (Wacker et al., 2014; Bazzone et al., 2017). Thus, *R. capsulatus* CcoI containing a C-terminal Myc-His tag was expressed in *E. coli* C43(DE3) cells, purified to homogeneity (**Supplementary Figure S2**), and reconstituted into liposomes (CcoI-LPs) at a 5:1 lipid-toprotein ratio (LPR). After adsorption of the CcoI-LPs to the sensor surface, the electrogenic response of the protein was monitored as transient currents established over time. The use of purified CcoI, reconstituted into liposomes, offers the unique advantage of monitoring its Cu translocation properties in the absence of any other protein.

To optimize the background signal-to-noise ratio of the SSM measurements and minimize any unspecific interaction of Cu(I) with the polar head group of the lipids, various lipid and buffer components were tested (**Supplementary Figure S3**). Three lipid mixtures were used to generate liposomes (LPs): (a) *E. coli* polar lipids (Avanti Polar Lipids) (b) *E. coli* polar lipids supplemented with the neutral phospholipid PC (phosphatidylcholine) in a 3:2 ratio, and (c) a mixture of pure phospholipids, containing 18:0 PC (DSPC; 1,2-distearoyl-sn-glycero-3-phosphocholine), 16:1 PE (1,2-dipalmitoleoyl-sn-glycero-3-phosphoethanolamine), 18:0–18:1 PG (1-stearoyl-2-oleoyl-sn-glycero-3-phospho-(1'-rac-glycerol; sodium salt)), DGTS (1,2-dipalmitoyl-sn-glycero-3-O-4'-(N,N,N-trimethyl)-homoserine) in a 2:3.5:3.5:1 ratio.

The best experimental conditions were obtained when the vesicles were prepared using pure lipids (**Supplementary Figures S3A, S4**) and the non-activating (NA)-solution was composed of 25 mM Tris-HCl, pH 7.4, 300 mM KCl, 5 mM $MgCl_2$, 10 mM ascorbic acid and 20 mM cysteine (plus 300 μM $CuCl_2$ or 250 μM ATP, as indicated). To investigate the effect of ATP in the presence of Cu(I), both NA- and activating (A)-solutions contained Cu, while ATP was only present in the A-solution. Likewise, to probe the effect of Cu in the presence of ATP, both solutions contained ATP, but only the A-solution had Cu. Under these conditions, when CcoI-LPs were subject to a concentration jump of ATP (250 μM) in the presence of Cu (300 μM), a transient current with an average amplitude of 1.3 nA was recorded (**Figure 2A**, black trace), in line with a Cu(I) translocation event. In contrast, a control experiment using LPs subjected to the same cycle of solutions yielded a much smaller increase in amperage (**Figure 2A**, red trace), reflecting residual interactions of Cu(I) or ATP with the lipid environment. In the converse experiment, i.e., when CcoI-LP were flushed with A-solution containing 300 μM Cu(I) in a background of 250 μM ATP, similar current increases were also detected with only minor signals when LPs were used (**Figure 2B**). On average, the electrogenic signals observed for both the ATP-induced or Cu(I)-induced transient currents showed comparable amplitudes (**Supplementary Figure S5A**).

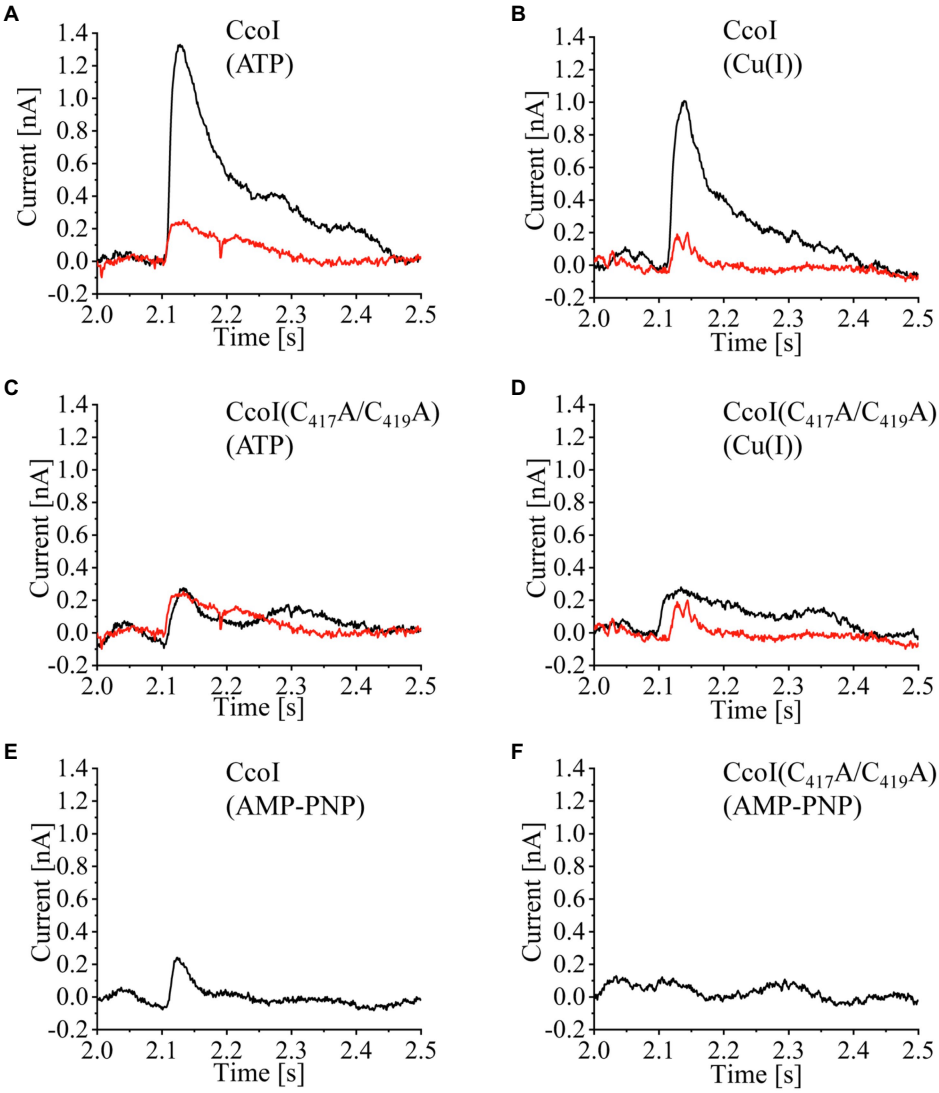

FIGURE 2 | ATP-dependent Cu(I) translocation by CcoI. Wild-type CcoI **(A,B,E)**, and the CcoI($C_{417}A/C_{419}A$) variant with a mutated TM-MBS1 **(C,D,F)**, were reconstituted at a 5:1 LPR (lipid-to-protein ratio) in liposomes (LP) prepared using a mixture of DSPC(1,2-distearoyl-sn-glycero-3-phospho-choline), POPE (1,2-dipalmitoleoyl-sn-glycero-3-phosphatidyl-ethanolamine), SOPG (1-stearoyl-2-oleoyl-sn-glycero-3-phospho-(1'-rac-glycerol)), and DGTS (1,2-dipalmitoyl-sn-glycero-3-O-4'-(N,N,N-trimethyl)-homoserine) at a 2:3.5:3.5:1 ratio. Representative current traces are shown. These traces were obtained when CcoI-LP (CcoI reconstituted in liposomes, black line) or LP (liposomes, red line) were adsorbed to a sensor unit and subsequently exposed to concentration jumps of 250 μM ATP in the presence of 300 μM Cu(I) **(A,C)**. In addition, traces of concentration jumps of 300 μM Cu(I) in the presence of 250 μM ATP were recorded **(B,D)**. **(E)** Same setup as in **(A)**, except that 250 μM of the non-hydrolysable ATP analog AMP-PNP was used. **(F)** As in **(E)**, but the CcoI($C_{417}A/C_{419}A$) variant was analyzed. All signals were recorded using a SURFE^{2}R-N1 (Nanion Technologies, Munich, Germany).

No significant responses were recorded when the CcoI($C_{417}A/C_{419}A$) variant was reconstituted into LPs (**Figures 2C,D**). In this variant, alanine residues replaced the conserved cysteine residues from the Cu-binding TM-MBS1 motif. As expected, CcoI($C_{417}A/C_{419}A$)-LPs did not show any electrogenic response upon activation by ATP (**Figure 2C**) or Cu(I) (**Figure 2D**). Similarly, when CcoI-LPs or CcoI($C_{417}A/C_{419}A$)-LPs were activated with Cu(I) in the presence of the non-hydrolysable ATP analogue AMP-PNP, there was no electrogenic response, demonstrating that ATP hydrolysis is required for Cu(I) translocation by CcoI (**Figures 2E,F**). Additional controls included the activation of CcoI-LPs with ATP in a Cu(I) background containing the Cu(I)-chelator bathocuproinedisulfonic acid (BCS; 5 mM) or in a background of 300 μM Co(II) ions. In all these cases, the recorded transient currents were only residual (**Supplementary Figures S5B, S5C**).

Therefore, the overall data are consistent with an ATP-driven Cu(I) translocation by CcoI, and substantiate the earlier hypothesis that the absence of cbb_3-Cox activity in the Δ*ccoI* strain is due to an impaired Cu-transport from the cytosol to the periplasm (Koch et al., 1998, 2000; Kulajta et al., 2006).

High Cu(I) but Not Cu(II) Concentrations Inhibit ATPase Activity of CcoI

The N-terminal metal binding site of CopA-like ATPases is suggested to serve as a Cu sensor that regulates the ATPase activity (Huster and Lutsenko, 2003; Mandal and Arguello, 2003; Wu et al., 2008). Considering the presence of two distinct N-MBSs in CcoI-like ATPases (**Figure 1**), the ATPase activity of detergent-solubilized, purified CcoI in the presence of different Cu(I) concentrations was analyzed by monitoring ^{33}P-γ-ATP hydrolysis. The data revealed a Cu(I)-concentration-dependent decrease of the ATPase activity. Even at the lowest concentration tested (2 μM), the ATPase activity was reduced by approx. 20% (**Figure 3A**). In contrast to Cu(I), the addition of Cu(II) up to a concentration of 32 μM had no drastic effect on the ATPase activity of CcoI (**Figure 3A**). As Cu(I) was generated and maintained in its reduced state by the presence of ascorbic acid, the influence of equivalent ascorbic acid concentrations were also tested, but concentrations up to 4 mM did not significantly influence the ATPase activity (**Figure 3B**).

Cu(I)-dependent inhibition of the ATPase activity was also observed for *Thermotoga maritima* CopA, but this required higher Cu(I) concentrations, and likely does not involve any MBSs (Hatori et al., 2008). The possible involvement of the CcoI-MBSs in Cu(I) mediated ATPase inhibition was analyzed by expressing three plasmid-borne *ccoI* mutant alleles in the Δ*ccoI* strain. The first CcoI variant contained alanine replacements in the glutaredoxin-like N-MBS1 [*ccoI*($C_{25}A/C_{28}A$)], the second had similar replacements in the CopZ-like N-MBS2 [*ccoI*($C_{57}A/C_{60}A$)], and the third was mutated in the TM-MBS1 [*ccoI*($C_{417}A/C_{419}A$)], which was also used in the SSM experiments (**Figure 2**). These mutated CcoI variants were purified to homogeneity and their ATPase activity was analyzed.

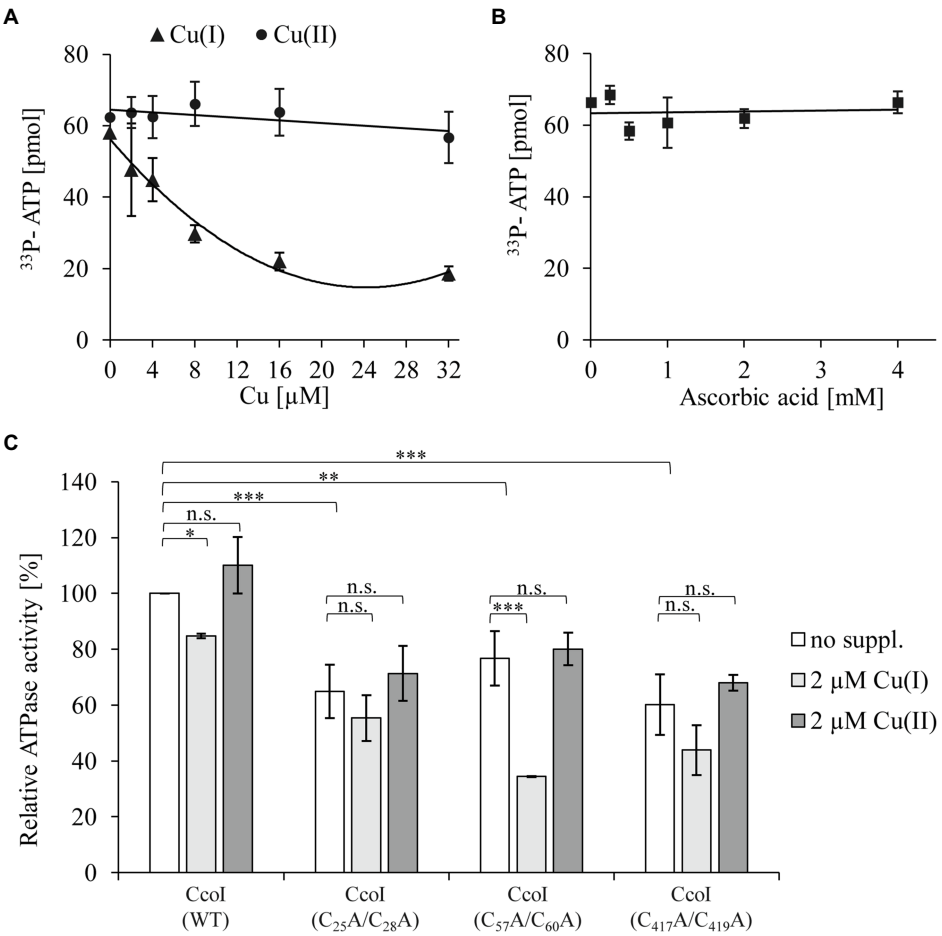

FIGURE 3 | The ATPase activity of CcoI is inhibited by Cu(I) **(A)** The ATPase activity of CcoI was determined by quantifying the hydrolysis of ^{33}P-γ-ATP in the presence of 1 μM purified CcoI in detergent and at increasing concentrations of Cu(I) (▲, with ascorbic acid) or Cu(II) (●, without ascorbic acid). Released ^{33}P was quantified *via* a scintillation counter. Error bars represent the standard deviation (SD) of three technical replicates. **(B)** As in A, but the ATPase activity of purified CcoI was analyzed in the presence of ascorbic acid concentrations (■) equivalent to the ones used in **(A)** for Cu(I). **(C)** The influence of the different CcoI metal binding sites (MBSs) to the ATPase activity in the absence (no suppl., white bars) and presence of either 2 μM Cu(I) (light grey bars) or 2 μM Cu(II) (dark grey bars). The amount of hydrolyzed ATP by wild type CcoI in the absence of added Cu was set to 100% and the relative ^{33}P release was calculated. Error bars represent the standard deviation (SD) of the mean values of three technical replicates. Statistical analyses were performed with the Satterthwaite corrected unpaired Students t-test. *refers to values of $p \leq 0.05$; **to values of $p \leq 0.01$; ***to values of $p \leq 0.001$ and (n.s.) to not significant.

The N-MBS1 mutation reduced the ATPase activity by approx. 30% (**Figure 3C**), compared to the wild type CcoI activity. This activity was further reduced by approx. 20% in the presence of Cu(I) (**Figure 3C**), similar to the inhibitory effect on wild type CcoI. The N-MBS2 mutation also reduced the ATPase activity by approx. 25%, compared to the wild type, but in this mutant, the addition of Cu(I) had a more pronounced inhibitory effect as it reduced the ATPase activity by 50%. The TM-MBS1 also showed an approx. 30% reduction of the ATPase activity, which dropped further in the presence of Cu(I). The inhibitory effect of Cu(I) on the TM-MBS1 mutant was comparable to that observed for wild type CcoI and the N-MBS1 mutant. As observed for the wild type (**Figures 3A,C**), the addition of 2 μM Cu(II) did not significantly influence the ATPase activity in any of the CcoI mutants.

The ATPase activity of the TM-MBS1 mutant, which does not translocate Cu(I) based on the SSM experiments (**Figure 2**), indicates that ATP hydrolysis is not strictly coupled to Cu(I) binding or translocation. The data further show that the ATPase activity of CcoI is inhibited by already rather low Cu(I) concentrations, and that Cu(I) inhibition is more pronounced in the absence of N-MBS2. This finding suggests that, unlike CopA (Hatori et al., 2008), Cu(I) inhibition of CcoI activity is influenced by the MBSs, and that the ATPase activity of CcoI is particularly sensitive to Cu(I) in the absence of the N-MBS2. Note that the SSM experiments with CcoI-LPs were performed at Cu(I) concentrations that inhibited the ATPase activity of purified CcoI in detergent (**Figures 2, 3**). The lack of inhibition in the SSM experiments is probably explained by the presence of 20 mM cysteine in the SSM buffers, which act as a strong Cu chelator and Cu donor (Pujol et al., 2011).

Dissecting the Contributions of the CcoI Metal Binding Sites to cbb_3-Cox Activity

In the absence of CcoI, cbb_3-Cox maturation is inhibited, resulting in very low amounts of the catalytic subunit CcoN and only background cbb_3-Cox activities (Koch et al., 2000; Utz et al., 2019). This indicates that cbb_3-Cox is a primary target of CcoI-mediated Cu(I) translocation. For dissecting further the contribution of the different MBSs in CcoI for cbb_3-Cox activity in *R. capsulatus* cells, NADI-staining was performed as semi-quantitative assay for cbb_3-Cox activity. In the presence of an active cbb_3-Cox, α-naphthol and DMPD are converted to indophenol blue, which is detectable as blue color in *R. capsulatus* colonies (Koch et al., 1998; **Figure 4A**). Wild type MT1131 colonies turned blue within seconds ($NADI^+$), while the Δ*ccoI* strain did not show any color reaction (i.e., $NADI^-$), even on Cu-supplemented media (10 μM or 25 μM additional Cu; **Figure 4A; Supplementary Figure S6A**). Expressing a plasmid-borne copy of *ccoI* in the Δ*ccoI* strain restored the NADI reaction (i.e., cbb_3-Cox activity).

The *ccoI*($C_{25}A/C_{28}A$) allele containing the mutated N-MBS1 in the Δ*ccoI* strain, resulted in a $NADI^{slow}$ phenotype on media without Cu supplementation, and in a $NADI^+$ phenotype on Cu-supplemented media (**Figure 4A**). In contrast, the *ccoI*($C_{57}A/C_{60}A$; N-MBS2 mutant) allele failed to restore cbb_3-Cox activity on media without Cu supplementation ($NADI^-$), but these cells showed a $NADI^+$ phenotype on Cu-supplemented media (**Figure 4A**). The expression of the *ccoI*($C_{417}A/_{419}A$) allele in the Δ*ccoI* strain did not support cbb_3-Cox activity (i.e., $NADI^-$), in agreement with its inability to transport Cu (**Figure 2**). Immune detection using α-Myc antibodies on whole cells expressing the different *ccoI* versions, revealed reduced amounts of all three mutated CcoI variants in comparison to wild type CcoI (**Figure 4B; Supplementary Figure S6B**), possibly indicating their reduced stability. Importantly, the addition of Cu did not significantly change the levels of wild type CcoI or its variants (**Figure 4B; Supplementary Figure S6B**). The $NADI^-$ phenotype of Δ*ccoI* strains expressing the different *ccoI* alleles with mutated MBS was validated by monitoring the presence of the Cu-containing catalytic subunit CcoN of cbb_3-Cox *via* immune detection. CcoN was readily detectable in wild type membranes, and basically absent in Δ*ccoI* membranes (**Figure 4C**). When wild type CcoI was expressed in the Δ*ccoI* strain, the CcoN levels became comparable to the wild type. However, upon expression of the N-MBS mutant alleles, only a weak CcoN band could be detected (**Figure 4C; Supplementary Figure S6C**), supporting the results from the NADI staining in the absence of additional Cu supplementation. CcoN was basically absent when the TM-MBS1 mutant allele was tested in the Δ*ccoI* strain.

The semi-quantitative analyses *via* NADI staining were confirmed by DMPD-oxidation based on quantitative photometric cbb_3-Cox activity assays using whole cells (**Figure 4D**). The activity in wild type (MT1131) cells grown without additional Cu was set to 100% and this value increased by approx. 30% when cells were grown in the presence of additional 25 μM Cu. No activity was observed in the cbb_3-Cox mutant strain GK32 (*ΔccoNO*), which contains a chromosomal deletion of the *ccoN* and *ccoO* structural genes of cbb_3-Cox (Koch et al., 1998). The Δ*ccoI* strain exhibited less than 10% of the wild type activity, which increased to approx. 30% when cells were grown in the presence of additional Cu (10 μM Cu). This is different from the previous results based on O_2-consumption assays using purified membranes, which showed no influence of Cu supplementation to cbb_3-Cox activity in the Δ*ccoI* strain (Koch et al., 1998; Kulajta et al., 2006). Whether this is related to the different assay conditions or to cbb_3-Cox independent DMPD oxidation was not further evaluated. Almost wild-type cbb_3-Cox activity was detected in the Δ*ccoI* strain expressing the plasmid-borne *ccoI* copy. In the Δ*ccoI* strain expressing the *ccoI*($C_{25}A/C_{28}A$) allele, approx. 25% of the wild type activity was detected, which increased to full wild type activity in Cu-supplemented (10 μM Cu) media. *CcoI*($C_{57}A/C_{60}A$) expressing cells also showed approx. 25% of wild type activity without Cu supplementation, but the addition of Cu only increased the activity to approx. 60% of the wild type. Finally, the *ccoI*($C_{417}A/_{419}A$) allele only allowed for 2% of the wild type activity, which was increased to approx. 10% when cells were grown in the presence of additional Cu (**Figure 4D**).

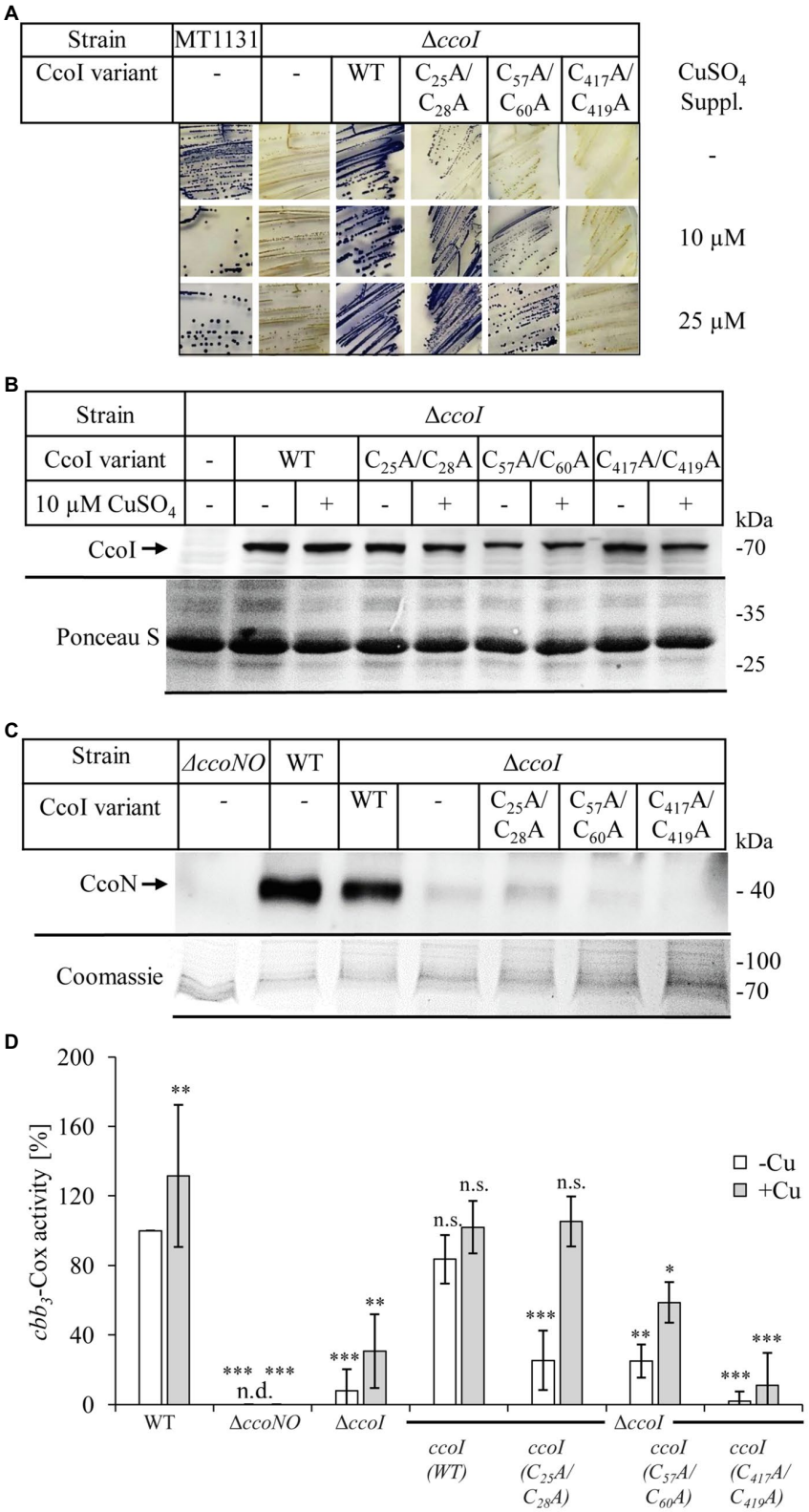

FIGURE 4 | Distinct effects of the CcoI MBSs on cbb_3-Cox activity. **(A)** NADI staining of wild type *R. capsulatus* MT1131 or the Δ*ccoI* strain, expressing different plasmid-encoded *ccoI* variants. The strains were grown semi-anaerobically on MPYE media, supplemented with 10 µM, 25 µM $CuSO_4$ or without copper

(continued)

FIGURE 4 | supplementation (–). 0.2% *L*-ara was added to the strains that carried a *ccoI* plasmid-borne copy to allow expression. Images showing the entire agar-plates are displayed in **Supplementary Figure S6A**. **(B)** 10^8 cells of the indicated strains grown in the presence of 10 μM $CuSO_4$ or without copper supplementation were TCA precipitated, separated on a 12% SDS-PAGE and immune-blotted with antibodies against the Myc-tag (upper panel). As a loading control, the lower part of the same membrane was stained with Ponceau S (lower panel). Quantification of three biological replicates is shown in **Supplementary Figure S6B**. **(C)** Cytoplasmic membranes of the different *R. capsulatus* strains were isolated and 10 μg of total protein were separated on a 16.5% SDS-Tris-Tricine polyacrylamide gel, immune-blotted and decorated with antibodies against CcoN (upper panel). As a loading control, the upper part of the gel was stained with Coomassie brilliant blue (lower panel). Quantification of three biological replicates is shown in **Supplementary Figure S6C**. **(D)** cbb_3-Cox activity was determined *via* a DMPD oxidation assay. For each strain, 10^8 cells grown to exponential phase were mixed with 1 mM DMPD and monitored for 4 min spectrophotometrically at 554 nm. The WT activity was set to 100% and the relative activities of the other strains were calculated. The bars represent the mean values of three biological replicates with three technical repetitions each and the standard deviation is indicated by error bars ($n = 9$). Statistical analyses were performed with the Satterthwaite corrected unpaired two-sided Student t-test, using the activity of the wild type grown in the absence of additional Cu as reference.*refers to values of $p \leq 0.05$; **to values of $p \leq 0.01$, and ***to values of $p \leq 0.001$.

Overall data indicated that the function of the different MBSs in CcoI is dependent on external Cu availability. While the inactivation of the glutaredoxin-like N-MBS1 can be fully restored by Cu supplementation, the CopZ-like N-MBS2 yielded an intermediate phenotype that could only be rescued partially by Cu addition. Considering that the CopZ-like N-MBS2 is conserved between CcoI and CopA, while the presence of the N-MBS1 is a particular feature of the high-affinity CcoI, these findings suggested that N-MBS1 might be important for receiving Cu from an alternative Cu donor different than CopZ, such as glutaredoxin or even glutathione (Maghool et al., 2020; Stewart et al., 2020).

The N-Terminal Metal Binding Sites Are Important Under Low Intracellular Copper Concentrations

The partial or full complementation of cbb_3-Cox activity in the N-MBS mutants by Cu supplementation of the medium is likely due to increased intracellular Cu concentrations, which might exceed those usually observed in bacteria (Heldal et al., 1985; Rae et al., 1999; Ekici et al., 2014). Recent data indicated that deleting CopZ or CopA also increases the intracellular Cu concentrations (Utz et al., 2019). Thus, whether or not the two CcoI N-MBSs mutants could support cbb_3-Cox assembly in the absence of CopZ or CopA was analyzed.

The CcoI variants were conjugated into a Δ*ccoI*Δ*copZ* strain and the cells were grown on MPYE medium without Cu supplementation and with 10 μM or 25 μM $CuSO_4$ addition. The Δ*ccoI*Δ*copZ* strain showed a $NADI^-$ phenotype independent of Cu supplementation (**Figure 5A**) and was rescued to $NADI^+$ phenotype with a plasmid-borne copy of *ccoI*, supporting the earlier observation that CopZ is involved in, but not essential for cbb_3-Cox assembly (Utz et al., 2019). This is also confirmed by the $NADI^+$ phenotype of the Δ*copZ* single mutant (Utz et al., 2019). When the *ccoI*($C_{25}A/C_{28}A$) or the *ccoI*($C_{57}A/C_{60}A$) alleles were expressed in the Δ*ccoI* strain, the external Cu-dependent cbb_3-Cox activities were observed as before (**Figures 4A, 5A**). However, the expression of the *ccoI*($C_{25}A/C_{28}A$) allele in the Δ*ccoI*Δ*copZ* double mutant allowed for a weak $NADI^+$ even in the absence of additional Cu (**Figure 5A**). The *ccoI*($C_{57}A/C_{60}A$) allele started to restore the NADI phenotype of the Δ*ccoI*Δ*copZ* double mutant strain at 10 μM $CuSO_4$ or above (**Figure 5A; Supplementary Figure S7**). As a control, expression of the *ccoI*($C_{417}A/C_{419}A$) allele did not rescue the cbb_3-Cox activity of the Δ*ccoI*Δ*copZ* strain, even in the presence of Cu supplementation, indicating that the rescue phenotypes observed were specific to the N-MBS mutants of CcoI.

When CopA is missing, the increase of intracellular Cu concentration is even more pronounced than that seen in the Δ*copZ* strain (Utz et al., 2019). When the CcoI N-MBS mutant alleles were expressed in the Δ*ccoI*Δ*copA* double mutant, both of these alleles were able to rescue cbb_3-Cox activity even without any Cu supplementation (**Figure 5B**), while the TM-MBS1 mutant could not regain any cbb_3-Cox activity (**Figure 5B; Supplementary Figure S7**).

In summary, these data indicate that increasing the intracellular Cu concentration due to the absence of the CopZ-CopA-mediated Cu export pathway is sufficient to compensate for the absence of the N-MBSs in CcoI, while the inactivation of TM-MBS1 cannot be bypassed by even large amounts of extracellular Cu supplementation. The different responses of the CcoI N-MBS1 and N-MBS2 mutants to external Cu addition both in the presence and absence of CopZ support the idea that the two N-MBSs have distinct roles in CcoI function.

The CcoI-SenC Interaction Is Required For cbb_3-Cox Activity

Due to the toxicity of free Cu, most cellular Cu is chelated by dedicated cytosolic and periplasmic Cu chaperones (Andrei et al., 2020), which transiently interact with P_{1B}-type ATPases to deliver or receive Cu (Gonzalez-Guerrero et al., 2009; Fu et al., 2013; Padilla-Benavides et al., 2014). A transient interaction of CopZ with CcoI on the cytoplasmic side of the membrane was recently observed (Utz et al., 2019). However, whether CcoI also interacts with periplasmic chaperones, like SenC or PccA, remains unknown. For detecting possible contacts between CcoI and SenC or PccA, BN-PAGE analyses were performed, followed by immune detection using c-Myc antibodies. The data indicated that wild-type CcoI runs as a stable entity at approx. 150 kDa (**Supplementary Figure S8A**), which would be consistent with a CcoI dimer. Dimerization of P_{1B}-type ATPases has been observed before for ATP7B in humans and for CopA in *A. fulgidus* (Jayakanthan et al., 2017). However, when CcoI-containing membranes were solubilized with SDS (instead of DDM) prior to BN-PAGE, the 150 kDa band remained intact (**Supplementary Figure S8B**), suggesting that it rather reflected a CcoI monomer. Determining the exact size of a protein complex *via* BN-PAGE is difficult and many proteins/

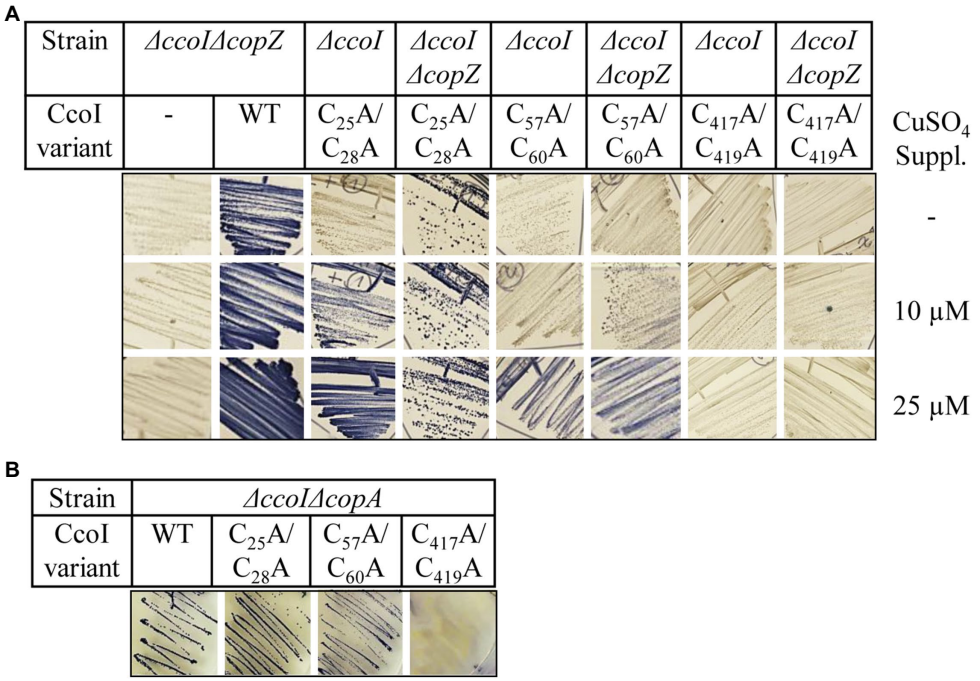

FIGURE 5 | The cytoplasmic copper concentration influences metal acquisition by CcoI. **(A)** NADI staining of different *R. capsulatus* strains expressing either wild type *ccoI* from a plasmid (WT) or the indicated variants. Cells were grown on MPYE plates in the presence of 10 μM or 25 μM $CuSO_4$ or without copper supplementation. **(B)** NADI staining of the *R. capsulatus* Δ*ccoI*Δ*copA* double-knock-out expressing different *ccoI* alleles. Images showing the entire agar-plates are displayed in **Supplementary Figure S7**.

protein complexes show aberrant migrations on BN-PAGE due to the binding of DDM and Coomassie (Heuberger et al., 2002; Kulajta et al., 2006). The 150 kDa band was also observed in membranes of the Δ*ccoI* strain expressing the modified MBS alleles of CcoI (**Supplementary Figure S8A**) while it was absent in Δ*ccoI* membranes. Upon Cu supplementation, additional weaker bands became visible in all strains at 250 kDa, 400 KDa, and 600 kDa (**Supplementary Figure S8A**). However, these entities were also visible in the Δ*senC* and Δ*pccA* strains and antibodies against SenC or PccA do not recognize any of them (data not shown), suggesting that SenC and PccA are not present in these complexes.

Our earlier findings demonstrated that the periplasmic chaperone SenC is crucial for cbb_3-Cox assembly at low Cu concentrations as its absence abolishes almost completely cbb_3-Cox activity (Lohmeyer et al., 2012; Trasnea et al., 2016, 2018). SenC was also shown to directly interact with cbb_3-Cox (Lohmeyer et al., 2012). In contrast, deleting PccA reduces cbb_3-Cox activity only by 30% and the corresponding strain retains its $NADI^+$ phenotype (Trasnea et al., 2016). We reasoned that if SenC serves as a periplasmic Cu acceptor for the CcoI-transported Cu, then a CcoI-SenC fusion protein should facilitate Cu transfer to cbb_3-Cox. Such an approach has been employed before for monitoring electron-transfer reactions (Lee et al., 2008). A CcoI-SenC fusion protein was therefore constructed in which the C-terminus of CcoI was fused in-frame with the N-terminal TM of SenC. As controls, the TM-MBS1 of CcoI, and the Cu-binding site of SenC were mutated in two separate CcoI-SenC fusion constructs, generating the *ccoI(M)-senC and ccoI-senC(M)* alleles, respectively (**Figure 6A**). The wild type fusion construct and its mutant variants were expressed in the $NADI^-$ Δ*ccoI* and Δ*senC* strains and their NADI phenotypes were monitored. The CcoI-SenC fusion protein was able to rescue both the Δ*ccoI* and Δ*senC* strains to $NADI^+$ (**Figure 6B**), demonstrating that this entity is produced in an active form in these strains. Conversely, the *ccoI(M)-senC* allele failed to rescue the Δ*ccoI* strain, and similarly, the *ccoI-senC(M)* allele failed to rescue the Δ*senC* strain (**Figure 6B**), indicating that the CcoI-SenC fusion protein is fully functional only when the Cu binding sites in both proteins are intact. The functionality of the CcoI-SenC fusion furthermore supports their close interaction and the possibility of a direct Cu transfer from CcoI to SenC.

Although not essential for cbb_3-Cox assembly, PccA can exchange Cu(I) with SenC, suggesting that it might also cooperate with SenC for Cu transfer to cbb_3-Cox, at least under certain conditions. Thus, the CcoI-SenC fusion constructs were also tested in a Δ*senC*Δ*pccA* double mutant, which is $NADI^-$ due to the absence of SenC. As expected, expression of the wild type CcoI-SenC fusion protein restored the $NADI^+$ phenotype in the Δ*senC*Δ*pccA* strain, while that of the *ccoI-senC(M)* allele was unable to do so (**Figure 6C**), showing that the fusion protein was also active in a strain where a native CcoI was also present. In summary, these data suggest that a CcoI-SenC interaction is critical for cbb_3-Cox assembly and that it likely naturally occurs in *R. capsulatus* membranes.

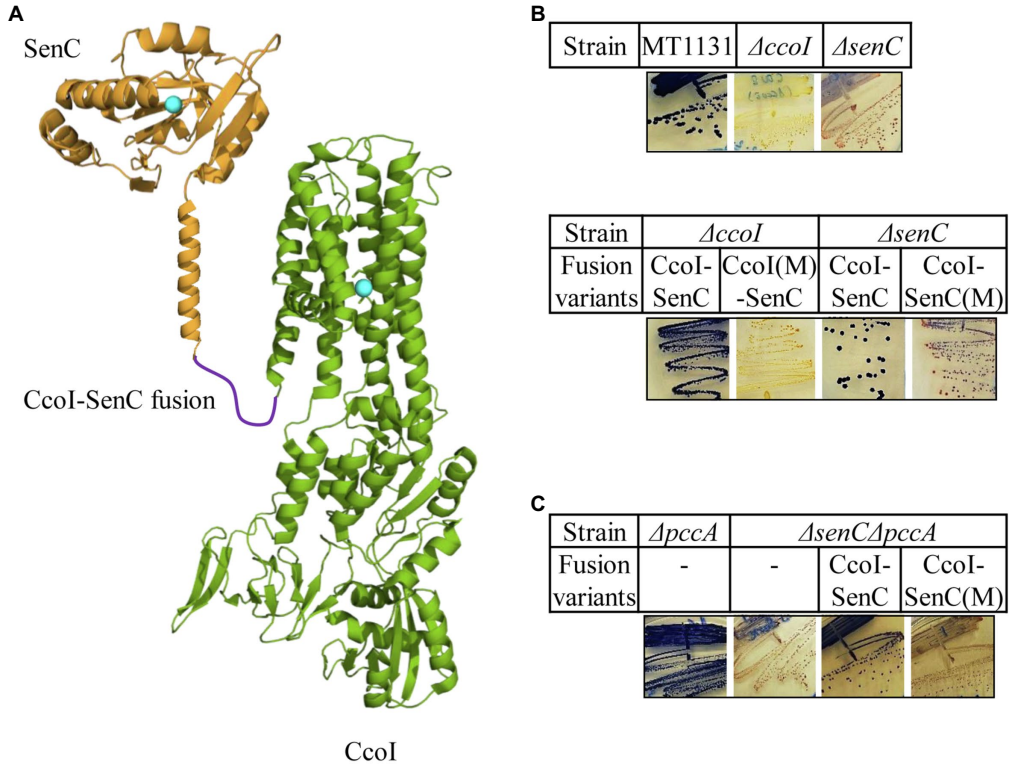

FIGURE 6 | A CcoI-SenC fusion protein is sufficient for Cu delivery to *cbb*$_3$-Cox. **(A)** Cartoon showing the genetically fused CcoI-SenC fusion protein, using known structures of the SenC-homologue ScoI (PDB 4WBR) and of CopA (PDB 3RFU). The Cu binding site in SenC and the TM-MBS1 of CcoI are indicated by turquoise spheres. **(B)** NADI staining of the wild type MT1131 and the Δ*ccoI* and Δ*senC* single mutants (upper panel), and the Δ*ccoI* or Δ*senC* single mutants expressing different CcoI-SenC fusion proteins (lower panel) CcoI(M)-SenC designates a fusion protein in which the fusion protein contains the *ccoI*($C_{417}A/C_{419}A$) mutation in TM-MBS1. CcoI-SenC(M) designates a fusion protein in which the Cu binding site of SenC is mutated (*senC*($C_{89}A/C_{87}A$) mutation). **(C)** NADI staining of the Δ*pccA* single and a Δ*pccA*Δ*senC* double knock-out strain expressing the CcoI-SenC fusion proteins when indicated.

DISCUSSION

In the current work, the P_{1B}-type ATPase CcoI of *R. capsulatus* was investigated. In contrast to its well-studied paralog CopA, which acts as the primary Cu exporter when cells are exposed to high Cu concentrations (Yang et al., 2007; Gonzalez-Guerrero and Arguello, 2008; Ekici et al., 2014; Mattle et al., 2015; Purohit et al., 2018; Utz et al., 2019; Abeyrathna et al., 2020), a detailed characterization of CcoI was hitherto lacking. Previous studies had demonstrated that CcoI is essential for the assembly and activity of *cbb*$_3$-Cox in bacteria, including *R. capsulatus* (Koch et al., 2000; Kulajta et al., 2006; Utz et al., 2019), *Bradyrhizobium japonicum* (Preisig et al., 1996) and *Rubrivivax gelatinosus* (Hassani et al., 2010). Based on the high sequence conservation between CopA and CcoI (33.2% sequence identity; **Supplementary Figure S1**), including its putative metal-specificity conferring amino acids (Ekici et al., 2014), it was proposed that CcoI could export Cu for the assembly of the heme *b*-Cu_B binuclear center in CcoN, the catalytic subunit of *cbb*$_3$-Cox (Kulajta et al., 2006). However, it was also found that the addition of external Cu could not rescue *cbb*$_3$-Cox activity in the Δ*ccoI* strain (Koch et al., 1998, 2000; Kulajta et al., 2006). In contrast, in strains lacking the periplasmic Cu chaperones SenC or PccA, the *cbb*$_3$-Cox activity can be rescued by increased external Cu concentrations (Lohmeyer et al., 2012; Trasnea et al., 2016, 2018). This observation is rather surprising because both chaperones are thought to transfer Cu from CcoI to *cbb*$_3$-Cox during maturation (Lohmeyer et al., 2012; Trasnea et al., 2016). In addition, the *cbb*$_3$-Cox defect in the Δ*ccoI* strain is also not remediated by increasing the cellular amounts of CopA, even though this was found to enhance Cu transport into the periplasm and to confer Cu resistance (Utz et al., 2019).

Despite sharing high sequence conservation with CopA and having an undisputed involvement in *cbb*$_3$-Cox assembly, the ultimate proof that CcoI indeed transports Cu was lacking. For addressing this, we have produced and purified CcoI, reconstituted it into liposomes and performed solid-supported membrane (SSM)-based electrophysiology measurements, in analogy to what was done for CopA-like P_{1B}-type ATPases (Abeyrathna et al., 2020). Our results revealed that the presence of CcoI is absolutely required to observe electrogenic transient currents with amplitudes well above background, and these can only be elicited by Cu(I) when ATP (but not a non-hydrolysable analog) is present. These results clearly establish that, like CopA, CcoI also functions as an ATP-dependent Cu exporter.

Next, the role of the two N-MBSs of CcoI was analyzed. Many bacterial CopA-like ATPases contain one or two N-MBSs, which are characterized by a CopZ-like (MxCxxC) Cu binding

motif and a ferredoxin-like fold (Fan et al., 2001; Banci et al., 2002; Mandal and Arguello, 2003; Wu et al., 2008; Zhou et al., 2012; Drees et al., 2015). In some cases, these motifs are separated by only a few amino acids, like in *B. subtilis* (Singleton et al., 2008), while in *E. coli*, they are 34 amino acids apart, which probably favors their independent communication with the other CopA domains (Barry et al., 2010; Leshane et al., 2010; Drees et al., 2015). While the TM-MBSs are essential for Cu translocation (Gonzalez-Guerrero et al., 2008, 2009), the N-MBSs in bacterial CopA-like ATPases appear to be non-essential (Fan et al., 2001; Gonzalez-Guerrero and Arguello, 2008; Drees et al., 2015). Instead, they are proposed to regulate the ATPase activity in response to Cu availability (Wu et al., 2008; Arguello et al., 2016) and to support Cu-loading of the TM-MBSs (**Figure 7**; Drees et al., 2015; Maghool et al., 2020). Current models suggest that in the absence of Cu, the N-MBS is interacting with the N- and the A-domains of CopA, preventing either ATP binding or phosphorylation of the P-domain (Tsivkovskii et al., 2001; Wu et al., 2008; Gonzalez-Guerrero et al., 2009).

Remarkably, although the TM-MBSs are conserved between the CopA-like and CcoI-like ATPases, there are differences in the N-MBSs. In *Rhizobium meliloti* and *B. japonicum*, the CcoI-like ATPase FixI contains only one N-MBS (Preisig et al., 1996), which resembles the CopZ-like Cu binding motif, but lacks the Met residue upstream of the CxxC motif. In *R. capsulatus* and *R. sphaeroides*, CcoI contains two N-MBSs, separated by 28 amino acids. N-MBS1 contains a glutaredoxin-like CPAC motif (Ströher and Millar, 2012), while N-MBS2 contains a CVAC motif, which also lacks the typical upstream Met residue of CopZ-like motifs. The presence of a glutaredoxin-like motif in N-MBS1 and the absence of the typical Met residue in the CopZ-like N-MBS2, conceivably allows CcoI to receive Cu also from Cu donors other than CopZ (**Figure 7**). The absence of the Met residue in CopZ-like Cu binding motifs does not influence Cu binding, but it increases the flexibility of this motif (Palm-Espling et al., 2013), most likely by reducing interactions with other hydrophobic residues (Rosenzweig et al., 1999; Poger et al., 2005). The absence of the Met residue in the N-MBS2 of CcoI could potentially position the cysteine residues in a more flexible conformation, suitable to receive Cu from alternative Cu donors, including glutaredoxin and small molecules, like glutathione or cysteine (**Figure 7**; Helbig et al., 2008; Banci et al., 2010c; Singleton et al., 2010; Aliaga et al., 2016; Bhattacharjee et al., 2017; Dolgova et al., 2017). These molecules have been linked to Cu metabolism in other species (Li et al., 2004; Helbig et al., 2008) and have been shown to interact with P_{1B}-type ATPases (Rosenzweig et al., 1999; Maghool et al., 2020). A CopZ independent Cu transfer to CcoI would also explain, why cbb_3-Cox activity is reduced by only 30% in the absence of CopZ (Utz et al., 2019).

Our data show that the function of both N-MBSs and the TM-MBS in *R. capsulatus* CcoI can be functionally dissected. The mutated CcoI variants are produced at a comparable level (**Figure 4B**), but show distinct effects on cbb_3-Cox activity. Mutating either N-MBS in CcoI reduces cbb_3-Cox activity by about 75%, while mutating the TM-MBS1 reduces it completely (**Figure 4D**). This indicates that both of the N-MBSs are important but not essential for CcoI-mediated Cu translocation (**Figure 7**). However, cbb_3-Cox activity in the N-MBS1 mutant can be fully restored by additional Cu, while the N-MBS2 mutant is only partially rescued. This is different for the TM-MBS1 mutant, which does not support cbb_3-Cox assembly even at higher Cu concentrations. The observation that the cbb_3-Cox related phenotype of the N-MBS2 mutant lies between the phenotypes observed for the N-MBS1 and TM-MBS1 mutants, suggests that the main function of N-MBS2 is to increase the local Cu concentration in close proximity to the TM-MBSs, while Cu-binding to N-MBS1 is additionally required for regulating the ATPase activity (**Figure 7**). Although further studies are needed to firmly establish a regulatory role of N-MBS1, this possibility is in line with the reduced ATPase activity of the N-MBS1 mutant and increased Cu(I) sensitivity when N-MBS2 is mutated. Due to the similarity between the N-MBS2 of CcoI and the Cu binding motif of CopZ, it appears likely that Cu is transferred from CopZ to N-MBS2, similarly as observed for CopA-like ATPases (**Figure 7**; Mandal and Arguello, 2003; Singleton and Le Brun, 2007; Rodriguez-Granillo and Wittung-Stafshede, 2008; Boal and Rosenzweig, 2009; Gonzalez-Guerrero et al., 2009; Banci et al., 2010b; Argüello et al., 2013). This is in line with the transient interaction between CcoI and CopZ that has been observed in *R. capsulatus* (Utz et al., 2019). Cu-loading of N-MBS2 by CopZ possibly enhances the subsequent Cu translocation step (Arguello et al., 2016), which would explain why the N-MBS2 mutant cannot be fully rescued by increased Cu concentrations. The partial rescue of the N-MBS2 mutant by increasing Cu concentrations (**Figure 7**) might be due to the presence of a conserved Cu entrance platform on the cytoplasmic side of TM2 in CcoI. In CopA, this site has been shown to serve as an additional contact site for direct Cu delivery to TM-MBSs (Gonzalez-Guerrero and Arguello, 2008).

Our data show that the *in vitro* ATPase activity of CcoI is inhibited by rather low Cu(I), but not Cu(II), concentrations. At Cu concentrations of 5–40 μM, which are often used for stimulating CopA-like ATPases (Drees et al., 2015), the CcoI-like ATPase is almost completely inhibited. CopA-like ATPases can also be inhibited by high Cu(I) concentrations, but this does not depend on the MBSs (Hatori et al., 2008), and rather appears to be unspecific because it has also been observed for Zn^{2+}/Cd^{2+}- transporting P-type ATPases (Schurig-Briccio and Gennis, 2012). This inhibition is different in the case of CcoI, as our data show that inactivation of N-MBS2 significantly increases Cu(I) sensitivity, while inactivating N-MBS1 does not influence Cu(I) inhibition. In *R. capsulatus*, Cu(I) induced inhibition of CcoI is likely physiologically relevant for coordinating Cu export *via* either CopA or CcoI. CopA-like ATPases are transcriptionally up-regulated in response to 10 μM Cu supplementation (Quintana et al., 2017; Utz et al., 2019), while the expression of CcoI is down-regulated (Utz et al., 2019). However, at lower Cu concentrations (5 μM), there is no significant change in the CcoI protein levels (Selamoglu et al., 2020). Thus, Cu(I)-induced substrate inhibition of CcoI might fine-tune the Cu export pathways, as its inhibition would prevent an

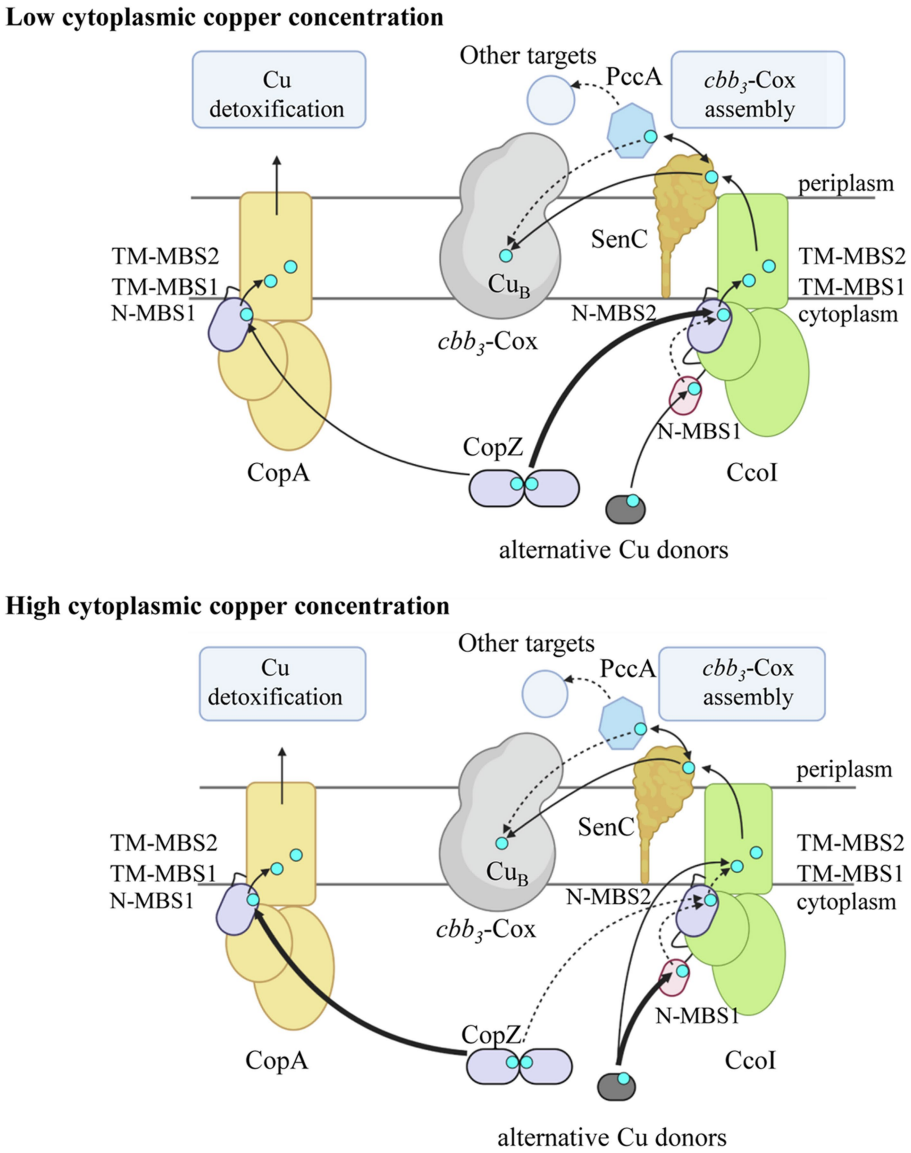

FIGURE 7 | Model on Cu concentration-dependent Cu loading of CcoI in *R. capsulatus*. At low cytoplasmic Cu concentration, the CopA levels (light orange) are low and the N-terminal metal binding site N-MBS2 (purple) of CcoI (green) is loaded primarily by the cytoplasmic Cu-chaperone CopZ (purple; thick arrow). Cu loading of N-MBS2 is suggested to facilitate the Cu translocation reaction *via* the two transmembrane Cu binding sites (TM-MBS1 & TM-MBS2). The glutaredoxin-like N-MBS1 is likely accepting Cu from alternative Cu donors such as glutaredoxin or glutathione (dark gray) and Cu-loading of N-MBS1 is likely involved in regulating the ATPase activity of CcoI. Whether Cu can be transferred from N-MBS1 to N-MBS2 is not known (dotted arrow). From CcoI, Cu is transferred *via* the periplasmic Cu chaperone SenC (dark orange) to cbb_3-Cox (light gray) for maturation of the heme *b*-Cu_B binuclear center in CcoN. SenC can also exchange Cu with the periplasmic Cu chaperone PccA (blue hexagon), which potentially could metalate other cuproproteins. At high cytoplasmic Cu concentrations, CopZ transfers Cu preferentially to CopA for Cu detoxification (thick arrow). As most CopZ is occupied with Cu delivery to CopA, Cu loading of CcoI is preferentially achieved by alternative Cu donors (thick arrow), likely *via* N-MBS1, but residual loading of N-MBS2 by CopZ can still occur (dotted arrow). In the absence of either N-MBS1 or N-MBS2 or CopZ, Cu translocation by CcoI can still occur, likely because the alternative Cu donors can deliver Cu also directly to TM-MBS1 for Cu translocation. At high Cu concentrations, SenC can be bypassed by an unknown mechanism (not shown). All Cu transfer pathways likely occur at all Cu concentrations, but the preferred use is defined by cytoplasmic Cu concentrations. The figure was prepared using biorender (*biorender.com*).

overload of the Cu-delivery pathway to cbb_3-Cox, while simultaneously boosting Cu-detoxification *via* the CopZ-CopA pathway.

P_{1B}-type ATPases transfer Cu from cytosolic to periplasmic Cu chaperones and thus provide the link between the cytosolic and periplasmic Cu homeostasis systems (Rensing and Grass, 2003; Argüello et al., 2013; Andrei et al., 2020). *R. capsulatus* contains two characterized periplasmic Cu chaperones, SenC and PccA (Lohmeyer et al., 2012; Trasnea et al., 2016), which are predicted to transfer Cu from CcoI to cbb_3-Cox (**Figure 7**; Andrei et al., 2020). A SenC-PccA complex has been observed *in vivo* (Trasnea et al., 2016) and copper exchange between both proteins can

occur *in vitro* (Trasnea et al., 2018). However, it was still unknown whether SenC or PccA was the primary acceptor of CcoI-mediated Cu translocation. Our study now revealed that a genetically fused CcoI-SenC complex is sufficient to support cbb_3-Cox assembly, even in the absence of PccA. This is in line with data showing that a Δ*pccA* strain still exhibits 60% of wild type cbb_3-Cox activity, while the activity is dropped to less than 10% in the Δ*senC* strain, which is also characterized by increased cytosolic Cu concentrations (Trasnea et al., 2016). However, both mutants are fully rescued by increasing the Cu concentration in the medium (Lohmeyer et al., 2012; Trasnea et al., 2016). SenC has been shown to directly interact with cbb_3-Cox by chemical cross-linking (Lohmeyer et al., 2012), suggesting that SenC transfers Cu from CcoI to cbb_3-Cox (**Figure 7**). Although we cannot exclude that the mobility of SenC's periplasmic Cu-binding domain might be partially restricted in the CcoI-SenC fusion protein, the fusion protein is active as indicated by its ability to rescue both the Δ*ccoI* and Δ*senC* strains. A functional link between CcoI and SenC is also deduced from the observation that *senC* is transcriptionally upregulated at high Cu concentrations in the Δ*ccoI* strain (Lohmeyer et al., 2012).

The role of PccA in Cu transfer to cbb_3-Cox is less clear; PccA could be involved in conveying Cu to some periplasmic cuproproteins, including SenC. Detailed studies on the assembly of the di-copper center (Cu_A center) in subunit II of the aa_3-type cytochrome *c* oxidase of *Bradyrhizobium diazoefficiens* have recently demonstrated that the first Cu is provided by the SenC-homologue Sco1 and that the PccA-homologue PcuC is required for regenerating Cu-loaded Sco1 and for providing the second Cu ion for the assembly of the Cu_A center (Canonica et al., 2019a, b). The Cu_B center of cbb_3-Cox contains only one Cu and our data suggest that Cu-loading of SenC likely occurs *via* CcoI. Yet, PccA could serve as a back-up strategy for Cu loading of SenC (**Figure 7**), as supported by the observation that the SenC-PccA complex is stabilized in the absence of CcoI (Trasnea et al., 2016).

In summary, our study provides further insight into the complexity of cuproprotein biogenesis by demonstrating the ATP-dependent Cu translocation by CcoI, by dissecting the different functions of its two distinct N-terminal metal binding sites (N-MBSs), and by showing that a CcoI-SenC fusion protein is fully functional in Cu delivery to cbb_3-Cox (**Figure 7**). This physical proximity suggests that SenC likely serves as acceptor for Cu that is translocated by CcoI into the periplasm and destined for cbb_3-Cox maturation. Future studies monitoring direct Cu transfer from CcoI *via* SenC to cbb_3-Cox will hopefully further validate this pathway.

DATA AVAILABILITY STATEMENT

The original contributions presented in the study are included in the article/**Supplementary Material**, further inquiries can be directed to the corresponding author.

AUTHOR CONTRIBUTIONS

AA, MR, YÖ, FD, SA, and H-GK contributed to the design of the study, the acquisition, analysis, and interpretations of the data. AM, ND, FF, and JR contributed to the acquisition, analysis, and interpretations of the data. All authors contributed to the article and approved the submitted version.

FUNDING

This work was supported by grants from the Deutsche Forschungsgemeinschaft (DFG; RTG 2202, Project-ID 278002225 to H-GK and SA; SFB1381 Project-ID 403222702 to H-GK), and the Else-Kröner Fresenius Stiftung/Motivate MD college of the University Freiburg Medical School to JR. FD was supported by grants from NIH GM 38237 and the Division of Chemical Sciences, Geosciences, and Biosciences, Office of Basic Energy Sciences of Department of Energy [DOE DE-FG02-91ER20052]. MR was supported in part by the Excellence Initiative of the German Research Foundation (GSC-4, Spemann Graduate School) and in part by the Ministry for Science, Research and Arts of the State of Baden-Wuerttemberg. YÖ gratefully acknowledges support by Philipp-Schwartz-Initiative of the Alexander von Humboldt Foundation.

ACKNOWLEDGMENTS

We are grateful to Narcis-Adrian Petriman for fruitful discussions and to Julia Fröbel for her kind introduction into establishing the CcoI purification protocol. Work included in this study has also been performed in partial fulfillment of the requirements for the doctoral thesis of AA.

SUPPLEMENTARY MATERIAL

The Supplementary Material for this article can be found online at: https://www.frontiersin.org/articles/10.3389/fmicb.2021.712465/full#supplementary-material

REFERENCES

Abeyrathna, N., Abeyrathna, S., Morgan, M. T., Fahrni, C. J., and Meloni, G. (2020). Transmembrane Cu(I) P-type ATPase pumps are electrogenic uniporters. *Dalton Trans.* 49, 16082–16094. doi: 10.1039/D0DT01380C

Agarwal, S., Hong, D., Desai, N. K., Sazinsky, M. H., Arguello, J. M., and Rosenzweig, A. C. (2010). Structure and interactions of the C-terminal metal binding domain of Archaeoglobus fulgidus CopA. *Proteins* 78, 2450–2458. doi: 10.1002/prot.22753

Aliaga, M. E., Lopez-Alarcon, C., Bridi, R., and Speisky, H. (2016). Redox-implications associated with the formation of complexes between copper ions and reduced or oxidized glutathione. *J. Inorg. Biochem.* 154, 78–88. doi: 10.1016/j.jinorgbio.2015.08.005

Andrei, A., Öztürk, Y., Khalfaoui-Hassani, B., Rauch, J., Marckmann, D., Trasnea, P. I., et al. (2020). Cu homeostasis in bacteria: The ins and outs. *Membranes* 10:242. doi: 10.3390/membranes10090242

Arguello, J. M., Eren, E., and Gonzalez-Guerrero, M. (2007). The structure and function of heavy metal transport P1B-ATPases. *Biometals* 20, 233–248. doi: 10.1007/s10534-006-9055-6

Arguello, J. M., Patel, S. J., and Quintana, J. (2016). Bacterial cu+-ATPases: models for molecular structure-function studies. *Metallomics* 8, 906–914. doi: 10.1039/C6MT00089D

Argüello, J. M., Raimunda, D., and Padilla-Benavides, T. (2013). Mechanisms of copper homeostasis in bacteria. *Front. Cell. Infect. Microbiol.* 3:73. doi: 10.3389/fcimb.2013.00073

Aygun-Sunar, S., Mandaci, S., Koch, H.-G. G., Murray, I. V. J. J., Goldfine, H., and Daldal, F. (2006). Ornithine lipid is required for optimal steady-state amounts of c-type cytochromes in *Rhodobacter capsulatus*. *Mol. Microbiol.* 61, 418–435. doi: 10.1111/j.1365-2958.2006.05253.x

Banci, L., Bertini, I., Cantini, F., and Ciofi-Baffoni, S. (2010a). Cellular copper distribution: a mechanistic systems biology approach. *Cell. Mol. Life Sci.* 67, 2563–2589. doi: 10.1007/s00018-010-0330-x

Banci, L., Bertini, I., Cantini, F., Inagaki, S., Migliardi, M., and Rosato, A. (2010b). The binding mode of ATP revealed by the solution structure of the N-domain of human ATP7A. *J. Biol. Chem.* 285, 2537–2544. doi: 10.1074/jbc.M109.054262

Banci, L., Bertini, I., Ciofi-Baffoni, S., Del Conte, R., and Gonnelli, L. (2003). Understanding copper trafficking in bacteria: interaction between the copper transport protein CopZ and the N-terminal domain of the copper ATPase CopA from Bacillus subtilis. *Biochemistry* 42, 1939–1949. doi: 10.1021/bi027096p

Banci, L., Bertini, I., Ciofi-Baffoni, S., D'onofrio, M., Gonnelli, L., Marhuenda-Egea, F. C., et al. (2002). Solution structure of the N-terminal domain of a potential copper-translocating P-type ATPase from Bacillus subtilis in the apo and cu(I) loaded states. *J. Mol. Biol.* 317, 415–429. doi: 10.1006/jmbi.2002.5430

Banci, L., Bertini, I., Ciofi-Baffoni, S., Kozyreva, T., Zovo, K., and Palumaa, P. (2010c). Affinity gradients drive copper to cellular destinations. *Nature* 465, 645–648. doi: 10.1038/nature09018

Barry, A. N., Shinde, U., and Lutsenko, S. (2010). Structural organization of human cu-transporting ATPases: learning from building blocks. *J. Biol. Inorg. Chem.* 15, 47–59. doi: 10.1007/s00775-009-0595-4

Bazzone, A., Barthmes, M., and Fendler, K. (2017). SSM-based electrophysiology for transporter research. *Methods Enzymol.* 594, 31–83. doi: 10.1016/bs.mie.2017.05.008

Bazzone, A., Costa, W. S., Braner, M., Călinescu, O., Hatahet, L., and Fendler, K. (2013). Introduction to solid supported membrane based electrophysiology. *J. Vis. Exp.* 75:e50230. doi: 10.3791/50230

Bhattacharjee, A., Chakraborty, K., and Shukla, A. (2017). Cellular copper homeostasis: current concepts on its interplay with glutathione homeostasis and its implication in physiology and human diseases. *Metallomics* 9, 1376–1388. doi: 10.1039/C7MT00066A

Boal, A. K., and Rosenzweig, A. C. (2009). Structural biology of copper trafficking. *Chem. Rev.* 109, 4760–4779. doi: 10.1021/cr900104z

Canonica, F., Hennecke, H., and Glockshuber, R. (2019a). Biochemical pathway for the biosynthesis of the cu(A) center in bacterial cytochrome c oxidase. *FEBS Lett.* 593, 2977–2989. doi: 10.1002/1873-3468.13587

Canonica, F., Klose, D., Ledermann, R., Sauer, M. M., Abicht, H. K., Quade, N., et al. (2019b). Structural basis and mechanism for metallochaperone-assisted assembly of the cu(A) center in cytochrome oxidase. *Sci. Adv.* 5:eaaw8478. doi: 10.1126/sciadv.aaw8478

Crisponi, G., Nurchi, V. M., Fanni, D., Gerosa, C., Nemolato, S., and Faa, G. (2010). Copper-related diseases: From chemistry to molecular pathology. *Coord. Chem. Rev.* 254, 876–889. doi: 10.1016/j.ccr.2009.12.018

Daldal, F., Cheng, S., and Applebaum, J. (1986). Cytochrome c2 is not essential for photosynthetic growth of Rhodopseudomonas capsulata. *Proc. Natl. Acad. Sci. U. S. A.* 83, 2012–2016. doi: 10.1073/pnas.83.7.2012

Dolgova, N. V., Yu, C., Cvitkovic, J. P., Hodak, M., Nienaber, K. H., Summers, K. L., et al. (2017). Binding of copper and cisplatin to Atox1 is mediated by glutathione through the formation of metal-sulfur clusters. *Biochemistry* 56, 3129–3141. doi: 10.1021/acs.biochem.7b00293

Drees, S. L., Beyer, D. F., Lenders-Lomscher, C., and Lubben, M. (2015). Distinct functions of serial metal-binding domains in the *Escherichia coli* P1 B -ATPase CopA. *Mol. Microbiol.* 97, 423–438. doi: 10.1111/mmi.13038

Ekici, S., Pawlik, G., Lohmeyer, E., Koch, H.-G., and Daldal, F. (2012). Biogenesis of cbb(3)-type cytochrome c oxidase in *Rhodobacter capsulatus*. *Biochim. Biophys. Acta* 1817, 898–910. doi: 10.1016/j.bbabio.2011.10.011

Ekici, S., Turkarslan, S., Pawlik, G., Dancis, A., Baliga, N. S., Koch, H.-G., et al. (2014). Intracytoplasmic copper homeostasis controls cytochrome c oxidase production. *MBio* 5:e01055-01013. doi: 10.1128/mBio.01055-13

Fan, B., Grass, G., Rensing, C., and Rosen, B. P. (2001). *Escherichia coli* CopA N-terminal Cys(X)(2) Cys motifs are not required for copper resistance or transport. *Biochem. Biophys. Res. Commun.* 286, 414–418. doi: 10.1006/bbrc.2001.5367

Fu, Y., Tsui, H. C., Bruce, K. E., Sham, L. T., Higgins, K. A., Lisher, J. P., et al. (2013). A new structural paradigm in copper resistance in *Streptococcus pneumoniae*. *Nat. Chem. Biol.* 9, 177–183. doi: 10.1038/nchembio.1168

Gantner, M. (2017). Exploring solid supported membrane based electrophysiology as an alternative platform to probe activity of membrane transport proteins. doctoral thesis. Leeds (UK): The University of Leeds School of Biomedical Sciences.

Gonzalez-Guerrero, M., and Arguello, J. M. (2008). Mechanism of cu+−transporting ATPases: soluble cu+ chaperones directly transfer cu+ to transmembrane transport sites. *Proc. Natl. Acad. Sci. U. S. A.* 105, 5992–5997. doi: 10.1073/pnas.0711446105

Gonzalez-Guerrero, M., Eren, E., Rawat, S., Stemmler, T. L., and Arguello, J. M. (2008). Structure of the two transmembrane cu+ transport sites of the cu+ -ATPases. *J. Biol. Chem.* 283, 29753–29759. doi: 10.1074/jbc.M803248200

Gonzalez-Guerrero, M., Hong, D., and Arguello, J. M. (2009). Chaperone-mediated cu+ delivery to cu+ transport ATPases: requirement of nucleotide binding. *J. Biol. Chem.* 284, 20804–20811. doi: 10.1074/jbc.M109.016329

Gonzalez-Guerrero, M., Raimunda, D., Cheng, X., and Arguello, J. M. (2010). Distinct functional roles of homologous cu+ efflux ATPases in *Pseudomonas aeruginosa*. *Mol. Microbiol.* 78, 1246–1258. doi: 10.1111/j.1365-2958.2010.07402.x

Gray, K. A., Grooms, M., Myllykallio, H., Moomaw, C., Slaughter, C., and Daldal, F. (1994). *Rhodobacter capsulatus* contains a novel cb-type cytochrome c oxidase without a CuA center. *Biochemistry* 33, 3120–3127. doi: 10.1021/bi00176a047

Grewer, C., Gameiro, A., Mager, T., and Fendler, K. (2013). Electrophysiological characterization of membrane transport proteins. *Annu. Rev. Biophys.* 42, 95–120. doi: 10.1146/annurev-biophys-083012-130312

Hassani, B. K., Astier, C., Nitschke, W., and Ouchane, S. (2010). CtpA, a copper-translocating P-type ATPase involved in the biogenesis of multiple copper-requiring enzymes. *J. Biol. Chem.* 285, 19330–19337. doi: 10.1074/jbc.M110.116020

Hatori, Y., Hirata, A., Toyoshima, C., Lewis, D., Pilankatta, R., and Inesi, G. (2008). Intermediate phosphorylation reactions in the mechanism of ATP utilization by the copper ATPase (CopA) of *Thermotoga maritima*. *J. Biol. Chem.* 283, 22541–22549. doi: 10.1074/jbc.M802735200

Hatori, Y., and Lutsenko, S. (2016). The role of copper chaperone atox1 in coupling redox homeostasis to intracellular copper distribution. *Antioxidants* 5:25. doi: 10.3390/antiox5030025

Helbig, K., Bleuel, C., Krauss, G. J., and Nies, D. H. (2008). Glutathione and transition-metal homeostasis in *Escherichia coli*. *J. Bacteriol.* 190, 5431–5438. doi: 10.1128/JB.00271-08

Heldal, M., Norland, S., and Tumyr, O. (1985). X-ray microanalytic method for measurement of dry matter and elemental content of individual bacteria. *Appl. Environ. Microbiol.* 50, 1251–1257. doi: 10.1128/aem.50.5.1251-1257.1985

Heuberger, E. H., Veenhoff, L. H., Duurkens, R. H., Friessen, R. H., and Poolman, B. (2002). Oligomeric state of membrane transport proteins analyzed with blue native electrophoresis and analytical ultracentrifugation. *J. Mol. Biol.* 317, 591–600. doi: 10.1006/jmbi.2002.5416

Huster, D., and Lutsenko, S. (2003). The distinct roles of the N-terminal copper-binding sites in regulation of catalytic activity of the Wilson's disease protein. *J. Biol. Chem.* 278, 32212–32218. doi: 10.1074/jbc.M305408200

Imhoff, J. F. (1991). Polar lipids and fatty acids in the genus Rhodobacter. *Syst. Appl. Microbiol.* 14, 228–234. doi: 10.1016/S0723-2020(11)80373-5

Jayakanthan, S., Braiterman, L. T., Hasan, N. M., Unger, V. M., and Lutsenko, S. (2017). Human copper transporter ATP7B (Wilson disease protein) forms stable dimers *in vitro* and in cells. *J. Biol. Chem.* 292, 18760–18774. doi: 10.1074/jbc.M117.807263

Koch, H. G., Hwang, O., and Daldal, F. (1998). Isolation and characterization of *Rhodobacter capsulatus* mutants affected in cytochrome cbb3 oxidase activity. *J. Bacteriol.* 180, 969–978. doi: 10.1128/JB.180.4.969-978.1998

Koch, H.-G., Winterstein, C., Saribas, A. S. S., Alben, J. O., and Daldal, F. (2000). Roles of the ccoGHIS gene products in the biogenesis of the cbb3-type cytochrome c oxidase. *J. Mol. Biol.* 297, 49–65. doi: 10.1006/jmbi.2000.3555

Kulajta, C., Thumfart, J. O., Haid, S., Daldal, F., and Koch, H. G. (2006). Multi-step assembly pathway of the cbb3-type cytochrome c oxidase complex. *J. Mol. Biol.* 355, 989–1004. doi: 10.1016/j.jmb.2005.11.039

Lee, D. W., Ozturk, Y., Osyczka, A., Cooley, J. W., and Daldal, F. (2008). Cytochrome bc(1)-c(y) fusion complexes reveal the distance constraints for functional electron transfer between photosynthesis components. *J. Biol. Chem.* 283, 13973–13982. doi: 10.1074/jbc.M800091200

Leshane, E. S., Shinde, U., Walker, J. M., Barry, A. N., Blackburn, N. J., Ralle, M., et al. (2010). Interactions between copper-binding sites determine the redox status and conformation of the regulatory N-terminal domain of ATP7B. *J. Biol. Chem.* 285, 6327–6336. doi: 10.1074/jbc.M109.074633

Li, K., Hein, S., Zou, W., and Klug, G. (2004). The glutathione-glutaredoxin system in *Rhodobacter capsulatus*: part of a complex regulatory network controlling defense against oxidative stress. *J. Bacteriol.* 186, 6800–6808. doi: 10.1128/JB.186.20.6800-6808.2004

Lohmeyer, E., Schroder, S., Pawlik, G., Trasnea, P. I., Peters, A., Daldal, F., et al. (2012). The ScoI homologue SenC is a copper binding protein that interacts directly with the cbb(3)-type cytochrome oxidase in *Rhodobacter capsulatus*. *Biochim. Biophys. Acta* 1817, 2005–2015. doi: 10.1016/j.bbabio.2012.06.621

Maghool, S., Fontaine, S., Roberts, B. R., Kwan, A. H., and Maher, M. J. (2020). Human glutaredoxin-1 can transfer copper to isolated metal binding domains of the P(1B)-type ATPase, ATP7B. *Sci. Rep.* 10:4157. doi: 1038/s41598-020-60953-z

Mandal, A. K., and Arguello, J. M. (2003). Functional roles of metal binding domains of the Archaeoglobus fulgidus cu(+)-ATPase CopA. *Biochemistry* 42, 11040–11047. doi: 10.1021/bi034806y

Mandal, A. K., Yang, Y., Kertesz, T. M., and Arguello, J. M. (2004). Identification of the transmembrane metal binding site in cu+−transporting PIB-type ATPases. *J. Biol. Chem.* 279, 54802–54807. doi: 10.1074/jbc.M410854200

Marckmann, D., Trasnea, P. I., Schimpf, J., Winterstein, C., Andrei, A., Schmollinger, S., et al. (2019). The cbb 3-type cytochrome oxidase assembly factor CcoG is a widely distributed cupric reductase. *Proc. Natl. Acad. Sci. U. S. A.* 116, 21166–21175. doi: 10.1073/pnas.1913803116

Mattle, D., Zhang, L., Sitsel, O., Pedersen, L. T., Moncelli, M. R., Tadini-Buoninsegni, F., et al. (2015). A sulfur-based transport pathway in cu+-ATPases. *EMBO Rep.* 16, 728–740. doi: 10.15252/embr.201439927

Padilla-Benavides, T., George Thompson, A. M., Mcevoy, M. M., and Arguello, J. M. (2014). Mechanism of ATPase-mediated cu+ export and delivery to periplasmic chaperones: the interaction of Escherichia coli CopA and CusF. *J. Biol. Chem.* 289, 20492–20501. doi: 10.1074/jbc.M114.577668

Palm-Espling, M. E., Andersson, C. D., Björn, E., Linusson, A., and Wittung-Stafshede, P. (2013). Determinants for simultaneous binding of copper and platinum to human chaperone Atox1: hitchhiking not hijacking. *PLoS One* 8:e70473. doi: 10.1371/journal.pone.0070473

Palmgren, M. G., and Nissen, P. (2011). P-type ATPases. *Annu. Rev. Biophys.* 40, 243–266. doi: 10.1146/annurev.biophys.093008.131331

Pawlik, G., Kulajta, C., Sachelaru, I., Schröder, S., Waidner, B., Hellwig, P., et al. (2010). The putative assembly factor CcoH is stably associated with the cbb3-type cytochrome oxidase. *J. Bacteriol.* 192, 6378–6389. doi: 10.1128/JB.00988-10

Poger, D., Fuchs, J. F., Nedev, H., Ferrand, M., and Crouzy, S. (2005). Molecular dynamics study of the metallochaperone Hah1 in its apo and cu(I)-loaded states: role of the conserved residue M10. *FEBS Lett.* 579, 5287–5292. doi: 10.1016/j.febslet.2005.08.052

Post, R. L., Hegyvary, C., and Kume, S. (1972). Activation by adenosine triphosphate in the phosphorylation kinetics of sodium and potassium ion transport adenosine triphosphatase. *J. Biol. Chem.* 247, 6530–6540. doi: 10.1016/S0021-9258(19)44725-X

Preisig, O., Zufferey, R., and Hennecke, H. (1996). The Bradyrhizobium japonicum fixGHIS genes are required for the formation of the high-affinity cbb3-type cytochrome oxidase. *Arch. Microbiol.* 165, 297–305. doi: 10.1007/s002030050330

Pujol, A. M., Gateau, C., Lebrun, C., and Delangle, P. (2011). A series of tripodal cysteine derivatives as water-soluble chelators that are highly selective for copper(I). *Chemistry* 17, 4418–4428. doi: 10.1002/chem.201003613

Purohit, R., Ross, M. O., Batelu, S., Kusowski, A., Stemmler, T. L., Hoffman, B. M., et al. (2018). Cu(+)-specific CopB transporter: revising P(1B)-type ATPase classification. *Proc. Natl. Acad. Sci. U. S. A.* 115, 2108–2113. doi: 10.1073/pnas.1721783115

Quintana, J., Novoa-Aponte, L., and Argüello, J. M. (2017). Copper homeostasis networks in the bacterium *Pseudomonas aeruginosa*. *J. Biol. Chem.* 292, 15691–15704. doi: 10.1074/jbc.M117.804492

Rae, T. D., Schmidt, P. J., Pufahl, R. A., Culotta, V. C., and O'halloran, T. V. (1999). Undetectable intracellular free copper: the requirement of a copper chaperone for superoxide dismutase. *Science* 284, 805–808. doi: 10.1126/science.284.5415.805

Raimunda, D., Gonzalez-Guerrero, M., Leeber, B. W. 3rd, and Arguello, J. M. (2011). The transport mechanism of bacterial cu+-ATPases: distinct efflux rates adapted to different function. *Biometals* 24, 467–475. doi: 10.1007/s10534-010-9404-3

Rensing, C., and Grass, G. (2003). *Escherichia coli* mechanisms of copper homeostasis in a changing environment. *FEMS Microbiol. Rev.* 27, 197–213. doi: 10.1016/S0168-6445(03)00049-4

Rodriguez-Granillo, A., and Wittung-Stafshede, P. (2008). Structure and dynamics of cu(I) binding in copper chaperones Atox1 and CopZ: a computer simulation study. *J. Phys. Chem. B* 112, 4583–4593. doi: 10.1021/jp711787x

Rosenzweig, A. C., Huffman, D. L., Hou, M. Y., Wernimont, A. K., Pufahl, R. A., and O'halloran, T. V. (1999). Crystal structure of the Atx1 metallochaperone protein at 1.02 A resolution. *Structure* 7, 605–617. doi: 10.1016/S0969-2126(99)80082-3

Rosenzweig, A. C., and O'halloran, T. V. (2000). Structure and chemistry of the copper chaperone proteins. *Curr. Opin. Chem. Biol.* 4, 140–147. doi: 10.1016/S1367-5931(99)00066-6

Rycovska-Blume, A., Lü, W., Andrade, S., Fendler, K., and Einsle, O. (2015). Structural and functional studies of NirC from salmonella typhimurium. *Methods Enzymol.* 556, 475–497. doi: 10.1016/bs.mie.2014.12.034

Schulz, P., Garcia-Celma, J. J., and Fendler, K. (2008). SSM-based electrophysiology. *Methods* 46, 97–103. doi: 10.1016/j.ymeth.2008.07.002

Schurig-Briccio, L. A., and Gennis, R. B. (2012). Characterization of the PIB-type ATPases present in Thermus thermophilus. *J. Bacteriol.* 194, 4107–4113. doi: 10.1128/JB.00849-12

Selamoglu, N., Önder, Ö., Öztürk, Y., Khalfaoui-Hassani, B., Blaby-Haas, C. E., Garcia, B. A., et al. (2020). Comparative differential cuproproteomes of *Rhodobacter capsulatus* reveal novel copper homeostasis related proteins. *Metallomics* 12, 572–591. doi: 10.1039/c9mt00314b

Singleton, C., Banci, L., Ciofi-Baffoni, S., Tenori, L., Kihlken, M. A., Boetzel, R., et al. (2008). Structure and cu(I)-binding properties of the N-terminal soluble domains of Bacillus subtilis CopA. *Biochem. J.* 411, 571–579. doi: 10.1042/BJ20071620

Singleton, C., and Le Brun, N. E. (2007). Atx1-like chaperones and their cognate P-type ATPases: copper-binding and transfer. *Biometals* 20, 275–289. doi: 10.1007/s10534-006-9068-1

Singleton, W. C., Mcinnes, K. T., Cater, M. A., Winnall, W. R., Mckirdy, R., Yu, Y., et al. (2010). Role of glutaredoxin1 and glutathione in regulating the activity of the copper-transporting P-type ATPases, ATP7A and ATP7B. *J. Biol. Chem.* 285, 27111–27121. doi: 10.1074/jbc.M110.154468

Sistrom, W. R. (1960). A requirement for sodium in the growth of Rhodopseudomonas-spheroides. *J. Gen. Microbiol.* 22, 778–785. doi: 10.1099/00221287-22-3-778

Smith, A. T., Barupala, D., Stemmler, T. L., and Rosenzweig, A. C. (2015). A new metal binding domain involved in cadmium, cobalt and zinc transport. *Nat. Chem. Biol.* 11, 678–684. doi: 10.1038/nchembio.1863

Smith, A. T., Smith, K. P., and Rosenzweig, A. C. (2014). Diversity of the metal-transporting P1B-type ATPases. *J. Biol. Inorg. Chem.* 19, 947–960. doi: 10.1007/s00775-014-1129-2

Steimle, S., Van Eeuwen, T., Ozturk, Y., Kim, H. J., Braitbard, M., Selamoglu, N., et al. (2021). Cryo-EM structures of engineered active bc(1)-cbb(3) type CIII(2)CIV super-complexes and electronic communication between the complexes. *Nat. Commun.* 12:929. doi: 10.1038/s41467-021-21051-4

Stewart, L. J., Ong, C.-L. Y., Zhang, M. M., Brouwer, S., Mcintyre, L., Davies, M. R., et al. (2020). A role for glutathione in buffering excess intracellular copper in *Streptococcus pyogenes*. *MBio* 11:e02804-20. doi: 10.1128/mBio.02804-20

Ströher, E., and Millar, A. H. (2012). The biological roles of glutaredoxins. *Biochem. J.* 446, 333–348. doi: 10.1042/BJ20112131

Thompson, A. K., Gray, J., Liu, A., and Hosler, J. P. (2012). The roles of Rhodobacter sphaeroides copper chaperones PCu(A)C and Sco (PrrC) in

the assembly of the copper centers of the aa(3)-type and the cbb(3)-type cytochrome c oxidases. *Biochim. Biophys. Acta* 1817, 955–964. doi: 10.1016/j.bbabio.2012.01.003

Toyoshima, C. (2009). How Ca2+-ATPase pumps ions across the sarcoplasmic reticulum membrane. *Biochim. Biophys. Acta, Mol. Cell Res.* 1793, 941–946. doi: 10.1016/j.bbamcr.2008.10.008

Trasnea, P. I., Andrei, A., Marckmann, D., Utz, M., Khalfaoui-Hassani, B., Selamoglu, N., et al. (2018). A copper relay system involving two periplasmic chaperones drives cbb3-type cytochrome c oxidase biogenesis in *Rhodobacter capsulatus*. *ACS Chem. Biol.* 13, 1388–1396. doi: 10.1021/acschembio.8b00293

Trasnea, P. I., Utz, M., Khalfaoui-Hassani, B., Lagies, S., Daldal, F., and Koch, H. G. (2016). Cooperation between two periplasmic copper chaperones is required for full activity of the cbb3 -type cytochrome c oxidase and copper homeostasis in *Rhodobacter capsulatus*. *Mol. Microbiol.* 100, 345–361. doi: 10.1111/mmi.13321

Tsivkovskii, R., Macarthur, B. C., and Lutsenko, S. (2001). The Lys1010-Lys1325 fragment of the Wilson's disease protein binds nucleotides and interacts with the N-terminal domain of this protein in a copper-dependent manner. *J. Biol. Chem.* 276, 2234–2242. doi: 10.1074/jbc.M003238200

Utz, M., Andrei, A., Milanov, M., Trasnea, P. I., Marckmann, D., Daldal, F., et al. (2019). The cu chaperone CopZ is required for cu homeostasis in *Rhodobacter capsulatus* and influences cytochrome cbb3 oxidase assembly. *Mol. Microbiol.* 111, 764–783. doi: 10.1111/mmi.14190

Völlmecke, C., Drees, S. L., Reimann, J., Albers, S. V., and Lübben, M. (2012). The ATPases CopA and CopB both contribute to copper resistance of the thermoacidophilic archaeon Sulfolobus solfataricus. *Microbiology* 158, 1622–1633. doi: 10.1099/mic.0.055905-0

Wacker, T., Garcia-Celma, J. J., Lewe, P., and Andrade, S. L. (2014). Direct observation of electrogenic NH4(+) transport in ammonium transport (Amt) proteins. *Proc. Natl. Acad. Sci. U. S. A.* 111, 9995–10000. doi: 10.1073/pnas.1406409111

Wenk, M., Ba, Q., Erichsen, V., Macinnes, K., Wiese, H., Warscheid, B., et al. (2012). A universally conserved ATPase regulates the oxidative stress response in *Escherichia coli*. *J. Biol. Chem.* 287, 43585–43598. doi: 10.1074/jbc.M112.413070

Wu, C. C., Rice, W. J., and Stokes, D. L. (2008). Structure of a copper pump suggests a regulatory role for its metal-binding domain. *Structure* 16, 976–985. doi: 10.1016/j.str.2008.02.025

Yang, Y., Mandal, A. K., Bredeston, L. M., Gonzalez-Flecha, F. L., and Arguello, J. M. (2007). Activation of Archaeoglobus fulgidus cu(+)-ATPase CopA by cysteine. *Biochim. Biophys. Acta* 1768, 495–501. doi: 10.1016/j.bbamem.2006.09.013

Yen, H. C., Hu, N. T., and Marrs, B. L. (1979). Characterization of the gene transfer agent made by an overproducer mutant of Rhodopseudomonas capsulata. *J. Mol. Biol.* 131, 157–168. doi: 10.1016/0022-2836(79)90071-8

Zhou, L., Singleton, C., and Le Brun, N. E. (2012). CopAb, the second N-terminal soluble domain of Bacillus subtilis CopA, dominates the cu(I)-binding properties of CopAab. *Dalton Trans.* 41, 5939–5948. doi: 10.1039/c2dt30126a

Tadini-Buoninsegni, F. (2020). Protein adsorption on solid supported membranes: monitoring the transport activity of P-type ATPases. *Molecules* 25:4167. doi: 10.3390/molecules25184167

Conflict of Interest: The authors declare that the research was conducted in the absence of any commercial or financial relationships that could be construed as a potential conflict of interest.

Publisher's Note: All claims expressed in this article are solely those of the authors and do not necessarily represent those of their affiliated organizations, or those of the publisher, the editors and the reviewers. Any product that may be evaluated in this article, or claim that may be made by its manufacturer, is not guaranteed or endorsed by the publisher.

frontiers in Microbiology

REVIEW
published: 01 October 2021
doi: 10.3389/fmicb.2021.735666

Shedding Light on Primary Donors in Photosynthetic Reaction Centers

Michael Gorka[1], Amgalanbaatar Baldansuren[2], Amanda Malnati[2], Elijah Gruszecki[2], John H. Golbeck[1,3] and K. V. Lakshmi[2]**

[1] Department of Biochemistry and Molecular Biology, The Pennsylvania State University, University Park, PA, United States, [2] Department of Chemistry and Chemical Biology and The Baruch '60 Center for Biochemical Solar Energy Research, Rensselaer Polytechnic Institute, Troy, NY, United States, [3] Department of Chemistry, The Pennsylvania State University, University Park, PA, United States

Chlorophylls (Chl)s exist in a variety of flavors and are ubiquitous in both the energy and electron transfer processes of photosynthesis. The functions they perform often occur on the ultrafast (fs–ns) time scale and until recently, these have been difficult to measure in real time. Further, the complexity of the binding pockets and the resulting protein-matrix effects that alter the respective electronic properties have rendered theoretical modeling of these states difficult. Recent advances in experimental methodology, computational modeling, and emergence of new reaction center (RC) structures have renewed interest in these processes and allowed researchers to elucidate previously ambiguous functions of Chls and related pheophytins. This is complemented by a wealth of experimental data obtained from decades of prior research. Studying the electronic properties of Chl molecules has advanced our understanding of both the nature of the primary charge separation and subsequent electron transfer processes of RCs. In this review, we examine the structures of primary electron donors in Type I and Type II RCs in relation to the vast body of spectroscopic research that has been performed on them to date. Further, we present density functional theory calculations on each oxidized primary donor to study both their electronic properties and our ability to model experimental spectroscopic data. This allows us to directly compare the electronic properties of hetero- and homodimeric RCs.

Keywords: primary donor, reaction center, heterodimer, homodimer, chlorophyll, electron paramagnetic resonance, density functional theory

OPEN ACCESS

Edited by:
Catarina M. Paquete, Universidade Nova de Lisboa, Portugal

Reviewed by:
Heiko Lokstein, Charles University, Czechia
Dong-Woo Lee, Yonsei University, South Korea

****Correspondence:***
John H. Golbeck
jhg5@psu.edu
K. V. Lakshmi
lakshk@rpi.edu

Specialty section:
This article was submitted to Microbial Physiology and Metabolism, a section of the journal Frontiers in Microbiology

Received: *03 July 2021*
Accepted: *30 August 2021*
Published: *01 October 2021*

Citation:
Gorka M, Baldansuren A, Malnati A, Gruszecki E, Golbeck JH and Lakshmi KV (2021) Shedding Light on Primary Donors in Photosynthetic Reaction Centers. Front. Microbiol. 12:735666. doi: 10.3389/fmicb.2021.735666

INTRODUCTION

Photosynthesis is perhaps one of the most important processes in nature. The ability of oxygenic photosynthesis to utilize the virtually inexhaustible supply of solar energy has powered the planet for billions of years. Some of the earliest signs of the presence of anoxygenic phototrophs, found in South Africa, date to more than 3.4 Ga (Tice and Lowe, 2004) and are believed to have used hydrogen (H_2) and/or iron (Fe) as the source reducing equivalents for carbon fixation (Widdel et al., 1993; Fischer et al., 2016). In the modern era, evolutionary history is marked by the advent of cyanobacteria [$\sim$ 2.4 Ga (Hofmann, 1976; Bekker et al., 2004; Rasmussen et al., 2008)] that utilizes the free energy provided by the sun to generate a highly oxidizing species that splits water,

producing reducing equivalents that are ultimately stored as NADPH or 'biohydrogen' for use in atmospheric CO_2 fixation. This process has evolved to be incredibly efficient, with a quantum efficiency of 0.97 for energy capture (Şener et al., 2011). Furthermore, the energy loss in these systems is mitigated by electron-transfer processes where approx. 60% of the energy of a red photon is conserved (Ke et al., 1973).

Light-driven electron-transfer in photosynthesis originates in a structure known as the reaction center (RC). Reaction centers are large, multi-subunit pigment-protein complexes that harvest light energy through a network of internal or external chlorophyll (Chl) or bacteriochlorophyll (BChl) molecules and store the energy through charge separation and mobilization (Golbeck, 2006; Vinyard et al., 2013). Photoexcitation of the RC leads to rapid charge separation between two (or more) (B)Chl molecules bound in the polypeptide core of the RC. The initial charge separation is subsequently stabilized by electron transfer through a series of cofactors, which extends the lifetime of charge separation from the picosecond to the physiologically relevant millisecond time scale. There are two types of RCs in nature, Type I and Type II, that can be differentiated in several ways. The most obvious difference is the identity of the terminal electron acceptors of the RCs. The electron transfer pathway(s) in Type I RCs utilize iron-sulfur ([4Fe–4S]) clusters, whereas, Type II RCs use quinone molecules as terminal acceptors. Moreover, the identity and orientation of the primary electron acceptor(s) are different in Type I and II RCs (**Figure 1**). The primary acceptor of Type II RCs is a (bacterio)pheophytin [(B)Pheo], lacking a central metal ion, whereas the primary donor of the RC [with the exception of the RC from *Acaryochloris marina* (Chen et al., 2005; Tomo et al., 2007)] is a (B)Pheo derivative, (B)Chl, of the same type. In contrast, Type I RCs always contain (B)Chl *a* (or related derivative) as the primary acceptor regardless of the identity of the primary donor (Orf et al., 2018).

Reaction centers can be further categorized as homodimers and heterodimers. The core of homodimeric RCs is comprised of a dimer of polypeptide subunits that are encoded by a single gene, *e.g.*, the RC of *Heliobacterium modesticaldum*. Homodimeric RCs tend to be simpler in function, containing fewer polypeptide subunits and electron-transfer cofactors (Gisriel et al., 2017). While there are two branches of symmetric cofactors available for electron transfer in homodimeric RCs, it is predicted that since there is no means of differentiating between the two branches, it is axiomatic that both are employed equally. In contrast, heterodimeric RCs contain two distinct polypeptide subunits with reasonably high sequence homology. These RCs also contain two branches of cofactors for electron transfer, which appear symmetric. However, the heterogeneity of the protein-matrix leads to significant differences in the usage and time scales of electron transfer. For example, in the heterodimeric Type I RC of cyanobacteria, photosystem I (PS I), electron transfer in the A-branch is preferred over the B-branch by a factor of $\sim$ 2 (Agalarov and Brettel, 2003; Poluektov et al., 2005). This situation is pushed to the extreme in heterodimeric Type II RCs, such as, photosystem II (PS II) and the bacterial RC (bRC) from *Rhodobacter (Rba.) sphaeroides* and *Rhodopseudomonas (Rps.) viridis*, where the A-branch is exclusively used for electron transfer (Mimuro et al., 1995; Wakeham and Jones, 2005; Williams and Allen, 2009; Vinyard et al., 2013). Although the protein matrix effects responsible for the free energy differences that lead to branch specificity in RCs are yet to be fully elucidated (Wakeham and Jones, 2005), the study of site-specific genetic variants has yielded partial insight on the factors that influence directionality in heterodimeric RCs (Kirmaier et al., 1991, 1999; de Boer et al., 2002).

(Bacterio)chlorophyll molecules are amongst the most ubiquitous cofactors in RCs, with BChls commonly found in anoxygenic phototrophic bacteria, such as, the green sulfur bacterium, *Chlorobaculum tepidum*, and purple bacterium, *Rba. sphaeroides*, while Chls are found in oxygenic phototrophs, such as, higher plants and cyanobacteria (Oren, 2011). Both Chl and BChl molecules are tetrapyrrole macrocycles that bind a central metal ion, which is usually Mg^{2+} (but also Zn^{2+} in rare cases) (Tomi et al., 2007; He et al., 2019; Charles et al., 2020). The (B)Chl molecules can be distinguished by the extent of delocalization of the π-system across the tetrapyrrole macrocycle, which leads to a shift in the absorbance maximum, with the BChls absorbing farther to the red (Strain and Svec, 1966). The (B)Chls can be further divided into different 'flavors,' differentiated by the substituents on the macrocycle and are often denoted by a letter, such as, Chl *a* and Chl *b*. There are six Chl molecules, Chl *a*, 8^1-hydroxy-Chl *a*, divinyl-Chl *a*/*b*, Chl *b*, Chl *d*, and Chl *f*, and six BChl molecules, BChl *a*, BChl *b*, BChl *c*, BChl *d*, BChl *e* and BChl *g*, currently known (Chew and Bryant, 2007). Divinyl (DV)Chls are a variation of Chls, where the ethyl group of the pyrrole ring (II) is changed to a vinyl group (Steglich et al., 2003; Ito and Tanaka, 2011; Barrera-Rojas et al., 2018). This relatively minor change allows for absorption of blue light with virtually no impact on the lifetime of the excited state (see below) or their fluorescence quantum yield (Steglich et al., 2003). They are predominately found in *Prochlorococcus*, a deep-sea growing marine cyanobacterium that uses DVChls to absorb the plentiful blue light found deeper in the water column (Ralf and Repeta, 1992; Moore et al., 1995; Partensky et al., 1999). In general, the various substituents on the (B)Chl macrocycles lead to changes of the extended π-system, which results in shifts of the absorbance bands. The structures of three of the most common (B)Chl molecules are shown in **Figure 2**. In addition to a functionalized tetrapyrrole macrocycle, (B)Chls contain a long hydrophobic tail that is often a phytol group (Chew and Bryant, 2007), but can also be other substituents, such as, farnesol in heliobacteria (Hb) (Kobayashi et al., 1991) and green sulfur bacteria (Gsb) (Frigaard et al., 2006). While the function of the phytol tail is likely to serve as a lipophilic anchor within the hydrophobic trans-membrane region(s) of proteins, it has been suggested that steric effects can impact the electronic properties of the macrocycle, as well as control the chelation properties of the central metal ion (Fiedor et al., 2008).

The arrangement of (B)Chl molecules in Type I and Type II RCs are presented in **Figure 1**. For the purposes of this review article, we will follow a common nomenclature for the (B)Chl cofactors across a variety of hetero- and homodimeric RCs. The two branches of cofactors will be denoted as 'A' and 'B,' as is common for Type I RCs. It should be noted that for Type II RCs,

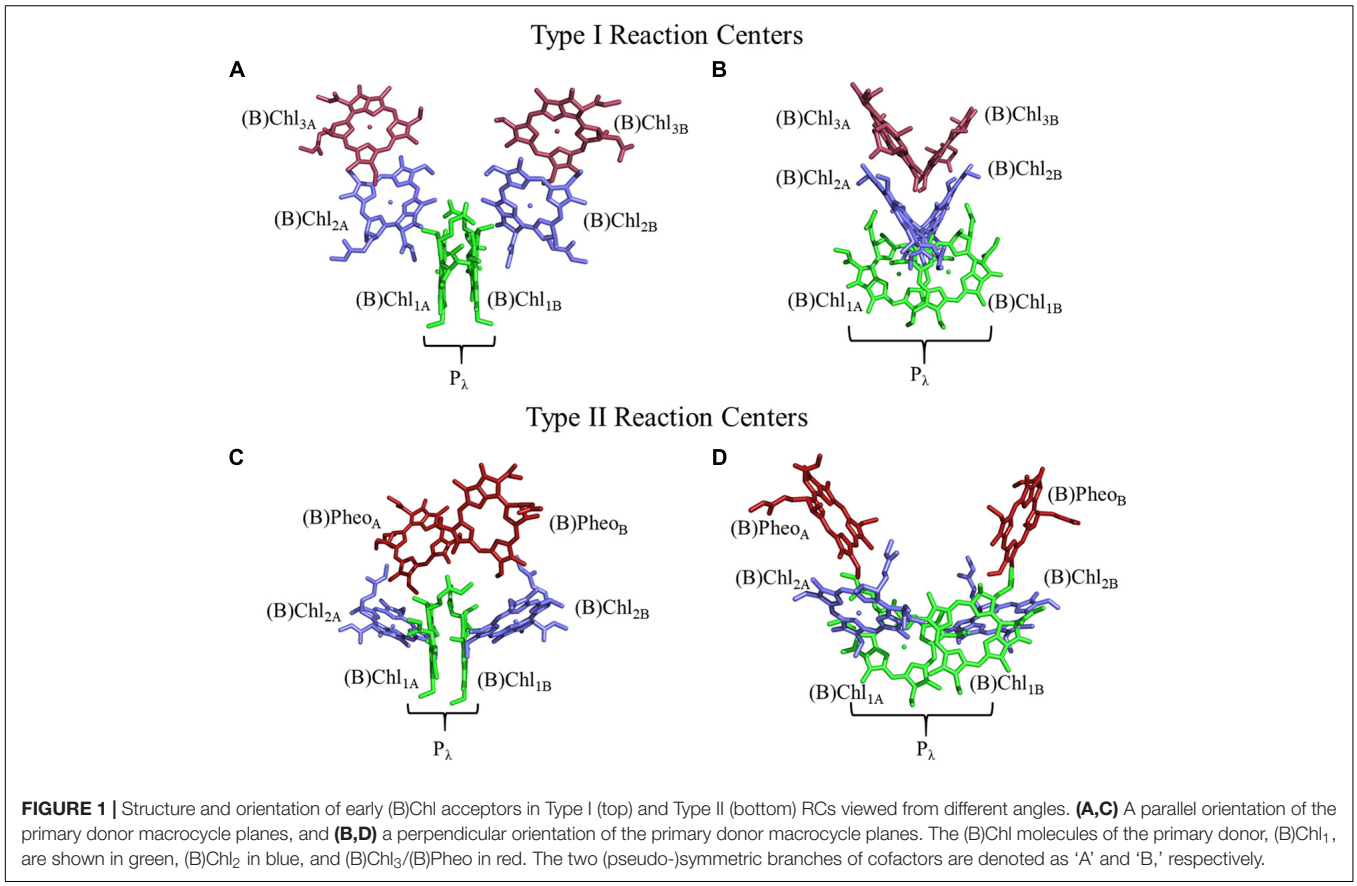

FIGURE 1 | Structure and orientation of early (B)Chl acceptors in Type I (top) and Type II (bottom) RCs viewed from different angles. **(A,C)** A parallel orientation of the primary donor macrocycle planes, and **(B,D)** a perpendicular orientation of the primary donor macrocycle planes. The (B)Chl molecules of the primary donor, (B)Chl_1, are shown in green, (B)Chl_2 in blue, and (B)Chl_3/(B)Pheo in red. The two (pseudo-)symmetric branches of cofactors are denoted as 'A' and 'B,' respectively.

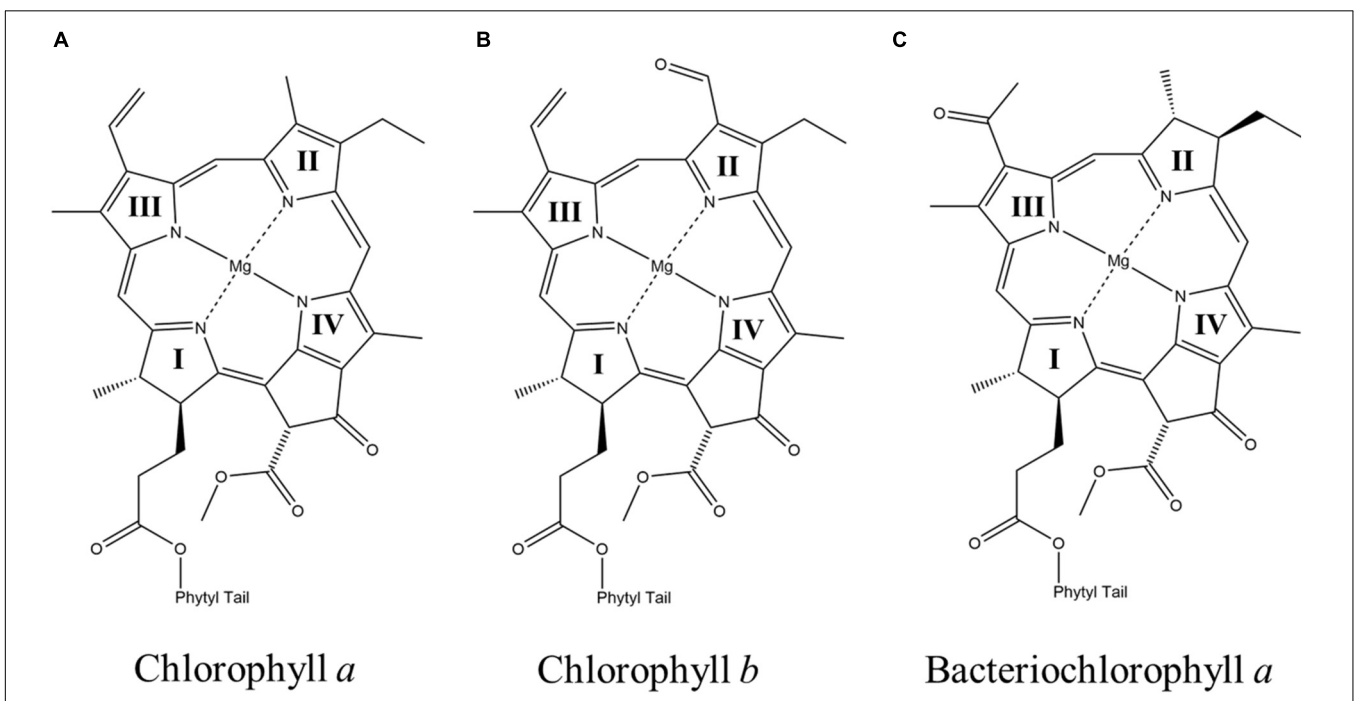

FIGURE 2 | The chemical structures of **(A)** chlorophyll *a* (Chl *a*) **(B)** chlorophyll *b* (Chl *b*), and **(C)** bacteriochlorophyll *a* (BChl *a*). The nitrogen atoms of the four pyrrole rings in each macrocycle are labeled as I, II, III, and IV, respectively.

'A' corresponds to the 'L' and 'D1' branches of the bRC and PS II, respectively. Similarly, 'B' refers to the 'M' and 'D2' branches of the bRC and PS II, respectively. The two closely spaced (B)Chl molecules near the luminal side of each RC are termed Chl_{1X}, where X is the associated A- or B-branch (**Figure 1**). These dimeric (B)$Chl_{1A/1B}$ molecules comprise the primary donor, P_{λ}, where λ is the wavelength of maximal absorbance. As both the chemical identity of the pair of (B)Chls in the primary donor, and the surrounding electrostatic environment vary between species, the value of λ is unique for each RC. We term the second pair of (B)Chl molecules of the RC as '(B)$Chl_{2A/2B}$.' The (B)Chl in this position is also commonly referred to as the 'accessory (B)Chl,' as well as $B_{A/B}$ and $Chl_{A/B}$ in the bRC and PS II, respectively. The orientation of (B)$Chl_{2A/2B}$ in Type I RCs is nearly perpendicular to the membrane plane, and parallel to the plane of (B)$Chl_{3A/3B}$, while Type II RCs display a roughly parallel orientation of (B)$Chl_{2A/2B}$ with the membrane plane and are almost perpendicular to the neighboring (B)Pheo. We label the final pair of (B)Chl molecules in the RC as (B)$Chl_{3A/3B}$, but we refer to these cofactors as (B)$Pheo_{A/B}$ in Type II RCs (this in keeping with the nomenclature used for Type II RCs). The (B)$Chl_{3A/3B}$ molecules are also commonly referred to as $H_{A/B}$ and A_0 in the bRC and PS I, respectively.

There are several reasons that (B)Chl molecules are ubiquitous in photosynthesis [reviewed in Mauzerall et al. (1976) and Björn et al. (2009)], and in the interest of brevity we will only address a few reasons here. First, Chl molecules have an extended and modifiable π-system, drastically reducing the energy gap between the highest occupied molecular orbital (HOMO) and lowest unoccupied molecular orbital (LUMO), which allows for absorption of photons in the visible region of the electromagnetic spectrum. As described below, slight modification of the π-system of Chl derivatives allows for the absorption of different wavelengths of light. This, in turn, allows organisms to exist in a variety of different ecological niches, or to switch their relative Chl abundance in response to changes in the environment (Humbeck et al., 1984). Second, the extended lifetime of Chl excitation allows for efficient photochemistry. It should be noted that the time scale of Chl de-excitation *in vivo* is ∼ 0.3–2.3 ns (Brody and Rabinowitch, 1957; Mar et al., 1972; Morales et al., 2001) which is marginally faster than *in vitro* [5.1 and 3.9 ns for Chl *a* and Chl *b*, respectively (Brody and Rabinowitch, 1957; Brody, 2002)]. The enhanced time scale of de-excitation of Chl molecules *in vivo* is due to the interaction with the surrounding protein matrix. Regardless, these values are significantly slower than charge separation events, which occur with lifetimes of ∼ 100 fs (Shelaev et al., 2010) therefore providing ample time for photochemistry to occur.

Another important factor that dictates the use of (B)Chls is the tunability of the electronic properties through interactions with the surrounding protein matrix. **Figure 3** showcases the redox potentials (both *in vitro* and *in vivo*) for a variety of monomeric (B)Chl molecules and primary donors of RCs. While smart protein-matrix interactions are not unique to (B)Chls, there are a multitude of methods by which the protein matrix can affect the redox properties of a Chl monomer or multimer (Srinivasan and Golbeck, 2009; Olson et al., 2013; Allen and Williams, 2014). One method for shifting a (B)Chl toward either a more positive or more negative redox potential is through the addition or elimination of charged residues within a distance of ∼10 Å of the cofactor (Williams et al., 2001; Johnson and Parson, 2002; Johnson et al., 2002; Ishikita et al., 2006). This method has immense flexibility in altering the potential depending on the charge of the added residue, with the impact being roughly controlled by the distance to that residue. The amplitude of this shift has been observed to vary for different cofactors, with a ∼50–60 mV shift (in either direction) for P_{865} (Allen and Williams, 2014) from the bRC, and up to +144 mV for the phylloquinones and iron-sulfur cluster, F_X, of PS I (Karyagina et al., 2007; Srinivasan and Golbeck, 2009). Hydrogen bonding provides yet another means of tuning the redox properties of cofactors, with the added benefit of serving as a structural component. The redox potential of P_{865} has been shown to increase by 60–125 mV when a hydrogen bond is added, while removal of a preexisting bond decreases the potential by a similar amount (Allen and Williams, 2014). This effect is mirrored in the quinone acceptors of PS I (Srinivasan and Golbeck, 2009) and the bRC (Taguchi et al., 2013; Vermaas et al., 2015), to such an extent that the $Gly225_L$ residue that is hydrogen bonded to the secondary quinone acceptor, Q_B, of the bRC is thought to be primarily responsible for the difference of the redox potential between the primary and secondary quinone, Q_A, and Q_B (Wraight, 1979; Kleinfeld et al., 1984a; Taguchi et al., 2013).

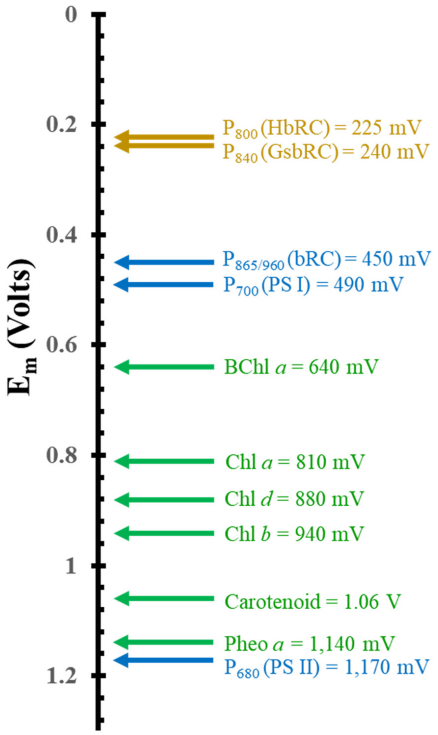

FIGURE 3 | Comparison of the mid-point potential of a variety of (B)Chls *in vitro* and primary donors *in vivo*. Isolated *in vitro* values are depicted in green and hetero and homodimeric primary donors are in blue and dark yellow, respectively.

Indeed, the addition of a hydrogen bond to the phylloquinone acceptor, A_1, in PS I (by altering the axial ligand of the Chl_3 molecule) shifts its redox potential such that it is too positive to participate in forward electron transfer (Sun et al., 2014; Gorka et al., 2021a).

While the addition of charged residues and hydrogen bonds constitute common strategies for controlling the redox properties of cofactors in proteins, there are aspects that are unique to (B)Chls in RCs. First, a typical strategy involves π-stacking of a nearby amino acid residue or neighboring cofactor. This has an ancillary benefit of facilitating the binding of cofactors (Mao et al., 2003), however, it is limited in that π-stacking only alters the potential in one direction, *i.e.,* toward a more negative potential. This strategy has been used to alter the potential of the phylloquinone cofactors, $A_{1A/1B}$, of PS I leading to a decrease in the potential from approx. 27 mV (Srinivasan and Golbeck, 2009) to 150 mV (Kaupp, 2002) by the presence of a π-stacked $Trp679_A/Trp677_B$ residue. To date, there have been few studies of this phenomenon in (B)Chl molecules, but given the extended π-system of the (B)Chls, and the recent discovery of a π-stacked Phe residue in the green-sulfur bacterial (Gsb)RC (Chen et al., 2020), this appears to be a feasible approach. Additionally, the wide variety of available axial ligands that are employed in the binding of (B)Chls in RCs can have a sizeable impact on the redox potential (Heimdal et al., 2007). While most Chl molecules in the photosynthetic antenna complexes are bound by the imidazole of a His residue, as expected by hard-soft acid-base theory (Pearson, 1963), other groups are frequently employed as axial ligands as well. For example, a Met residue is used to bind the Chl molecules, $Chl_{3A/3B}$, involved in electron transfer in PS I (Jordan et al., 2001), and changes to this axial ligand have been demonstrated to significantly impact the electronic (Gorka et al., 2021a) and electron-transfer (Cohen et al., 2004; Dashdorj et al., 2005; van der Est et al., 2009; Santabarbara et al., 2010) properties of $Chl_{3A/3B}$. Finally, planar ring distortions can lead to changes in the absorptive features of (B)Chl molecules (Zucchelli et al., 2007). These protein matrix effects work in tandem to help tune the spectral, electronic, and redox properties of (B)Chl molecules so as to serve multiple functions, even within the same RC.

(B)Chls are critical to photosynthesis as they are not only used to harvest solar energy but these are the only pigments used to generate a charge-separated state, and play an integral role in photosynthetic electron transfer. Light harvesting in photosynthesis is often performed through a pool of densely packed (B)Chl molecules that allow energy transfer to neighboring pigments over very short time scales using fluorescence resonance energy transfer (FRET) (Oppenheimer and Schwinger, 1941; Şener et al., 2011). In the case of PS I, the antenna pool is contained within the RC itself (Jordan et al., 2001; Şener et al., 2011) and is comprised of nearly 100 Chl molecules, although additional antenna complexes are also formed under differing physiological conditions (Bibby et al., 2001). For example, the bacterial reaction center (bRC) and PS II contain light-harvesting complexes (LHCs), termed LHC-I and LHC-II, which aid in light harvesting and energy transfer through closely packed (B)Chl molecules (Deisenhofer et al., 1985; McDermott et al., 1995; Koepke et al., 1996; Papiz et al., 2003; Roszak et al., 2003; Şener et al., 2011; van Amerongen and Croce, 2013). This process can also occur externally through energy transfer from the chlorosome to the RC via the Fenna-Matthews-Olson (FMO) protein (Olson, 2004), as is the case for green sulfur bacteria (Olson, 2013). However, energy transfer to the RC in green sulfur bacteria is unusually inefficient (Blankenship et al., 1995; Francke et al., 1996; Neerken et al., 1998; Oh-oka et al., 1998; Olson, 1998), with an estimated value of only ∼ 30%. The energy of an absorbed photon migrates across this network of (B)Chl molecules until the energy finds its way to a thermodynamic well in the RC, known as the trap. Excitation of the trap leads to the charge-separation reaction in the RC. This process occurs on ultrafast time scales, from fs (Shelaev et al., 2010; Song et al., 2021) to ps (Holzapfel et al., 1989; Peloquin et al., 1994; Holzwarth and Müller, 1996), and has thus been difficult to study. Recent advances in theoretical and experimental techniques have led to several proposed models for charge separation in RCs. While a detailed analysis of every model is outside the scope of this review article, we will provide brief descriptions of the types that have been put forth. It should also be noted that given the variations in cofactor identity, structure, and organization in the different RCs, the exact mechanism of charge separation may vary between them. Therefore, the models for each RC are described in greater detail in the respective sections [for a comprehensive review, please see Savikhin and Jankowiak (2014)].

In general, three categories of models for charge-separation have been proposed in the literature, where the process originates either at the: (i) primary donor, (ii) accessory Chl, or (ii) a larger group of highly coupled cofactors. Shown in **Scheme 1** is a simple representation of the models.

For many years, the primary donor (P) had been thought of as the initial site for charge separation (White et al., 1996; Savikhin et al., 2000; Gibasiewicz et al., 2001; Gobets and van Grondelle, 2001; Gobets et al., 2001; Melkozernov, 2001; Savikhin and Jankowiak, 2014), whereby this electronically coupled special pair of (B)Chl molecules serves as an energy sink for the antenna complexes. While it was unclear whether the act of charge separation or energy transfer to the trap was the limiting factor, all of the models assumed that the low-potential reductant emerged from the primary donor, initially reducing $(B)Chl_2$. Advances in ultrafast optical spectroscopy have made it possible to investigate the femto- and picosecond transient states of the RCs, which led to various proposed models for the charge separation reaction. A thorough review of ultrafast optical spectroscopy methods can be found in Berera et al. (2009) and Schlau-Cohen et al. (2012). Ultrafast spectroscopy has been employed for the study of the bRC (Van Brederode et al., 1997; van Brederode et al., 1998, 1999; van Stokkum et al., 1997; Vos et al., 1997; van Brederode and van Grondelle, 1999; Konar et al., 2018; Ma et al., 2019), PS II (Schatz et al., 1987; Peterman et al., 1998; Novoderezhkin et al., 2007; Myers et al., 2010), PS I (Müller et al., 2003, 2010; Holzwarth et al., 2006a; Cherepanov et al., 2017, 2020, 2021), and the HbRC (Kojima et al., 2020; Song et al., 2021). Early research on the bRC demonstrated that charge separation with the successful formation of the reduced $Q_A^{\cdot -}$ state still occurs in site-directed genetic variants with significantly slower energy transfer from

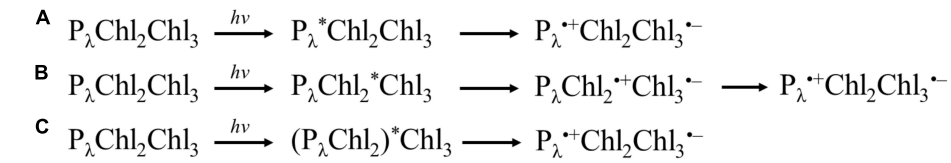

SCHEME 1 | Simple archetypes of charge separation models. **(A)** Excitation of primary donor, P_λ, leading to charge separation between P_λ and Chl_3. **(B)** Excitation of Chl_2, leading to charge separation between Chl_2 and Chl_3, followed by the hole on Chl_2 being filled by P_λ. **(C)** Excitation of highly coupled P_λ, Chl_2 (and potentially Chl_3). Please note that Chl_3 is a Pheo in Type II RCs.

$BChl_{2A}$* to P_{865} (Van Brederode et al., 1997; van Brederode et al., 1998). These results, coupled with the observation that direct excitation of $BChl_{2A}$ resulted in the formation of P_{865}*, led to a model in which $BChl_{2A}$ was the genesis of the charge-separated state. Other studies around the same time period suggested instead that the early BChls should be considered a hexamer, where both P_{865} and $BChl_2$ can be coherently excited (Vos et al., 1997). Much later, multiple two-dimensional electronic spectroscopy with better time resolution showed that when vibrational and electronic factors are considered, it is more reasonable to conclude that P_{865} initiates charge separation (Niedringhaus et al., 2018; Ma et al., 2019) and that P_{865} and $BChl_{2A/2B}$ are electronically coupled, allowing for excited state migration (Konar et al., 2018). In principle, this could lead to the presence of multiple redundant mechanisms of charge separation in the system.

Analogous models for charge separation were also proposed for PS I using ultrafast spectroscopy methods. Ultrafast difference spectroscopy of wild-type (WT) PS I showed a mixture of the excited P_{700}* state and the radical states associated with the charge-separated state, $P_{700}^{\bullet+}Chl_{2A/B}^{\bullet-}$. Moreover, perturbation of the protein environment surrounding the $Chl_{2A/2B}$ cofactors through site-directed genetic variants appeared to slow the formation of the charge-separated state in the symmetric branch, e.g., changes to Chl_{2B} suppressed the formation of $P_{700}^{\bullet+}Chl_{2A}^{\bullet-}$ state. This suggested the presence of a highly coupled system of Chl molecules in PS I. Most recently, ultrafast spectroscopy of both WT PS I and genetic variants of the protein environment in the vicinity of the Chl_2 cofactor have suggested the formation of an initial excited state $(Chl_{2A}P_{700}Chl_{2B})$* (Cherepanov et al., 2020, 2021), which rapidly leads to the formation of the first charge-separated state, $P_{700}^{\bullet+}Chl_2^{\bullet-}$.

In contrast, Müller and coworkers have proposed a mechanism of charge separation in PS I that originates at Chl_2 (Müller et al., 2003; Holzwarth et al., 2006a), where the first charge-separated state is $Chl_2^{\bullet+}Chl_3^{\bullet-}$. Here, the hole on Chl_2 was suggested to be reduced by P_{700} (Chl_1), forming the first stable charge-separated state, $P_{700}^{\bullet+}Chl_3^{\bullet-}$. Theoretical studies of PS II have found that this is a promising model, as Chl_2 was observed to have the lowest site energy of the initial Chl/Pheo molecules in the core (Sirohiwal et al., 2020). Recent findings have indicated common ground with both of the models described above, suggesting that the initial four (or six) Chl molecules of PS I are highly electronically coupled, and participate in charge separation to various extents. Similar models have also been proposed for the homodimeric RC from *H. modesticaldum*, invoking both the $BChl_2/BChl_3$ pair (Song et al., 2021) and/or all six core BChl molecules (Kojima et al., 2020; Song et al., 2021) in the excited state. It should be noted that these models are not necessarily mutually exclusive as different models likely take priority under different excitation conditions and may vary between RCs.

With the recent availability of the X-ray crystal and cryo-electron microscopy structures of the HbRC and GsbRC (Gisriel et al., 2017; Chen et al., 2020), respectively, we have the unique opportunity to compare the electronic structure of the primary donors in a variety of RCs. The goal of this article is to review research on the geometric and electronic structure of a variety of primary donors of hetero and homodimeric RCs, with an emphasis on pulsed electron paramagnetic resonance (EPR) and density functional theory (DFT) methods. We will focus on six RCs: (i) The heterodimers, P_{700} of Photosystem I (PS I), P_{680} of Photosystem II (PS II), P_{865} and P_{960} of the bRCs from *Rba. sphaeroides* and *Rps. viridis*, respectively, and (ii) homodimers, P_{800} of *H. modesticaldum* and P_{840} of the green-sulfur bacterium, *C. tepidum*.

GEOMETRIC STRUCTURES

Geometric Structure of the Primary Donor of Heterodimeric Reaction Centers

The Primary Donor, P_{700}, of Photosystem I

We begin by describing the extensively studied primary donor, P_{700}, of PS I. Cyanobacterial PS I [reviewed in Golbeck (2006)] is a composed of 12 or 13 polypeptide subunits that bind the light-harvesting and electron-transfer cofactors. There are 90 Chl *a* molecules that function as the light-harvesting antenna while the electron-transfer cofactors are comprised of two pseudo-symmetric branches of six Chl *a* molecules ($Chl_{1A/1B}$, $Chl_{2A/2B}$, and $Chl_{3A/3B}$), two phylloquinones ($A_{1A/1B}$), and three [4Fe–4S] clusters, F_X, F_A and F_B (**Figures 4A,B**). The electron-transfer cofactors are largely bound in the transmembrane PsaA and PsaB polypeptide subunits, with the terminal [4Fe–4S] clusters, F_A and F_B, bound by PsaC on the stromal side of the RC (**Figure 4A**).

There is currently a lack of consensus on the mechanism of charge separation in PS I. Early models had suggested that P_{700} functioned as the source of the electron (White et al., 1996; Savikhin et al., 2000; Gibasiewicz et al., 2001; Gobets and van Grondelle, 2001; Gobets et al., 2001; Melkozernov, 2001;

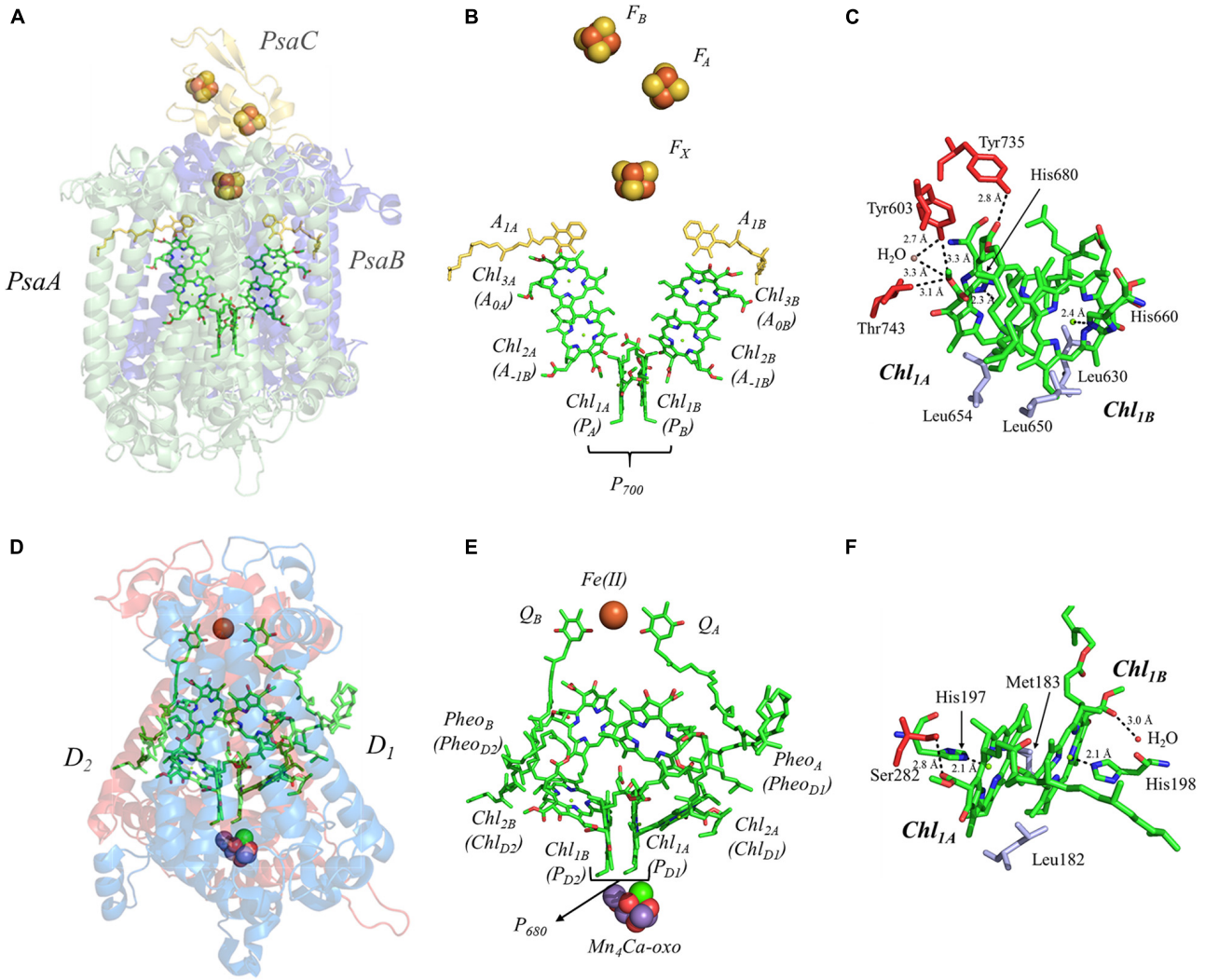

FIGURE 4 | (A) The core subunits (PsaA, green; PsaB, blue; and PsaC, yellow) and cofactors of PS I as observed by X-ray crystallography (PDB ID: 1jb0), **(B)** the cofactors that participate in the primary electron transfer pathway of PS I and **(C)** the binding pocket of the primary donor, P_{700}. **(D)** The core subunits (D1, red; D2, blue) and cofactors of PS II as observed by X-ray crystallography (PDB ID: 3wu2), **(E)** the cofactors that participate in the primary electron transfer pathway of PS II and **(F)** the binding pocket of the primary donor, P_{680}. Commonly used labels are in parentheses. Part **(C,F)** emphasize the prominent protein-matrix effects of the primary donor of PS I and PS II, respectively, where the residues that are hydrogen bonded to the primary donors are shown in red, and nearby non-polar or π-stacked residues are colored in gray.

Savikhin and Jankowiak, 2014), whereby the dimerization of Chl_{1A}/Chl_{1B} created a lower energy site that traps the excitation energy. Subsequently, it was proposed that Chl_2, instead of acting as the first electron acceptor, served to trap the energy and was the source of the charge-separated state (Müller et al., 2003; Holzwarth et al., 2006a). It was proposed that Chl_2 would reduce Chl_3 and the hole that was generated would migrate to P_{700}, ultimately creating the charge-separated $P_{700}^{\cdot+}Chl_3^{\cdot-}$ state. However, theoretical studies have suggested that the redox potentials of the Chl_2/Chl_3 pair make this mechanism thermodynamically unlikely (Ptushenko et al., 2008). More recently, advances in theoretical and experimental methods have led to a highly electronically coupled model, wherein $(P_{700}Chl_{2A}Chl_{2B})^*$ form an exciplex, with the negative charge localized primarily on Chl_2 (Cherepanov et al., 2020, 2021). While there are differences that remain in the field, and the mechanism may vary based on experimental conditions and across organisms, it should be noted that similar models have been proposed in other Type I RCs (Kojima et al., 2020; Song et al., 2021).

While the overall mechanism remains under study, the lifetime of the various electron-transfer steps of PS I are reasonably well understood. Exciton migration from the antenna system to the trap appears to be the limiting step in charge separation, occurring with a lifetime of $\sim$ 5 ps (Wasielewski et al., 1987; Shelaev et al., 2010). However, charge separation is known to occur within 100 fs of photoexcitation of the trap (Shelaev et al., 2010). It is upon charge separation that

the electron-transfer pathway bifurcates between the A- and B-branches, forming the $P_{700}^{\cdot+}A_{0A}^{\cdot-}$ or $P_{700}^{\cdot+}A_{0B}^{\cdot-}$ state. Unlike Type II RCs, each branch is utilized, albeit unequally, with the A-branch being favored in cyanobacteria by a factor of two in comparison with the B-branch (Agalarov and Brettel, 2003; Poluektov et al., 2005). Electron transfer then proceeds to the A_{1A} and A_{1B} cofactors within ∼ 30–50 ps (Brettel, 1997; Itoh et al., 2001), and then within 20 or 200 ns, respectively (Agalarov and Brettel, 2003; Kurashov et al., 2018) to the inter-polypeptide [4Fe–4S] cluster, F_X, where the A- and B-branches are known to converge (**Figure 4B**). Subsequently, electron transfer occurs linearly though the F_A and then F_B clusters (Díaz-Quintana et al., 1998) with a lifetime of ∼ 200 ns, after which the electron is transferred to a soluble electron acceptor, ferredoxin (Mondal and Bruce, 2018) or flavodoxin (Pierella Karlusich and Carrillo, 2017), for downstream processes. For a detailed analysis of the electron-transfer and charge-recombination lifetimes in PS I, please see (Kurashov et al., 2018).

It is important to understand the structural and electronic factors that influence the redox and kinetic properties of the primary donor, P_{700}, as it is critical for light-driven electron transfer in PS I. P_{700} is a dimer of a Chl *a*' and Chl *a* molecules, Chl_{1A} and Chl_{1B}, where Chl *a*' is the 13^2 epimer of Chl *a* (Kobayashi, 1996; Webber and Lubitz, 2001; **Figure 4C**). Of all of the primary donors that are discussed in this review, P_{700} appears to have the most extensive and asymmetric protein-cofactor interactions based on the X-ray crystal structure (Jordan et al., 2001). Perhaps an obvious indication is the striking asymmetry of the hydrogen (H)-bonding environment of the two Chl molecules, Chl_{1A} and Chl_{1B}, that comprise the primary donor. As can be seen in **Figure 4C**, Chl_{1A} has three hydrogen bonds, provided by the $Tyr735_{PsaA}$, $Tyr603_{PsaA}$, and $Thr743_{PsaA}$ residues, with a hydrogen H-bonding distance of 2.8, 3.3, and 3.1 Å, respectively. Additionally, there is a water molecule within 3.3 Å of Chl_{1A}, which is not present near Chl_{1B}. While it is possible that the hydrogen bonds may facilitate selective binding of the Chl *a*' epimer, these are also likely to serve as a means to alter the redox potential of Chl_{1A} relative to Chl_{1B}, providing strict control over the distribution of electron density. The hydrogen bonds do not appear to be the only significant deviation in the protein matrix that could influence asymmetry between Chl_{1A} and Chl_{1B}, as three Leu residues ($Leu630_{PsaB}$, $Leu650_{PsaA}$, and $Leu654_{PsaA}$) preferentially interact with Chl_{1B}, although $Leu654_{Psa}$ and $Leu630_{PsaB}$ are found in the non-overlapping regions of the rings. Beyond this, both contain axially ligated His residues, which should not contribute to any asymmetrical effects.

Alterations to the primary donor, P_{700}, of PS I from C*hlamydomonas reinhardtii* with the axial ligands, $His656_{PsaB}$ and $His676_{PsaA}$, have demonstrated profound effects on its properties. Initial studies, where the $His656_{PsaB}$ residue was replaced by Asn or Ser, displayed a shift in the mid-point potential of P_{700} by +40 mV, with a corresponding alteration in its spectral features. While such changes are to be expected, electron-nuclear double resonance (ENDOR) spectroscopy of $P_{700}^{\cdot+}$ in the genetic variants revealed an increase in electron spin density at the methyl group in position 12 by ∼ 20%, suggesting a significant effect on the electron delocalization over the two halves of the dimer (Webber et al., 1996). Subsequently, additional variants were studied that included changes to the axial ligand of Chl_{1A} on the A-side, $His676_{PsaA}$, and non-polar, acidic, basic, and uncharged residues in the vicinity. Changes to the redox properties of P_{700} displayed an expected pattern, where soft base ligands, such as, the S atom of a Cys residue, had the most profound effect on the redox potential, shifting the potential by up to ∼ + 140 mV. The effects on the electronic properties of $P_{700}^{\cdot+}$ were subtle and highly asymmetric.

Shown in **Figure 5A** are the inter-cofactor distances and orientation of the $Chl_{1A/1B}$ molecules of P_{700}. P_{700} has perhaps the most archetypal parallel orientation of the two Chl macrocycles of Chl_{1A} and Chl_{1B} in the dimer, with the distance between the macrocycles varying from 3.5–3.6 Å. There is significant overlap of the ring planes of the Chl_{1A} and Chl_{1B} macrocycles, as the center-to-center distance between the two Mg^{2+} ions is 6.3 Å. Much like every other primary donor, the most prominent overlap occurs over the pyrrole group of the N^3 atom, with a small overlap of the pyrrole of N^2. The space-filling model in **Figure 6A** shows the extent of the overlap between the two macrocycles. Because of the significant overlap, the nearest ring nitrogen atoms are amongst the closest amongst all of the RCs discussed here. The most relevant are the N^{3A}–N^{3B}, N^{2A}–N^{2B}, and N^{3A}–N^{2B} distances of 3.7, 4.4, and 4.9 Å, respectively. These values are shown in **Table 1** for comparison with analogous distances in other RCs. **Figure 6A** also highlights the typical orientation of the phytol tail of P_{700} in comparison with that of other Type I RCs, i.e., a configuration that is tight to the central rings of the macrocycles with a small bend influenced by the presence of a water molecule.

The Primary Donor, P_{680}, of Photosystem II

This section is focused on the Type II heterodimeric RC, photosystem II (PS II) [reviewed in Vinyard et al. (2013) and Lakshmi et al. (2014)]. The primary electron-transfer cofactors of PS II are present in the core polypeptide subunits, D1 and D2, and encompassed by ∼ 22–23 smaller polypeptides, whose identity varies among differing organisms. The primary electron-transfer pathway of PS II is composed of the following cofactors that are common to heterodimeric Type II RCs: four pseudo-symmetric Chl *a* molecules, two pheophytins ($Pheo_A$ and $Pheo_B$) and two quinones (Q_A and Q_B) (**Figures 4D,E**). In contrast to other Type II RCs, the electron-transfer pathways also contain two redox-active tyrosine residues, Y_D and Y_Z, and a unique tetranuclear manganese calcium-oxo (Mn_4Ca-oxo) cluster, which is the well-known water-splitting catalytic moiety of PS II. The redox properties of the primary donor, P_{680}, further differentiate PS II from other Type I and Type II RCs. The primary donor, P_{680}, of PS II is by far the most oxidizing of any RC discovered thus far, with an E_m of ∼ 1,200 mV (Rappaport et al., 2002; Ishikita et al., 2005, 2006; **Figure 3**). In fact, it is one of the most oxidizing species that is found in nature. The evolutionary reason for this is clear, as P_{680} needs to be a strong oxidant in order to allow for successive oxidations of the Mn_4Ca-oxo cluster that leads to the catalytic conversion of two substrate water molecules into dioxygen. The extremely high oxidizing potential of P_{680}

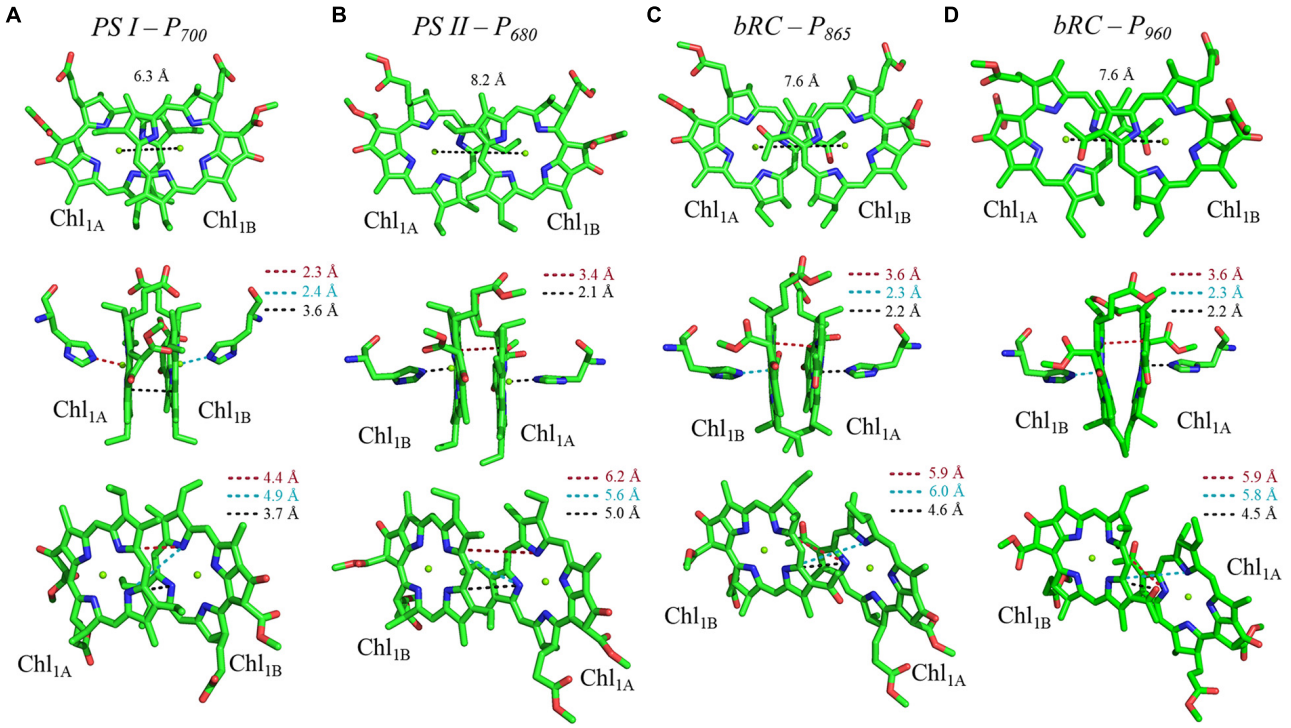

FIGURE 5 | Analysis of inter-cofactor distances and relative orientation of primary donors from the heterodimeric RCs: **(A)** Photosystem I, **(B)** Photosystem II, and the bacterial RC from **(C)** *Rba. sphaeroides* and **(D)** *Rps. viridis*.

showcases the amazing ability of nature in modulating the redox potential of identical or highly similar cofactors for different purposes (Ishikita et al., 2006).

Once again, there are various proposals in literature on the location of the primary charge separation of PS II, but recent findings suggest that charge separation originates at the 'accessory' Chl, termed Chl_{2A} (Groot et al., 2005; Holzwarth et al., 2006b; Romero et al., 2010; Duan et al., 2017; Sirohiwal et al., 2020; Tamura et al., 2020). Theoretical modeling of site energies has indicated that contrary to previous assumptions, Chl_{2A} has the lowest energy of all of the initial Chls. The reason for this deviation from other Type II heterodimeric RCs (see below) is attributed to the need to incorporate the Mn_4Ca-oxo cluster used in water splitting (Tamura et al., 2020). In other studies, Stark spectroscopy was used to observe multiple mixed exciton charge-transfer states: $(Chl_{1B}{}^{\delta+}Chl_{1A}{}^{\delta-}Chl_{2A})^*$, $(Chl_{2A}{}^{\delta+}Pheo_D{}^{\delta-})^*$, and $(Chl_{1B}{}^{+}Chl_{1A}{}^{-})^{\delta*}$, suggesting a highly electronically coupled model. Interestingly, multiple empirical methods have found two events associated with charge separation, at 100–400 fs and ∼1.8 ps (Romero et al., 2010; Duan et al., 2017). Regardless of the mechanism, within ∼ 1.5 ps of photoexcitation of the trap, an electron is transferred to $Pheo_A$, forming the charge-separated $[P_{680}{}^{\cdot+}Pheo_A{}^{\cdot-}]$ state. Unlike PS I, electron transfer within PS II is branch specific, only occurring through the A-side involving the cofactors associated with the D1 polypeptide subunit (with the exception of the primary quinone, Q_A, that is bound in the D2 polypeptide). The stabilization of the relatively short-lived $P_{680}{}^{\cdot+}Pheo_A{}^{\cdot-}$ state is achieved through rapid forward electron transfer to the primary quinone acceptor, Q_A, within 200 ps and then to the secondary quinone, Q_B, within ∼ 200–400 μs. Much like the bRC, Q_B is doubly reduced and doubly protonated after two turnovers of the RC, forming the labile quinol, Q_BH_2, with the second electron transfer step occurring notably slower than the first one (∼500–800 μs) (Bowes et al., 1980; Robinson and Crofts, 1983; de Wijn and van Gorkom, 2001; Sauer and Yachandra, 2004).

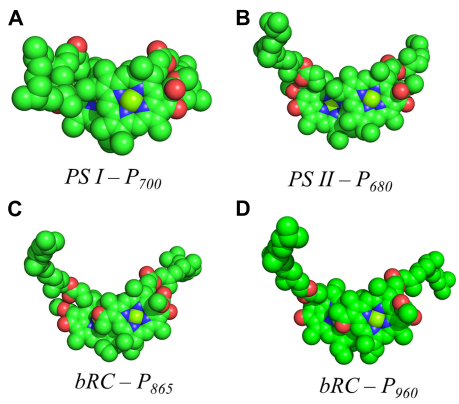

FIGURE 6 | Space filling models of **(A)** P_{700} from PS I, **(B)** P_{680} from PS II, **(C)** P_{865} from the bRC of *Rba. Sphaeroides* and **(D)** P_{960} from the bRC of *Rps. Viridis*.

TABLE 1 | Distance parameters of the primary donors of heterodimeric and homodimeric RCs.

Heterodimeric RCs						
Primary Donor	**Mg^{2+}–Mg^{2+}**	**Ring–Ring**	**Nearest Nitrogens***			
			N^{3A}–N^{3B}	**N^{2A}–N^{2B}**	**N^{3A}–N^{2B}**	**N^{2A}–N^{3B}**
P_{700}	6.3 Å	3.4–3.6 Å	3.7 Å	4.4 Å	4.9 Å	4.9 Å
P_{680}	8.2 Å	3.4–3.6 Å	5.0 Å	6.2 Å	5.6 Å	6.8 Å
P_{865}	7.6 Å	3.6–3.8 Å	4.6 Å	6.3 Å	6.0 Å	5.9 Å
P_{960}	7.6 Å	3.6–3.8 Å	4.5 Å	6.2 Å	5.9 Å	5.8 Å
Homodimeric RCs						
Primary Donor	**Mg^{2+}–Mg^{2+}**	**Ring–Ring**	**Nearest Nitrogens**			
			N^3–N^3	**N^2–N^2**	**N^3–N^2**	**N^2–N^3**
P_{800}	5.7 Å	3.1–3.5 Å	3.1 Å	4.7 Å	4.7 Å	4.7 Å
P_{840}	6.4 Å	3.3–3.6 Å	3.9 Å	5.7 Å	5.5 Å	5.4 Å

**The labels A and B refer to $BChl_{1A}$ and $BChl_{1B}$ for P_{680}, P_{960}, and P_{865}.*

As previously mentioned, the terminal quinone acceptors are a hallmark of Type II RCs as are the [4Fe–4S] clusters of the Type I RC, PS I. Meanwhile, on the acceptor side, the hole on $P_{680}^{\cdot+}$ is reduced by the redox-active tyrosine, Y_Z, which, in turn, is re-reduced by the Mn_4Ca-oxo cluster. Two turnovers of PS II are required for the complete reduction of Q_B and a total of four turnovers results in the oxidation of two molecules of substrate water to dioxygen at the catalytic Mn_4Ca-oxo cluster (Vinyard et al., 2013).

The primary donor of PS II, P_{680}, is a dimer of Chl *a* molecules, Chl_{1A} and Chl_{1B}. In contrast with P_{700}, which displays an asymmetry of interactions with the protein matrix, P_{680} of shows less asymmetry in the protein matrix for each Chl *a* molecule. P_{680} contains one hydrogen bond at each Chl *a* provided by the $Ser282_{D2}$ residue and a water molecule at Chl_{1A} and Chl_{1B}, respectively (**Figure 4F**). Moreover, the axial ligand to each Chl *a* is a His residue, $His197_{D1}$ and $His198_{D2}$, where the $His197_{D1}$ residue also serves to bind a water molecule in proximity of the Chl_{1A} cofactor. It should be noted that the importance of the $His198_{D2}$ residue is in question and may well be species-dependent. While the alteration of the $His198_{D2}$ residue in PS II from *Synechocystis* sp. PCC 6803 displayed changes in the spectral profile of P_{680} with a corresponding drop in the redox potential of $\sim$ 80 mV (Diner et al., 2001), analogous genetic variants of $His198_{D2}$ in PS II from *Thermosynechococcus elongatus* displayed no discernable effects on the spectral, redox, or kinetic properties of P_{680} (Sugiura et al., 2008). Aside from the H-bonding interactions, the only other deviation between the environment of Chl_{1A} and Chl_{1B} of P_{680} are the residues $Leu182_{D2}$ (near Chl_{1B}) and $Met183_{D1}$ (near Chl_{1B}), in the non-overlapping region of the Chl *a* macrocycles.

The primary donor, P_{680}, further differentiates itself from P_{700} in terms of the inter-cofactor distances and relative orientation of the Chl *a* molecules. While the macrocycles adopt a parallel orientation with a similar distance between the ring planes of Chl_{1A} and Chl_{1B} of 3.4–3.6 Å, the distance between the Mg^{2+} ions increases to 8.2 Å in P_{680}. This results in minimal overlap of Chl_{1A} and Chl_{1B}, which is evident only in part of the N^3 pyrrole group (**Figure 5B**, Top Panel). The limited overlap of the ring planes is further manifest as an increased distance between the nearest nitrogen atoms of Chl_{1A} and Chl_{1B}. The distance for the three nearest nitrogen atoms are: N^{3D1}–N^{3D2} (5.0 Å), N^{3D1}–N^{2D2} (5.6 Å), and N^{2D1}–N^{2D2} (6.2 Å) (**Figure 5B**, bottom panel). This reveals that not only is there an increase in the distance between proximal nitrogen atoms of Chl_{1A} and Chl_{1B}, but the longest distance of the three nitrogen atoms is observed in N^{2D1}–N^{2D2} (as opposed to N^{3A}–N^{2B} for P_{700}). This suggests that the macrocycles exhibit a small degree of 'outward' rotation relative to each other. However, the orientation of the tail of P_{680} is typical of other Type II RCs, where it extends outward toward the stromal side of the protein. The space-filling model shown in **Figure 6B** provides a visual representation of the change in ring overlap, slight outward rotation, and the change of the tail orientation of P_{680}.

The Primary Donor, P_{865} and P_{960}, of the Bacterial Reaction Centers

The final set of heterodimeric primary donors is that of the bRCs from *Rba. sphaeroides* and *Rps. viridis* (more recently known as *Bl. viridis*) [reviewed in Leonova et al. (2011) and Savikhin and Jankowiak (2014)]. The determination of the X-ray crystal structure of these RCs dates back to several decades. Indeed, the first X-ray crystal structure of a membrane protein ever obtained was from *Rps. viridis*, for which Hartmut Michel, Robert Huber, and Johann Deisenhofer were awarded the Nobel Prize in chemistry in 1988 (Deisenhofer et al., 1985). In contrast with the other heterodimeric RCs, the bRC is relatively simple, being composed of only three polypeptide subunits, L, M, and H. An additional subunit containing four cytochrome *c* polypeptides is present in *Rps. viridis*, but the electron-transfer cofactors are entirely contained within the L and M subunits of the bRC. Similar to PS II, the electron transfer chain of the bRC is comprised of four bacteriochlorophylls (BChl), two

bacteriopheophytins ($BPheo_A$ and $BPheo_B$) and two quinones (Q_A and Q_B) (**Figures 7A,B,D,E**).

The predominant model of charge separation in the bRC includes the initiation of electron transfer at the primary donor (Niedringhaus et al., 2018), P_{865} and P_{960}, in *Rba. sphaeroides* and *Rps. viridis*, respectively. Theoretical studies have even suggested that charge separation can occur in the primary donor between $BChl_{1A}$ and $BChl_{1B}$ itself (Xu et al., 2002). However, Huang and coworkers used polarization selective spectroscopic methods to demonstrate that the excitation of $BChl_2$ can lead to two sub-populations, wherein there is rapid formation of $BChl_{2A}^{\cdot+}Pheo_A^{\cdot-}$ in approximately half of the RCs, and the excitation migrates to P_{865} in the remaining RCs (Huang et al., 2012). The photoexcitation of the primary donor results in charge separation within 3–5 ps in *Rba. sphaeroides* (Martin et al., 1986; Holzapfel et al., 1989; Lauterwasser et al., 1991; Peloquin et al., 1994; Holzwarth and Müller, 1996) and a slightly faster rate of ∼ 2 ps in *Rps. viridis* (Wasielewski and Tiede, 1986; Huppman et al., 2002). The rapid formation of the $Pheo_A^{\cdot-}$ state is unexpected given its long distance from the primary donor. Hence, it was proposed that the accessory BChl, $BChl_2$, may play a role in charge separation. Through a combination of transient absorption spectroscopy (Arlt et al., 1993; van Stokkum et al., 1997), ultrafast mid-IR spectroscopy (Pawlowicz et al., 2008), mutagenesis (Shkuropatov and Shuvalov, 1993; Heller et al., 1996; Kennis et al., 1997; Roberts et al., 2001), and cofactor replacement experiments (Kirmaier et al., 1995a,b), the presence of $BChl_2^{\cdot-}$ was indeed detected and it was found to play an integral role in electron transfer. However, the first stable electron transfer intermediate is largely considered to be $Pheo_A^{\cdot-}$, after which the electron is transferred to the primary quinone, Q_A, in ∼ 200 ps. The

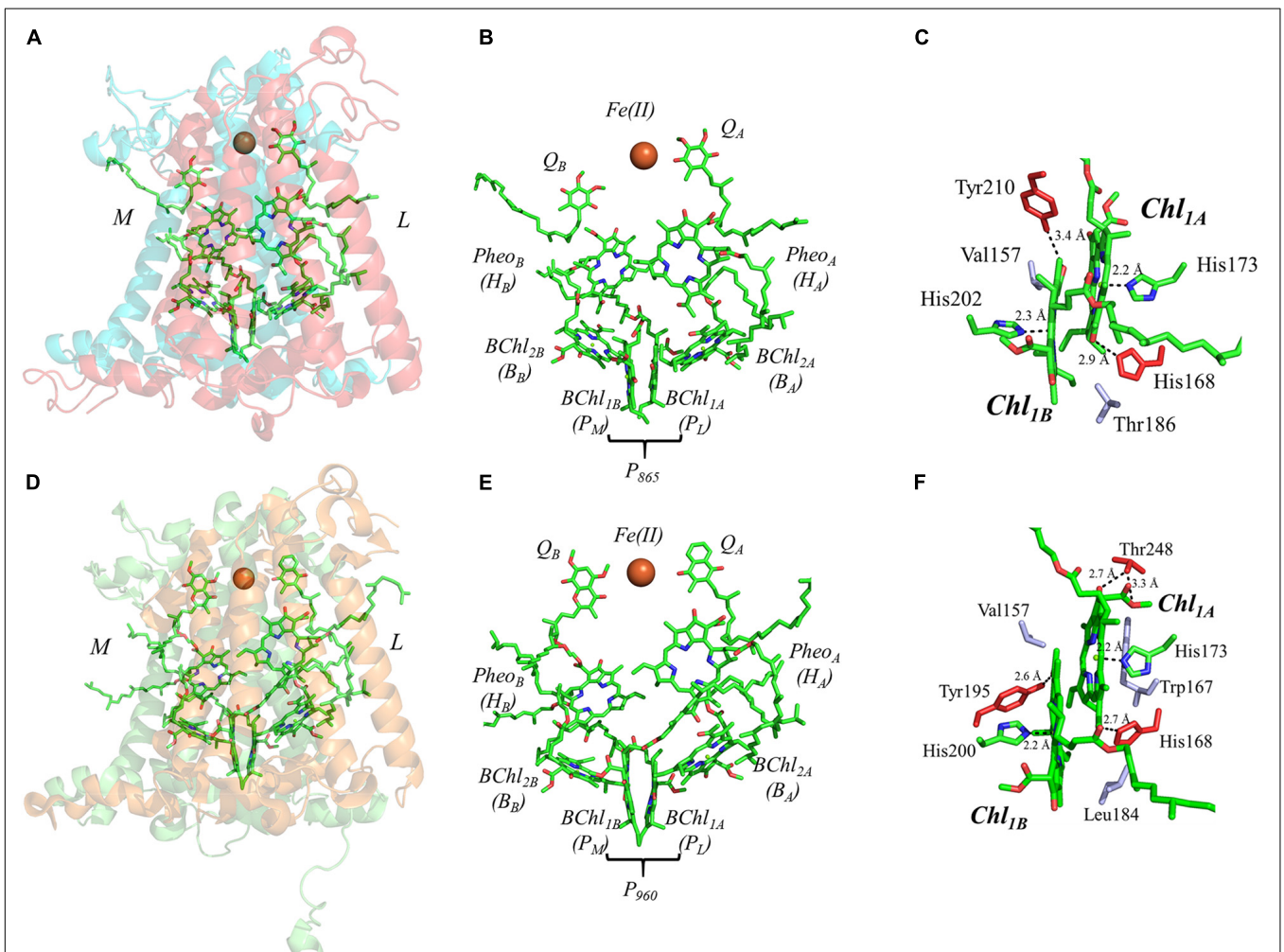

FIGURE 7 | (A) The core subunits (M, blue; and L, red) and cofactors of the bRC from *Rba. sphaeroides* as observed by X-ray crystallography (PDB ID: 1aij), **(B)** the cofactors that participate in the primary electron transfer pathway of the bRC from *Rba. sphaeroides* and **(C)** the binding pocket of the primary donor, P_{865}. **(D)** The core subunits (M, blue; and L, red) and cofactors of the bRC from *Rps. viridis* as observed by X-ray crystallography (PDB ID: 2jbl), **(E)** the cofactors that participate in the primary electron transfer pathway of the bRC from *Rps. viridis* and **(F)** the binding pocket of the primary donor, P_{960}. Commonly used labels are in parentheses. Part **(C,F)** emphasize the prominent protein-matrix effects of the primary donor of the bRC from *Rba. sphaeroides* and *Rps. viridis*, respectively, where the residues that are hydrogen bonded to the primary donors are shown in red, and nearby non-polar or π-stacked residues are colored in gray.

reduction of Q_A, and the subsequent change in the presence of an electric field causes a structural perturbation to the solvation (and ultimately the protein) structure (Arata and Parson, 1981; Kleinfeld et al., 1984b; McMahon et al., 1998), which allows for the final step of electron transfer and the reduction of the secondary quinone, Q_B. Similar to PS II, two turnovers of the bRC are required for the complete reduction of Q_B, which functions as a two-electron/two-proton acceptor, forming the quinol, Q_BH_2 (Wraight, 2004).

The primary donor of the bRC is a dimer of two BChl molecules that are bound by the L and M polypeptide subunits. It is interesting that the identity of the BChls, and thus the spectral features of the primary donors, P_{865} and P_{960}, of the bRC from *Rba. sphaeroides* and *Rps. viridis* are different. In *Rba. sphaeroides,* the primary donor, P_{865}, is a dimer of BChl *a* molecules, while P_{960} of *Rps. viridis* is a dimer of BChl *b* molecules. In this section, we will focus on both bRCs as the differences between the two are minor. The binding site of P_{865} and P_{960} suggests a moderately asymmetric H-bonding environment that could influence the relative redox potential of each primary donor. As shown in **Figures 7C,F**, there is a hydrogen bond to the BChl molecules of P_{865} and P_{960} from the $Tyr210_L$ and $Tyr195_L$ residue that are within 3.4 and 2.6 Å, of $BChl_{1B}$, respectively, and the $His168_L$ that is within 2.9 and 2.7 Å of $BChl_{1A}$ in P_{865} and P_{960}, respectively. There is an additional residue that provides a hydrogen bond to $BChl_{1A}$ in P_{960}, $Thr248_L$, with the hydroxyl and carboxyl group at a distance of 2.7 and 3.3 Å, respectively. Additional differences between the two bRCs include the residues that are located in the non-overlapping region of the BChl rings. In P_{960}, there are two non-polar residues, $Val157_L$ and $Leu184_M$, whereas, in P_{865} there is a non-polar, $Val157_L$, and an unusual polar residue, $Thr186_M$. The axial ligands of all of the BChl molecules, however, remain similar to all of the other primary donors, with $His202_M$ (P_{865})/$His200_M$ (P_{960}) and $His173_L$ ligating $BChl_{1B}$ and $BChl_{1A}$, respectively.

Further analysis of the inter-cofactor distances and relative orientation of the BChl macrocycles of P_{865} of the bRC from *Rba. sphaeroides* reveals a structure that is similar to P_{680} of PS II, albeit with unusual features. A view of the macrocycle plane (**Figure 5C**, Top Panel) indicates an overlapping structure that is similar to PS II, whereby the overlap of the two BChl rings is nearly exclusively on the pyrrole associated with N^3. The Mg–Mg distance of P_{865} is 7.6 Å, which is in between PS II (8.2 Å) and PS I (6.3 Å); however, there is significantly more overlap than exists in P_{680}. But perhaps the most defining feature of the BChl dimer of P_{865} is in how it deviates from a parallel orientation of the ring planes. The macrocycles form a 'V' shape when viewed parallel to the ring plane, pointing toward the luminal side of the protein. While most prominently seen in *Rps. viridis*, it is also observed in *Rba. sphaeroides* (**Figures 5C,D**). As expected, this results in a change of the distance between the nearest nitrogen atoms of the macrocycles. While the N^3 nitrogen atoms remain the closest at 4.6 Å and the $N^3{}_M$–$N^2{}_L$ distance is next at 6.0 and 5.9 Å in P_{865} and P_{960}, respectively, $N^2{}_M$ is located at a distance of 5.9 and 5.8 Å from $N^3{}_L$ in P_{865} and P_{960}, respectively, which is different from the pattern that is observed in other RCs. The space-filling model P_{865} and P_{960} shown in **Figures 6C,D** displays the macrocycle overlap and tail orientation that is common to other Type II RCs.

Geometric Structure of the Primary Donor of Homodimeric Reaction Centers

The Primary Donor, P_{800}, of *Heliobacterium modesticaldum*

The homodimeric RC from *H. modesticaldum*, HbRC, is a simplified complex which is often considered an exemplar of ancestral Type I RCs (Ferlez et al., 2016; Orf et al., 2018). It has long been known that the HbRC is composed of a dimer of PshA polypeptide subunits, but it was not until the availability of the X-ray crystal structure that another identical pair of polypeptide subunits, PshX, were found on the periphery of each PshA polypeptide subunit (Gisriel et al., 2017; **Figure 8A**). The electron-transfer cofactors are completely housed in the PshA polypeptide core, and are comprised of four symmetric BChl *g* molecules, two 8^1-OH Chl *a* molecules, and a single inter-polypeptide [4Fe–4S] cluster, F_X (**Figure 8B**). Note the lack of the two quinones and two additional [4Fe–4S] clusters bound by a small soluble ferredoxin-like protein present in the other Type I RC, PS I, discussed above (Romberger and Golbeck, 2012).

The mechanism(s) of primary charge separation in the HbRC has been the focus of several recent studies. The unusual pigment composition of the HbRC, where multiple types of (B)Chl molecules are involved in electron transfer, lends itself particularly well to the direct observation of the transient excited states using optical spectroscopic methods. Ultrafast pump-probe spectroscopy was initially employed to study energy transfer amongst the various pools of BChl molecules as well as the initial states of charge separation, suggesting a highly coupled system of early BChl molecules (Kojima et al., 2020). Subsequently, global analysis of two-dimensional electronic spectra suggested multiple pathways of charge separation. The direct photoexcitation of the trap was suggested to generate the excited state $[BChl_2/Chl_3]^*$, which then extended to $[P_{800}/BChl_2/Chl_3]^*$ in $\sim$ 90 fs and led to the formation of the first charge-separated state, $[P_{800}/BChl_2]^{\cdot-}Chl_3{}^{\cdot+}$, within 900 fs (Song et al., 2021). Alternately, the excitation of the antenna system led to the formation of the initial charge-separated state, $[P_{800}/BChl_2]^{\cdot-}Chl_3{}^{\cdot+}$, within 2.2 ps. Regardless of which mechanism is involved, the final charge separated state, $P_{800}{}^{\cdot+}A_0{}^{\cdot-}$, was formed within 20–25 ps, which is in agreement with previous observations (Chauvet et al., 2013; Kojima et al., 2020). Once the stable $P_{800}{}^{\cdot+}A_0{}^{\cdot-}$ state is formed in the HbRC, the electron is transferred to the F_X cluster in 600–800 ps (Nuijs et al., 1985a; Chauvet et al., 2013).

Much like PS I, the primary donor of the HbRC, P_{800}, is composed of an epimer of the primary pigment of the RC, which is BChl *g*' (Kobayashi et al., 1991). The P_{800} dimer may be the most interesting of all the cases discussed here, not because it contains extensive protein-matrix effects like those observed for P_{700}, but rather due to the lack of apparent protein matrix effects from the surrounding environment. While FTIR spectroscopy had previously suggested that a cysteine residue, either Cys469 or Cys601, may be hydrogen bonded to the primary donor itself

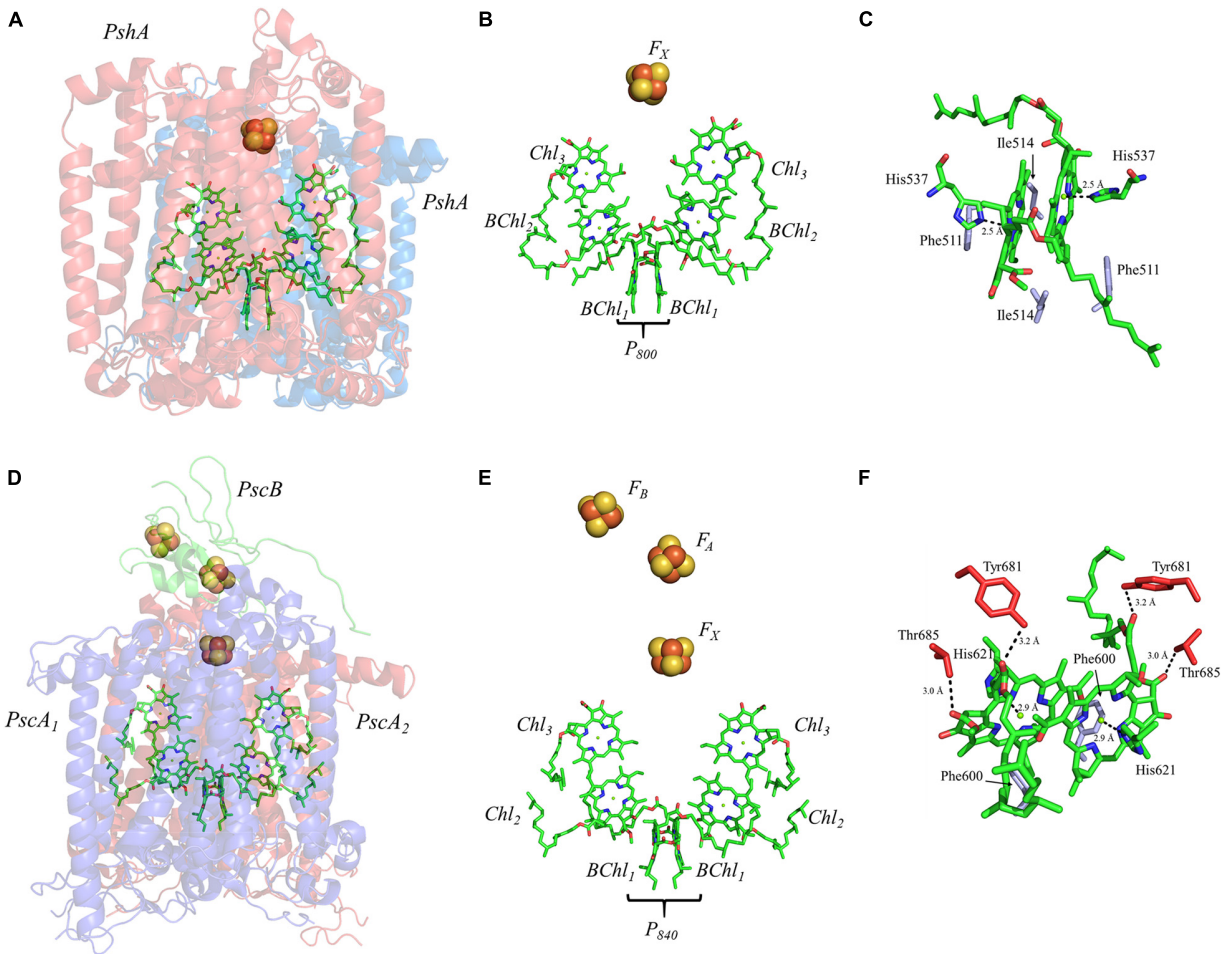

FIGURE 8 | (A) The core subunits (PshA, Blue and Red) and cofactors of the HbRC from *H. modesticaldum* as observed by X-ray crystallography (PDB ID: 5v8k), **(B)** the cofactors that participate in the primary electron transfer pathway of the HbRC and **(C)** the binding pocket of the primary donor, P_{800}. **(D)** The core subunits ($PscA_1$, blue; $PscA_2$, red; and PscB, green) and cofactors GsbRC from *C. tepidum* as observed by cryo-electron microscopy (PDB ID: 6m32), **(E)** the cofactors that participate in the primary electron transfer pathway of the GsbRC and **(F)** the binding pocket of the primary donor, P_{840}. The residues in part **(C,F)** that are providing hydrogen bonds are shown in red, and nearby non-polar or π-stacked residues are colored in gray.

(Noguchi et al., 1997), the high-resolution X-ray crystal structure of the HbRC has revealed that this is not the case (Gisriel et al., 2017). Instead, the differential signal at 2550/2560 cm^{-1} that was observed in the FTIR spectra was likely due to Cys601, a residue that is in close proximity to the axial His ligands, His537, of P_{800}. Indeed, there are no apparent hydrogen bonds that have been observed in either of the BChl *g*' molecules of the HbRC (**Figure 8C**). Also lacking are any effects from neighboring water molecules. The only observable residues are Ile514 that resides in the non-overlapping region of the BChl *g*' macrocycles and a nearby Phe511 residue within 4.4 Å that is oriented in a pseudo π-stacked fashion.

Several facets of the inter-cofactor distances and relative macrocycle orientation further showcase the unique nature of the BChl *g*' dimer of P_{800}. The Mg–Mg distance is the shortest of all known RCs, at 5.7 Å, which results in a significant amount overlap of the BChl *g*' macrocycles (**Figure 9A**). Moreover, while the macrocycles maintain a roughly parallel orientation, there is a minor bend in each BChl, which causes the distance between the rings to vary from 3.1 to ∼ 3.5 Å, the former being the shortest distance between ring planes seen thus far. An interesting artifact of the macrocycle structure is reflected in the distance between the nearest nitrogen atoms of the rings. Not only is N^3–N^3 distance of 3.1 Å representative of the closest point between the two macrocycles, the distance between N^2–N^2 and N^3–N^2 for each ring is identical at 4.7 Å (the distance parameters for homodimeric RCs are summarized in **Table 1**). This suggests a highly coupled dimer resulting in nearly symmetric electron density on each macrocycle. The extensive overlap of the two macrocycles of P_{800} is evident in the space-filling model shown in **Figure 10A**, with a tail orientation typical of Type I RCs.

The Primary Donor, P_{840}, of *Chlorobaculum tepidum*

The RC from the green sulfur bacterium *C. tepidum*, GsbRC, is a homodimer of the membrane-bound PscA polypeptide subunit (**Figures 8D,E**), which is encoded by a single gene, *pscA*

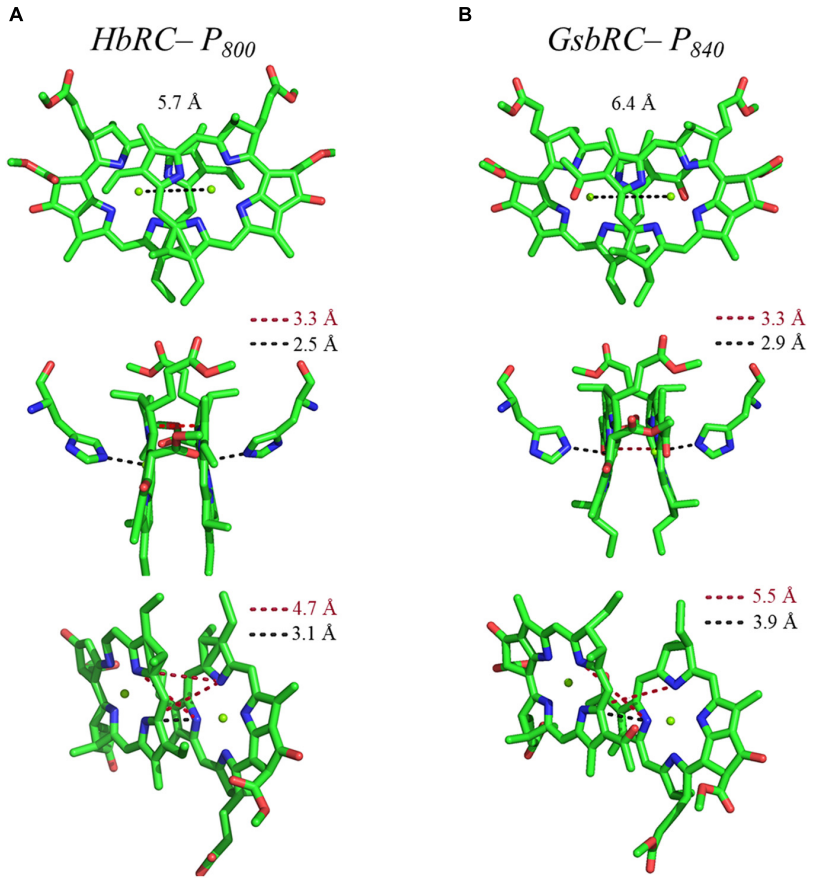

FIGURE 9 | Analysis of inter-cofactor distances and relative orientation of primary donors from the homodimeric RCs: **(A)** P_{800} from the HbRC, and **(B)** P_{840} from the GsbRC.

(Hager-Braun et al., 1999; Hauska et al., 2001). The GsbRC core also includes PscB, a polypeptide analogous to PsaC in PS I, however, this polypeptide subunit is less tightly bound than PsaC and can be removed with detergent treatment (Miller et al., 1992; Schmidt et al., 2000) or at relatively low salt concentration (Miller et al., 1992; Jagannathan and Golbeck, 2008). While the polypeptide core and accompanying cofactors of the GsbRC should be considered a homodimer, the symmetry is broken by the PscB polypeptide, whose arbitrary orientation (in conjunction with PscD) directs the binding of the FMO-1, -2, and -3 proteins on the cytoplasmic side of the membrane (Chen et al., 2020). The electron-transfer cofactors reside within the homodimeric core and are comprised of two BChl molecules that constitute the primary donor, P_{840}, four Chl *a* molecules, and three [4Fe–4S] clusters, F_X, F_A, and F_B. Similar to the HbRC, note the absence of any quinones between Chl_3 and the [4Fe–4S] clusters. For a detailed review of the GsbRC, please see (Hauska et al., 2001).

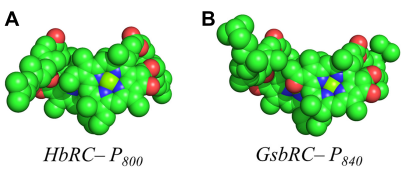

FIGURE 10 | Space filling models of **(A)** P_{800} from the HbRC and **(B)** P_{840} from the GsbRC.

Charge separation in the GsbRC appears to follow a pattern similar to that of other Type I RCs. Time-resolved transient absorption spectroscopy at various temperatures has suggested that a highly electronically coupled system of (B)Chls are responsible for energy trapping and primary charge separation (Neerken et al., 1998, 1999). It should be noted that similar data is not available for the homodimeric HbRC, hence, a detailed comparison of the mechanism is not possible here. Regardless, photoexcitation of the trap appears to be complete within 2 ps, allowing charge separation to occur within 25 ps (Francke et al., 1996; Neerken et al., 1998, 1999), a lifetime that is nearly identical to the HbRC. Optical spectroscopy on the picosecond time scale showed that subsequent electron transfer from $A_0^{\cdot -}$ to F_X occurs within 600 ps (Nuijs et al., 1985b; Shuvalov et al., 1986), notably slower than $A_0^{\cdot -}$ oxidation in PS I. Electron transfer then proceeds linearly through the two [4Fe–4S] clusters, F_A and F_B, that are bound by the PscB subunit in <5 μs (Hauska et al., 2001).

Similar to PS I and HbRC, the primary donor of the GsbRC is comprised of a 13^2-epimer, BChl *a*' (Kobayashi et al., 2000). Examination of the primary donor of the GsbRC in **Figure 8F** reveals that the protein-matrix effects are much more pronounced than those of the analogous homodimeric RC, the HbRC, from *H. modesticaldum*. As discussed recently, the markedly lower resolution of the cryo-electron microscopy structure (as compared to other X-ray structures) suggests that assignments of protein matrix interactions should be considered tentative (Gisriel et al., 2021). There exists a total of four hydrogen bonds, two on each BChl macrocycle, provided by the Tyr681 and Thr685 residues (**Figure 8F**). However, as this is a homodimeric RC, it is expected that the effects of these interactions will impact the redox properties of each BChl *a* molecule equally and only serve to alter the redox potential of the primary donor, P_{840}, as opposed to influencing the localization of the charge density. Another interesting feature of the protein matrix is the identity of the non-polar residues that fill the non-overlapping region of the macrocycles. While these tend to be amino acid residues with a short aliphatic side chain, such as Val and Ile in both heterodimeric and homodimeric RCs, there are aromatic residues in the GsbRC, *e.g.,* Phe600. The side chain of the Phe residues are orthogonal to the BChl *a* macrocycles, suggesting that there are no π-stacking interactions present. However, the aromatic residues are within a distance of 3.1 Å of the BChl *a* macrocycles and are likely to impact the redox properties of the P_{840} dimer.

The inter-cofactor distances and relative orientation of the BChl *a* macrocycles of the primary donor, P_{840}, appear to be similar to P_{700} and P_{800} of PS I and the HbRC, respectively. The Mg–Mg distance of 6.4 Å for P_{840} (**Figure 9B**, Top Panel) is close to that of the P_{700} donor of PS I (6.3 Å), resulting in significant overlap of the two macrocycles, including both the pyrrole rings of N^3 and to a lesser extent the pyrrole ring associated with N^2. However, when viewed along the ring planes, it is clear that the macrocycles remain in a roughly parallel orientation, but adopt a non-planar or domed shape. While analogous to the HbRC, the deviation from planarity is much more extensive in P_{840}. This bending results in a slight deviation in the identity of the nearest nitrogens of the macrocycles, where N^3s remain proximal to each other at 3.9 Å, and both N^2s are proximal to the opposing N^3, at 5.4 and 5.5 Å. The space-filling model shows overlapping rings and a tail orientation that shares a high similarity to that of P_{700} (**Figure 10B**).

ELECTRONIC STRUCTURE OF THE PRIMARY DONOR OF HETERODIMERIC AND HOMODIMERIC REACTION CENTERS

Continuous-Wave and Pulsed Electron Paramagnetic Resonance Spectroscopy Measurements

Continuous-wave (*CW*) and pulsed electron paramagnetic resonance (EPR) spectroscopy has been used for the study of the electronic structure and function of (B)Chl cofactors of RCs (Commoner et al., 1956; Käβ et al., 1995, 1996; Käβ and Lubitz, 1996). As described above, developments in protein crystallization and X-ray crystallography led to outstanding high-resolution structures of PS I, PS II, the bRC and HbRC from cyanobacteria, purple bacteria and heliobacteria, respectively (Stowell et al., 1997; Jordan et al., 2001; Umena et al., 2011; Gisriel et al., 2017). These advances have been complemented by other techniques, such as, cryo-electron microscopy, that provided the structure of the GsbRC from green sulfur bacteria (Chen et al., 2020). While these structures have delivered insight on the geometry and relative topology of the (B)Chl dimers in the neutral ground state, spectroscopic measurements have been instrumental in determining the electronic properties of the individual primary donors. *CW* and pulsed EPR methods have been especially well suited to probe the structure of the oxidized primary donors as the high sensitivity and specificity of the detection of unpaired electron spin(s) has helped overcome limitations of the large size of the RCs, and the use of powder samples has largely eliminated the need for soluble or crystalline material.

Photooxidation of the primary donor, P, generates a paramagnetic center with an unpaired electron spin, S, of 1/2 which makes it possible to probe the $P^{\cdot+}$ state by EPR spectroscopy. The EPR signal of $P^{\cdot+}$ is known to display a relatively small *g*-anisotropy, with a featureless resonance at X-band (9.6 GHz) frequency (Commoner et al., 1956; Norris et al., 1971). One of the earliest applications of *CW* EPR spectroscopy demonstrated that steady-state photoaccumulation of the primary donor cation, $P_{700}^{\cdot+}$, of PS I (Commoner et al., 1956), resulted in a signal at a g value of 2.0025. Subsequently, Norris and coworkers showed that the EPR signal of $P_{700}^{\cdot+}$ arises from a strongly excitonically coupled Chl *a* dimer (Norris et al., 1971; Davis et al., 1993; Mac et al., 1998; Käβ et al., 2001) with a line width that is narrower than that of monomeric Chl $a^{\cdot+}$ *in vitro* (Norris et al., 1971). This observation provided initial evidence for the delocalization of the unpaired electron spin across the dimeric $Chl_{1A/1B}$ cofactors of $P_{700}^{\cdot+}$ (Norris et al., 1971). The line width of the excitonically coupled dimeric $Chl_{1A/1B}$ molecules of $P_{700}^{\cdot+}$ is related to the width of a monomeric cation signal through the relationship, $\Delta H_N = 1/\sqrt{N} \cdot \Delta H_M$ (where ΔH_N and ΔH_M are the line width of the multimeric chlorophyll cation with spin delocalization, $Chl_N^{\cdot+}$, and a monomeric $Chl^{\cdot+}$ cation, respectively). The presence of a narrower line width, and hence the possible delocalization of the unpaired electron spin, was also observed in the primary donor, $P_{680}^{\cdot+}$ and $P_{865}^{\cdot+}$, of PS II and the bRC from *Rba. sphaeroides*, respectively (van Gorkom et al., 1974; Davis et al., 1979).

Although the *g*-anisotropy of an oxidized primary donor, $P^{\cdot+}$, is not resolved at X-band (9.6 GHz) frequency, it is possible to observe the anisotropy at higher EPR frequencies (Webber and Lubitz, 2001). One of us has previously demonstrated that the *g*-anisotropy of $P_{700}^{\cdot+}$ can be resolved at D-band (130 GHz) EPR frequency using perdeuterated PS I from *Synechococcus lividus* (Poluektov et al., 2002). These studies suggested that the *g*-anisotropy of $P_{700}^{\cdot+}$ is smaller than that of monomeric Chl $a^{\cdot+}$ *in vitro*, which was explained by the delocalized electronic

character of $P_{700}^{\cdot+}$ or a heteromeric model of the primary donor. Using higher EPR frequencies, Angerhofer, Redding and coworkers determined the *g*-anisotropy of $P_{700}^{\cdot+}$ of PS I from *Chlamydomonas reinhardtii* (Petrenko et al., 2004) and higher plants (Bratt et al., 1997, 2000), which suggested that the electron spin distribution of $P_{700}^{\cdot+}$ may be more monomeric than dimeric. A similar comparison of the *g*-anisotropy of $P_{865}^{\cdot+}$ of the bRC from *Rba. sphaeroides* with monomeric BChl $a^{\cdot+}$ *in vitro* also revealed little difference in the respective line widths (Burghaus et al., 1993). However, these results were in contrast with previous experimental and computational studies. Thus, it appeared that the magnitude of *g*-anisotropy of the primary donor cation, $P^{\cdot+}$, alone was not sufficient to provide definitive evidence on the extent of the delocalization of the electron spin over the (B)Chl molecules.

In principle, the direct measurement of magnetic hyperfine couplings between the unpaired electron spin and NMR-active nuclei could reveal the distribution of the electron spin density and hence, the electronic structure of the $Chl_{1A/1B}$ dimer in the oxidized primary donor, $P^{\cdot+}$. However, it is not possible to measure the electron-nuclear hyperfine interactions using *CW* EPR spectroscopy due to the inhomogeneous broadening of the peaks in the spectrum. Therefore, hyperfine spectroscopy methods, such as ENDOR, electron-spin-echo envelope modulation (ESEEM) and two-dimensional (2D) hyperfine sub-level correlation (HYSCORE) spectroscopy, in conjunction with computational modeling, have been used to obtain information on the electronic structure of the oxidized primary donors (Britt, 1993; Deligiannakis et al., 2000; Lakshmi and Brudvig, 2000, 2001; Prisner et al., 2001; Harmer et al., 2009). The electron-nuclear hyperfine interactions determined by both experimental and computational methods have been used to identify the *CW* EPR signals, characterize the surrounding environment and coordination geometry, and quantitatively determine the hyperfine couplings and electron spin density distribution of the oxidized primary donors, $P^{\cdot+}$, in RCs. These measurements have included hyperfine interactions of the unpaired electron spin of the oxidized primary donor, $P^{\cdot+}$, with NMR-active nuclei, such as ^{1}H, ^{13}C, ^{15}N and ^{14}N of the (B)Chl molecules.

Electron-nuclear double resonance spectroscopy is a double resonance technique with reasonably high spectral resolution that has typically allowed for the measurement of small hyperfine couplings. Initial ENDOR spectroscopy studies of $P^{\cdot+}$ utilized *CW* radio-frequency irradiation, although this was replaced by pulsed methods, such as, Mims and Davies ENDOR, which have the advantage of more selective measurement of the nuclear hyperfine couplings (Hoffman, 2003; Kulik and Lubitz, 2009). More recently, ESEEM spectroscopy has been applied to the study of the oxidized primary donor, $P^{\cdot+}$, as it overcomes the inhomogeneous broadening of EPR resonances and provides access to unresolved electron-nuclear hyperfine couplings (Deligiannakis et al., 2000). The hyperfine couplings that are measured by ENDOR and ESEEM spectroscopy are orientation dependent, which means that information on the hyperfine anisotropy is lost in powder EPR samples with random orientations. Therefore, the hyperfine measurements of $P^{\cdot+}$ have also been performed on single-crystals of RCs or at high EPR frequencies, where the *g*-anisotropy of $P^{\cdot+}$ is better resolved making it possible to select for specific orientations of the molecules with respect to the applied magnetic field.

The nuclear transitions of multiple abundant spins, such as, ^{1}H or ^{14}N, in powder samples or frozen solutions have often been difficult to resolve by one-dimensional ENDOR and ESEEM spectroscopy due to spectral overcrowding of signals. Hence, we and others have been employing HYSCORE spectroscopy, which is a two-dimensional version of ESEEM, to obtain correlations between nuclear transitions to facilitate the detection and assignment of multiple hyperfine-coupled proton and nitrogen atoms of the oxidized primary donors, $P^{\cdot+}$, in two-dimensional frequency space (Höfer et al., 1986). All three of the hyperfine methods, ENDOR, ESEEM and HYSCORE, are highly sensitive as the electron spin-coupled nuclear transitions are monitored through the observation of a paramagnetic electron spin (Webber and Lubitz, 2001). Additionally, these methods are versatile as they can detect weak hyperfine couplings to less sensitive nuclei with smaller magnetic moments, such as, ^{14}N and ^{15}N atoms.

The hyperfine interactions of protons (^{1}H), carbon (^{13}C) and nitrogen (both ^{14}N and isotope-labeled ^{15}N) atoms of the oxidized primary donor, $P_{700}^{\cdot+}$, $P_{865}^{\cdot+}$, $P_{960}^{\cdot+}$, $P_{680}^{\cdot+}$, and $P_{840}^{\cdot+}$ of the heterodimeric RCs, PS I, the bRC from *Rba. sphaeroides* and *Rps. viridis*, PS II and the homodimeric RCs, GsbRC from *Chlorobium limicola* and *Chloroacidobacterium thermophilum* (*Cab*. RC) (Charles et al., 2020), respectively, have been determined by pulsed EPR spectroscopy methods. As shown in **Figures 4C,F**, **7C,F**, **8F**, the primary donors of PS I, PS II, the bRCs and GbRC are comprised of a dimer of $(B)Chl_{1A}$ and $(B)Chl_{1B}$ molecules (Stowell et al., 1997; Jordan et al., 2001; Umena et al., 2011). Earliest estimates of the hyperfine coupling parameters of $P_{700}^{\cdot+}$ of PS I were obtained by Dikanov, Astashkin and coworkers using ENDOR and ESEEM spectroscopy of the nitrogen atoms (both ^{14}N and ^{15}N) of the Chl *a* and Chl *a*' macrocycles interacting with the unpaired electron spin (Dikanov et al., 1983; Astashkin et al., 1987). It was observed that the unpaired electron spin of $P_{700}^{\cdot+}$ displayed magnetic interactions with four nitrogen atoms, where two of the nitrogens were strongly hyperfine coupled with an isotropic hyperfine coupling, A_{iso}, of $\sim$ 2 MHz, and two other nitrogens were weakly coupled with a much smaller A_{iso} of $\sim$ 0.2 MHz. While the early results were semi-qualitative, they established the feasibility of hyperfine measurements on $P_{700}^{\cdot+}$ and highlighted the need for measurements that would yield higher spectral resolution.

Subsequently, the unpaired electron spin density distribution of the oxidized primary donors was determined by quantitative measurements of the hyperfine interactions of the protons and nitrogen atoms, which were compared with those of monomeric Chl $a^{\cdot+}$ and BChl $a^{\cdot+}$ *in vitro* (Astashkin et al., 1988). There is broad consensus in the field that the oxidized heterodimeric primary donors are comprised of a dimer of coupled (B)Chl molecules, albeit with small differences on the extent of asymmetry of the electron spin delocalization across the dimer. The asymmetric spin density distribution (ratio 3:1 to 5:1) of $P_{700}^{\cdot+}$ has been observed by ^{1}H, ^{14}N and ^{15}N ENDOR, HYSCORE and single crystal EPR and

ENDOR measurements (Käβ et al., 1995; Käβ and Lubitz, 1996; Deligiannakis and Rutherford, 2001; Käβ et al., 2001; Webber and Lubitz, 2001; Chestnut et al., 2021). Recently, using ^{14}N HYSCORE spectroscopy we conclusively established that there are at least four distinct ^{14}N atoms (and likely more than four nitrogen atoms if we consider the possibility of overlapping cross-peaks in the spectrum) that are interacting with the unpaired electron spin of $P_{700}^{\cdot+}$ (Gorka et al., 2021b). The isotropic hyperfine couplings, A_{iso}, range from 1.4–2.8 MHz, indicating that the electron spin is distributed on at least four nitrogen atoms. In conjunction with previous and current findings, this indicates that $P_{700}^{\cdot+}$ is comprised of a strongly electronically coupled Chl *a* dimer, where the unpaired electron spin density distribution is asymmetric over the two Chl a molecules (Käβ et al., 1995; Käβ and Lubitz, 1996; Deligiannakis and Rutherford, 2001; Käβ et al., 2001; Webber and Lubitz, 2001; Chestnut et al., 2021). A summary of the experimental hyperfine and quadrupolar couplings of the nitrogen atoms of $P_{700}^{\cdot+}$ is presented in **Table 2**.

Early experimental measurements of $P_{865}^{\cdot+}$ of the bRC from *Rba. sphaeroides* had determined two or four nitrogen hyperfine coupling tensors, which were on average smaller than those of the monomeric BChl $a^{\cdot+}$ *in vitro* by a factor of 2 (Lubitz et al., 1984). At the time, this seemed adequate as only four reduced hyperfine couplings were expected for the nitrogen atoms in a symmetric BChl dimer model of $P_{865}^{\cdot+}$. Consequently, the first ENDOR and ESEEM spectroscopy studies were interpreted on the basis of an essentially symmetric spin density distribution across $BChl_{1A}$ and $BChl_{1B}$ of $P_{865}^{\cdot+}$ (Lubitz et al., 1984; Lin et al., 1986; Astashkin et al., 1988). A detailed ^1H ENDOR study performed on single crystals of the bRC from *Rba. sphaeroides* near room temperature showed that the 3:1 electron spin density distribution in favor of the Chl_{1A} (Lendzian et al., 1993), which was also observed for $P_{960}^{\cdot+}$ of the bRC from *Rps. viridis* (Lendzian et al., 1988). This observation was further supported by the determination of ^{15}N hyperfine couplings under similar conditions using ^{15}N-labeled single crystals of the bRC (Lendzian et al., 1992). However, the complete hyperfine tensors were not determined in these experiments and hence, the assignment of the hyperfine couplings was only possible by comparison with molecular orbital calculations. These results were further confirmed by ESEEM measurements of $P_{865}^{\cdot+}$ and $P_{960}^{\cdot+}$ of the bRC from *Rba. sphaeroides* and *Rps. viridis* (Davis et al., 1993). Subsequently, a combined ESEEM and HYSCORE spectroscopy study of monomeric ^{15}N-labeled BChl $a^{\cdot+}$ in solution and $P_{865}^{\cdot+}$ in ^{15}N-labeled bRC from *Rba. sphaeroides* yielded a much higher asymmetry of the spin density ratio of approximately 5:1 (Käβ et al., 1995; **Table 2**).

Proton ENDOR and HYSCORE spectroscopy have also been employed for the study of the primary donor cation, $P_{680}^{\cdot+}$, in core preparations of PS II containing the D1, D2 and cytochrome b_{559} polypeptides (Rigby et al., 1994a). The hyperfine parameters of the protons of methyl groups obtained from ^1H ENDOR spectroscopy was used to calculate the electron spin density distribution of $P_{680}^{\cdot+}$. Comparison of the hyperfine parameters and electron spin density distribution of $P_{680}^{\cdot+}$ with the Chl $a^{\cdot+}$ monomer *in vitro* indicated an apparent reduction in the unpaired electron spin density for $P_{680}^{\cdot+}$. Similar to $P_{700}^{\cdot+}$ and $P_{865}^{\cdot+}$, these studies suggested that $P_{680}^{\cdot+}$ was a weakly coupled $Chl_{1A/1B}$ dimer with 82% of the unpaired electron spin located on one of the chlorophyll molecules. Based on the experimental hyperfine parameters of $P_{700}^{\cdot+}$, $P_{865}^{\cdot+}$, $P_{960}^{\cdot+}$, and $P_{680}^{\cdot+}$, it is evident that the asymmetric spin density distribution that is observed does not appear to be caused by the structural difference of the (B)Chl molecules of $P^{\cdot+}$ in heterodimeric RCs, but by the interaction of the cofactors with the protein environment.

There have been far fewer reports on the primary donors of the homodimeric RC, HbRC and GsbRC. The oxidized primer donor, $P_{840}^{\cdot+}$, of the GsbRC in *Chlorobium limicola* membranes was studied by ^1H ENDOR and Triple electron-nuclear-nuclear spectroscopy (Rigby et al., 1994b). These studies showed that $P_{840}^{\cdot+}$ is comprised of a BChl *a* dimer with a

TABLE 2 | Experimental ^{14}N isotropic hyperfine couplings of the nitrogen atoms of $P_{700}^{\cdot+}$, $P_{865}^{\cdot+}$, and $P_{840}^{\cdot+}$ of the GsbRC and *Cab*. RC.

Nitrogen	$P_{700}^{\cdot+}$				$P_{865}^{\cdot+}$	$P_{840}^{\cdot+}$	$P_{840}^{\cdot+}$
	A_{iso} [MHz][a]	A_{iso} [MHz][b]	A_{iso} [MHz][c]	A_{iso} [MHz][d]	A_{iso} [MHz][e]	A_{iso} [MHz][f]	A_{iso} [MHz][g]
N^{I}	2.8 ± 0.1	2.8 ± 0.4	2.13	2.36	2.65	1.14	0.90 ± 0.2
N^{II}	2.4 ± 0.2	2.3 ± 0.3	2.06	1.95	2.48	1.35	1.10 ± 0.2
N^{III}	1.77 ± 0.1	1.4 ± 0.2	1.95	1.13	2.11	1.35	0.90 ± 0.2
N^{IV}	1.37 ± 0.2	1.2 ± 0.2	2.19	0.67	1.86	1.65	1.00 ± 0.2
N^{V}		0.47 ± 0.07		0.25	0.52		
N^{VI}		0.45 ± 0.07			0.48		
N^{VII}					0.39		
N^{VIII}					0.37		

[a] *Gorka et al. (2021b).*
[b] *Chestnut et al. (2021).*
[c] *Mac et al. (1998).*
[d] *Käβ et al. (1996).*
[e] *Käβ et al. (1995).*
[f] *Bratt et al. (1996).*
[g] *Charles et al. (2020).*

highly symmetrical distribution of electron spin density between $BChl_{1A}$ and $BChl_{1B}$. Moreover, Triple spectroscopy resolved the separate contributions of the two halves of the dimeric primary donor and revealed small deviations from a 1:1 electron spin density distribution. Subsequently, ^{14}N ESEEM spectroscopy of the GsbRC in *Chlorobium limicola* membranes (**Table 2**) confirmed that the electron spin density distribution of $P_{840}^{\cdot+}$ is shared equally between the two BChl *a* molecules (Bratt et al., 1996). In these studies, $P_{840}^{\cdot+}$ was found to be closest yet to the symmetrical 'dimer' that was originally thought to exist in bRCs.

Most recently, we probed the oxidized primary donor, $P_{840}^{\cdot+}$, of *Chloroacidobacterium* (*Cab.*) *thermophilum* with ^{14}N and ^{67}Zn HYSCORE spectroscopy (Charles et al., 2020). *Cab. thermophilum* is a microaerophilic, chlorophototrophic species in the phylum *Acidobacteria* that employs a homodimeric RC with BChl molecules. The *Cab*. RC is highly unusual, as pigment analyses have shown the presence of three (B)Chl molecules, BChl a_P, Chl a_{PD}, and Zn^{2+}-BChl a_P', in the ratio 7.1:5.4:1 (He et al., 2019). While Chl a_{PD} was shown to be the primary electron acceptor, we demonstrated that the primary electron donor, P_{840}, contains a dimer of Zn^{2+}-BChl a_P' molecules. The ^{14}N and ^{67}Zn hyperfine couplings (**Table 2**) and DFT calculations have indicated that the electron spin density is distributed nearly symmetrically over the two Zn^{2+}-(B)Chl a_P' molecules of $P_{840}^{\cdot+}$ (Charles et al., 2020), as expected in a homodimeric RC. To our knowledge, this is the only example of a photochemical RC in which the (B)Chl molecules of the primary donor are metalated differently from those of the antenna.

Computational Studies of the Spin Density Distribution

The electronic structure of the oxidized primary donors, $P_{700}^{\cdot+}$, $P_{680}^{\cdot+}$, $P_{865}^{\cdot+}$, and $P_{960}^{\cdot+}$, of the heterodimeric RC, PS I, PS II and the bRC, have been probed by semi-empirical molecular orbital, quantum mechanics/molecular modeling (QM/MM) and density functional theory (DFT) methods. Early RHF-INDO/SP calculations by Lubitz and coworkers suggested that $P_{700}^{\cdot+}$ of PS I is formed by a dimer of Chl *a* and Chl *a*' molecules, Chl_{1A} and Chl_{1B}, respectively, with an asymmetric charge and electron spin density distribution in favor of the Chl *a* half of the dimer (Käß et al., 1995; Webber and Lubitz, 2001; Plato et al., 2003). The predicted asymmetry of the charge and spin density distribution across Chl_{1A} and Chl_{1B} was in agreement with previously reported EPR and ENDOR spectroscopy studies (Käß et al., 2001). Interestingly, the stepwise inclusion of the electrostatic interactions of the Chl_{1A} and Chl_{1B} molecules of $P_{700}^{\cdot+}$ with the neighboring amino acid residues, such as, $Thr743_{PsaA}$, which forms a putative hydrogen bond with the keto group of Chl *a*', and $His680_{PsaA}$ and $His660_{PsaB}$, serving as axial ligands to the Mg atoms of Chl_{1A} and Chl_{1B}, respectively, led to systematic enhancement of the electronic asymmetry that yielded a spin density ratio of almost 5:1. Molecular orbital calculations indicated that hydrogen bonding specifically stabilized the Chl_{1B} molecule of the dimer, which suggested that the unpaired electron of $P_{700}^{\cdot+}$ would predominantly reside at this site. This was corroborated by the DFT calculations performed by Sun and coworkers, who found that the asymmetry of the spin density of $P_{700}^{\cdot+}$ was mainly due to the hydrogen bond to the 13^1-keto-O group of Chl_{1A} (Sun et al., 2004). More recently, using QM/MM methods Saito and Ishikita (Saito and Ishikita, 2011) estimated the asymmetry of spin density of $P_{700}^{\cdot+}$ as 22.4:77.6 in favor of the Chl_{1B} molecule. This ratio was in good agreement with the experimental value of 25:75–20:80 that was obtained for the spin density distribution for $P_{700}^{\cdot+}$ of PS I from spinach (Davis et al., 1993) and 15:85 for $P_{700}^{\cdot+}$ of PS I from *Thermosynechococcus elongatus* (Käß et al., 2001). The general consensus has been that there are three factors that significantly contribute to a larger spin population of Chl_{1B} relative to that of Chl_{1A}, namely, (i) the presence of the $Thr743_{PsaA}$ residue that forms a hydrogen bond with the 13^1-keto-O group of Chl_{1A}, which is absent in Chl_{1B}, (ii) the identity of Chl_{1A} as a Chl *a* epimer, which leads the methyl ester group of Chl_{1A} and Chl_{1B} to be oppositely oriented with respect to the chlorin plane and (iii) the conserved pair of $Arg750_{PsaA}$ and $Ser734_{PsaB}$ residues that interact with Chl_{1A} and Chl_{1B}.

The charge and spin density distribution of $P_{680}^{\cdot+}$ of PS II has also been studied by DFT and QM/MM methods. The charge distribution determined by natural population analysis indicated that the positive charge of $P_{680}^{\cdot+}$ was significantly delocalized over the two Chl *a* molecules, Chl_{1A} and Chl_{1B}, with a slight bias in favor of the Chl_{1B} molecule (ratio of 0.46:0.54) (Takahashi et al., 2008). However, the charge delocalization, and similar spin density distribution, on Chl_{1A} and Chl_{1B} of $P_{680}^{\cdot+}$ in this study (Takahashi et al., 2008) was in contrast with experimental observations that the charge is mostly localized on one of the Chl *a* molecules, Chl_{1A}, of $P_{680}^{\cdot+}$ (Rigby et al., 1994b). More recently, the delocalization of the charge and spin density across the Chl_{1A} and Chl_{1B} dimer of $P_{680}^{\cdot+}$ was studied by Saito and coworkers using QM/MM methods (Saito and Ishikita, 2011). The Chl_{1A}:Chl_{1B} charge and spin density distribution was found to be 76.9:23.1 and 80.6:19.4, respectively, based on the complete structure of PS II that was obtained from the 1.9 Å X-ray crystal structure (Umena et al., 2011). The calculated spin density distribution was more asymmetric than the charge delocalization in the previous QM/MM study, which was also observed in computational studies of the other oxidized heterodimeric primary donors. The ratio of the spin density distribution on the Chl_{1A} and Chl_{1B} dimer of 80.6:19.4 was in agreement with the ratio of 82:18 that was obtained from experimental ^1H ENDOR spectroscopy of $P_{680}^{\cdot+}$ of PS II from spinach (Rigby et al., 1994a) and the ratio of 80:20 from flash-induced spectroscopic studies of PS II from *Synechocystis* sp. PCC 6803 (Diner et al., 2001). This suggested a preferential localization of the cationic state on Chl_{1A} over Chl_{1B} irrespective of the homology of the protein sequences between the D1 and D2 polypeptide subunits of PS II. Interestingly, the removal of the protein subunits of PS II in the QM/MM calculations yielded an isolated Chl_{1A}:Chl_{1B} ratio of 57.5:42.5 in vacuum. The significantly lower ratio of Chl_{1A}:Chl_{1B} in the absence of the polypeptide subunits, in comparison with that obtained in their presence, suggested that the remarkable asymmetric distribution of the cationic state among Chl_{1A} and Chl_{1B} of $P_{680}^{\cdot+}$ was not due to the geometry of the Chl molecules but due to the

asymmetric protein environment provided by PS II. Based on this observation, it was concluded that the Chl_{1A}:Chl_{1B} ratio of ∼ 80:20 was mainly due to the difference in the amino acid residues that were interacting with Chl_{1A} and Chl_{1B} of P_{680}.

Initial semi-empirical RHF-INDO/SP calculations of the ^{15}N hyperfine couplings of $P_{865}^{\cdot+}$ of the bRC had yielded a spin density ratio of 1.8:1 across the $BChl_{1A}$ and $BChl_{1B}$ dimer, which appeared to be in agreement with the early ^{1}H ENDOR data (Lendzian et al., 1992). However, later ENDOR, ESEEM and HYSCORE spectroscopy measurements of both single-crystal and powder samples of the bRC from *Rba. sphaeroides* and *Rps. viridis* indicated that the ratio of the electron spin density distribution is 3:1 or 5:1 in favor of $BChl_{1A}$ (Lendzian et al., 1988, 1992, 1993). Subsequent semi-empirical molecular orbital calculations by Lubitz and coworkers on the oxidized primary donor, $P_{865}^{\cdot+}$, using RHF-INDO/SP methods (Käß et al., 1995) reproduced the experimental isotropic hyperfine couplings to within 10% error, which facilitated the assignment of the hyperfine couplings of all of the nitrogen atoms of the $BChl_{1A}$ and $BChl_{1B}$ dimer and a ratio of the electron spin density distribution of 5:1 was deduced from the measured and assigned hyperfine couplings of the ^{15}N atoms of $P_{865}^{\cdot+}$. Most recently, the asymmetry of the spin density distribution and electronic coupling of the (B)Chl molecules of the oxidized primary donor, $P_{865}^{\cdot+}$, from *Rba. sphaeroides*, as well as $P_{700}^{\cdot+}$ and $P_{680}^{\cdot+}$, of PS I and PS II from *Synechococcus elongatus*, and *Thermosynechococcus vulcanus*, respectively, was estimated by frozen-density embedding diabatic (FDE-diab) methodology (Artiukhin and Neugebauer, 2018). The calculated ratio of spin densities was in agreement with previous experimental results for PS II and the bRC, where 82% and 66% of the spin density of $P_{680}^{\cdot+}$ and $P_{865}^{\cdot+}$ was found to be located on the Chl_{1A} molecule.

Density functional theory and QM/MM methods are powerful tools for the investigation of the electronic structure of the oxidized primary donors. As described above, there are several reports in literature on computational studies of $P_{700}^{\cdot+}$, $P_{680}^{\cdot+}$, $P_{865}^{\cdot+}$, and $P_{960}^{\cdot+}$ of PS I, PS II and the bRC from *Rba. sphaeroides* and *Rps. viridis*, respectively. However, to our best knowledge quantum-mechanical calculations to determine the hyperfine and quadrupolar parameters of the ^{14}N atoms of the primary donors of the homodimeric RCs, with the exception of the *Cab*. RC (Charles et al., 2020), are lacking at this time. This may be because the high-resolution structures of homodimeric RCs have been determined only very recently. In order to facilitate a comparison of the oxidized primary donor of hetero- and homodimeric RCs, we performed DFT calculations on computational models of $P_{800}^{\cdot+}$ and $P_{840}^{\cdot+}$ of the HbRC and GsbRC from heliobacteria and green sulfur bacteria, respectively. The goal is to obtain a better understanding of the effect of the relative geometry, symmetry and protein matrix effects on the electronic structure of the dimeric BChl molecules in the oxidized primary donor of homodimeric RCs.

In order to assess the computational methods that were employed in this study, we performed DFT calculations on models of $P_{700}^{\cdot+}$, $P_{680}^{\cdot+}$ $P_{865}^{\cdot+}$, and $P_{960}^{\cdot+}$ that were derived from the X-ray crystal structure of PS I (Jordan et al., 2001) (PDB ID: 1jb0), PS II (Umena et al., 2011) (PDB ID: 3wu2) and the bRC from *Rba. sphaeroides* (PDB ID: 1pcr) (Ermler et al., 1994) and *Rps. viridis* (PDB ID: 1prc) (Deisenhofer et al., 1995). The computational model of each primary donor included the dimeric (B)Chl molecules, $(B)Chl_{1A}$ and $(B)Chl_{1B}$, the axial histidine ligands of the (B)Chls and proximal hydrogen-bonding and hydrophobic residues in the protein matrix as observed in the respective structures (**Figures 4C,F**, **7C,F**). The dimeric models contained the complete (B)Chl molecules with the exception that the phytol tail was truncated by a methyl group after 23 carbon atoms. Please note that there may be an effect of the accessory (B)Chl molecules, $(B)Chl_{2A}$ and $(B)Chl_{2B}$, on the spin density distribution of the oxidized primary donors, which was not investigated in this study.

The single-point energy of each model was calculated employing the hybrid-generalized gradient approximation (hybrid-GGA) B3LYP functional (Dunham et al., 1971; Becke, 1988; Lee et al., 1988) along with the special EPR-optimized EPR-II (Barone, 1995) basis set for the lighter atoms and 6-31G(d) for magnesium, respectively, for most calculations, and the valence polarization basis sets (SVP and TZVP) (Schäfer et al., 1992; Weigend and Ahlrichs, 2005; Weigend, 2006) with the decontracted auxiliary basis sets (i.e., the coulomb fitting def2/J) (Weigend, 2006) when necessary. The calculations were performed in the spin-unrestricted mode for nuclear quadrupole couplings and isotropic hyperfine interactions of pyrrole nitrogen atoms. To account for the influence of solvent effects, a model of uniform dielectric constant of solvents using the conductor-like polarizable continuum model (CPCM) was used in the calculations (Klamt and Schüürmann, 1993; Cossi et al., 2003). The CPCM used a dielectric constant, ε, of 4.0 for incorporating the effects of the protein environment in all of the DFT calculations. All of the calculations included dispersion correction using a DFT-D3 approach with Becke-Johnson damping (D3BJ). In order to estimate the effect of the exchange functional, the hyperfine tensor calculations were also performed with the hybrid-meta-GGA TPSSh (Tao et al., 2003) functional along with the chain of spheres (RIJCOSX) (Staroverov et al., 2003; Neese et al., 2009) approximation and an EPR-II (Barone, 1995) and 6-31G(d) basis set for the lighter atoms and magnesium, that were previously used in the single-point energy calculations. The DFT calculations of $P_{700}^{\cdot+}$, $P_{680}^{\cdot+}$, $P_{865}^{\cdot+}$, and $P_{960}^{\cdot+}$ were validated by comparison of the calculated and previously published experimental hyperfine coupling constants of the ^{14}N atoms. Although the absorbance features of chromophores have been reasonably estimated through quantum mechanical calculations [e.g., the primary donor of *Rba. sphaeroides* (Eccles et al., 1988)], we focused on the prediction of hyperfine coupling constants for the purpose of this review article.

As a starting point for the DFT calculations, we selected a simple computational model for $P_{700}^{\cdot+}$ that was comprised only of the Chl_{1A} and Chl_{1B} molecules. In this model, the electron spin density across the singly occupied molecular orbital (SOMO) of isolated $Chl_{1A/1B}^{\cdot+}$ was distributed predominantly on the Chl_{1A} molecule. This was in contrast with experimental findings where the electron spin was predominantly located on Chl_{1B} (see above). To determine the effects of protein-cofactor

interactions, we systematically expanded the computational model of $P_{700}^{\cdot+}$ to include the axial ligands, $His680_{PsaA}$ and $His660_{PsaB}$, putative hydrogen-bonding residues, $Thr743_{PsaA}$, $Tyr735_{PsaA}$, and $Tyr603_{PsaA}$ and the hydrophobic residues, $Leu630_{PsaB}$ and $Leu650_{PsaA}$. As observed in **Figure 4C**, the protein matrix effects appear to be completely asymmetric across the $Chl_{1A/1B}$ dimer of P_{700} as the hydrogen bonding and electrostatic interactions are limited to Chl_{1A}, while the hydrophobic effects are localized in the vicinity of Chl_{1B}. We observed that despite the presence of the axial His ligands and putative hydrogen bonding residues, the asymmetric electron spin density distribution in the SOMO that was observed in the DFT calculations was still in favor of Chl_{1A}, albeit there was a slight change in the distribution of the spin density within the Chl_{1A} molecule. Interestingly, it was the introduction of the hydrophobic effects from the addition of the residues, $Leu630_{PsaB}$ and $Leu650_{PsaA}$, which resulted in a shift of the spin density distribution in favor of the Chl_{1B} half of the dimer of $P_{700}^{\cdot+}$.

For the DFT calculations of $P_{865}^{\cdot+}$ of the bRC from *Rba. sphaeroides*, the computational model included the $Tyr210_L$, $Val157_M$, $His202_L$, $Thr186_L$, $His168_M$, and $His173_M$ residues that are proximal to the $BChl_{1A}$ and $BChl_{1B}$ molecules in the X-ray crystal structure (**Figure 7C**; Ermler et al., 1994). Similarly, the computational model of $P_{960}^{\cdot+}$ of the bRC from *Rps. viridis* contained the $Val157_M$, $Tyr195_L$, $His200_L$, $Leu184_L$, $His168_M$, $Trp167_M$, $His173_M$, and $Thr248_M$ residues (**Figure 7F**). We observed that the calculated electron spin density distribution in the SOMO of $P_{865}^{\cdot+}$ and $P_{960}^{\cdot+}$ was in favor of the $BChl_{1A}$ molecule, both in the absence and presence of the hydrogen-bonding and hydrophobic amino acid residues. We observed a similar trend in the DFT calculation of $P_{680}^{\cdot+}$ of PS II with a model comprised of the Chl_{1A} and Chl_{1B} dimer with the $Ser282_{D1}$, $Leu182_{D2}$, $Met183_{D1}$, $His197_{D1}$, and $His198_{D2}$ residues (**Figure 4F**), where the spin density in the SOMO was located on the Chl_{1A} half of the dimer. The localization of the electron spin density on the (B)Chl_{1A} molecule of $P_{865}^{\cdot+}$, $P_{960}^{\cdot+}$, and $P_{680}^{\cdot+}$ was in contrast with that of $P_{700}^{\cdot+}$, where the asymmetric distribution of the electron spin density was in favor of the Chl_{1B} molecule.

The hyperfine coupling constants of the ^{14}N atoms of the oxidized primary donors, (B)Chl_{1A} and (B)Chl_{1B}, of $P_{700}^{\cdot+}$, $P_{680}^{\cdot+}$, $P_{865}^{\cdot+}$, and $P_{960}^{\cdot+}$ that were obtained from the DFT calculations are presented in **Table 3**. In the case of $P_{700}^{\cdot+}$ and $P_{865}^{\cdot+}$ of PS I and the bRC from *Rba. sphaeroides*, respectively, a comparison of the experimental (**Table 2**) and calculated (**Table 3**) ^{14}N hyperfine couplings indicates that the calculations corroborate the experimental values obtained by ENDOR, ESEEM and HYSCORE spectroscopy. Further, the ratio of the asymmetric spin density distribution across the (B)Chl_{1A} and (B)Chl_{1B} dimer of $P_{700}^{\cdot+}$ and $P_{865}^{\cdot+}$ that was estimated from the spin populations was 5.7:1 and 5.6:1, respectively, which was in good agreement with the approximate estimate of Chl_{1B}:Chl_{1A}:5:1 and $BChl_{1A}$:$BChl_{1B}$:5:1 that was obtained from spectroscopic measurements of $P_{700}^{\cdot+}$ and $P_{865}^{\cdot}$+ (Käβ et al., 1995; Käβ et al., 1995; Käβ and Lubitz, 1996; Deligiannakis and Rutherford, 2001; Käβ et al., 2001; Chestnut et al., 2021). To our best knowledge, the ^{14}N hyperfine coupling constants of $P_{680}^{\cdot+}$ are not available in literature. However, the asymmetric spin density distribution that was determined in the DFT calculations of $P_{680}^{\cdot+}$ of Chl_{1A}:Chl_{1B}:6:1 was roughly in agreement with the ratio of Chl_{1A}:Chl_{1B}:80:20 in literature. The broad agreement between the calculated and experimental hyperfine coupling constants and the high asymmetry of the electron spin density distribution of the oxidized heterodimeric primary donors indicates that the DFT methods used in this study are comparable with the experimental data in literature. However, it is important to note that the Kohn-Sham DFT methods employed may have resulted in slight over delocalization of the electron spin density across the oxidized primary donors (Artiukhin and Neugebauer, 2018). Further studies are in progress to address this possibility.

The DFT calculations on the oxidized heterodimeric primary donors of PS I, PS II and the bRC were consistent the magnetic parameters and asymmetric electron spin distribution over the (B)Chl dimer of $P_{700}^{\cdot+}$, $P_{680}^{\cdot+}$, $P_{865}^{\cdot+}$, and $P_{960}^{\cdot+}$. Following which, we performed DFT calculations to understand better the effects of the electronic structure and local symmetry on the hyperfine and quadrupolar parameters of the ^{14}N atoms in the oxidized primary donors, $P_{800}^{\cdot+}$ and $P_{840}^{\cdot+}$, of the RC from the HbRC and GsbRC, respectively. The coordinates for the atoms in the computational models of P_{800} and P_{840} were derived from the structures of the HbRC and GsbRC from *H. modesticaldum* (PDB ID: 5v8k) (Gisriel et al., 2017) and *C. tepidum* (PDB ID: 6m32) (Chen et al., 2020), respectively. Similar to the computational models of the heterodimeric primary donors, the models for the homodimeric ones included the dimeric BChl molecules,

TABLE 3 | Calculated ^{14}N isotropic hyperfine coupling parameters of the nitrogen atoms of $P_{700}^{\cdot+}$, $P_{865}^{\cdot+}$, $P_{960}^{\cdot+}$, $P_{680}^{\cdot+}$, $P_{800}^{\cdot+}$, $P_{840}^{\cdot+}$ (of the GsbRC).

Nitrogen	$P_{700}^{\cdot+}$ A_{iso} [MHz]	$P_{865}^{\cdot+}$ A_{iso} [MHz]	$P_{960}^{\cdot+}$ A_{iso} [MHz]	$P_{680}^{\cdot+}$ A_{iso} [MHz]	$P_{800}^{\cdot+}$ A_{iso} [MHz]	$P_{840}^{\cdot+}$ A_{iso} [MHz]
N^{I}	2.88	2.88	2.76	3.72	−0.68	1.10
N^{II}	2.34	2.59	2.26	2.44	−1.01	1.26
N^{III}	1.64	2.29	2.17	2.19	−0.90	1.37
N^{IV}	1.26	1.67	1.75	1.55	−1.29	1.61
N^{V}	0.39	0.35	0.30	0.40	−0.67	1.10
N^{VI}	0.36	0.15	0.20	0.30	−1.01	1.27
N^{VII}	0.18	0.14	0.15	0.10	−0.91	1.38
N^{VIII}	0.11	0.12	0.13	0.10	−1.29	1.63

$BChl_{1A}$ and $BChl_{1B}$, and the axial ligands to each BChl monomer (**Figures 8C,F**). Once again, the models contained the complete BChl molecules with the exception that the farnesol tail was truncated by a methyl group after 23 carbon atoms. Both the HbRC and GsbRC are comprised of a homodimeric polypeptide subunit core encoded by the single genes, *pshA* and *pscA*, respectively. However, the symmetry of the homodimeric core of the GsbRC is broken by the presence of an additional PscB polypeptide (Chen et al., 2020). Additionally, while the primary donor, P_{840}, of the GsbRC contains a symmetric BChl *a*' dimer with four hydrogen-bonding residues (**Figure 8F**), two on each BChl molecule, P_{800} of the HbRC is comprised of a dimer of BChl *g*′ molecules that lack hydrogen-bonding interactions (**Figure 8C**). However, it is expected that the effects of the hydrogen-bonding interactions of P_{840} of the GsbRC will impact the BChl molecules equally, which will not influence the localization of the charge or spin density distribution. Since there are no residues that appear to be participating in hydrogen bonds with P_{800} of the HbRC, the spin density is also expected to be completely symmetric.

The DFT calculations of the oxidized primary donor models, $P_{800}^{\cdot+}$ and $P_{840}^{\cdot+}$, of the HbRC and GsbRC were also performed with B3LYP level of theory using an EPR-II and 6-31G(d) basis set for the lighter atoms and Mg, respectively. The calculated ^{14}N hyperfine coupling constants (**Table 3**) and the spin populations of $BChl_{1A}$ and $BChl_{1B}$ that were obtained from the DFT calculations indicated that the ratio of the electron spin density distribution across the dimer of $P_{800}^{\cdot+}$ and $P_{840}^{\cdot+}$ of the HbRC and GsbRC, respectively, are completely symmetric. The unpaired electron spin density distribution in the singly occupied molecular orbital (SOMO) of $P_{800}^{\cdot+}$ and $P_{840}^{\cdot+}$ was also symmetric (**Figures 11A,B**). The calculated hyperfine couplings of the nitrogen atoms of $P_{800}^{\cdot+}$ of the HbRC and $P_{840}^{\cdot+}$ of the GsbRC (**Table 3**) were in agreement with the experimental couplings obtained from ^{14}N ESEEM and HYSCORE spectroscopy measurements of $P_{840}^{\cdot+}$ from *Chlorobium limicola* and *Cab. thermophilum* membranes, respectively (**Table 2**), respectively. This is indeed interesting as P_{800} of the HbRC is comprised of a BChl *g*' dimer, while P_{840} of *Cab. thermophilum* has been shown to a dimer of Zn^{2+}-BChl *a*′ molecules. This suggests that the protein environment surrounding $P^{\cdot+}$ in the HbRC and GsbRC is likely similar to that of the *Cab. thermophilum* RC.

Although the symmetry of the homodimeric core in the structure of the GsbRC is broken due to the presence of the additional PscB polypeptide, it appears that this did not impact the magnetic parameters of the BChl dimer of $P_{840}^{\cdot+}$. This finding is in agreement with the ^{1}H ENDOR and HYSCORE spectroscopy studies that demonstrated that the electron distribution of $P_{840}^{\cdot+}$ of the GsbRC from *Chlorobium limicola* was symmetrical in nature (Rigby et al., 1994b). However, there is the possibility that the small asymmetric effects from the extended protein environment, leading to minor deviations from total symmetry were not observed in the DFT calculations. This would most likely be due to the limited computational model of $P_{840}^{\cdot+}$ that was adopted in this study.

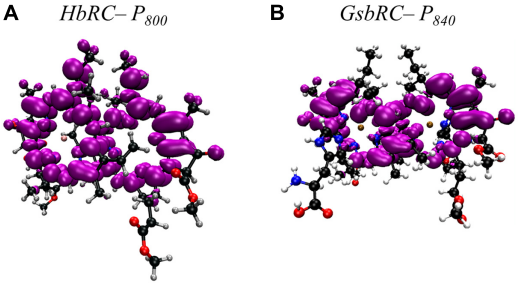

FIGURE 11 | Electron spin density distribution on the Chl_{1A} macrocycles of the homodimeric oxidized primary donor **(A)** $P_{800}^{\cdot+}$ of the HbRC from *Heliobacterium modesticaldum* (PDB ID: 5v8k) (Gisriel et al., 2017) and **(B)** $P_{840}^{\cdot+}$ of the GsbRC from *Chlorobaculum tepidum* (PDB ID: 6m32) (Chen et al., 2020) in the singly occupied molecular orbital (SOMO) as determined through DFT calculations.

The spatial arrangements of (B)Chl molecules in the primary donor of PS I, PS II, and the bRC are similar, where there are small differences in the inter-cofactor distance and relative orientation of the (B)Chl molecules. However, the protein matrix effects on the two halves of the (B)Chl dimer are highly asymmetric and this results in the localization of the spin density on a single (B)Chl molecule. We observed that the asymmetry of the spin density distribution is not solely caused by the structural differences of the (B)Chl macrocycles, but by the interaction of the cofactors with the protein environment. In contrast, these asymmetric effects are not present in homodimeric RCs, resulting in nearly equal sharing of spin density between the two BChl molecules (**Figures 11A,B**). The absence of asymmetric electrostatic and/or hydrophobic effects from the surrounding protein environment leads to a symmetric distribution of the charge and spin density in the homodimeric primary donors, $P_{800}^{\cdot+}$ and $P_{840}^{\cdot+}$. This effect is also mirrored in the distance between the macrocycles to ensure that spin density is not localized on one molecule. A direct consequence of the symmetric electronic structure of P_{800} and P_{840} is that it allows for electron transfer through both branches of cofactors with equal efficiency, which is not the case with the heterodimers examined in this study.

COMPARISON OF THE PRIMARY DONORS IN HETERO AND HOMODIMERIC REACTION CENTERS

Overall, the DFT calculations of the hetero- and homodimeric oxidized primary donors indicated that the presence of the surrounding protein matrix has profound effects on the distribution of the electron spin density across the (B)Chl molecules. Although the spatial arrangement of (B)Chl molecules in the primary donor of PS I, PS II, and the bRC are similar, there are small differences in the inter-cofactor distance and relative orientation of the (B)Chl molecules. As expected, at larger inter-molecular separations the spin density distribution becomes more localized on a single (B)Chl molecule. The increased localization of spin density in the cationic state is

caused by the absolute magnitudes of the electronic coupling that decreases exponentially with the inter-molecular separation. It appears that this asymmetry of the spin density distribution is not solely caused by the structural differences of the (B)Chl macrocycles, but by the interaction of the cofactors with the protein environment. This is perhaps most apparent in P_{700}, where the protein environment is highly asymmetric with respect to hydrogen bonds and non-polar residues around the two Chls. Interestingly, it is the combination of both hydrogen bonds and non-polar residues that provide the preferential localization on Chl_{1B}, since, in the absence of the Leu residues, localization is expected to be completely inverted in favor of Chl_{1A}. This observation may merit further detailed investigation. In contrast, these asymmetric effects are not present in homodimeric RCs, resulting in nearly equal sharing of spin density between the two BChl molecules.

The protein environment and its effect on the neutral P_{700} state was recently probed by Mitsuhashi et al. using a combination of computational methods (QM/MM/PCM and time-dependent DFT). They found that this asymmetric environment led to a high coupling for the HOMO of the neutral Chl_{1A}/Chl_{1B} pair (85 meV), but a low coupling of the LUMO (15 meV) (Mitsuhashi et al., 2021). They concluded that this caused a preferential (but not exclusive) localization of the excited state on Chl_{1A}, resulting the strong preference for A-branch electron transfer. Interestingly, this does not extend to the bRC, where the neutral HOMO and LUMO couplings were found to be high (115 and 134 meV, respectively), implying that the excited state is shared nearly equally among the two BChl molecules. The deciding factor in branch specificity instead occurs at the $BChl_{2A}$ level, in line with previous mutagenesis experiments (Kirmaier et al., 2001). It appears that manipulations to the electronic structure of the primary donor alone are not enough to confer the quantitative branch specificity required in Type II RCs, but are sufficient to lend a slight preference to branch usage, as observed in PS I. This may explain why Type II RCs display less asymmetry of protein matrix effects while attaining high asymmetry in the branch usage.

In addition to affecting the electronic coupling between the two (B)Chl monomers, the protein matrix also influences the dimer as a whole. As highlighted in **Figure 3**, the monomeric (B)Chls as well as the primary donors exist on a wide distribution of possible redox potentials. From most oxidizing species, P_{680} of PS II with a potential of $\sim$ 1,200 mV, to the least oxidizing, P_{800} of the HbRC at $\sim$ 225 mV, the E_m values span a range of nearly 1,000 mV, thus showcasing both the versatility and profound impact that the protein matrix effects can have in altering the electronic properties of (B)Chl molecules. An interesting example is the comparison of P_{700} of PS I to the P_{865} and P_{960} of the bRCs. There are significant differences in redox properties of BChl *a* [$E_m = +640$ mV (Fajer et al., 1975)], Chl *a* [$E_m = +800$ mV (Fajer et al., 1982; Maggiora et al., 1985)], and Chl *b* [$E_m = +940$ mV (Kobayashi et al., 2007)], and yet the primary donors of P_{700} (composed of Chl *a*), P_{865} (composed of BChl *a*), and P_{865} (composed of BChl *b*) that have nearly the same redox potential of $\sim$ 500 mV (Moss et al., 1991; Williams et al., 1992; Nagarajan et al., 1993; Lin et al., 1994; Brettel, 1997; Alric et al., 2004). It should be noted that the redox potential for BChl *b* is unknown, but it is likely more oxidizing than BChl *a* and close to that of Chl *a*. Regardless, through a combination of (B)Chl dimerization and implementation of extensive protein-matrix effects, heterodimeric RCs can modulate the redox potential of the primary donors by at least 300 mV as compared to the respective monomers. Perhaps even more impressive is the remarkably precise control that proteins have to tailor their interactions with chemically dissimilar molecules to achieve a highly similar mid-point potential.

Not only are RCs capable of tuning the mid-point potentials of disparate Chls to similar values, but the reverse is also observed, where proteins are able to modify chemically identical primary donors to achieve vastly different redox potentials. Nowhere is this effect more pronounced than in the comparison of P_{680} and P_{700} of PS II and PS I, respectively. Even though P_{680} and P_{700} are both composed of Chl *a* molecules, their redox potentials vary by over 600 mV, with the E_m of P_{680} and P_{700} $\sim$ 1,200 mV (Rappaport et al., 2002; Ishikita et al., 2005) and $\sim$ 500 mV, respectively. Indeed, nature is able to take a modestly oxidizing species and form one of the most oxidizing cofactors in biology. Please note that the value of the redox potential of P_{700} is approximate, as it has been shown to vary in different organisms, with P_{700} of spinach PS I reporting a value of +470 and $\sim$ +400 mV for the cyanobacterium *Gloeobacter violaceus* (Nakamura et al., 2011). Regardless, the difference of $\sim$700 mV for a dimer of chemically identical Chl molecules is noteworthy. While this difference is staggering, it must be acknowledged that these RCs ultimately are primed to serve vastly different functions. PS I must generate a low potential reductant sufficient to reduce a soluble ferredoxin, while PS II needs to generate a strong oxidant for water splitting at the Mn_4Ca-oxo cluster.

In contrast to heterodimers, the primary donors of homodimeric reaction centers exhibit remarkably similar midpoint potentials. Redox titrations on the primary donor, P_{840}, of the GsbRC yielded a reduction potential of +217 (Azai et al., 2016)–+240 mV (Fowler et al., 1971; Prince and Olson, 1976; Hauska et al., 2001). Related experiments on P_{800} from the HbRC yielded a surprisingly similar E_m of +225 mV (Prince et al., 1985). This is notable given the differences in the surrounding protein environment and chemical identity of the BChl molecules. While they share the same axial ligands, P_{800} lacks any hydrogen bonds while P_{840} has two putative hydrogen bonds to each BChl in the dimer and two unique aromatic residues in close proximity. There are currently no empirical measurements in the literature for the E_m of BChl *g*, so it is difficult to assess the degree to which the redox potential of P_{800} must be altered to achieve a value of +225 mV. However, the fact that the HbRC, containing BChl *g*, can achieve the same redox potential as GsbRC, containing BChl *a*, without the extensive protein-matrix effects suggests a more oxidizing potential of BChl *g*. The reason for the E_m of each RC to shift by $\sim$ 250 mV in comparison to the heterodimeric Type I RC, PS I, is not well understood, as both RCs are capable of reducing soluble ferredoxins (Seo et al., 2001; Romberger and Golbeck, 2012). It should be noted that the more simplified RCs have fewer electron transfer cofactors and therefore do not need to account for the loss of ΔG. However, that the GsbRC

is associated with a cytochrome c_{551} that is only 53 mV more negative than P_{840} (Kusumoto et al., 1999) may be a contributing factor. Further insight can be gained from the HbRC, as the BChl *g* pigments that compose the primary donor are subject to relatively controlled oxidation to Chl a_{ox} in the presence of light and O_2. Interestingly, partial oxidation of the pair, resulting in BChl *g*/Chl a_{ox} remains functionally active and able to generate a charge-separated state (Ferlez et al., 2015). However, full oxidation of both BChl *g* molecules results in a loss of activity. Whether this loss of activity arises from a decoupling of the dimer, a shifting of its redox potential, or another substantial change to its electronic properties remains an open question.

Alterations to the redox and electronic properties of primary donors and its effects on the efficiency of charge separation have been studied in literature. Interestingly, small changes to the local protein environment can substantially impact the redox potential of the primary donor. Allen and Williams (Allen and Williams, 1995) investigated a series of site-specific genetic variants that either altered, added, or deleted hydrogen bonds to P_{865}. Removing all of the hydrogen bonds by replacing a His residue by a Phe decreased the redox potential of P_{865} by 95 mV, while the addition of three His residues resulting in a total of four hydrogen bonds increased the potential by 260 mV. Concomitant with increase of the redox potential was a decrease of the recombination rate of the $P_{865}^{\cdot+}Q_A^{\cdot-}$ state by 60% and an increase in the lifetime of the excited state decay by $\sim$ 15 times. Similar genetic variants of other bRCs have displayed similar effects (Jia et al., 1993; Wachtveitl et al., 1993a,b). For example, a change in the electrostatic environment when the $Tyr210_L$ residue in the bRC from *Rps. viridis* was replaced by Phe, Ile, or Trp, each resulted in a redox potential that was sequentially more positive (Alden et al., 1996). A better understanding of the factors that influence the redox properties of primary donors has allowed for exciting progress in re-directing electron transfer within the bRCs (Wakeham and Jones, 2005; Williams and Allen, 2009).

Nature has many robust tools for the tuning and control of photosynthetic electron transfer cofactors that are tailored to its various needs, especially the primary donors of photosynthetic RCs. It has demonstrated the ability to not only align the redox potential of differing cofactors, but also push identical molecules to extreme oxidative potentials. Protein-matrix effects have a profound impact on the electronic properties of both the neutral and oxidized states of the primary donor, which we are just beginning to understand. As shown in this review, modern computational methods can be employed to model these states and accurately re-create the electronic properties that are observed experimentally. As we are able to understand better the influence of hydrogen bonds, charged and/or hydrophobic residues, the geometry and relative orientation of the (B)Chls, and protein motion (Gorka et al., 2020) on the highly efficient processes of light harvesting and electron transfer, it delivers insight on the evolutionary photosynthetic origins in our past and provides a blueprint for the design of artificial photosynthetic systems in the future.

AUTHOR CONTRIBUTIONS

MG, KVL, and JHG were responsible for the writing of the manuscript. MG and KVL were responsible for the geometric analysis of reaction centers, while AB, AM, EG, and KVL performed the computational analysis. All authors contributed to the article and approved the submitted version.

FUNDING

This study is supported by the Photosynthetic Systems Program, Office of Basic Energy Sciences of the United States Department of Energy under the contracts DE-FG02-07ER15903 (KVL) and DE-FG-05-05-ER46222 (JHG).

ACKNOWLEDGMENTS

The authors acknowledge support from the NSF REU Program in Physics (Grant no. 1560266) for EG and AM and thank the Center for Computational Innovations at RPI for computational resources.

REFERENCES

Agalarov, R., and Brettel, K. (2003). Temperature dependence of biphasic forward electron transfer from the phylloquinone(s) A_1 in photosystem I: only the slower phase is activated. *Biochim. Biophys. Acta* 1604, 7–12. doi: 10.1016/s0005-2728(03)00024-0

Alden, R. G., Parson, W. W., Chu, Z. T., and Warshel, A. (1996). Orientation of the OH dipole of tyrosine (M)210 and its effect on electrostatic energies in photosynthetic bacterial reaction centers. *J. Phys. Chem.* 100, 16761–16770. doi: 10.1021/jp961271s

Allen, J. P., and Williams, J. C. (1995). Relationship between the oxidation potential of the bacteriochlorophyll dimer and electron transfer in photosynthetic reaction centers. *J. Bioenerg. Biomembr.* 27, 275–283. doi: 10.1007/BF02110097

Allen, J. P., and Williams, J. C. (2014). "Energetics of cofactors in photosynthetic complexes: relationship between protein–cofactor interactions and midpoint potentials," in *The Biophysics of Photosynthesis*, eds J. Golbeck and A. van der Est (New York City, NY: Springer), 275–295.

Alric, J., Cuni, A., Maki, H., Nagashima, K. V. P., Verméglio, A., and Rappaport, F. (2004). Electrostatic interaction between redox cofactors in photosynthetic reaction centers. *J. Biol. Chem.* 279, 47849–47855. doi: 10.1074/jbc.M408888200

Arata, H., and Parson, W. W. (1981). Enthalpy and volume changes accompanying electron transfer from P_{870} to quinones in *Rhodopseudomonas sphaeroides* reaction centers. *Biochim. Biophys. Acta* 636, 70–81. doi: 10.1016/0005-2728(81)90077-3

Arlt, T., Schmidt, S., Kaiser, W., Lauterwasser, C., Meyer, M., Scheer, H., et al. (1993). The accessory bacteriochlorophyll: a real electron carrier in primary photosynthesis. *Proc. Natl. Acad. Sci. U S A* 90, 11757–11761. doi: 10.1073/pnas.90.24.11757

Artiukhin, D. G., and Neugebauer, J. (2018). Frozen-density embedding as a quasi-diabatization tool: charge-localized states for spin-density calculations. *J. Chem. Phys.* 148:214104. doi: 10.1063/1.5023290

Astashkin, A. V., Dikanov, S. A., and Tsvetkov, Y. D. (1987). Spectrometer dead time: effect on electron spin echo modulation spectra in disordered

systems. *Chem. Phys. Lett.* 136, 204–208. doi: 10.1016/0009-2614(87)80442-6

Astashkin, A. V., Dikanov, S. A., and Tsvetkov, Y. D. (1988). Hyperfine interactions of deuterium nuclei in the nearest surroundings of trapped electrons in alkaline glass. *Chem. Phys. Lett.* 144, 258–264. doi: 10.1016/0009-2614(88)87150-1

Azai, C., Sano, Y., Kato, Y., Noguchi, T., and Oh-oka, H. (2016). Mutation-induced perturbation of the special pair P_{840} in the homodimeric reaction center in green sulfur bacteria. *Sci. Rep.* 6:19878. doi: 10.1038/srep19878

Barone, V. (1995). "Structure, magnetic properties and reactivities of open-shell species from density functional and self-consistent hybrid methods," in *Recent Advances in Density Functional Methods*, ed. D. P. Chong (Singapore: World Scientific), 287–334.

Barrera-Rojas, J., de la Vara, L. G., Ríos-Castro, E., Leyva-Castillo, L. E., and Gómez-Lojero, C. (2018). The distribution of divinyl chlorophylls *a* and *b* and the presence of ferredoxin-$NADP^+$ reductase in *Prochlorococcus marinus* MIT9313 thylakoid membranes. *Heliyon* 4, e01100. doi: 10.1016/j.heliyon.2018.e01100

Becke, A. D. (1988). Density-functional exchange-energy approximation with correct asymptotic behavior. *Phys. Rev. A* 38, 3098–3100. doi: 10.1103/PhysRevA.38.3098

Bekker, A., Holland, H. D., Wang, P. L., Rumble, D., Stein, H. J., Hannah, J. L., et al. (2004). Dating the rise of atmospheric oxygen. *Nature* 427, 117–120. doi: 10.1038/nature02260

Berera, R., van Grondelle, R., and Kennis, J. T. M. (2009). Ultrafast transient absorption spectroscopy: principles and application to photosynthetic systems. *Photosynth. Res.* 101, 105–118. doi: 10.1007/s11120-009-9454-y

Bibby, T. S., Nield, J., and Barber, J. (2001). Iron deficiency induces the formation of an antenna ring around trimeric photosystem I in cyanobacteria. *Nature* 412, 743–745. doi: 10.1038/35089098

Björn, L. O., Papageorgiou, G. C., Blankenship, R. E., and Govindjee. (2009). A viewpoint: why chlorophyll *a*? *Photosynth. Res.* 99, 85–98. doi: 10.1007/s11120-008-9395-x

Blankenship, R. E., Olson, J. M., and Miller, M. (1995). "Antenna complexes from green photosynthetic bacteria," in *Anoxygenic Photosynthetic Bacteria*, eds R. E. Blankenship, M. T. Madigan, and C. E. Bauer (Dordrecht, Netherland: Springer), 399–435.

Bowes, J., Crofts, A. R., and Arntzen, C. J. (1980). Redox reactions on the reducing side of photosystem II in chloroplasts with altered herbicide binding properties. *Arch. Biochem. Biophys.* 200, 303–308. doi: 10.1016/0003-9861(80)90359-8

Bratt, P. J., Muhiuddin, I. P., Evans, M. C. W., and Heathcote, P. (1996). ^{14}N electron spin echo envelope modulation (ESEEM) spectroscopy of the cation radical P_{840}^+, the primary electron donor of the *Chlorobium limicola* reaction center. *Photochem. Photobiol.* 64, 20–25. doi: 10.1111/j.1751-1097.1996.tb02416.x

Bratt, P. J., Poluektov, O. G., Thurnauer, M. C., Krzystek, J., Brunel, L.-C., Schrier, J., et al. (2000). The g-factor anisotropy of plant chlorophyll $a^{\cdot+}$. *J. Phys. Chem. B* 104, 6973–6977.

Bratt, P. J., Rohrer, M., Krzystek, J., Evans, M. C. W., Brunel, L.-C., and Angerhofer, A. (1997). Submillimeter high-feld EPR studies of the primary donor in plant photosystem I $P_{700}^{\cdot+}$. *J. Phys. Chem. B* 101, 9686–9689. doi: 10.1021/jp9725238

Brettel, K. (1997). Electron transfer and arrangement of the redox cofactors in photosystem I. *Biochim. Biophys. Acta Bioenerg.* 1318, 322–373. doi: 10.1016/S0005-2728(96)00112-0

Britt, R. D. (1993). Time-domain electron paramagnetic resonance spectroscopy. *Curr. Opin. Struct. Biol.* 3, 774–779. doi: 10.1016/0959-440X(93)90063-Q

Brody, S. S. (2002). Fluorescence lifetime, yield, energy transfer and spectrum in photosynthesis, 1950–1960*. *Photosynth. Res.* 73:127. doi: 10.1023/A:1020405921105

Brody, S. S., and Rabinowitch, E. (1957). Excitation lifetime of photosynthetic pigments *in vitro* and *in vivo*. *Science* 125:555. doi: 10.1126/science.125.3247.555

Burghaus, O., Plato, M., Rohrer, M., Moebius, K., MacMillan, F., and Lubitz, W. (1993). 3-mm High-field EPR on semiquinone radical anions Q^- related to photosynthesis and on the primary donor P^+ and acceptor Q_A^- in reaction centers of *Rhodobacter sphaeroides* R-26. *J. Phys. Chem. B* 97, 7639–7647.

Charles, P., Kalendra, V., He, Z., Khatami, M. H., Golbeck, J. H., van der Est, A., et al. (2020). Two-dimensional ^{67}Zn HYSCORE spectroscopy reveals that a Zn-bacteriochlorophyll a_P' dimer is the primary donor (P_{840}) in the type-1 reaction centers of *Chloracidobacterium thermophilum*. *Phys. Chem. Chem. Phys.* 22, 6457–6467. doi: 10.1039/c9cp06556c

Chauvet, A., Sarrou, J., Lin, S., Romberger, S. P., Golbeck, J. H., Savikhin, S., et al. (2013). Temporal and spectral characterization of the photosynthetic reaction center from *Heliobacterium modesticaldum*. *Photosynth. Res.* 116, 1–9. doi: 10.1007/s11120-013-9871-9

Chen, J.-H., Wu, H., Xu, C., Liu, X.-C., Huang, Z., Chang, S., et al. (2020). Architecture of the photosynthetic complex from a green sulfur bacterium. *Science* 370:eabb6350. doi: 10.1126/science.abb6350

Chen, M., Telfer, A., Lin, S., Pascal, A., Larkum, A. W. D., Barber, J., et al. (2005). The nature of the photosystem II reaction centre in the chlorophyll *d*-containing prokaryote, *Acaryochloris marina*. *Photochem. Photobiol. Sci.* 4, 1060–1064. doi: 10.1039/b507057k

Cherepanov, D. A., Shelaev, I. V., Gostev, F. E., Aybush, A. V., Mamedov, M. D., Shuvalov, V. A., et al. (2020). Generation of ion-radical chlorophyll states in the light-harvesting antenna and the reaction center of cyanobacterial photosystem I. *Photosynth. Res.* 146, 55–73. doi: 10.1007/s11120-020-00731-0

Cherepanov, D. A., Shelaev, I. V., Gostev, F. E., Mamedov, M. D., Petrova, A. A., Aybush, A. V., et al. (2017). Mechanism of adiabatic primary electron transfer in photosystem I: femtosecond spectroscopy upon excitation of reaction center in the far-red edge of the Q_Y band. *Biochim. Biophys. Acta Bioenerg.* 1858, 895–905. doi: 10.1016/j.bbabio.2017.08.008

Cherepanov, D. A., Shelaev, I. V., Gostev, F. E., Petrova, A., Aybush, A. V., Nadtochenko, V. A., et al. (2021). Primary charge separation within the structurally symmetric tetrameric $Chl_{2A}P_AP_BChl_{2B}$ chlorophyll exciplex in photosystem I. *J. Photochem. Photobiol. B* 217:112154. doi: 10.1016/j.jphotobiol.2021.112154

Chestnut, M. M., Milikisiyants, S., Chatterjee, R., Kern, J., and Smirnov, A. I. (2021). Electronic structure of the primary electron donor $P_{700}^{\cdot+}$ in photosystem I studied by multifrequency HYSCORE spectroscopy at X- and Q-Band. *J. Phys. Chem. B* 125, 36–48. doi: 10.1021/acs.jpcb.0c09000

Chew, A. G. M., and Bryant, D. A. (2007). Chlorophyll biosynthesis in bacteria: the origins of structural and functional diversity. *Annu. Rev. Microbiol.* 61, 113–129. doi: 10.1146/annurev.micro.61.080706.093242

Cohen, R. O., Shen, G., Golbeck, J. H., Xu, W., Chitnis, P. R., Valieva, A. I., et al. (2004). Evidence for asymmetric electron transfer in cyanobacterial photosystem I: analysis of a methionine-to-leucine mutation of the ligand to the primary electron acceptor A_0. *Biochemistry* 43, 4741–4754. doi: 10.1021/bi035633f

Commoner, B., Heise, J. J., and Townsend, J. (1956). Light-induced paramagnetism in chloroplasts. *Proc. Natl. Acad. Sci. U S A* 42, 710–718. doi: 10.1073/pnas.42.10.710

Cossi, M., Rega, N., Scalmani, G., and Barone, V. (2003). Energies, structures, and electronic properties of molecules in solution with the C-PCM solvation model. *J. Comput. Chem.* 24, 669–681. doi: 10.1002/jcc.10189

Dashdorj, N., Xu, W., Cohen, R. O., Golbeck, J. H., and Savikhin, S. (2005). Asymmetric electron transfer in cyanobacterial photosystem I: charge separation and secondary electron transfer dynamics of mutations near the primary electron acceptor A_0. *Biophys. J.* 88, 1238–1249. doi: 10.1529/biophysj.104.050963

Davis, I. H., Heathcote, P., MacLachlan, D. J., and Evans, M. C. W. (1993). Modulation analysis of the electron spin echo signals of *in vivo* oxidised primary donor ^{14}N chlorophyll centres in bacterial, P_{870} and P_{960}, and plant photosystem I, P_{700}, reaction centres. *Biochim. Biophys. Acta Bioenerg.* 1143, 183–189. doi: 10.1016/0005-2728(93)90141-2

Davis, M. S., Forman, A., and Fajer, J. (1979). Ligated chlorophyll cation radicals: their function in photosystem II of plant photosynthesis. *Proc. Natl. Acad. Sci. USA* 76, 4170–4174. doi: 10.1073/pnas.76.9.4170

de Boer, A. L., Neerken, S., de Wijn, R., Permentier, H. P., Gast, P., Vijgenboom, E., et al. (2002). B-branch electron transfer in reaction centers of *Rhodobacter sphaeroides* assessed with site-directed mutagenesis. *Photosynth. Res.* 71, 221–239. doi: 10.1023/A:1015533126685

de Wijn, R., and van Gorkom, H. J. (2001). Kinetics of electron transfer from Q_A to Q_B in photosystem II. *Biochemistry* 40, 11912–11922. doi: 10.1021/bi010852r

Deisenhofer, J., Epp, O., Miki, K., Huber, R., and Michel, H. (1985). Structure of the protein subunits in the photosynthetic reaction centre of *Rhodopseudomonas*

viridis at 3Å resolution. *Nature* 318, 618–624. doi: 10.1038/318618a0

Deisenhofer, J., Epp, O., Sinning, I., and Michel, H. (1995). Crystallographic refinement at 2.3 Å resolution and refined model of the photosynthetic reaction centre from *Rhodopseudomonas viridis*. *J. Mol. Biol.* 246, 429–457. doi: 10.1006/jmbi.1994.0097

Deligiannakis, Y., Louloudi, M., and Hadjiliadis, N. (2000). Electron Spin Echo Envelope Modulation (ESEEM) spectroscopy as a tool to investigate the coordination environment of metal centers. *J. Coord. Chem.* 204, 1–112. doi: 10.1016/S0010-8545(99)00218-0

Deligiannakis, Y., and Rutherford, A. W. (2001). Electron spin echo envelope modulation spectroscopy in photosystem I. *Biochim. Biophys. Acta Bioenerg.* 1507, 226–246. doi: 10.1016/S0005-2728(01)00201-8

Díaz-Quintana, A., Leibl, W., Bottin, H., and Sétif, P. (1998). Electron transfer in photosystem I reaction centers follows a linear pathway in which iron-sulfur cluster F_B is the immediate electron donor to soluble ferredoxin. *Biochemistry* 37, 3429–3439. doi: 10.1021/bi972469l

Dikanov, S. A., Astashkin, A. V., Tsvetkov, Y. D., and Goldfeld, M. G. (1983). Comparative modulation analysis of electron spin echo signals from oxidized chlorophyll a *in vitro* and P_{700} centres in chloroplasts. *Chem. Phys. Lett.* 101, 206–210. doi: 10.1016/0009-2614(83)87372-2

Diner, B. A., Schlodder, E., Nixon, P. J., Coleman, W. J., Rappaport, F., Lavergne, J., et al. (2001). Site-directed mutations at D1-His198 and D2-His197 of Photosystem II in Synechocystis PCC 6803: sites of primary charge separation and cation and triplet stabilization. *Biochemistry* 40, 9265–9281. doi: 10.1021/bi010121r

Duan, H.-G., Prokhorenko, V. I., Wientjes, E., Croce, R., Thorwart, M., and Miller, R. J. D. (2017). Primary charge separation in the photosystem II reaction center revealed by a global analysis of the two-dimensional electronic spectra. *Sci. Rep.* 7:12347. doi: 10.1038/s41598-017-12564-4

Dunham, W. R., Bearden, A. J., Salmeen, I. T., Palmer, G., Sands, R. H., Orme-Johnson, W. H., et al. (1971). The two-iron ferredoxins in spinach, parsley, pig adrenal cortex, *Azotobacter vinelandii*, and *Clostridium pasteurianum*: studies by magnetic field Mössbauer spectroscopy. *Biochim. Biophys. Acta Bioenerg.* 253, 134–152. doi: 10.1016/0005-2728(71)90240-4

Eccles, J., Honig, B., and Schulten, K. (1988). Spectroscopic determinants in the reaction center of *Rhodopseudomonas viridis*. *Biophys. J.* 53, 137–144. doi: 10.1016/S0006-3495(88)83075-3

Ermler, U., Fritzsch, G., Buchanan, S. K., and Michel, H. (1994). Structure of the photosynthetic reaction centre from *Rhodobacter sphaeroides* at 2.65 Å resolution: cofactors and protein-cofactor interactions. *Structure* 2, 925–936. doi: 10.1016/s0969-2126(94)00094-8

Fajer, J., Brune, D. C., Davis, M. S., Forman, A., and Spaulding, L. D. (1975). Primary charge separation in bacterial photosynthesis: oxidized chlorophylls and reduced pheophytin. *Proc. Natl. Acad. Sci. U S A* 72, 4956–4960. doi: 10.1073/pnas.72.12.4956

Fajer, J., Fujita, I., Davis, M. S., Forman, A., Hanson, L. K., Smith, K. M., et al. (1982). "Electrochemical and spectrochemical studies of biological redox components," in *ACS division of analytical chemistry*, ed. K. M. Kadish (Atlanta, GA: ACS Publication), 489–513.

Ferlez, B., Cowgill, J., Dong, W., Gisriel, C., Lin, S., Flores, M., et al. (2016). Thermodynamics of the electron acceptors in *Heliobacterium modesticaldum*: an exemplar of an early homodimeric Type I photosynthetic reaction center. *Biochemistry* 55, 2358–2370. doi: 10.1021/acs.biochem.5b01320

Ferlez, B., Dong, W., Siavashi, R., Redding, K., Hou, H. J. M., Golbeck, J. H., et al. (2015). The effect of bacteriochlorophyll *g* oxidation on energy and electron transfer in reaction centers from *Heliobacterium modesticaldum*. *J. Phys. Chem. B* 119, 13714–13725. doi: 10.1021/acs.jpcb.5b03339

Fiedor, L., Kania, A., Myśliwa-Kurdziel, B., Orzeł, Ł, and Stochel, G. (2008). Understanding chlorophylls: central magnesium ion and phytyl as structural determinants. *Biochim. Biophys. Acta Bioenerg.* 1777, 1491–1500. doi: 10.1016/j.bbabio.2008.09.005

Fischer, W. W., Hemp, J., and Johnson, J. E. (2016). Evolution of oxygenic photosynthesis. *Annu. Rev. Earth Planet Sci.* 44, 647–683. doi: 10.1146/annurev-earth-060313-054810

Fowler, C. F., Nugent, N. A., and Fuller, R. C. (1971). The isolation and characterization of a photochemically active complex from *Chloropseudomonas ethylica*. *Proc. Natl. Acad. Sci. USA* 68, 2278–2282. doi: 10.1073/pnas.68.9.2278

Francke, C., Otte, S. C. M., Miller, M., Amesz, J., and Olson, J. M. (1996). Energy transfer from carotenoid and FMO-protein in subcellular preparations from green sulfur bacteria. Spectroscopic characterization of an FMO-reaction center core complex at low temperature. *Photosynth. Res.* 50, 71–77. doi: 10.1007/BF00018222

Frigaard, N.-U., Maqueo Chew, A. G., Maresca, J. A., and Bryant, D. A. (2006). "Bacteriochlorophyll biosynthesis in green bacteria," in *Chlorophylls and Bacteriochlorophylls: Biochemistry, Biophysics, Functions and Applications*, eds B. Grimm, R. J. Porra, W. Rüdiger, and H. Scheer (Netherlands: Springer), 201–221.

Gibasiewicz, K., Ramesh, V. M., Melkozernov, A. N., Lin, S., Woodbury, N. W., Blankenship, R. E., et al. (2001). Excitation dynamics in the core antenna of PS I from *Chlamydomonas reinhardtii* CC 2696 at room temperature. *J. Phys. Chem. B* 105, 11498–11506. doi: 10.1021/jp012089g

Gisriel, C., Sarrou, I., Ferlez, B., Golbeck, J. H., Redding, K. E., and Fromme, R. (2017). Structure of a symmetric photosynthetic reaction center-photosystem. *Science* 357, 1021–1025. doi: 10.1126/science.aan5611

Gisriel, C. J., Azai, C., and Cardona, T. (2021). Recent advances in the structural diversity of reaction centers. *Photosynth. Res.* doi: 10.1007/s11120-021-00857-9

Gobets, B., and van Grondelle, R. (2001). Energy transfer and trapping in photosystem I. *Biochim. Biophys. Acta Bioenerg.* 1507, 80–99. doi: 10.1016/s0005-2728(01)00203-1

Gobets, B., van Stokkum, I. H., Rögner, M., Kruip, J., Schlodder, E., Karapetyan, N. V., et al. (2001). Time-resolved fluorescence emission measurements of photosystem I particles of various cyanobacteria: a unified compartmental model. *Biophys. J.* 81, 407–424. doi: 10.1016/S0006-3495(01)75709-8

Golbeck, J. H. (2006). *Photosystem I: The Light-Driven Plastocyanin: Ferredoxin Oxidoreductase*. Dordrecht: Springer.

Gorka, M., Charles, P., Kalendra, V., Baldansuren, A., Lakshmi, K. V., and Golbeck, J. H. (2021a). A dimeric chlorophyll electron acceptor differentiates type I from type II photosynthetic reaction centers. *iScience* 24:102719. doi: 10.1016/j.isci.2021.102719

Gorka, M., Cherepanov, D. A., Semenov, A. Y., and Golbeck, J. H. (2020). Control of electron transfer by protein dynamics in photosynthetic reaction centers. *Crit. Rev. Biochem. Mol. Biol.* 55, 425–468. doi: 10.1080/10409238.2020.1810623

Gorka, M., Gruszecki, E., Charles, P., Kalendra, V., Lakshmi, K. V., and Golbeck, J. H. (2021b). Two-dimensional HYSCORE spectroscopy reveals a histidine imidazole as the axial ligand to Chl_{3A} in the $M688H_{PsaA}$ genetic variant of Photosystem I. *Biochim. Biophys. Acta Bioenerg.* 1862:148424. doi: 10.1016/j.bbabio.2021.148424

Groot, M. L., Pawlowicz, N. P., van Wilderen, L. J. G. W., Breton, J., van Stokkum, I. H. M., and van Grondelle, R. (2005). Initial electron donor and acceptor in isolated photosystem II reaction centers identified with femtosecond mid-IR spectroscopy. *Proc. Natl. Acad. Sci. USA* 102, 13087–13092. doi: 10.1073/pnas.0503483102

Hager-Braun, C., Zimmermann, R., and Hauska, G. (1999). "The homodimeric reaction center of chlorobium," in *The Phototrophic Prokaryotes*, eds G. A. Peschek, W. Löffelhardt, and G. Schmetterer (Boston, MA: Springer), 169–181.

Harmer, J., Mitrikas, G., and Schweiger, A. (2009). "Advanced pulse EPR methods for the characterization of metalloproteins," in *High Resolution EPR: Applications to Metalloenzymes and Metals in Medicine*, eds L. Berliner and G. Hanson (New York City, NY: Springer), 13–61. doi: 10.1039/b701568b

Hauska, G., Schoedl, T., Remigy, H., and Tsiotis, G. (2001). The reaction center of green sulfur bacteria. *Biochim. Biophys. Acta* 1507, 260–277. doi: 10.1016/S0005-2728(01)00200-6

He, Z., Ferlez, B., Kurashov, V., Tank, M., Golbeck, J. H., and Bryant, D. A. (2019). Reaction centers of the thermophilic microaerophile, *Chloracidobacterium thermophilum* (*Acidobacteria*) I: biochemical and biophysical characterization. *Photosynth. Res.* 142, 87–103. doi: 10.1007/s11120-019-00650-9

Heimdal, J., Jensen, K. P., Devarajan, A., and Ryde, U. (2007). The role of axial ligands for the structure and function of chlorophylls. *J. Biol. Inorg. Chem.* 12, 49–61. doi: 10.1007/s00775-006-0164-z

Heller, B. A., Holten, D., and Kirmaier, C. (1996). Effects of Asp residues near the L-side pigments in bacterial reaction centers. *Biochemistry* 35, 15418–15427. doi: 10.1021/bi961362f

Höfer, P., Grupp, A., Nebenführ, H., and Mehring, M. (1986). Hyperfine sublevel correlation (HYSCORE) spectroscopy: a 2D ESR investigation of the squaric acid radical. *Chem. Phys. Lett.* 132, 279–282. doi: 10.1016/0009-2614(86)80124-5

Hoffman, B. M. (2003). Electron-nuclear double resonance spectroscopy (and electron spin-echo envelope modulation spectroscopy) in bioinorganic chemistry. *Proc. Natl. Acad. Sci. USA* 100, 3575–3578. doi: 10.1073/pnas.0636464100

Hofmann, H. J. (1976). Precambrian microflora, Belcher Islands, Canada: significance and systematics. *J. Paleontol.* 50, 1040–1073. doi: 10.2307/1303547

Holzapfel, W., Finkele, U., Kaiser, W., Oesterhelt, D., Scheer, H., Stilz, H. U., et al. (1989). Observation of a bacteriochlorophyll anion radical during the primary charge separation in a reaction center. *Chem. Phys. Lett.* 160, 1–7. doi: 10.1016/0009-2614(89)87543-8

Holzwarth, A. R., and Müller, M. G. (1996). Energetics and kinetics of radical pairs in reaction centers from *Rhodobacter sphaeroides*. A femtosecond transient absorption study. *Biochemistry* 35, 11820–11831. doi: 10.1021/bi9607012

Holzwarth, A. R., Müller, M. G., Niklas, J., and Lubitz, W. (2006a). Ultrafast transient absorption studies on photosystem I reaction centers from *Chlamydomonas reinhardtii*. 2: mutations near the P_{700} reaction center chlorophylls provide new insight into the nature of the primary electron donor. *Biophys. J.* 90, 552–565. doi: 10.1529/biophysj.105.059824

Holzwarth, A. R., Müller, M. G., Reus, M., Nowaczyk, M., Sander, J., and Rögner, M. (2006b). Kinetics and mechanism of electron transfer in intact photosystem II and in the isolated reaction center: pheophytin is the primary electron acceptor. *Proc. Natl. Acad. Sci. USA* 103, 6895–6900. doi: 10.1073/pnas.0505371103

Huang, L., Ponomarenko, N., Wiederrecht, G. P., and Tiede, D. M. (2012). Cofactor-specific photochemical function resolved by ultrafast spectroscopy in photosynthetic reaction center crystals. *Proc. Natl. Acad. Sci. USA* 109, 4851–4856. doi: 10.1073/pnas.1116862109

Humbeck, K., Schumann, R., and Senger, H. (1984). "The influence of blue light on the formation of chlorophyll-protein complexes in *Scenedesmus*," in *Blue Light Effects in Biological Systems*, ed. H. Senger (Berlin, Heidelberg: Springer), 359–365.

Huppman, P., Arlt, T., Penzkofer, H., Schmidt, S., Bibikova, M., Dohse, B., et al. (2002). Kinetics, energetics, and electronic coupling of the primary electron transfer reactions in mutated reaction centers of *Blastochloris viridis*. *Biophys. J.* 82, 3186–3197. doi: 10.1016/S0006-3495(02)75661-0

Ishikita, H., Loll, B., Biesiadka, J., Saenger, W., and Knapp, E.-W. (2005). Redox potentials of chlorophylls in the photosystem II reaction center. *Biochemistry* 44, 4118–4124. doi: 10.1021/bi047922p

Ishikita, H., Saenger, W., Biesiadka, J., Loll, B., and Knapp, E.-W. (2006). How photosynthetic reaction centers control oxidation power in chlorophyll pairs P_{680}, P_{700}, and P_{870}. *Proc. Natl. Acad. Sci. USA* 103, 9855–9860. doi: 10.1073/pnas.0601446103

Ito, H., and Tanaka, A. (2011). Evolution of a divinyl chlorophyll-based photosystem in *Prochlorococcus*. *Proc. Natl. Acad. Sci. USA* 108, 18014–18019. doi: 10.1073/pnas.1107590108

Itoh, S., Iwaki, M., and Ikegami, I. (2001). Modification of photosystem I reaction center by the extraction and exchange of chlorophylls and quinones. *Biochim. Biophys. Acta Bioenerg.* 1507, 115–138. doi: 10.1016/s0005-2728(01)00199-2

Jagannathan, B., and Golbeck, J. H. (2008). Unifying principles in homodimeric type I photosynthetic reaction centers: properties of PscB and the F_A, F_B and F_X iron–sulfur clusters in green sulfur bacteria. *Biochim. Biophys. Acta Bioenerg.* 1777, 1535–1544. doi: 10.1016/j.bbabio.2008.09.001

Jia, Y., DiMagno, T. J., Chan, C. K., Wang, Z., Popov, M. S., Du, M., et al. (1993). Primary charge separation in mutant reaction centers of *Rhodobacter capsulatus*. *J. Phys. Chem.* 97, 13180–13191. doi: 10.1021/j100152a024

Johnson, E. T., Müh, F., Nabedryk, E., Williams, J. C., Allen, J. P., Lubitz, W., et al. (2002). Electronic and vibronic coupling of the special pair of bacteriochlorophylls in photosynthetic reaction centers from wild-type and mutant strains of *Rhodobacter sphaeroides*. *J. Phys. Chem. B* 106, 11859–11869. doi: 10.1021/jp021024q

Johnson, E. T., and Parson, W. W. (2002). Electrostatic interactions in an integral membrane protein. *Biochemistry* 41, 6483–6494. doi: 10.1021/bi012131y

Jordan, P., Fromme, P., Witt, H. T., Klukas, O., Saenger, W., and Krauss, N. (2001). Three-dimensional structure of cyanobacterial photosystem I at 2.5 Å resolution. *Nature* 411, 909–917. doi: 10.1038/35082000

Käß, H., Rautter, J., Boenigk, B., Hoefer, P., and Lubitz, W. (1995). 2D ESEEM of the ^{15}N-labeled radical cations of bacteriochlorophyll a and of the primary donor in reaction centers of *Rhodobacter sphaeroides*. *J. Phys. Chem.* 99, 436–448. doi: 10.1021/j100001a065

Karyagina, I., Pushkar, Y., Stehlik, D., van der Est, A., Ishikita, H., Knapp, E.-W., et al. (2007). Contributions of the protein environment to the midpoint potentials of the A_1 phylloquinones and the F_X iron-sulfur cluster in photosystem I. *Biochemistry* 46, 10804–10816. doi: 10.1021/bi700846z

Käß, H., Fromme, P., Witt, H. T., and Lubitz, W. (2001). Orientation and electronic structure of the primary donor radical cation in photosystem I: a single crystal EPR and ENDOR Study. *J. Phys. Chem. B* 105, 1225–1239. doi: 10.1021/jp0032311

Kaupp, M. (2002). The function of photosystem I. quantum chemical insight into the role of tryptophan-quinone interactions. *Biochemistry* 41, 2895–2900. doi: 10.1021/bi0159783

Käß, H., Bittersmann-Weidlich, E., Andréasson, L. E., Bönigk, B., and Lubitz, W. (1995). ENDOR and ESEEM of the ^{15}N labelled radical cations of chlorophyll *a* and the primary donor P_{700} in photosystem I. *Chem. Phys.* 194, 419–432. doi: 10.1016/0301-0104(95)00021-F

Käß, H., Fromme, P., and Lubitz, W. (1996). Quadrupole parameters of nitrogen nuclei in the cation radical $P_{700}^{\cdot+}$ determined by ESEEM of single crystals of photosystem I. *Chem. Phys. Lett.* 257, 197–206. doi: 10.1016/0009-2614(96)00533-7

Käß, H., and Lubitz, W. (1996). Evaluation of 2D ESEEM data of ^{15}N-labeled radical cations of the primary donor P_{700} in photosystem I and chlorophyll *a*. *Chem. Phys. Lett.* 251, 193–203. doi: 10.1016/0009-2614(96)00129-7

Ke, B., Hansen, R. E., and Beinert, H. (1973). Oxidation-reduction potentials of bound iron-sulfur proteins of photosystem I. *Proc. Natl. Acad. Sci. USA* 70, 2941–2945. doi: 10.1073/pnas.70.10.2941

Kennis, J. T. M., Shkuropatov, A. Y., van Stokkum, I. H. M., Gast, P., Hoff, A. J., Shuvalov, V. A., et al. (1997). Formation of a long-lived $P^+B_A^-$ state in plant pheophytin-exchanged reaction centers of *Rhodobacter sphaeroides* R26 at low temperature. *Biochemistry* 36, 16231–16238. doi: 10.1021/bi9712605

Kirmaier, C., Gaul, D., DeBey, R., Holten, D., and Schenck, C. (1991). Charge separation in a reaction center incorporating bacteriochlorophyll for photoactive bacteriopheophytin. *Science* 251, 922–927. doi: 10.1126/science.2000491

Kirmaier, C., He, C., and Holten, D. (2001). Manipulating the direction of electron transfer in the bacterial reaction center by swapping Phe for Tyr near $BChl_M$ (L181) and Tyr for Phe near $BChl_L$ (M208). *Biochemistry* 40, 12132–12139. doi: 10.1021/bi0113263

Kirmaier, C., Laporte, L., Schenck, C. C., and Holten, D. (1995a). The nature and dynamics of the charge-separated intermediate in reaction centers in which bacteriochlorophyll replaces the photoactive bacteriopheophytin. 1. spectral characterization of the transient state. *J. Phys. Chem.* 99, 8903–8909. doi: 10.1021/j100021a067

Kirmaier, C., Laporte, L., Schenck, C. C., and Holten, D. (1995b). The nature and dynamics of the charge-separated intermediate in reaction centers in which bacteriochlorophyll replaces the photoactive bacteriopheophytin. 2. the rates and yields of charge separation and recombination. *J. Phys. Chem.* 99, 8910–8917. doi: 10.1021/j100021a068

Kirmaier, C., Weems, D., and Holten, D. (1999). M-side electron transfer in reaction center mutants with a lysine near the nonphotoactive bacteriochlorophyll. *Biochemistry* 38, 11516–11530. doi: 10.1021/bi9908585

Klamt, A., and Schüürmann, G. (1993). COSMO: a new approach to dielectric screening in solvents with explicit expressions for the screening energy and its gradient. *J. Chem. Soc. Perkin Trans.* 2, 799–805. doi: 10.1039/P29930000799

Kleinfeld, D., Okamura, M. Y., and Feher, G. (1984a). Electron transfer in reaction centers of *Rhodopseudomonas sphaeroides*. I. determination of the charge recombination pathway of $D^+Q_AQ_{-B}$ and free energy and kinetic relations between $Q^{-A}Q_B$ and $Q_AQ_B^-$. *Biochim. Biophys. Acta Bioenerg.* 766, 126–140. doi: 10.1016/0005-2728(84)90224-x

Kleinfeld, D., Okamura, M. Y., and Feher, G. (1984b). Electron-transfer kinetics in photosynthetic reaction centers cooled to cryogenic temperatures in the charge-separated state: evidence for light-induced structural changes. *Biochemistry* 23, 5780–5786. doi: 10.1021/bi00319a017

Kobayashi, M. (1996). Study of precise pigment composition of photosystem 1-type reaction centers by means of normal-phase HPLC. *J. Plant Res.* 109, 223–230.

Kobayashi, M., Ohashi, S., Iwamoto, K., Shiraiwa, Y., Kato, Y., and Watanabe, T. (2007). Redox potential of chlorophyll d in vitro. *Biochim. Biophys. Acta Bioenerg.* 1767, 596–602. doi: 10.1016/j.bbabio.2007.02.015

Kobayashi, M., Oh-oka, H., Akutsu, S., Akiyama, M., Tominaga, K., Kise, H., et al. (2000). The primary electron acceptor of green sulfur bacteria, bacteriochlorophyll 663, is chlorophyll a esterified with Δ 2,6-phytadienol. *Photosynth. Res.* 63, 269–280. doi: 10.1023/A:1006480629059

Kobayashi, M., van de Meent, E. J., Erkelens, C., Amesz, J., Ikegami, I., and Watanabe, T. (1991). Bacteriochlorophyll *g* epimer as a possible reaction center component of heliobacteria. *Biochim. Biophys. Acta Bioenerg.* 1057, 89–96. doi: 10.1016/S0005-2728(05)80087-8

Koepke, J., Hu, X., Muenke, C., Schulten, K., and Michel, H. (1996). The crystal structure of the light-harvesting complex II (B800-850) from *Rhodospirillum molischianum*. *Structure* 4, 581–597. doi: 10.1016/s0969-2126(96)00063-9

Kojima, R., Yamamoto, H., Azai, C., Uragami, C., Hashimoto, H., Kosumi, D., et al. (2020). Energy transfer and primary charge separation upon selective femtosecond excitation at 810 nm in the reaction center complex from *Heliobacterium modesticaldum*. *J. Photochem. Photobiol. A* 401:112758. doi: 10.1016/j.jphotochem.2020.112758

Konar, A., Sechrist, R., Song, Y., Policht, V. R., Laible, P. D., Bocian, D. F., et al. (2018). Electronic interactions in the bacterial reaction center revealed by two-color 2D electronic spectroscopy. *J. Phys. Chem. Lett.* 9, 5219–5225. doi: 10.1021/acs.jpclett.8b02394

Kulik, L., and Lubitz, W. (2009). Electron-nuclear double resonance. *Photosynth. Res.* 102, 391–401. doi: 10.1007/s11120-009-9401-y

Kurashov, V., Gorka, M., Milanovsky, G. E., Johnson, T. W., Cherepanov, D. A., Semenov, A. Y., et al. (2018). Critical evaluation of electron transfer kinetics in P_{700}-F_A/F_B, P_{700}-F_X, and P_{700}-A_1 photosystem I core complexes in liquid and in trehalose glass. *Biochim. Biophys. Acta Bioenerg.* 1859, 1288–1301. doi: 10.1016/j.bbabio.2018.09.367

Kusumoto, N., Sétif, P., Brettel, K., Seo, D., and Sakurai, H. (1999). Electron transfer kinetics in purified reaction centers from the green sulfur bacterium Chlorobium tepidum studied by multiple-flash excitation. *Biochemistry* 38, 12124–12137. doi: 10.1021/bi990452s

Lakshmi, K. V., and Brudvig, G. W. (2000). "Electron paramagnetic resonance distance measurements in photosystems," in *Distance Measurements in Biological Systems by EPR*, eds L. J. Berliner, G. R. Eaton, and S. S. Eaton (Boston, MA: Springer), 513–567.

Lakshmi, K. V., and Brudvig, G. W. (2001). Pulsed electron paramagnetic resonance methods for macromolecular structure determination. *Curr. Opin. Struct. Biol.* 11, 523–531. doi: 10.1016/s0959-440x(00)00242-6

Lakshmi, K. V., Coates, C. S., Smith, S., and Chatterjee, R. (2014). "The radical intermediates of photosystem II," in *The Biophysics of Photosynthesis*, eds J. Golbeck and A. van der Est (New York City, NY: Springer), 299–320.

Lauterwasser, C., Finkele, U., Scheer, H., and Zinth, W. (1991). Temperature dependence of the primary electron transfer in photosynthetic reaction centers from *Rhodobacter sphaeroides*. *Chem. Phys. Lett.* 183, 471–477. doi: 10.1016/0009-2614(91)80161-P

Lee, C., Yang, W., and Parr, R. G. (1988). Development of the Colle-Salvetti correlation-energy formula into a functional of the electron density. *Phys. Rev. B* 37, 785–789. doi: 10.1103/physrevb.37.785

Lendzian, F., Geβern, C., Bönigk, B., Plato, M., Möbius, K., and Lubitz, W. (1992). "^{15}N- and ^{1}H-ENDOR/TRIPLE resonance of the primary donor cation radical $D^{+\cdot}$ in isotopically labelled reaction centers of *Rhodobacter sphaeroides*," in *Research in Photosynthesis, Proceedings of the IXth International Congress on Photosynthesis, Nagoya, Japan*, ed. N. Murata (Dordrecht, Netherland: Springer), 433–436.

Lendzian, F., Huber, M., Isaacson, R. A., Endeward, B., Plato, M., Bönigk, B., et al. (1993). The electronic structure of the primary donor cation radical in *Rhodobacter sphaeroides* R-26: ENDOR and TRIPLE resonance studies in single crystals of reaction centers. *Biochim. Biophys. Acta Bioenerg.* 1183, 139–160. doi: 10.1016/0005-2728(93)90013-6

Lendzian, F., Lubitz, W., Scheer, H., Hoff, A. J., Plato, M., Tränkle, E., et al. (1988). ESR, ENDOR and TRIPLE resonance studies of the primary donor radical cation $P_{960}^{+\cdot}$ in the photosynthetic bacterium *Rhodopseudomonas viridis*. *Chem. Phys. Lett.* 148, 377–385. doi: 10.1016/0009-2614(88)87191-4

Leonova, M. M., Fufina, T. Y., Vasilieva, L. G., and Shuvalov, V. A. (2011). Structure-function investigations of bacterial photosynthetic reaction centers. *Biochemistry (Mosc)* 76, 1465–1483. doi: 10.1134/S0006297911130074

Lin, C. P., Bowman, M. K., and Norris, J. R. (1986). Analysis of electron spin echo modulation in randomly oriented solids: ^{15}N modulation of radical cations of bacteriochlorophyll *a* and the primary donor of photosynthetic bacterium *Rhodospirillum rubrum*. *J. Chem. Phys.* 85, 56–62. doi: 10.1063/1.451582

Lin, X., Murchison, H. A., Nagarajan, V., Parson, W. W., Allen, J. P., and Williams, J. C. (1994). Specific alteration of the oxidation potential of the electron donor in reaction centers from *Rhodobacter sphaeroides*. *Proc. Natl. Acad. Sci. U S A.* 91, 10265–10269. doi: 10.1073/pnas.91.22.10265

Lubitz, W., Isaacson, R. A., Abresch, E. C., and Feher, G. (1984). ^{15}N electron nuclear double resonance of the primary donor cation radical $P_{865}^{+\cdot}$ in reaction centers of *Rhodopseudomonas sphaeroides*: additional evidence for the dimer model. *Proc. Natl. Acad. Sci. USA* 81, 7792–7796. doi: 10.1073/pnas.81.24.7792

Ma, F., Romero, E., Jones, M. R., Novoderezhkin, V. I., and van Grondelle, R. (2019). Both electronic and vibrational coherences are involved in primary electron transfer in bacterial reaction center. *Nat. Commun.* 10:933. doi: 10.1038/s41467-019-08751-8

Mac, M., Bowlby, N. R., Babcock, G. T., and McCracken, J. (1998). Monomeric spin density distribution in the primary donor of photosystem I as determined by electron magnetic resonance: functional and thermodynamic implications. *J. Am. Chem. Soc.* 120, 13215–13223.

Maggiora, L. L., Petke, J. D., Gopal, D., Iwamoto, R. T., and Maggiora, G. M. (1985). Experimental and theoretical studies of Schiff base chlorophylls. *Photochem. Photobiol.* 42, 69–75. doi: 10.1021/bi00236a011

Mao, L., Wang, Y., and Hu, X. (2003). π−π stacking interactions in the peridinin-chlorophyll-protein of *Amphidinium carterae*. *J. Phys. Chem. B* 107, 3963–3971. doi: 10.1021/jp0276496

Mar, T., Govindjee, Singhal, G. S., and Merkelo, H. (1972). Lifetime of the excited state in vivo. I. chlorophyll a in algae, at room and at liquid nitrogen temperatures; rate constants of radiationless deactivation and trapping. *Biophys. J.* 12, 797–808. doi: 10.1016/S0006-3495(72)86123-X

Martin, J.-L., Breton, J., Hoff, A. J., Migus, A., and Antonetti, A. (1986). Femtosecond spectroscopy of electron transfer in the reaction center of the photosynthetic bacterium *Rhodopseudomonas sphaeroides* R-26: direct electron transfer from the dimeric bacteriochlorophyll primary donor to the bacteriopheophytin acceptor with a time constant of 2.8 ± 0.2 psec. *Proc. Natl. Acad. Sci. USA* 83, 957–961. doi: 10.1073/pnas.83.4.957

Mauzerall, D., Neuberger, A., and Kenner, G. W. (1976). Chlorophyll and photosynthesis. *Philos. Trans. R Soc. B* 273, 287–294. doi: 10.1098/rstb.1976.0014

McDermott, G., Prince, S. M., Freer, A. A., Hawthornthwaite-Lawless, A. M., Papiz, M. Z., Cogdell, R. J., et al. (1995). Crystal structure of an integral membrane light-harvesting complex from photosynthetic bacteria. *Nature* 374, 517–521. doi: 10.1038/374517a0

McMahon, B. H., Muller, J. D., Wraight, C. A., and Nienhaus, G. U. (1998). Electron transfer and protein dynamics in the photosynthetic reaction center. *Biophys. J.* 74, 2567–2587. doi: 10.1016/S0006-3495(98)77964-0

Melkozernov, A. N. (2001). Excitation energy transfer in Photosystem I from oxygenic organisms. *Photosynth. Res.* 70, 129–153. doi: 10.1023/A:1017909325669

Miller, M., Liu, X., Snyder, S. W., Thurnauer, M. C., and Biggins, J. (1992). Photosynthetic electron-transfer reactions in the green sulfur bacterium *Chlorobium vibrioforme*: evidence for the functional involvement of iron-sulfur redox centers on the acceptor side of the reaction center. *Biochemistry* 31, 4354–4363. doi: 10.1021/bi00132a028

Mimuro, M., Tomo, T., Nishimura, Y., Yamazaki, I., and Satoh, K. (1995). Identification of a photochemically inactive pheophytin molecule in the spinach D_1-D_2-cyt b_{559} complex. *Biochim. Biophys. Acta Bioenerg.* 1232, 81–88. doi: 10.1016/0005-2728(95)00116-2

Mitsuhashi, K., Tamura, H., Saito, K., and Ishikita, H. (2021). Nature of asymmetric electron transfer in the symmetric pathways of

photosystem I. *J. Phys. Chem. B* 125, 2879–2885. doi: 10.1021/acs.jpcb.0c10885

Mondal, J., and Bruce, B. D. (2018). Ferredoxin: the central hub connecting photosystem I to cellular metabolism. *Photosynthetica* 56, 279–293. doi: 10.1007/s11099-018-0793-9

Moore, L. R., Goericke, R., and Chisholm, S. W. (1995). Comparative physiology of *Synechococcus* and *Prochlorococcus*: influence of light and temperature on growth, pigments, fluorescence and absorptive properties. *Mar. Ecol. Prog. Ser.* 116, 259–275.

Morales, F., Moise, N., Quílez, R., Abadía, A., Abadía, J., and Moya, I. (2001). Iron deficiency interrupts energy transfer from a disconnected part of the antenna to the rest of photosystem II. *Photosynth. Res.* 70, 207–220. doi: 10.1023/A:1017965229788

Moss, D. A., Leonhard, M., Bauscher, M., and Mäntele, W. (1991). Electrochemical redox titration of cofactors in the reaction center from *Rhodobacter sphaeroides*. *FEBS Lett.* 283, 33–36. doi: 10.1016/0014-5793(91)80547-g

Müller, M. G., Niklas, J., Lubitz, W., and Holzwarth, A. R. (2003). Ultrafast transient absorption studies on photosystem I reaction centers from *Chlamydomonas reinhardtii*. 1. a new interpretation of the energy trapping and early electron transfer steps in photosystem I. *Biophys. J.* 85, 3899–3922. doi: 10.1016/S0006-3495(03)74804-8

Müller, M. G., Slavov, C., Luthra, R., Redding, K. E., and Holzwarth, A. R. (2010). Independent initiation of primary electron transfer in the two branches of the photosystem I reaction center. *Proc. Natl. Acad. Sci. U S A* 107, 4123–4128. doi: 10.1073/pnas.0905407107

Myers, J. A., Lewis, K. L. M., Fuller, F. D., Tekavec, P. F., Yocum, C. F., and Ogilvie, J. P. (2010). Two-dimensional electronic spectroscopy of the D_1-D_2-cyt b_{559} photosystem II reaction center complex. *J. Phys. Chem.* 1, 2774–2780. doi: 10.1021/jz100972z

Nagarajan, V., Parson, W. W., Davis, D., and Schenck, C. C. (1993). Kinetics and free energy gaps of electron-transfer reactions in *Rhodobacter sphaeroides* reaction centers. *Biochemistry* 32, 12324–12336. doi: 10.1021/bi00097a008

Nakamura, A., Suzawa, T., Kato, Y., and Watanabe, T. (2011). Species dependence of the redox potential of the primary electron donor P_{700} in photosystem I of oxygenic photosynthetic organisms revealed by spectroelectrochemistry. *Plant Cell. Physiol.* 52, 815–823. doi: 10.1093/pcp/pcr034

Neerken, S., Permentier, H. P., Francke, C., Aartsma, T. J., and Amesz, J. (1998). Excited states and trapping in reaction center complexes of the green sulfur bacterium *Prosthecochloris aestuarii*. *Biochemistry* 37, 10792–10797. doi: 10.1021/bi9806899

Neerken, S., Schmidt, K. A., Aartsma, T. J., and Amesz, J. (1999). Dynamics of energy conversion in reaction center core complexes of the green sulfur bacterium *Prosthecochloris aestuarii* at low temperature. *Biochemistry* 38, 13216–13222. doi: 10.1021/bi9910981

Neese, F., Wennmohs, F., Hansen, A., and Becker, U. (2009). Efficient, approximate and parallel Hartree–Fock and hybrid DFT calculations. A 'chain-of-spheres' algorithm for the Hartree–Fock exchange. *Chem. Phys.* 356, 98–109. doi: 10.1016/j.chemphys.2008.10.036

Niedringhaus, A., Policht, V. R., Sechrist, R., Konar, A., Laible, P. D., Bocian, D. F., et al. (2018). Primary processes in the bacterial reaction center probed by two-dimensional electronic spectroscopy. *Proc. Natl. Acad. Sci. USA* 115, 3563–3568. doi: 10.1073/pnas.1721927115

Noguchi, T., Fukami, Y., Oh-oka, H., and Inoue, Y. (1997). Fourier transform infrared study on the primary donor P_{798} of *Heliobacterium modesticaldum*: cysteine S-H coupled to P_{798} and molecular interactions of carbonyl groups. *Biochemistry* 36, 12329–12336. doi: 10.1021/bi970853c

Norris, J. R., Uphaus, R. A., Crespi, H. L., and Katz, J. J. (1971). Electron spin resonance of chlorophyll and the origin of signal I in photosynthesis. *Proc. Natl. Acad. Sci. USA* 68, 625–628. doi: 10.1073/pnas.68.3.625

Novoderezhkin, V. I., Dekker, J. P., and van Grondelle, R. (2007). Mixing of exciton and charge-transfer states in photosystem II reaction centers: modeling of Stark Spectra with modified Redfield theory. *Biophys. J.* 93, 1293–1311. doi: 10.1529/biophysj.106.096867

Nuijs, A. M., Dorssen, R. J. V., Duysens, L. N. M., and Amesz, J. (1985a). Excited states and primary photochemical reactions in the photosynthetic bacterium *Heliobacterium chlorum*. *Proc. Natl. Acad. Sci. USA* 82, 6865–6868. doi: 10.1073/pnas.82.20.6865

Nuijs, A. M., Vasmel, H., Joppe, H. L. P., Duysens, L. N. M., and Amesz, J. (1985b). Excited states and primary charge separation in the pigment system of the green photosynthetic bacterium *Prosthecochloris aestuarii* as studied by picosecond absorbance difference spectroscopy. *Biochim. Biophys. Acta Bioenerg.* 807, 24–34.

Oh-oka, H., Kamei, S., Matsubara, H., Lin, S., van Noort, P. I., and Blankenship, R. E. (1998). Transient sbsorption spectroscopy of energy-transfer and trapping processes in the reaction center complex of *Chlorobium tepidum*. *J. Phys. Chem. B* 102, 8190–8195. doi: 10.1021/jp981478g

Olson, J. M. (1998). Chlorophyll organization and function in green photosynthetic bacteria. *Photochem. Photobiol.* 67, 61–75. doi: 10.1111/j.1751-1097.1998.tb05166.x

Olson, J. M. (2004). The FMO Protein. *Photosynth. Res.* 80, 181–187. doi: 10.1023/B:PRES.0000030428.36950.43

Olson, J. M. (2013). "Green bacteria: the light-harvesting chlorosome," in *Encyclopedia of Biological Chemistry*, Second Edn, eds W. J. Lennarz and M. D. Lane (Waltham: Academic Press), 513–516.

Olson, T. L., Williams, J. C., and Allen, J. P. (2013). Influence of protein interactions on oxidation/reduction midpoint potentials of cofactors in natural and *de novo* metalloproteins. *Biochim. Biophys. Acta Bioenerg.* 1827, 914–922. doi: 10.1016/j.bbabio.2013.02.014

Oppenheimer, J. R., and Schwinger, J. (1941). On the interaction of mesotrons and nuclei. *Phys. Rev.* 60, 150–152. doi: 10.1103/PhysRev.60.150

Oren, A. (2011). "Characterization of pigments of prokaryotes and their use in taxonomy and classification," in *Methods in Microbiology*, eds F. Rainey and A. Oren (Cambridge: Academic Press), 261–282.

Orf, G. S., Gisriel, C., and Redding, K. E. (2018). Evolution of photosynthetic reaction centers: insights from the structure of the heliobacterial reaction center. *Photosynth. Res.* 138, 11–37. doi: 10.1007/s11120-018-0503-2

Papiz, M. Z., Prince, S. M., Howard, T., Cogdell, R. J., and Isaacs, N. W. (2003). The structure and thermal motion of the B800-850 LH2 complex from *Rps. acidophila* at 2.0 Å resolution and 100 K: new structural features and functionally relevant motions. *J. Mol. Biol.* 326, 1523–1538. doi: doi: 10.1016/s0022-2836(03)00024-x

Partensky, F., Hess, W. R., and Vaulot, D. (1999). *Prochlorococcus*, a marine photosynthetic prokaryote of global significance. *Microbiol. Mol. Biol. Rev.* 63, 106–127. doi: 10.1128/MMBR.63.1.106-127.1999

Pawlowicz, N. P., van Grondelle, R., van Stokkum, I. H. M., Breton, J., Jones, M. R., and Groot, M. L. (2008). Identification of the first steps in charge separation in bacterial photosynthetic reaction centers of *Rhodobacter sphaeroides* by ultrafast mid-infrared spectroscopy: electron transfer and protein dynamics. *Biophys. J.* 95, 1268–1284. doi: 10.1529/biophysj.108.130880

Pearson, R. G. (1963). Hard and soft acids and bases. *J. Am. Chem. Soc.* 85, 3533–3539. doi: 10.1021/ja00905a001

Peloquin, J. M., Williams, J. C., Lin, X., Alden, R. G., Taguchi, A. K. W., Allen, J. P., et al. (1994). Time-dependent thermodynamics during early electron transfer in reaction centers from *Rhodobacter sphaeroides*. *Biochemistry* 33, 8089–8100. doi: 10.1021/bi00192a014

Peterman, E. J. G., van Amerongen, H., van Grondelle, R., and Dekker, J. P. (1998). The nature of the excited state of the reaction center of photosystem II of green plants: a high-resolution fluorescence spectroscopy study. *Proc. Natl. Acad. Sci. USA* 95, 6128–6133. doi: 10.1073/pnas.95.11.6128

Petrenko, A., Maniero, A. L., van Tol, J., MacMillan, F., Li, Y., Brunel, L.-C., et al. (2004). A high-field EPR study of $P_{700}^{+\cdot}$ in wild-type and mutant photosystem I from *Chlamydomonas reinhardtii*. *Biochemistry* 43, 1781–1786. doi: 10.1021/bi035466j

Pierella Karlusich, J. J., and Carrillo, N. (2017). Evolution of the acceptor side of photosystem I: ferredoxin, flavodoxin, and ferredoxin-$NADP^+$ oxidoreductase. *Photosynth. Res.* 134, 235–250. doi: 10.1007/s11120-017-0338-2

Plato, M., Krauß, N., Fromme, P., and Lubitz, W. (2003). Molecular orbital study of the primary electron donor P_{700} of photosystem I based on a recent X-ray single crystal structure analysis. *Chem. Phys.* 294, 483–499. doi: 10.1016/S0301-0104(03)00378-1

Poluektov, O. G., Paschenko, S. V., Utschig, L. M., Lakshmi, K. V., and Thurnauer, M. C. (2005). Bidirectional electron transfer in photosystem I: direct evidence from high-frequency time-resolved EPR spectroscopy. *J. Am. Chem. Soc.* 127, 11910–11911. doi: 10.1021/ja053315t

Poluektov, O. G., Utschig, L. M., Schlesselman, S. L., Lakshmi, K. V., Brudvig, G. W., Kothe, G., et al. (2002). Electronic structure of the P_{700} special pair from high-frequency electron paramagnetic resonance spectroscopy. *J. Phys. Chem. B* 106, 8911–8916. doi: 10.1021/jp021465+

Prince, R. C., Gest, H., and Blankenship, R. E. (1985). Thermodynamic properties of the photochemical reaction center of *Heliobacterium chlorum*. *Biochim. Biophys. Acta Bioenerg.* 810, 377–384. doi: 10.1016/0005-2728(85)90224-5

Prince, R. C., and Olson, J. M. (1976). Some thermodynamic and kinetic properties of the primary photochemical reactants in a complex from a green photosynthetic bacterium. *Biochim. Biophys. Acta Bioenerg.* 423, 357–362. doi: 10.1016/0005-2728(76)90191-2

Prisner, T., Rohrer, M., and MacMillan, F. (2001). Pulsed EPR spectroscopy: biological applications. *Annu. Rev. Phys. Chem.* 52, 279–313. doi: 10.1146/annurev.physchem.52.1.279

Ptushenko, V. V., Cherepanov, D. A., Krishtalik, L. I., and Semenov, A. Y. (2008). Semi-continuum electrostatic calculations of redox potentials in photosystem I. *Photosynth. Res.* 97:55. doi: 10.1007/s11120-008-9309-y

Ralf, G., and Repeta, D. J. (1992). The pigments of *Prochlorococcus marinus*: the presence of divinylchlorophyll a and b in a marine procaryote. *Limnol. Oceanogr.* 37, 425–433. doi: 10.4319/lo.1992.37.2.0425

Rappaport, F., Guergova-Kuras, M., Nixon, P. J., Diner, B. A., and Lavergne, J. (2002). Kinetics and pathways of charge recombination in photosystem II. *Biochemistry* 41, 8518–8527. doi: 10.1021/bi025725p

Rasmussen, B., Fletcher, I. R., Brocks, J. J., and Kilburn, M. R. (2008). Reassessing the first appearance of eukaryotes and cyanobacteria. *Nature* 455, 1101–1104. doi: 10.1038/nature07381

Rigby, S. E. J., Nugent, J. H. A., and O'Malley, P. J. (1994a). ENDOR and special triple resonance studies of chlorophyll cation radicals in photosystem 2. *Biochemistry* 33, 10043–10050. doi: 10.1021/bi00199a031

Rigby, S. E. J., Thapar, R., Evans, M. C. W., and Heathcote, P. (1994b). The electronic structure of $P_{840}^{+\cdot}$ the primary donor of the *Chlorobium limicola* f. sp. *thiosulphatophilum* photosynthetic reaction centre. *FEBS Lett.* 350, 24–28. doi: 10.1016/0014-5793(94)00724-1

Roberts, J. A., Holten, D., and Kirmaier, C. (2001). Primary events in photosynthetic reaction centers with multiple mutations near the photoactive electron carriers. *J. Phys. Chem. B* 105, 5575–5584. doi: 10.1021/jp010280k

Robinson, H. H., and Crofts, A. R. (1983). Kinetics of the oxidation—reduction reactions of the photosystem II quinone acceptor complex, and the pathway for deactivation. *FEBS Lett.* 153, 221–226. doi: 10.1016/0014-5793(83)80152-5

Romberger, S. P., and Golbeck, J. H. (2012). The F_X iron-sulfur cluster serves as the terminal bound electron acceptor in heliobacterial reaction centers. *Photosynth. Res.* 111, 285–290. doi: 10.1007/s11120-012-9723-z

Romero, E., van Stokkum, I. H. M., Novoderezhkin, V. I., Dekker, J. P., and van Grondelle, R. (2010). Two different charge separation pathways in photosystem II. *Biochemistry* 49, 4300–4307. doi: 10.1021/bi1003926

Roszak, A. W., Howard, T. D., Southall, J., Gardiner, A. T., Law, C. J., Isaacs, N. W., et al. (2003). Crystal structure of the RC-LH1 core complex from *Rhodopseudomonas palustris*. *Science* 302, 1969–1972. doi: 10.1126/science.1088892

Saito, K., and Ishikita, H. (2011). Cationic state distribution over the P_{700} chlorophyll pair in photosystem I. *Biophys. J.* 101, 2018–2025. doi: 10.1016/j.bpj.2011.09.010

Santabarbara, S., Kuprov, I., Poluektov, O., Casal, A., Russell, C. A., Purton, S., et al. (2010). Directionality of electron-transfer reactions in photosystem I of prokaryotes: universality of the bidirectional electron-transfer model. *J. Phys. Chem. B* 114, 15158–15171. doi: 10.1021/jp1044018

Sauer, K., and Yachandra, V. K. (2004). The water-oxidation complex in photosynthesis. *Biochim. Biophys. Acta* 1655, 140–148. doi: 10.1016/j.bbabio.2003.07.004

Savikhin, S., and Jankowiak, R. (2014). "Mechanism of primary charge separation in photosynthetic reaction centers," in *The Biophysics of Photosynthesis*, eds J. H. Golbeck and A. van der Est (New York, NY: Springer), 193–240.

Savikhin, S., Xu, W., Chitnis, P. R., and Struve, W. S. (2000). Ultrafast primary processes in PS I from *Synechocystis* sp. PCC 6803: roles of P_{700} and A_0. *Biophys. J.* 79, 1573–1586. doi: 10.1016/S0006-3495(00)76408-3

Schäfer, A., Horn, H., and Ahlrichs, R. (1992). Fully optimized contracted Gaussian basis sets for atoms Li to Kr. *J. Chem. Phys.* 97, 2571–2577. doi: 10.1063/1.463096

Schatz, G. H., Brock, H., and Holzwarth, A. R. (1987). Picosecond kinetics of fluorescence and absorbance changes in photosystem II particles excited at low photon density. *Proc. Natl. Acad. Sci. USA* 84, 8414–8418. doi: 10.1073/pnas.84.23.8414

Schlau-Cohen, G. S., Dawlaty, J. M., and Fleming, G. R. (2012). Ultrafast multidimensional spectroscopy: principles and applications to photosynthetic systems. *IEEE J. Sel. Top Quantum Electron.* 18, 283–295. doi: 10.1109/JSTQE.2011.2112640

Schmidt, K. A., Neerken, S., Permentier, H. P., Hager-Braun, C., and Amesz, J. (2000). Electron transfer in reaction center core complexes from the green sulfur bacteria *Prosthecochloris aestuarii* and *Chlorobium tepidum*. *Biochemistry* 39, 7212–7220. doi: 10.1021/bi992861u

Şener, M., Strümpfer, J., Hsin, J., Chandler, D., Scheuring, S., Hunter, C. N., et al. (2011). Förster energy transfer theory as reflected in the structures of photosynthetic light-harvesting systems. *Chem. Phys. Chem.* 12, 518–531. doi: 10.1002/cphc.201000944

Seo, D., Tomioka, A., Kusumoto, N., Kamo, M., Enami, I., and Sakurai, H. (2001). Purification of ferredoxins and their reaction with purified reaction center complex from the green sulfur bacterium *Chlorobium tepidum*. *Biochim. Biophys. Acta Bioenerg.* 1503, 377–384. doi: 10.1016/s0005-2728(00)00245-0

Shelaev, I. V., Gostev, F. E., Mamedov, M. D., Sarkisov, O. M., Nadtochenko, V. A., Shuvalov, V. A., et al. (2010). Femtosecond primary charge separation in *Synechocystis* sp. PCC 6803 photosystem I. *Biochim. Biophys. Acta* 1797, 1410–1420. doi: 10.1016/j.bbabio.2010.02.026

Shkuropatov, A. Y., and Shuvalov, V. A. (1993). Electron transfer in pheophytin a-modified reaction centers from *Rhodobacter sphaeroides* (R-26). *FEBS Lett.* 322, 168–172. doi: 10.1016/0014-5793(93)81561-d

Shuvalov, V. A., Amesz, J., and Duysens, L. N. M. (1986). Picosecond spectroscopy of isolated membranes of the photosynthetic green sulfur bacterium *Prosthecochloris aestuarii* upon selective excitation of the primary electron donor. *Biochim. Biophys. Acta Bioenerg.* 851, 1–5. doi: 10.1016/0005-2728(86)90242-2

Sirohiwal, A., Neese, F., and Pantazis, D. A. (2020). Protein matrix control of reaction center excitation in photosystem II. *J. Am. Chem. Soc.* 142, 18174–18190. doi: 10.1021/jacs.0c08526

Song, Y., Sechrist, R., Nguyen, H. H., Johnson, W., Abramavicius, D., Redding, K. E., et al. (2021). Excitonic structure and charge separation in the heliobacterial reaction center probed by multispectral multidimensional spectroscopy. *Nat. Commun.* 12:2801. doi: 10.1038/s41467-021-23060-9

Srinivasan, N., and Golbeck, J. H. (2009). Protein-cofactor interactions in bioenergetic complexes: the role of the A_{1A} and A_{1B} phylloquinones in photosystem I. *Biochim. Biophys. Acta* 1787, 1057–1088. doi: 10.1016/j.bbabio.2009.04.010

Staroverov, V. N., Scuseria, G. E., Tao, J., and Perdew, J. P. (2003). Comparative assessment of a new nonempirical density functional: molecules and hydrogen-bonded complexes. *J. Chem. Phys.* 119, 12129–12137. doi: 10.1063/1.1626543

Steglich, C., Mullineaux, C. W., Teuchner, K., Hess, W. R., and Lokstein, H. (2003). Photophysical properties of *Prochlorococcus marinus* SS120 divinyl chlorophylls and phycoerythrin *in vitro* and *in vivo*. *FEBS Lett.* 553, 79–84. doi: 10.1016/s0014-5793(03)00971-2

Stowell, M. H. B., McPhillips, T. M., Rees, D. C., Soltis, S. M., Abresch, E., and Feher, G. (1997). Light-induced structural changes in photosynthetic reaction center: implications for mechanism of electron-proton transfer. *Science* 276, 812–816. doi: 10.1126/science.276.5313.812

Strain, H. H., and Svec, W. A. (1966). "Extraction, separation, estimation, and isolation of the chlorophylls," in *The Chlorophylls*, eds L. P. Vernon and G. R. Seely (Cambridge: Academic Press), 21–66.

Sugiura, M., Boussac, A., Noguchi, T., and Rappaport, F. (2008). Influence of Histidine-198 of the D_1 subunit on the properties of the primary electron donor, P_{680}, of photosystem II in *Thermosynechococcus elongatus*. *Biochim. Biophys. Acta Bioenerg.* 1777, 331–342. doi: 10.1016/j.bbabio.2008.01.007

Sun, J., Hao, S., Radle, M., Xu, W., Shelaev, I., Nadtochenko, V., et al. (2014). Evidence that histidine forms a coordination bond to the A_{0A} and A_{0B} chlorophylls and a second H-bond to the A_{1A} and A_{1B} phylloquinones in $M688H_{PsaA}$ and $M668H_{PsaB}$ variants of *Synechocystis* sp. PCC 6803. *Biochim. Biophys. Acta Bioenerg.* 1837, 1362–1375. doi: 10.1016/j.bbabio.2014.04.004

Sun, Y., Wang, H., Zhao, F., and Sun, J. (2004). The effect of axial Mg^{2+} ligation and peripheral hydrogen bonding on chlorophyll *a*. *Chem. Phys. Lett.* 387, 12–16. doi: 10.1016/j.cplett.2004.01.103

Taguchi, A. T., Mattis, A. J., O'Malley, P. J., Dikanov, S. A., and Wraight, C. A. (2013). Tuning cofactor redox potentials: the 2-methoxy dihedral angle generates a redox potential difference of >160 mV between the primary (Q_A) and secondary (Q_B) quinones of the bacterial photosynthetic reaction center. *Biochemistry* 52, 7164–7166. doi: 10.1021/bi4011896

Takahashi, R., Hasegawa, K., and Noguchi, T. (2008). Effect of charge distribution over a chlorophyll dimer on the redox potential of P_{680} in photosystem II as studied by density functional theory calculations. *Biochemistry* 47, 6289–6291. doi: 10.1021/bi8007998

Tamura, H., Saito, K., and Ishikita, H. (2020). Acquirement of water-splitting ability and alteration of the charge-separation mechanism in photosynthetic reaction centers. *Proc. Natl. Acad. Sci. USA* 117, 16373–16382. doi: 10.1073/pnas.2000895117

Tao, J., Perdew, J. P., Staroverov, V. N., and Scuseria, G. E. (2003). Climbing the density functional ladder: nonempirical meta–generalized gradient approximation designed for molecules and solids. *Phys. Rev. Lett.* 91:146401. doi: 10.1103/PhysRevLett.91.146401

Tice, M. M., and Lowe, D. R. (2004). Photosynthetic microbial mats in the 3,416-Myr-old ocean. *Nature* 431, 549–552. doi: 10.1038/nature02888

Tomi, T., Shibata, Y., Ikeda, Y., Taniguchi, S., Haik, C., Mataga, N., et al. (2007). Energy and electron transfer in the photosynthetic reaction center complex of *Acidiphilium rubrum* containing Zn-bacteriochlorophyll *a* studied by femtosecond up-conversion spectroscopy. *Biochim. Biophys. Acta* 1767, 22–30. doi: 10.1016/j.bbabio.2006.10.008

Tomo, T., Okubo, T., Akimoto, S., Yokono, M., Miyashita, H., Tsuchiya, T., et al. (2007). Identification of the special pair of photosystem II in a chlorophyll *d*-dominated cyanobacterium. *Proc. Natl. Acad. Sci. USA* 104, 7283–7288. doi: 10.1073/pnas.0701847104

Umena, Y., Kawakami, K., Shen, J. R., and Kamiya, N. (2011). Crystal structure of oxygen-evolving photosystem II at a resolution of 1.9 A. *Nature* 473, 55–60. doi: 10.1038/nature09913

van Amerongen, H., and Croce, R. (2013). Light harvesting in photosystem II. *Photosynth. Res.* 116, 251–263. doi: 10.1007/s11120-013-9824-3

Van Brederode, M. E., Jones, M. R., Van Mourik, F., Van Stokkum, I. H. M., and Van Grondelle, R. (1997). A new pathway for transmembrane electron transfer in photosynthetic reaction centers of *Rhodobacter sphaeroides* not involving the excited special pair. *Biochemistry* 36, 6855–6861. doi: 10.1021/bi9703756

van Brederode, M. E., Ridge, J. P., van Stokkum, I. H. M., van Mourik, F., Jones, M. R., and van Grondelle, R. (1998). On the efficiency of energy transfer and the different pathways of electron transfer in mutant reaction centers of *Rhodobacter sphaeroides*. *Photosynth. Res.* 55, 141–146. doi: 10.1023/A:1005925917867

van Brederode, M. E., and van Grondelle, R. (1999). New and unexpected routes for ultrafast electron transfer in photosynthetic reaction centers. *FEBS Lett.* 455, 1–7. doi: 10.1016/s0014-5793(99)00810-8

van Brederode, M. E., van Mourik, F., van Stokkum, I. H. M., Jones, M. R., and van Grondelle, R. (1999). Multiple pathways for ultrafast transduction of light energy in the photosynthetic reaction center of *Rhodobacter sphaeroides*. *Proc. Natl. Acad. Sci. USA* 96, 2054–2059. doi: 10.1073/pnas.96.5.2054

van der Est, A., Chirico, S., Karyagina, I., Cohen, R., Shen, G., and Golbeck, J. H. (2009). Alteration of the axial Met ligand to electron acceptor A_0 in photosystem I: an investigation of electron transfer at different temperatures by multifrequency time-resolved and CW EPR. *Appl. Magn. Reson.* 37:103. doi: 10.1007/s00723-009-0043-1

van Gorkom, H. J., Tamminga, J. J., and Haveman, J. (1974). Primary reactions, plastoquinone and fluorescence yield in subchloroplast fragments prepared with deoxycholate. *Biochim. Biophys. Acta* 347, 417–438. doi: 10.1016/0005-2728(74)90080-2

van Stokkum, I. H. M., Beekman, L. M. P., Jones, M. R., van Brederode, M. E., and van Grondelle, R. (1997). Primary electron transfer kinetics in membrane-bound *Rhodobacter sphaeroides* reaction centers: A global and target analysis. *Biochemistry* 36, 11360–11368. doi: 10.1021/bi9707943

Vermaas, J. V., Taguchi, A. T., Dikanov, S. A., Wraight, C. A., and Tajkhorshid, E. (2015). Redox potential tuning through differential quinone binding in the photosynthetic reaction center of *Rhodobacter sphaeroides*. *Biochemistry* 54, 2104–2116. doi: 10.1021/acs.biochem.5b00033

Vinyard, D. J., Ananyev, G. M., and Dismukes, C. (2013). Photosystem II: the reaction center of oxygenic photosynthesis. *Annu. Rev. Biochem.* 82, 577–606. doi: 10.1146/annurev-biochem-070511-100425

Vos, M. H., Breton, J., and Martin, J.-L. (1997). Electronic energy transfer within the hexamer cofactor system of bacterial reaction centers. *J. Phys. Chem. B* 101, 9820–9832. doi: 10.1021/jp971486h

Wachtveitl, J., Farchaus, J. W., Das, R., Lutz, M., Robert, B., and Mattioli, T. A. (1993a). Structure, spectroscopic, and redox properties of *Rhodobacter sphaeroides* reaction centers bearing point mutations near the primary electron donor. *Biochemistry* 32, 12875–12886. doi: 10.1021/bi00210a041

Wachtveitl, J., Farchaus, J. W., Mathis, P., and Oesterhelt, D. (1993b). Tyrosine 162 of the photosynthetic reaction center L-subunit plays a critical role in the cytochrome c2 mediated rereduction of the photooxidized bacteriochlorophyll dimer in *Rhodobacter sphaeroides*. 2. Quantitative kinetic analysis. *Biochemistry* 32, 10894–10904. doi: 10.1021/bi00091a045

Wakeham, M. C., and Jones, M. R. (2005). Rewiring photosynthesis: engineering wrong-way electron transfer in the purple bacterial reaction centre. *Biochem. Soc. Trans.* 33, 851–857. doi: 10.1042/BST0330851

Wasielewski, M. R., Fenton, J. M., and Govindjee. (1987). The rate of formation of P_{700}^{+}–A_0^{-} in photosystem I particles from spinach as measured by picosecond transient absorption spectroscopy. *Photosynth. Res.* 12, 181–189. doi: 10.1007/BF00047947

Wasielewski, M. R., and Tiede, D. M. (1986). Sub-picosecond measurements of primary electron transfer in *Rhodopseudomonas viridis* reaction centers using near-infrared excitation. *FEBS Lett.* 204, 368–372. doi: 10.1016/0014-5793(86)80845-6

Webber, A. N., and Lubitz, W. (2001). P_{700}: the primary electron donor of photosystem I. *Biochim. Biophys. Acta Bioenerg.* 1507, 61–79. doi: 10.1016/s0005-2728(01)00198-0

Webber, A. N., Su, H., Bingham, S. E., Käβ, H., Krabben, L., Kuhn, M., et al. (1996). Site-directed mutations affecting the spectroscopic characteristics and midpoint potential of the primary donor in photosystem I. *Biochemistry* 35, 12857–12863. doi: 10.1021/bi961198w

Weigend, F. (2006). Accurate Coulomb-fitting basis sets for H to Rn. *Phys. Chem. Chem. Phys.* 8, 1057–1065. doi: 10.1039/b515623h

Weigend, F., and Ahlrichs, R. (2005). Balanced basis sets of split valence, triple zeta valence and quadruple zeta valence quality for H to Rn: design and assessment of accuracy. *Phys. Chem. Chem. Phys.* 7, 3297–3305. doi: 10.1039/b508541a

White, N. T. H., Beddard, G. S., Thorne, J. R. G., Feehan, T. M., Keyes, T. E., and Heathcote, P. (1996). Primary charge separation and energy transfer in the photosystem I reaction center of higher plants. *J. Phys. Chem.* 100, 12086–12099. doi: 10.1021/jp9604709

Widdel, F., Schnell, S., Heising, S., Ehrenreich, A., Assmus, B., and Schink, B. (1993). Ferrous iron oxidation by anoxygenic phototrophic bacteria. *Nature* 362, 834–836. doi: 10.1038/362834a0

Williams, J. C., Alden, R. G., Murchison, H. A., Peloquin, J. M., Woodbury, N. W., and Allen, J. P. (1992). Effects of mutations near the bacteriochlorophylls in reaction centers from *Rhodobacter sphaeroides*. *Biochemistry* 31, 11029–11037. doi: 10.1021/bi00160a012

Williams, J. C., and Allen, J. P. (2009). "Directed modification of reaction centers from purple bacteria," in *The Purple Phototrophic Bacteria*, eds C. N. Hunter, F. Daldal, M. C. Thurnauer, and J. T. Beatty (Netherlands: Springer), 337–353.

Williams, J. C., Haffa, A. L. M., McCulley, J. L., Woodbury, N. W., and Allen, J. P. (2001). Electrostatic interactions between charged amino acid residues and the bacteriochlorophyll dimer in reaction centers from *Rhodobacter sphaeroides*. *Biochemistry* 40, 15403–15407. doi: 10.1021/bi011574z

Wraight, C. (2004). Proton and electron transfer in the acceptor quinone complex of photosynthetic reaction centers from *Rhodobacter sphaeroides*. *Front. Biosci.* 9, 309–337. doi: 10.2741/1236

Wraight, C. A. (1979). Electron acceptors of bacterial photosynthetic reaction centers II. H^{+} binding coupled to secondary electron transfer in the quinone acceptor complex. *Biochim. Biophys. Acta Bioenerg.* 548, 309–327. doi: 10.1016/0005-2728(79)90138-5

Xu, H., Zhang, R.-B., Ma, S.-H., Qu, Z.-W., Zhang, X.-K., and Zhang, Q.-Y. (2002). Theoretical studies on the mechanism of primary electron transfer in the photosynthetic reaction center of *Rhodobacter sphaeroides*. *Photosynth. Res.* 74, 11–36. doi: 10.1023/A:1020811911956

Zucchelli, G., Brogioli, D., Casazza, A. P., Garlaschi, F. M., and Jennings, R. C. (2007). Chlorophyll ring deformation modulates Q_Y electronic energy in chlorophyll-protein complexes and generates spectral sorms. *Biophys. J.* 93, 2240–2254. doi: 10.1529/biophysj.107.104554

Conflict of Interest: The authors declare that the research was conducted in the absence of any commercial or financial relationships that could be construed as a potential conflict of interest.

Publisher's Note: All claims expressed in this article are solely those of the authors and do not necessarily represent those of their affiliated organizations, or those of the publisher, the editors and the reviewers. Any product that may be evaluated in this article, or claim that may be made by its manufacturer, is not guaranteed or endorsed by the publisher.

Advantages of publishing in Frontiers

OPEN ACCESS
Articles are free to read for greatest visibility and readership

FAST PUBLICATION
Around 90 days from submission to decision

HIGH QUALITY PEER-REVIEW
Rigorous, collaborative, and constructive peer-review

TRANSPARENT PEER-REVIEW
Editors and reviewers acknowledged by name on published articles

Frontiers
Avenue du Tribunal-Fédéral 34
1005 Lausanne | Switzerland

Visit us: www.frontiersin.org
Contact us: frontiersin.org/about/contact

REPRODUCIBILITY OF RESEARCH
Support open data and methods to enhance research reproducibility

DIGITAL PUBLISHING
Articles designed for optimal readership across devices

FOLLOW US
@frontiersin

IMPACT METRICS
Advanced article metrics track visibility across digital media

EXTENSIVE PROMOTION
Marketing and promotion of impactful research

LOOP RESEARCH NETWORK
Our network increases your article's readership